The Hilbert-Hankel Transform and its Application to Shallow Water Ocean Acoustics

RLE Technical Report No. 513

January 1986

Michael S. Wengrovitz

Research Laboratory of Electronics
Massachusetts Institute of Technology
Cambridge, MA 02139 USA

Massachusetts Institute of Technology
Department of Electrical Engineering and Computer Science
Research Laboratory of Electronics
Room 36-615
Cambridge, MA   02139

The Hilbert-Hankel Transform and its Application

to Shallow Water Ocean Acoustics

Michael S. Wengrovitz

Technical Report No. 513

January 1986

SECURITY CLASSIFICATION OF THIS PAGE

REPORT DOCUMENTATION PAGE

1. REPORT SECURITY CLASSIFICATION	1b. RESTRICTIVE MARKINGS
2a. SECURITY CLASSIFICATION AUTHORITY	3. DISTRIBUTION/AVAILABILITY OF REPORT
2b. DECLASSIFICATION/DOWNGRADING SCHEDULE	Approved for public release; distribution unlimited

4. PERFORMING ORGANIZATION REPORT NUMBER(S)	5. MONITORING ORGANIZATION REPORT NUMBER(S)

6a. NAME OF PERFORMING ORGANIZATION	6b. OFFICE SYMBOL (If applicable)	7a. NAME OF MONITORING ORGANIZATION
Research Laboratory of Electronics Massachusetts Institute of Technology		Office of Naval Research Mathematical and Information Scien. Div.

6c. ADDRESS (City, State and ZIP Code)	7b. ADDRESS (City, State and ZIP Code)
77 Massachusetts Avenue Cambridge, MA 02139	800 North Quincy Street Arlington, Virginia 22217

8a. NAME OF FUNDING/SPONSORING ORGANIZATION	8b. OFFICE SYMBOL (If applicable)	9. PROCUREMENT INSTRUMENT IDENTIFICATION NUMBER
Advanced Research Projects Agency		N00014-81-K-0742

8c. ADDRESS (City, State and ZIP Code)	10. SOURCE OF FUNDING NOS.			
1400 Wilson Boulevard Arlington, Virginia 22217	PROGRAM ELEMENT NO.	PROJECT NO.	TASK NO.	WORK UNIT NO.
			NR 049-506	

11. TITLE (Include Security Classification) The Hilbert-Hankel Transform and its Application to...

12. PERSONAL AUTHOR(S) Michael S. Wengrovitz

13a. TYPE OF REPORT	13b. TIME COVERED	14. DATE OF REPORT (Yr., Mo., Day)	15. PAGE COUNT
Technical	FROM _____ TO _____	January 1986	482

16. SUPPLEMENTARY NOTATION

17. COSATI CODES			18. SUBJECT TERMS (Continue on reverse if necessary and identify by block number)
FIELD	GROUP	SUB. GR.	

19. ABSTRACT (Continue on reverse if necessary and identify by block number)

In the shallow water acoustics problem, a time-harmonic source is placed in the ocean and a hydrophone records the acoustic pressure field as a function of range from the source. In this thesis, new techniques related to the synthetic generation, acquisition, and inversion of this data are developed.

A hybrid method for accurate shallow water synthetic data generation is presented. The method is based on computing the continuum portion of the field using the Hankel transform and computing the trapped portion analytically. In the related problem of extracting the reflection coefficient, it is shown that the inversion can be highly sensitive to errors in the Green's function estimate. This sensitivity can be eliminated by positioning the source and receiver above the invariant critical depth (cont.)

20. DISTRIBUTION/AVAILABILITY OF ABSTRACT	21. ABSTRACT SECURITY CLASSIFICATION
UNCLASSIFIED/UNLIMITED ☒ SAME AS RPT. ☐ DTIC USERS ☐	Unclassified

22a. NAME OF RESPONSIBLE INDIVIDUAL	22b. TELEPHONE NUMBER (Include Area Code)	22c. OFFICE SYMBOL
Kyra M. Hall RLE Contract Reports	(617) 253-2569	

19. Abstract continued

of the waveguide.

The theory of a new transform, referred to as the Hilbert-Hankel transform, is developed. Its consistency with the Hankel transform leads to an approximate real-part/imaginary-part sufficiency condition for acoustic fields. An efficient reconstruction method for obtaining the complex-valued acoustic field from a single quadrature component is developed and applied to synthetic and experimental data. The Hilbert-Hankel transform is a unilateral version of the Hankel transform and its application to this problem is based on the outgoing nature of the acoustic field. The theory of this transform and its one-dimensional counterpart can be applied to a wide class of problems.

The Hilbert-Hankel Transform
and its Application to
Shallow Water Ocean Acoustics

by

Michael S. Wengrovitz

Abstract

In the shallow water acoustics problem, a time-harmonic source is placed in the ocean and a hydrophone records the acoustic pressure field as a function of range from the source. In this thesis, new techniques related to the synthetic generation, acquisition, and inversion of this data are developed.

A hybrid method for accurate shallow water synthetic data generation is presented. The method is based on computing the continuum portion of the field using the Hankel transform and computing the trapped portion analytically. In the related problem of extracting the reflection coefficient, it is shown that the inversion can be highly sensitive to errors in the Green's function estimate. This sensitivity can be eliminated by positioning the source and receiver above the invariant critical depth of the waveguide.

The theory of a new transform, referred to as the Hilbert-Hankel transform, is developed. Its consistency with the Hankel transform leads to an approximate real-part/imaginary-part sufficiency condition for acoustic fields. An efficient reconstruction method for obtaining the complex-valued acoustic field from a single quadrature component is developed and applied to synthetic and experimental data. The Hilbert-Hankel transform is a unilateral version of the Hankel transform and its application to this problem is based on the outgoing nature of the acoustic field. The theory of this transform and its one-dimensional counterpart can be applied to a wide class of problems.

Thesis Supervisors:
Alan V. Oppenheim, Professor of Electrical Engineering,
    Massachusetts Institute of Technology.
George V. Frisk, Associate Scientist,
    Woods Hole Oceanographic Institution.

Acknowledgements

2

To Debbie and Steven

Contents

6 Reconstruction of a Complex-Valued Acoustic Field From its Real or Imaginary Part   368

7 Summary   470

Chapter 1

Introduction

1.1 Background

This thesis is concerned with the signal processing of sound pressure fields in shallow water oceanic waveguides. We have studied a simplified version of the general problem, and have assumed that the pressure field is due to a time-harmonic point source located within the waveguide. The waveguide and the underlying ocean bottom are assumed to be horizontally stratified fluid media. The three main components of the problem to be addressed in this thesis are: 1) determination of the acoustic field given the specifications of the geoacoustic model, 2) determination of certain geoacoustic model parameters given measurements of the acoustic field, and 3) development of related digital signal processing theory and algorithms.

The theory of propagation in horizontally stratified fluid media has been studied by numerous researchers for some time [1][2][3][4][5]. Given the specific geoacoustic properties of the various layers, it is possible to develop mathematical expressions for the acoustic field as a function of spatial position. However, the inverse problem of determining geoacoustic model parameters from acoustic pressure field measurements

is of more recent interest and remains an active research area. Our motivation has been to develop signal processing theory and algorithms in order to partially solve this problem.

Our interest in the topic of signal processing of shallow water acoustic fields stems from recent work done by others in the two related areas of deep water ocean acoustics [6], and borehole acoustics[7]. In their research, a similar problem of extracting geoacoustic information from measurements of an acoustic field was addressed. Although there are some similarities between these two problems and the shallow water problem, there are also some essential differences, as will now be discussed.

In deep water, the sound transmitted by a point source located within the ocean arrives at a receiver hydrophone, also located within the ocean, via a direct path and a single reflected path. The portion of the field which reflects off the surface of a deep ocean can be gated out in time. The portion of the acoustic field which reflects off the ocean bottom contains information related to the properties of the bottom. In principle, if the reflected field can be separated from the direct field, it is possible to infer information about the ocean bottom. The information, which may be summarized in terms of a reflection coefficient, is obtained by applying signal processing techniques to the acoustic field measurements, collected as a function of range.

In a borehole, the sound transmitted by a source located within the borehole arrives at a single receiving hydrophone, or at an array of hydrophones, also located within the borehole. In this environment, the sound follows a complicated path due to the multiple reflections which occur at the borehole boundaries. The non-direct portion of the received field contains information related to the properties of the media surrounding the borehole. In principle, if the direct and non-direct portions of the field can be separated, it is possible to infer information about the surrounding media. The information, which may be summarized in terms of a reflection coefficient,

7

is obtained by applying signal processing techniques, which include dereverberation, to the acoustic field measurements, collected as a function of depth.

In shallow water, the sound transmitted by a point source located within the ocean arrives at a receiver hydrophone, also located in the ocean, via a direct path and a complicated path comprised of multiple reflections off the ocean surface and bottom. Although the reverberation within the shallow water waveguide is more closely related to the borehole problem, the shallow water measurement geometry is more closely related to the deep water problem. In principle, it is also possible to infer information about the ocean bottom, which may be summarized in terms of the reflection coefficient by applying signal processing techniques which include dereverberation to the acoustic field measurements, collected as a function of range. Thus, the shallow water problem contains certain features of both the deep water and the acoustic borehole problems.

However, there are also essential differences which imply that the shallow water problem is not just a simple extension or trivial combination of these problems. For example, although there are multiple reflections in both the borehole waveguide and the shallow water waveguide, the reflection mechanisms differ. By this, we mean that only *one* type of reflection can occur in the borehole waveguide, due to the impedance contrast at the edge of the borehole, while *two* types of reflection can occur in the shallow water waveguide, due to the impedance contrast at both the surface and bottom of the ocean. The difference implies that while there are only two basic components of the field in a borehole waveguide (radially incoming and radially outgoing), there are four basic components in the shallow water waveguide (vertically upgoing and downgoing at the source, and vertically upgoing and downgoing at the receiver). The manner in which these components can constructively and destructively interfere has important impact on the character of the field in these two problems. Additionally, while the geometric difference between oceanic waveguide and the borehole waveguide may seem trivial, in that the oceanic waveguide is the borehole waveguide turned on

8

its side, there are important differences in symmetry which occur. For example, cylindrical stratification in the borehole problem implies that measurements collected in depth can be related to a one-dimensional vertical wavenumber decomposition, expressed in terms of a one-dimensional Fourier transform. Horizontal stratification in the shallow water problem implies that measurements collected in range are related to a one-dimensional horizontal wavenumber decomposition, expressed in terms of a one-dimensional Hankel transform. The difference in the fundamental transform which relates the measurement and wavenumber decomposition in these two problems is indicative of the different signal processing techniques which must apply.

In fact, the shallow water problem is much more closely related to the deep water problem than to the borehole problem, due to the fact that a Hankel transform is involved. In the case of horizontal stratification, both deep and shallow water acoustic fields can be expressed in terms of the Hankel transform of a Green's function. The Green's function for the shallow water problem incorporates the reverberation effects due to the presence of the ocean surface. In this sense, the deep water problem, in which there is no surface present, can be considered as a special case of the more general shallow water problem. A number of results in this thesis, developed in the context of the shallow water problem, can be applied to the deep water problem as well.

A portion of this thesis will focus on the development of the theoretical properties of the Green's function. One of these properties will be exploited in a new method for synthetic data generation. A second property can be used to determine a geoacoustic property directly from the Green's function without first determining the reflection coefficient. A third property relates to a fundamental sensitivity problem which occurs in extracting the reflection coefficient in a reverberant environment. Additionally, certain theoretical aspects of the Hankel transform have led to us to consider a related transform, referred to as the Hilbert-Hankel transform. A major component of this thesis consists of the application of this transform to the shallow water problem.

In addition to having a theoretical component, this thesis contains an experimental component as well. A number of signal processing algorithms, based on the theoretical properties of the Green's function and Hilbert-Hankel transform, are applied to experimentally collected data. This acoustic data was obtained in several ocean experiments conducted by the Woods Hole Oceanographic Institution[8]. The typical configuration for obtaining the experimental data used in this thesis is shown in Figure 1.1. The ocean experiment consists of towing a harmonic source at fixed depth away from one or more moored hydrophone receivers, over an aperture which extends from zero range to several kilometers. The receivers quadrature demodulate the harmonic pressure signal and digitally record the real and imaginary components of the spatial part of the acoustic field. Typically, the field is sampled at a spatial rate of at least two samples per acoustic wavelength. Explaining certain features of this experimental data also provided the motivation for developing several new signal processing methods discussed in this thesis.

Radar Ranging System

PRESSURE
RELEASE
SURFACE

SURFACE BUOY

13.9 m

SOURCE
$Z_0 = 6.1$ m
$f_1 = 140$ Hz
$f_2 = 220$ Hz

Synthetic Aperture

RECEIVER 2
$Z_2 = 7.1$ m

$C = 1500$ m/s
$\rho = 1.0$ g/cm^3

RECEIVER 1
$Z_1 = 12.5$ m

Anchor

HORIZONTALLY STRATIFIED BOTTOM
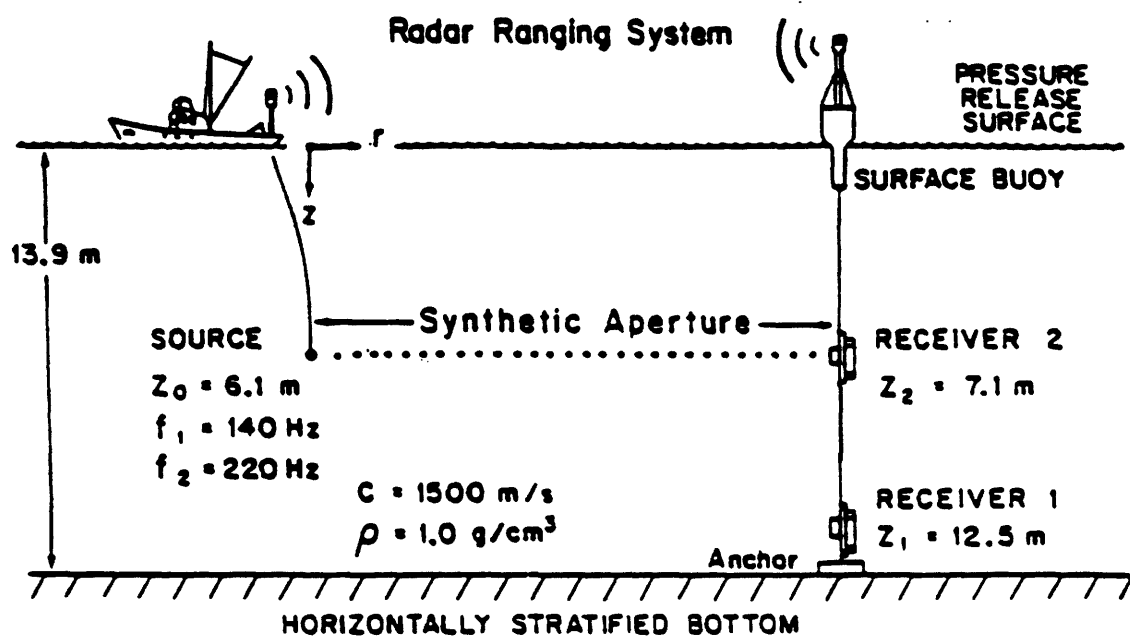
Figure 1.1: Ocean Experiment Configuration

1.2 Outline

The thesis begins in Chapter 2 with a review of the theory of propagation of an acoustic pressure field within a shallow water waveguide. The relationships between the Green's function, the Hankel transform, and the acoustic field are developed. In order to study these relationships further, a simple waveguide model, referred to as a Pekeris waveguide, consisting of an isovelocity water column overlying an isovelocity halfspace is next considered. The model provides the framework for relating poles, branch-cuts, and the behavior of the Green's function on differing Riemann sheets. Several existing viewpoints are unified in the discussion and a numerical example involving a Pekeris Green's function and its associated Riemann sheets is provided. The theory of a more general waveguide, consisting of a non-isovelocity waveguide overlying a horizontally stratified ocean bottom, is next considered. A new technique of Green's function migration, which will form the basis for numerical examples throughout the thesis, is developed. A number of important properties of the reflection coefficient and Green's function are derived.

The basic transform which relates the shallow water acoustic field to the Green's function is the Hankel transform. In our work, we have developed a new transform which also applies to this problem. The transform, referred to as the Hilbert-Hankel transform, is a unilateral version of the Hankel transform. In Chapter 3, the theory of unilateral transforms in both one and two dimensions is developed. To do this, we first focus on the simpler one-dimensional theory. The theory of analytic signals and the Hilbert transform is first reviewed. The analytic signal, can be directly related to a unilateral inverse Fourier transform, since the Fourier transform of an analytic signal is one-sided or causal. However, the theory is extended in this chapter to develop the concept of a signal which is approximately analytic. In particular, we will focus on the complex-valued even signal, which is the one-dimensional counterpart of the two-dimensional complex-valued circularly symmetric signal. The

condition of causality does not apply since the Fourier transform of an even signal must also be even. However, we will show that under some conditions there exists a relationship between an even signal and its unilateral inverse Fourier transform. A number of statements regarding an approximate real-part/imaginary-part sufficiency condition, the unilateral inverse Fourier transform, and the unilateral Fourier transform are made, and a numerical example is provided. The theory is then extended to the two-dimensional circularly symmetric signal. A number of statements regarding an approximate real-part/imaginary-part sufficiency condition, the Hilbert-Hankel transform, and the complex Hankel transform are made. The connection between the Hilbert-Hankel transform and an outgoing acoustic field is discussed. An asymptotic version of the Hilbert-Hankel transform is next considered and its relationship to both one and two-dimensional unilateral transforms is developed. Several important properties of this transform are derived and signal processing applications to acoustic fields are discussed.

To demonstrate the application of the Hilbert-Hankel transform and to study aspects of the shallow water inversion problem, we developed a new synthetic data generation technique for shallow water acoustic fields. This technique is discussed in detail in Chapter 4. In the first portion of the chapter, a review of existing methods for synthetic data generation is given. Next, the theory of the new method, based on decomposing the Green's function into the sum of a trapped portion plus a continuum portion, is presented. Although the decomposition is theoretically straightforward, some important details related to the numerical implementation are discussed. Several extensions of the method are then developed. These include an alternate method for determining poles and residues and a method for computing the continuum portion of the shallow water field. Numerical examples which illustrate the basic method and the extensions are provided. Finally, the new technique is compared and contrasted with several existing methods, and we point out that the method can also be applied to deep water synthetic field generation.

In Chapter 5, two aspects of the shallow water inversion problem are addressed. In the first portion of the chapter, we define the quantity of residual phase for a shallow water acoustic field. The acoustic field residual phase is a complementary quantity to the acoustic field magnitude and can be used in the context of forward modelling. Although it has been previously thought that a major advantage of determining the Green's function is that both magnitude and phase information is available, we show that useful magnitude and phase information is available in the pressure field domain as well. We point out that features such as modal cycle distance can be determined not only from the field magnitude but also from the residual phase. Other applications of the residual phase are considered. These include determining the acoustic source phase, which is an essential step required in the extraction of the ocean bottom reflection coefficient, and determining range-dependent waveguide features. The residual phase curves for several experimental fields are presented and discussed. In the second portion of the chapter, the problem of extracting the reflection coefficient from shallow water measurements is considered in detail. We show that there is a fundamental limitation in performing this inversion for certain configurations of the acoustic experiment. The relationship between points of infinite sensitivity in the inversion and invariant zeros of the Green's function is discussed, and the invariant critical depth for a waveguide is defined. In the last portion of this chapter, synthetic data is inverted in order to demonstrate that points of infinite sensitivity do not exist if the source and receiver do not exceed the invariant critical depth.

In Chapter 6, the reconstruction of a complex-valued acoustic field from its real or imaginary part is discussed. The approximate real-part/imaginary-part sufficiency condition is a consequence of consistency between the Hilbert-Hankel transform and the Hankel transform, and is based on theoretical properties presented in Chapter 3. A reconstruction algorithm in which the real (or imaginary) component of an acoustic field is obtained from the imaginary (or real) component is discussed. The algorithm is applied to both deep and shallow water synthetic data, produced by the hybrid method. The reconstruction quality is assessed in terms of acoustic field magnitude

and residual phase. We demonstrate that a reasonable approximation to the ocean bottom reflection coefficient can be obtained by collecting complex samples in range at a rate of one complex sample per acoustic wavelength. The reconstruction method is applied to several experimentally collected shallow water acoustic fields, and it is shown that samples of one quadrature channel can be successfully recovered from samples of the alternate channel.

Bibliography

[1] L.M. Brekhovskikh. *Waves in Layered Media.* Academic Press, New York, 1960.

[2] K. Aki and P.G. Richards. *Quantitative Seismology Theory and Methods.* W.H. Freeman and Co., San Francisco, 1980.

[3] James R. Wait. *Electromagnetic Waves in Stratified Media.* Macmillan Co, New York, 1962.

[4] L.B. Felsen and N. Marcuvitz. *Radiation and Scattering of Waves.* Prentice-Hall, Englewood Cliffs, NJ, 1973.

[5] I. Tolstoy and C.S. Clay. *Ocean Acoustics.* McGraw-Hill, New York, 1966.

[6] D.R. Mook. *The Numerical Synthesis and Inversion of Acoustic Fields Using the Hankel Transform with Application to the Estimation of the Plane Wave Reflection Coefficient of the Ocean Bottom.* Technical Report, Sc.D. Thesis, MIT/WHOI Joint Program, Cambridge Ma., Jan. 1983.

[7] Andrew L. Kurkjian. *The Estimation of the Cylindrical Wave Reflection Coefficient.* Technical Report, Ph.D. Thesis, Massachusetts Institute of Technology, Cambridge, Ma., July 1982.

[8] George V. Frisk, James F. Lynch, and James A. Doutt. The determination of geoacoustic models in shallow water. Presented at Symposium on Ocean Seismo-Acoustics, La Spezia, Italy, June 10-14 1985.

Chapter 2

Propagation of an Acoustic Pressure Field in a Waveguide

2.1 Introduction

In this chapter, we address a number of theoretical issues related to the propagation of an acoustic pressure field due to a point harmonic source in a waveguide. Much of the theory is presented as background for the remaining chapters in this thesis and has been addressed by numerous researchers in underwater acoustics, and in related disciplines [1][2][3][4]. However, in reviewing this background material, we present several new perspectives on the problem which will lead to the development of some important properties of the field and its associated Green's function. We will exploit a number of these properties in the signal processing methods and theory discussed in later chapters of this thesis.

In Section 2.2, we discuss the representation of the acoustic field in terms of the Hankel transform of a function. A more formal approach which demonstrates that this function is a Green's function will be pursued initially. Next, we follow a more

intuitive approach based on expressing the field in terms of an infinite number of reflections which can occur at the surface and bottom of the waveguide. In Section 2.3, we will consider the field for a simple geoacoustic model, consisting of an isovelocity waveguide overlying an isovelocity halfspace, in more detail. The relationships between modes, virtual modes, branch-cuts and Riemann sheets will be discussed. These relationships will form the important components of a new synthetic data generation method, which will be discussed in detail in Chapter 4. In Section 2.4, the more general waveguide, consisting of an isovelocity water column overlying a horizontally stratified fluid bottom, is considered. The results will be extended to the non-isovelocity waveguide. In developing expressions for the Green's function and field, we will review an existing method for migrating the reflection coefficient, and present a new method for migrating the Green's function. These migration methods also provide the means for identifying some important properties regarding the symmetry of the reflection coefficient and Green's function. These properties will be derived in this chapter and will be referred to in later chapters of this thesis. Finally, in Section 2.5, a summary of the important points in this chapter will be presented.

2.2 Integral Representation of the Field

In this section, we discuss the integral representation of the acoustic pressure field in a waveguide. There are numerous ways to construct this representation, and in this section two separate methods are considered. The first method is based on directly solving the governing partial differential equation and is important because it emphasizes that the solution involves a Green's function [1][5]. The properties of the specific Green's function for this problem are important and will form the basis for many of the results which we will present later in this thesis. The second method to be discussed is essentially a superposition approach which consists of decomposing the source field into its constituent horizontal wavenumber components, determining how each component propagates within the waveguide, and resynthesizing the complete field from the propagated components [1]. The method is important because it provides an intuitive description of acoustic propagation in the reverberant waveguide environment. We will provide intuitive and physical explanations for many of the theoretical results presented throughout this thesis.

The assumptions involved in the problem of determining the acoustic field in an isovelocity waveguide are now reviewed. As shown in Figure 2.1, the isovelocity waveguide is assumed to be bounded above by a series of layers underlying a halfspace, and bounded below by a series of layers overlying a halfspace. The acoustic source, located within the waveguide at the point S shown in Figure 2.1, is assumed to have a harmonic time-dependence and can be expressed mathematically as $\delta(\mathbf{r} - \mathbf{r}_0)e^{-j\omega t}$. The layers are assumed to have fixed geoacoustic properties which are independent of range, and to be of fixed thickness. Although the problem is inherently three-dimensional, only two dimensions are required to describe the spatial dependence of the acoustic field, because of the horizontal stratification. The problem is *cylindrically* or *circularly* symmetric because of the fact that the field depends only on range and depth, as opposed to azimuth, range, and depth. The layers and halfspaces are
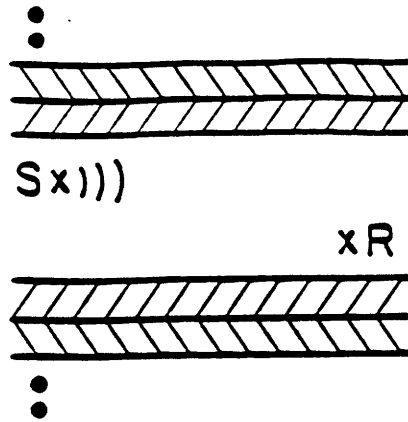
Figure 2.1: Horizontally Stratified Waveguide Model

assumed to be fluids and therefore only compressional field components can exist. The problem at hand is to describe the acoustic field within the waveguide as a function of the position of the receiver R. In a later section, we will also determine the field in the case that the source and receiver reside in different layers.

Although the exact specifications of the layers, i.e. the density, velocity, attenuation, and thickness, are important in terms of their influence on the field within the waveguide, it is possible to completely characterize their effect in terms of two quantities. One of these quantities incorporates the effect that the overlying medium has on the propagation within the waveguide, and is referred to as the *surface reflection coefficient*. The other quantity incorporates the effect that the underlying medium has on the propagation within the waveguide, and is referred to as the *bottom reflection coefficient*. Each quantity completely characterizes the influence that a stack of layers has on an impinging plane-wave. By knowing the layer properties, it is possible to determine the reflection coefficient which relates the complex amplitude of the reflected plane-wave to the complex amplitude of the incident wave. Because of the fact that the two reflection coefficients completely describe the influence of the underlying and overlying media on incident plane-waves, they will be of fundamental importance in our study.
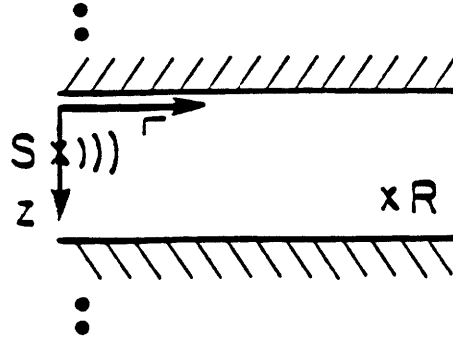
Figure 2.2: Waveguide Model and Coordinate System

We will next develop an expression for the integral representation of the acoustic pressure field $p(\mathbf{r}; \mathbf{r}_0)$ due to a point harmonic source within the waveguide, using a Green's function approach. The spatial partial differential equation which applies to the problem is

$$[\nabla^2 + k^2]p(\mathbf{r}; \mathbf{r}_0) = -4\pi\delta(\mathbf{r} - \mathbf{r}_0) \qquad (2.1)$$

where $\nabla^2 = \partial^2/\partial x^2 + \partial^2/\partial y^2 + \partial^2/\partial z^2$, and where $k = \omega/c$ is the wavenumber within the waveguide. Also in this equation, $\mathbf{r}_0 = (x_0, y_0, z_0)$ refers to the spatial position of the source and $\mathbf{r} = (x, y, z)$ refers to the spatial position of the receiver at an arbitrary point within the waveguide. Equation (2.1), referred to as the *Helmholtz equation*, is the temporal Fourier transform of the acoustic wave equation, evaluated at the harmonic frequency ω of the source. The equation describes the spatial behavior of the field, and the temporal behavior of the field is harmonic with a form identical to that of the source.

The coordinate system in which this problem is solved can be positioned so that the source is located at $\mathbf{r}_0 = (0, 0, z_0)$, with the z-axis pointing downward, as shown in Figure 2.2. Although the conditions of circular symmetry could be incorporated in the first steps of the derivation, so that $p(\mathbf{r}, \mathbf{r}_0) = p(r, z; r_0, z_0)$ where $r = (x^2 + y^2)^{1/2}$ and $r_0 = (x_0^2 + y_0^2)^{1/2}$, we refrain initially from imposing this symmetry. By doing this, it

20

is possible to pursue the development of the solution in terms of the two-dimensional Fourier transform, rather than in terms of the (one-dimensional) Hankel transform. The approach emphasizes the relationship between the the two-dimensional Fourier transform and the Hankel transform [6], [7], and we will discuss this relationship further in the next chapter of this thesis.

We proceed by expressing the acoustic field in terms of a two-dimensional inverse Fourier transform

$$p(x, y, z; z_0) = \frac{1}{(2\pi)^2} \int_{-\infty}^{\infty} \int_{-\infty}^{\infty} \tilde{g}(k_x, k_y, z; z_0) e^{j(k_x x + k_y y)} dk_x dk_y \qquad (2.2)$$

In this equation, $\tilde{g}(k_x, k_y, z; z_0)$ is the two-dimensional Fourier transform of the acoustic field and thus

$$\tilde{g}(k_x, k_y, z; z_0) = \int_{-\infty}^{\infty} \int_{-\infty}^{\infty} p(x, y, z; z_0) e^{-j(k_x x + k_y y)} dx dy \qquad (2.3)$$

Note that $\tilde{g}$ is a function of the receiver depth z, as well as the source depth z_0, since the two-dimensional Fourier transform of p involves integration only over x and y. Applying the operator $\partial^2/\partial x^2 + \partial^2/\partial y^2$ to both sides of equation (2.1), we find that

$$\mathcal{F}\{(\frac{\partial^2}{\partial x^2} + \frac{\partial^2}{\partial y^2}) p(x, y, z; z_0)\} = -(k_x^2 + k_y^2) \tilde{g}(k_x, k_y, z; z_0) \qquad (2.4)$$

where $\mathcal{F}$ represents the two-dimensional Fourier transform.

By determining the two-dimensional Fourier transform of both sides of equation (2.1), and by using equation (2.4), it follows that

$$(-k_x^2 - k_y^2 + \frac{d^2}{dz^2} + k^2) \tilde{g}(k_x, k_y, z; z_0) = -4\pi\delta(z - z_0) \qquad (2.5)$$

Note that for fixed values of k_x and k_y, $\tilde{g}(k_x, k_y, z; z_0)$ is a Green's function because of the fact that it solves a homogeneous differential equation at every value of depth z except at the single fixed depth z_0. Also note that, if this equation could be solved for $\tilde{g}(k_x, k_y, z; z_0)$, the integral representation for the acoustic field would simply be the two-dimensional inverse Fourier transform of the Green's function $\tilde{g}$.

21

We now determine the two-dimensional Fourier transform of the field under the assumption that it is circularly symmetric. Using the definitions

$$
\begin{aligned}
k_x &= k_r \cos\phi & x &= r\cos\theta \\
k_y &= k_r \sin\phi & y &= r\sin\theta \\
k_r &= (k_x^2 + k_y^2)^{1/2} & z &= (x^2 + y^2)^{1/2}
\end{aligned}
\tag{2.6}
$$

equation (2.3) can be re-written as

$$
\tilde{g}(k_r, \phi, z; z_0) = \int_0^{2\pi} \int_0^\infty p(r, \theta, z; z_0) e^{-jk_r r \cos(\theta - \phi)} r\,dr\,d\theta
\tag{2.7}
$$

Using the fact that p is circularly symmetric so that it is independent of θ, this equation becomes

$$
\tilde{g}(k_r, \phi, z; z_0) = \int_0^\infty p(r, z; z_0) [\int_0^{2\pi} e^{-jk_r r \cos(\theta - \phi)} d\theta] r\,dr
\tag{2.8}
$$

so that

$$
\tilde{g}(k_r, z; z_0) = 2\pi \int_0^\infty p(r, z; z_0) J_0(k_r r) r\,dr
\tag{2.9}
$$

where the integral definition for the zeroth-order Bessel function $J_0(k_r r)$ has been used [8]. Note that in equation (2.9), the variables ϕ and θ no longer appear. This is consistent with the fact that the two-dimensional Fourier transform of a circularly symmetric function must also be circularly symmetric [6].

We will also find it convenient to use the definition

$$
\tilde{g}(k_r, z; z_0) \equiv 2\pi g(k_r, z; z_0)
\tag{2.10}
$$

so that $g(k_r, z; z_0)$ and $p(r, z; z_0)$ are related directly via the Hankel transform as

$$
g(k_r, z; z_0) = \int_0^\infty p(r, z; z_0) J_0(k_r r) r\,dr
\tag{2.11}
$$

Using the properties of $J_0(k_r r)$, or alternately using the properties of two-dimensional Fourier transforms, it is easily shown that the Hankel transform is self-inverse, so that

$$
p(r, z; z_0) = \int_0^\infty g(k_r, z; z_0) J_0(k_r r) k_r\,dk_r
\tag{2.12}
$$

22

Next, using the definition $\bar{g} = 2\pi g$, equation (2.5) becomes

$$(\frac{d^2}{dz^2} + k^2 - k_r^2)g(k_r, z; z_0) = -2\delta(z - z_0) \qquad (2.13)$$

Before continuing further, we summarize what has been done. It has been shown that the field can be represented as the two-dimensional inverse Fourier transform of a quantity $\bar{g}(k_x, k_y, z; z_0)$ so that

$$p(x, y, z; z_0) \xleftarrow{\mathcal{F}} \bar{g}(k_x, k_y, z; z_0) \qquad (2.14)$$

The quantity $\bar{g}(k_x, k_y, z; z_0)$ represents the solution of an ordinary second-order differential equation. Because of the cylindrical symmetry involved, the two-dimensional Fourier transform collapses to a one-dimensional Hankel transform so that

$$p(r, z; z_0) \xleftarrow{\mathcal{J}_0} 2\pi\bar{g}(k_r, z; z_0) \qquad (2.15)$$

where the symbol $\mathcal{J}_0$ represents the Hankel transform operation. Finally, the quantity $g(k_r, z; z_0)$ has been defined so that

$$p(r, z; z_0) \xleftarrow{\mathcal{J}_0} g(k_r, z; z_0) \qquad (2.16)$$

where $g(k_r, z; z_0)$ satisfies the equation for a Green's function

$$(\frac{d^2}{dz^2} + k^2 - k_r^2)g(k_r, z; z_0) = -2\delta(z - z_0) \qquad (2.17)$$

The integral representation for the acoustic field within the waveguide is the Hankel transform of the Green's function $g(k_r, z; z_0)$. The quantity $g(k_r, z; z_0)$ is also referred to as the *depth-dependent Green's function* to emphasize its dependence on the source and receiver depths [9]. In our discussions, we will often eliminate the implicit dependence of g on z and z_0, in order to simplify the notation, and we will additionally refer to g as simply the Green's function.

The problem of determining the acoustic field has now been transformed to the problem of solving equation (2.17). The boundary conditions for this second-order

differential equation are determined by the impedance conditions at the surface and bottom of the waveguide. We will initially consider the waveguide to be isovelocity and the non-isovelocity case will be treated later. As mentioned previously, the impedance boundary conditions incorporate the influence on the field of the media outside the waveguide. The impedance conditions can be written in terms of the reflection coefficients at the top and bottom of the waveguide, defined as $R_S(k_r)$ and $R_B(k_r)$. We further define two solutions to the homogeneous version of equation (2.17) which satisfy the impedance boundary conditions in terms of these reflection coefficients. Therefore, the Green's function $g(k_r)$ has the form [1]

$$
\begin{aligned}
g(k_r) &= a(e^{-jk_z z} + R_S e^{jk_z z}) & z \leq z_0 \\
&= b(e^{jk_z(z-h)} + R_B e^{-jk_z(z-h)}) & z \geq z_0
\end{aligned}
\tag{2.18}
$$

where h is the waveguide thickness. The constants a and b in this expression are not arbitrary, since we have incorporated the two boundary conditions, and are now determined [10]. To do this, the continuity of the solution at $z = z_0$ is imposed, so that the solution is written in terms of a new constant c as

$$
\begin{aligned}
g(k_r) &= c(e^{-jk_z z} + R_S e^{jk_z z})(e^{jk_z(z_0-h)} + R_B e^{-jk_z(z_0-h)}) & z \leq z_0 \\
&= c(e^{jk_z(z-h)} + R_B e^{-jk_z(z-h)})(e^{-jk_z z_0} + R_S e^{jk_z z_0}) & z \geq z_0
\end{aligned}
\tag{2.19}
$$

Note that this solution is continuous with respect to z, at $z = z_0$. Next, the fact that the first derivative of $g(k_r)$ must undergo a step change of -2 at $z = z_0$ in order for the left side of equation (2.17) to match the right side is used. Taking the derivative of equation (2.19) with respect to z, and evaluating at $z = z_0$ yields

$$
c j k_z [(e^{jk_z(z_0-h)} - R_B e^{-jk_z(z_0-h)})(e^{-jk_z z_0} + R_S e^{jk_z z_0}) -
$$

$$
(-e^{-jk_z z_0} + R_S e^{jk_z z_0})(e^{jk_z(z_0-h)} + R_B e^{-jk_z(z_0-h)})] = -2
\tag{2.20}
$$

Solving for the constant c gives

$$
c = \frac{j}{k_z e^{-jk_z h}(1 - R_S R_B e^{j2k_z h})}
\tag{2.21}
$$

---

[1]In the remainder of this section, we will drop the explicit dependence of the reflection coefficients on k_r in order to simplify the notation.

Substituting this result for c into equation (2.19), and factoring the term $e^{-jk_z h}$ from the numerator and the denominator, we obtain

$$g(k_r) = \frac{j(e^{-jk_z z_l} + R_S e^{jk_z z_l})(e^{jk_z z_g} + R_B e^{jk_z(2h - z_g)})}{k_z(1 - R_S R_B e^{j2k_z h})} \tag{2.22}$$

where the notation $z_g \equiv max(z, z_0)$ and $z_l \equiv min(z, z_0)$ has been used to summarize the solution for both $z \leq z_0$, and $z \geq z_0$.

To summarize, it has been shown that the integral solution for the acoustic field in a waveguide is

$$p(r, z; z_0) = \int_0^\infty g(k_r, z; z_0) J_0(k_r r) k_r \, dk_r \tag{2.23}$$

where $g(k_r, z; z_0)$ satisfies the ordinary differential equation

$$(\frac{d^2}{dz^2} + k^2 - k_r^2) g(k_r, z; z_0) = -2\delta(z - z_0) \tag{2.24}$$

By solving this differential equation for g, the integral representation for p becomes

$$p(r, z; z_0) = \int_0^\infty \frac{j(e^{-jk_z z_l} + R_S e^{jk_z z_l})(e^{jk_z z_g} + R_B e^{jk_z(2h - z_g)})}{k_z(1 - R_S R_B e^{j2k_z h})} J_0(k_r r) k_r \, dk_r \tag{2.25}$$

We have previously presented a method for obtaining the integral representation for the acoustic field within a waveguide based on solving the Green's function differential equation. Although the method emphasizes that a Green's function is involved in the solution for the field, we now provide an alternate, more intuitive, development which is based on the concept of decomposing, weighting, and resynthesizing the acoustic field in terms of its spatial wavenumber components.

To do this, the harmonic point source is first expanded [1] as

$$p_S(r) = \int_0^\infty \frac{j e^{jk_z|z - z_0|}}{k_z} J_0(k_r r) k_r \, dk_r \tag{2.26}$$

An interpretation of this integral is that for each value of horizontal wavenumber k_r, there exists a plane wave component, $e^{jk_z|z - z_0|}$. For values of k_r less than the water wavenumber, this component travels vertically and accumulates phase. For $z > z_0$

25

the plane-wave component is downgoing, as is easily established from the presence of the term $e^{jk_z z}$ in the integrand of equation (2.26) and the assumed time dependence $e^{-j\omega t}$. For $z < z_0$, the plane wave component is upgoing because of the presence of the term $e^{-jk_z z}$ in the integrand. In the situation that this harmonic source is located within a waveguide, we must consider the effect that the waveguide has on both the upgoing and downgoing components.

First consider a downgoing component produced by the source. As the plane wave component propagates downward, it is reflected and its amplitude is scaled by the reflection coefficient R_B. This component then reverses direction due to its reflection and then travels upward until it reflects off the surface of the waveguide, where in a similar manner, it is scaled by the surface reflection coefficient R_S and is reversed in direction. Therefore, for a source field component of the form $e^{jk_z(z-z_0)}$, the effect of the waveguide is to produce the series of reflected terms

$$e^{jk_z(z-z_0)} + R_B e^{jk_z(2h-(z+z_0))} + R_S R_B e^{jk_z(2h+(z-z_0))} + R_B R_S R_B e^{jk_z(4h-(z+z_0))} + ...$$

The symbol below each of these components denotes the path that each has followed prior to arriving at the receiver depth z. The phase factor associated with each term can be derived as follows. At the bottom interface, $z = h$, the downgoing wave is changed only by the reflection coefficient scaling. Although the component reverses direction, its phase just after reflection is unaltered with the possible exception of a phase change due to a non-zero argument of R_B. For example, at $z = h$, the first and second terms of the above series have the identical phase, and the second term has been scaled by the reflection coefficient.

A similar argument can be applied to an upgoing component produced by the source. As the plane wave component propagates upward, it is reflected at the surface and its amplitude is scaled by R_S. The component then reverses direction due to its reflection and travels downward until it reflects off the bottom of the waveguide, where it is scaled by the bottom reflection coefficient R_B. The effect of the waveguide on

26

the upgoing source component, $e^{-jk_z z}$, is to produce the series of reflected terms

$$R_S e^{jk_z(z+z_0)} + R_B R_S e^{jk_z(2h-(z-z_0))} + R_S R_B R_S e^{jk_z(2h+(z+z_0))} + ...$$

Again, the symbol below each term denotes the path that a plane wave has travelled prior to arriving at depth z. Note also, that the phase factors are consistent with the length of the path that the component has followed, multiplied by the vertical wavenumber k_z.

If the two series are added together and the common term is factored, the resultant sum becomes

$$[e^{jk_z(z-z_0)} + R_S e^{jk_z(z+z_0)} + R_B e^{jk_z(2h-(z+z_0))} + R_B R_S e^{jk_z(2h-(z-z_0))}] S(k_r) \qquad (2.27)$$

where

$$S(k_r) = 1 + R_S R_B e^{j2k_z h} + (R_S R_B)^2 e^{jk_z 4h} + ... \qquad (2.28)$$

It can be seen that there are four kinds of propagating components involved in the synthesis of the total field. Their direction of propagation as they encounter the depth z and their interaction with either the surface, bottom, or both, is symbolically indicated by arrows in the above expression. We will see later in Chapter 5, that there are two possible ways in which these plane wave components can cancel at specific values of horizontal wavenumber.

The term $S(k_r)$, in equation (2.27), incorporates the higher order reflections that each one of these four components basic experiences in travelling from the source to the receiver. That is, the nth term in $S(k_r)$ represents an additional n vertical traversals of the waveguide, with corresponding n reflections off the surface and bottom. The phase factor of the nth term is consistent with the path length $2nh$, times the vertical wavenumber. If the $S(k_r)$ summation is written in closed form [2] so that

$$S(k_r) = \frac{1}{1 - R_S R_B e^{j2k_z h}} \qquad (2.29)$$

---

[2] Convergence of the sum is guaranteed if an arbitrarily small amount of attenuation is assumed[1].

and the four terms in equation (2.27) are factored into a product of two terms, we obtain the result that for each of the individual components of the source field, $e^{jk_z|z-z_0|}$, the effect of the waveguide is to produce the component

$$\frac{(e^{-jk_z z_0} + R_S e^{jk_z z_0})(e^{jk_z z} + R_B e^{jk_z(2h-z)})}{1 - R_S R_B e^{j2k_z h}}$$

If the entire field is synthesized using the correct weighting for each of the source components, it is apparent that

$$p(r, z; z_0) = \int_0^\infty \frac{j(e^{-jk_z z_0} + R_S e^{jk_z z_0})(e^{jk_z z} + R_B e^{jk_z(2h-z)})}{k_z(1 - R_S R_B e^{j2k_z h})} J_0(k_r r) k_r dk_r \qquad (2.30)$$

Equation (2.30) was derived for the case that $z > z_0$. In the situation that $z \leq z_0$, it can also be shown that field expression is identical to equation (2.30), with the variables z and z_0 interchanged. Thus, the total field for either of these cases can be written in a combined form as

$$p(r, z; z_0) = \int_0^\infty \frac{j(e^{-jk_z z_l} + R_S e^{jk_z z_l})(e^{jk_z z_g} + R_B e^{jk_z(2h-z_g)})}{k_z(1 - R_S R_B e^{j2k_z h})} J_0(k_r r) k_r dk_r \qquad (2.31)$$

where $z_g \equiv max(z, z_0)$ and $z_l \equiv min(z, z_0)$.

This expression for the field within the waveguide is identical to the expression derived previously in equation (2.25). The approaches used in deriving the two expressions differed significantly however. In the first approach, the solution was obtained as the two-dimensional inverse Fourier transform of the Green's function solution. Because of the symmetry involved, the two-dimensional inverse Fourier transform became a Hankel transform. In the second approach, a more intuitive development was presented. The waveguide was interpreted in terms of its effect on the plane wave components of the source. In the following section, we will examine the expressions for the Green's function and acoustic field in more detail for specific assumptions regarding the waveguide and surrounding media.

2.3   The Field in a Pekeris Waveguide

In the previous section, an expression for the field in a waveguide was presented in terms of the Hankel transform of a Green's function. In this section, we consider a simpler geoacoustic model which consists of a waveguide surrounded by two halfspaces. The overlying halfspace is assumed to be air so that the surface reflection coefficient is -1, i.e. the upper interface of the waveguide is assumed to be a pressure-release boundary. Below the waveguide, the medium is assumed to be a lossless liquid halfspace with constant parameters of compressional speed and density.

The propagation of sound in this model was a problem first considered by Pekeris in 1948 [11], and the model is correspondingly referred to as the *Pekeris model*. Although Pekeris considered the propagation of sound due to an explosive source in this waveguide, a number of researchers have since considered the propagation due to a harmonic source [2], [12], [13], [14], [15]. The two problems are related, as the field due to the explosive source is the inverse Fourier transform of the field due to the single harmonic source weighted by its frequency spectrum.

The Pekeris waveguide problem, which is a special case of the more general waveguide problem, is important to study for several reasons. First, the model is sufficienctly complicated so that most of the propagation phenomena associated with more general problems also occur in the Pekeris waveguide. For this reason, the Pekeris model will form the basis for a number of examples in later chapters of this thesis. Additionally, the model is simple enough so that expressions for the field can be written in terms of the geoacoustic parameters. In our work, we have found this to be quite important, as it provided a way in which to validate several numerical techniques related to both the synthesis and inversion of acoustic fields. Finally, the study of the model is important because, in some instances, it may be representative of the situation which occurs in a real-life shallow ocean context. For these reasons, we now study the propagation of acoustic fields in a Pekeris waveguide in more detail.

The approach to be followed consists of applying the results of the previous section to the simplified geoacoustic model. The approach taken is not new and other researchers have also considered the propagation of sound in the Pekeris waveguide in a similar manner [2], [15], [16], [17], [18], [19], [20]. However, in the literature there are a number of differing viewpoints regarding the choice of a branch-cut and its relationship to the poles of the Green's function. In the review and discussion in this section, we will unify several of these viewpoints, and relate alternate methods for describing the field in this waveguide. To do this, we will begin with the Hankel transform representation for the field in a Pekeris model waveguide. Next, in anticipating the application of Cauchy's theorem, the equation which describes the location of the poles of $g(k_r)$ in the complex k_r-plane will be derived. The equation which describes these poles is ambiguous in that it does not specify how the signs of several square roots are to be determined. In order to explain how these should be chosen, we will consider the problem in terms of Riemann sheets. In the discussion, we will review several important concepts of Riemann sheets for a much simpler function prior to considering the Green's function itself. Given this review, Cauchy's theorem will be utilized to derive an expression for the field as a sum, due to pole contributions, plus an integral, due to a branch-point contribution. We will point out that the definition of this branch-cut is completely arbitrary and that different choices lead to different representations of an identical field.

We begin by restating the Hankel transform integral representation of the field presented in the previous section,

$$p(r) = \int_0^\infty g(k_r) J_0(k_r r) k_r \, dk_r \qquad (2.32)$$

where the Green's function, $g(k_r)$, is

$$g(k_r) = \frac{j(e^{-jk_z z_l} + R_S(k_r)e^{jk_z z_l})(e^{jk_z z_s} + R_B(k_r)e^{jk_z(2h-z_s)})}{k_z(1 - R_S(k_r)R_B(k_r)e^{j2k_z h})} \qquad (2.33)$$

For the Pekeris waveguide, the surface reflection coefficient, R_S, is -1 so that the

Green's function becomes

$$g(k_r) = \frac{2\sin k_z z_l}{k_z} e^{jk_z z_g} \frac{(1 + R_B(k_r)e^{j2k_z(h - z_g)})}{(1 + R_B(k_r)e^{j2k_z h})} \qquad (2.34)$$

Because of the simple structure of the medium underlying the waveguide, the reflection coefficient at the bottom of the waveguide, $R_B(k_r)$, is the Rayleigh reflection coefficient. We will also use the notation k_{z0} to refer to the vertical wavenumber in medium 0, the waveguide, and the notation k_{z1} to refer to the vertical wavenumber in the underlying halfspace, medium 1. Additionally, the density ratio b is defined as $b = \rho_0/\rho_1$ where ρ_i refers to the density in medium i.

The Rayleigh reflection coefficient for the interface at the bottom of the waveguide can be shown [1] to be

$$R_B(k_r) = \frac{k_{z0} - bk_{z1}}{k_{z0} + bk_{z1}} \qquad (2.35)$$

where $k_{z0} = (k_0^2 - k_r^2)^{1/2}$, $k_{z1} = (k_1^2 - k_r^2)^{1/2}$, $k_1 = \omega/c_0$, $k_1 = \omega/c_1$, and c_0, c_1 are the compressional wave speeds in medium 0 and 1. If these results are substituted in the equation for the Green's function, (2.34), the following expression results,

$$g(k_r) = \frac{2\sin k_{z0} z_l}{z_l} e^{jk_{z0} z_g} \frac{(k_{z0} + bk_{z1}) + (k_{z0} - bk_{z1})[\cos k_{z0}(h - z_g) + j\sin k_{z0}(h - z_g)]^2}{[(k_{z0} + bk_{z1}) + (k_{z0} - bk_{z1})][\cos k_{z0}h + j\sin k_{z0}h]^2} \qquad (2.36)$$

This expression can be further simplified to yield the result

$$g(k_r) = \frac{2\sin k_{z0} z_l}{k_{z0}} \frac{[k_{z0}\cos k_{z0}(h - z_g) - jbk_{z1}\sin k_{z0}(h - z_g)]}{[k_{z0}\cos k_{z0}h - jbk_{z1}\sin k_{z0}h]} \qquad (2.37)$$

Although the Hankel transform integral representation in equation (2.32) requires integration along the real-k_r axis only, it is possible to use Cauchy's integral theorem and equation (2.37) to obtain alternate representations for $p(r)$. To do this, $g(k_r)$ must be considered as a function of complex k_r. To apply Cauchy's theorem, we first recognize the fact that $g(k_r)$ is an even function of k_r. As can be seen from equation (2.37), $g(k_r)$ depends only indirectly on k_r via the terms k_{z0} and k_{z1}, and since these terms are even functions of k_r, $g(k_r)$ must also be even. Using this fact, and the

31

representation for the Bessel function $J_0(k_r r)$ in terms of Hankel functions [8] as

$$J_0(k_r r) = \frac{1}{2} \left[H_0^{(1)}(k_r r) - H_0^{(1)}(e^{j\pi} k_r r) \right] \tag{2.38}$$

the following integral expression [3] is obtained,

$$p(r) = \frac{1}{2} \int_{-\infty}^{\infty} g(k_r) H_0^{(1)}(k_r r) k_r \, dk_r \tag{2.39}$$

where $g(k_r)$ refers to equation (2.37). Note that equation (2.39) is equivalent to the Hankel transform expression presented earlier, i.e.

$$p(r) = \int_0^{\infty} g(k_r) J_0(k_r r) k_r \, dk_r$$

since $g(k_r)$ is an even function of k_r. Thus, the relationship between p and g in equation (2.39) is sometimes also referred to as a Hankel transform. The path followed by the Hankel transform integration contour in the complex k_r-plane and the branch-cut associated with the Hankel function [8] are shown in Figure 2.3.

In order to evaluate the integral in equation (2.39) using Cauchy's theorem, it is necessary to determine the singularities of the integrand. Two kinds of singularities in equation (2.37) must be considered. First, it may be possible for the denominator to become zero whenever

$$k_{z0} \cos k_{z0} h - j b k_{z1} \sin k_{z0} h = 0 \tag{2.40}$$

This type of singularity is represented by a pole in the complex k_r-plane. Note that although the denominator of equation (2.37) can also become zero when $k_{z0} = 0$, a straightforward application of L'Hopital's rule shows that $g(k_r)$ remains finite in this case. Second, branch-point singularities exist in equation (2.37), due to the ambiguity in choosing the signs of square roots. We will show shortly that the ambiguity exists

---

[3] The integral representation is valid only for $r > 0$. In the remainder of this chapter we will assume, in order to simplify notation, that all field expressions are valid *only* for $r > 0$, with the implication that the field for negative values of r can be determined from the condition that $p(r)$ must be an even function of r.
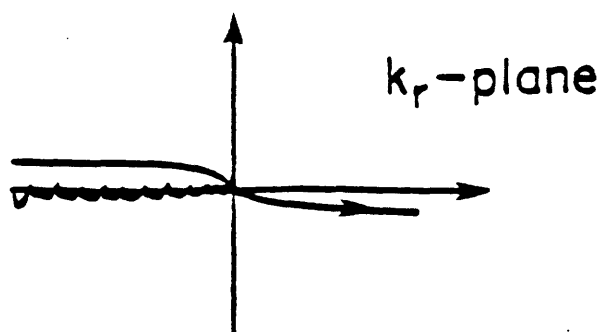
Figure 2.3: Complex k_r-plane indicating path of contour integration and Hankel function branch-cut.

only for the choice of the sign associated with k_{z1}. Specifically, the value that $g(k_r)$ assumes for a particular value of k_r depends only on the choice of the sign of k_{z1}, and not on the choice of the sign of k_{z0}.

One way of resolving this ambiguity is to separately consider the behavior of $g(k_r)$ on two planes or *Riemann sheets* [21]. On one sheet the sign is chosen one way, and on the other sheet sheet the sign is chosen the opposite way. It is noted, from equation (2.37), that the choice of the sign associated with k_{z0} is arbitrary since $g(k_r)$ is an even function of k_{z0} ; either sign choice yields the same value when $g(k_r)$ is evaluated. Therefore, the ambiguity exists only in the choice of the sign of k_{z1} and only two Riemann sheets are required. The ambiguity in the choice of the sign implies that $g(k_r)$ is not analytic along a line in the k_r-plane. In order to better explain the relationship between ambiguity and analyticity, we will digress to discuss the Riemann sheets for the much simpler function $z^{1/2}$.

Consider the polar representation of the complex number $z = x + jy$ as $Me^{j\theta}$. The square root of z can be easily determined as $z^{1/2} = M^{1/2}e^{j\theta/2}$. There is an inherent ambiguity in this expression however, related to the proper definition of θ.

33

z-plane

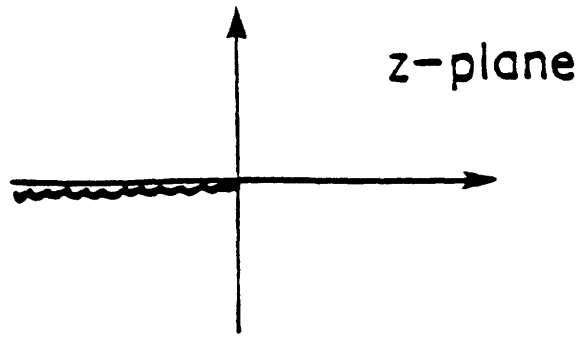Figure 2.4: Complex z-plane indicating the branch-cut corresponding to the principal value definition $-\pi < \theta \leq \pi$.

For example, although $z_1 = Me^{j\theta}$ and $z_2 = Me^{j(\theta+2\pi)}$ correspond to the same point, $z_1^{1/2} = M^{1/2}e^{j\theta/2}$ and $z_2^{1/2} = M^{1/2}e^{j(\theta/2+\pi)}$ correspond to two different points - the same point apparently has two possible values associated with its square root. To resolve this ambiguity, θ must be defined as a principal-valued quantity, which assumes values only over an interval of length 2π. For example, θ defined over the interval $[-\pi, \pi)$, or over the interval $[0, 2\pi)$, are two possible definitions of principal value which eliminate the ambiguity. However, for a given principal value specification, there exists for every value of M, a value θ_c such that

$$\lim_{\epsilon \to 0} \left[Me^{j(\theta_c+\epsilon)} - Me^{j(\theta_c-\epsilon)} \right]^{1/2} \neq 0 \qquad (2.41)$$

In other words, $z^{1/2}$ is discontinuous and therefore not analytic in the vicinity of the point $Me^{j\theta_c}$. As an example, consider $-\pi < \theta \leq \pi$. We note that $\left[1e^{j(\pi-\epsilon)}\right]^{1/2} \simeq j$ while $\left[1e^{j(-\pi+\epsilon)}\right]^{1/2} \simeq -j$, and thus $z^{1/2}$ is discontinuous and not analytic at this point.

. The values of z at which the function $z^{1/2}$ is discontinuous are indicated in the z-plane by the presence of a jagged line, referred to as the *branch-line*, or *branch-cut*, as indicated in Figure 2.4. In this figure the principal value definition for θ is $-\pi < \theta \leq \pi$, so that $z^{1/2}$ is discontinuous along the ray which extends from 0 to $-\infty$. More general principal value definitions can also depend on the magnitude of z. It is noted that, from the principal value definition it is possible to predict the branch-

34

z−plane
Top Sheet

z−plane
Bottom Sheet
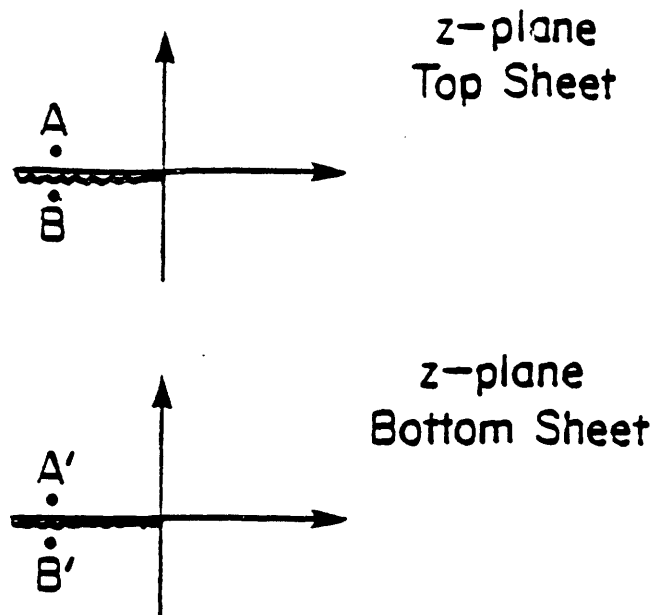
Figure 2.5: Top and bottom Riemann sheets. The function remains continuous as a path from A to B' or from A' to B is followed. Point A is close to point B' and point A' is close to point B.

line position, or alternately, from the branch-line position it is possible to predict the principal value value definition.

By introducing Riemann sheets and connecting these sheets along the branch-line, it is possible to resolve the ambiguity and consider the analyticity of $z^{1/2}$. To see this, consider Figure 2.5 which illustrates the Riemann sheets for $z^{1/2}$ with the principal value definition of $-\pi < \theta \leq \pi$. The ambiguity in the choice of the square root sign is represented by the presence of the two Riemann sheets, and the discontinuous behavior is indicated by the presence of the branch-line on both sheets. The function $z^{1/2}$ is not continuous as a path is followed from point A on the top sheet to point B on the top sheet. Similarly, $z^{1/2}$ is discontinuous as a path is followed from the point A' on the bottom sheet to the point B' on the bottom sheet. However, if a path is defined from point A on the top sheet to point B' on the bottom sheet, or from point A' on the bottom sheet to point B on the top sheet, the function $z^{1/2}$ will remain continuous along this path. However, the definition of the square root must change along the path, if either of the latter two paths are followed. In a sense, A is considered as close to B', and A' is considered as close to B, with an implication
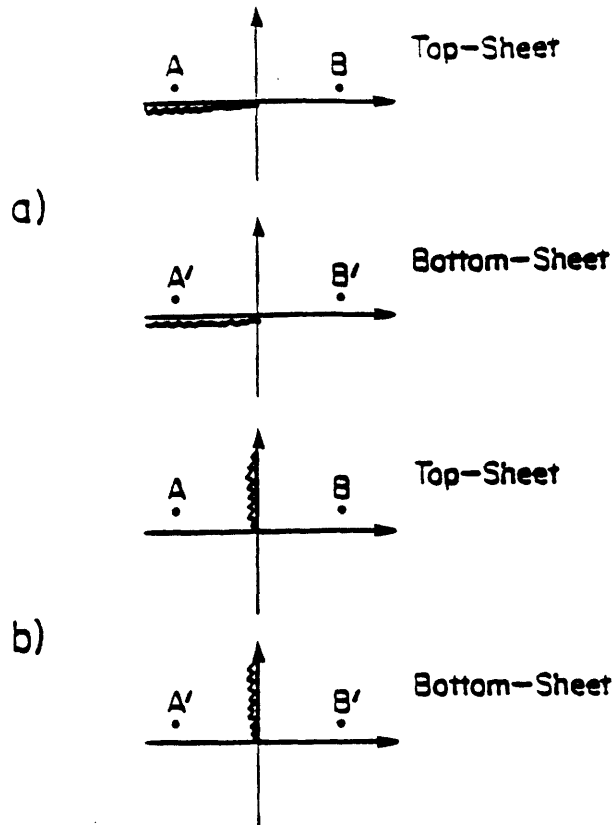
Figure 2.6: Top and bottom Riemann sheets for two different branch-cut definitions.

of analyticity. Alternately, A cannot be considered close to B, because the function becomes discontinuous as a path is traversed from A to B.

Note that both the principal value definition and the sheet specification, i.e. the specification of which sheet is the top sheet, are required in order to completely specify how the square root is to be performed for each value of z. For example, Figure 2.6 displays the Riemann sheets for two different choices of the definition of the principal value of θ, i.e. for two different branch cut definitions. In Figure 2.6a, the four points A, B, A', B' are defined such that A and A' are at the same location in the k_r-plane but lie on the top and bottom sheets respectively. The values of $z^{1/2}$ at the locations A, B, A', B' are also defined as a, b, a', b' respectively. Note that $a' = -a$ and $b' = -b$. In Figure 2.6b, the principal value definition has been changed as indicated by the different location of the branch-cut, and the top sheet was defined such that the value of $z^{1/2}$ at the point B is again b. However, it can be easily shown that the value of

$z^{1/2}$ at the point A for the two branch-cut definitions differs. Specifically, $z^{i/2}$ at the point labelled A in Figure 2.6b is actually a', while $z^{1/2}$ at the point A in Figure 2.6a is a. In other words, although the position of the point A is fixed and lies on the top Riemann sheet in both cases, the particular specification of the branch-cut yields different values for the associated square root.

A convenient mechanism for keeping track of the behavior of a function as the position of the branch-cut is changed is now provided. Consider slowly twisting the cut from its position in Figure 2.6a to its position in Figure 2.6b. As the cut encounters the points A and A', we can consider the point on the top sheet falling to the bottom sheet and vice versa. In other words, the sheets are considered as connected at the branch-cut and as the cut is twisted, points from one sheet move to the other sheet. For example, as the cut is twisted from its position in Figure 2.7a to its position in Figure 2.7b, we see that the point A has moved to the bottom sheet and that the point A' has moved to the top sheet. Using this concept, it is possible to predict the values of $z^{1/2}$ for alternate branch-cut selections assuming that $z^{1/2}$ is known fully for one branch-cut selection. As the cut is moved, points on the bottom sheet migrate to the top sheet and points on the top sheet migrate to the bottom sheet.

To summarize, we have shown that specifying the principal value definition is equivalent to selecting the position of the branch-cut. Specifying the square root at every point in the z-plane can be done by specifying the location of the branch-cut, and by defining which sheet is the top sheet. The location of the branch-cut is arbitrary and can be chosen for convenience with the constraints that it must begin at $z = 0$, end at $z = \infty$, and not cross itself. The choice of which sheet is the top sheet is not arbitrary and depends on the particular problem. Typically, some physical constraint dictates which sheet is the top sheet, and the sheet selection process for the Green's function will be considered shortly.

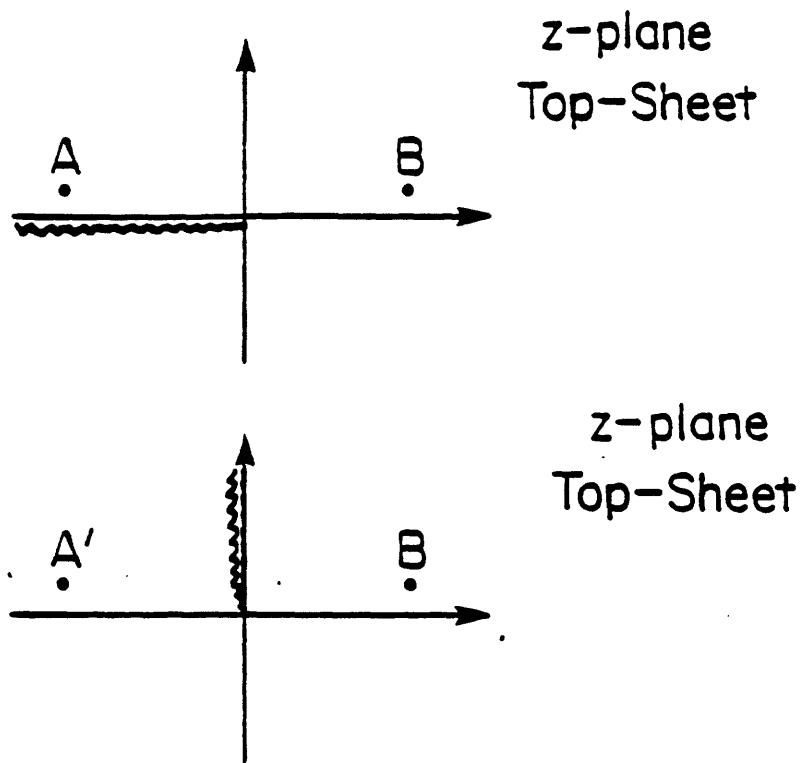Given this review of Riemann sheets for the function $z^{1/2}$, we next discuss the more

Figure 2.7: Top Riemann sheet for two different branch-cut definitions. As the branch cut is twisted from its position in a) to its position in b), point A falls to the bottom sheet and point A' rises to the top sheet. Point B remains on the top sheet.

complicated function $g(k_r)$ for the Pekeris geoacoustic model. Recall from equation (2.37) that $g(k_r)$ depends only on k_r through the quantities k_{z0}, and k_{z1}. As discussed previously, only the sign of k_{z1} must be specified - the sign of k_{z0} may be chosen arbitrarily since $g(k_r)$ is an even function of k_{z0}. We wish to obtain the square root of k_{z1}^2 in the manner similar to obtaining the square root of z. There is an additional complication however, in that the integration is to be performed in the k_r-plane, while the principal value definition applies to the k_{z1}^2-plane. An implication is that the branch-cut which is present in the k_{z1}^2 plane must be mapped to the k_r-plane, using the relationship $k_{z1} = (k_1^2 - k_r^2)^{1/2}$.

In Figure 2.8 are shown a number of branch-cuts in the k_{z1}^2-plane and their corresponding mapping to the k_r-plane. The branch-cut depicted in Figure 2.8a is referred as the *Ewing-Jardetzky-Press* (EJP) cut [2] and the cut is specified via $Im\{k_{z1}\} = 0$. Values of $g(k_r)$ on the top Riemann sheet sheet for this cut are obtained by computing k_{z1}, and choosing the sign of k_{z1} such that $Im\{k_{z1}\} \geq 0$. It is noted that most computer complex variable subroutines define the square root operation using the principal value definition shown in Figure 2.8d. Note that in Figure 2.8g, the vertical cut in the k_r-plane corresponds to a principal value definition in the k_{z1}^2-plane which is a function of magnitude. This vertical branch-cut in the k_r-plane is referred as the *Pekeris cut* [19].

The concepts discussed concerning the behavior of the function $z^{1/2}$ on the Riemann sheets are also applicable to the more general function $g(k_r)$. For example, if a path is traversed in the k_r-plane which crosses the branch-cut, the function $g(k_r)$ will change discontinuously. However, if the path begins on the top sheet, crosses the cut, and continues onto the bottom sheet, $g(k_r)$ will remain continuous and analytic. This also has direct impact on the application of Cauchy's integral theorem, which requires a function to be analytic everywhere inside an integration contour except at isolated singular points. The implication is that the integration contour must either dodge the branch-cut, where the function becomes non-analytic along a line, or alternately
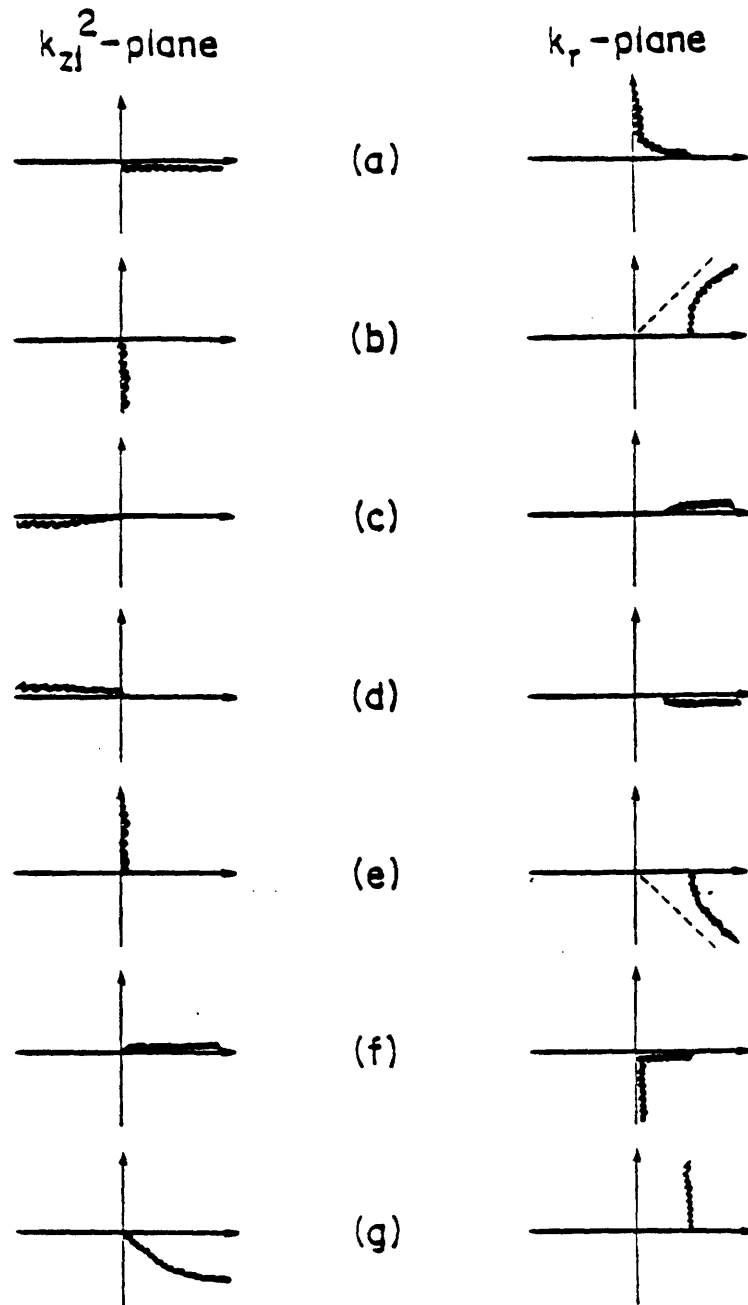
Figure 2.8: Branch cuts in the k_{z1}^2-plane and their corresponding mappings to the k_r-plane.

must continue under the cut, onto the bottom sheet.

The Green's function $g(k_r)$ has significantly different behavior for specific values of k_r dependent on the sheet chosen. For example, consider equation (2.40) which describes the location of the poles for the Pekeris model Green's function, and further assume that the branch-cut is specified as $Im\{k_{s1}\} = 0$, i.e. as the EJP branch-cut. It can be shown [4] [22] that this equation may only have solutions, k_{ri}, such that k_{ri} is purely-real and $k_1 < k_{ri} < k_0$. In particular, there can be no poles on this Riemann sheet which are in quadrant I of the k_r-plane except those on the real-k_r axis. This restriction does not apply to the poles on the bottom sheet. In fact, as discussed by Stickler [22], bottom sheet poles which have non-zero imaginary parts may exist. Note that since $g(k_r)$ is an even function of k_r, poles which appear in quadrant I must also appear in quadrant III. However, we will ignore these poles in our discussion as the Hankel transform integration contour will be closed in the upper k_r-plane, and thus the poles in quadrant III are of no interest. A point to be emphasized is that although a pole at some value of k_{ri} on the bottom Riemann sheet may exist, this singularity is, in general, not present on the top Riemann sheet.

We next consider the effects caused by the proximity of poles on the top and bottom Riemann sheets to the real k_r-axis. As an example, consider the pole in quadrant I of the bottom Riemann sheet depicted in Figure 2.9. Although the pole does not appear on the top Riemann sheet, the effects of the pole are felt when $g(k_r)$ is evaluated at values of k_r on the top sheet *near* the pole. An essential point here is that the top and bottom sheets are connected along the branch-cut. In this figure, the point A on the top sheet is near the pole on the bottom sheet and thus it is expected that the Green's function evaluated at point A will have large magnitude. Similarly, points located just below the real axis on the top Riemann sheet will be strongly influenced by the pole on the bottom Riemann sheet. Therefore, poles on *both* the top *and* bottom sheets near the real-k_r axis are responsible for the resonances in $g(k_r)$ evaluated for real values of k_r, provided that the branch-cut is in the appropriate

41
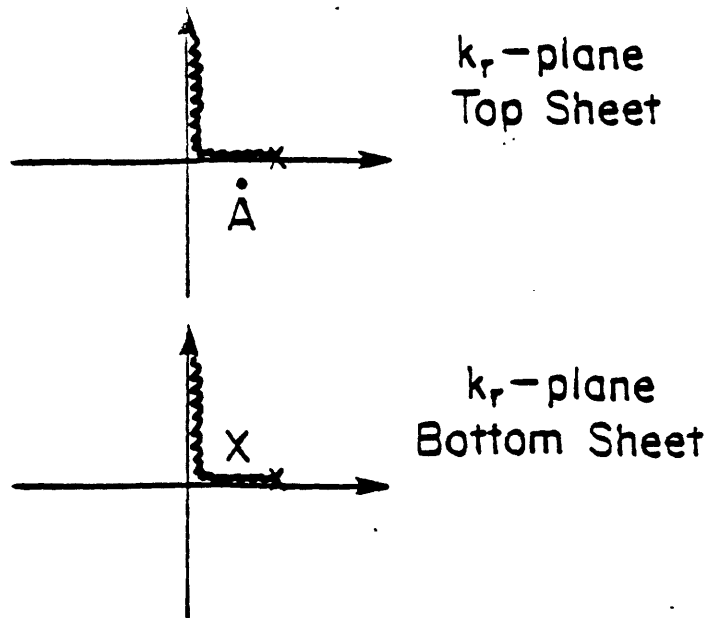
Figure 2.9: Top and bottom Riemann sheets indicating a pole on the bottom sheet near the branch-cut.

position. This effect is now illustrated in more detail using a numerical example.

The Green's function for the specific set cf Pekeris model geoacoustic parameters summarized in Table 2.1 was computed, and its magnitude is plotted as a function of real-k_r in Figure 2.10. [4] We have selected the EJP branch-cut and the top Riemann sheet in order to evaluate k_{r1} in computing the Green's function. For this choice of the geoacoustic parameters, there are two poles of $g(k_r)$ which are located on the real-k_r axis, and these two points are identified in Figure 2.10 as A and B. There is an additional resonance near $k_r = 0.13$ which has been labelled as C in this figure. This plot displays the magnitude of $g(k_r)$ evaluated along a single line in the complex k_r-plane. In order to see the effects of on-axis and off-axis poles more clearly, we next display in Figure 2.11 a perspective plot of the magnitude of $g(k_r)$ as a function of k_r within quadrant I of the complex k_r-plane. The location of the EJP branch-cut is shown in this figure as the jagged line. The figure indicates that two poles are present along the real-k_r axis and these poles have been labelled as A and B. It is apparent that the poles labelled as A and B in Figure 2.11 are responsible for the resonances

---

[4] To be more precise, this function was computed along a horizontal line in the complex k_r-plane displaced by ϵ below the real-k_r axis.

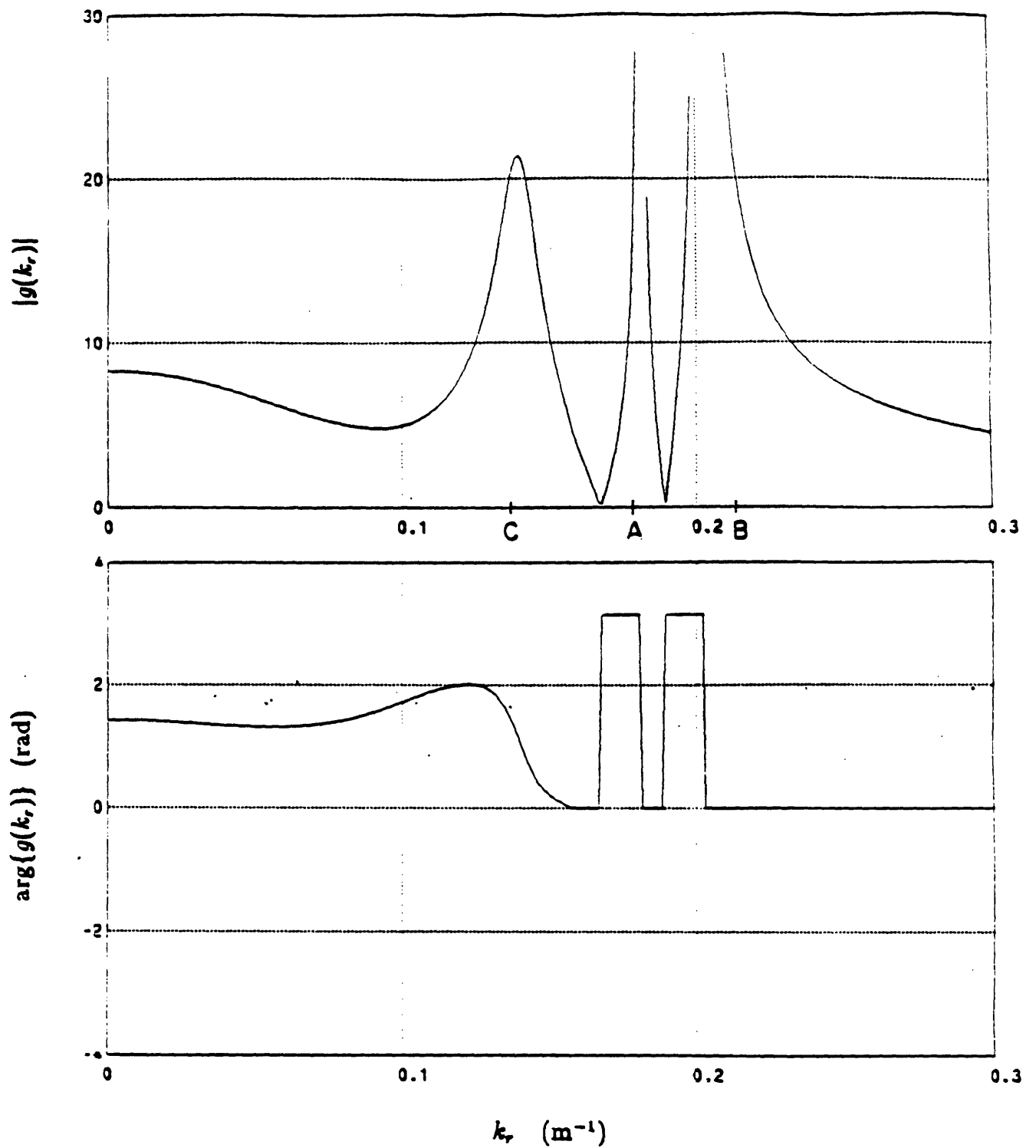| Depth of source	z_0	=	25 m
Depth of receiver	z	=	25 m
Waveguide thickness	h	=	50 m
Frequency	f	=	50 Hz
Water velocity	c_0	=	1500 m/sec
Sediment velocity	c_1	=	2000 m/sec
Water density	ρ_0	=	1 g/cm^3
Sediment density	ρ_1	=	1.5 g/cm^3

Table 2.1: Geoacoustic Parameters for the Pekeris Model

Figure 2.10: Magnitude and phase of Green's function $g(k_r)$. The function was evaluated along a line just below the real k_r axis.
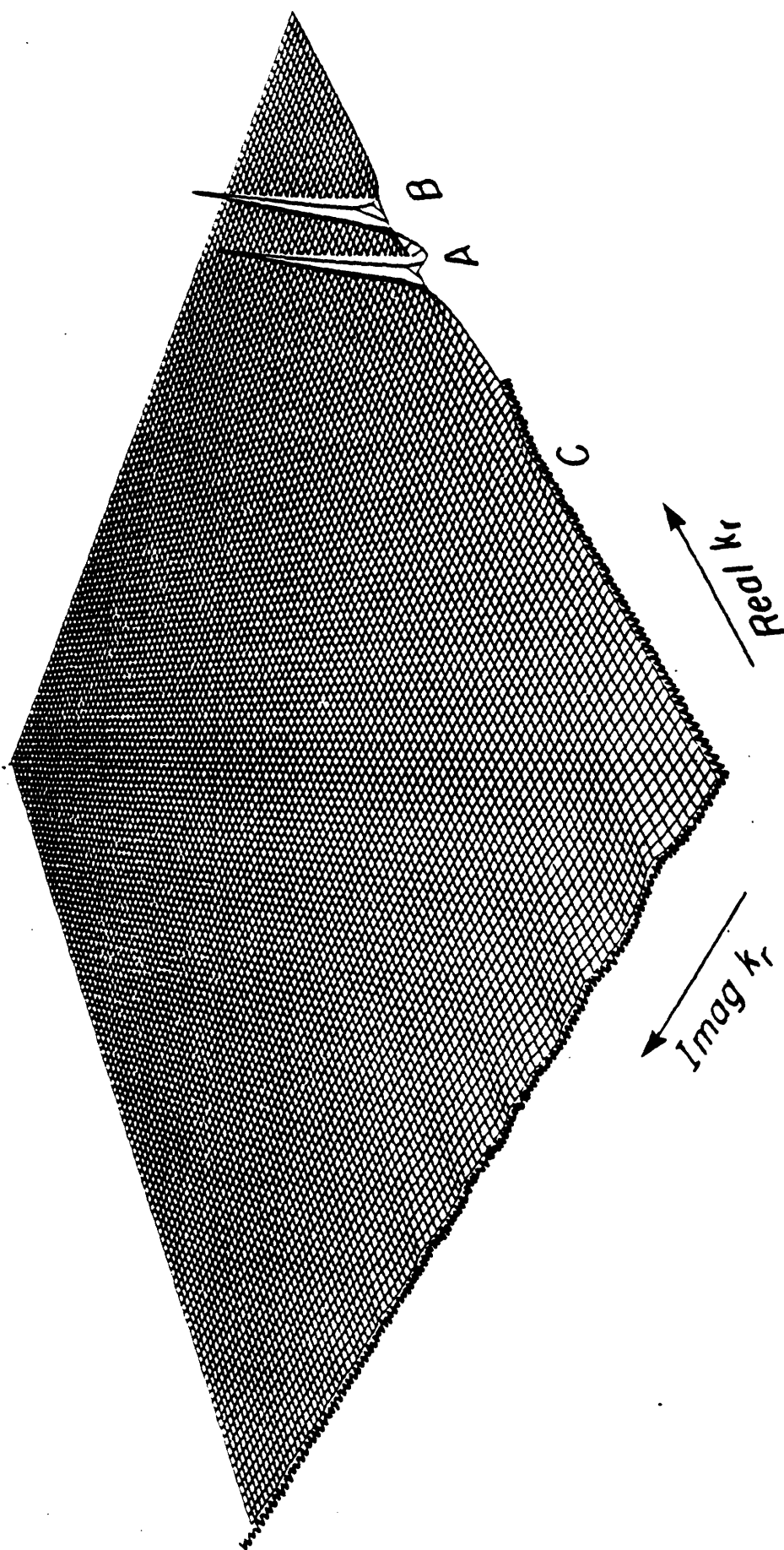
Figure 2.11: Perspective plot of $|g(k_r)|$ in quadrant I of top Riemann sheet for the EJP branch-cut.

labelled as A and B in Figure 2.10. The resonance labelled as C in Figure 2.10 can also be seen in Figure 2.11, however there is no pole in quadrant I which gives rise to this resonance. It can be similarly shown that there is no pole in quadrant IV of the complex k_r-plane which is responsible for this resonance. The off-axis pole which causes the resonance at C must be located on the bottom Riemann sheet.

In order to see this, we next display in Figure 2.12 a perspective plot of quadrant I of the bottom Riemann sheet. The display indicates that there are a number of poles near the imaginary axis of the complex k_r-plane on the bottom Riemann sheet. The relative heights, or amplitudes, of these poles are not accurately displayed due to the sampling grid on which this function was computed. The two most interesting features of this display however, are the poles labelled as C and D. From our discussion earlier, it is apparent that certain points along the real-k_r axis on the top sheet are close to the pole on the bottom sheet labelled C because of the intervening EJP branch-cut. The implication is that the pole labelled as C in Figure 2.12 is responsible for the resonance labelled as C in Figure 2.10. However, the pole labelled as D on the bottom sheet has negligible impact on the behavior of the Green's function along the real axis on the top Riemann sheet - it is not close to any points on the top Riemann sheet because there is no intervening branch-cut.

In our previous discussions, we pointed out that it is sometimes convenient to visualize the effects of top and bottom sheet poles on the Green's function by twisting the branch-cut from one position to another. We indicated that as the cut twists, points from the top Riemann sheet fall to the bottom Riemann sheet and points from the bottom Riemann sheet rise to the top Riemann sheet. We will now illustrate this effect, in the context of this example, by twisting the branch-cut from its EJP position, in Figures 2.11 and 2.12, to a vertical, or Pekeris-cut, position. In Figure 2.13 is shown a display of quadrant I of the top Riemann sheet for the Pekeris branch-cut definition. As the cut was twisted from its previous position to this vertical position, poles previously on the bottom sheet, near the imaginary axis, have now risen to
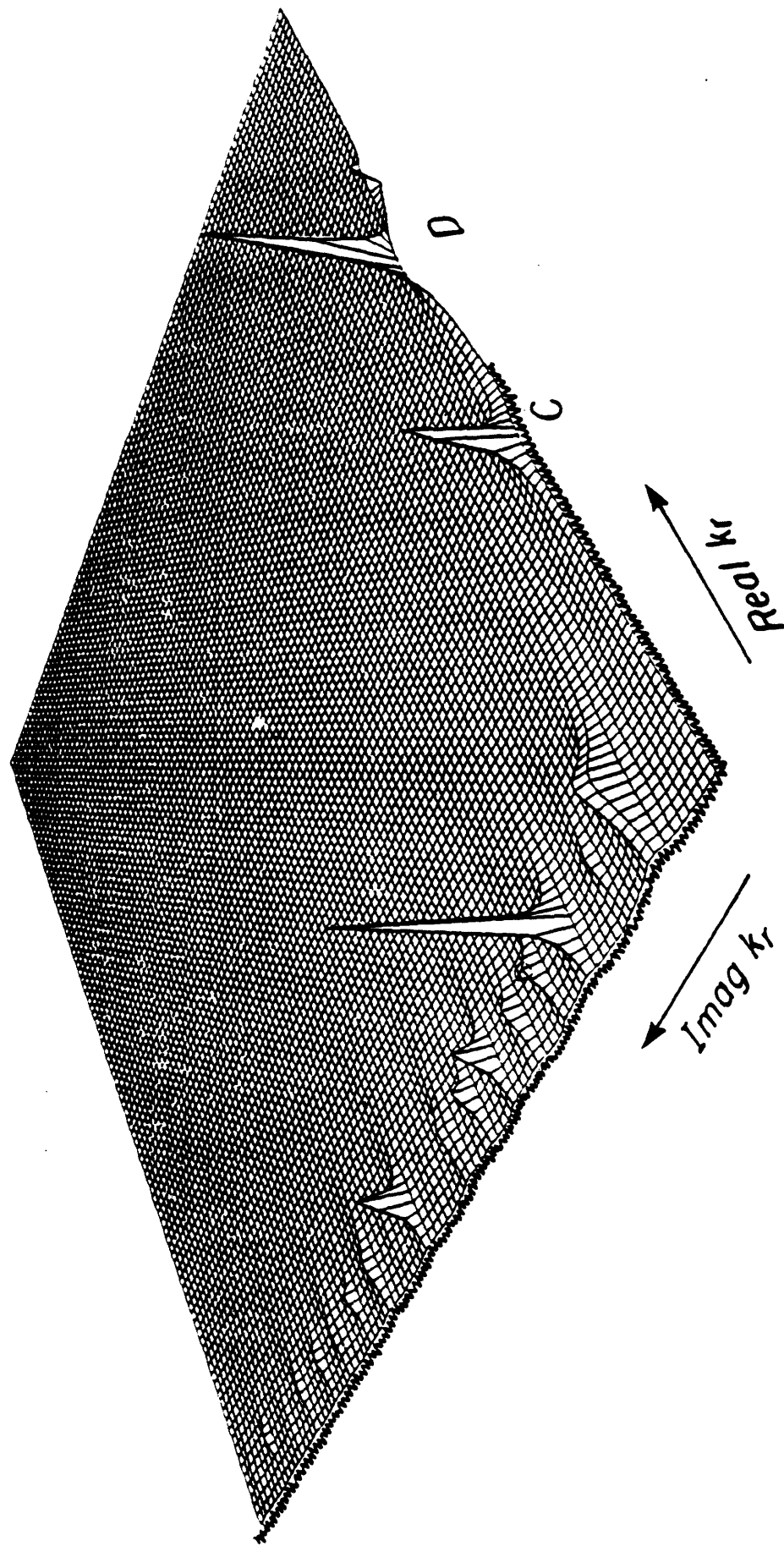
Figure 2.12: Perspective plot of $|g(k_r)|$ in quadrant I of bottom Riemann sheet for the EJP branch-cut.
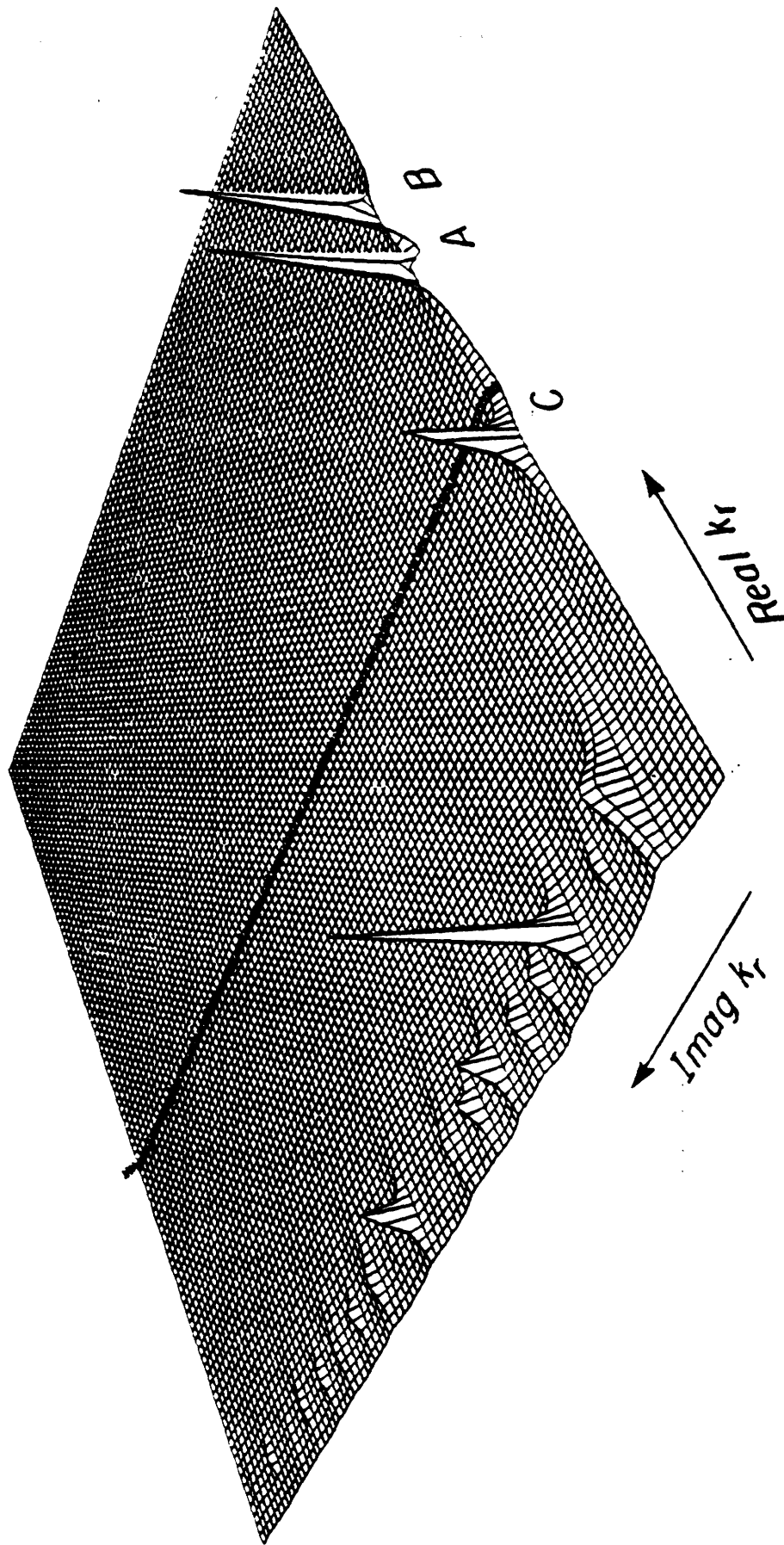
Figure 2.13: Perspective plot of $|g(k_r)|$ in quadrant I of top Riemann sheet for the Pekeris branch-cut.

become top-sheet poles. Additionally the cut has been twisted far enough so that the pole labelled C is also exposed on the top sheet. The poles labelled as A and B remain in place however, because they have not been encountered as the cut is twisted. Additionally, the pole labelled as D remains on the bottom sheet for this reason.

Given the selection of the vertical branch-cut, the cause of the resonance at C in Figure 2.10 is now quite evident - it is due to the presence of the off-axis pole on the top Riemann sheet depicted in Figure 2.13. The resonance at point C in Figure 2.10 is thus explained by the proximity of an off-axis pole to points along the real axis. However, we emphasize that the definition of the branch-cut has absolutely no effect on the computation of $g(k_r)$ for *real* values of k_r. That is, the display of $g(k_r)$ shown in Figure 2.10 does not depend on the selection of either the EJP or Pekeris branch-cut - the function is identical in either case provided that the top sheet is selected properly. [5] The branch-cut definition affects $g(k_r)$ only for values of k_r off the real axis. The selection of a particular cut is completely arbitrary - in this case we have used different definitions to demonstrate that the resonance at C in Figure 2.10 is due to an off-axis pole. The off-axis pole appeared either on the top or bottom Riemann sheet dependent on the specific choice of the cut.

To summarize, we have demonstrated that it is useful to consider the behavior of $g(k_r)$ on dual Riemann sheets. In analogy with the description of the sheets for $z^{1/2}$, $g(k_r)$ exhibits different behavior on the two sheets. In particular, a pole located at a particular position on one sheet is, in general, not located at the same position on the alternate sheet. The relationship between the different choices of branch-cuts can be conveniently visualized by twisting the cut from one position to another, and correspondingly moving points off one sheet and onto the other. Finally, we have pointed out that pseudo-resonances in $g(k_r)$ evaluated along the real-k_r axis are due to the proximity of poles. A pole may appear on the top or bottom sheet depending

---

[5]In the remainder of this section, the top sheet can also be considered as the physical sheet.

on the selection of the cut. However, for any branch-cut choice, the effect of the pole on $g(k_r)$ along the real-k_r axis is identical, provided that the proper top sheet is selected.

We next discuss the application of Cauchy's theorem as a means for determining the Hankel transform of $g(k_r)$. The presence of the branch-cuts and Riemann sheets makes applying Cauchy's integral theorem non-trivial in this context. The development which is followed is based on the Hankel transform integral representation discussed earlier, as opposed to alternate methods based on eigenfunction expansions. The two approaches will be related in Chapter 4 of this thesis. An advantage of the Hankel transform approach is that it leads naturally to the technique for synthetic data generation, which is also discussed in Chapter 4.

Consider the Riemann sheet diagram shown in Figure 2.14 which displays the position of the EJP branch-cut, a typical pole configuration, and the path of integration for the Hankel transform integral

$$p(r) = \frac{1}{2} \int_{-\infty}^{\infty} g(k_r) H_0^{(1)}(k_r r) k_r \, dk_r \tag{2.42}$$

The branch-cut associated with the Hankel function $H_0^{(1)}(k_r r)$ is assumed to lie along the negative real-k_r axis and is not shown in Figure 2.14. The choice of the top, or physical, Riemann sheet on which the integration in equation (2.42) is to be performed must be made based on some physical constraint. The constraint invoked is that the radiation condition must be satisfied. In simple terms, the radiation condition implies that fields cannot grow exponentially as a function of distance from the source.

The selection of the choice of the physical sheet cannot be made by applying the radiation condition to the field within the waveguide. In fact, performing the Hankel transform of the Green's function on the bottom sheet yields a field which satisfies the radiation condition, but which is physically *incorrect*. The selection of the sheet on which the Hankel transform integration is to be performed can only be made by considering the behavior of the field outside of the waveguide in the underlying

50
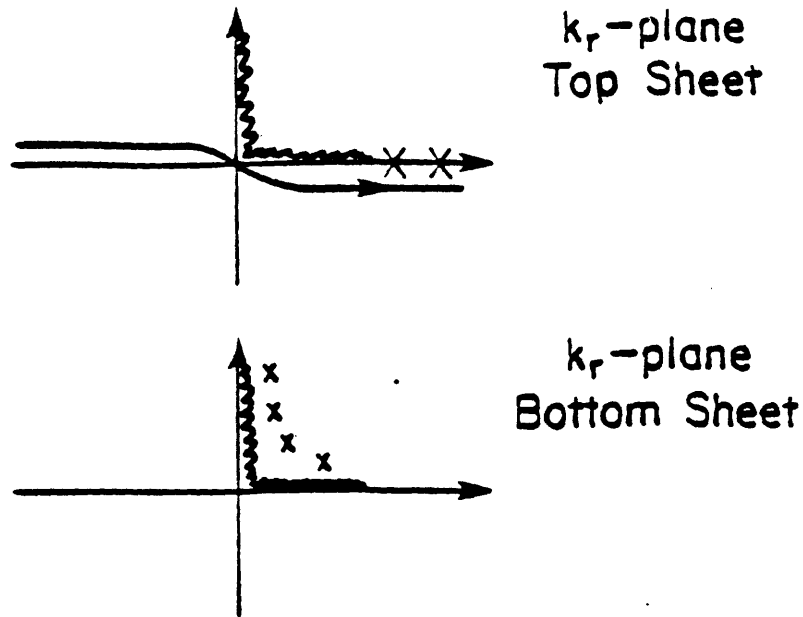
Figure 2.14: Top and bottom Riemann sheets indicating Hankel transform integration contour on top sheet and a typical pole configuration.

halfspace.

There are several ways of obtaining the integral representation in the underlying halfspace. One approach is based on analytically continuing the Green's function, or equivalently, analytically continuing the field. By invoking the continuity of pressure and vertical derivative of particle velocity, the field in the bottom for the Pekeris model can be expressed as

$$p_B(r) = \int_{-\infty}^{\infty} g_B(k_r) H_0^{(1)}(k_r r) k_r \, dk_r \tag{2.43}$$

where

$$g_B(k_r) = \frac{\sin k_{z0} z_l \, e^{jk_{z1}(z-h)}}{k_{z0} \cos k_{z0} h - j b k_{z1} \sin k_{z0} h} \tag{2.44}$$

It can be verified that $p_B(r)$ satisfies the required continuity conditions with respect to the function $p(r)$. Specifically, by comparing equations (2.37), (2.39) and (2.43), (2.44), it can be shown that

$$
\begin{aligned}
p(\mathbf{r})|_{z=h} &= p_B(\mathbf{r})|_{z=h} \\
\frac{1}{\rho_0} \frac{\partial p(\mathbf{r})}{\partial z}\Big|_{z=h} &= \frac{1}{\rho_1} \frac{\partial p_B(\mathbf{r})}{\partial z}\Big|_{z=h}
\end{aligned}
\tag{2.45}
$$

Equation (2.44) can be used to determine the physical Riemann sheet. In this

equation there is a term present which has the form $e^{jk_{z1}z}$, and this exponential suggests the method for choosing the physical sheet. Specifically, consider values of $k_r > k_1$ so that k_{z1} becomes purely imaginary. The term $e^{jk_{z1}z}$ is either exponentially growing, or decaying, with depth z, depending on the choice of the sign of k_{z1}. Application of the radiation condition implies that the minus sign must be chosen so that the field does not grow exponentially with increasing depth. In other words, the top or physical Riemann sheet should be selected so that $Im\{k_{z1}\} > 0$ for real-$k_r > k_1$. Note that the radiation condition does not imply that $Im\{k_{z1}\} \geq 0$ for all k_r, which is the condition for the entire physical sheet, assuming the EJP branch-cut. Rather, the radiation condition suggests the way in which the physical sheet is determined for *any* branch cut. The procedure for determining the physical Riemann sheet which describes the physically correct field within the waveguide is to therefore: 1) select a convenient branch-cut which emanates from the branch-point at $k_r = k_1$, 2) define the physical sheet, i.e. the sheet on which the integration is to be performed, by choosing the sign of $Im\{k_{z1}\}$ as positive, for values of real-$k_r > k_1$. It is emphasized that the physical Riemann sheet is selected by applying the radiation condition to the acoustic field at large depth, as opposed to large range, from the source.

Given this discussion, we can now evaluate the Hankel transform in equation (2.42) using Cauchy's theorem. The approach is to choose an arbitrary branch-cut and to select the physical sheet on which the integration is to be performed. Initially, we will select the EJP branch-cut. Note that the integrand of the Hankel transform becomes exponentially small for $|k_r|$ large when $Im\{k_r\} > 0$, so that the integration contour can be closed in the upper-half of the k_r-plane, as shown in Figure 2.15. Using Cauchy's theorem and Figure 2.15, it is apparent that

$$\left[\int_{-\infty}^{\infty} + \int_{C_1} + \int_{C_2}\right] \frac{g(k_r)}{2} H_0^{(1)}(k_r r) k_r \, dk_r = \pi j \sum_i a_i k_{ri} H_0^{(1)}(k_{ri} r) \qquad (2.46)$$

where k_{ri} is the ith pole, a_i is the residue at this pole, and the sum is over all poles which appear inside the contour of integration. Using equation (2.46), the fact that
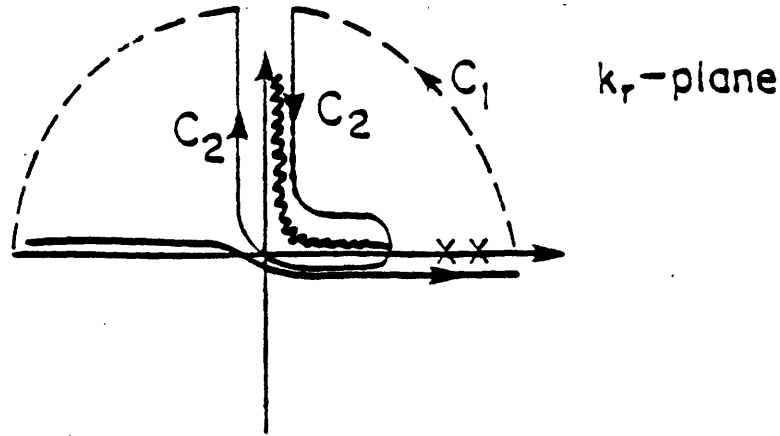
Figure 2.15: Complex k_r-plane indicating poles and integration contour.

$\int_{C_1} = 0$, and recalling that the desired field has the integral representation

$$p(r) = \frac{1}{2} \int_{-\infty}^{\infty} g(k_r) H_0^{(1)}(k_r r) k_r dk_r,$$ (2.47)

it is apparent that an equivalent representation for $p(r)$ is

$$p(r) = p_T(r) + p_C(r)$$ (2.48)

where

$$p_T(r) = \pi j \sum_i a_i k_{ri} H_0^{(1)}(k_{ri} r)$$ (2.49)

and

$$p_C(r) = - \int_{C_2} \frac{g(k_r)}{2} H_0^{(1)}(k_r r) k_r dk_r$$ (2.50)

The field has now been decomposed into the sum of two components as indicated by equation (2.48). The first component, $p_T(r)$, consisting of a finite sum of terms, is the *trapped* or *normal* mode sum. Each term in this sum corresponds to a value of horizontal wavenumber at which perfectly constructive interference occurs within the waveguide. In other words, at this wavenumber, the downgoing plane wave produced at the source adds perfectly in phase with all higher-order multiples due to additional reflections off both the surface and bottom. Similarly, the upgoing component produced at the source adds perfectly in phase with all higher-order multiples. Because

of the fact that there is no attenuation included in the Pekeris geoacoustic model and the fact that the plane waves experience total internal reflection at both the surface and bottom of the waveguide, i.e. the magnitude of the bottom reflection coefficient must be unity, each mode is trapped within the waveguide.

The second term in equation (2.48) is referred to as the *continuum* contribution [19] [23]. This term represents the superposition of the remaining plane-wave components within the waveguide which do not interfere in a perfectly constructive manner. We emphasize that the integral expression for the continuum, $p_C(r)$, shown in equation (2.50), is *not* a Hankel transform. Although the integrand of this expression has the correct form of a Hankel transform, the limits of the integral do not. However, in Chapter 4 of this thesis, we will develop a different method which does express the continuum in terms of a Hankel transform. Specifically, the continuum portion of the field will be defined in terms of the Hankel transform of the continuum portion of the Green's function. The method will form the key element of a hybrid method for synthetically generating acoustic fields not only within a Pekeris waveguide, but in more general waveguides as well.

Given the form of the Green's function for the Pekeris model, it is possible to derive specific expressions for the continuum and trapped mode contributions. The expression for the continuum portion of the field, assuming that the EJP branch-cut has been selected, is

$$p_C(r) = - \int_{C_2} \frac{\sin k_{z0} z_l}{k_{z0}} \frac{[k_{z0} \cos k_{z0}(h - z_g) - j b k_{z1} \sin k_{z0}(h - z_g)]}{[k_{z0} \cos k_{z0} h - j b k_{z1} \sin k_{z0} h]} H_0^{(1)}(k_r r) k_r dk_r$$

(2.51)

where the contour C_2 is defined in Figure 2.15. Substituting $k_{z1} = (k_1^2 - k_r^2)^{1/2}$ into equation (2.51) yields

$$p_C(r) = \int_0^\infty \frac{\sin k_{z0} z_l}{k_{z0}} \frac{[k_{z0} \cos k_{z0}(h - z_g) - j b k_{z1} \sin k_{z0}(h - z_g)]}{[k_{z0} \cos k_{z0} h - j b k_{z1} \sin k_{z0} h]} H_0^{(1)}(k_r r) k_{z1} dk_{z1}$$

(2.52)

$$+ \int_{-\infty}^0 \frac{\sin k_{z0} z_l}{k_{z0}} \frac{[k_{z0} \cos k_{z0}(h - z_g) - j b k_{z1} \sin k_{z0}(h - z_g)]}{[k_{z0} \cos k_{z0} h - j b k_{z1} \sin k_{z0} h]} H_0^{(1)}(k_r r) k_{z1} dk_{z1}$$

54

If the integration variable in the second expression is changed from $-k_{z1}$ to k_{z1}, the second integral can be combined with the first to yield

$$p_C(r) = 2jm \int_0^\infty \frac{\sin k_{z0}z_0 \sin k_{z0}z \, k_{z1}^2}{k_{z0}^2 m^2 \cos^2 k_{z0}h + k_{z1}^2 \sin^2 k_{z0}h} H_0^{(1)}(k_r r) dk_{z1} \qquad (2.53)$$

We again emphasize that this expression cannot be directly converted to the form of a Hankel transform.

Similarly, an expression for the trapped mode contribution in the Pekeris geoacoustic model, assuming the selection of the EJP branch-cut, can be determined. Previously, it was shown that the poles, k_{ri}, must satisfy the equation

$$k_{z0} \cos k_{z0}h - jbk_{z1} \sin k_{z0}h|_{k_r=k_{ri}} = 0 \qquad (2.54)$$

The residue, a_i, at the pole, k_{ri}, must also satisfy the equation

$$a_i \equiv \lim_{k_r \to k_{ri}} g(k_r)k_r = \frac{\sin k_{z0}z_l}{k_{z0}} \frac{[k_{z0} \cos k_{z0}(h-z_g) - jbk_{z1} \sin k_{z0}(h-z_g)]}{\frac{\partial}{\partial k_r}[k_{z0} \cos k_{z0}h - jbk_{z1} \sin k_{z0}h]}\Big|_{k_r=k_{ri}} \qquad (2.55)$$

By performing the $\partial/\partial k_r$ operation on the denominator and expanding the cosine and sine terms in the numerator, the expression for a_i becomes

$$a_i = \frac{\sin k_{z0}z \sin k_{z0}z_0 \, k_{z0}}{hk_{z0} \sin k_{z0}h \cos k_{z0}h - b^2 \sin k_{z0}h \tan k_{z0}h}\Big|_{k_r=k_{ri}} \qquad (2.56)$$

To proceed further, we use the relationship that

$$b = \frac{k_{z0}}{jk_{z1}h}\Big|_{k_r=k_{ri}} \qquad (2.57)$$

obtained from the pole equation, and a trigonometric identity for $\sin k_{z0}h \cos k_{z0}h$ to get

$$a_i = \frac{\sin k_{z0}z \sin k_{z0}z_0}{k_r(h - \frac{\sin 2k_{z0}h}{2k_{z0}} + j\frac{b\sin^2 k_{z0}h}{k_{z1}})}\Big|_{k_r=k_{ri}} \qquad (2.58)$$

Therefore, the trapped modal portion, $p_T(r)$, of the field in a Pekeris waveguide, assuming the EJP branch-cut choice, is

$$p_T(r) = \pi j \sum_{i=1}^N \frac{\sin k_{z0}z \sin k_{z0}z_0}{\frac{h}{2} - \frac{\sin 2k_{z0}h}{4k_{z0}} + j\frac{b\sin^2 k_{z0}h}{2k_{z1}}} H_0^{(1)}(k_{ri}r) \qquad (2.59)$$

55

where N is the number of poles of $g(k_r)$ on the physical Riemann sheet. This equation is identical to expressions for $p_T(r)$ found in both Tindle [14] and Bucker [19].

To summarize briefly, we have used Cauchy's theorem, for the Pekeris waveguide model and the choice of the EJP branch-cut, to decompose the field within the waveguide as

$$p(r) = p_T(r) + p_C(r) \qquad (2.60)$$

where $p_T(r)$ is the trapped modal sum and $p_C(r)$ is the continuum. The components of the modal sum are perfectly trapped because the corresponding poles of $g(k_r)$ are located on the real-k_r axis. Because the integration contour encloses these poles, they contribute to the total integral as a residue sum. The continuum, or branch-cut, integral must be retained because the integration contour cannot cross the branch-cut if $g(k_r)$ is to remain analytic. In deriving the one-sided integral expression for the continuum in equation (2.53), we have used the fact that algebraic cancellation of the real part of the Green's function occurs across the branch-cut. In the following section of this chapter, we will see that the behavior of $g(k_r)$ on both sides of the branch-cut also forms the basis of an important property concerning the finite extent of the imaginary part of $g(k_r)$. Additionally, in the next chapter we will see that the cancellation of the real part across the EJP branch-cut, is directly connected with the property of real-part/imaginary-part sufficiency for the Green's function.

We next consider the effect of selecting a different branch-cut. We point out that the total field *cannot* depend on the choice of the branch-cut since the Hankel transform integral representation does not depend on the choice of the branch-cut. We will show however, that the specification of the branch-cut determines how the total field is *partitioned* between the modal sum and the continuum. Consider the Riemann sheet diagram shown in Figure 2.16 where the branch-cut has been twisted from its position in Figure 2.15 to its present position. The selection of this particular branch-cut yields an additional physical sheet pole in quadrant I, as indicated in Figure 2.16. In effect, the branch-cut has been twisted to expose one of the poles
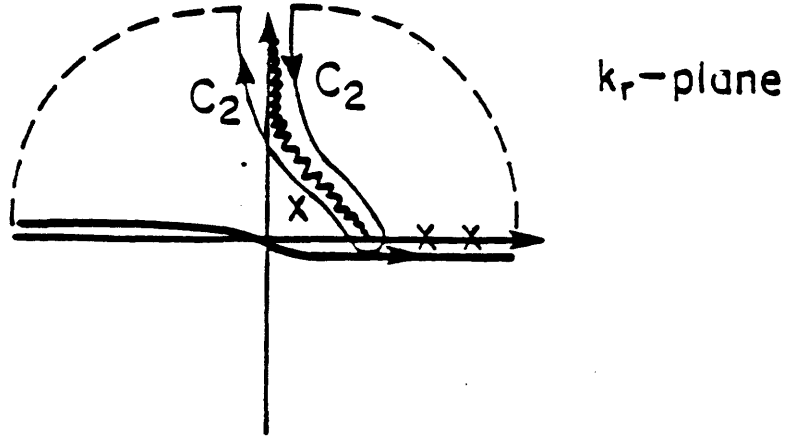
Figure 2.16: Complex k_r-plane indicating new choice of the branch-cut and an additional pole which has been exposed.

on the bottom Riemann sheet, near the imaginary axis of the complex k_r-plane, as previously displayed in Figure 2.11. Cauchy's theorem can again be applied to obtain the representation

$$p(r) = p_T(r) + p_C(r) \tag{2.61}$$

However, the precise decomposition differs from the one previously presented. Specifically, the sum $p_T(r)$ for this choice of the cut differs from the sum $p_T(r)$ for the EJP branch-cut due to the additional pole in quadrant I which is now enclosed within the contour of integration. In addition, the continuum contribution differs from that presented earlier. Specifically, although the mathematical expression for the continuum is identical to the expression presented earlier,

$$p_C(r) = - \int_{C_2} \frac{g(k_r)}{2} H_0^{(1)}(k_r r) k_r \, dk_r \tag{2.62}$$

the continuum field itself differs due to the change in the contour path C_2.

The change in $p_T(r)$ due to the new choice of branch-cut can be simply described. By examining equation (2.59) and the equations immediately preceding (2.46), it can be seen that the assumption of the EJP branch-cut is not used in the derivation of the trapped modal sum. Thus, the form of the trapped modal sum given in (2.59)

must apply to other branch-cut selections as well. The choice of the branch-cut affects *only* the number of poles which appear on the physical sheet and the manner in which the sign of k_{zi} is determined in equation (2.59). In particular, the sum corresponding to the new choice of branch-cut is identical to the sum previously discussed except that one additional pole contribution is included. The additional pole has a positive imaginary part so that the corresponding Hankel function in the sum behaves asymptotically in range as a decaying exponential. Physically, plane waves produced by the source, which have a horizontal wavenumber corresponding to the real part of this pole, undergo a partial interference which is nearly, but not completely, perfect. [*] In other words, there is a partial but not complete resonance in the corresponding wavenumber decomposition. Essentially, the sum which has resulted from the new choice of the branch-cut is no longer a trapped modal sum, but rather a modal sum, due to the additional term which is not perfectly trapped.

The above analysis can be applied to other selections of branch-cuts as well. The choice of the previous branch-cut caused one additional pole on the bottom sheet to appear on the physical sheet. By twisting the cut further towards the Pekeris cut, additional poles are exposed on the physical sheet and produce additional contributions to the modal sum. Although the corresponding modal sum changes, the continuum integral also changes in such a way that the sum of the two contributions, $p(r)$, remains fixed. The sum must be fixed because the Hankel transform integral itself does not depend on the choice of the branch cut. Essentially, the EJP branch-cut and the Pekeris branch-cut choices [17] represent extreme cases of an infinite number of equivalent field representations. For the selection of the EJP cut, there are no physical sheet poles located off the real-k_r axis. As the cut is twisted toward a vertical position, i.e. toward the Pekeris cut, poles are exposed one-by-one until an infinite number of poles [22] contribute to the modal sum. In this case, there is still a non-

---

[*]This partial interference occurs both in magnitude and phase, i.e. it is not possible to state that the plane-wave component undergoes perfectly constructive interference with respect to phase, but loses energy to the bottom due to a non-unity reflection coefficient magnitude.

zero continuum contribution, even though there are an infinite number of terms in the modal sum.

We have pointed out that the continuum portion of the field consists of plane-wave components which do not interfere in a perfectly constructive manner. An implication is that, at large ranges, the perfectly trapped modal portion of the field dominates the continuum portion. In many applications, it is reasonable to assume that the field is adequately represented by the trapped modal sum only. However, in other applications, particularly those involving the determination of the bottom reflection coefficient, the contribution of the continuum cannot be neglected. However, the difficulty in numerically computing the continuum contribution has lead to a number of different techniques for its synthesis.

One such approach, suggested by Tindle et.al. [14] , consists of approximating the continuum in a Pekeris waveguide via a sum of *virtual* modes. These virtual modes are due to the imperfect pseudo-resonances, or virtual poles of the Green's function. In Tindle's approach, the branch-line integral is approximately computed by asymptotically expanding the integrand in the vicinity of the pseudo-resonances. The locations of these pseudo-resonances are determined by the hard bottom eigenvalue equation. The result is a virtual mode sum which resembles the trapped mode sum, except that the virtual modes decay exponentially in range, and are weighted by a different amplitude factor. The theory presented by Tindle is similar to the theory presented above, in that both model portions of the continuum by including the contributions due to resonances in the Green's function. However, there are a number of important differences between the virtual mode formalism presented by Tindle and the theory which we have just presented. In particular, Tindle determines the locations of these resonances approximately by using the hard bottom eigenvalue equation. [7] In our approach however, we have shown that the equation which describes the exact loca-

---

[7] The hard bottom eigenvalue equation is only an approximation since the reflection coefficient at the virtual pole locations has a non-zero imaginary part.

tion of the virtual poles is *identical* to the equation used to determine the trapped modes - only the choice of the sign of the square root must be specified carefully. Also, Tindle incorporates the contribution of a virtual pole by asymptotically expanding the Hankel transform integral in the vicinity of the resonance. In our approach, the contribution of a virtual pole is included exactly via the use of Cauchy's theorem. In other words, the virtual pole contributes to the modal sum in exactly the same manner as a trapped mode contributes to the modal sum, except that the imaginary part of the virtual pole is non-zero. Thus, the virtual mode sum has an identical form as the trapped mode sum except that the poles are complex. Note that the amplitude of the virtual mode contribution in Tindle's approach is based on several assumptions, while in the theory just presented, an exact expression for the amplitude has been developed. In particular, the modal amplitude, related to the residue a_i at the off-axis pole, is described exactly in equation (2.59). Finally, we have pointed out that the error in approximating the continuum portion of the field by the virtual mode sum is identically the Pekeris branch-line integral.

An implication of these conclusions is that a more accurate virtual mode sum could be developed as a means for approximating the continuum. However, such a sum would still neglect the remaining branch-line contribution. That is, if the infinite number of off-axis poles were included using the above theory based on Cauchy's theorem, it would still be necessary to compute the Pekeris branch-cut integral in order to synthesize the field exactly. In our work, we have chosen not to develop such an approximate method. Rather, we have chosen to compute the branch-line integral exactly and efficiently by relating it to a Hankel transform, and relying on the use of computationally efficient methods for computing the Hankel transform. The method applies not only to the Pekeris model but to more complicated waveguide models as well, and will be discussed further in Chapter 4.

To summarize, in this section we have considered a number of the issues relating to the determination of the acoustic field in a Pekeris waveguide. We began with the

Hankel transform integral expression in terms of the Green's function for the Pekeris model. The Green's function was examined in detail and was shown to possess an ambiguity in the specification of a square root. To explain the ambiguity we considered the simpler function $z^{1/2}$ and its associated Riemann sheets. This explanation was then extended to the Green's function and a numerical example illustrating the Riemann sheets, poles, branch-cuts and their relationships was presented. We pointed out that an infinite number of representations for the acoustic field exist, dependent on the definition of the branch-cut. The EJP branch-cut and Pekeris branch-cut were shown to represent the extreme cases of these representations. Finally, we related Cauchy's theorem and the off-axis poles with the virtual mode theory discussed by Tindle, and pointed out their differences. In the following section, we will extend a number of these ideas to more complicated waveguide models.

2.4 The Field in a Layered Fluid Waveguide

In the previous section, the Green's function and the acoustic field for the simple Pekeris geoacoustic model were discussed in detail. In some situations, the Pekeris model is adequate for describing the behavior of an acoustic field within a waveguide. In other situations however, a more complicated non-isovelocity waveguide [8] overlying a horizontally stratified bottom is required. In the most general case, the properties of these layers may vary as a function of range and may support shear as well as compressional propagation. This general problem is not completely solved and is beyond the scope of this thesis. Instead, we will focus, in this section, on developing expressions for the Green's function and acoustic field in a waveguide which consists of fluid layers with range-independent properties.

In our discussion, we will, as in the case of the Pekeris waveguide, relate the acoustic field within the waveguide to the depth-dependent Green's function via the Hankel transform. Therefore, most of the presentation will concentrate on developing the Green's function for the horizontally stratified fluid model. This basic idea of relating the acoustic field to the Green's function is not new and has been discussed by a number of researchers. In fact, there are a number of techniques already in existence for determining the Green's function for a layered model [2], [9], [24], [25], [26] . These techniques yield identical theoretical results but have differing properties with respect to numerical accuracy and computational efficiency. In our work, a new technique, referred to as *Green's function migration*, has been developed which again yields a theoretically identical result for the Green's function. While we are not proposing that the technique has superior numerical properties, it has been implemented numerically and compares favorably with other techniques in terms of accuracy and efficiency. The advantage of the new approach however, is that it provides the basis for developing a number of important properties of the Green's function. We will find these properties

---

[8]Non-isovelocity refers to the source and receiver residing within layers having different acoustic properties.
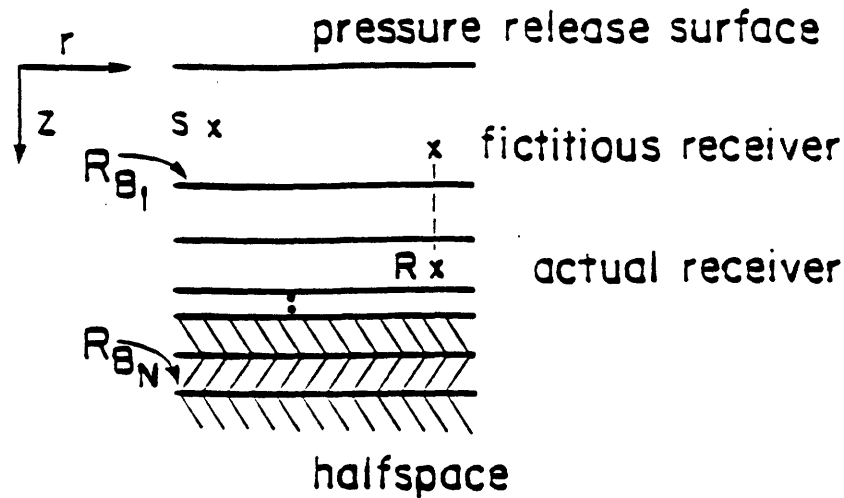
Figure 2.17: Non-isovelocity waveguide with a pressure release surface. The fictitious receiver is located in the same layer as the source while the actual receiver is located in an underlying layer.

to be useful in later chapters of this thesis.

The essential idea of the new technique is to determine the Green's function for a non-isovelocity waveguide by first determining a fictitious Green's function, in which the source and receiver reside within the same layer, and then migrating the Green's function down through the layers to the appropriate depth. To see this more clearly, consider the non-isovelovity waveguide depicted in Figure 2.17. To determine the Green's function for this configuration of the source and receiver, we will first determine the Green's function for the fictitious receiver located in the top layer and then migrate the Green's function to the actual receiver depth. The method relies on the fact that it is straightforward to determine the Green's function for the fictitious receiver. This Green's function corresponds to an isovelocity waveguide overlying a layered media, and has the identical form as the Pekeris model Green's function except that the bottom reflection coefficient, R_{B_1}, differs. [9]

---

[9]In the remainder of this section, we will often omit the explicit dependence of reflection coefficients and Green's functions on the horizontal wavenumber k_r, for notational convenience.

Specifically, the reflection coefficient R_{B_1} for the layered model is not a Rayleigh reflection coefficient, and must be determined from the geoacoustic properties of all underlying layers and the halfspace. Again, numerous methods exist for computing this reflection coefficient. However, we will focus on a particular existing method [27], [28] for computing the reflection coefficient. The method is based on determining the reflection coefficient R_{B_1} by first determining the reflection coefficient, R_{B_N}, at the interface between the lowest layer and the underlying halfspace, and then migrating this reflection coefficient up through the layers. The reflection coefficient R_{B_N} is simply determined since it is a Rayleigh reflection coefficient. This approach for determining R_{B_1}, which we will refer to as *reflection coefficient migration*, can be contrasted with alternate propagator matrix based methods. In these latter methods, both the upgoing fields and downgoing fields are propagated across layers, and at the top layer their ratio is computed to yield the reflection coefficient. In the reflection coefficient migration method however, the ratio itself is propagated, or migrated, directly. An advantage of the formulation is that properties of the reflection coefficient, particularly with respect to the influence of underlying layers, are more easily established by working with this ratio throughout. Additionally, the reflection coefficient migration technique yields the partial reflection coefficient at each intermediate layer interface. The sequence of these partial reflection coefficients will be shown to be an important component in the Green's function migration method. The reflection coefficient migration method also provides the basis for a convenient computational algorithm for determining the reflection coefficient.

The material in this section is organized as follows. First, the reflection coefficient migration approach will be discussed in detail. Next, using this approach, we will derive two important properties of the reflection coefficient. The first property relates to the number of branch points present in the case that there are multiple layers. The second is a symmetry property in the complex k_r-plane and will be required in later discussions. Next, we will consider the situation that the source and receiver are located within different layers, i.e. the non-isovelocity waveguide case. We will

refer to the corresponding Green's function as the *extended Green's function*. The expression for the extended Green's function will be developed using the Green's function migration method. Three important properties of the Green's function and extended Green's function will then be derived. First, it will be shown that although there are multiple layers present, the square root ambiguity implies that only two Riemann sheets are present. Next, a symmetry property for the Green's function and extended Green's function is presented. Using this property, we will next develop a property related to the finite extent of the imaginary part of these Green's functions. Finally, we will consider the application of Cauchy's theorem. Because there are only two Riemann sheets of $g(k_r)$ present, most of the issues related to branch-cut selection, resonances, and virtual modes are identical to those presented in the previous section. Expressions for the pole locations and coresponding residues will be presented, and these expressions will be used in the numerical examples in Chapter 4.

We begin the discussion by restating the form of the Green's function for an isovelocity waveguide, in terms of the reflection coefficients at its top and bottom

$$g(k_r) = \frac{j(e^{-jk_z z_l} + R_S e^{jk_z z_l})(e^{jk_z z_s} + R_B e^{jk_z(2h - z_s)})}{k_z(1 - R_S R_B e^{j2k_z h})} \qquad (2.63)$$

In order to develop the relationship between $g(k_r)$ and the geoacoustic parameters of the underlying media, the specific relationship between R_B and these parameters is required. We will now develop this relationship based on the reflection coefficient migration approach.

To do this, consider the layered structure shown in Figure 2.18. Using the reflection coefficient migration method, we will relate the reflection coefficient R_{B_i}, at the $(i - 1)/i$ interface to the reflection coefficient $R_{B_{i+1}}$, at the next lower interface, $i/(i + 1)$. By relating these, it is possible to obtain the set of all reflection coefficients at the layer interfaces, and we will refer to the complete set, $\{R_{B_i}\}$, as the *reflectivity series*. Although it is only the first term in the reflectivity series which is required in the isovelocity waveguide Green's function expression, we will later see that the other terms are required for the extended Green's function construction. Note that each
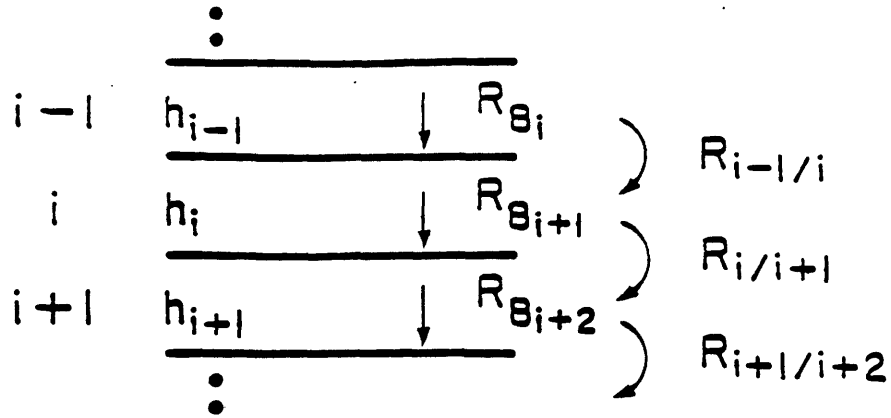
Figure 2.18: Layer structure and various reflection coefficients. The reflection coefficient R_{B_i} refers to the total reflection coefficient looking down from layer $i - 1$. The reflection coefficient $R_{i/i+1}$ refers to the Rayleigh reflection coefficient at the boundary between layer i and $i + 1$.

term in the reflectivity series is not the Rayleigh reflection coefficient between two adjacent layers. Rather, the properties of all underlying layers influence each reflection coefficient in the reflectivity series. Therefore, as illustrated in Figure 2.18, R_{B_i} refers to the total reflection coefficient looking down from the $(i - 1)^{th}$ layer. In this figure, the reflection coefficient $R_{i/i+1}$ refers to the Rayleigh reflection coefficient looking down from the ith to the $(i + 1)^{th}$ layer.

Referring again to Figure 2.18, consider a particular plane-wave k_r component of the acoustic field propagating within layer i. The z-dependence of this component must have the form

$$f(k_r; z; i) = c[e^{jk_{ni}z} + R_{B_{i+1}} e^{-jk_{ni}z}] \qquad (2.64)$$

which consists of a downgoing component, plus an upgoing component which is weighted by the reflection coefficient at the $i/(i + 1)$ interface. At this interface we have assumed that $z = 0$, and the ratio of the second term to the first term above is simply $R_{B_{i+1}}$. At the top of layer i just below the interface, $z = -h_i$ and this

66

component has the form

$$f(k_r; z; i)|_{z=-h_i} = c[e^{-jk_{zi}h_i} + R_{B_{i+1}}e^{jk_{zi}h_i}] \tag{2.65}$$

Next, assume that the wavenumber component within layer $(i - 1)$ is of the form

$$f(k_r; z; i - 1) = c[ae^{jk_{zi-1}(z+h_i)} + be^{-jk_{zi-1}(z+h_i)}] \tag{2.66}$$

This expression also consists of the sum of an upgoing term plus a downgoing term, weighted by a reflection coefficient. By definition, the reflection coefficient at the bottom of the $(i - 1)^{th}$ layer, where $z = -h_i$, is $R_{B_i} = b/a$. In order to determine the coefficients a and b, we invoke the continuity conditions across the $(i - 1)/i$ boundary

$$f(k_r; z; i - 1)|_{z=-h_i} = f(k_r; z; i)|_{z=-h_i}$$
$$\frac{1}{\rho_{i-1}}\frac{\partial f(k_r; z; i-1)}{\partial z}\Big|_{z=-h_i} = \frac{1}{\rho_i}\frac{\partial f(k_r; z; i)}{\partial z}\Big|_{z=-h_i} \tag{2.67}$$

Performing the required algebra to solve for a and b, and computing their ratio, we obtain

$$R_{B_i} = \frac{R_{i-1/i} + R_{B_{i+1}}e^{j2k_{zi}h_i}}{1 + R_{i-1/i}R_{B_{i+1}}e^{j2k_{zi}h_i}} \,. \tag{2.68}$$

In deriving this well known expression [27], [28], the reflection coefficient $R_{B_{i+1}}$ at the lower interface has been migrated through a layer and across the next higher interface to obtain the reflection coefficient R_{B_i}. From this expression, it is apparent that R_{B_i} depends on the properties of layer i and on the properties of all underlying media via $R_{B_{i+1}}$. Additionally, although the reflection coefficient has been migrated through only a single layer, the approach for migrating it through additional layers is clear - the reflection coefficient R_{B_i} at the bottom of layer $i - 1$ can be migrated through this layer to obtain the reflection coefficient at the bottom of layer $i - 2$, etc. Thus, the method for obtaining all the terms in the reflectivity series is to: 1) determine the Rayleigh reflection between the lowest layer and the underlying halfspace, 2) migrate the reflection coefficient up through each higher layer i using equation (2.68).

Although the form of the migrated reflection coefficient in equation (2.68) was derived mathematically by matching boundary conditions, this form has a physical

interpretation as well. Specifically, equation (2.68) incorporates all possible paths of reflection which can occur when a plane wave is incident at the $(i-1)/i$ interface. To see that this is the case, assume for simplicity that $i = 1$. The reflection coefficient R_{B_1} is written in terms of R_{B_2} using equation (2.68) as

$$R_{B_1} = \frac{R_{0/1} + R_{B_2} e^{j2k_{z1}h_1}}{1 + R_{0/1} R_{B_2} e^{j2k_{z1}h_1}} \qquad (2.69)$$

The denominator of this expression can be expanded as a series so that

$$R_{B_1} = (R_{0/1} + R_{B_2} e^{j2k_{z1}h_1})[1 - R_{0/1} R_{B_2} e^{j2k_{z1}h_1} + (R_{0/1} R_{B_2} e^{j2k_{z1}h_1})^2 - ...] \qquad (2.70)$$

Combining terms and simplifying, it is apparent that

$$R_{B_1} = R_{0/1} + (1 - R_{0/1}{}^2) R_{B_2} e^{j2k_{z1}h_1} - R_{0/1}(1 - R_{0/1}^2) R_{B_2}{}^2 e^{j4k_{z1}h_1} + ... \qquad (2.71)$$

Now, using the definition of the transmission coefficient $T_{0/1} \equiv 1 - R_{0/1}$ and the identity $R_{1/0} = -R_{0/1}$, where the notation $1/0$ indicates propagation from medium 1 to medium 0, we have that

$$R_{B_1} = R_{0/1} + T_{0/1} R_{B_2} T_{1/0} e^{j2k_{z1}h_1} + T_{0/1} R_{B_2} R_{1/0} R_{B_2} T_{1/0} e^{j4k_{z1}h_1} + ... \qquad (2.72)$$

From this series, it is apparent that R_{B_1} accounts for all of the possible ways in which the incident plane wave can be reflected. Specifically, the first term in equation (2.72) accounts for the Rayleigh reflection due to the impedance contrast between medium 0 and medium 1. The second term in the series accounts for the reflection due to transmission into media 1, reflection at the 1/2 interface, and re-transmission from medium 1 to medium 0. Similarly, the higher order terms in equation (2.72) represent the multiple reflections which can occur within layer 1. The associated phase factor of each term accounts for the length of the path followed by each reflected component. Also note that in the case that medium 1 is a thick high-speed layer, the imaginary vertical wavenumber which occurs when $k_r > k_1$, yields a reflection coefficient which is approximately the Rayleigh reflection coefficient. That is,

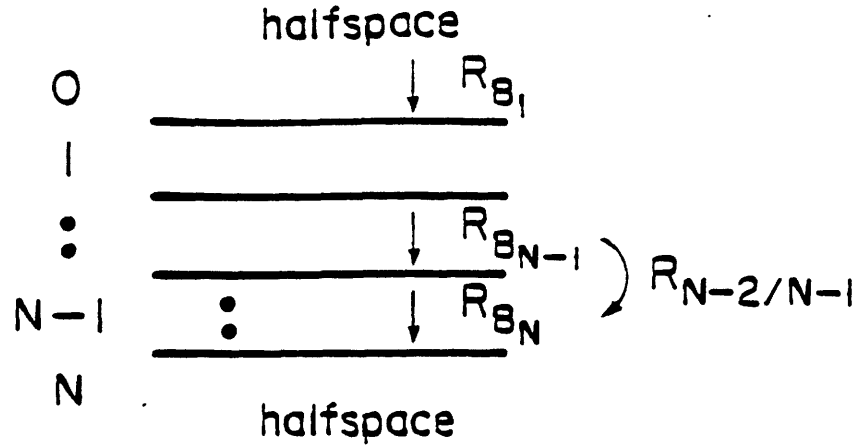$$R_{B_1} \sim R_{0/1} \qquad (2.73)$$

68

Figure 2.19: Layer model indicating overlying and underlying halfspaces.

when k_{z1} is purely imaginary and h_1 is large, as can be concluded by examining equation (2.69). Similarly, it can be shown that the partial reflection coefficient at any interface which overlies a thick high-speed layer approaches the Rayleigh reflection coefficient, for horizontal wavenumbers greater than the layer wavenumber. The physical interpretation is that the underlying layers have negligible effect due to the fact that insignificant penetration of energy occurs.

We have defined the reflectivity series as the set of all intermediate reflection coefficients at layer interfaces within a stack of layers. Each term in the reflectivity series is related to an adjacent term via equation (2.68), and a physical interpretation of this equation has been provided. Referring to Figure 2.19, it can be seen that the first term in this set is most important. This reflection coefficient, R_{B_1}, incorporates the geoacoustic properties of all underlying layers and summarizes the effect that the stack of layers has on an impinging plane wave. This reflection coefficient is also required in the expression for the isovelocity waveguide Green's function. In this case the source and receiver are assumed to reside in layer 0, and the corresponding Green's function expression is written as

$$g(k_r) = \frac{j(e^{-jk_{z0}z_r} + R_S e^{jk_{z0}z_r})(e^{jk_{z0}z_s} + R_{B_1} e^{jk_{z0}(2h_0 - z_s)})}{k_{z0}(1 - R_S R_{B_1} e^{j2k_{z0}h_0})} \qquad (2.74)$$

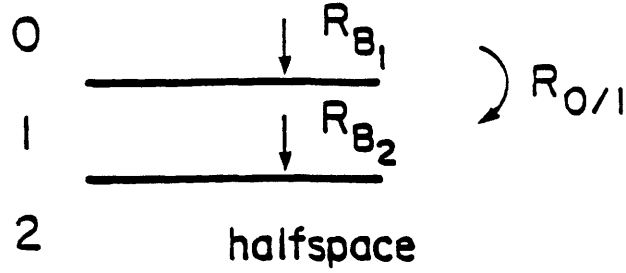Because of its importance, we will now derive two useful properties of the reflection

69

Figure 2.20: Simplified one layer model.

coefficient R_{B_1}. The first of these properties is well known [2], [29], however we believe the second property to be new.

The first property to be developed is that R_{B_1} is an even function of each vertical wavenumber k_{zi}. Essentially, the presence of additional k_{zi} terms within the reflection coefficient migration method suggests that additional square root ambiguities might exist. In order to demonstrate that this is not the case, we will now show that R_{B_1} is an even function of these wavenumbers. To prove this, consider the simplified layered model depicted in Figure 2.20, and the reflection coefficient migration expression

$$R_{B_1} = \frac{R_{0/1} + R_{B_2}e^{j2k_{z1}h_1}}{1 + R_{0/1}R_{B_2}e^{j2k_{z1}h_1}} \tag{2.75}$$

Since medium 2 is a halfspace, both $R_{0/1}$ and R_{B_2} are Rayleigh reflection coefficients and thus

$$R_{B_2} = \frac{k_{z1} - b_1 k_{z2}}{k_{z1} + b_1 k_{z2}} \quad \text{where } b_1 \equiv \rho_1/\rho_2 \tag{2.76}$$

and

$$R_{0/1} = \frac{k_{z0} - b_0 k_{z1}}{k_{z0} + b_0 k_{z1}} \quad \text{where } b_0 \equiv \rho_0/\rho_1 \tag{2.77}$$

Suppose that R_{B_1} for this model is evaluated at the same value of k_r but with the opposite sign choice for k_{z1}. Notationally, we will use ′ to denote evaluation of a

70

quantity using the opposite choice of the sign of k_{z1}. Therefore,

$$R'_{B_2} = \frac{-k_{z1} - b_1 k_{z2}}{-k_{z1} + b_1 k_{z2}} = 1/R_{B_2} \qquad (2.78)$$

and

$$R'_{0/1} = \frac{k_{z0} + b_0 k_{z1}}{k_{z0} - b_0 k_{z1}} = 1/R_{0/1} \qquad (2.79)$$

Substituting these values into the expression for R'_{B_1}, it is apparent that

$$R'_{B_1} = \frac{R'_{0/1} + R'_{B_2} e^{-j2k_{z1}h_1}}{1 + R'_{0/1} R'_{B_2} e^{-j2k_{z1}h_1}} = \frac{1/R_{0/1} + 1/R_{B_2} e^{-j2k_{z1}h_1}}{1 + (1/R_{0/1})(1/R_{B_2}) e^{-j2k_{z1}h_1}} \qquad (2.80)$$

Multiplying numerator and denominator by $R_{0/1} R_{B_2} e^{j2k_{z1}h_1}$, we see that

$$R'_{B_1} = \frac{R_{0/1} + R_{B_2} e^{j2k_{z1}h_1}}{1 + R_{0/1} R_{B_2} e^{j2k_{z1}h_1}} = R_{B_1} \qquad (2.81)$$

Thus, the choice of the sign of the vertical wavenumber within layer 1, does not affect the value of the reflection coefficient R_{B_1}.

This analysis can be applied in an identical manner to further prove that the reflection coefficient does not depend on the choice of the sign of the vertical wavenumber within *any* layer, in the situation that multiple layers are present. It is straightforward to show that the reflection coefficient *does* depend on the choice of the sign of the vertical wavenumber in any halfspace. For example, referring to Figure 2.19, where media 0 and N are assumed to be isovelocity halfspaces, it can be shown that $R_{B_1}(k_r)$ is not an even function of k_{z0}, and not an even function of k_{zN}. An implication is that it is necessary to consider four Riemann sheets, when evaluating the reflection coefficient in the complex k_r-plane.

The next property to be developed is the conjugate symmetry property for the reflection coefficient

$$R_{B_1}(k_r^*) = R_{B_1}^*(k_r) \qquad (2.82)$$

This property is important because it implies constraints on the poles, zeros, and residues of the reflection coefficient. The property applies separately on each Riemann

71

sheet and is only valid in the case that EJP branch-cuts are selected in determining k_{z0} and k_{zN}. In evaluating this expression for real values of k_r, we point out that since there are branch-cuts which lie along a portion of the real axis, the expression must be evaluated as the real axis is approached from either above or below. Additionally, we will show that this property applies not only to the first term in the reflectivity series but to all terms in this series as well.

To prove this, consider the reflection coefficient $R_{B_{N-1}}$ for the model shown in Figure 2.19 where medium N is assumed to be an isovelocity halfspace. Using the reflection coefficient migration equation, we have that

$$R_{B_{N-1}}(k_r) = \frac{R_{N-2/N-1} + R_{B_N} e^{j2k_{zN-1}h_{N-1}}}{1 + R_{N-2/N-1} R_{B_N} e^{j2k_{zN-1}h_{N-1}}} \qquad (2.83)$$

Recall that R_{B_N} is the Rayleigh reflection coefficient

$$R_{B_N}(k_r) = \frac{k_{zN-1} - b_{N-1}k_{zN}}{k_{zN-1} + b_{N-1}k_{zN}} \quad \text{where } b_{N-1} = \rho_{N-1}/\rho_N \qquad (2.84)$$

and that the vertical wavenumber in the ith medium is $k_{zi} = \pm(k_i^2 - k_r^2)^{1/2}$. From earlier arguments, all sign choices are arbitrary except for the sign associated with k_{zN}. We therefore choose all square root signs such that $Im\{k_{zi}\} \geq 0$, corresponding to the EJP cut for each of these square roots. If we let $k_r' \equiv k_r^*$, it is apparent that $k_{zi}' = \pm k_{zi}^*$, where the sign must be chosen such that $Im\{k_{zi}\} \geq 0$, and thus $k_{zi}' = -k_{zi}^*$. Substituting this result into equation (2.84) for R_{B_N}, we find that

$$R_{B_N}(k_r^*) = R_{B_N}^*(k_r) \qquad (2.85)$$

Similarly, it is easily shown that $R_{N-2/N-1}(k_r^*) = R_{N-2/N-1}^*(k_r)$. Substituting these results into the reflection coefficient migration equation (2.83), we have that

$$R_{B_{N-1}}(k_r^*) = \frac{R_{N-2/N-1}^* + R_{B_N}^* e^{-j2k_{zN-1}^* h_{N-1}}}{1 + R_{N-2/N-1}^* R_{B_N}^* e^{-j2k_{zN-1}^* h_{N-1}}} = R_{B_{N-1}}^*(k_r) \qquad (2.86)$$

Continuing in this manner, it follows that all reflection coefficients in the reflectivity series must satisfy the property that $R_{B_i}(k_r^*) = R_{B_i}^*(k_r)$.

It is also possible to develop other interesting and important properties of the reflection coefficient and the reflectivity series in a similar style. For example, by relating adjacent terms in the reflectivity series using equation (2.68), statements concerning constraints on the poles of these reflection coefficients can be made. Although we have chosen not to further develop these properties in this thesis, their development is suggested as an interesting topic for future research. Instead, given the expression in equation (2.63) for the Green's function corresponding to an isovelocity waveguide overlying a layered medium, we will next discuss a method for obtaining the extended Green's function. With analogy to the reflection coefficient migration method, we will develop the Green's function migration method as a means for determining the extended Green's function.

Consider the form of the Green's function in equation (2.63) for the source and receiver in layer 0. To emphasize the fact that the receiver resides within layer 0, we will use the subscript 0, and re-write this expression as

$$g_0(k_r) = c_0(e^{jk_{z0}z_s} + R_{B_1}e^{j2k_{z0}h_0}e^{-jk_{z0}z_s})$$ (2.87)

where

$$c_0 = \frac{j(e^{-jk_{z0}z_l} + R_S e^{jk_{z0}z_l})}{k_{z0}(1 - R_S R_{B_1} e^{j2k_{z0}h_0})}$$ (2.88)

Now suppose that this fictitious receiver is moved downward towards the bottom of layer 0. At some depth, the receiver depth z must exceed the source depth z_0. Thus, for larger receiver depths, $z_s = z$, and $z_l = z_0$, and the corresponding Green's function, $g_0(k_r)$, is written as

$$g_0(k_r) = c_0(e^{jk_{z0}z} + R_{B_1}e^{j2k_{z0}h_0}e^{-jk_{z0}z})$$ (2.89)

This form of the Green's function indicates that, at each horizontal wavenumber, there exists a downgoing component, $e^{jk_{z0}z}$, plus an upgoing component, $e^{-jk_{z0}z}$, weighted in amplitude by the reflection coefficient at the next lower interface. The downgoing and upgoing components propagate with the vertical wavenumber in medium 0.

The Green's function for the receiver located in the next lower layer must be of the form

$$g_1(k_r) = ae^{jk_{z1}z} + be^{-jk_{z1}z} \qquad (2.90)$$

in order to satisfy the homogeneous ordinary differential equation for the Green's function, as discussed in Section 2.2. The constants a and b must be chosen to satisfy the continuity boundary conditions at the 0/1 interface - the two continuity conditions exactly specify the two apparent degrees of freedom in the solution [28]. By matching this Green's function with the Green's function in equation (2.89), we have migrated the Green's function across the boundary between layer 0 and layer 1.

A slightly more convenient choice for the Green's function $g_1(k_r)$ is

$$g_1(k_r) = c_1(e^{jk_{z1}(z-h_0)} + R_{B_2}e^{j2k_{z1}h_1}e^{-jk_{z1}(z-h_0)}) \qquad (2.91)$$

Note that this form for $g_1(k_r)$ is similar to the form for $g_0(k_r)$, shown in equation (2.89). In other words, this form of $g_1(k_r)$ contains a downgoing component plus an upgoing component weighted by the reflection coefficient R_{B_2}. These components propagate with the vertical wavenumber in medium 1, and at $z = h_0 + h_1$, the ratio of the upgoing component to the downgoing component is R_{B_2}. Also note that there is only one apparent degree of freedom in this expression. In order for the expression to be a valid expression for the Green's function, it is necessary that c_1 satisfy both boundary conditions at the 0/1 interface. We now determine c_1 and show that this choice satisfies both of these boundary conditions.

The pressure continuity condition which must be satisfied is

$$g_0(k_r)|_{z=h_0} = g_1(k_r)|_{z=h_0} \qquad (2.92)$$

Substituting $z = h_0$ into equations (2.89) and (2.91) for g_0 and g_1 yields the relationship

$$c_0e^{jk_{z0}h_0}(1 + R_{B_1}) = c_1(1 + R_{B_2}e^{j2k_{z1}h_1}) \qquad (2.93)$$

Thus, in order for the pressure continuity condition to be satisfied, c_1 must be chosen such that

$$c_1 = e^{jk_{z0}h_0}\frac{(1 + R_{B_1})}{(1 + R_{B_2}e^{jk_{z1}h_1})}c_0 \tag{2.94}$$

It is possible to put this expression in an alternate form using the formula for reflection coefficient migration developed previously. Specifically, since

$$R_{B_1} = \frac{R_{0/1} + R_{B_2}e^{j2k_{z1}h_1}}{1 + R_{0/1}R_{B_2}e^{j2k_{z1}h_1}} \tag{2.95}$$

R_{B_2} can be related to R_{B_1} as

$$R_{B_2} = \frac{R_{B_1} - R_{0/1}}{1 - R_{B_1}R_{0/1}}e^{-j2k_{z1}h_1} \tag{2.96}$$

Substituting this expression for R_{B_2} into equation (2.94) and performing some algebra, it is straightforward to show that

$$\frac{1 + R_{B_1}}{1 + R_{B_2}e^{jk_{z1}h_1}} = \frac{1}{2}\left(\frac{k_{z0}}{k_{z1}} + \frac{\rho_0}{\rho_1}\right)(1 - R_{B_1}R_{0/1})\frac{\rho_1}{\rho_0} \tag{2.97}$$

and thus

$$c_1 = \frac{1}{2}e^{jk_{z0}h_0}\left(\frac{k_{z0}}{k_{z1}} + \frac{\rho_0}{\rho_1}\right)(1 - R_{B_1}R_{0/1})\frac{\rho_1}{\rho_0}c_0 \tag{2.98}$$

We now show that this choice of c_1 also satisfies the particle velocity continuity condition at the 0/1 interface. Specifically, evaluating the boundary condition

$$\frac{1}{\rho_0}\frac{\partial g_0(k_r)}{\partial z}\Big|_{z=h_0} = \frac{1}{\rho_1}\frac{\partial g_1(k_r)}{\partial z}\Big|_{z=h_0} \tag{2.99}$$

using equations (2.89) and (2.91) for g_0 and g_1 yields

$$\frac{1}{\rho_0}c_0jk_{z0}e^{jk_{z0}h_0}(1 - R_{B_1}) = \frac{1}{\rho_1}c_1jk_{z1}(1 - R_{B_2}e^{j2k_{z1}h_1}) \tag{2.100}$$

and thus

$$c_1 = \frac{\rho_1 k_{z0}}{\rho_0 k_{z1}}e^{jk_{z0}h_0}\frac{(1 - R_{B_1})}{(1 - R_{B_2}e^{j2k_{z1}h_1})}c_0 \tag{2.101}$$

Substituting the relationship between R_{B_2} and R_{B_1} in equation (2.96) into this equation and performing some algebra yields

$$c_1 = \frac{1}{2}e^{jk_{z0}h_0}\left(\frac{k_{z0}}{k_{z1}} + \frac{\rho_0}{\rho_1}\right)(1 - R_{B_1}R_{0/1})\frac{\rho_1}{\rho_0}c_0 \tag{2.102}$$

Note that this choice of c_1 is identical to the value shown in equation (2.98) and thus c_1 satisfies both continuity conditions.

To summarize, the form for the Green's function, when the receiver is located in either medium 0 or medium 1 is

$$
\begin{aligned}
g_0(k_r) &= c_0(e^{jk_{z0}z} + R_{B_1}e^{j2k_{z0}h_0}e^{-jk_{z0}z}) & z_0 < z < h_0 \\
g_1(k_r) &= c_1(e^{jk_{z1}(z-h_0)} + R_{B_2}e^{j2k_{z1}h_1}e^{-jk_{z1}(z-h_0)}) & h_0 < z < h_1
\end{aligned}
\tag{2.103}
$$

where

$$
\begin{aligned}
c_0 &= j(e^{-jk_{z0}z_l} + R_S e^{jk_{z0}z_l})/[k_{z0}(1 - R_S R_{B_1}e^{j2k_{z0}h})] \\
c_1 &= \tfrac{1}{2}e^{jk_{z0}h_0}(\tfrac{k_{z0}}{k_{z1}} + \tfrac{\rho_0}{\rho_1})(1 - R_{B_1}R_{0/1})\tfrac{\rho_1}{\rho_0}c_0
\end{aligned}
\tag{2.104}
$$

The migration approach can also be used to determine the Green's function in the case that the receiver resides within layer 2. In this situation, the form of the Green's function must be

$$
g_2(k_r) = c_2(e^{jk_{z2}(z-H_1)} + R_{B_3}e^{j2k_{z2}h_2}e^{-jk_{z2}(z-H_1)})
\tag{2.105}
$$

where $H_1 \equiv h_0 + h_1$. It is straightforward to show that c_2 can be chosen such that both continuity conditions at the 1/2 interface are satisfied, i.e. so that

$$
\begin{aligned}
g_1(k_r)|_{z=h_1} &= g_2(k_r)|_{z=h_1} \\
\tfrac{1}{\rho_1}\tfrac{\partial g_1(k_r)}{\partial z}\Big|_{z=h_1} &= \tfrac{1}{\rho_2}\tfrac{\partial g_2(k_r)}{\partial z}\Big|_{z=h_1}
\end{aligned}
\tag{2.106}
$$

Performing the required algebra, we have that

$$
c_2 = \frac{1}{2}e^{jk_{z1}h_1}\Big(\frac{k_{z1}}{k_{z2}} + \frac{\rho_1}{\rho_2}\Big)(1 - R_{B_2}R_{1/2})\frac{\rho_2}{\rho_1}c_1
\tag{2.107}
$$

Note the similarity between equation (2.107), which relates c_2 to c_1, and equation (2.104), which relates c_1 and c_0.

Proceeding inductively, if the receiver is located in an arbitrary layer i, the migration method yields the extended Green's function expression,

$$
g_i(k_r) = c_i(e^{jk_{zi}(z-H_{i-1})} + R_{B_{i+1}}e^{j2k_{zi}h_i}e^{-jk_{zi}(z-H_{i-1})})
\tag{2.108}
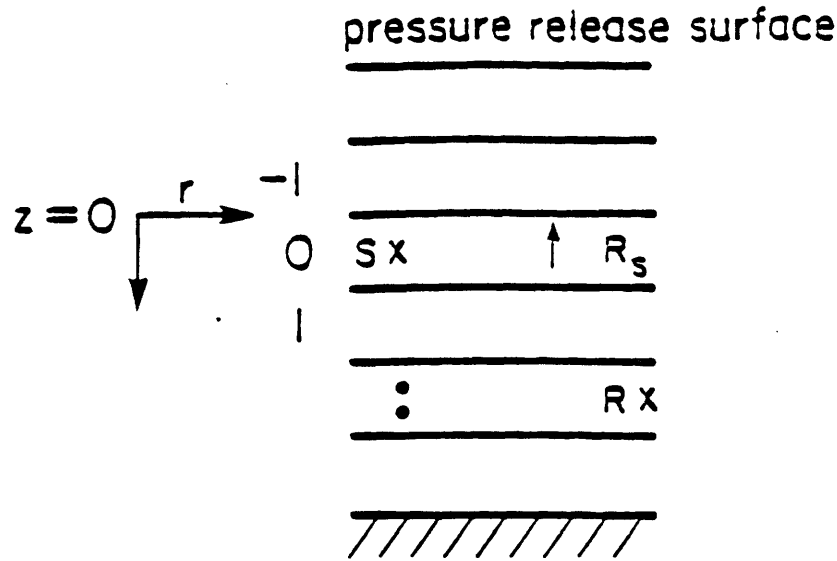$$

76

pressure release surface

Figure 2.21: Non-isovelocity waveguide in which the source is not in the top layer. The coordinate system can be re-defined so that the overlying layer structure is incorporated in the surface reflection coefficient.

where

$$H_i \equiv h_0 + h_1 + ...h_i \qquad (2.109)$$

$$c_i = \frac{1}{2}e^{jk_{zi-1}h_{i-1}}\left(\frac{k_{zi-1}}{k_{zi}} + \frac{\rho_{i-1}}{\rho_i}\right)(1 - R_{B_i}R_{i-1/i})\frac{\rho_i}{\rho_{i-1}}c_{i-1} \quad i > 0 \qquad (2.110)$$

and

$$c_0 = \frac{j(e^{-jk_{z0}z_1} + R_S e^{jk_{z0}z_1})}{k_{z0}(1 - R_S R_{B_1}e^{j2k_{z0}h_0})} \qquad (2.111)$$

Note that the terms R_{B_i}, which are required in the recursive computation of the extended Green's function, are also the elements of the reflectivity series, discussed earlier.

For the case in which the source is not in the top layer, an expression for the Green's function and extended Green's function can be obtained from equations (2.108) and (2.110) in a straightforward manner. The approach is to redefine the coordinate system so that $z = 0$ corresponds to the top of the layer in which the source is located. For example, as shown in Figure 2.21, the source is no longer in the top layer. However, by defining all depth variables with respect to $z = 0$ at the 0/-1 interface, and by determining an expression for R_S looking from medium 0 toward

medium -1, equations (2.108) and (2.110) apply. In addition, R_S for this case can be determined by using the reflection coefficient migration method applied to the overlying layers.

To summarize, an expression for the extended Green's function has been determined using the Green's function migration method. In this method, the isovelocity waveguide Green's function is migrated across layer boundaries. In addition, we have pointed out that the source need not reside within the top layer. In this case, the location of the $z = 0$ coordinate is simply re-defined as the nearest interface above the source, and the effects of the overlying media are incorporated in the definition of the surface reflection coefficient, R_S. In our analyis, we have assumed that the receiver is located at a depth greater than that of the source. In the opposite case, the expressions for the Green's function and extended Green's function remain the same, except that the variables z and z_0 are interchanged, from reciprocity. We will next prove three important properties of the Green's function and extended Green's function.

Previously, it was shown that the reflection coefficient $R_{B_1}(k_r)$ does not depend on the choice of the sign of the vertical wavenumber within any layer. However, $R_{B_1}(k_r)$ depends on the signs of both k_{z0} and k_{zN}. In the isovelocity waveguide problem however, the important quantity to consider is not $R_{B_1}(k_r)$, but rather the Green's function $g(k_r)$. From the definition [10] of $g(k_r)$, it is apparent that since the $R_{B_1}(k_r)$ is even in $k_{z1}, k_{z2}, ...k_{zN-1}$, $g(k_r)$ must also be even in these variables. It can also be shown that both $R_{B_1}(k_r)$ and $g(k_r)$ depend on the choice of the sign of the wavenumber in the underlying halfspace. We now show that, although $R_{B_1}(k_r)$ is not even in k_{z0}, $g(k_r)$ must be even in k_{z0}. To do this, we must prove that $g(k_r)$ in equation (2.74) is

---

[10]Recall that $g_0(k_r)$ and $g(k_r)$ are identical functions. Both apply to the case that the receiver and source reside within layer 0. We will refer to both $g(k_r)$ and $g_0(k_r)$ as the Green's function, and to $g_i(k_r)$ for $i \neq 0$ as the extended Green's function.

even in k_{z0}. Consider replacing k_{z0} by $-k_{z0}$ in this equation so that

$$g'(k_r) = \frac{j(e^{jk_{z0}z_s} + R'_S e^{-jk_{z0}z_s})(e^{-jk_{z0}z_s} + R'_{B_1} e^{-jk_{z0}(2h_0-z_s)})}{-k_{z0}(1 - R'_S R'_{B_1} e^{-j2k_{z0}h_0})} \tag{2.112}$$

Using the facts that, $R'_{B_1}(k_r) = 1/R_{B_1}(k_r)$, and $R'_S(k_r) = 1/R_S(k_r)$, where $'$ indicates the alternate choice of the sign of k_{z0}, and performing some algebra, it can be shown that

$$g'(k_r) = g(k_r) \tag{2.113}$$

Thus, $g(k_r)$ does not depend on the choice of the sign in *any* layer, including layer 0.

Similarly, the extended Green's function does not depend on the choice of the sign of the vertical wavenumber in any layer. It is difficult to argue this statement algebraically. However, this fact can be established using an alternate line of reasoning. Consider the source and receiver positioned within the top layer. The presence or lack of a branch point in the complex k_r-plane associated with a square root ambiguity must be independent of the specific locations of the source and receiver within the layer, i.e. independent of z and z_0. This must also be the case if the receiver is re-positioned out of this layer. For example, if the receiver is located within layer 1, the presence or lack of presence of a branch point must be independent of the position of the receiver within this layer. Now, suppose that the receiver is located just below the 0/1 interface, i.e. at $z = h_0$. Using the continuity condition that

$$g_0(k_r)|_{z=h_0} = g_1(k_r)|_{z=h_0} \tag{2.114}$$

we note that if g_0 depends on the sign of a particular vertical wavenumber, g_1 must also depend on this choice of sign, in order to satisfy this continuity condition. Similarly, if g_0 is independent of a particular choice of square root sign, g_1 must also be independent of this choice. Thus, by invoking the continuity conditions at each interface, it is seen that the extended Green's function must depend on the signs of k_{zi} in *exactly* the same manner as g_0 depends on these quantities.

We have shown that both the Green's function and extended Green's function are independent of the sign choice of the vertical wavenumber in any layer. However,

these functions do depend on the sign of the vertical wavenumber in the overlying and underlying halfspaces, assuming that each halfpace can support propagation. In the ocean acoustics context, a reasonable assumption is that the uppermost interface is pressure-release and thus propagation cannot be supported in the overlying halfspace. In other words, the vertical wavenumber is not defined for this overlying halfspace. An implication is that the Green's function and extended Green's function are independent of the sign choice of all vertical wavenumbers except the vertical wavenumber in the underlying halfspace. Thus, both the Green's function and extended Green's function have a single branch-point in the complex k_r-plane at $k_r = \pm k_N$. In the remainder of this thesis, we will assume that propagation is not supported in the overlying halfspace.

The next property to be developed is the conjugate symmetry property $g_i(k_r^*) = g_i^*(k_r)$. This property is only valid if the EJP branch-cut has been selected. A related symmetry property that does not depend on the branch-cut definition is $g_i(k_r) = g_i(-k_r)$. The latter property follows from the fact that the Green's function and extended Green's function depend on k_r only via the vertical wavenumbers, which are even functions of k_r. In order to demonstrate that $g_i(k_r^*) = g_i^*(k_r)$, we utilize the property that

$$R_{B_1}(k_r^*) = R_{B_1}^*(k_r) \qquad (2.115)$$

which was developed earlier in this section. Substituting this relationship into equation (2.87) and performing some algebra, it can be shown that

$$g_0(k_r^*) = g_0^*(k_r) \qquad (2.116)$$

The property can also be derived for the extended Green's function, i.e. for $i \neq 0$, using the same line of reasoning as previously presented for the branch point. Namely, by invoking continuity across layer boundaries and by recognizing that equation (2.116) is independent of z and z_0, it can be argued that the symmetry property

also applies to the extended Green's function i.e.

$$g_i(k_r^*) = g_i^*(k_r) \qquad (2.117)$$

Note that this symmetry property applies separately on both Riemann sheets, as can be determined by assuming that $Im\{k_{zi}\} < 0$ in the previous derivation.

The conjugate symmetry condition in equation (2.117) implies a number of constraints involving the poles and residues of the Green's function and extended Green's function. For example, if $g_i(k_r)$ has a pole at $k_r = k_{ri}$ where k_{ri} is real, and the corresponding residue is a_i, the property $g_i(-k_r) = g_i(k_r)$ implies that $g_i(k_r)$ also has a pole at $k_r = -k_{ri}$ with residue $-a_i$. Furthermore, since $g_i(k_r^*) = g_i^*(k_r)$, a_i must be real. Similarly, it can be argued that if $g_i(k_r)$ has a complex pole at $k_r = k_{ri}$, it must also have poles at $k_r = -k_{ri}, k_{ri}^*, -k_{ri}^*$ and corresponding residues of $-a_i, a_i^*, -a_i^*$.

The final property to be discussed relates to the finite extent of the imaginary part of the Green's function and the extended Green's function. In particular, we will now show that

$$Im\{g_i(k_r)\} = 0 \qquad (2.118)$$

for real-$k_r > k_N$, and furthermore that $Im\{g_i(k_r)\} = 0$ only at isolated points for real-$k_r < k_N$. The fact that the deep-water Green's function can be approximated as a function which has finite extent to the water wavenumber, i.e. that the magnitude of the deep-water Green's function is approximately zero for $k_r > k_0$, has been derived elsewhere [30]. The property which is to be derived here relates not to the approximate finite extent of $g(k_r)$ at the water wavenumber, but rather to the exact finite extent of $Im\{g(k_r)\}$ at the underlying halfspace wavenumber. The property which we will develop can be exploited in an inversion scheme to directly determine a geoacoustic property from the Green's function. In particular, if $p(r)$ is measured and $g(k_r)$ is obtained by computing the Hankel transform of $p(r)$, the maximum value of k_r at which $Im\{g(k_r)\}$ is non-zero corresponds to the branch point at $k_N = \omega/c_N$, where c_N is the velocity in the underlying halfspace. This property is valid independent

81

of the velocities and densities of any intervening layers. The property is also useful in the context of shallow water synthetic data generation and will be referred to in Chapter 4.

There are several ways to derive the finite extent property. One way is to demonstrate the property algebraically, using the reflection coefficient migration equation and the Green's function migration equation. A disadvantage of this approach is that it requires the consideration of a number of special cases. For example, separate treatment of high speed and low speed layers within the media underlying the waveguide is required. An alternate, more direct approach, which uses the two properties of $g_i(k_r)$ just presented, is now followed.

The first property to be used is that $g_i(k_r)$ contains the single branch point at $k_r = k_N$. Note that this property is valid independent of whether or not high or low speed layers are present in the media which underlies the waveguide. In stating this property, we have assumed that the overlying halfspace does not support propagation. The second property to be used is $g_i(k_r^*) = g_i^*(k_r)$, for the EJP branch cut assumption. Together, these two properties imply the property in equation (2.118). To see this, consider Figure 2.22 which depicts quadrants I and IV of the k_r-plane and the EJP branch cut emanating from the branch point at $k_r = k_N$. Also shown in this figure are two points labelled k_A and $k_{A'}$. These two points are assumed to be located at symmetric locations about the real-k_r axis so that $k_{A'} = k_A^*$. Furthermore, these points are chosen such that $Re\{k_{A'}\} = Re\{k_A\} < k_N$. Now, defining the value of the extended Green's function $g_i(k_r)$ at the point $k_r = k_A$ as

$$g_i(k_r)|_{k_r=k_A} \equiv g_R + j g_I \qquad (2.119)$$

it can be seen, from the expression $g_i(k_r^*) = g_i^*(k_r)$, that

$$g_i(k_r)|_{k_r=k_{A'}} = g_R - j g_I \qquad (2.120)$$

Next consider moving the points k_A and $k_{A'}$ closer to the real-k_r axis while retaining their symmetry about the axis. In particular, suppose k_A is located ϵ above the real-k_r
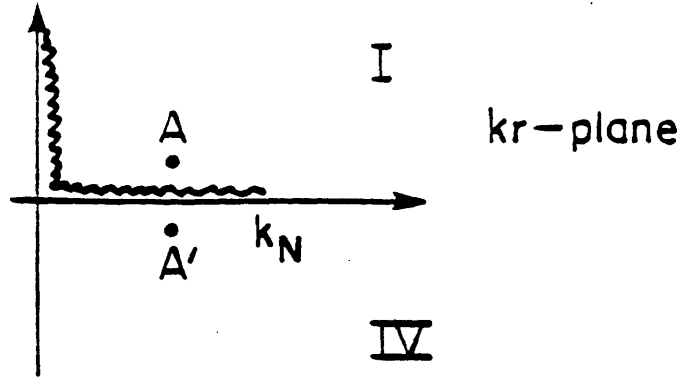
82

Figure 2.22: Quadrant I and IV of the complex k_r-plane. Points A and A' are symmetrically located about the real axis. The EJP branch-cut was selected.

axis and $k_{A'}$ is located ϵ below the real axis with $Re\,\{k_{A'}\} = Re\,\{k_A\} < k_N$. We note that the conjugate symmetry property $g_i(k_r^*) = g_i^*(k_r)$ is still valid so that equations (2.119) and (2.120) apply. However, because the branch cut passes between these two points, $g_i(k_r)$ cannot be continuous in a region which includes points on either side of the cut. Since the real part of $g_i(k_r)$ is identical at the two points, the imaginary part must change discontinuously from k_A to $k_{A'}$. Therefore, the imaginary part of $g_i(k_r)$ cannot be zero in a region along the real-k_r axis for $k_r < k_N$. If it were zero in such a region, the conjugate symmetry condition $g_i(k_r^*) = g_i^*(k_r)$ would imply a gap in the branch cut.

Now consider a similar argument for $Re\,\{k_{A'}\} = Re\,\{k_A\} > k_N$. The conjugate symmetry property for $g_i(k_r)$ must apply, and $g_i(k_r)$ must be continuous across the real-k_r axis except at isolated poles since there is no branch-cut here. Continuity across the real-k_r axis therefore requires that

$$g_i(k_r)|_{k_r = k_A} = g_i(k_r)|_{k_r = k_{A'}}$$ (2.121)

and conjugate symmetry requires that

$$g_i(k_r)|_{k_r = k_A} = g_i^*(k_r)|_{k_r = k_{A'}}$$ (2.122)

83

2.5 Summary

In this chapter, we have discussed the representation of an acoustic field within a waveguide in terms of the Hankel transform of a Green's function. In Section 2.2, we developed this integral representation using both a more formal approach, based on solving the underlying partial differential equation and a more intuitive approach, based on the superposition of plane waves. In the second approach, it was emphasized that the field in a waveguide consists of four types of components. In Chapter 5, we will see that the cancellation between these components has some important consequences in the context of the inversion problem.

In Section 2.3, we considered a simple waveguide consisting of a fluid layer overlying a fluid halfspace. In the discussion, we considered the behavior of the corresponding Green's function on two different Riemann sheets, in order to point out the relationship between Cauchy's theorem, trapped poles, virtual poles, and the branch-cut definition. This theory was compared and contrasted with an alternate approach for approximately describing the continuum in terms of virtual modes.

In Section 2.4, a more general layered fluid waveguide was considered. Here, we developed expressions for the Green's function and extended Green's function, using the Green's function migration method. In doing this, we found it convenient to define and derive the reflectivity series, which is the set of all intermediate reflection coefficients at layer boundaries. The individual terms in this series were derived by migrating the deepest reflection coefficient upwards through the layers. The reflection coefficient migration method provided a means for deriving several properties of the reflection coefficient. Additionally, several properties related to the symmetry of Green's function and the finite extent of its imaginary part were presented. In applying Cauchy's theorem, we pointed out the similarity with the theory in the previous section, and provided equations for describing the pole locations and their associated residues.

Green's function $g_0(k_r)$, can be determined from equation (2.104) as

$$(1 - R_S(k_r)R_{B_1}(k_r)e^{j2k_{z0}h_0})|_{k_r=k_{ri}} = 0 \tag{2.124}$$

The same equation must also prescribe the locations of poles for the extended Green's function $g_i(k_r)$. This fact can be argued by using the continuity condition of the extended Green's function across layer boundaries. The residue a_n at the pole k_{rn} can be determined by expressing $g_i(k_r)$ as

$$g_i(k_r) \equiv \frac{N(k_r)}{D(k_r)} \tag{2.125}$$

as in equation (2.108) and computing the residue as

$$a_n = \frac{N(k_r)}{\partial D(k_r)/\partial k_r}|_{k_r=k_{rn}} \tag{2.126}$$

In summary, in this section we have discussed the Green's function and acoustic field for the layered fluid waveguide. We have presented a method for migrating the reflection coefficient and for migrating the Green's function. These methods led to the development of several properties of the reflection coefficient and the extended Green's function. Specifically, we showed that the reflection coefficient does not depend on the sign of the vertical wavenumber within any layer and that it has a conjugate symmetry property. Additionally, assuming that propagation is not supported in the overlying halfspace, we showed that the extended Green's function depends only on the choice of the sign of the vertical wavenumber in the underlying halfspace and that it also has a conjugate symmetry property. These two properties were used to derive a finite extent property for the imaginary part of the Green's function and extended Green's function. Finally, in considering the application of Cauchy's theorem, we pointed out that the theory presented in the previous section is applicable to this more general case as well. Expressions for the poles and residues of the Green's function and extended Green's function were given.

Therefore, the imaginary part of $g_i(k_r)$ must be zero in order to satisfy both of these conditions.

Thus, when evaluated along the real k_r-axis, the imaginary part of the Green's function and extended Green's function must be of finite extent, and must be zero for horizontal wavenumbers greater than the wavenumber of the underlying halfspace, k_{zN}. Although there can be isolated zero crossings of the imaginary part for $Re\{k_r\} < k_{N_i}$, no such region may exist as its presence would imply a gap in the branch cut. The finite extent property is exact only under the conditions that all media are lossless and that the overlying halfspace does not support propagation. The property does not depend on the specific velocities and densities of intermediate layers.

In the final part of this section, we will consider the application of Cauchy's theorem to the layered waveguide problem. In the previous section, we pointed out that Cauchy's theorem can be applied to the Pekeris model Green's function as one means of evaluating its Hankel transform. The resultant acoustic field was written as

$$p(r) = p_T(r) + p_C(r) \tag{2.123}$$

where $p_T(r)$ represents the modal sum, and $p_C(r)$ represents the continuum. There are an infinite number of ways in which this partioning of $p(r)$ can be achieved, dependent on how the branch-cut is defined. In fact, the *identical theory* can be applied to the more general Green's functions discussed in this section. Thus, we can define trapped and virtual modes in the more general case as well. The virtual modes are again due to the off-axis poles which reside on either the top or bottom Riemann sheet, depending on the branch-cut selection and they contribute to the total field as terms in a residue sum. The only differences between the Pekeris waveguide model and the more general layered model are the specific equations which describe the pole locations and their associated residues. These equations are included here for completeness.

The equation which describes the pole locations, k_{r_i} for the isovelocity waveguide

Bibliography

[1] L.M. Brekhovskikh. *Waves in Layered Media.* Academic Press, New York, 1960.

[2] W.M. Ewing, W.S. Jardetsky, and F. Press. *Elastic Waves in Layered Media.* McGraw-Hill, New York, 1957.

[3] James R. Wait. *Electromagnetic Waves in Stratified Media.* Macmillan Co, New York, 1962.

[4] K. Aki and P.G. Richards. *Quantitative Seismology Theory and Methods.* W.H. Freeman and Co., San Francisco, 1980.

[5] P.M. Morse and H. Feshbach. *Methods of Theoretical Physics.* Volume 1,2, McGraw-Hill, New York, 1953.

[6] A. Papoulis. *Systems and Transforms with Applications to Optics.* McGraw-Hill, New York, 1968.

[7] Alan V. Oppenheim, George V. Frisk, and David R. Martines. Computation of the Hankel transform using projections. *J. Acoust. Soc. Am.*, 68(2):523–529, Aug. 1980.

[8] M. Abramowitz and I. Stegun. *Handbook of Mathematical Functions.* National Bureau of Standards, 1964.

[9] George V. Frisk, Alan V. Oppenheim, and D.R. Martines. A technique for measuring the plane-wave reflection coefficient of the ocean bottom. *J. Acoust. Soc.*

Am., 68(2), Aug. 1980.

[10] Bernard Friedman. *Principles and Techniques of Applied Mathematics.* John Wiley and Sons, New York, 1956.

[11] C.L. Pekeris. Theory of propagation of explosive sound in shallow water. *Geol.Soc.Am.*, Mem. 27, 1948.

[12] I. Tolstoy and C.S. Clay. *Ocean Acoustics.* McGraw-Hill, New York, 1966.

[13] F.M. Labianca. Normal modes, virtual modes, and alternative representations in the theory of surface duct sound propagation. *J. Acoust. Soc. Am.*, 53:1137–1147, 1973.

[14] C.T. Tindle, A.P. Stamp, and K.M. Guthrie. Virtual modes and the surface boundary condition in underwater acoustics. *J.Sound Vib.*, 49:231–240, 1976.

[15] D.C. Stickler. Normal-mode program with both the discrete and branch line contributions. *J. Acoust. Soc. Am.*, 57(4):856–861, Apr., 1975.

[16] C.B. Officer. *Introduction to the Theory of Sound Transmission with Application to the Ocean.* McGraw-Hill, New York, 1958.

[17] C.L. Bartberger. Comparison of two normal-mode solutions based on different branch cuts. *J. Acoust. Soc. Am.*, 61:1643, 1977.

[18] A.O Williams. Pseudoresonances and virtual modes in underwater sound propagation. *J. Acoust. Soc. Am.*, 64(5):1487–1491, Nov., 1978.

[19] H.P. Bucker. Propagation in a liquid layer lying over a liquid half-space (Pekeris cut). *J. Acoust. Soc. Am.*, 65(4):906–908, Apr., 1979.

[20] G.V. Frisk and J.F. Lynch. Shallow water waveguide characterization using the Hankel transform. *J. Acoust. Soc. Am.*, 76(1), July 1984.

[21] R.V. Churchill. *Complex Variables and Applications.* McGraw-Hill, 1960.

[22] D.C. Stickler and E. Ammicht. Uniform asymptotic evaluation of the continuous spectrum contribution for the Pekeris model. *J. Acoust. Soc. Am.*, 67(1):2018–2024, 1980.

[23] E. Ammicht and D.C. Stickler. Uniform asymptotic evaluation of the continuous spectrum contribution for a stratified ocean. *J. Acoust. Soc. Am.*, 76:186–191, July 1984.

[24] F.R. DiNapoli and R.L. Deavenport. Theoretical and numerical Green's function solution in a plane multilayered medium. *J. Acoust. Soc. Am.*, 67:92–105, 1980.

[25] H.W. Kutschale. *Rapid Computation by Wave Theory of Propagation Loss in the Arctic Ocean.* Technical Report Rep. CU-8-73, Columbia University, 1973.

[26] Henrik Schmidt and Finn B. Jensen. A full wave solution for propagation in multilayered viscoelastic media with application to Gaussian beam reflection at fluid-soild interfaces. *J. Acoust. Soc. Am.*, 77(3):813–825, Mar. 1985.

[27] C.S. Clay and H. Medwin. *Acoustical Oceanography.* John Wiley and Sons, New York, 1977.

[28] L. Brekhovskikh and Yu. Lysanov. *Fundamentals of Ocean Acoustics.* Springer-Verlag, New York, 1982.

[29] L.B. Felsen and N. Marcuvitz. *Radiation and Scattering of Waves.* Prentice-Hall, Englewood Cliffs, NJ, 1973.

[30] Douglas R. Mook, George V. Frisk, and Alan V. Oppenheim. A hybrid numerical/analytic technique for the computation of wave fields in stratified media based on the Hankel transform. *J. Acoust. Soc. Am.*, 76(1):222–243, July 1984.

Chapter 3

Unilateral Transforms in One and Two Dimensions

3.1 Introduction

In the previous chapter, we reviewed the Hankel transform relationship between the Green's function and the acoustic field in a waveguide. In this chapter, it is shown that a unilateral version of the Hankel transform is also applicable to this problem. The theory and properties of the unilateral transform will form an important foundation for many of results to be presented in later chapters of this thesis.

It is well-known that a one-dimensional complex-valued signal which can be synthesized in terms of a one-sided Fourier transform has an exact relationship between its real and imaginary components. Similarly, a two-dimensional complex-valued signal has an exact relationship between its real and imaginary components if it can be synthesized in terms a Fourier transform which is zero in a halfplane. In our work, we have found that it is possible for signals to possess an approximate real-part/imaginary-part sufficiency condition under other circumstances. For example, in

90

some cases, it is possible for a one-dimensional complex-valued even signal, which has an even Fourier transform, or a two-dimensional complex-valued circularly symmetric signal, which has a circularly symmetric Fourier transform, to have an approximate real-part/imaginary-part sufficiency condition. In this chapter, we will consider these signals and their relationship to one and two-dimensional unilateral transforms in detail.

In the first portion of Section 3.2 a review of one-dimensional analytic signals is provided. The connection between an analytic signal, the unilateral inverse Fourier transform, and the Hilbert transform is developed. In the second portion of the section, the theory of one-dimensional approximate analytic signals is presented. A number of statements involving the unilateral Fourier transform, the unilateral inverse Fourier transform, causality, and approximate real-part/imaginary-part sufficiency are made. A numerical example is also provided.

In Section 3.3, the theory is extended to two-dimensional circularly symmetric signals. These signals, which can be equivalently described in terms of the Hankel transform, are directly related to acoustic pressure fields propagating in a circularly symmetric media. We will show that, under some conditions, it is possible to approximately relate the real and imaginary components of the acoustic field, which is described in terms of the Hankel transform of the Green's function. To do this, we will develop a unilateral version of the Hankel transform, referred to as the Hilbert-Hankel transform. The transform can be used to approximately synthesize an outgoing acoustic field, and its consistency with the Hankel transform will be shown to imply an approximate relationship between the real and imaginary components of the outgoing field. The properties of the Hilbert-Hankel transform, and its relationship to several other transforms, will be considered.

In Section 3.4, an asymptotic version of the Hilbert-Hankel transform is developed. The transform is related to the Fast-Field-Program (FFP)[1], used to synthetically

generate underwater acoustic fields. In addition to forming the basis for an efficient computational algorithm, the asymptotic Hilbert-Hankel transform has other important properties. These properties arise because of the close connection between the asymptotic Hilbert-Hankel transform and the one-dimensional unilateral inverse Fourier transform. Several of these properties and their applications to the acquisition and processing of acoustic fields are discussed.

3.2 One-Dimensional Exact and Approximate Analytic Signals

In this section, we will consider the relationship between the real and imaginary components of a one-dimensional complex-valued signal. In general, these components are completely unrelated, as they may be specified independently. However, for certain classes of signals, there exists an exact coupling relationship between these two components. In the first portion of this section, we will review some of the well-known theory of signals which possess this exact condition. In the second portion of the section, we consider the related property of approximate real-part/imaginary-part sufficiency. Several statements concerning approximate causality and approximate real-part/imaginary-part sufficiency will be made, and a numerical example will be provided.

3.2.1 Analytic Signals and the Hilbert Transform

We begin the discussion by considering a complex-valued function of a complex-valued variable. From the theory of analytic functions, the complex-valued function is analytic at a point if it is both single-valued and has a unique derivative. By unique, it is meant that the derivative is independent of the direction in which the derivative is taken. A necessary condition for a unique derivative is that the real and imaginary components of the function satisfy the Cauchy-Riemann conditions[2], which involve the partial derivatives of the function. If these partial derivatives are also continuous, the Cauchy-Riemann conditions form a necessary and sufficient condition for analyticity at a given point.

The Cauchy-Riemann conditions imply that the real and imaginary components of a function cannot be chosen independently, if the function is to be analytic. These

conditions imply that if the real (or imaginary) component is specified within the region of analyticity, the imaginary (or real) component can be determined. In some cases, knowledge of one of the components along only the boundary of the analytic region is sufficient to determine the alternate component [3] [4]. For example, if the region of analyticity is a circle centered at the origin of the complex plane, integral relationships between the real and imaginary components of the function referred to as Poisson integrals have been developed. Similarly, if the region of analyticity is a halfplane which includes the real or imaginary axis, integral relationships between the real and imaginary components of the function along the axis, referred to as Hilbert transform integrals, have been developed.

In a signal processing context, we are perhaps more familiar with the concept that a one-sided, or causal, condition in one domain implies a real-part/imaginary-part sufficiency condition in the alternate domain. That is, a complex-valued signal has a real-part/imaginary-part sufficiency condition if its Fourier transform is causal and vice versa. A signal which can be exactly synthesized in terms of a one-sided Fourier transform is referred to as an *analytic signal*.

To explore this further, consider an arbitrary real-valued signal $f(t)$ which has a Fourier transform $F(\omega)$. An analytic signal $z(t)$, which is related to $f(t)$, can be constructed by synthesizing over only the positive frequency components of $F(\omega)$. That is, the complex-valued signal $z(t)$ can be synthesized as

$$z(t) = \frac{1}{\pi} \int_0^\infty F(\omega)e^{j\omega t} d\omega \qquad (3.1)$$

Here, $z(t)$ is an analytic signal, since its Fourier transform is a causal function of ω. The synthesis equation for $z(t)$ is valid for both real and complex values of t. It can be shown that the one-sided integral in equation (3.1) implies that $z(t)$ is an analytic function in the upper half of the complex t-plane[5][6]. This one-sided condition connects the theory of the analytic signal with the theory of the analytic function.

94

The relationship between the real and imaginary components of $z(t)$ is now determined. Equating real parts on both sides of equation (3.1) yields

$$Re[z(t)] = \frac{1}{\pi}\int_0^\infty Re[F(\omega)e^{j\omega t}]d\omega$$

$$= \frac{1}{2\pi}\int_0^\infty[F(\omega)e^{j\omega t} + F^*(\omega)e^{-j\omega t}]d\omega \qquad (3.2)$$

$$= \frac{1}{2\pi}\int_{-\infty}^\infty F(\omega)e^{j\omega t}d\omega = f(t)$$

Thus, the real part of the analytic signal $z(t)$ is $f(t)$. Similarly, equating the imaginary parts on both sides of equation (3.1), we find that

$$\hat{f}(t) \equiv Im[z(t)] = \frac{1}{2\pi j}\int_0^\infty F(\omega)e^{j\omega t}d\omega + \frac{1}{2\pi j}\int_{-\infty}^0 -F^*(-\omega)e^{j\omega t}d\omega \qquad (3.3)$$

so that

$$\hat{f}(t) = \frac{1}{2\pi}\int_{-\infty}^\infty -j\,sgn[\omega]F(\omega)d\omega \qquad (3.4)$$

The relationships between the real and imaginary components of $z(t)$ and their Fourier transforms can be summarized as follows

$$f(t) \stackrel{\mathcal{F}}{\longleftrightarrow} F(\omega)$$

$$z(t) = f(t) + j\hat{f}(t) \stackrel{\mathcal{F}}{\longleftrightarrow} 2F(\omega)U(\omega) \qquad (3.5)$$

$$\hat{f}(t) \stackrel{\mathcal{F}}{\longleftrightarrow} -j\,sgn[\omega]F(\omega)$$

The signals $f(t)$ and $\hat{f}(t)$ are said to form a *Hilbert transform pair*.

Although the Hilbert transform relationship between $f(t)$ and $\hat{f}(t)$ is conveniently summarized in the frequency domain, it is also possible to use the convolution property of Fourier transforms to state the relationship in the time domain. Determining the inverse Fourier transform of $-j\,sgn[\omega]$, we find that

$$\hat{f}(t) = \frac{1}{\pi t} * f(t) \qquad (3.6)$$

and similarly that

$$f(t) = -\frac{1}{\pi t} * \hat{f}(t) \qquad (3.7)$$

where the integrals are interpreted as Cauchy principal valued.

In our work, we have been interested in extending some of the properties of analytic signals to signals which do not possess a one-sided Fourier transform. Our primary interest has been in two-dimensional circularly symmetric signals, which are related to the two-dimensional circularly symmetric Fourier transform, or equivalently to the Hankel transform. However, the extension of the theory of analytic functions can best be presented by first considering the one-dimensional case. In the remainder of this section the theory of one-dimensional signals which are approximately analytic is developed, and a numerical example is provided. In the next section, the analogous theory for two-dimensional circularly symmetric signals is presented.

3.2.2 Approximate Analytic Signals and the Unilateral Inverse Fourier transform

Consider a one-dimensional complex-valued signal $f(t)$ which has the Laplace transform $F_0(s)$ given by

$$F_0(s) = \int_{-\infty}^{\infty} f(t)e^{-st}dt \tag{3.8}$$

The signal $f(t)$ is restricted to be a stable signal, so that its Fourier transform $F(\omega) = F_0(s)|_{s=j\omega}$ exists. We will further assume that the Fourier transform $F(\omega)$ is a two-sided function of ω and thus the signal $f(t)$ can be described in terms of the inverse Fourier transform synthesis integral as

$$f(t) = \frac{1}{2\pi} \int_{-\infty}^{\infty} F(\omega)e^{j\omega t}d\omega \tag{3.9}$$

We will find it convenient to define the related signal $f_u(t)$ in terms of the unilateral inverse Fourier transform as follows

$$f_u(t) \equiv \frac{1}{2\pi} \int_{0}^{\infty} F(\omega)e^{j\omega t}d\omega \tag{3.10}$$

Note that $f_u(t)$ is an analytic signal, since its Fourier transform is causal.

To extend the theory of analytic signals to the signal $f(t)$ which has a two-sided Fourier transform, we require that

$$f(t) \sim f_u(t) \tag{3.11}$$

That is, a signal $f(t)$ which can be approximated by a unilateral version of its inverse Fourier transform can be considered as approximately analytic.

The condition that a signal can be accurately synthesized in terms of its unilateral inverse Fourier transform is rather restrictive, and certainly does not apply to any arbitrary signal. For example, consider a signal, comprised of a sum of complex exponentials, which has a rational Laplace transform. In Figure 3.1, we have indicated the positions of several poles in the s-plane, corresponding to the arbitrarily chosen
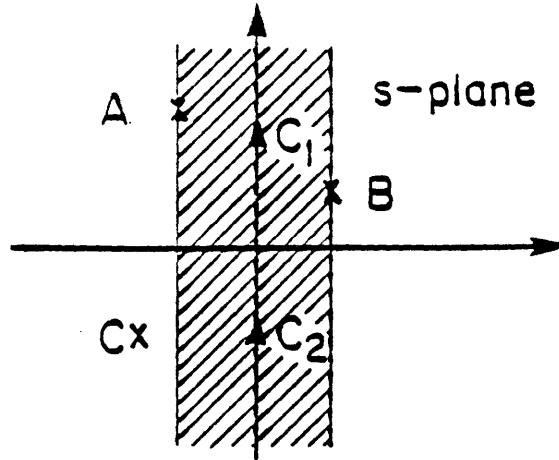
Figure 3.1: Complex s-plane indicating positions of poles, the inverse Laplace transform integration contour, and the Laplace transform region of convergence.

signal, as well as the region of convergence for the Laplace transform. The condition that $f(t) \sim f_u(t)$ is equivalent to the statement that the inverse Laplace transform contour $C_1 + C_2$, can be approximately replaced by the contour C_1. The approximation will be poor if a pole, such as C, is located in Quadrant III or IV of the s-plane. Essentially, the effects of this pole, quite important in determining the character of the corresponding signal $f(t)$, are only negligibly included by integrating along the positive imaginary axis only. That is, if $f(t)$ is exactly synthesized as

$$f(t) = \frac{1}{2\pi j} \int_{C_1 + C_2} F_0(s) e^{st} ds \qquad (3.12)$$

so that

$$f(t) = \frac{1}{2\pi j} \int_{C_1} F_0(s) e^{st} ds + \frac{1}{2\pi j} \int_{C_2} F_0(s) e^{st} ds \qquad (3.13)$$

the pole at position C contributes primarily to the second of these. Thus, the approximation

$$f(t) \sim \frac{1}{2\pi j} \int_{C_1} F_0(s) e^{st} ds = \frac{1}{2\pi} \int_0^\infty F(\omega) e^{j\omega t} d\omega \quad t > 0 \qquad (3.14)$$

is not accurate because of the position of pole C in the s-plane. Alternately, if there are no poles in quadrant III or IV of the s-plane, the unilateral inverse transform can yield an accurate version of $f(t)$. This can be argued informally based on the fact that

only the tails of the poles, such as A and B, are incorporated within the integrand of the second integral in equation (3.13).

This concept of approximate analyticity is intuitive - if the signal $f(t)$ can be approximated by the analytic signal $f_a(t)$, $f(t)$ is certainly approximately analytic. Although it is possible to develop an approximate relationship between the real and imaginary components of $f(t)$, there are no further consequences of the relationship $f(t) \sim f_a(t)$. However, as will be indicated in the remainder of this section, many interesting consequences occur if additional restrictions are placed on the signal $f(t)$ and the definition of approximate analyticity is slightly modified. For example, there are interesting consequences which arise if $f(t)$ is restricted to be a causal signal. In our work, we have explored the consequences of requiring $f(t)$ to be even. Essentially, by considering $f(t)$ to be an even signal, the case of the causal signal can be treated as well, since an even (or causal) signal can always be invertibly constructed from a causal (or even) signal. As will be discussed in the next section, the even signal in one-dimension is completely analogous to the circularly symmetric signal in two dimensions.

It is pointed out that *any* stable even function $f(t)$ can be directly related to a Fourier transform which is analytic. This follows from the fact that the Fourier transform of the causal portion of $f(t)$ must be analytic in the ω domain. Our interest is in the property of analyticity *not* in the ω domain, but rather in the t domain.

To develop the theory, consider the even, complex-valued signal $f(t)$ which has a Laplace transform $F_0(s)$. The signal is again required to be stable, so that its Fourier transform $F(\omega) = F_0(s)|_{s=j\omega}$ exists. Since the signal is even, it follows that its Fourier transform and Laplace transform must also be even. We will find it convenient to define not only the Fourier transform and inverse Fourier transform, but their unilateral counterparts as well. Thus,

$$f(t) \equiv \mathcal{F}^{-1}\{F(\omega)\} \equiv \frac{1}{2\pi} \int_{-\infty}^{\infty} F(\omega)e^{j\omega t}d\omega \qquad (3.15)$$

$$f_u(t) \equiv \mathcal{F}_u^{-1}\{F(\omega)\} \equiv \frac{1}{2\pi}\int_0^\infty F(\omega)e^{j\omega t}\,d\omega \tag{3.16}$$

and

$$F(\omega) \equiv \mathcal{F}\{f(t)\} \equiv \int_{-\infty}^\infty f(t)e^{-j\omega t}\,dt \tag{3.17}$$

$$F_u(\omega) \equiv \mathcal{F}_u\{f(t)\} \equiv \int_0^\infty f(t)e^{-j\omega t}\,dt \tag{3.18}$$

where $f_u(t)$ represents the unilateral inverse Fourier transform of $F(\omega)$, and $F_u(\omega)$ represents the unilateral Fourier transform of $f(t)$. Symbolically, $\mathcal{F}$ and $\mathcal{F}^{-1}$ represent the Fourier transform and inverse Fourier transform operations, and $\mathcal{F}_u$ and $\mathcal{F}_u^{-1}$ represent the unilateral Fourier transform and unilateral inverse Fourier transform operations.

It is pointed out that, while $\mathcal{F}$ and $\mathcal{F}^{-1}$ are necessarily inverse operations, $\mathcal{F}_u$ and $\mathcal{F}_u^{-1}$ are *not* necessarily inverse operations. Additionally, it is recognized that both $f_u(t)$ and $F_u(\omega)$ are analytic signals, since their Fourier transforms are causal. Therefore, the real and imaginary components of $f_u(t)$ are exactly related by the Hilbert transform, and the real and imaginary components of $F_u(\omega)$ are exactly related by the Hilbert transform. Additionally, it is noted that since $f(t)$, and thus $F(\omega)$, are even signals, they can be synthesized in terms of the cosine transform as

$$f(t) = \frac{1}{\pi}\int_0^\infty F(\omega)\cos\omega t\,d\omega \tag{3.19}$$

$$F(\omega) = 2\int_0^\infty f(t)\cos\omega t\,dt \tag{3.20}$$

To extend the theory of analytic signals to the signal $f(t)$, we will require that $f(t)$ satisfy the condition

$$f(t) \sim f_u(t) \quad t > 0 \tag{3.21}$$

That is, only those functions $f(t)$ which can be approximated by the unilateral inverse Fourier transform for positive values of t will be considered. Note that this condition differs from the condition in (3.11). Specifically, the unilateral inverse Fourier transform is required to synthesize the even signal $f(t)$ for positive values of t only. The

even function $f(t)$ will be defined as approximately analytic if the condition in (3.21) is satisfied. To the extent that the approximation in equation (3.21) is valid, there will also exist an approximate relationship between the real and imaginary components of $f(t)$, for $t > 0$. This result is the basis for a number of statements which will now be made.

Statement 1 *If $f(t) \sim f_u(t)$ for $t > 0$, then the real and imaginary components of $f(t)$ must be approximately related by the Hilbert transform for $t > 0$.*

The signal $f_u(t)$ must be analytic since its Fourier transform is causal in ω. Equating the real and imaginary parts on both sides of equation (3.21) for $t > 0$, we have that $Re[f(t)]$ and $Im[f(t)]$ must be related via the Hilbert transform, since $Re[f_u(t)]$ and $Im[f_u(t)]$ are related by the Hilbert transform.

The condition that the causal portion of a signal can be accurately synthesized by a unilateral version of the inverse Fourier transform is rather restrictive. For example, consider the even signal $f(t)$, comprised of complex exponentials, which has the Laplace transform $F_0(s)$. In Figure 3.2, we have indicated the positions of several poles in the s-plane for an arbitrarily chosen even signal. The poles labelled A', B', and C' are in symmetrically-located positions with respect to the poles A, B, and C, due to the fact that $F_0(s)$ must be even. The condition that $f(t) \sim f_u(t), t > 0$ is equivalent to the statement that the inverse Laplace transform contour $C_1 + C_2$, can be approximately replaced by the contour C_1. The approximation will be poor if a pole, such as C, is located in Quadrant III of the s-plane. Essentially, the effects of this pole, quite important in determining the character of the corresponding signal $f(t)$ for $t > 0$, are only negligibly included by integrating along the positive imaginary axis only. [1] That is, if $f(t)$ is exactly synthesized as

$$f(t) = \frac{1}{2\pi j} \int_{C_1 + C_2} F_0(s) e^{st} ds \tag{3.22}$$

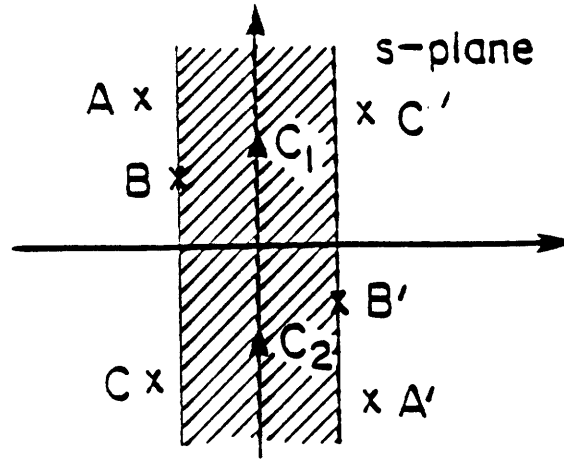[1]The pole at C' determines the behavior of the function $f(t)$ primarily for values of $t < 0$.

Figure 3.2: Complex s-plane indicating positions of poles, the inverse Laplace transform integration contour, and the Laplace transform region of convergence.

so that

$$f(t) = \frac{1}{2\pi j} \int_{C_1} F_0(s)e^{st}ds + \frac{1}{2\pi j} \int_{C_2} F_0(s)e^{st}ds \qquad (3.23)$$

the pole at position C contributes primarily to the second of these two integrals, for values of $t > 0$. Thus, the approximation

$$f(t) \sim \frac{1}{2\pi j} \int_{C_1} F_0(s)e^{st}ds = \mathcal{F}_\omega^{-1}\{F(\omega)\} \qquad (3.24)$$

is not accurate for $t > 0$ because of the position of pole C in the s-plane.

Alternately, if there are no poles or other singularities in quadrant III of the s-plane, (and thus in quadrant I since $F_0(s)$ is even), the unilateral inverse transform can yield an accurate version of $f(t)$ for values of $t > 0$. This can be argued informally based on the fact that only the tails of the poles, such as A and B, are incorporated within the integrand of the second integral in equation (3.23). More formally, if $F_0(s)$ is analytic in quadrant III, under the weak condition that $F_0(s) \to 0$, as $|s| \to \infty$ in this quadrant, the contour C_2 can be deformed [2] from its position along the negative imaginary s axis, to a position C_2' along the negative real axis, as shown in Figure 3.3. In this case, $f(t)$ can be written exactly as

---

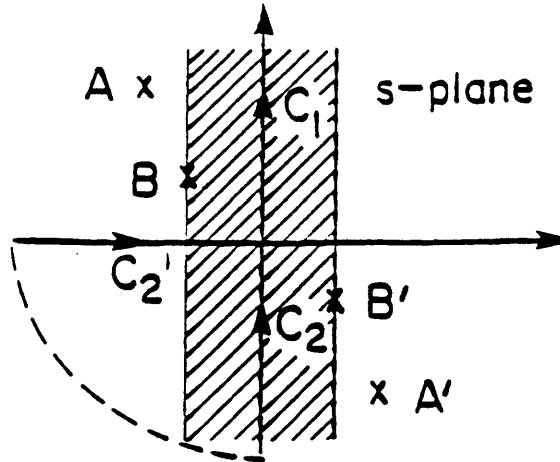[2]The fact that the contour integral at infinite radius is zero can be proved using Jordan's Lemma.

Figure 3.3: Complex s-plane and integration contour deformation. The integrals along C_2 and C_2' are identical.

$$f(t) = \frac{1}{2\pi j} \int_{C_1} F_0(s)e^{st}\,ds + \frac{1}{2\pi j} \int_{C_2'} F_0(s)e^{st}\,ds \qquad (3.25)$$

From this equation, it is seen that the second integral consists of exponential terms which are purely decaying in t. The implication is that, to the degree that these exponential decaying terms can be neglected in the synthesis of $f(t)$ for $t > 0$, the approximation $f(t) \sim f_u(t), t > 0$ is valid. Additionally, the validity of the approximation increases for larger values of t.

Similarly, it can be argued that as the imaginary part of a pole located in quadrant II, increases, so must the quality of the unilateral inverse Fourier transform synthesis. Essentially, the contribution along the negative imaginary axis, due to the tail of this pole, decreases as the pole is displaced upwards. Additionally, as the magnitude of the real part of a pole increases, i.e. the Q-factor of the pole decreases, the unilateral approximation becomes worse. However, as the magnitude of the real part of a pole increases, its relative contribution to the signal $f(t)$ also decreases for $t \gg 0$. This fact is consistent with the statement that the unilateral inverse Fourier transform yields a signal $f_u(t)$ which more closely approximates $f(t)$ for $t \gg 0$.

It is possible to determine an exact expression for the error in the unilateral inverse

Fourier transform synthesis of a signal $f(t)$. Specifically, by examining the definitions of $f(t)$ and $f_u(t)$, the error in the approximation $f(t) \sim f_u(t), t > 0$ can be written as

$$\epsilon(t) \equiv f(t) - f_u(t) = \frac{1}{2\pi} \int_{-\infty}^{0} F(\omega)e^{j\omega t}d\omega \quad t > 0 \tag{3.26}$$

This integral can be evaluated analytically by utilizing cosine and sine transform tables, or it can be evaluated numerically, as is done in the example later in this section. It is also possible to establish bounds on the error as a function of t. However, we have chosen not to pursue the mathematical evaluation of the error function in great detail. We focus instead, on other consequences of the unilateral approximation $f(t) \sim f_u(t), t > 0$. Specifically, in the following statement, the approximation is used to develop a causality property for $f_u(t)$.

Statement 2 *If* $f(t) \sim f_u(t)$ *for* $t > 0$, *then the unilateral inverse Fourier transform* $f_u(t)$ *is approximately causal.*

Note from equation (3.16), that the unilateral inverse Fourier transform is defined for all values of t. Thus, the causality condition stated above is not a consequence of the definition of the unilateral inverse Fourier transform, but rather is a consequence of the condition that $f(t) \sim f_u(t), t > 0$. To justify the statement, we note that $f(t) \sim f_u(t), t > 0$ implies that

$$\frac{1}{2\pi} \int_{-\infty}^{0} F(\omega)e^{j\omega t}d\omega \sim 0 \quad t > 0 \tag{3.27}$$

so that

$$\frac{1}{2\pi} \int_{0}^{\infty} F(\omega)e^{-j\omega t}d\omega \sim 0 \quad t > 0 \tag{3.28}$$

The latter step follows from the fact that $F(\omega)$ is even in ω. From equation (3.28), and the definition of the unilateral inverse Fourier transform, it can be seen that

$$f_u(-t) \sim 0, \quad t > 0 \tag{3.29}$$

and thus

$$f_u(t) \sim 0, \quad t < 0 \tag{3.30}$$

Thus, under the condition that $f(t) \sim f_u(t)$ for $t > 0$, the unilateral inverse Fourier transform must be approximately causal.

As pointed earlier, in general, the unilateral Fourier transform and unilateral inverse Fourier transform are not inverse operations. However, the following statement summarizes the relationship between these two transforms under the condition that $f(t) \sim f_u(t), t > 0$ is valid.

Statement 3 *If $f(t) \sim f_u(t)$ for $t > 0$, then the unilateral Fourier transform and unilateral inverse Fourier transform are related via*

$$\mathcal{F}_u\{\mathcal{F}_u^{-1}\{F(\omega)\}\} \sim F(\omega)U(\omega) \tag{3.31}$$

To justify this, note that

$$\mathcal{F}_u\{\mathcal{F}_u^{-1}\{F(\omega)\}\} = \mathcal{F}_u\{f_u(t)\} \tag{3.32}$$

from the definition of $f_u(t)$. Next, it follows that

$$\mathcal{F}_u\{f_u(t)\} \sim \mathcal{F}\{f_u(t)\} \tag{3.33}$$

since $f_u(t)$ is approximately causal, from the preceding theorem. However, from the definition of $f_u(t)$, it is also apparent that

$$\mathcal{F}\{f_u(t)\} = F(\omega)U(\omega) \tag{3.34}$$

Combining the three previous equations establishes the validity of the statement.

The next property to be discussed is a real-part/imaginary-part sufficiency condition which occurs in the ω domain. The fact that $F(\omega)$ has an approximate real-part/imaginary-part sufficiency condition is not completely unexpected, since, as previously discussed, there exists an approximate causality condition in the alternate t domain. The real-part/imaginary-part sufficiency condition for $F(\omega)$ is summarized in the following statement.

Statement 4 *If $f(t) \sim f_u(t)$ for $t > 0$, then the real and imaginary components of $F(\omega)$ must be related by the Hilbert transform for $\omega > 0$.*

To justify this, Statement 3 is used to establish that

$$\mathcal{F}_u\{\mathcal{F}_u^{-1}\{F(\omega)\}\} \sim F(\omega)U(\omega) \qquad (3.35)$$

so that

$$\mathcal{F}_u\{f_u(t)\} \sim F(\omega)U(\omega) \qquad (3.36)$$

The signal $F(\omega)U(\omega)$ is approximately analytic since it is related to the one-sided Fourier transform on the left hand side of equation (3.36). Thus, since $F(\omega)U(\omega)$ is approximately analytic, its real and imaginary parts must be related via the Hilbert transform.

Although we have previously considered several statements involving the relationships between the Fourier transform, inverse Fourier transform and their unilateral counterparts, it is also possible to derive a number of interesting relationships between the cosine and sine transforms which comprise these. To develop the relationships, the additional notation for cosine and sine transforms is defined as

$$C\{F(\omega)\} \equiv \frac{1}{\pi} \int_0^\infty F(\omega) \cos \omega t \, d\omega \qquad (3.37)$$

$$S\{F(\omega)\} \equiv \frac{1}{\pi} \int_0^\infty F(\omega) \sin \omega t \, d\omega \qquad (3.38)$$

Note that since the signal $f(t)$ is even, and thus its Fourier transform $F(\omega)$ is also even, equations (3.15) and (3.17) can be written in terms of cosine transforms as

$$f(t) = \mathcal{F}^{-1}\{F(\omega)\} = C\{F(\omega)\} \qquad (3.39)$$

$$F(\omega) = \mathcal{F}\{f(t)\} = 2\pi C\{f(t)\} \qquad (3.40)$$

Additionally, the unilateral inverse Fourier transform and unilateral Fourier transform, in equations (3.16) and (3.18), can be written in terms of cosine and sine transforms as

$$f_u(t) = \mathcal{F}_u^{-1}\{F(\omega)\} = \frac{1}{2}C\{F(\omega)\} + j\frac{1}{2}S\{F(\omega)\} \qquad (3.41)$$

106

and

$$F_u(\omega) = \mathcal{F}_u\{f(t)\} = \pi C\{f(t)\} - j\pi S\{f(t)\} \tag{3.42}$$

Under the condition that $f(t) \sim f_u(t), t > 0$, the following statement, involving the relationships between the various cosine and sine transforms, can be made.

Statement 5 *If $f(t) \sim f_u(t)$ for $t > 0$, then the cosine and sine transforms of the real and imaginary components of $F(\omega)$ are related, for $t > 0$, via*

$$C\{Re[F(\omega)]\} \sim -S\{Im[F(\omega)]\} \tag{3.43}$$

$$C\{Im[F(\omega)]\} \sim S\{Re[F(\omega)]\} \tag{3.44}$$

Additionally, the cosine and sine transforms of the real and imaginary components of $f(t)$ are related, for $\omega > 0$, via

$$C\{Re[f(t)]\} \sim S\{Im[f(t)]\} \tag{3.45}$$

$$C\{Im[f(t)]\} \sim -S\{Re[f(t)]\} \tag{3.46}$$

To derive the first pair of equations, the fact that $f(t) \sim f_u(t), t > 0$ implies

$$\mathcal{F}^{-1}\{F(\omega)\} \sim \mathcal{F}_u^{-1}\{F(\omega)\} \quad t > 0 \tag{3.47}$$

is used. Substituting equation (3.39) into the left-hand portion of the expression and equation (3.41) into the right-hand portion of the expression, and equating real and imaginary parts on both sides, yields the first pair of equations. To derive the second pair of equations, we utilize Statement 3, which relates the unilateral inverse Fourier transform and the unilateral Fourier transform, to derive that

$$\mathcal{F}\{f(t)\} \sim \mathcal{F}_u\{f(t)\} \quad \omega > 0 \tag{3.48}$$

Substituting equation (3.40) into the left-hand portion of the expression and equation (3.42) into the right-hand portion of the expression, and equating real and imaginary parts on both sides, yields the second pair of equations in the statement.

107

Another interesting consequence of the validity of the unilateral synthesis of $f(t)$ for $t > 0$ is presented in the following statement.

Statement 6 *If $f(t) \sim f_u(t)$ for $t > 0$, then $f(t)$ can be approximately synthesized, for $t > 0$, in terms of either the real, or imaginary components of $F(\omega)$, as*

$$f(t) \sim 2\mathcal{F}_u^{-1}\{Re[F(\omega)]\} \tag{3.49}$$

$$f(t) \sim 2j\,\mathcal{F}_u^{-1}\{Im[F(\omega)]\} \tag{3.50}$$

Additionally, $F(\omega)$ can be approximately analyzed, for $\omega > 0$, in terms of either the real, or imaginary components of $f(t)$, as

$$F(\omega) \sim 2\mathcal{F}_u\{Re[f(t)]\} \tag{3.51}$$

$$F(\omega) \sim 2j\,\mathcal{F}_u\{Im[f(t)]\} \tag{3.52}$$

These relationships may be of importance if only one component of the signal (or Fourier transform) is available and it is desirable to determine the Fourier transform (or signal). To obtain equations (3.128) and (3.129), the fact that $f(t) \sim f_u(t), t > 0$ implies

$$f(t) \sim \mathcal{F}_u^{-1}\{F(\omega)\} \quad t > 0 \tag{3.53}$$

is used. Next, the right-hand side of this equation is expressed in terms of cosine and sine transforms, as in equation (3.41). The relationships stated in the first part of Statement 5 are then substituted to derive equations (3.49) and (3.50). To obtain the second pair of equations, we utilize Statement 3, which relates the unilateral inverse Fourier transform and unilateral Fourier transform, to derive that

$$F(\omega) \sim \mathcal{F}_u\{f(t)\} \quad \omega > 0 \tag{3.54}$$

Next, the right-hand side of this equation is expressed in terms of cosine and sine transforms, using equation (3.42). The relationships stated in the second part of Statement 4 are then substituted to derive equations (3.51) and (3.52).
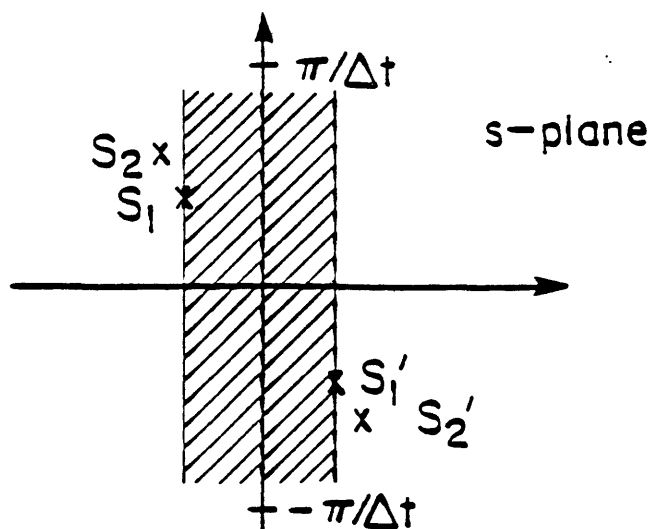
Figure 3.4: Complex s-plane indicating the location of poles s_1, s_2, and their symmetrically-located versions.

Before concluding this section, we will consider a numerical example in order to better illustrate the statements which have been made. To do this, we will choose a simple signal $f(t)$, comprised of complex exponentials, having the form

$$f(t) = \sum_{i=1}^{N} a_i e^{s_i|t|} \quad Re[s_i] < 0 \tag{3.55}$$

which has the Laplace transform

$$F_0(s) = \sum_{i=1}^{N} \frac{2a_i s_i}{s^2 - s_i^2} \tag{3.56}$$

Evaluating $F_0(s)$ at $s = j\omega$, the Fourier transform is obtained as

$$F(\omega) = \sum_{i=1}^{N} \frac{-2a_i s_i}{\omega^2 + s_i^2} \tag{3.57}$$

From these expressions, it is seen that $f(t)$, $F_0(s)$, and $F(\omega)$ are even functions. In the example, N was chosen as 2, and, s_1, s_2 were selected to lie in quadrant II of the s-plane, as indicated in Figure 3.4.

A difficulty which arises in constructing a numerical example is that the preceding theory applies to continuous functions of t and ω. By necessity, demonstrating the theory numerically involves discretization. Although it is possible to develop the

theory for discrete signals, we have chosen not to pursue this development in this thesis. We are thus faced with the problem of demonstrating properties involving continuous signals using their discrete representations. Thus, instead of computing the Fourier transform, inverse Fourier transform, cosine transform, etc., it is the discrete versions of these transforms which must be computed. The detailed algorithms used to implement these discrete transforms are well-known, and will not be discussed here. We point out however, that in constructing the discrete version of the inverse Fourier transform and unilateral inverse Fourier transform it was necessary to map the $j\omega$ axis to the unit circle in the z-transform domain, and in our approach, the impulse invariant technique was used.

In the example, the specific values

$$s_1 = (-8.0 * 10^{-3} + j1.5)/\Delta t \tag{3.58}$$

$$s_2 = (-7.0 * 10^{-3} + j1.6)/\Delta t$$

and

$$a_1 = 0.5e^{j0.5} \tag{3.59}$$

$$a_2 = 0.4e^{j1.0}$$

were chosen. The factor Δt in these expressions is arbitrary and corresponds to the sampling rate associated with the discrete version of the continuous-time signal. Thus, the discrete version of the signal $f(t)$ is written as

$$f[n] \equiv f(t)|_{t=n\Delta t} = \sum_{i=1}^{2} a_i e^{s_i \Delta t |n|} \tag{3.60}$$

The magnitude and phase of this signal are displayed in Figure 3.5. From the figure, it is seen that this signal is even and that it decays in $|t|$ due to the non-zero real parts of s_1 and s_2. The phase varies quite rapidly, and the slowly varying pattern in the magnitude is related to the difference between the imaginary parts of s_1 and s_2. The magnitude and phase of the Fourier transform of this signal are displayed in
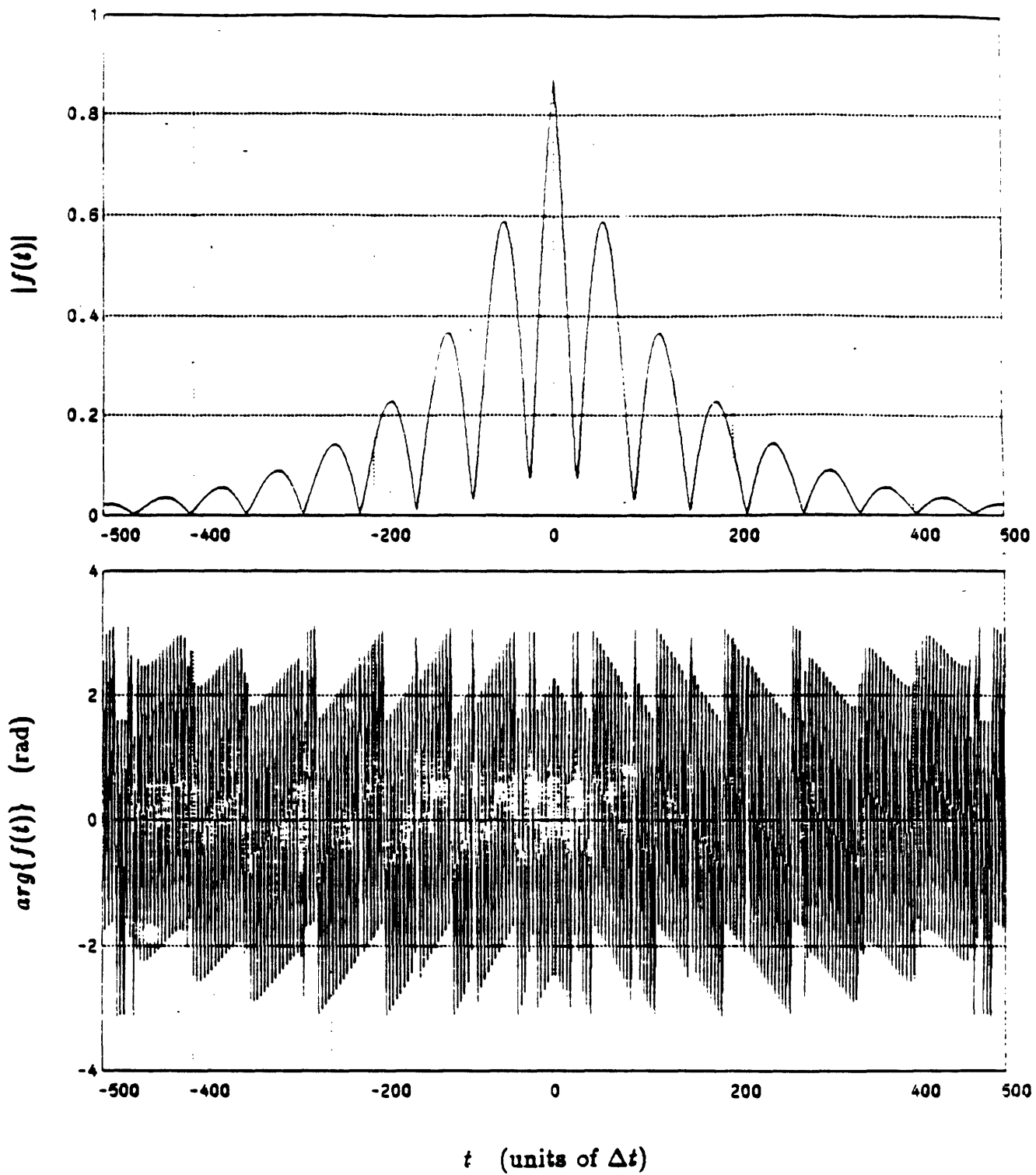
110

Figure 3.5: Magnitude and phase of the signal comprised of two complex exponentials.
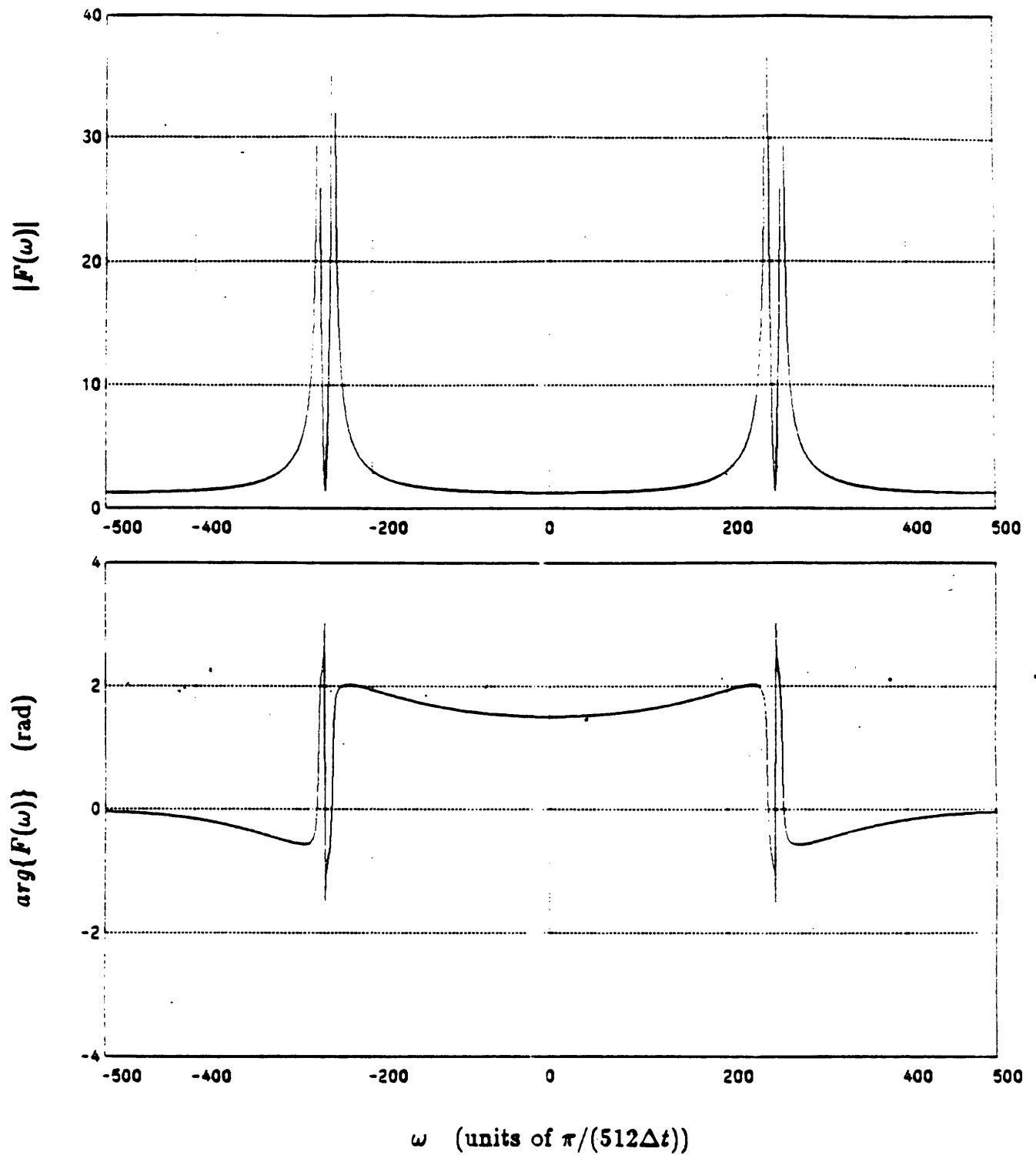
Figure 3.6: Magnitude and phase of the Fourier transform of the signal in the preceding figure.

Figure 3.6. From the figure, it can be seen that the Fourier transform is even in ω. The presence of the off-axis poles in the s-plane, which are close to the $j\omega$ axis, are indicated by the large peaks in the magnitude of the Fourier transform.

The preceding two figures indicate that the condition of *exact* analyticity is *not* applicable to the signal or to its Fourier transform. Specifically, the signal (or Fourier transform) is not causal so that the Fourier transform (or signal) cannot be analytic. However, we will show that the theory of approximate analyticity is applicable to this signal.

To begin, consider Statement 1, which summarizes the approximate real-part/imaginary-part sufficiency condition for $f(t)$. To demonstrate that $f(t)$, shown in Figure 3.5, has this property, the imaginary component was set to zero and then reconstructed from the real component using the Hilbert transform. To compute the Hilbert transform, the Fourier transform was computed and multiplied by $2U(\omega)$. The inverse Fourier transform was then computed. The magnitude of the signal consisting of the real component and the reconstructed imaginary component is displayed in Figure 3.7b for positive values of t. The magnitude of the true signal for positive t is also displayed in Figure 3.7a, for comparison. The curves compare closely except at small values of t where the unilateral inverse Fourier transform synthesis approximation is not valid, as discussed earlier. A comparison of the rapidly varying [3] phase curves is not shown here.

To demonstrate Statement 2, the unilateral inverse Fourier transform of $F(\omega)$ was computed. The magnitude of the resultant signal is shown in Figure 3.8b for both positive and negative values of t. For comparison, the original signal magnitude is also shown in Figure 3.8a. The curves indicate that for values of $t > 0$, the signal $f(t)$ is approximately synthesized by the unilateral inverse Fourier transform. To better illustrate this, the error $\epsilon(t)$, as defined in equation (3.26) was computed. The

---

[3] In a later chapter, when the two-dimensional extension of this theory is considered, we will present a method for displaying rapidly varying phase curves in a more meaningful manner.
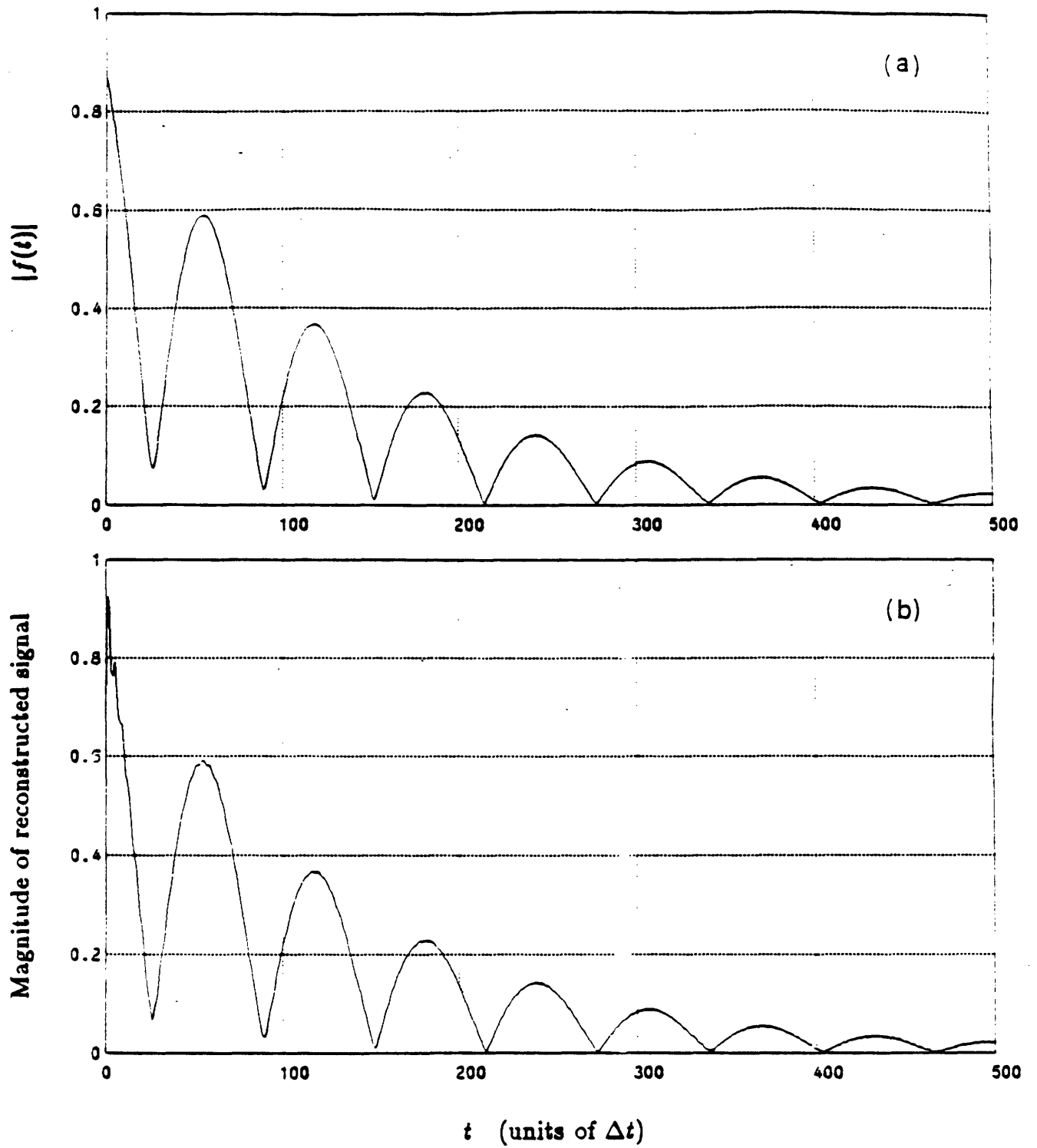
113

Figure 3.7: Magnitude of the original signal for positive values of t (a). Magnitude of the reconstructed signal for positive values of t (b).
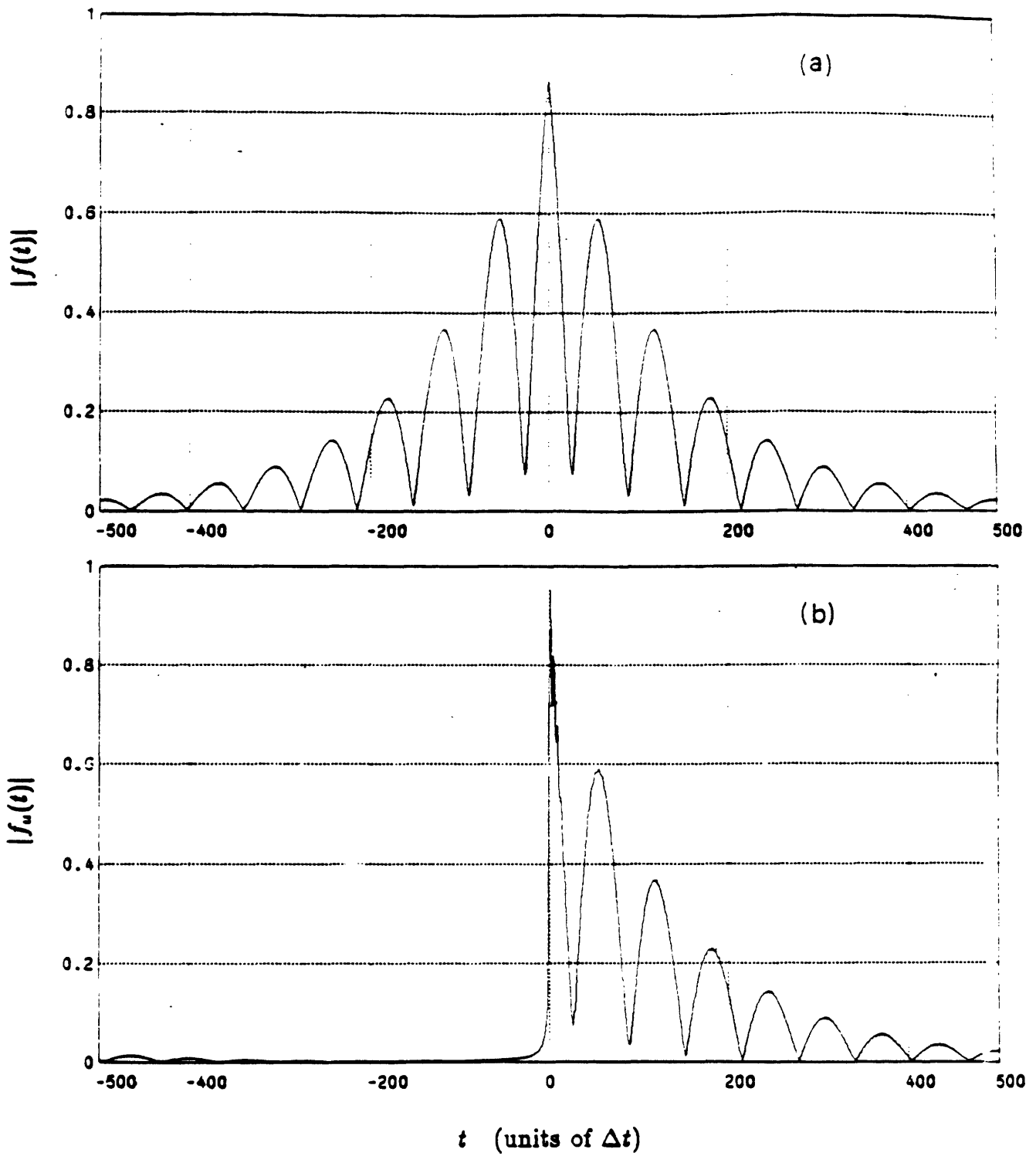
Figure 3.8: Magnitude of the original signal for positive and negative values of t (a). Magnitude of the signal synthesized by the unilateral inverse Fourier transform for positive and negative values of t (b).

magnitude of the error for positive values of t is displayed in Figure 3.9b, and the original signal magnitude is plotted in Figure (3.9)a for reference. The largest error in the synthesis occurs at small positive values of t, consistent with the theory which was discussed earlier. For additional reference, the error is displayed on a logarithmic scale in Figure 3.10.

As can be seen from Figure 3.8, the signal synthesized by the unilateral inverse Fourier transform is approximately causal, which is also consistent with Statement 2. The departure from exact causality occurs primarily for small negative values of t. The slight oscillations in $f_u(t)$ for large negative values of t are due to the aliasing which has occurred due to the use of the discrete version of the unilateral inverse Fourier transform.

Statement 3 indicates that under the condition that the unilateral inverse Fourier transform approximates the signal $f(t)$ for $t > 0$, there exists an inverse relationship between the unilateral Fourier transform and the unilateral inverse Fourier transform. To demonstrate this, we computed the unilateral inverse Fourier transform, followed by the unilateral Fourier transform. The magnitude of the result is plotted in Figure 3.11b for positive and negative values of ω. For comparison, the magnitude of the true Fourier transform $F(\omega)$ is also plotted in Figure 3.11a. From these curves, it can be seen that $\mathcal{F}_u\{\mathcal{F}_u^{-1}\{F(\omega)\}\} \sim F(\omega)U(\omega)$ as was predicted in Statement 3.

Statement 4 indicates that under the condition that the unilateral inverse Fourier transform approximates the signal $f(t)$ for $t > 0$, there exists an approximate real-part/imaginary-part sufficiency condition for $F(\omega)U(\omega)$. To demonstrate that the Fourier transform $F(\omega)$ has this property, the imaginary component was set to zero and then reconstructed from the real component using the Hilbert transform. To compute the Hilbert transform, the inverse Fourier transform of $Re[F(\omega)U(\omega)]$ was computed, and multiplied by $2U(t)$. The inverse Fourier transform was then computed. The magnitude of the Fourier transform, consisting of the real component
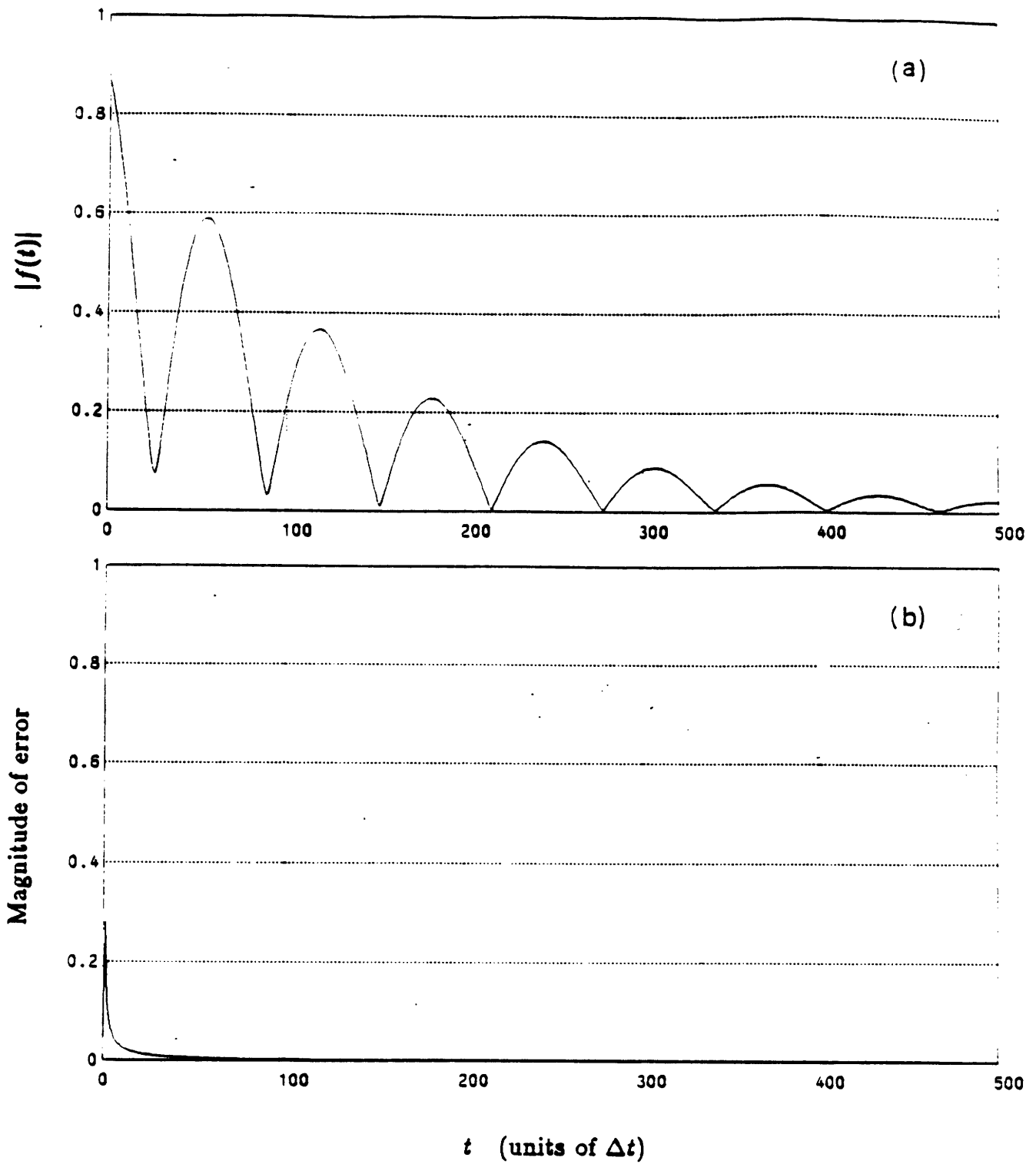
Figure 3.9: Magnitude of the original signal for positive values of t (a). Error in the unilateral inverse Fourier transform synthesis for positive values of t (b).
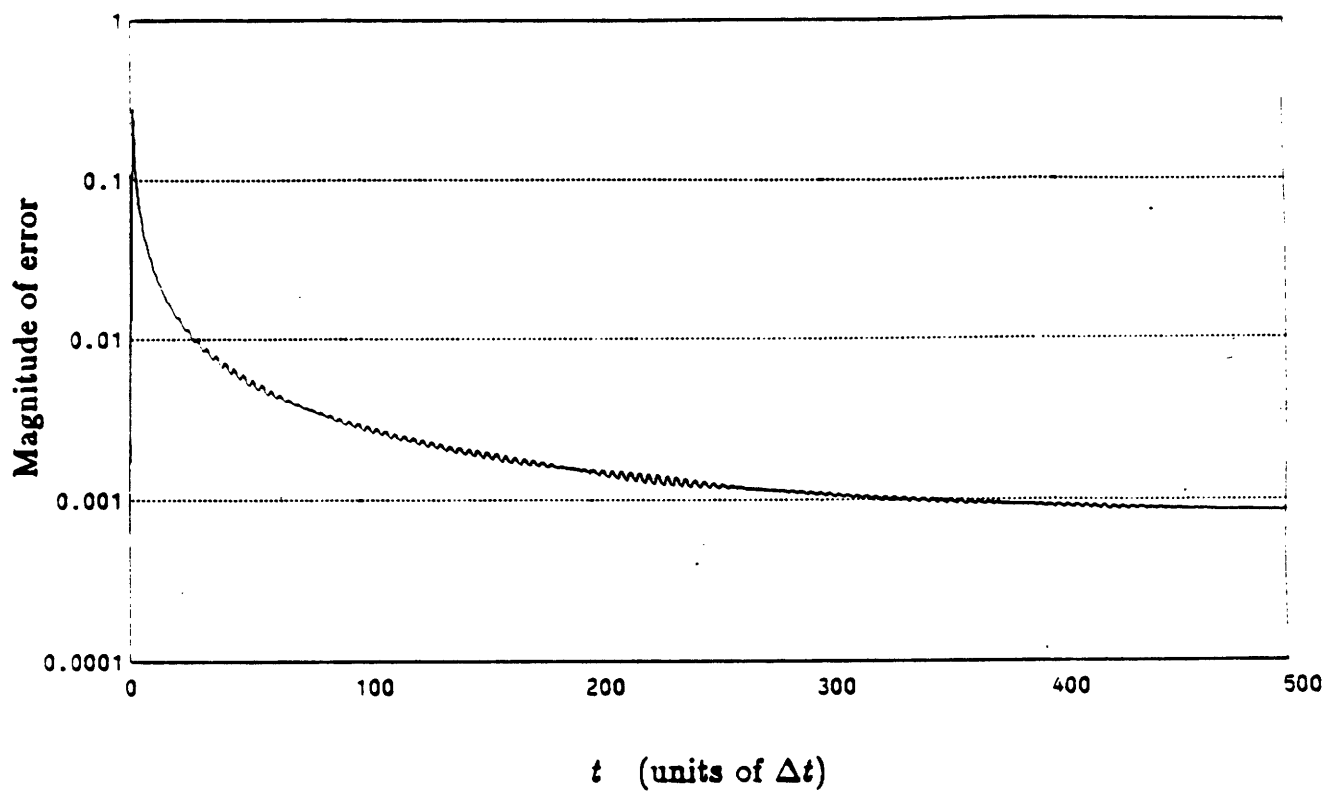
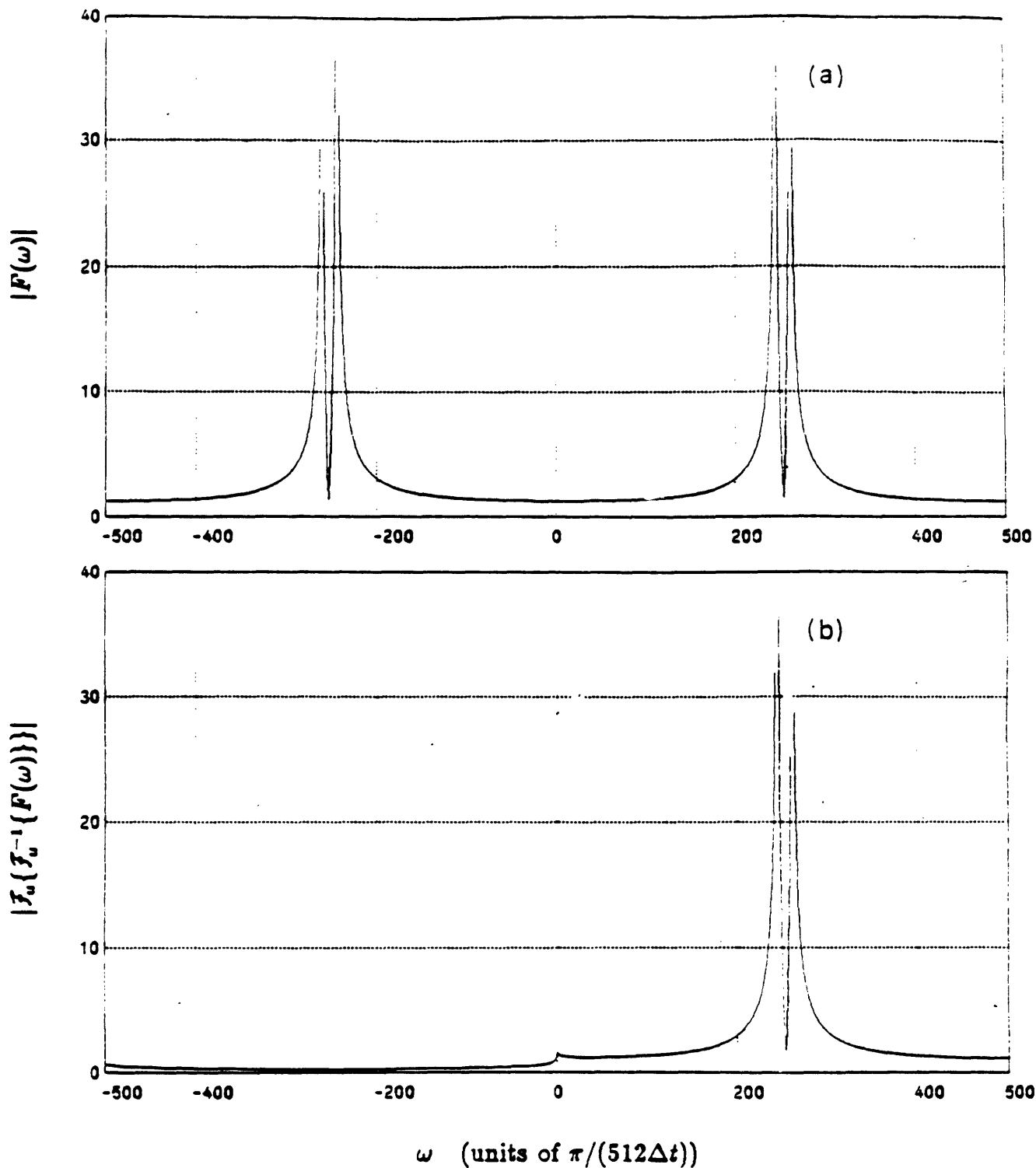Figure 3.10: Magnitude of the error in the unilateral inverse Fourier transform synthesis.

Figure 3.11: Magnitude of the original Fourier transform for positive and negative values of ω (a). Magnitude of the function $\mathcal{F}_u\{\mathcal{F}_u^{-1}\{F(\omega)\}\}$ for positive and negative values of ω (b).

and the reconstructed imaginary component, is displayed in Figure 3.12b for values of $\omega > 0$. The magnitude of the original Fourier transform for this range of ω is also displayed in Figure 3.12a for comparison. Although there are several differences between the curves, attributed to both the approximation in the theory and the numerical implementation, the agreement is quite good.

In order to demonstrate the relationship between the cosine and sine transforms of the real and imaginary components, we have chosen to illustrate only the first property in Statement 5, which is

$$C\{Re[F(\omega)]\} \sim -S\{Im[F(\omega)]\} \quad t > 0 \tag{3.61}$$

To demonstrate this, the discrete cosine transform was used to compute the left-hand side of this expression and the discrete sine transform was used to compute the right-hand side of the expression. In Figure 3.13a is shown the real-valued signal for $t > 0$ resulting from the cosine transform, and in Figure 3.13b is shown the real-valued signal for $t > 0$ resulting from the sine transform. The two curves compare quite closely, as is further confirmed by examining a plot of the difference between these two functions, shown in Figure 3.14.

Finally, in considering Statement 6, we have chosen to illustrate only the first property which is

$$f(t) \sim 2\mathcal{F}_u^{-1}\{Re[F(\omega)]\} \quad t > 0 \tag{3.62}$$

To demonstrate this property, the discrete version of the unilateral inverse Fourier transform was used to compute the right-hand side of this expression, and the magnitude of the resulting signal is shown for $t > 0$ in Figure 3.15b. For comparison, the magnitude of $f(t)$ for $t > 0$ is also shown in Figure 3.15a. The curves agree, although some differences, attributed to both the approximations in the theory and the numerical implementation, are evident.

In summary, we have reviewed the theory of exact and approximate analytic signals. The theory of exact analytic signals was presented in terms of the properties
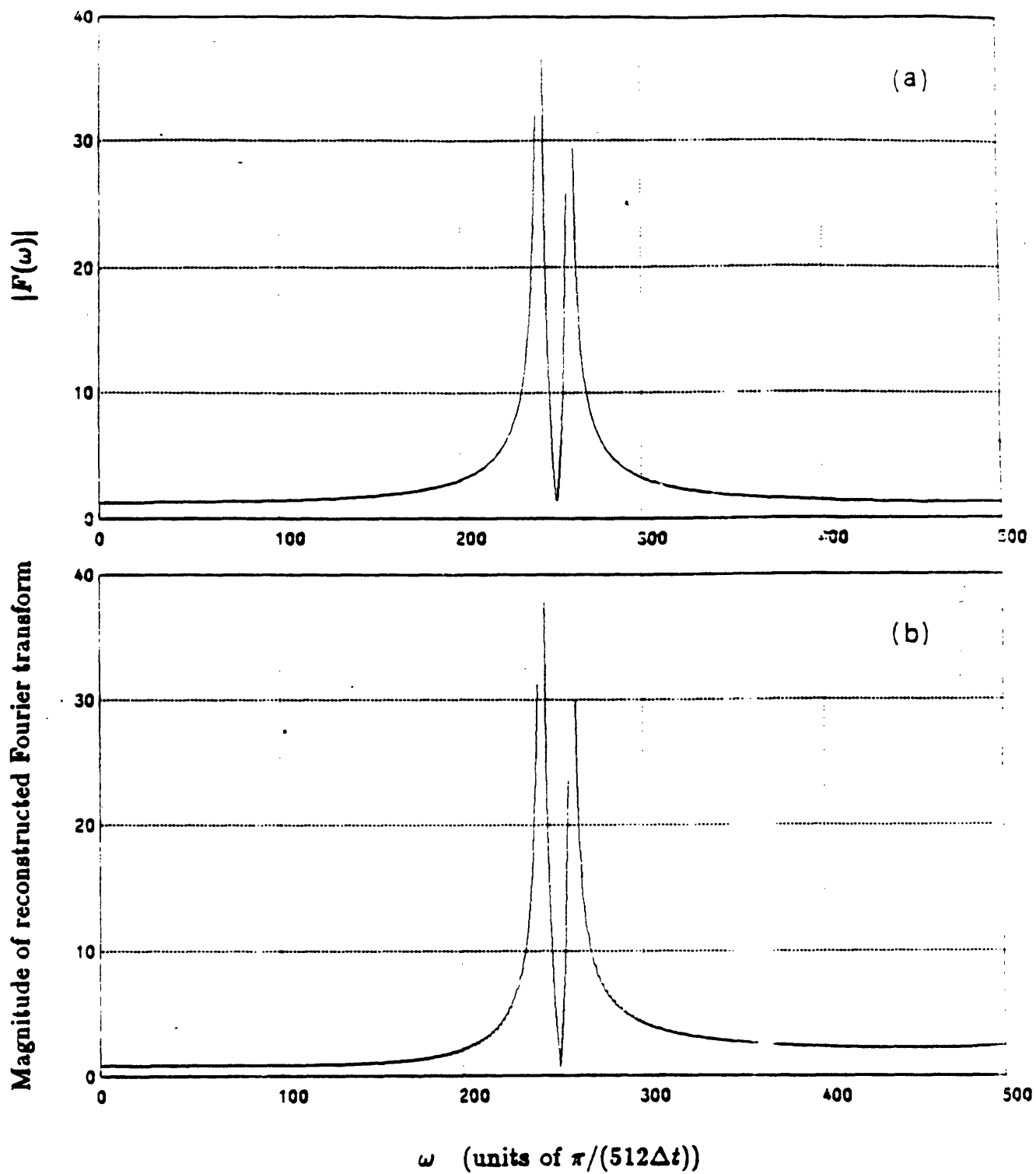
Figure 3.12: Magnitude of the original Fourier transform for positive values of ω (a). Magnitude of the reconstructed Fourier transform for positive values of ω (b).
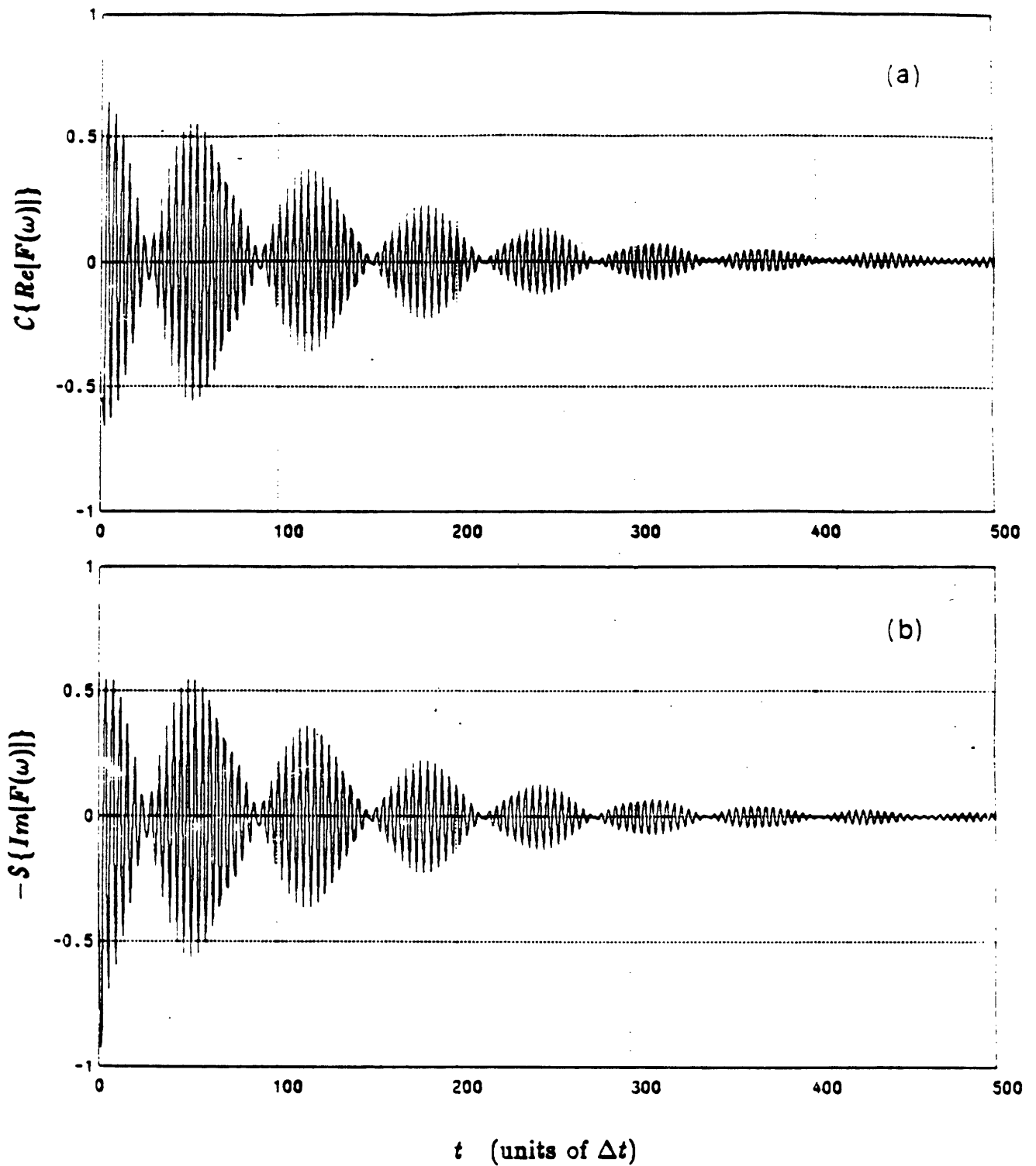
121

Figure 3.13: Cosine transform of $Re[F(\omega)]$ for positive values of t (a). Sine transform of $Im[F(\omega)]$ for positive values of t (b).
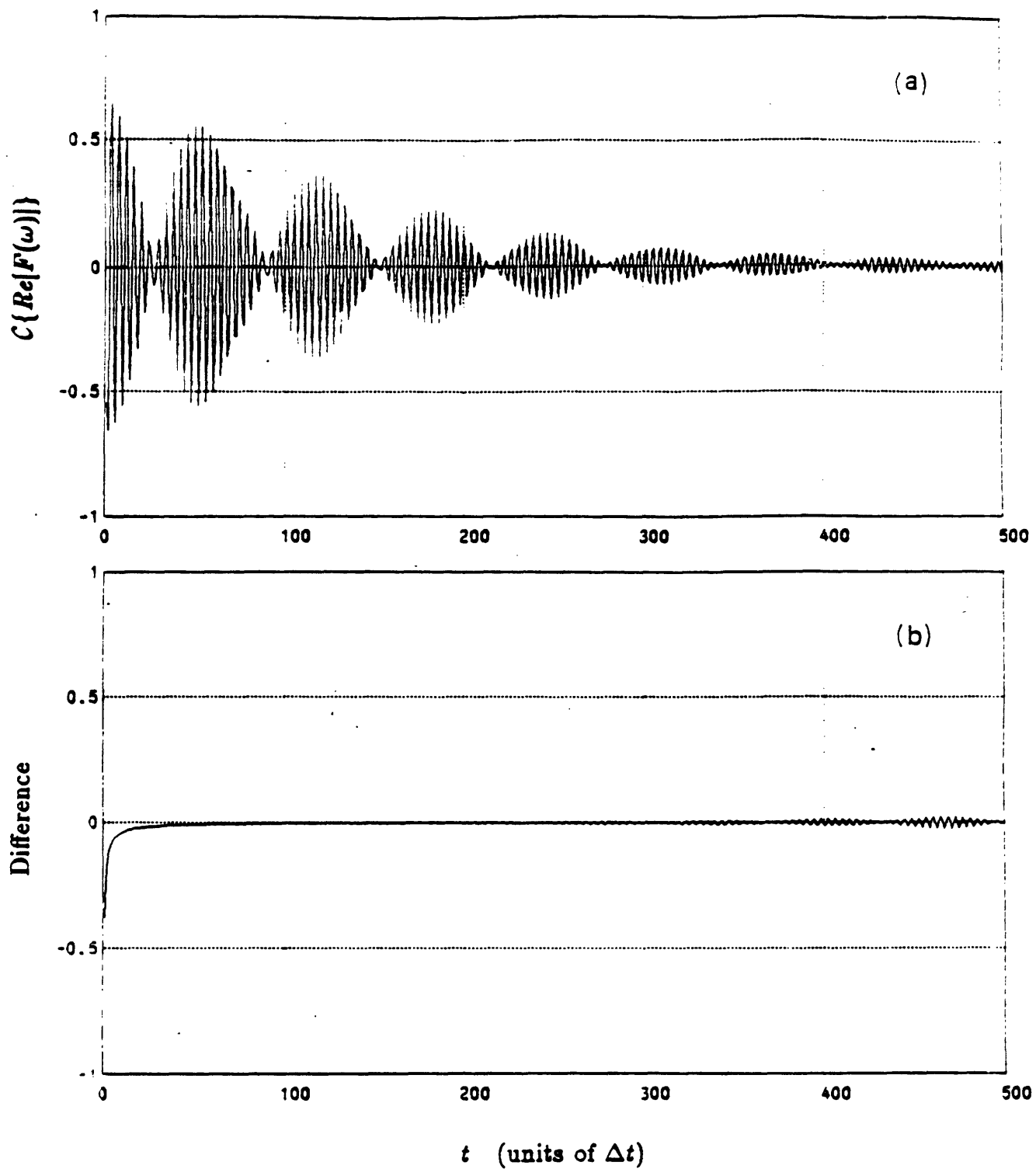
Figure 3.14: Cosine transform of the real part of $F(\omega)$ as a function of positive values of t (a). Difference between $C\{Re[F(\omega)]\}$ and $-S\{Im[F(\omega)]\}$ as function of positive values t (b).
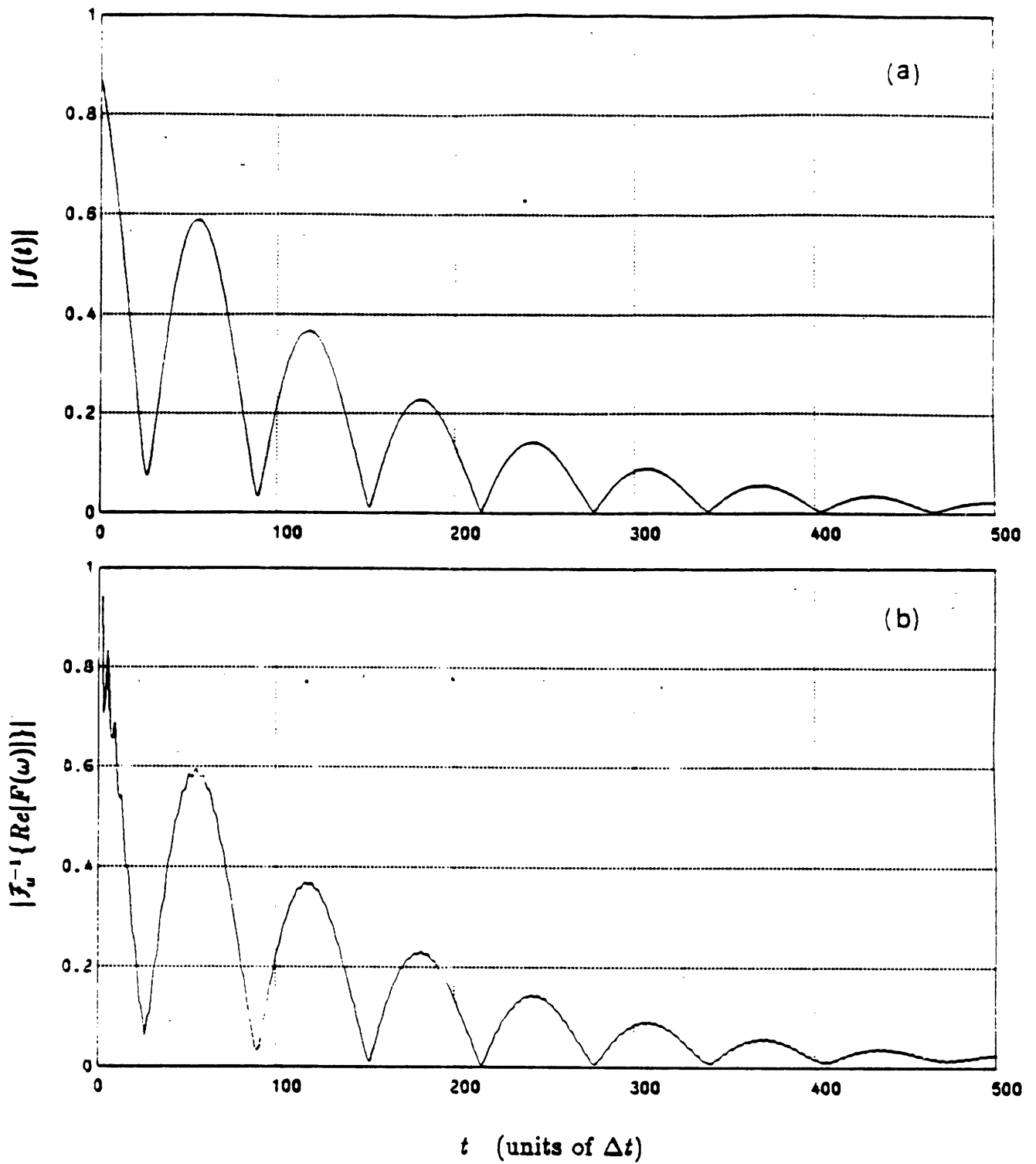
Figure 3.15: Magnitude of the original signal as a function of positive t (a). Unilateral inverse Fourier transform of the real part of $F(\omega)$ (b).

of the Fourier transform. The theory was then extended to develop the notion of a signal which is approximately analytic. Although such a signal does not have a causal Fourier transform, its real and imaginary parts can be approximately related by the Hilbert transform. The necessary condition for a even signal to possess this property is that its causal portion must be accurately synthesized by the unilateral inverse Fourier transform. If this is the case, there are a number of other interesting consequences including an approximate real-part/imaginary-part sufficiency for both the causal part of the signal and the causal part of its Fourier transform, and an inverse relationship between the unilateral Fourier transform and unilateral inverse Fourier transform. These consequences were summarized in several statements. Although the theory was presented for one-dimensional even functions, its principal application within this thesis will be to the two-dimensional circularly symmetric case. As will be pointed out in the following section, the validity of the unilateral synthesis is particularly applicable to signals which correspond to propagating fields in a circularly symmetric environment.

3.3 The Hilbert-Hankel Transform

In the preceding section, it was shown that in the context of the one-dimensional Fourier transform, the condition of causality in one domain implies the condition of real-part/imaginary-part sufficiency condition in the alternate domain. Specifically, it was shown that causality of the one-dimensional Fourier transform implies an exact relationship between the real and imaginary components of the corresponding signal. If the Fourier transform of the signal is not one-sided, the real and imaginary components are generally not related. However, in the special case that the signal can be approximated by a unilateral version of the inverse Fourier transform, it was shown that the signal possesses an approximate real-part/imaginary-part sufficiency condition. Further, if the signal is even, it has an approximate real-part/imaginary-part sufficiency condition if its causal portion can be approximated by the unilateral inverse Fourier transform. In this section, we will extend the theory of approximate analyticity to the two-dimensional circularly symmetric signal. Although the theory can be developed for the general multidimensional case, by considering the multidimensional version of the unilateral inverse Fourier transform, we will focus primarily on the special case of two-dimensional circularly symmetric signals. The motivation for studying this special case is that the corresponding two-dimensional signal is closely related to the propagating acoustic pressure field, considered in the previous chapter.

In the last chapter, the important relationship between the two-dimensional Fourier transform of a circularly symmetric function and the Hankel transform was reviewed. Specifically, it was shown that for fixed values of z and z_0, the acoustic pressure field $p(x, y, z; z_0)$ was related to the Green's function $g(k_x, k_y, z; z_0)$ via the two-dimensional Fourier transform. Under the condition of circularly symmetry, the relationship can be equivalently expressed in terms of the Hankel transform as

$$p(r, z; z_0) = \int_0^\infty g(k_r, z; z_0) J_0(k_r r) k_r \, dk_r \tag{3.63}$$

Dropping the explicit dependence on z and z_0, this expression can also be written as

$$p(r) = \int_0^\infty g(k_r) J_0(k_r r) k_r \, dk_r \qquad (3.64)$$

This relationship implies that $p(r)$ must be an even function of r, since $J_0(k_r r)$ is an even function of r. Only positive values of k_r are involved in the expression and thus $g(k_r)$ can in principle, be arbitrary for negative values of k_r. However, in writing the inverse relationship between $g(k_r)$ and $p(r)$ as

$$g(k_r) = \int_0^\infty p(r) J_0(k_r r) r \, dr \qquad (3.65)$$

it can be seen that $g(k_r)$ must also be an even function of k_r, since $J_0(k_r r)$ is an even function of k_r. The causality condition, which was important in establishing the exact real-part/imaginary-part sufficiency condition in the one-dimensional case, is not applicable to the Hankel transform, since both $g(k_r)$ and $p(r)$ are even, and thus not causal. In the remainder of this section however, we will show that under some circumstances, there exists an approximate real-part/imaginary-part sufficiency condition for $p(r)$ and $g(k_r)$. The theory which we will present will closely parallel the one-dimensional theory presented in the previous section.

In order to develop the property of approximate analyticity for a two-dimensional circularly symmetric signal, we must develop a unilateral version of the Hankel transform. That is, with analogy to the one-dimensional bilateral inverse Fourier transform and one-dimensional unilateral inverse Fourier transform, we wish to develop the Hankel transform and its unilateral version. In examining equation (3.64) it appears that the Hankel transform is already unilateral, since the limits of integration are from zero to infinity. However, this version of the Hankel transform is actually analogous to the one-sided cosine transform considered in the previous section. Here, we must develop the transform analogous to the Fourier transform, and then consider its unilateral counterpart.

In order to do this, the zeroth-order Bessel function of the first kind is written in

terms of Hankel functions[7] as

$$J_0(k_r r) = \frac{1}{2}[H_0^{(1)}(k_r r) + H_0^{(2)}(k_r r)] \tag{3.66}$$

so that equation (3.64) becomes

$$p(r) = \frac{1}{2}\int_0^\infty g(k_r)H_0^{(1)}(k_r r)k_r dk_r + \frac{1}{2}\int_0^\infty g(k_r)H_0^{(2)}(k_r r)k_r dk_r \tag{3.67}$$

which is valid for both positive and negative values of r. The expression can be simplified by using the property [8] that

$$H_0^{(2)}(ze^{-j\pi}) = -H_0^{(1)}(z) \tag{3.68}$$

to yield [4]

$$p(r) = \frac{1}{2}\int_{-\infty}^\infty g(k_r)H_0^{(1)}(k_r r)k_r dk_r, \quad r > 0 \tag{3.69}$$

The signal $p(r)$ can be determined for negative values of r by utilizing this equation and the fact that $p(r) = p(-r)$. It is important to recognize that the bilateral transform in equation (3.69) correctly synthesizes the acoustic pressure field $p(r)$ for positive values of r only. Specifically, although $p(r)$ is an even function of r, the Hankel function $H_0^{(1)}(k_r r)$ is not an even function of r, nor is $g(k_r)$ an odd function of k_r, and thus the expression in equation (3.69) is not correct for $r < 0$. The correct expression for $r < 0$ can be obtained, using properties of $H_0^{(1)}(k_r r)$ and $H_0^{(2)}(k_r r)$, as

$$p(r) = \frac{1}{2}\int_{-\infty}^\infty g(k_r)H_0^{(2)}(k_r r)k_r dk_r, \quad r < 0 \tag{3.70}$$

Alternately, a bilateral expression which describes $p(r)$ correctly for both positive and negative values of r can be written as

$$p(r) \equiv \mathcal{H}^{-1}\{g(k_r)\} \equiv \frac{1}{2}\int_{-\infty}^\infty g(k_r)H_0^{(1)}(k_r|r|)k_r dk_r \tag{3.71}$$

The transform in equation (3.71) will be referred to as the *bilateral inverse Hankel transform.*

---

[4]More precisely, the substitution yields $p(r) = \frac{1}{2}\int_{\infty e^{j\pi}}^\infty g(k_r)H_0^{(1)}(k_r r)k_r dk_r$, for $r > 0$.

We will define the unilateral version of the transform in equation (3.71) as

$$p_u(r) \equiv \mathcal{H}_u^{-1}\{g(k_r)\} \equiv \frac{1}{2}\int_0^\infty g(k_r)H_0^{(1)}(k_r r)k_r\,dk_r \qquad (3.72)$$

The operator $\mathcal{H}_u^{-1}$ could be referred to as the unilateral inverse Hankel transform. However, because the Hankel transform in equation (3.64) is already unilateral, the name unilateral Hankel transform is ambiguous. Instead, we will refer to the transform defined in equation (3.72) as the *Hilbert-Hankel transform*, because of its close relationship to the Hankel transform and because, as will be discussed shortly, the transform implies an approximate relationship between the real and imaginary components of $p(r)$.

The bilateral inverse Hankel transform and the Hilbert-Hankel transform can be written in alternate forms by utilizing the relationship that

$$H_0^{(1)}(k_r r) = J_0(k_r r) + jY_0(k_r r) \qquad (3.73)$$

where $Y_0(k_r r)$ is the zeroth-order Bessel function of the second kind, also referred to as the Weber function[8] or Neumann function[7]. We note that both $J_0(k_r r)$ and $Y_0(k_r r)$ are real-valued functions for real-valued arguments. Using this relationship, the bilateral inverse Hankel transform can be written as

$$\mathcal{H}^{-1}\{g(k_r)\} \equiv \frac{1}{2}\int_{-\infty}^\infty g(k_r)[\,J_0(k_r r) + jY_0(k_r|r|)\,]k_r\,dk_r \qquad (3.74)$$

and the Hilbert-Hankel transform can be written as

$$\mathcal{H}_u^{-1}\{g(k_r)\} \equiv \frac{1}{2}\int_0^\infty g(k_r)[\,J_0(k_r r) + jY_0(k_r r)\,]k_r\,dk_r \qquad (3.75)$$

It is also possible to develop a bilateral transform for the inverse relationship between $p(r)$ and $g(k_r)$. Using equation (3.65) and the relationship in equation (3.68), we obtain that

$$g(k_r) \equiv \mathcal{H}\{p(r)\} \equiv \frac{1}{2}\int_{-\infty}^\infty p(r)H_0^{(1)}(|k_r|r)r\,dr \qquad (3.76)$$

This expression will be referred to as the *bilateral Hankel transform*. Note that the bilateral Hankel transform and bilateral inverse Hankel transform are identical operators although they apply to different domains.

The most obvious definition for the unilateral version of this transform is obtained by replacing the lower limit in equation (3.76) by zero. However, we will find it convenient to define the transform differently. In particular, the unilateral version of the transform will be defined as

$$g_u(k_r) \equiv \mathcal{H}_u\{p(r)\} \equiv \frac{1}{2}\int_0^\infty p(r)[J_0(k_r r) - j\mathbf{H}_0(k_r r)]r\,dr \qquad (3.77)$$

The function $\mathbf{H}_0(z)$ is the zeroth-order Struve function [8][9], which is a particular solution [5] of the differential equation

$$z^2\frac{d^2w}{dz^2} + z\frac{dw}{dz} + z^2 w = \frac{2z}{\pi} \qquad (3.78)$$

Additionally, the zeroth-order Struve function, $\mathbf{H}_0(z)$, and the zeroth-order Bessel function of the first kind, $J_0(z)$, form a Hilbert transform pair [6]. To see this, $J_0(z)$ is expressed in terms of a Fourier synthesis integral as

$$J_0(z) = \frac{1}{2\pi}\int_{-1}^1 \frac{2}{(1-\omega^2)^{1/2}}e^{j\omega z}d\omega \qquad (3.79)$$

To compute the Hilbert transform $\hat{J}_0(z)$, the integrand in this expression is multiplied by $-j\,sgn[\omega]$ to yield

$$\hat{J}_0(z) = \frac{1}{2\pi}\int_{-1}^1 -j\,sgn[\omega]\frac{2}{(1-\omega^2)^{1/2}}e^{j\omega z}d\omega = \frac{2}{\pi}\int_0^1 \frac{\sin\omega z}{(1-\omega^2)^{1/2}}d\omega \qquad (3.80)$$

The last integral is also the integral representation for the zeroth-order Struve function[8].

The transform defined in equation (3.77) has also been considered by Papoulis[6][10] and has been referred to as the *complex Hankel transform* [6]. It is noted that $g_u(k_r)$

---

[5] The homogeneous solutions of this equation are $J_0(z)$ and $Y_0(z)$.

[6] The complex Hankel transform defined by Papoulis did not have a preceding factor of 1/2. However, we will find it convenient to retain this factor here.
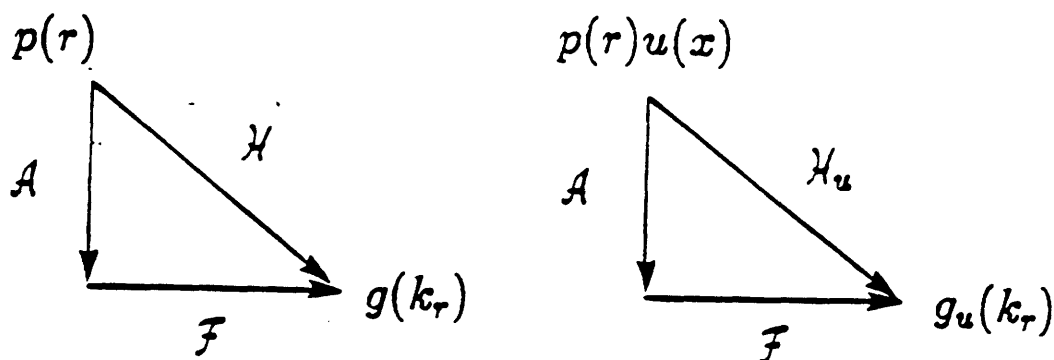
130

Figure 3.16: Relationships between the Abel, Fourier, Hankel, and complex Hankel transforms.

must be an analytic signal, since its real and imaginary components are related by the Hilbert transform. From preceding discussions, this implies that the one-dimensional Fourier transform of $g_u(k_r)$ must be causal. This fact, and the use of the projection slice theorem for two-dimensional Fourier transforms [11][12], provides the basis for expressing the complex Hankel transform in terms of the Abel transform, which is the projection of the two-dimensional circularly symmetric function, and the one-dimensional Fourier transform. Specifically, the complex Hankel transform of $p(r)$ can be determined by computing the Abel transform of $p(r)$, retaining the causal portion, and computing the one-dimensional Fourier transform. The relationships between the Abel, Fourier, Hankel, and complex Hankel transforms are summarized in Figure 3.16. In this figure, the operator A refers to the Abel transform defined as

$$p_A(x) = A\{p(r)\} \equiv \frac{1}{2\pi} \int_{-\infty}^{\infty} p(r)dy \qquad (3.81)$$

where $r = (x^2 + y^2)^{1/2}$. We note that

$$A\{p(r)u(x)\} = \frac{1}{2\pi} \int_{-\infty}^{\infty} p(r)u(x)dy = p_A(x)u(x) \qquad (3.82)$$

The definitions for the bilateral and unilateral transforms are now summarized

131

below

$$p(r) \equiv \mathcal{H}^{-1}\{g(k_r)\} \equiv \frac{1}{2}\int_{-\infty}^{\infty} g(k_r)[J_0(k_r r) + jY_0(k_r|r|)]k_r\,dk_r \tag{3.83}$$

$$p_u(r) \equiv \mathcal{H}_u^{-1}\{g(k_r)\} \equiv \frac{1}{2}\int_{0}^{\infty} g(k_r)[J_0(k_r r) + jY_0(k_r r)]k_r\,dk_r \tag{3.84}$$

$$g(k_r) \equiv \mathcal{H}\{p(r)\} \equiv \frac{1}{2}\int_{-\infty}^{\infty} p(r)[J_0(k_r r) + jY_0(|k_r|r)]r\,dr \tag{3.85}$$

$$g_u(k_r) \equiv \mathcal{H}_u\{p(r)\} \equiv \frac{1}{2}\int_{0}^{\infty} p(r)[J_0(k_r r) - j\mathbf{H}_0(k_r r)]r\,dr \tag{3.86}$$

where $p_u(r)$ represents the Hilbert-Hankel transform of $g(k_r)$ and $g_u(k_r)$ represents the complex Hankel transform of $p(r)$. These equations are analogous to equations (3.15)-(3.18), developed in the one-dimensional context in the preceding section. It is also convenient to define the following transforms and symbolic notation.

$$\mathbf{J}_0\{g(k_r)\} \equiv \int_{0}^{\infty} g(k_r)J_0(k_r r)k_r\,dk_r \tag{3.87}$$

$$\mathbf{Y}_0\{g(k_r)\} \equiv \int_{0}^{\infty} g(k_r)Y_0(k_r r)k_r\,dk_r \tag{3.88}$$

$$\mathbf{H}_0\{g(k_r)\} \equiv \int_{0}^{\infty} g(k_r)\mathbf{H}_0(k_r r)k_r\,dk_r \tag{3.89}$$

To develop the theory of two-dimensional circularly symmetric signals which are approximately analytic, we will require that

$$p(r) \sim p_u(r) \quad r > 0 \tag{3.90}$$

That is, only circularly symmetric signals $p(r)$ which can be approximated by the Hilbert-Hankel transform for $r > 0$ will be considered as approximately analytic. This condition is analogous to the condition stated in the previous section that $f(t) \sim f_u(t), t > 0$. To the extent that the approximation in equation (3.90) is valid, there will also exist an approximate relationship between the real and imaginary components of $p(r)$, for $r > 0$. This result is the basis for the first of several statements which will now be discussed. The statements will closely parallel the one-dimensional versions in the preceding section.

Statement 1 *If $p(r) \sim p_u(r)$ for $r > 0$, then the real and imaginary components of $p(r)$ must be approximately related for $r > 0$, as*

$$Re[p(r)] \sim -Y_0\{J_0\{Im[p(r)]\}\}$$

$$Im[p(r)] \sim Y_0\{J_0\{Re[p(r)]\}\} \tag{3.91}$$

The statement can be justified as follows. The condition that $p(r) \sim p_u(r), r > 0$ can be equivalently written as

$$J_0\{g(k_r)\} \sim \mathcal{H}_u^{-1}\{g(k_r)\} \quad r > 0 \tag{3.92}$$

so that

$$J_0\{g(k_r)\} \sim \frac{1}{2}J_0\{g(k_r)\} + j\frac{1}{2}Y_0\{g(k_r)\} \quad r > 0 \tag{3.93}$$

Using the facts that J_0 and Y_0 are real operators and that $Re[p(r)] = J_0\{Re[g(k_r)]\}$, $Im[p(r)] = J_0\{Im[g(k_r)]\}$, the statement is established by equating real and imaginary parts on both sides of equation (3.93).

The condition that $p(r) \sim p_u(r), r > 0$ is restrictive in the context of the general class of circularly symmetric signals $p(r)$. For example, in Figure 3.17, the positions of several poles in the k_r-plane corresponding to a rational function $g(k_r)$ are indicated. The poles labelled A', B', and C' are in symmetrically-located positions with respect to poles A, B, and C, due to the fact that $g(k_r)$ is even. The condition that $p(r) \sim p_u(r), r > 0$ is equivalent to the statement that the bilateral inverse Hankel transform integration contour $C_1 + C_2$, can be approximately replaced by the contour C_1. Clearly, the approximation will be poor if a pole, such as C, is located in Quadrant II of the k_r-plane. Essentially, the effects of this pole, quite important in determining the character of the corresponding signal $p(r)$ for $r > 0$, are only negligibly included by integrating along the positive real axis only. [7] That is, if $p(r)$ for $r > 0$ is exactly synthesized as

$$p(r) = \frac{1}{2}\int_{C_1+C_2} g(k_r)H_0^{(1)}(k_r r)k_r\,dk_r \tag{3.94}$$

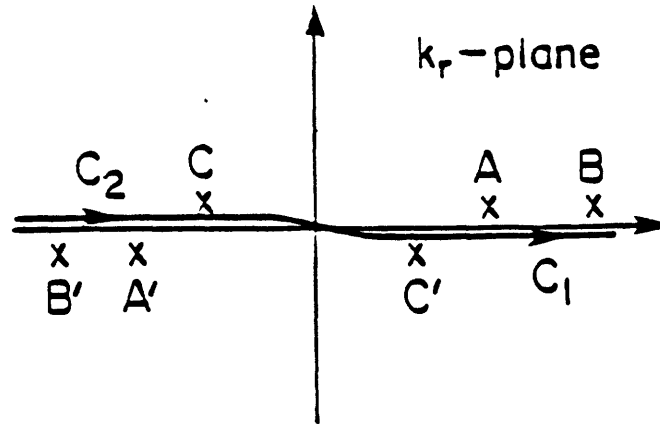[7]The pole at C' determines the behavior of the signal $p(r)$ primarily for values of $r < 0$.

Figure 3.17: Complex k_r-plane indicating positions of poles and the bilateral inverse Hankel transform contour.

so that

$$p(r) = \frac{1}{2}\int_{C_1} g(k_r)H_0^{(1)}(k_r r)k_r\,dk_r + \frac{1}{2}\int_{C_2} g(k_r)H_0^{(1)}(k_r r)k_r\,dk_r \qquad (3.95)$$

the pole at position C contributes primarily to the second of these two integrals, for values of $r > 0$. Thus, the approximation

$$p(r) \sim \frac{1}{2}\int_{C_1} g(k_r)H_0^{(1)}(k_r r)k_r\,dk_r = \mathcal{H}_u^{-1}\{g(k_r)\} \qquad (3.96)$$

is not accurate for $r > 0$, because of the position of pole C in the k_r-plane.

Although the condition that $p(r) \sim p_u(r), r > 0$ is a restrictive condition for the general class of two-dimensional circularly symmetric functions $p(r)$, the condition is apparently much less restrictive in the context of wave propagation. Essentially, the condition $p(r) \sim p_u(r), r > 0$, when written in the form

$$p(r) \sim \frac{1}{2}\int_0^\infty g(k_r)H_0^{(1)}(k_r r)k_r\,dk_r \quad r > 0 \qquad (3.97)$$

can be interpreted as the statement that $p(r)$ is accurately approximated by a superposition of positive, or *outgoing*, wavenumber components only. Here, the term outgoing has been associated with the function $H_0^{(1)}(k_r r)$. This association can be justified by asymptotically expanding $H_0^{(1)}(k_r r)$, for $r \gg 0$. For example, the propagating acoustic field, with temporal variation included, can be written for $r \gg 0$

134

as

$$p(r, t) \sim \frac{1}{(2\pi)^{1/2}} \int_0^\infty \frac{g(k_r)e^{-j\pi/4}}{(k_r r)^{1/2}} e^{j(k_r r - \omega t)} k_r dk_r \qquad (3.98)$$

The field is seen to be comprised of the superposition of outgoing plane-waves of the form $e^{j(k_r r - \omega t)}$. It is also possible to write the error in the Hilbert-Hankel transform approximation as

$$\epsilon(r) \equiv p(r) - p_u(r) = \frac{1}{2} \int_0^\infty g(k_r) H_0^{(2)}(k_r r) k_r dk_r, \quad r > 0 \qquad (3.99)$$

The error can be interpreted as a synthesis over the *incoming* wavenumber components of $p(r)$. Here, the term incoming has been associated with the function $H_0^{(2)}(k_r r)$. This association can be justified by asymptotically expanding $H_0^{(2)}(k_r r)$, for $r \gg 0$. The error, with temporal variation included, can thus be written as

$$\epsilon(r, t) \sim \frac{1}{(2\pi)^{1/2}} \int_0^\infty \frac{g(k_r)e^{-j\pi/4}}{(k_r r)^{1/2}} e^{-j(k_r r + \omega t)} k_r dk_r \qquad (3.100)$$

The error is seen to be comprised of the superposition of incoming plane-waves of the form $e^{-j(k_r r + \omega t)}$.

The unilateral synthesis implied by the condition $p(r) \sim p_u(r), r > 0$ is widely used in the area of underwater acoustics. For example, the unilateral synthesis implied by the Hilbert-Hankel transform is an important component in a number of synthetic data-generation methods for acoustic fields, such as the Fast-Field-Program (FFP). This is due to the fact that, in many cases, it is reasonable to assume that an acoustic field is comprised of outgoing components only. In Chapter 4 of this thesis, we will show several examples of acoustic fields, generated synthetically to represent realistic ocean environments, which support the statement that the acoustic field can be adequately described in terms of its outgoing components only. The implication is that the two-dimensional theory of approximately analytic signals, based on the condition $p(r) \sim p_u(r), r > 0$, is applicable to the wide class of outwardly propagating acoustic fields. In Chapter 6 of this thesis, we will present a number of examples of acoustic fields which possess the property of approximate real-part/imaginary-part sufficiency as a further justification of the preceding theory. In the remainder of this section, we

135

will consider other theoretical consequences of the approximation $p(r) \sim p_u(r), r > 0$.

Statement 2 *If $p(r) \sim p_u(r)$ for $r > 0$, then the Hilbert-Hankel transform, $p_u(r)$, is approximately causal.*

Note from equation (3.84), that the Hilbert-Hankel transform is defined for all values of r. Thus, the causality condition stated above is not a consequence of the definition of the Hilbert-Hankel transform, but rather is a consequence of the condition that $p(r) \sim p_u(r), r > 0$. To justify the statement, we note that $p(r) \sim p_u(r), r > 0$ implies that

$$\frac{1}{2} \int_{-\infty}^{0} g(k_r) H_0^{(1)}(k_r r) k_r \, dk_r \sim 0 \quad r > 0 \tag{3.101}$$

so that

$$-\frac{1}{2} \int_{0}^{\infty} g(k_r) H_0^{(1)}(-k_r r) k_r \, dk_r \sim 0 \quad r > 0 \tag{3.102}$$

The latter step follows from the fact that $g(k_r)$ is even in k_r. From this equation, and the definition of the Hilbert-Hankel transform, it can be seen that

$$p_u(-r) \sim 0 \quad r > 0 \tag{3.103}$$

and thus

$$p_u(r) \sim 0 \quad r < 0 \tag{3.104}$$

Therefore, under the condition that $p(r) \sim p_u(r), r > 0$, the Hilbert-Hankel transform must be approximately causal.

In general, the Hilbert-Hankel transform and the complex Hankel transform are not inverse operations. However, the following statement summarizes the relationship between these two transforms, under the condition that $p(r) \sim p_u(r), r > 0$.

Statement 3 *If $p(r) \sim p_u(r)$ for $r > 0$, then the Hilbert-Hankel transform and complex Hankel transform are related via*

$$\mathcal{H}_u\{\mathcal{H}_u^{-1}\{g(k_r)\}\} \sim g(k_r) u(k_r) \tag{3.105}$$

136

To justify the statement, the complex Hankel transform is written in terms of the operators J_0, Y_0, and $\mathbf{H}_0$ as

$$\mathcal{H}_u\{p_u(r)\} = \frac{1}{4}g(k_r) + \frac{1}{4}\mathbf{H}_0\{\ Y_0\{g(k_r)\}\ \} + \frac{1}{4}j(\ J_0\{\ Y_0\{g(k_r)\}\ \} - \mathbf{H}_0\{\ J_0\{g(k_r)\}\ \}\ )$$

(3.106)

which is valid for all k_r. Next, from the approximation $p(r) \sim p_u(r), r > 0$, it follows that

$$J_0\{g(k_r)\} \sim \frac{1}{2}J_0\{g(k_r)\} + \frac{1}{2}jY_0\{g(k_r)\}\ \ r > 0$$

(3.107)

so that

$$J_0\{g(k_r)\} \sim jY_0\{g(k_r)\}\ \ r > 0$$

(3.108)

Substituting this expression into equation (3.106), we find that

$$\mathcal{H}_u\{p_u(r)\} \sim \frac{1}{4}g(k_r) + \frac{1}{4}\mathbf{H}_0\{Y_0\{g(k_r)\}\} + \frac{1}{4}j(\ -jJ_0\{J_0\{g(k_r)\}\} - j\mathbf{H}_0\{Y_0\{g(k_r)\}\}\ )$$

(3.109)

valid for all k_r. Substituting the orthogonality relationships [13] [14]

$$J_0\{\ J_0\{g(k_r)\}\ \} = g(k_r)$$

(3.110)

and

$$\mathbf{H}_0\{\ Y_0\{g(k_r)\}\ \} = sgn[k_r]g(k_r)$$

(3.111)

into equation (3.109) justifies the statement that

$$\mathcal{H}_u\{p_u(r)\} \sim g(k_r)u(k_r)$$

(3.112)

The next statement concerns a real-part/imaginary-part sufficiency condition which occurs in k_r domain. The fact that $g(k_r)$ has an approximate real-part/imaginary-part sufficiency condition is not completely unexpected, since, as previously discussed, there exists an approximate causality condition in the alternate r domain. The real-part/imaginary-part sufficiency condition for $g(k_r)$ is summarized in the following statement.

Statement 4 *If* $p(r) \sim p_u(r)$ *for* $r > 0$, *then the real and imaginary components of* $g(k_r)$ *must be related by the Hilbert transform for* $k_r > 0$.

To justify this, Statement 3 is used to obtain the expression

$$\mathcal{H}_u\{p_u(r)\} \sim g(k_r)u(k_r) \tag{3.113}$$

Writing the operator $\mathcal{H}_u$ in terms of the operators J_0 and Y_0 yields

$$J_0\{Re[p_u(r)]\} + \mathbf{H}_0\{Im[p_u(r)]\} + j(-\mathbf{H}_0\{Re[p_u(r)]\} + J_0\{Im[p_u(r)]\})$$

$$\sim Re[g(k_r)] + j\,Im[g(k_r)] \quad k_r > 0 \tag{3.114}$$

It is noted that the real and imaginary components on the left-hand side of this expression form a Hilbert transform pair, so that the real and imaginary components on the right-hand side are also related approximately by the Hilbert transform.

Although we have previously considered several statements involving the relationships between the Hilbert-Hankel transform and the complex Hankel transform, it is also possible to derive a number of interesting relationships between the J_0, Y_0, and $\mathbf{H}_0$ transforms which comprise these. To develop these relationships, we write the Hilbert-Hankel transform and complex Hankel transform as

$$p_u(r) = \mathcal{H}_u^{-1}\{g(k_r)\} = \frac{1}{2}J_0\{g(k_r)\} + j\frac{1}{2}Y_0\{g(k_r)\} \tag{3.115}$$

and

$$g_u(k_r) = \mathcal{H}_u\{p(r)\} = \frac{1}{2}J_0\{p(r)\} - j\frac{1}{2}\mathbf{H}_0\{p(r)\} \tag{3.116}$$

Using these relationships, two statements involving the relationships between the J_0, Y_0, and $\mathbf{H}_0$ transforms are now made.

Statement 5 *If* $p(r) \sim p_u(r)$ *for* $r > 0$, *then the* J_0 *and* Y_0 *transforms of the real and imaginary components of* $g(k_r)$ *are related for* $r > 0$ *via*

$$J_0\{Re[g(k_r)]\} \sim -Y_0\{Im[g(k_r)]\} \tag{3.117}$$

138

$$J_0\{Im[g(k_r)]\} \sim Y_0\{Re[g(k_r)]\} \qquad (3.118)$$

Additionally, the J_0 and Y_0 transforms of the real and imaginary components of $p(r)$ are related for $k_r > 0$ via

$$J_0\{Re[p(r)]\} \sim \mathbf{H}_0\{Im[p(r)]\} \qquad (3.119)$$

$$J_0\{Im[p(r)]\} \sim -\mathbf{H}_0\{Re[p(r)]\} \qquad (3.120)$$

To justify the first part of this statement, the condition $p(r) \sim p_u(r), r > 0$ is written as

$$J_0\{g(k_r)\} \sim \frac{1}{2}J_0\{g(k_r)\} + j\frac{1}{2}Y_0\{g(k_r)\} \quad r > 0 \qquad (3.121)$$

so that

$$J_0\{g(k_r)\} \sim jY_0\{g(k_r)\} \quad r > 0 \qquad (3.122)$$

If the real and imaginary parts on both sides of this expression are equated, the first pair of equations in the statement are obtained. To derive the second pair of equations, we use Statement 3, which relates the Hilbert-Hankel transform and the complex Hankel transform, to derive that

$$J_0\{p(r)\} \sim \mathcal{H}_u\{p(r)\} \quad k_r > 0 \qquad (3.123)$$

Using equation (3.116), this expression becomes

$$J_0\{g(k_r)\} \sim \frac{1}{2}J_0\{p(r)\} - j\frac{1}{2}\mathbf{H}_0\{p(r)\} \quad k_r > 0 \qquad (3.124)$$

so that

$$J_0\{p(r)\} \sim -j\mathbf{H}_0\{p(r)\} \quad k_r > 0 \qquad (3.125)$$

Equating the real and imaginary parts on both sides of this expression yields the second pair of equations.

An additional consequence of the validity of the unilateral synthesis of $p(r)$ for $r > 0$ is summarized in the following statement.

139

Statement 6 *If $p(r) \sim p_a(r)$ for $r > 0$, then $p(r)$ can be approximately synthesized, for $r > 0$, in terms of either the real, or imaginary components of $g(k_r)$, as*

$$p(r) \sim 2\mathcal{H}_a^{-1}\{Re[g(k_r)]\} \tag{3.126}$$

$$p(r) \sim 2j\mathcal{H}_a^{-1}\{Im[g(k_r)]\} \tag{3.127}$$

Additionally, $g(k_r)$ can be approximately analyzed, for $k_r > 0$, in terms of either the real, or imaginary components of $p(r)$, as

$$g(k_r) \sim 2\mathcal{H}_a\{Re[p(r)]\} \tag{3.128}$$

$$g(k_r) \sim 2j\mathcal{H}_a\{Im[p(r)]\} \tag{3.129}$$

These relationships may be of importance if only one component of the pressure field (or Green's function) is available and it is desirable to determine both components of the Green's function (or pressure field). To develop the first pair of equations, we use the fact that

$$p(r) \sim \frac{1}{2}J_0\{g(k_r)\} + j\frac{1}{2}Y_0\{g(k_r)\} \quad r > 0 \tag{3.130}$$

If equations (3.117) and (3.118) are substituted into the right-hand side of this expression, the first pair of equations are obtained. To derive the second pair, we use Statement 3, which relates the Hilbert-Hankel transform and complex Hankel transform, to derive that

$$g(k_r) \sim \mathcal{H}_a\{p(r)\} \quad k_r > 0 \tag{3.131}$$

If equations (3.119) and (3.120) are substituted into the right-hand side of this expression, the second pair of equations is obtained.

In the previous section, a numerical example was presented in order to demonstrate the one-dimensional theory of approximate analyticity. In the two-dimensional circularly symmetric case, presenting an analogous example is more difficult due to fact that there is no efficient numerical algorithm for computing the Hilbert-Hankel transform. That is, although efficient algorithms exist for computing the Hankel transform,

and the complex Hankel transform, no such algorithm exists for the Hilbert-Hankel transform. In the next section however, we will develop the asymptotic version of the Hilbert-Hankel transform. The asymptotic version of the Hilbert-Hankel transform not only forms the basis for a computationally efficient algorithm, but has a number of other interesting and important properties as well. These properties will be developed in the next section, and will be illustrated using numerical examples of acoustic fields in Chapter 6.

To summarize, in this section the property of approximate analyticity was extended to two-dimensional circularly symmetric signals. To do this, we developed a bilateral version of the inverse Hankel transform and its unilateral counterpart, referred to as the Hilbert-Hankel transform. Under the condition that the two-dimensional circularly symmetric signal is approximated by the Hilbert-Hankel transform for $r > 0$, it was shown that the real and imaginary parts of such a signal are approximately related. The Hilbert-Hankel transform was also related to another unilateral transform, referred to as the complex Hankel transform. A number of other consequences based on the validity of the Hilbert-Hankel transform were developed. The theory is of particular importance because of its application to outgoing acoustic fields.

3.4 The Asymptotic Hilbert-Hankel Transform

In the previous section of this chapter, the Hilbert-Hankel transform was defined and a number of its properties were developed. It was shown that if the causal portion of a circularly symmetric signal, described by the bilateral inverse Hankel transform, can be approximated by the Hilbert-Hankel transform, there are some important consequences. These include an approximate real-part/imaginary-part sufficiency condition for the signal.

The Hilbert-Hankel transform is the unilateral version of the bilateral inverse Hankel transform, and can be expressed as

$$p_u(r) \equiv \mathcal{H}_u^{-1}\{g(k_r)\} = \frac{1}{2}\int_0^\infty g(k_r)[\, J_0(k_r r) + jY_0(k_r r)]k_r\, dk_r \qquad (3.132)$$

The Hilbert-Hankel transform can be analytically evaluated by recognizing that

$$\mathcal{H}_u^{-1}\{g(k_r)\} = \frac{1}{2}J_0\{g(k_r)\} + \frac{1}{2}jY_0\{g(k_r)\} \qquad (3.133)$$

and by using existing integral tables to compute the J_0 and Y_0 transforms[7]. In contrast with the complex Hankel transform, there does not exist an efficient numerical algorithm for computing the Hilbert-Hankel transform. However, in this section we will consider the asymptotic version of the Hilbert-Hankel transform. This transform not only provides the basis for efficient computing an approximation to $p_u(r)$, but has a number of interesting and important properties as well.

To develop the asymptotic transform, the Hankel function is expressed asymptotically for large $|k_r r|$ as

$$H_0^{(1)}(k_r r) \sim (\frac{2}{\pi k_r r})^{1/2} e^{j(k_r r - \pi/4)} \qquad (3.134)$$

Substituting this relationship into equation (3.132) we define the resulting transform as

$$p_{au}(r) \equiv \mathcal{H}_{au}^{-1}\{g(k_r)\} \equiv \frac{1}{2}\int_0^\infty g(k_r)(\frac{2}{\pi k_r r})^{1/2} e^{j(k_r r - \pi/4)} k_r\, dk_r \qquad (3.135)$$

This transform will be referred to as the *asymptotic Hilbert-Hankel transform.*

It is noted that since the asymptotic version of the Hankel function is valid for $r \gg 0$, the Hilbert-Hankel transform and asymptotic Hilbert-Hankel transform are related as

$$p_u(r) \sim p_{au}(r) \quad r \gg 0 \tag{3.136}$$

Additionally, if the Hilbert-Hankel transform approximates $p(r)$ for $r > 0$, we have that

$$p(r) \sim p_u(r) \quad r > 0 \tag{3.137}$$

Combining the two relationships, yields the relationship between the $p(r)$ and the asymptotic Hilbert-Hankel transform

$$p(r) \sim p_{au}(r) \quad r \gg 0 \tag{3.138}$$

The relationship described in equation (3.138) is the basis of the Fast-Field-Program (FFP), commonly used in underwater acoustics for synthetic acoustic field generation.

The FFP was primarily developed as a tool for efficient computation of acoustic fields[1]. Its efficiency stems from the fact that equation (3.135) can be written as

$$p_{au}(r)r^{1/2} = \frac{1}{2\pi} \int_0^\infty g(k_r)(\frac{2}{\pi k_r})^{1/2} e^{j(k_r r - \pi/4)} k_r dk_r \tag{3.139}$$

The right-hand side of equation (3.139) is in the form of an inverse Fourier transform, which can be rapidly computed using the inverse Fast-Fourier-Transform (FFT).

Essentially, the use of the FFP to generate the acoustic field $p(r)$ is based on two separate assumptions. The first assumption is that $p(r)$ can be accurately synthesized by the Hilbert-Hankel transform, for $r > 0$. The second assumption is that the asymptotic version of this transform is also applicable, for values of $r \gg 0$. Recalling that $p(r)$ can be expressed exactly, for all values of r, via

$$p(r) = \int_0^\infty g(k_r) J_0(k_r r) k_r dk_r \tag{3.140}$$

the FFP can be viewed as an algorithm for the approximate computation of the Hankel transform, for a special class of functions $p(r)$. Since the development of the FFP,

numerous alternate algorithms for efficient computation of the Hankel transform have been developed. These include, for example, algorithms based on the relationship between the two-dimensional Fourier transform and the Hankel transform. Such algorithms are in principle exact, and do not require any asymptotic approximations. Additionally, they do not require the validity of the approximation $p(r) \sim p_u(r), r > 0$, which is an important first approximation in the FFP. In the following chapter, we will present several examples of the comparison between an exact Hankel transform algorithm and the FFP, in the context of synthetic acoustic field generation.

It is interesting to note that there exists another efficient algorithm for approximate computation of $p(r)$ which requires only a single approximation, rather than the pair of approximations required in the FFP. This method requires that only the asymptotic approximation be made, and is thus applicable to functions which do not satisfy the condition

$$p(r) \sim p_u(r) \quad r > 0 \qquad (3.141)$$

The method can be developed by writing $p(r)$ in terms of the bilateral inverse Hankel transform [8] as

$$p(r) = \frac{1}{2} \int_{-\infty}^{\infty} g(k_r) H_0^{(1)}(k_r|r|) k_r \, dk_r \qquad (3.142)$$

and asymptotically expanding $H_0^{(1)}(k_r|r|)$ as

$$H_0^{(1)}(k_r|r|) \sim \left(\frac{2}{\pi k_r |r|}\right)^{1/2} e^{j(k_r|r| - \pi/4)} \qquad (3.143)$$

Substituting this approximation into equation (3.142) and simplifying yields

$$p(r) \sim \frac{1}{|r|^{1/2}} \int_0^{\infty} \frac{g(k_r) k_r^{1/2}}{\pi^{1/2}} [\cos k_r r + \sin k_r |r|] \, dk_r \qquad (3.144)$$

and therefore

$$p(r) r^{1/2} \sim \int_0^{\infty} \frac{g(k_r) k_r^{1/2}}{\pi^{1/2}} [\cos k_r r + \sin k_r r] \, dk_r, \quad r > 0 \qquad (3.145)$$

---

[8] The derivation can also be done by using the unilateral transform in equation (3.140) and the asymptotic expansion for $J_0(k_r r)$.

144

The right-hand side of this expression is in the form of a unilateral *Hartley transform* [15][16]. The unilateral Hartley transform differs from the unilateral Fourier transform and the unilateral inverse Fourier transform, because it does not contain the j term preceding $\sin k_r r$, as can be verified by examining equation (3.145). Therefore, defining the bilateral Hartley transform as

$$\mathcal{CAS}\{f(r)\} \equiv \int_{-\infty}^{\infty} f(r)[\cos k_r r + \sin k_r r]\,dk_r \qquad (3.146)$$

we see that

$$p(r) \sim \frac{1}{r^{1/2}}\mathcal{CAS}\{\frac{g(k_r)k_r^{1/2}u(k_r)}{\pi^{1/2}}\} \qquad (3.147)$$

for values of $r > 0$. The connection between the Hankel transform and the Hartley transform may have practical applications in the context of synthetic field generation. This is particularly true given the recent development of efficient algorithms to compute the Hartley transform [17][18]. Although we have chosen not to pursue this further, the Hartley transform is intermediate to the exact Hankel transform and the FFP, and may prove to be especially applicable to problems in which the unilateral approximation $p(r) \sim p_u(r)$ is not valid.

We have thus far emphasized the computational aspects of the relationships

$$p(r) \sim p_u(r) \quad r > 0 \qquad (3.148)$$

$$p_u(r) \sim p_{au}(r) \quad r \gg 0 \qquad (3.149)$$

where

$$p_{au}(r) = \mathcal{H}_{au}^{-1}\{g(k_r)\} = \frac{1}{2}\int_0^{\infty} g(k_r)(\frac{2}{\pi k_r r})^{1/2}e^{j(k_r r - \pi/4)}k_r\,dk_r \qquad (3.150)$$

In the remainder of this section, we will develop other important consequences of equations (3.148) - (3.150). To do this, the quantity $\bar{g}(k_r)$ is defined as

$$\bar{g}(k_r) = (2\pi|k_r|)^{1/2}g(k_r)e^{-j\pi/4} \qquad (3.151)$$

Equations (3.148) - (3.150) can thus be written as

$$p(r)r^{1/2} \sim p_{au}(r)r^{1/2} \quad r \gg 0 \qquad (3.152)$$

145

where

$$p_{aw}(r)r^{1/2} = \frac{1}{2\pi}\int_0^\infty \tilde{g}(k_r)e^{jk_r \cdot r}dk_r \qquad (3.153)$$

We note that the right-hand side of equation (3.153) is in the form of a unilateral inverse Fourier transform. From discussion earlier, this implies that the real and imaginary components of $p_{aw}(r)r^{1/2}$ are related exactly by the Hilbert transform. Additionally, since $p(r)r^{1/2} \sim p_{aw}(r)r^{1/2}$ for $r \gg 0$, it is seen that the signal $p(r)r^{1/2}$ has the property of one-dimensional approximate analyticity. In other words, since the signal $p(r)r^{1/2}$ can be approximated by a unilateral version of its inverse Fourier transform, the real and imaginary components of $r^{1/2}p(r)$ must be approximately related by the Hilbert transform. Thus, because of the special form of the asymptotic expansion of $H_0^{(1)}(k_r r)$, it is possible to apply either the two-dimensional theory of approximate analyticity, discussed in Section 3.3, to the signal $p(r)$, or alternately, the one-dimensional theory, discussed in Section 3.2, to the signal $p(r)r^{1/2}$. Mathematically, the connection between the two-dimensional and one-dimensional theory can be stated as

$$p(r) \sim \mathcal{H}_w^{-1}\{g(k_r)\} \quad r > 0 \qquad (3.154)$$

$$r^{1/2}p(r) \sim \mathcal{F}_w^{-1}\{\tilde{g}(k_r)\} \quad r \gg 0 \qquad (3.155)$$

where

$$\tilde{g}(k_r) = (2\pi|k_r|)^{1/2}g(k_r)e^{-j\pi/4} \qquad (3.156)$$

The primary difference between the one and two dimensional theories occurs at small values of r. In our applications, we have not found the difference to be particularly significant at values of r greater than several acoustic wavelengths.

In later chapters of this thesis, we will explore other consequences of the theory of one-dimensional analytic signals applied in the context of shallow water acoustics. Specifically, in Chapter 4, we will demonstrate that a realistic field $p(r)$, can be synthesized using the relationship

$$r^{1/2}p(r) \sim 2j\mathcal{F}_w^{-1}\{Im[\tilde{g}(k_r)]\} \qquad (3.157)$$

146

which follows from Statement 4 in Section 3.2. This method represents an important extension to the hybrid synthetic data generation which will be discussed. Also, in Chapter 6,.we will demonstrate a reconstruction algorithm which uses the FFT to reconstruct a sampled version of one quadrature channel of an acoustic field, from a sampled version of the alternate channel. The method will be applied to synthetically generated deep and shallow water acoustic fields, and to several experimentally collected acoustic fields.

The relationship between $p(r)$ and the one-dimensional Fourier transform has some important consequences. In particular, the properties of the exact Hankel transform are complicated and can often obscure much simpler behavior of $p(r)$ and $g(k_r)$, especially at large values of r and k_r. In considering equation (3.155) it is possible to develop approximate properties of $p(r)$ and $g(k_r)$ in terms of the simpler, one-dimensional Fourier transform. Several of these properties can be exploited in both the acquisition, and signal processing of acoustic field measurements. We will focus on four of these properties in the remainder of this section.

The shift theorem for the Fourier transform states that a shift in one domain implies a linear phase shift in the alternate domain. Recalling the definition of $p_{au}(r)$ as

$$p_{au}(r) = \mathcal{H}_{au}^{-1}\{g(k_r)\} = \frac{1}{r^{1/2}}\mathcal{F}_u^{-1}\{\bar{g}(k_r)\} \tag{3.158}$$

the application of the shift theorem yields

$$p_{au}(r + r_0) = \frac{1}{(r + r_0)^{1/2}}\mathcal{F}_u^{-1}\{\bar{g}(k_r)e^{jk_r r_0}\} \tag{3.159}$$

It is not always the case that the condition

$$p(r) \sim p_{au}(r) \quad r \gg 0 \tag{3.160}$$

implies the condition

$$p(r + r_0) \sim p_{au}(r + r_0) \quad r \gg 0 \tag{3.161}$$

For example, if r_0 is large and negative, the latter condition is not valid, as can be established by recognizing that $p(r)$ is an even function, and that $p_{ow}(r)$ is approximately causal. However, for small values of positive r_0, the condition is in equation (3.161) is reasonable. An implication is that it is possible to approximately correct for fixed range registration errors in the acquisition of $p(r)$, by multiplying $g(k_r)$ by a linear phase shift term. The correction technique may be important in a practical sense due to the difficulty in obtaining acoustic field measurements at short ranges in an ocean experiments. Of course, it is also possible to approximately compensate for a fixed range registration error by shifting the field prior to computing the Hankel transform. However, in some cases, the precise value of r_0 may be unknown, and the determination of its value may be more conveniently done in the wavenumber domain. Additionally, the acoustic field is typically acquired on a non-uniform grid and must be re-interpolated to a new grid prior to computing the Hankel transform. By exploiting the shift theorem, the re-interpolation of the field need not be performed for each choice of r_0. In Chapter 6, we will present a numerical example of the shift theorem in the context of extracting the reflection coefficient from a realistic acoustic field with range offset.

The dual property for the shift theorem is the modulation theorem. Using equation (3.158), the modulation theorem can be expressed as

$$p_{ow}(r)e^{-jk_\phi r} = \frac{1}{r^{1/2}}\mathcal{F}^{-1}\{\tilde{g}(k_r - k_\phi)u(k_r - k_\phi)\} \qquad (3.162)$$

Under the condition that

$$p(r) \sim p_{ow}(r) \quad r \gg 0 \qquad (3.163)$$

we see that

$$p(r)e^{-jk_\phi r} \sim \frac{1}{r^{1/2}}\mathcal{F}^{-1}\{\tilde{g}(k_r - k_\phi)u(k_r - k_\phi)\} \qquad (3.164)$$

In Chapter 5, we will consider a number of applications of removing the linear phase component $k_\phi r$ from the phase of a shallow water acoustic field. Equation (3.164) suggests that this effect can be interpreted in the k_r domain as well. Additionally,

equation (3.164) suggests a method for interpolating a non-uniformly sampled version of $p(r)$. Specifically, if the Green's function contains significant energy at a particular wavenumber, or within a small wavenumber interval, the equation suggests that by translating the Green's function in k_r, it may be possible to adequately re-interpolate the corresponding field $p(r)e^{-jk_\phi r}$ using a simple interpolation method. The method may be particularly applicable to the shallow water acoustic fields since the energy in the Green's function is typically concentrated near the trapped poles. Further aspects of this interpolation scheme will be discussed in Chapters 5 and 6.

The convolution property for the Fourier transform states that convolution in one domain corresponds to multiplication in the alternate domain. The dual property is the windowing property, which involves convolution in the alternate domain. These two properties have also been studied in the context of the Hankel transform where similar, but not identical, properties can be derived, based on using the asymptotic expansion of $J_0(k_r r)$. However, by using not only the asymptotic expansion but the unilateral approximation implied by the validity of the Hilbert-Hankel transform as well, the one-dimensional Fourier transform properties can be applied directly to $p(r)$ and $g(k_r)$.

The windowing property in the r domain implies that if

$$p_{\infty}(r) = \frac{1}{r^{1/2}} \mathcal{F}^{-1}\{\bar{g}(k_r)u(k_r)\} \tag{3.165}$$

then

$$p_{\infty}(r)w(r) = \frac{1}{2\pi r^{1/2}} \mathcal{F}^{-1}\{[\bar{g}(k_r)u(k_r)] * W(k_r)\} \tag{3.166}$$

where

$$W(k_r) \equiv \mathcal{F}\{w(r)\} \tag{3.167}$$

In the special case that $w(r)$ is the impulse train

$$w(r) = \sum_{n=-\infty}^{\infty} \delta(r - n\Delta r) \tag{3.168}$$

149
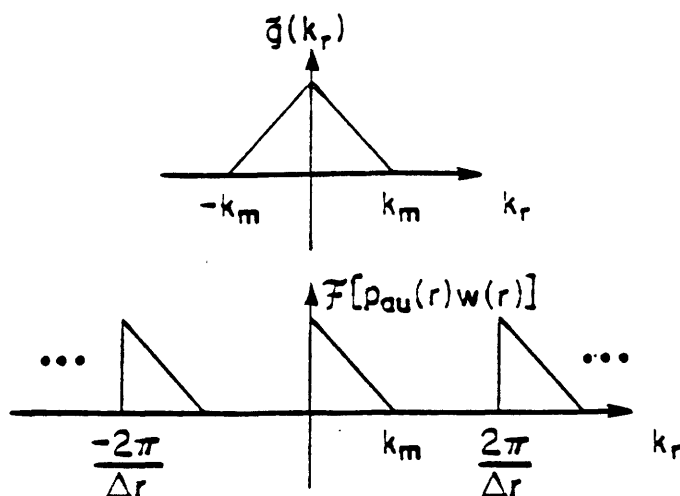
Figure 3.18: Typical function $\bar{g}(k_r)$ (a). Fourier transform of a sampled version of $p_{au}(r)$ (b).

it can be shown that

$$W(k_r) = \frac{2\pi}{\Delta r} \sum_{n=-\infty}^{\infty} \delta(k_r + \frac{2\pi n}{\Delta r}) \qquad (3.169)$$

Substituting these results in equation (3.166), we find that

$$p_{au}(r) \sum_{n=-\infty}^{\infty} \delta(r - n\Delta r) = \frac{1}{(r^{1/2}\Delta r)} \mathcal{F}^{-1}\{ \sum_{n=-\infty}^{\infty} \bar{g}(k_r + \frac{2\pi n}{\Delta r})u(k_r + \frac{2\pi n}{\Delta r}) \} \quad (3.170)$$

The left-hand side of this equation represents the sampled version of $p_{au}(r)$, with the corresponding sampling interval of Δr. The right-hand side of this expression consists of the superposition of replicated versions of $\bar{g}(k_r)u(k_r)$, with the corresponding replication interval of $2\pi/\Delta r$. To better illustrate this, consider Figure 3.18a where a typical function $\bar{g}$ is displayed. [9] In Figure 3.18b is shown the Fourier transform of the sampled version of $p_{au}(r)$. As indicated by the figure, it is possible to recover $p_{au}(r)$ from its sampled version provided that the replications do not overlap, i.e. provided that

$$\frac{2\pi}{\Delta r} > k_m. \qquad (3.171)$$

---

[9] Note that $\bar{g}(k_r)$ is an even function since the Green's function $g(k_r)$ is even.

Therefore, the sampling interval must be chosen so that

$$\Delta r < \frac{2\pi}{k_m} \qquad (3.172)$$

In the case that the acoustic field $p(r)$ can be approximated by

$$p(r) \sim p_{ou}(r) \quad r \gg 0 \qquad (3.173)$$

an implication is that $p(r)$ can be approximately recovered from its sampled version, as long as the sampling interval satisfies the condition in equation (3.172).

If $p(r)$ corresponds to an acoustic field in the ocean, a reasonable assumption is that the corresponding Green's function is small for $|k_r| > k_0$, where k_0 is the water wavenumber. This statement is based on the fact that the field is evanescent for wavenumbers larger than the water wavenumber. In the case that the source and receiver are separated vertically, the contribution due to these wavenumbers must be small. The effect will be described in further detail in the next chapter. In this context, the condition that $g(k_r)$ is small for $k_r > k_0$ implies that $k_m = k_0$, and thus $p(r)$ can be adequately represented by its sampled version provided that $\Delta r < 2\pi/k_0$. Defining the *water wavelength* as

$$\lambda_0 = \frac{2\pi}{k_0} \qquad (3.174)$$

it follows that $p(r)$ must be sampled at the minimum rate of *one* complex sample per water wavelength. This rate is a factor of two smaller than has been predicted elsewhere[19], and is a consequence of the fact that the outgoing nature of the field has been exploited. Essentially, there is an effective reduction in wavenumber extent when the field is assumed to be outgoing. The result is important in a practical sense because it potentially simplifies experimental constraints related to the acquisition of ocean acoustic field measurements. In Chapter 6, we will present several examples of this sampling result. In particular, we will show that a reasonable estimate of the ocean bottom reflection coefficient can be obtained from a synthetic field, which has been sampled at a rate of one complex sample per water wavelength.

Finally, the convolution property applied in the r domain is considered. Writing

$$p_{ou}(r) = \frac{1}{r^{1/2}} \mathcal{F}_u^{-1}\{\bar{g}(k_r)\} \tag{3.175}$$

this property can be mathematically expressed as

$$p_{ou}(r) * w(r) = \frac{1}{r^{1/2}} \mathcal{F}_u^{-1}\{\bar{g}(k_r)W(k_r)\} \tag{3.176}$$

In the special case that $W(k_r)$ is the impulse train

$$W(k_r) = \sum_{n=-\infty}^{\infty} \delta(k_r - n\Delta k_r) \tag{3.177}$$

equation (3.176) becomes

$$\frac{1}{\Delta k_r}\sum_{n=-\infty}^{\infty} p_{ou}(r + \frac{2\pi n}{\Delta k_r}) = \frac{1}{r^{1/2}} \mathcal{F}_u^{-1}\{\sum_{n=-\infty}^{\infty} \bar{g}(k_r)\delta(k_r - n\Delta k_r)\}$$

$$= \frac{1}{r^{1/2}}\frac{1}{2\pi}\sum_{n=0}^{\infty} \bar{g}(n\Delta k_r)e^{jn\Delta k_r r} \tag{3.178}$$

The right-hand side of this expression is the basis for the FFP algorithm. Specifically, if $\bar{g}(k_r)$ is wavenumber limited to k_m and Δk_r is chosen such that

$$N\Delta k_r = k_m \tag{3.179}$$

then equation (3.178) becomes

$$\frac{1}{\Delta k_r}\sum_{n=-\infty}^{\infty} p_{ou}(r + \frac{2\pi n}{\Delta k_r}) = \frac{1}{r^{1/2}}\frac{1}{2\pi}\sum_{n=0}^{N-1} \bar{g}(n\Delta k_r)e^{jn\Delta k_r r} \tag{3.180}$$

If $p_{ou}(r)$ is evaluated at the set of discrete ranges $r = m\Delta r$, this equation becomes

$$\frac{1}{\Delta k_r}\sum_{n=-\infty}^{\infty} p_{ou}(m\Delta r + \frac{2\pi n}{\Delta k_r}) = \frac{1}{(m\Delta r)^{1/2}}\frac{1}{2\pi}\sum_{n=0}^{N-1} \bar{g}(n\Delta k_r)e^{jn\Delta k_r m\Delta r} \tag{3.181}$$

If Δr is chosen to be related to Δk_r as $\Delta r = 2\pi/(N\Delta k_r)$, it follows that

$$\frac{1}{\Delta k_r}\sum_{n=-\infty}^{\infty} p_{ou}(m\Delta r + \frac{2\pi n}{\Delta k_r}) = \frac{1}{(m\Delta r)^{1/2}}\frac{1}{2\pi}\sum_{n=0}^{N-1} \bar{g}(n\Delta k_r)e^{j2\pi nm/N} \tag{3.182}$$

The right-hand side of this expression is in the form of an inverse discrete Fourier transform, and can be implemented efficiently using the inverse FFT. Under the condition that Δk_r is chosen as sufficiently small, so that the replications of $p_{au}(r)$ do not overlap in r, the expression in (3.182) can be written as

$$p_{au}(m\Delta r) = \frac{\Delta k_r}{(m\Delta r)^{1/2}} \frac{1}{2\pi} \sum_{n=0}^{N-1} \tilde{g}(n\Delta k_r) e^{j2\pi nm/N} \tag{3.183}$$

The expression, in conjunction with the approximation

$$p(m\Delta r) \sim p_{au}(m\Delta r) \quad m\Delta r \gg 0 \tag{3.184}$$

is the computational algorithm in the FFP.

A key step in the preceding derivation is the assumption that the replications of $p_{au}(r)$ do not overlap. Thus, the sampling interval Δk_r must be chosen as sufficiently small so that there is no aliasing in the r domain. However, in typical shallow water applications, it is quite difficult to sample $\tilde{g}(k_r)$ at a rate sufficient to avoid aliasing, because of the presence of trapped, or nearly trapped, poles in $g(k_r)$. For example, consider the case of a single trapped mode in the acoustic field which corresponds to a pole, k_{ri} on the real-k_r axis of the top Riemann sheet of $g(k_r)$. Asymptotically, the behavior of the corresponding mode is $e^{jk_{ri}r}/r^{1/2}$ for $r \gg 0$. Neglecting the effects of the continuum portion of the field, the computation of the FFP yields a sampled version of the quantity

$$p(r) = \frac{1}{r^{1/2}} [e^{jk_{ri}r}(1 + e^{jk_{ri}2\pi/\Delta k_r} + e^{jk_{ri}4\pi/\Delta k_r} + ...)] = \frac{e^{jk_{ri}r}}{r^{1/2}} \left(\frac{1}{1 - e^{jk_{ri}2\pi/\Delta k_r}} \right) \tag{3.185}$$

Therefore, the FFP synthesizes the actual mode multiplied by a scale factor, which can vary in magnitude from .5 to ∞. If the sampling rate of $g(k_r)$ is chosen such that $l\Delta k_r = k_{ri}$, where l is an integer, the corresponding synthesized mode may be in error by many orders of magnitude. The addition of attenuation into the problem reduces the effect of the aliasing. In this case, the scale factor can no longer become infinite, but can still be quite large when $l\Delta k_r = Re[k_{ri}]$. Therefore, the convolution property suggests that the use of the FFP in shallow water acoustic propagation applications

must be approached carefully. In the following chapter, we will present an alternate hybrid method, which can incorporate a discrete version of the asymptotic Hilbert-Hankel transform, but which is not subject to this severe aliasing effect.

To summarize, in this section we have discussed the asymptotic version of the Hilbert-Hankel transform. A discrete implementation of this transform is widely used in underwater acoustics as a means for computing synthetic acoustic fields accurately and efficiently and is referred to the FFP. We pointed out that two separate approximations are involved in the FFP. The first approximation is the condition $p(r) \sim p_a(r), r > 0$, which was also discussed in the previous section, in the context of the Hilbert-Hankel transform. The second approximation is the condition $p_a(r) \sim p_{aa}(r), r \gg 0$ where $p_{aa}(r)$ represents the asymptotic Hilbert-Hankel transform. The Hartley transform was also discussed as a related transform which is intermediate to the exact Hankel transform and the asymptotic Hilbert-Hankel transform. In addition to forming the basis for an efficient computational algorithm, the validity of the asymptotic Hilbert-Hankel transform was shown to have other important consequences. Specifically, the transform relates the theory of one and two-dimensional signals, which are approximately analytic, via the conditions

$$p(r) \sim \mathcal{H}_a^{-1}\{g(k_r)\} \quad r > 0 \tag{3.186}$$

$$r^{1/2}p(r) \sim \mathcal{F}_a^{-1}\{\tilde{g}(k_r)\} \quad r \gg 0 \tag{3.187}$$

where the function $\tilde{g}$ is defined in equation (3.151). The relationships indicate that it is possible to demonstrate the two-dimensional theory using the simpler one-dimensional unilateral inverse Fourier transform. Additionally, the relationship in equation (3.187) is important because it implies an approximate Fourier transform relationship between the Green's function and the acoustic field. Several consequences of the relationship were discussed.

3.5 Summary

In this chapter, we have reviewed the relationship between the analytic signal, the real-part/imaginary-part sufficiency condition, and the unilateral transform. The condition of exact analyticity, or exact real-part/imaginary-part sufficiency, is based on the causality of the Fourier transform. In our work, we have found that it is possible for a signal to be approximately analytic under other conditions. For example, in this chapter we developed the property of approximate real-part/imaginary-part sufficiency for the one-dimensional even signal, which has an even Fourier transform, and the two-dimensional circularly symmetric signal, which has a circularly symmetric Fourier transform.

In the one-dimensional context, discussed in Section 3.2, it was shown that in order for an even signal to have the property of approximate analyticity, its causal portion must be approximated by the unilateral version of the inverse Fourier transform. A number of relationships, based on the consistency between the approximate unilateral synthesis and the exact bilateral synthesis, were developed. A numerical example was provided to illustrate these relationships.

In the two-dimensional context, discussed in Section 3.3, it was shown that in order for a circularly symmetric signal to have the property of approximate analyticity, its causal portion must be approximated by the unilateral version of Hankel transform, referred to as the Hilbert-Hankel transform. A number of relationships, based on the consistency between the approximate Hilbert-Hankel transform synthesis and the exact bilateral inverse Hankel transform synthesis, were developed. The theory is of particular importance because of its applicability to outgoing acoustic fields.

In the final section, we pointed out that there is an interesting connection between the one and two-dimensional versions of the theory of approximate analyticity. To develop the connection, we defined the asymptotic Hilbert-Hankel transform. The

transform, which also forms the basis for an efficient computational algorithm, has a number of interesting properties. The properties were used to derive the fact that an outgoing acoustic field can be approximately represented in terms of its samples, spaced once per water wavelength. Additionally, the aliasing which occurs in synthetically generating shallow water acoustic fields was discussed in terms of the asymptotic Hilbert-Hankel transform. In the next chapter, we will present a method for shallow water synthetic data generation which is not subject to the severe effects of this aliasing.

Bibliography

[1] F.R. DiNapoli and R.L. Deavenport. Theoretical and numerical Green's function solution in a plane multilayered medium. *J. Acoust. Soc. Am.*, 67:92–105, 1980.

[2] R.V. Churchill. *Complex Variables and Applications*. McGraw-Hill, 1960.

[3] P.M. Morse and H. Feshbach. *Methods of Theoretical Physics*. Volume 1,2, McGraw-Hill, New York, 1953.

[4] E.A. Guillemin. *The Mathematics of Circuit Analysis*. M.I.T. Press, Cambridge, Massachusetts, 1949.

[5] A. Papoulis. *The Fourier Integral and its Applications*. McGraw-Hill, New York, 1962.

[6] A. Papoulis. *Systems and Transforms with Applications to Optics*. McGraw-Hill, New York, 1968.

[7] H. Bateman. *Higher Transcendental Functions Vol.2.* McGraw-Hill, New York, 1953.

[8] M. Abramowitz and I. Stegun. *Handbook of Mathematical Functions*. National Bureau of Standards, 1964.

[9] G.N. Watson. *A Treatise on the Theory of Bessel Functions*. Macmillan Company, New York, 1945.

[10] A. Papoulis. Optical systems, singularity functions, complex Hankel transforms. *Journal of the Optical Society of America*, 57:207–213, Feb. 1967.

[11] Ronald N. Bracewell. *The Fourier Transform and Its Applications.* McGraw-Hill, New York, 1978.

[12] Alan V. Oppenheim, George V. Frisk, and David R. Martinez. Computation of the Hankel transform using projections. *J. Acoust. Soc. Am.*, 68(2):523–529, Aug. 1980.

[13] H. Bateman. *Tables of Integral Transforms.* McGraw-Hill, New York, 1954.

[14] E.C. Titchmarsh. *Introduction to the Theory of Fourier Integrals.* Clarendon Press, Oxford, 1937.

[15] R.V. Hartley. A more symmetrical Fourier analysis applied to transmission problems. *Proc. IRE*, 30:144–150, Mar. 1942.

[16] R.N. Bracewell. The discrete Hartley transform. *Journal of the Optical Society of America*, 73:1832–1835, Dec. 1983.

[17] R.N. Bracewell. The fast Hartley transform. *Proceedings of the IEEE*, 72(8):1010–1018, Aug. 1984.

[18] A. Zakhor. *Error Properties of Hartley Transform Algorithms.* Technical Report, Masters Thesis, Massachusetts Institute of Technology, Cambridge Ma., Oct. 1985.

[19] Douglas R. Mook, George V. Frisk, and Alan V. Oppenheim. A hybrid numerical/analytic technique for the computation of wave fields in stratified media based on the Hankel transform. *J. Acoust. Soc. Am.*, 76(1):222–243, July 1984.

Chapter 4

Shallow Water Synthetic Acoustic Field Generation

4.1   Introduction

In the previous two chapters, the acoustic field and its relationship to the Green's function was discussed. In Chapter 2, the theory which relates the Green's function and the acoustic field in terms of the Hankel transform was presented, and a number of properties of the Green's function were developed. In Chapter 3, the relationship between the Hankel transform and the Hilbert-Hankel transform was discussed. In this chapter, we combine some of these ideas in order to develop a new technique for shallow water synthetic acoustic field generation.

A technique for generating synthetic shallow water acoustic fields is important for a number of reasons. First, it can be used to predict propagation loss in a shallow water environment and can form an important tool for developing intuition about the way sound propagates in this reverberant environment. For example, the technique can be used to predict the minimum range at which the propagation can be

approximated by a trapped modal sum only. Secondly, a technique for synthetic data generation can be used in the design of an actual experiment in which the acoustic pressure field is recorded. For example, use of the technique facilitates designing an ocean acoustic experiment in which a particular mode is either not present or is dominant at a specific receiver depth. Thirdly, a synthetic data generation technique can be used in an forward modelling or analysis-by-synthesis method to obtain the geoacoustic parameters using experimental measurements. In this approach, the input parameters to the synthetic data generation method are adjusted so that the synthetic data produced most closely matches the actual data recorded. Finally, the technique can be used to verify some of the interesting theoretical properties of shallow water acoustic fields. In the next chapter, we will use the technique to demonstrate that extraction of the bottom reflection coefficient is highly sensitive to errors in the Green's function, estimate under certain circumstances. In Chapter 6, we will use the method to demonstrate that realistic shallow water acoustic fields can be reconstructed from a single real or imaginary component.

The material in this chapter is organized as follows. In Section 4.2, a review of the existing methods for the generation of synthetic shallow water acoustic fields is given. Next, in Section 4.3, the theory for a new hybrid technique based on the decomposition of the field and its associated Green's function is developed. Details related to the numerical implementation of an algorithm based on this decomposition are next given in Section 4.4. In Section 4.5, several extensions to the basic method are given which are based on the use of the properties of the Green's function including its eigenfunction expansion and the real-part/imaginary-part sufficiency condition. In Section 4.6, the technique is related to three other techniques. Finally, in Section 4.7, a review of the important points in the chapter is provided.

4.2 Existing Approaches for Shallow Water Synthetic Acoustic Field Generation

In this section, we will review the existing approaches for generating synthetic acoustic fields in shallow water. It is possible to classify the existing approaches into three categories as follows: 1) Residue Methods, 2) Multipath methods, 3) Hankel transform based methods. We will exclude from the discussion methods based on the use of the parabolic equation. Although such methods, based on approximating the original hyperbolic partial differential equation with a parabolic model, are important because they can be extended to very complicated models including those which involve range-dependence, they depart significantly from the model of the field as an integral transform of a Green's function. As such, they will be excluded from our discussion here and the reader is referred to a number of sources regarding these methods [1] [2]. Although most other methods fit directly into this categorization, there are also several hybrid schemes which incorporate features of two or more of the above categories. The new technique to be presented in the next section is an example of one of these hybrid methods.

An excellent review of methods which perform the integration

$$p(r) = \int_0^\infty g(k_r) J_0(k_r r) k_r \, dk_r \tag{4.1}$$

in the context of wave propagation problems is provided in the 1980 paper by DiNapoli and Deavenport [3]. Their classification of existing approaches is very similar to that suggested above with the exception that the third class has been changed to include all Hankel transform based methods, as opposed to direct integration using the Fast-Field-Program (FFP) [3] [4]. The change in the last category has been made, in part, to include several Hankel transform based methods which have appeared since 1980 [5] [6] [7].

We begin the review of existing approaches with residue methods. A common

element in these techniques is the application of Cauchy's theorem to the integral in equation (4.1). As discussed in Chapter 2, the integration contour can be extended and closed in the upper half of the k_r-plane. Applying Cauchy's theorem yields the equivalent field representation of a sum, due to the pole contributions, plus a branch-line integral, due to the presence of a branch point. Dependent on the particular application required, the branch-line contribution, also referred to as the continuum, may become subdominant to the pole sum and may be neglected, particularly at large range offsets. The resulting approximation to the field is also referred to as the normal-mode sum.

There are a number of computer programs in existence which compute the acoustic field in a shallow water environment using the normal-mode sum. One such program was published by Newman and Ingenito in 1972 [8]. In their approach, the field was computed using the form

$$p(r) \approx \frac{j}{4} \sum_{i=1}^{N} u_i(z) u_i(z_0) H_0^{(1)}(k_{r_i} r) e^{-j\omega t} \tag{4.2}$$

As discussed later in this chapter, the functions $u_i(z)$ are the eigenfunctions of the homogeneous Green's function differential equation and the corresponding eigenvalues are the locations of the top-sheet poles of the Green's function. Essentially, the approach proposed by Newman and Ingenito and extended by Miller and Ingenito[9] was to solve the homogeneous version of the Green's function differential equation using a finite difference scheme. The technique allowed for the source and receiver to reside anywhere within a fluid layer with arbitrary velocity structure and constant density. The media underlying the shallow water waveguide consisted of a fluid layer with arbitrary velocity structure overlying a solid halfspace.

An improved version of this program, referred to as SNAP (Saclanten Normal mode Acoustic Program), was published by Jensen and Ferla in 1979 [10]. Although, the finite difference solution technique was identical to the previous technique, some improvements were made in program speed and size. Attenuation and shear effects

were also incorporated via loss mechanisms by including a non-zero imaginary part in the eigenvalues (poles) , $k_{r,i}$, in the sum shown in equation (4.2). In addition, SNAP simulated a range-dependent environment by dividing the full range into a number of smaller segments each with different range-independent properties. SNAP also provided a way to incorporate a rough waveguide surface into the normal-mode sum.

More recently, Baggeroer has introduced a modal solution by the solving the acoustic wave equation numerically [11]. His approach is based on determining the eigenvalues and eigenfunctions using a state-variable technique. Additionally, a newer version of SNAP has been introduced in 1985 which uses an improved algorithm for determining the eigenfunctions and eigenvalues[12].

The advantage of normal-mode expansions is that they may be determined quickly and accurately using finite difference algorithms or other approaches which exploit the eigenfunction structure of equation (4.2). In addition, if the properties of the waveguide vary slowly with range, the adiabatic approximation can be applied so that the normal modes are both depth and range dependent. The result is an approximation for the range dependent environment. The disadvantage of normal-mode expansions is that they are only accurate in the far-field of the source. This is due to the fact that the contribution of the branch-line integral has been neglected entirely. In applications where it is desired to compute the field at closer ranges, the continuum field cannot be neglected. For example, in applications where synthetic data is produced in order to study inversion techniques to obtain the bottom reflection coefficient, it is important to include the continuum contribution.

A number of techniques have been proposed to include the continuum contribution by adding this field to the normal-mode sum. One such technique was proposed by Stickler in 1975 [13]. In this technique, the continuum contribution was determined by directly computing the branch-line integral for the EJP branch-cut definition. This result was then added to a standard normal-mode expansion. The geoacoustic model

assumed a $1/c^2$-linear velocity profile and included compressional propagation only. The closed form integral expression for the continuum contribution was determined as

$$p_c(r) = \frac{j}{2\rho_0} \int_0^{k_B} C_1(k)p(z_0,k)p(z,k)H_0^{(1)}(kr)kdk \qquad (4.3)$$

$$+\frac{j}{2\rho_0} \int_0^\infty C_2(k)p(z_0,jk)p(z,jk)K_0(kr)kdk$$

where k_B refers to the branch point corresponding to the wavenumber in the underlying halfspace and where specific expressions [1] for the function $C_1(k)$ and $C_2(k)$ were given by Stickler [13]. Stickler provided several numerical examples which demonstrated that the continuum contribution can be important at ranges out to many times the waveguide thickness. It is noted that computation of the above integrals may be extensive, as each integral must be evaluated for each range point desired.

Bucker later studied the contribution of the continuum portion of the total acoustic field for the simpler case of a Pekeris waveguide [14]. In his approach, the Pekeris branch-cut was selected and an algorithm for calculating the corresponding branch-cut integral was given. In addition, Bucker considered the trajectory in the k_r-plane that a specific pole follows as a function of frequency or waveguide thickness. The algorithm also required a separate integration for each range point.

An alternate approach for including the continuum contribution in a residue method was suggested by Tindle, et.al. in 1976 [15]. Their approach was to approximately evaluate the EJP branch-cut integral only in the vicinity of the peaks in the integrand. The geoacoustic model considered was the Pekeris waveguide. By evaluating the integral approximately over a finite number of resonances, Tindle provided a modal-like sum which approximated the continuum contribution. We have previously remarked in Chapter 2 that this sum is actually an approximation to the residue sum corresponding to the bottom sheet poles. A more detailed discussion concerning this point will be provided in a later section of this chapter. In later papers, Williams[16]

---

[1]It appears that an extra k term appears in the functions $C_1(k)$ and $C_2(k)$ in [13].

and Tindle [17] considered the treatment of virtual modes and normal modes which are in the immediate vicinity of the branch point. They developed alternate techniques for including the virtual modes in the case of non-symmetric resonances for the Pekeris waveguide.

In 1980, Stickler and Ammicht proposed a technique which accounts for the continuum contribution in a more exact manner for the Pekeris waveguide model [18]. Their approach was based on representing the continuum portion of the field as an integral in the variable of vertical wavenumber as opposed to horizontal wavenumber. In this case, the integral contains only poles and no branch cut. The integrand is modelled as a pole expansion based on the theory of analytic functions, and the continuum field is approximated using a finite sum of terms. The approach was later modified and extended to more general shallow water waveguides[19].

In summary, the techniques which fit into the class of residue methods are based on decomposing the acoustic field into the sum of two contributions - the normal-mode sum and the continuum. In some methods, the continuum is neglected entirely. In other methods, the continuum is modelled as a finite sum of virtual modes with various mathematical forms. Finally, it is possible to numerically perform the branch-line integral to determine the continuum as is done in several methods. These approaches have in common the fact that the Hankel transform is no longer applicable after the application of Cauchy's theorem. In other words, although the original solution consists of the Hankel transform of the Green's function, the application of Cauchy's theorem yields a sum and a branch-line integral which is no longer in the form of a Hankel transform.

The multipath expansion method is also used to evaluate integrals in the form of equation (4.1). In this technique, the denominator of the Green's function is expanded into a series. Each term in the series may be identified as a ray and thus higher order terms represent the higher order multiples. The multipath expansion technique was

implicitly used in deriving the mathematical form of the Green's function in Chapter 2. Apparently, the technique is not in widespread use for the determination of synthetic acoustic fields in shallow water. It appears to be most suitable for generating the near-field in shallow water, when only a few terms in the expansion are required. The technique is more applicable to situations in which several rays are appropriate for modelling the field and has been applied to the problem of range-dependent deep water acoustic propagation [20].

The final class of synthetic data generation techniques to be reviewed consists of Hankel transform based approaches. Apparently, the first use of a numerical Hankel transform, in the context of synthetic field generation, was the Fast-Field-Program (FFP) [3] [4] [21]. In this approach, a fast numerical algorithm for computing the Hankel transform was applied directly to the Green's function. The date is significant in the fact that the direct integration used the fast Fourier transform which was proposed some two years earlier by Cooley and Tukey[22]. The novelty of the FFP approach was the use of an asymptotic expansion and the coupling of this expansion with an algorithm for fast computation. The FFP has a number of advantages including the fact that it computes the full-wave solution, i.e. all contributions to the field are included as opposed to including normal-modes only in the residue methods or the lower order multiples in the multipath expansion. In addition, the computer implementation is extremely fast due to the underlying fast Fourier transform. Generation times as small as several seconds for approximately 10^4 range samples were obtained by DiNapoli in 1971.

Since the introduction of the FFP in 1967, a number of field generation programs based on this approach have appeared. In 1971, DiNapoli used the FFP to generate synthetic data for a single exponential layer and a two-layer geoacoustic model [21]. A method for determining the acoustic field in the Arctic ocean based on the FFP was developed by Kutschale in 1970[23]. Again, this approach used the FFP to perform the direct integration of the Green's function. The Green's function was derived for

167

the more general case of fluid-solid layers and was modified to account for the surface ice structure.

In their 1980 paper, DiNapoli and Deavenport discuss the application of the FFP to propagation in media with certain canonic velocity structures including linear, $1/c^2$-linear, and exponential velocity profiles. In addition, several numerical examples are discussed and a technique for inverting the pressure field to obtain the Green's function is proposed. Reference is also made to the collapsed FFP, proposed by DiNapoli in 1971 [24]. In this technique, the sampling theorem for Fourier transforms is applied in such a way that the computation of the FFP is reduced at the cost of an increased sample spacing in the range domain. Essentially, the collapsed FFP generates an undersampled version of the pressure field by aliasing in the wavenumber domain.

The FFP remains a key component in synthetic acoustic field generation programs. As an example, the general program SAFARI for computing fields source has recently been developed by Schmidt and Jensen [7]. The SAFARI program computes the frequency-dependent Green's function for a layered fluid- solid media and has the flexibility of incorporating source and receiver spatial arrays. The field generation approach is based on computing the FFP of the Green's function.

In 1984, Thomson published a description of a computer technique based on the work of Kutschale[6]. This technique is designed to produce synthetic acoustic fields in a shallow water environment and also uses the FFP to directly generate the transform of the Green's function. The program also has the option of computing the field using a residue method. The interesting aspect of this option is that it uses the FFP algorithm to compute the continuum portion of the field. This is apparently the first use of the FFP in a manner other than directly computing the Hankel transform of the Green's function. The method is actually a hybrid method, as the residue method is used to decompose the field and the FFP is used to compute the continuum. In principle,

the method is similar to the new Hankel transform based method to be discussed in the next section of this thesis. However, there are a number of important differences which will be discussed in detail later. Essentially, the Kutschale-Thomson approach is based on the mathematical formulation of Stickler[13] and references the equation for the continuum contribution, which was presented earlier as equation (4.3). The novelty of their approach however is that the continuum is approximated by the first of these integrals only, and the FFP is used to evaluate this integral. The geoacoustic model includes attenuation and shear in the normal-mode sum.. However, only the compressional contribution to the continuum is included.

Another hybrid method for computing acoustic fields was proposed by Mook et.al. in 1984 [5]. In this approach, the Fourier-Bessel series was used to compute the Hankel transform of the deep water Green's function. Mook pointed out the difficulty in performing the integration if the Green's function contains singularities near the contour of integration. The singularity which presents the most difficulty in the deep water case is the branch point at the water wavenumber. As also pointed out, the deep water Green's function can become infinite in the case that the reflection coefficient has a pole on the real-k_r axis. This situation can occur if the underlying media contains low-speed layers. A method for removing the branch-point singularity and the poles in the reflection coefficient was suggested in [5], thereby easing the numerical requirements of performing the Hankel transform. The method proposed for determining the poles and associated residues involved the least-squares fit of a partial-fraction expansion for the reflection coefficient. The approach is significant in the fact that it is a Hankel transform based approach which accounts for inherent numerical difficulties caused by singularities on or near the real-k_r axis.

In a sense, the new technique for shallow water synthetic field generation is a Hankel transform based approach which is a combination and extension of the techniques proposed by Kutschale-Thomson and Mook. As will be described in the next section, the new technique also uses a transform to compute the continuum, as was done in

the Kutschale-Thomson technique. Their technique is approximate however, while the new technique is, in principle, exact. In addition, in the new method the quantity to be transformed is not in the closed-form shown in equation (4.3), but rather is related to the original Green's function, after the singularities have been removed. In this way the new technique is similar to that of Mook, in that a portion of the field is computed analytically, i.e. the modal portion, and the remaining portion is computed numerically, i.e. the continuum. Further discussion regarding the relationship of the new method to these methods will be presented in a later section of this chapter.

4.3 Theory of the New Hybrid Method

In this section, we present a new hybrid approach for shallow water synthetic field generation which decomposes the Green's function into two constituent parts. The need for a hybrid approach is based on the difficulty of accurately computing the numerical Hankel transform of the Green's function. This difficulty is due to the presence of poles in of the Green's function which are located in the vicinity of the Hankel transform integration contour. As pointed out in Chapter 3, the aliasing errors associated with the undersampling of the Green's function in the regions of real-k_r near these poles may be quite severe. The basis of the current approach is to modify the underlying transformation in such a way that the degradation due to aliasing is substantially reduced.

In Chapter 2, we considered the decomposition of an acoustic field into the sum of a modal field and a continuum field as

$$p(r) = p_T(r) + p_C(r) \tag{4.4}$$

As pointed out in the previous section of this chapter, this decomposition is also the basis of the residue methods. The linearity of the Hankel transform suggests that a similar decomposition exists for the corresponding Green's function. This fact forms the basis of for new hybrid method for shallow water synthetic field synthesis. If the decomposition into a trapped portion and a continuum portion is applied not to the field, but rather to the Green's function, we obtain

$$g(k_r) = g_T(k_r) + g_C(k_r) \tag{4.5}$$

Here, $g(k_r)$ is the Green's function, $g_T(k_r)$ is referred to as the modal portion of the Green's function and $g_C(k_r)$ is referred to as the continuum portion of the Green's function. In addition $g(k_r)$, $g_T(k_r)$ and $g_C(k_r)$ are defined such that

$$g(k_r) \xleftrightarrow{J_0} p(r) \tag{4.6}$$

171

$$g_T(k_r) \xleftrightarrow{J_0} p_T(r)$$

$$g_C(k_r) \xleftrightarrow{J_0} p_C(r)$$

Note that in this representation, the continuum is represented exactly by the Hankel transform of the continuum portion of the Green's function, $g_C(k_r)$. This is to be contrasted with other techniques which identify $p_C(r)$ as the result of a branch line integral and not as the result of a Hankel transform. An advantage of representing $p_C(r)$ in this way is that one of the numerous fast algorithms for efficient computation of the Hankel transform can be applied.

The basis of the hybrid approach for shallow water synthetic field generation is to compute analytically the Hankel transform of $g_T(k_r)$ and to compute numerically the Hankel transform of $g_C(k_r)$. As will be discussed shortly, the pole singularities of $g(k_r)$ near the real-k_r axis are included in $g_T(k_r)$ and not in $g_C(k_r)$. Therefore, the sampling requirements for the numerical Hankel transform are eased. Qualitatively, $g_C(k_r)$ is a smoother function than $g_T(k_r)$ and thus requires fewer samples to adequately represent it. Said another way, in the range domain, the continuum portion of the field decays much more rapidly than the modal portion and thus, the corresponding continuum portion of the Green's function can be sampled at a lower rate.

In order to perform the Green's function decomposition, the specific form for $g_T(k_r)$ must be determined. Using this form, the continuum portion of the Green's function can be simply determined since

$$g_C(k_r) = g(k_r) - g_T(k_r) \tag{4.7}$$

The modal portion of the Green's function must be in the form of a residue sum since $p_T(r)$ is a modal sum and $p_T(r)$ and $g_T(k_r)$ are related by the Hankel transform. The specific form for $g_T(k_r)$ will now be determined.

Assuming the form of the Green's function decomposition discussed above, it is

easily seen that

$$p_T(r) + p_C(r) = \int_0^\infty [g_T(k_r) + g_C(k_r)] J_0(k_r r) k_r \, dk_r \qquad (4.8)$$

If $g_T(k_r)$ is chosen to be an even function of k_r, $g_C(k_r)$ must also be an even function, since, as derived in Chapter 2, $g(k_r)$ must be an even function. If $g_T(k_r)$ and $g_C(k_r)$ are even functions, the Bessel function can be replaced by a Hankel function [2] and equation (4.8) becomes

$$p_T(r) + p_C(r) = \int_{-\infty}^\infty \frac{1}{2} [g_T(k_r) + g_C(k_r)] H_0^{(1)}(k_r r) k_r \, dk_r \qquad (4.9)$$

where the contour of integration lies ϵ above the negative real-k_r axis and ϵ below the positive real-k_r axis as discussed previously. Using Cauchy's theorem, equation 4.9, and the property that $g_T(k_r)$ is even, it can be shown that a term of the form $j\pi a_i k_{ri} H_0^{(1)}(k_{ri} r)$ in $p_T(r)$ must be due to a term of the form

$$\left(\frac{a_i}{k_r - k_{ri}} - \frac{a_i}{k_r + k_{ri}} \right) \qquad (4.10)$$

in $g_T(k_r)$. In this expression, a_i is the residue of $g_T(k_r)$ at the pole $k_r = k_{ri}$, i.e.

$$\lim_{k_r \to k_{ri}} (k_r - k_{ri}) g_T(k_r) = a_i \qquad (4.11)$$

Therefore, a modal sum of the form

$$p_T(r) = j\pi \sum_{i=1}^N a_i k_{ri} H_0^{(1)}(k_{ri} r) \qquad (4.12)$$

must be due to the modal portion of the Green's function

$$g_T(k_r) = \sum_{i=1}^N \frac{2 a_i k_{ri}}{(k_r^2 - k_{ri}^2)} \qquad (4.13)$$

To summarize, the relationship between the various quantities is summarized in the following figure. Using this figure, the hybrid approach for generating $p(r)$ can be summarized in five steps: 1) determine $g_T(k_r)$, 2) determine $p_T(r)$ using the analytic

---

[2] We will again assume in this chapter that all fields are evaluated for $r > 0$ and thus the Hankel function $H_0^{(1)}(k_r r)$ is chosen.

$$p(r) \quad = \quad j\pi \sum_{i=1}^{N} a_i k_{ri} H_0^{(1)}(k_{ri}r) \quad + \quad p_C(r)$$

$$\Big\updownarrow J_0 \qquad\qquad \Big\updownarrow J_0 \qquad\qquad\qquad \Big\updownarrow J_0$$

$$.g(k_r) \quad = \quad \sum_{i=1}^{N} \frac{2a_i k_{ri}}{(k_r^2 - k_{ri}^2)} \quad\qquad + \quad g_C(k_r)$$

Figure 4.1: Relationship between the modal and continuum portions of the field and Green's function which forms the basis of the hybrid method.

relationship between $g_T(k_r)$ and $p_T(r)$, 3) determine $g_C(k_r)$ using $g_C(k_r) = g(k_r) - g_T(k_r)$, 4) determine $p_C(r)$ by numerically computing the Hankel transform of $g_C(k_r)$, 5) determine $p(r)$ using $p(r) = p_T(r) + p_C(r)$.

The hybrid approach trades off the difficulty in numerically computing a Hankel transform with the difficulty in determining the quantity $g_T(k_r)$. To determine the values of the coefficients in $g_T(k_r)$, $g_T(k_r)$ must be related to $g(k_r)$ in a more direct manner. This is necessary because we have at our disposal only $g(k_r)$, and thus the coefficients a_i and k_{ri} must be determined from $g(k_r)$. We now show that the coefficients k_{ri} are the poles of $g(k_r)$ and that the coefficients a_i are the residues of $g(k_r)$ at the corresponding pole locations. Essentially, the proof shows that $g(k_r)$, which is not a rational function in k_r, can be decomposed into the sum of a rational function which contains the top-sheet poles of $g(k_r)$ plus an irrational function which has no poles. This type of decomposition is sometimes referred to as a Mittag-Leffler expansion and can be thought of as a generalization of the partial fraction expansion for a rational function [25].

The proof is based on the use of Cauchy's theorem. To proceed, consider the top Riemann sheet of the complex-k_r plane depicted in Figure 4.2. In this figure are shown the locations of the singularities of $g(k_r)$, the selected EJP branch cuts and a number of integration contours labelled $C_1 - C_{12}$. We have indicated only a single symmetric
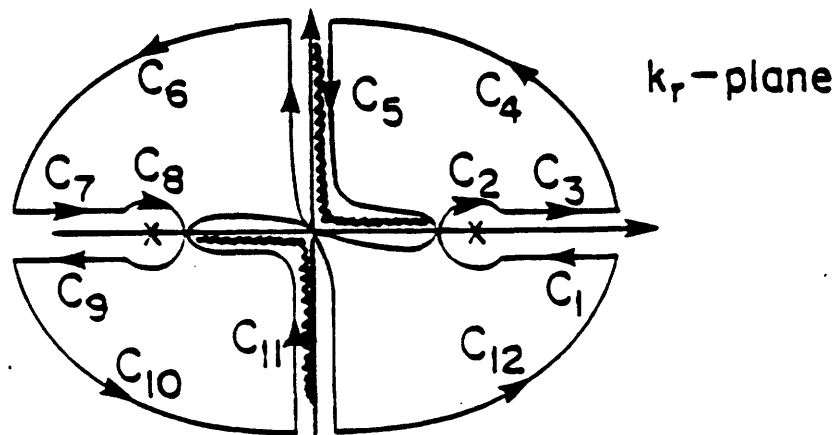
Figure 4.2: Top Riemann sheet of complex-k_r plane showing poles, branch-cuts, and various integration contours $C_1 - C_{12}$. The function $g(k_r)$ is analytic within the region prescribed by these contours.

pole in this diagram although multiple poles might also exist. In the interior of the region of the k_r plane prescribed by these contours, $g(k_r)$ is an analytic function and thus Cauchy's integral theorem is applicable, i.e.

$$g(k_r) = \frac{1}{2\pi j} \int_C \frac{g(k_r')}{k_r' - k_r} dk_r' \qquad (4.14)$$

where C denotes the sum of the integration contours C_1 through C_{12}. This contour integration is now simplified. First, consider positioning contours C_4, C_8, C_{10} and C_{12} at a large $|k_r|$ which approaches infinity. The integration along these contours becomes zero because $|g(k_r)|$ approaches zero as $|k_r|$ approaches infinity. The latter behavior can be proved by choosing an arbitrary square root definition for k_{z0} and evaluating the expression for $g(k_r)$ given in Chapter 2. Also, the integration along the contours C_1 and C_3 cancels, as does the integration along the contours C_7 and C_9. The integration around contour C_2 can be written as

$$\frac{1}{2\pi j} \int_{C_2} \frac{g(k_r')}{k_r' - k_r} dk_r' = Residue\{g(k_r')|_{k_r'=k_{ri}}\} \frac{1}{k_r - k_{ri}} \qquad (4.15)$$

where it is assumed that the pole is located at position k_{ri} within the contour C_2. Defining $Residue\{g(k_r')|_{k_r'=k_{ri}}\}$ as a_i, it is apparent that

$$\frac{1}{2\pi j} \int_{C_2} \frac{g(k_r')}{k_r' - k_r} dk_r' = \frac{a_i}{k_r - k_{ri}} \qquad (4.16)$$

Similarly, it is apparent that

$$\frac{1}{2\pi j} \int_{C_8} \frac{g(k_r')}{k_r' - k_r} dk_r' = \frac{-a_i}{k_r + k_{ri}} \qquad (4.17)$$

where the fact that $g(k_r)$ is an even function has been used in determining the sign of this residue. Using these facts, we have for the case of a single symmetric pole on the real-k_r axis of the top Riemann sheet that

$$g(k_r) = \frac{1}{2\pi j} \int_C \frac{g(k_r')}{k_r' - k_r} dk_r' = \frac{2a_i k_{ri}}{k_r^2 - k_{ri}^2} + \frac{1}{2\pi j} \int_{C_5 + C_{11}} \frac{g(k_r')}{k_r' - k_r} dk_r' \qquad (4.18)$$

Similarly, if N poles were present on the positive real-k_r axis, the form for the decomposition of $g(k_r)$ would be

$$g(k_r) = \sum_{i=1}^{N} \frac{2a_i k_{ri}}{k_r^2 - k_{ri}^2} + \frac{1}{2\pi j} \int_{C_5 + C_{11}} \frac{g(k_r')}{k_r' - k_r} dk_r' \qquad (4.19)$$

Note that equation (4.19) is in the form of

$$g(k_r) = g_T(k_r) + g_C(k_r) \qquad (4.20)$$

Furthermore, we note that k_{ri} and a_i correspond to the poles and residues of $g(k_r)$. Additionally, the poles have been incorporated within $g_T(k_r)$ and thus $g_C(k_r)$ is finite at the pole locations k_{ri}. Although equation (4.19) also provides an integral expression for $g_C(k_r)$, this expression is not used in the hybrid approach. The reason is that it is simpler to numerically compute $g_C(k_r)$ using $g_C(k_r) = g(k_r) - g_T(k_r)$. Alternately, there exists another method for computing $g_C(k_r)$ without directly estimating the poles and residues. This method is based on the real-part/imaginary-part sufficiency condition of $g(k_r)$ and is discussed in a later section of this chapter.

To summarize, the theory of the new hybrid method for generating synthetic acoustic fields in shallow water has been discussed. The approach is based on decomposing the Green's function into the sum of a modal component and a continuum component. The modal component, $g_T(k_r)$, has the form

$$g_T(k_r) = \sum_{i=1}^{N} \frac{2a_i k_{ri}}{k_r^2 - k_{ri}^2} \qquad (4.21)$$

where k_{ri} is the location of a pole of the Green's function and a_i is the corresponding residue. The continuum portion of the Green's function, $g_C(k_r)$, can be expressed as an integral or alternately as

$$g_C(k_r) = g(k_r) - g_T(k_r) \qquad (4.22)$$

An analytic expression for the Hankel transform of $g_T(k_r)$ can be simply derived as

$$p_T(r) = j\pi \sum_{i=1}^{N} a_i k_{ri} H_0^{(1)}(k_{ri} r) \qquad (4.23)$$

The continuum portion of the field can be obtained by computing a numerical Hankel transform of $g_C(k_r)$. Because the decomposition includes the singular behavior due to the poles in $g_T(k_r)$, the sampling requirements for computing the numerical transform of $g_C(k_r)$ are eased. The total field is constructed by adding the analytically computed modal field to the numerically computed continuum field.

177

4.4 Implementation of the Hybrid Method

In the previous section, the theory of the hybrid method for synthetic shallow water field generation was discussed. The method proposed is exact in that it does not rely on any approximations or asymptotic expressions. Rather, the method is based only on the linearity property of the Hankel transform. In practice however, there are a number of issues which cause this technique to depart from being exact. For example, the poles and residues cannot be determined exactly, nor can an exact numerical Hankel transform of $g_C(k_r)$ be computed. In this section, we consider several of the issues related to the numerical implementation of the hybrid method based on the Green's function decomposition.

We begin by examining the procedure for determining $g_T(k_r)$. Previously, it was shown that the coefficients in the expression for $g_T(k_r)$ are determined by the poles and residues of the Green's function. The philosophy which has been assumed in the numerical procedure for determining these poles and residues is to exploit the a priori information about the Green's function. For example, the complete mathematical expression for $g(k_r)$ corresponding to an arbitrary isovelocity layered bottom is known as discussed in Chapter 2. In fact, $g(k_r)$ depends on the specific geoacoustic properties of the underlying bottom only through the reflection coefficient $R_B(k_r)$. This a priori knowledge can be exploited in determining the poles and residues. We first show how this fact aids in the determination of the pole locations.

The approach chosen for determining the pole locations of $g(k_r)$ is based on using a numerical technique for locating the complex zeros of an analytic function. There are several well-known techniques for determining these zeros. The technique we have chosen is based on the IMSL standard computer function ZANLYT[26]. For the case at hand, we can determine the pole locations of $g(k_r)$ by searching for the zeros of the denominator of this function. The denominator of $g(k_r)$, when set to zero, is referred

to as the characteristic equation, as shown below

$$1 + R_B(k_r)e^{j2k_{z0}h} = 0 \qquad (4.24)$$

Thus, a possible method for determining the pole locations is to use the root-finding technique to determine the solutions of this equation. Unfortunately, the denominator of $g(k_r)$, i.e. the left-hand side of equation (4.24), is not an analytic function. Specifically, there are branch points located at both the water wavenumber and the wavenumber of the underlying halfspace. The non-analyticity of this function in the complex-k_r plane appears not only at the branch points but also along the two branch cuts emanating from these branch points. Note that the presence of the additional branch cut emanating from the water wavenumber is due to the fact that only the denominator of the Green's function is being considered as opposed to the complete Green's function expression. As discussed in Chapter 2, there is no branch-cut associated with the water wavenumber in the complete Green's function expression because $g(k_r)$ is an even function of k_{z0}. Additionally, the denominator of $g(k_r)$ may be non-analytic at isolated points corresponding to the poles of $R_B(k_r)$. Thus, there is a basic incompatibility between the numerical technique of searching for the zeros of an analytic function and the case at hand - the function of interest is not analytic.

In particular, if the branch cut emanating from the water wavenumber is chosen as an EJP-type cut, the root finding technique is forced to search for zeros in the immediate vicinity of this branch cut, i.e. in a region where the function is not analytic. Although this cut can be repositioned by assuming a different choice of the square root definition, numerical experiments have shown that the root finder is more reliable if the cut can be eliminated entirely. This can be accomplished if the zeros of $1/g(k_r)$ are determined instead of the zeros of the denominator of $g(k_r)$. In addition, the singularities due to the poles in the reflection coefficient are also eliminated using the expression $1/g(k_r)$. Thus, by exploiting a priori knowledge of the Green's function, the numerical technique for determining the pole locations has been made more reliable. In particular, by searching for the zeros of $1/g(k_r)$ as

opposed to the zeros of the denominator of $g(k_r)$, the presence of the branch cut and the singular behavior due to poles in the reflection coefficient has been eliminated. The root finder must still contend with the cut emanating from the branch point due to the underlying halfspace and point singularities corresponding to the poles of $1/g(k_r)$.

In practice, the root finder requires an initial guess for the location of each pole. In the situation that there are only several poles on or near the real-k_r axis present, this initial guess can be made by examining a plot of $|g(k_r)|$ versus real-k_r. Essentially, the a priori knowledge regarding the location of the peaks in this function can be used to initialize the root finder. This procedure may also be automated. In the situation that more than several poles are present, this initialization procedure becomes more difficult. In this case, the root finder tends to not detect one or more of the roots. A similar effect may occur if a root is in the immediate vicinity of the branch point. An alternate approach for determining the pole locations in these more complicated cases is discussed in the next section.

We now show that a priori knowledge about the Green's function can be exploited in a technique for determining the residues. In particular, although the residue a_i for a simple pole in $g(k_r)$ is defined as

$$a_i = \lim_{k_r \to k_{ri}} (k_r - k_{ri}) g(k_r) \qquad (4.25)$$

we have found that a numerical scheme based on this equation is unstable. A least-squares approach also yields residue estimates which are not accurate enough to remove the effects of a pole in $g(k_r)$ and tends to degrade significantly if more than a single pole is present. Instead, the a priori form of the Green's function can be incorporated within a numerical scheme for determining the residues. In effect, this scheme performs a portion of the residue computation analytically and a portion of the computation numerically. Specifically, if $g(k_r)$ is defined as

$$g(k_r) \equiv \frac{N(k_r)}{D(k_r)} \qquad (4.26)$$

then the residue at the pole location k_{ri} can be shown to be

$$a_i = \frac{N(k_r)}{\frac{\partial D(k_r)}{\partial k_r}}\Big|_{k_r = k_{ri}} \tag{4.27}$$

A portion of the operation $\partial D(k_r)/\partial k_r$ can be performed analytically using the known form of the Green's function. For example, for the case of the source and receiver in the top layer, with a surface reflection coefficient of -1, the Green's function expression in equation (2.34) can be used to determine the residue a_i at the pole location k_{ri}. The result is

$$a_i = 2\frac{\sin k_{z0}z_l}{k_{z0}}e^{jk_{z0}z_g}\frac{1 + R_B e^{j2k_{z0}(h-z_g)}}{\frac{\partial R_B}{\partial k_r}e^{j2k_{z0}h} - j2h\frac{k_r}{k_{z0}}R_B e^{j2k_{z0}h}}\Big|_{k_r = k_{ri}} \tag{4.28}$$

Note that the result is an expression for the residue in terms of the reflection coefficient and its derivative at $k_r = k_{ri}$. These two quantities can be numerically evaluated at the pole location and substituted into equation (4.28) to determine the residue. Numerical experiments have shown that this technique for estimating the residue based on exploiting the form of the Green's function is more accurate than alternate techniques such as a least-squares fit. The limitation of the technique appears to be the numerical determination of the pole location and the reflection coefficient derivative. In the next section, an alternate approach for determining the pole location is presented. A by-product of this alternate approach is another method for determining the residue which does not require the computation of the reflection coefficient derivative.

Although the numerical techniques just discussed aid in the accurate determination of the poles and residues, there is still some numerical error which occurs. In effect, in determining $g_C(k_r)$, we have attempted to remove the effects of a pole by placing a zero in the complex-k_r plane at the same location. If there is any error whatsoever in determining the position of the pole, a pole-zero pair will exist rather than a complete cancellation. However, the error in cancellation will be locally concentrated near the pole location. It seems that this error is compensated for exactly in the decomposition approach, since $g_C(k_r)$ has been computed as $g_C(k_r) = g(k_r) - g_T(k_r)$. In other words, if slight errors in determining the coefficients of $g_T(k_r)$ have been

made, then the associated negative error will also appear in $g_C(k_r)$. If the Hankel transforms of $g_C(k_r)$ and $g_T(k_r)$ are computed and added, any errors should cancel. The problem with this argument however, is that the exact Hankel transform of $g_C(k_r)$ cannot be computed numerically. In fact, the slight error in estimating a particular pole location and residue may be responsible for a sharp spike in $g_C(k_r)$ which occurs in the immediate vicinity of the pole location. The numerical Hankel transform of this function is subject to aliasing in a similar manner as was the original Hankel transform of the Green's function.

In order to remove the spike in $g_C(k_r)$ in the neighborhood of the pole, a local smoothing operator is applied to $g_C(k_r)$ at values of real-k_r near the pole. This operator averages N sample points of $g_C(k_r)$ around the real value of the pole location. We have typically chosen $N = 5$ for situations in which several thousand samples of $g_C(k_r)$ are computed over a k_r range of 0 to twice the water wavenumber. In effect, by applying this smoothing operator, the following statements are being made. The modal portion of the acoustic field is slightly in error due to inaccuracies in estimating the poles and residues. This error cannot be compensated for by computing the numerical Hankel transform of $g_C(k_r)$ because of the aliasing which occurs. Therefore, we accept the fact that the modal field may be slightly in error and apply the smoothing operator to improve the estimate of the continuum portion of the field.

As a specific numerical example of this procedure, we consider its application to the geoacoustic model summarized in Table 4.1. The Green's function for this model has a single trapped pole on the top Riemann sheet for the EJP branch cut and, in addition, has a pole located on the bottom sheet which is close to the real-k_r axis. The Green's function for this model was computed and its magnitude and phase are shown in Figure 4.3. The numerical root finding technique was used to determine the location of the top sheet pole at $k_{r,i} = 0.5623757$ and the associated residue was determined as $a_i = 0.1558157$ using equation (4.28). The continuum portion of the Green's function, $g_C(k_r)$, was computed by removing the pole and 2048 samples of
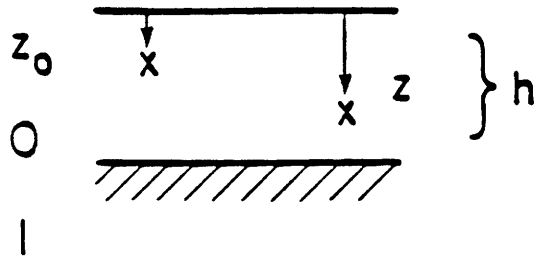
|		
z_0	=	6.096 m
z	=	7.03579 m
f	=	140.056 Hz
h	=	13.8684 m
c_0	=	1500 m/sec
ρ_0	=	1.0 g/cm^3
c_1	=	1800 m/sec
ρ_1	=	1.8 g/cm^3

Table 4.1: Pekeris Model Geoacoustic Parameters
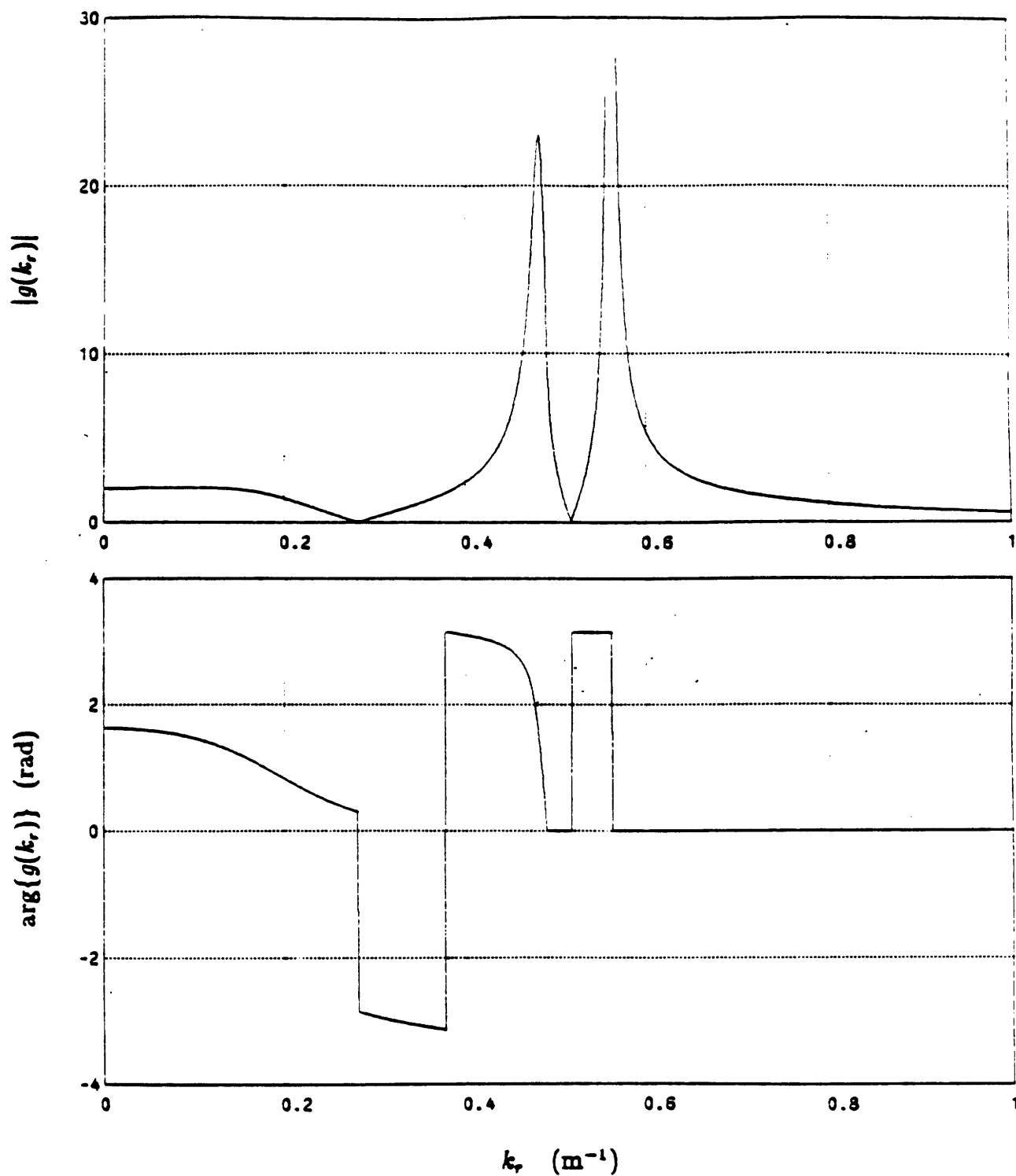
Figure 4.3: Magnitude and phase of the Green's function, $g(k_r)$, corresponding to the geoacoustic model in Table 4.1

the resultant magnitude and phase are shown in Figure 4.4. Note the presence of the spike in the magnitude of $g_C(k_r)$ at the value of $k_r = k_{r_i}$ caused by the slight error in estimating the pole and residue. In this particular case, the spike is quite small attesting to the accuracy in estimating the pole position and residue. The smoothing operator, with $N = 5$, was applied to $g_C(k_r)$ and the resultant magnitude and phase of $g_C(k_r)$ are shown in Figure 4.5. The effect of applying the smoothing operator is to eliminate the spike in $g_C(k_r)$ as can be verified by examining Figure 4.5.

In more complicated models which have multiple poles on the top Riemann sheet, the smoothing is sometimes less effective. This is due to the fact that accurate estimation of the pole parameters is more difficult and also due to the fact that the poles may be clustered. The proposed technique thus has a limitation in this respect. However, to this point we have considered only geoacoustic models which have zero attenuation. The result of including even small amounts of attenuation is to move the poles off the real-k_r axis and into the first quadrant of the complex-k_r plane. In this situation, when the continuum portion of the Green's function is evaluated at values of k_r along the real axis, no spikes are observed and the smoothing operator may be eliminated entirely. In this case, $g_C(k_r)$ is evaluated at values of k_r sufficiently far away from the pole-zero pair so that the cancellation is effective.

Several numerical issues related to the computation of the Hankel transform of $g_C(k_r)$ are now considered. The first is related to the finite extent of $g_C(k_r)$. All Hankel transform techniques have in common the fact that a maximum finite limit of integration must be chosen. The implication is that the integrand is exactly wavenumber limited to this maximum value. We first examine this assumption for the total Green's function and not $g_C(k_r)$. Using the expression for $g(k_r)$ given in Chapter 2, it can be shown that $g(k_r)$ behaves as

$$g(k_r) \sim \frac{e^{jk_{z0}(z_g - z_l)}}{k_{z0}} \qquad (4.29)$$

for large k_r. Note that if $z_g \neq z_l$, then this function decays at an exponential rate for k_r greater than the water wavenumber since k_{z0} is imaginary. However, in the situation

185
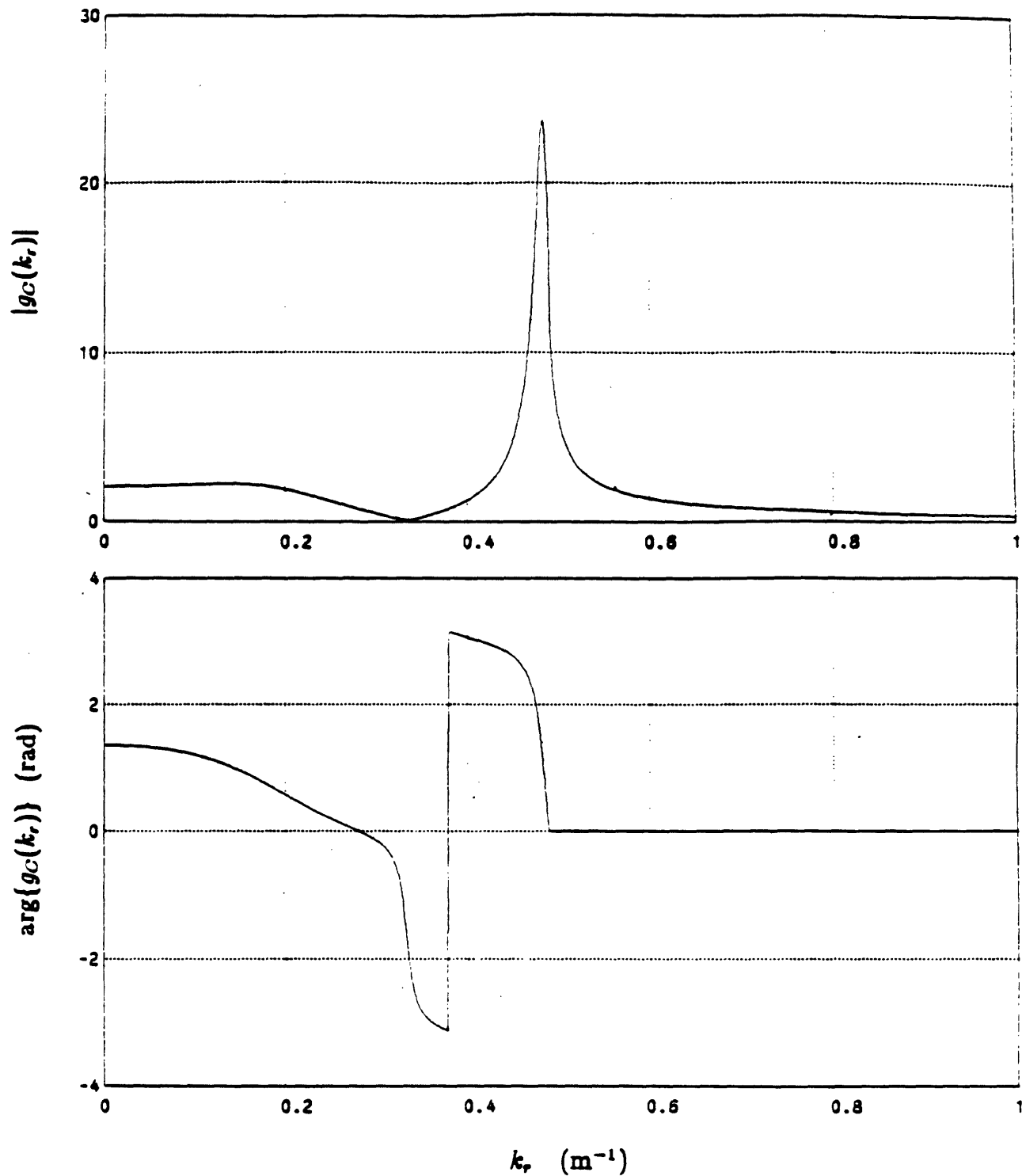
Figure 4.4: Magnitude and phase of the continuum portion of the Green's function, $g_C(k_r)$, corresponding to the geoacoustic model in Table 4.1. No smoothing has been applied and the error in pole, residue determination is evident as a spike in the magnitude at $k_r = 0.56$.
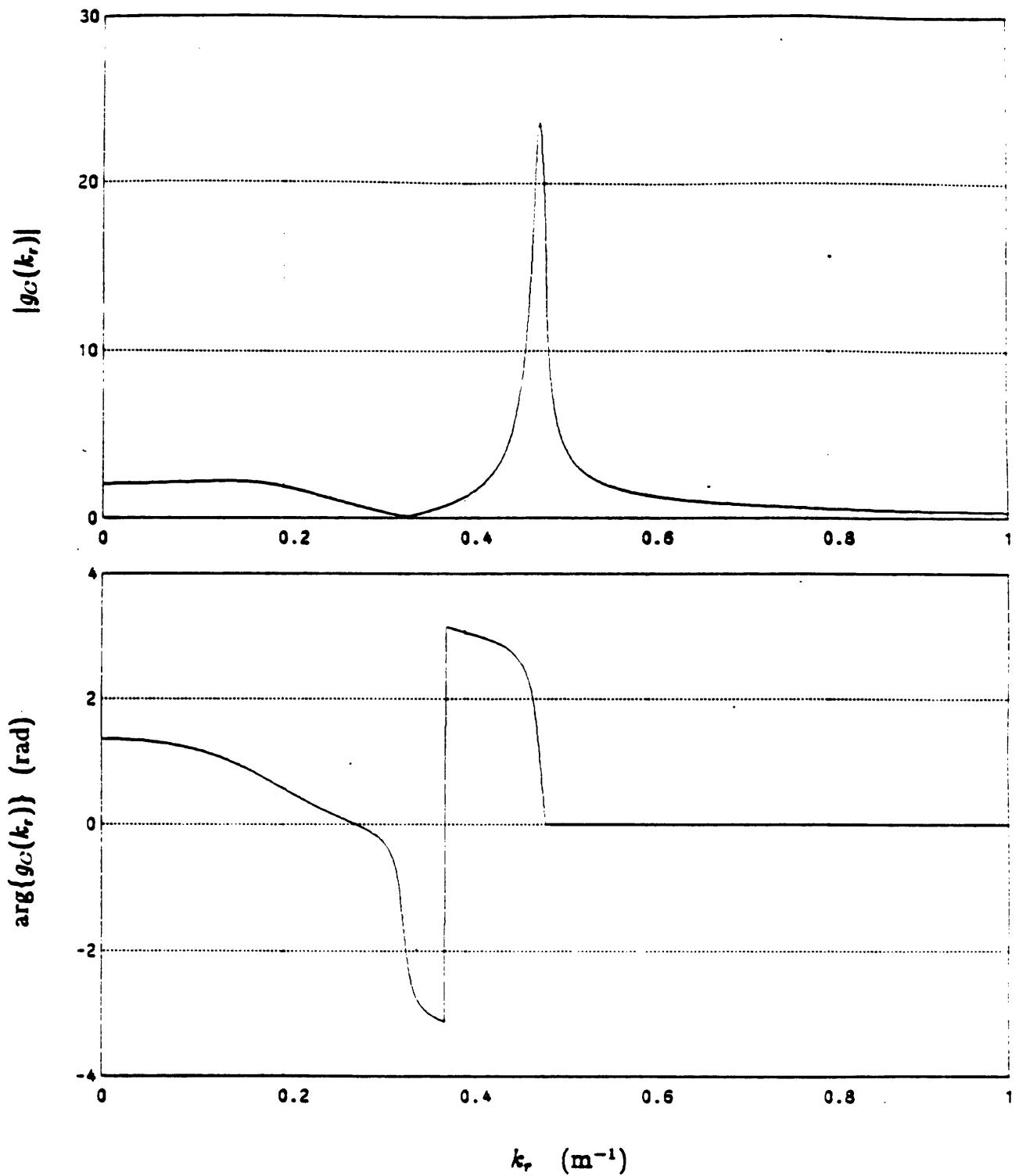
Figure 4.5: Magnitude and phase of the continuum portion of the Green's function, $g_C(k_r)$, after smoothing, corresponding to the geoacoustic model in Table 4.1.

that $z_g - z_l$ is small or zero, this rate may also be small or zero. In fact for the case that $z_g = z_l$, the magnitude of the Green's function behaves as $1/k_r$ for large k_r. To illustrate this effect, two different configurations of source and receiver depths within the waveguide summarized in Table 4.1 were considered. In Figure 4.6a is shown the log-magnitude of $g(k_r)$ for $z_g = 12.8684\ m$ and $z_l = 1.0\ m$ and in Figure 4.6b is shown the log-magnitude of $g(k_r)$ for $z_g = z_l = 7.03579\ m$. Both are plotted for real values of k_r extending well past the water wavenumber of 0.58666. Note that the Green's function magnitude decays quite rapidly in the first case and it can be considered as a wavenumber limited function. The exponential decay of the magnitude for values of k_r higher than the water wavenumber is due to the large value of $z_g - z_l$ in the model. In the second case however, the Green's function magnitude is seen to decay at the slow rate of $1/k_r$, as predicted in equation (4.29). The numerical example points out that it may not always be appropriate to consider $g(k_r)$ as a wavenumber limited function.

Although the above effect has been considered for the total Green's function, we have also observed a similar effect for the continuum portion of the Green's function. In other words, $g_C(k_r)$ may decay quite slowly for $k_r > k_0$. However the numerical transform still requires a maximum wavenumber to which the integration is performed. To reduce the effect of abruptly terminating the integration at some maximum wavenumber, a Hamming window is applied to $g_C(k_r)$ starting at the water wavenumber and extending to the maximum wavenumber chosen. Although the appropriate maximum wavenumber may depend on $z_g - z_l$, numerical experiments have shown that choosing a maximum wavenumber of between 1 and 2 times the water wavenumber and applying the Hamming window in this region, yields adequate results.

Once $g_C(k_r)$ is considered to be a wavenumber limited function, there are a number of applicable techniques for computing the Hankel transform in order to obtain $p_C(r)$. A survey of these techniques may be found in Mook [27]. Two different
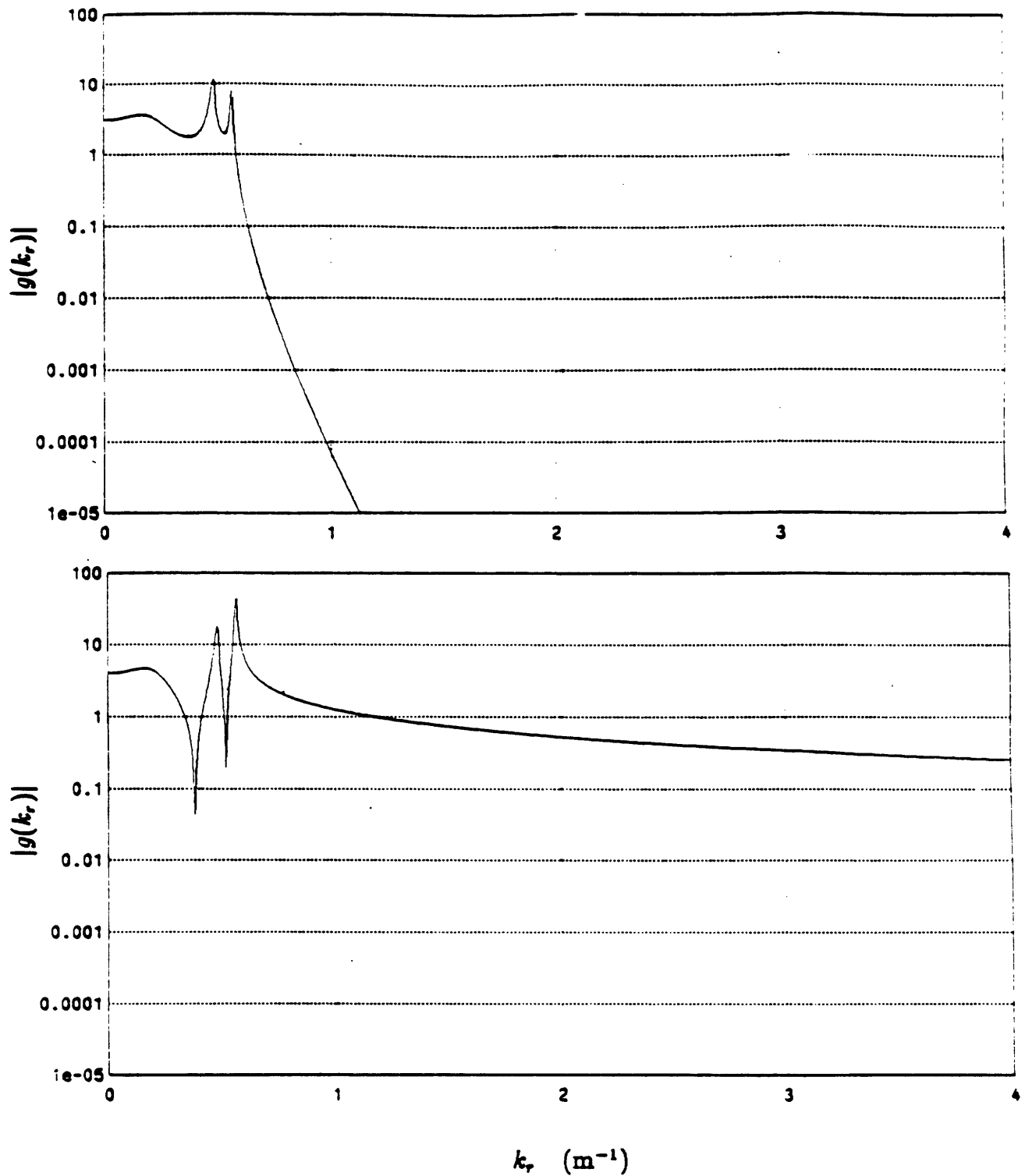
Figure 4.6: Magnitude of $g(k_r)$ on a logarithmic scale for two different source/receiver configurations for the geoacoustic model summarized in Table 4.1. In the top figure, $z_g = 12.8684\ m$ and $z_l = 1.0\ m$, and in the bottom figure $z_g = z_l = 7.03579\ m$.

techniques for computing the Hankel transform of $g_C(k_r)$ have been used in the numerical implementation of the hybrid method. The first technique is the Abel/Fourier transform approach [28]. This approach is based on the projection-slice theorem for two-dimensional Fourier transforms [29]. The projection operation for the circularly symmetric function is the Abel transform. Although several algorithms exist [30] [31] [32] for computing the Abel transform, we have chosen to use the technique proposed by Hansen [32] because of its accuracy and speed. This algorithm is based on the use of a state equation model to compute the Abel transform integral. The algorithm can be modified to operate on a function which has been sampled on any grid, however we have selected a linear grid to facilitate performing the discrete Fourier transform of the output sequence of the Abel transform. The second algorithm used for computing the Hankel transform is the asymptotic Hilbert-Hankel transform, discussed in Chapter 3. This algorithm was selected because it forms the basis for several numerical experiments concerning real-part/imaginary-part sufficiency and the reconstruction of the field from its real or imaginary part. Numerical examples related to the use of both of these transforms will be presented in a later section of this chapter, and in the following two chapters.

To summarize, in this section, we have discussed several detailed issues related to the numerical implementation of the hybrid method based on the decomposition of the Green's function. In particular, we have discussed a technique for determining the poles and residues which exploits the known form of the Green's function. By exploiting this form, a procedure has been developed for estimating the poles and residues when one or several poles are present on the top Riemann sheet. Although the technique is also applicable when more poles are present, there is a difficulty in initializing the root finder. An alternate approach which circumvents this difficulty will be presented in the next section. Also, the effect of errors obtained in determining the pole locations and residues was discussed. For small errors, the continuum portion of the Green's function can be corrected by locally smoothing over horizontal wavenumbers in the vicinity of the real part of the pole location. The smoothing

operation is not required in the case that a typical value of attenuation is included in the geoacoustic model. Issues related to the choice of the maximum wavenumber to which the Hankel transform is performed were also considered. Finally, the selection of Hankel transform techniques used to compute the continuum portion of the field was discussed.

4.5 Extensions

In this section, two extensions to the hybrid method for shallow water synthetic field generation are presented. The first extension is an alternate technique for computing the poles and residues of the Green's function. This technique exploits additional information about the Green's function to facilitate the pole and residue determination. The second extension is an alternate technique for computing the continuum portion of the field. As discussed earlier, the continuum portion of the field can be computed using any one of several numerical Hankel transform routines applied to $g_C(k_r)$. In this extension however, the Hilbert-Hankel transform is required for the computation of the continuum portion of the field. As will be discussed, this approach directly exploits the real-part/imaginary-part sufficiency condition as applied to the continuum portion of the Green's function.

4.5.1 Alternate Approach for Pole and Residue Determination

In this subsection, we discuss an alternate approach for determining the poles and residues of $g(k_r)$. There are several ways of explaining the alternate approach, depending on whether the method is considered in the range domain or in the wavenumber domain. Perhaps the simplest explanation is to consider it as a reversal of the first two steps in the original method. Recall that in the original method, the first step is to determine $g_T(k_r)$ and the second step is to determine $p_T(r)$ using the analytic relationship between $g_T(k_r)$ and $p_T(r)$. The function $g_T(k_r)$ is also required for the computation of $g_C(k_r)$, since $g_C(k_r) = g(k_r) - g_T(k_r)$. In the alternate approach, $p_T(r)$ is first determined and the analytic relationship between $p_T(r)$ and $g_T(k_r)$ is used to determine $g_T(k_r)$. The method exploits the fact that there are several efficient computer programs in existence which compute $p_T(r)$ - these are the normal mode

192

programs, several of which were discussed in Section 4.2.

To emphasize the difference between the two methods, a block diagram of the original method and a block diagram of the extension to the method are shown in Figures 4.7a and 4.7b respectively. As can be seen from the figure, the difference between the two methods is the manner in which $g_T(k_r)$ is determined. In the first method, $g_T(k_r)$ is constructed from the values of the pole locations and residues determined using the algorithm which locates the zeros of $1/g(k_r)$. In the second method, $g_T(k_r)$ is determined using a normal-mode computer code and the algebraic relationship between $p_T(r)$ and $g_T(k_r)$. The most interesting aspect of the alternate approach is that the poles and residues are not computed by using a numerical zero-finding algorithm. Rather, an alternate procedure based on the eigenfunction expansion of $p_T(r)$ is used.

The advantage of this extension to the hybrid approach is that a much larger number of poles can be accommodated. Recall from the discussion earlier that a disadvantage of the original approach is the difficulty in determining the location of the poles when more than several poles are present. This difficulty is due to establishing the proper initial values for the root-finding algorithm. In the extension to the technique, this initialization is not required because the normal mode technique determines the pole locations in an entirely different manner.

The alternate technique exploits additional a priori knowledge about $g(k_r)$. Namely, it exploits the fact that $g(k_r)$ is a Green's function, and as such, should satisfy the properties of a Green's function, which follow from the theory of ordinary differential equations. To develop this further, and to justify the improvement in the method based on exploiting a priori knowledge, we will now develop $g_T(k_r)$ in an eigenfunction expansion. Although, the properties and theory of Green's functions in terms of their eigenfunction expansions is presented in numerous places [33] [34] , the connection between this theory and $g_T(k_r)$ in the hybrid method has apparently not been made. Therefore, a brief derivation of the expansion of $g_T(k_r)$ in terms of eigenfunctions is
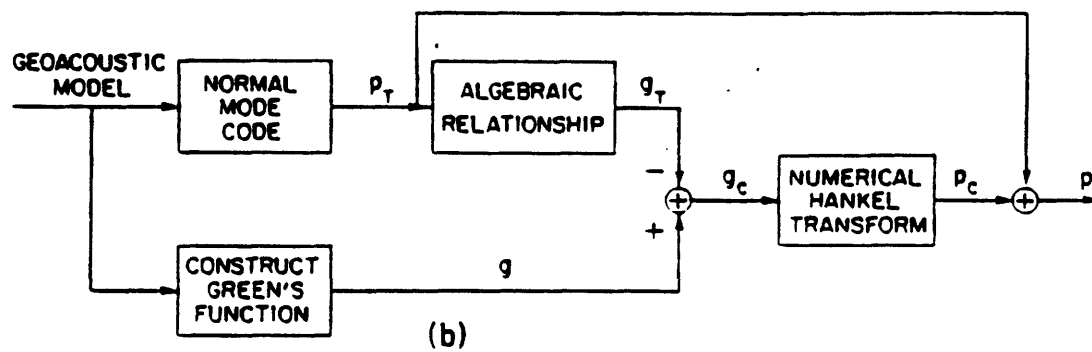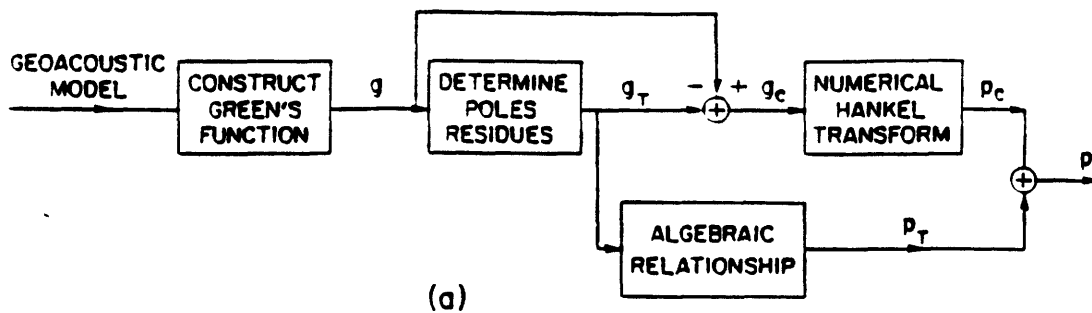
Figure 4.7: The top figure represents a block diagram of the algorithm for determining $p(r)$ by first determining the poles and residues to form $g_T(k_r)$. The bottom figure represents a block diagram of the extension to this method which is based on using normal-mode techniques to determine $p_T(r)$.

194

included here for completeness.

Recall from Chapter 2 that the Green's function for the acoustic propagation model is the solution to the ordinary differential equation

$$(\frac{d^2}{dz^2} + k^2 - k_r^2)g(k_r) = -2\delta(z - z_0) \tag{4.30}$$

where the source and receiver reside within the top layer. This equation results from applying a Hankel transform to the wave equation which describes the field within a layer. In the present situation, we wish to determine the solution at all depths for purposes of establishing eigenfunction orthogonality conditions. In this case, the governing partial differential equation must incorporate the effects of velocity and density changes from layer to layer. The appropriate equation is

$$\rho(z)\frac{\partial}{\partial z}\rho^{-1}(z)\frac{\partial p(r; z, z_0)}{\partial z} + k^2(z)p(r; z, z_0) \doteq -4\pi\delta(\mathbf{r} - \mathbf{r}_0) \tag{4.31}$$

where $\rho(z)$ is the density as a function of depth. By applying the Hankel transform to both sides of this expression, the ordinary differential equation which results is

$$\rho(z)\frac{d}{dz}\rho^{-1}(z)\frac{dg(k_r; z, z_0)}{dz} + (k^2(z) - k_r^2)g(k_r; z, z_0) = -2\delta(z - z_0) \tag{4.32}$$

where $g(k_r; z, z_0) \equiv g(k_r)$, $p(r; z, z_0) \equiv p(r)$ and $g(k_r)$ and $p(r)$ form a Hankel transform pair. To simplify the development which follows, we ignore the -2 term on the right-hand side of this equation and require that the final solution be multiplied by this factor. Thus, we consider the equation,

$$\rho(z)\frac{d}{dz}\rho^{-1}(z)\frac{dg(k_r)}{dz} + (k^2(z) - k_r^2)g(k_r) = \delta(z - z_0) \tag{4.33}$$

which can be also be written as

$$(L - \lambda)g(\lambda; z, z_0) = \delta(z - z_0) \tag{4.34}$$

where $L \equiv \rho(z)\frac{d}{dz}\rho^{-1}(z)\frac{d}{dz} + k^2(z)$, $\lambda \equiv k_r^2$ and $g(\lambda; z, z_0) \equiv g(k_r; z, z_0)$. It is straightforward to show that the operator L is self-adjoint under the orthogonality criteria

$$< \phi_n(z), \phi_m(z) >\equiv \int_0^\infty \frac{1}{\rho(z)}\phi_n(z)\phi_m(z)dz \tag{4.35}$$

195

Using an argument similar to the Mittag-Leffler expansion discussed earlier, Cauchy's theorem can be used to develop an expression for $g(\lambda; z, z_0)$ as

$$g(\lambda; z, z_0) = \frac{1}{2\pi j} \int_C \frac{g(\lambda'; z, z_0)}{\lambda' - \lambda} d\lambda' \tag{4.36}$$

and thus

$$g(\lambda; z, z_0) = -\sum_n \frac{R_n(z, z_0)}{\lambda_n - \lambda} + \frac{1}{2\pi j} \int_{BL} \frac{g(\lambda'; z, z_0)}{\lambda' - \lambda} d\lambda' \tag{4.37}$$

Here, the first term corresponds to the pole contributions in the λ plane and the second term corresponds to the branch-line integral. The numerator in the first term is the expression for the residue at the pole λ_n and is a function of both the source and receiver depths. By using this expansion for $g(\lambda; z, z_0)$, multiplying both sides of equation (4.34) by $\lambda - \lambda_m$ and taking the limit, we have that

$$\lim_{\lambda \to \lambda_m} (\lambda - \lambda_m)(L - \lambda)g = \lim_{\lambda \to \lambda_m} \delta(z - z_0) \tag{4.38}$$

$$\lim_{\lambda \to \lambda_m} (\lambda - \lambda_m)(L - \lambda)[-\sum_n \frac{R_n(z, z_0)}{\lambda_n - \lambda} + \frac{1}{2\pi j} \int_{BL}] = 0 \tag{4.39}$$

and thus

$$(L - \lambda_m)R_m(z, z_0) = 0 \tag{4.40}$$

From this equation, it can be seen that $R_m(z, z_0)$ is an eigenfunction of the operator L with the corresponding eigenvalue λ_m. Therefore, if $\phi_n(z)$ is a normalized eigenfunction which satisfies

$$(L - \lambda_n)\phi_n(z) = 0 \tag{4.41}$$

then $R_n(z, z_0) = cf_n(z_0)\phi_n(z)$ where the dependence on z_0 is included in $f_n(z_0)$ and c is included for normalization purposes.

By using the fact that L is a self-adjoint operator, and considering L_{z_0} as the operator L with a change of variables from z to z_0, it can be shown that $f_n(z_0) = \phi_n(z_0)/\rho(z_0)$ where $\phi_n(z_0)$ is an eigenfunction of the operator L_{z_0} with eigenvalue λ_n. Incorporating this into the expression for $R_n(z, z_0)$ we have that

$$R_n(z, z_0) = c\frac{\phi_n(z_0)\phi_n(z)}{\rho(z_0)} \tag{4.42}$$

It is straightforward to determine that $c = 1$ using the definition for orthogonality and thus the complete expression for $g(\lambda; z, z_0)$ becomes

$$g(\lambda; z, z_0) = \sum_n \frac{\phi_n(z)\phi_n(z_0)}{\lambda_n - \lambda} + g_C(\lambda; z, z_0) \qquad (4.43)$$

where the second term is the branch-line integral and $\phi_n(z)$ is the solution of the eigenvalue equation

$$(L - \lambda_n)\phi_n(z) = 0 \qquad (4.44)$$

and $\phi_n(z_0) = \phi_n(z)|_{z=z_0}$. This is the eigenfunction expansion for $g(\lambda; z, z_0)$ in terms of the variable λ. To relate it to the problem at hand, we return to the k_r domain. Making the substitution $\lambda = k_r^2$ and multiplying by the factor -2, we find that

$$g(k_r; z, z_0) = \sum_n \frac{2}{\rho(z_0)} \frac{\phi_n(z_0)\phi_n(z)}{k_r^2 - k_{r_n}^2} + g_C(k_r; z, z_0) \qquad (4.45)$$

The first term in equation (4.45) is the basis of the normal-mode approach for generating $p_T(r)$. Specifically, by taking the Hankel transform of this expression and retaining the contribution due to the sum, we have that

$$p_T(r) = \sum_i \frac{\pi j}{\rho(z_0)} \phi_i(z_0)\phi_i(z) H_0^{(1)}(k_{r_i} r) \qquad (4.46)$$

The values of k_{r_i}, $\phi_i(z)$, and $\phi_i(z_0)$ can be determined by numerically solving the eigenvalue equation (4.44) using a finite difference scheme. In other words, a trial solution for λ_n is made and the corresponding eigenfunction is determined. If the boundary conditions are satisfied, the solution has been determined, otherwise the trial value of λ_n is modified.

For the case at hand, we recognize that equation (4.45) is in the form of $g(k_r) = g_T(k_r) + g_C(k_r)$. Previously, we showed that

$$g_T(k_r) = \sum_i \frac{2a_i k_{r_i}}{k_r^2 - k_{r_i}^2} \qquad (4.47)$$

where k_{r_i} is a pole of $g(k_r)$ and a_i is the residue. Using the eigenfunction expansion, we see that

$$g_T(k_r) = \sum_i \frac{2}{\rho(z_0)} \frac{\phi_i(z_0)\phi_i(z)}{k_r^2 - k_{r_i}^2} \qquad (4.48)$$

197

Thus, an alternate approach for determining the poles is to solve the eigenvalue equation and use $k_{ri} = \lambda_i^{1/2}$. Furthermore, the alternate approach for determining the residue is to use the expression

$$a_i = \frac{\phi_i(z_0)\phi_i(z)}{\rho(z_0)k_{ri}} \qquad (4.49)$$

We note that different a priori knowledge about the Green's function has been exploited in the two approaches. In the original approach, the closed-form solution for $g(k_r)$ was used in order to determine the residue in terms of the reflection coefficient and its derivative at the pole. In the alternate approach, the knowledge used was that $g(k_r)$ satisfies an equation for a Green's function and, as such, can be expressed in an eigenfunction expansion. Note that the alternate approach also applies to the case in which the source and receiver are not necessarily located within the top layer, i.e. to the extended Green's function.

In practice, we have found that using a normal mode program to determine the roots and residues in this way works quite well. The SNAP normal mode program[10] was chosen for convenience. An interpolation routine was also added to SNAP in order to evaluate $\phi_i(z)$ and $\phi_i(z_0)$ for values of z, z_0 which do not lie on the finite difference grid.

As an example of the procedure, the Green's function for the geoacoustic model summarized in Table 4.2 was computed and the magnitude and phase of this function are plotted in Figure 4.8. Note that the source and receiver are not in the top layer and thus the extended Green's function equation developed in Chapter 2 was used. It is impossible to identify either the number of peaks or their approximate positions by examining the plot of the magnitude of $g(k_r)$ in Figure 4.8. Thus, the initialization of the root-finder is difficult. Alternately, the model was used as the input to the SNAP normal-mode program and the number of trapped poles was determined to be 14. The pole positions were determined by SNAP by solving for the eigenvalues of the homogeneous Green's function equation, and the residues were

1500 m/sec, 1.0 g/cm^3	1 m
1550 m/sec, 1.0 g/cm^3	1 m
1560 m/sec, 1.0 g/cm^3	21.8684 m
1650 m/sec, 1.5 g/cm^3	100 m
1800 m/sec, 1.8 g/cm^3	

z_0	=	6.096 m
z	=	7.03579 m
f	=	220.264 Hz

Table 4.2: Geoacoustic Model of a Non-Isovelocity Water Column Overlying a Thick Layer Overlying a Halfspace
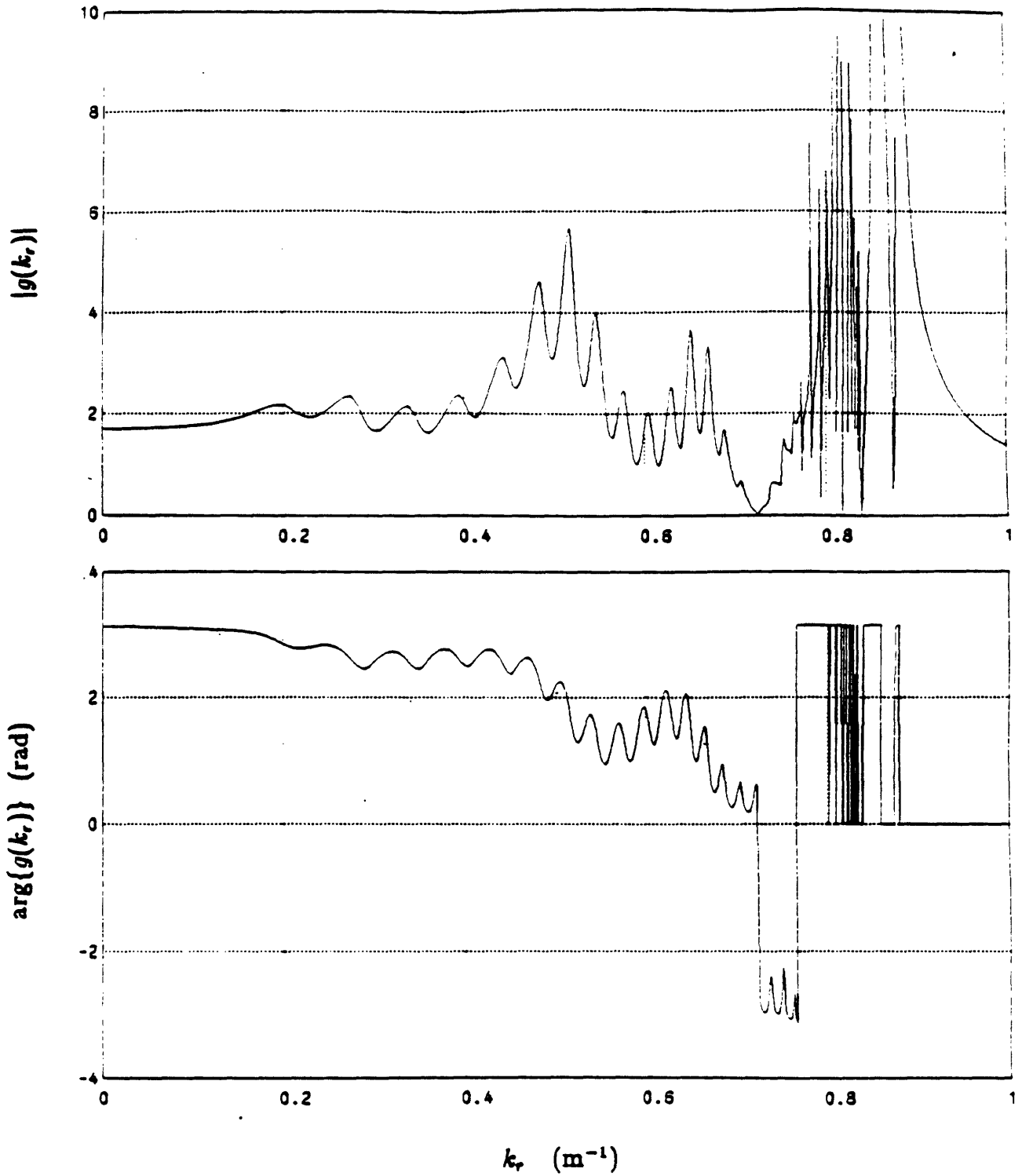
Figure 4.8: Magnitude and phase of the Green's function, $g(k_r)$, corresponding to the geoacoustic model in Table 4.2.

determined using equation (4.49). The mode amplitudes, m_i, defined as $m_i = \pi a_i k_{ri}$, were also computed and a list of the pole positions and the mode amplitudes for the geoacoustic model can be found in Table 4.3. $g_T(k_r)$ and $g_C(k_r)$ were computed using these values, and the resultant $g_C(k_r)$ magnitude and phase are displayed in Figure 4.9. Here, no smoothing operator has been applied and the effects of imperfect pole-zero cancellation are evident by the presence of several spikes in the neighborhood of the pole locations. Figure 4.10 shows the magnitude and phase of $g_C(k_r)$ after applying the smoothing operator in the neighborhood of the real parts of the poles with $N = 5$.

The presence of the spikes prior to smoothing and the residual error after smoothing in the vicinity of $k_r = .86$ can be attributed to errors in the pole and residue estimation. One source of error is that SNAP linearly interpolates between layers to determine the actual velocity at any given depth while the Green's function is computed based on isovelocity layers. The effect can be compensated for by incorporating thin intermediate layers within the geoacoustic model input to SNAP however this compensation is only approximate. A potentially more severe error is incurred in the interpolation procedure required in determining $\phi_i(z)$ and $\phi_i(z_0)$ at values of z, z_0 not on the finite difference grid. A linear interpolator was applied, however it is recognized that a more sophisticated scheme is required. Additionally, the finite difference scheme only provides an approximate solution to the underlying eigenvalue equation.

It is also possible to use the results of SNAP to provide the initialization values to the root-finding technique. For example, consider the dominant pole listed in Table 4.3, i.e. the pole with the largest mode amplitude, which is located at $k_{ri} = 0.8597293$ with $\pi a_i k_{ri} = 0.2140388$. The root-finder could be initialized to this value of k_{ri} and the residue could be computed using the numerical expression involving the reflection coefficient and its derivative. Presumably, the use of these values in the expression for $g_T(k_r)$ would improve the estimate of $g_C(k_r)$ although this has not been fully explored. For reference, in Figure 4.11 is shown the magnitude and phase of the smoothed $g_C(k_r)$

201

k_{r_i}	m_i
0.8804902	$9.4117895e - 02$
0.8597293	$2.1403880e - 01$
0.8382334	$5.7814509e - 04$
0.8366570	$2.5564961e - 03$
0.8340870	$7.1196225e - 03$
0.8306701	$1.8042102e - 02$
0.8267667	$3.8345765e - 02$
0.8225527	$4.0777378e - 02$
0.8172472	$2.1565886e - 02$
0.8105006	$1.0324701e - 02$
0.8024934	$5.7498589e - 03$
0.7933905	$3.6924945e - 03$
0.7834035	$2.4684239e - 03$
0.7730384	$1.0335498e - 03$

Table 4.3: Summary of pole locations k_{r_i} and mode amplitudes $m_i = \pi a_i k_{r_i}$ for the geoacoustic model in Table 4.2.
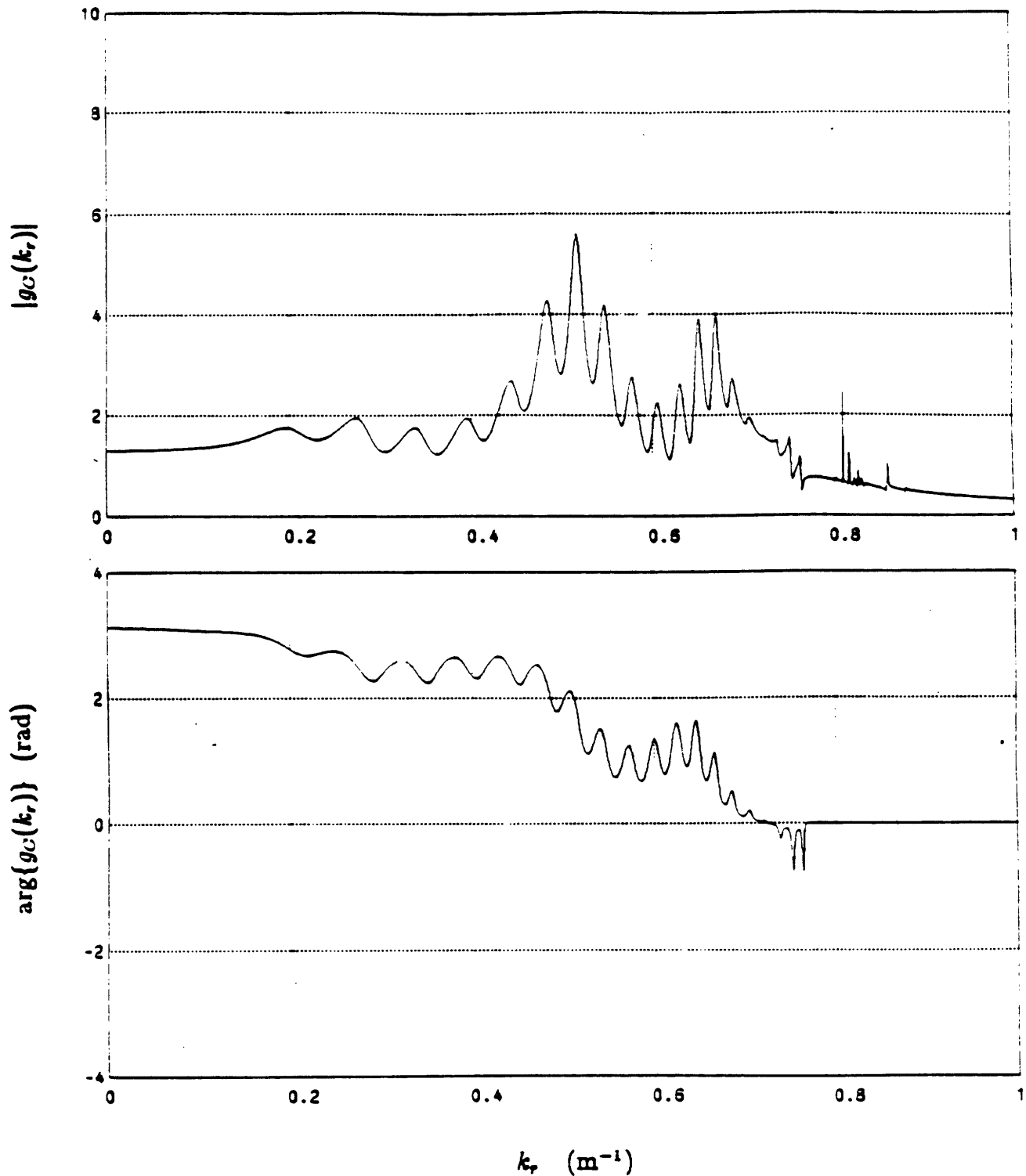
Figure 4.9: Magnitude and phase of the continuum portion of the Green's function, $g_C(k_r)$, corresponding to the geoacoustic model in Table 4.2. No smoothing has been applied and the errors in pole and residue estimation are visible as sharp spikes for values of $k_r > k_N = 0.7688$.
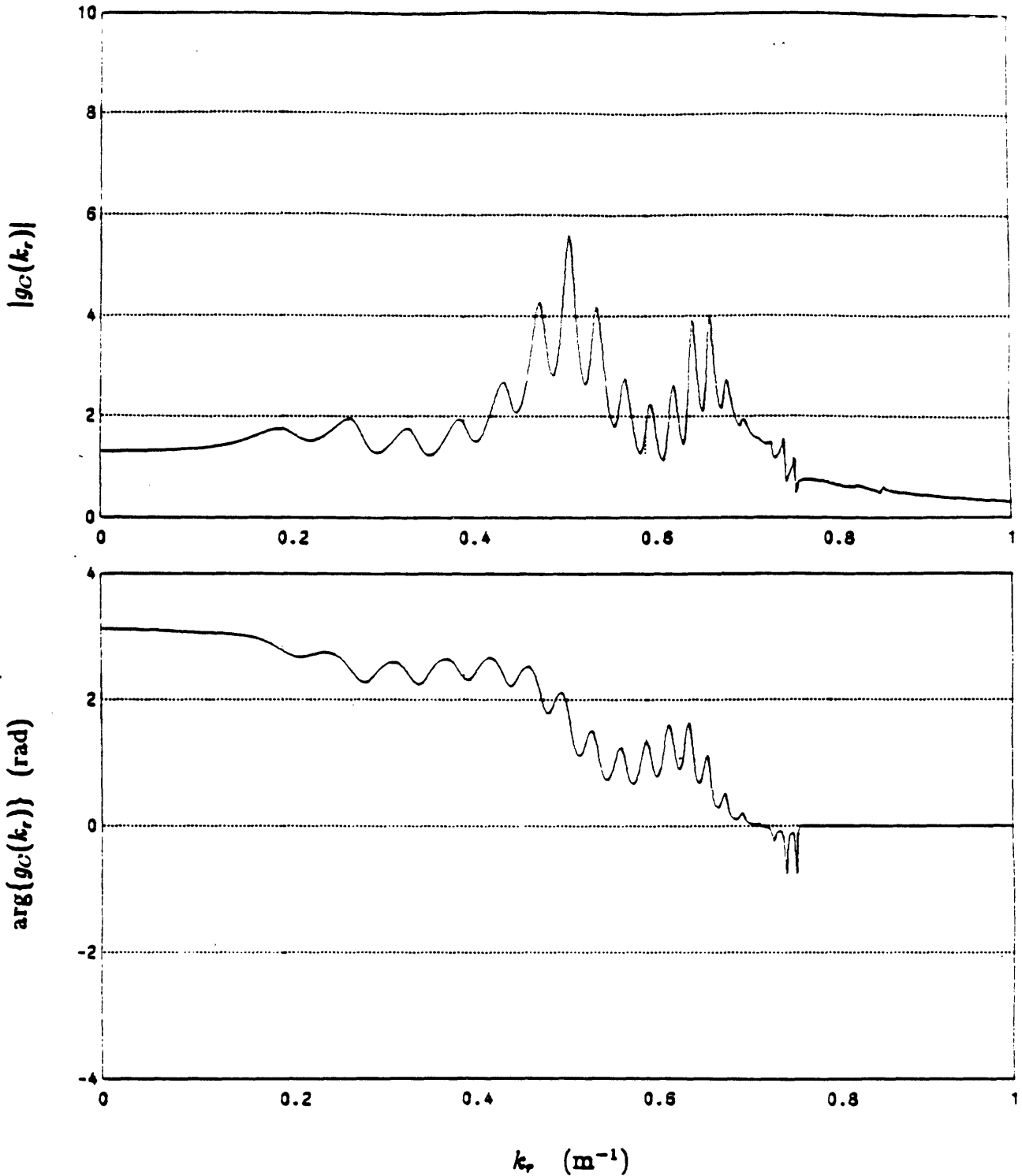
Figure 4.10: Magnitude and phase of the continuum portion of the Green's function, $g_C(k_r)$, after smoothing, corresponding to the geoacoustic model in Table 4.2. A slight residual error remains at $k_r \sim 0.86$ due to errors in estimating the parameters of the dominant pole located at $k_r = 0.8597293$.
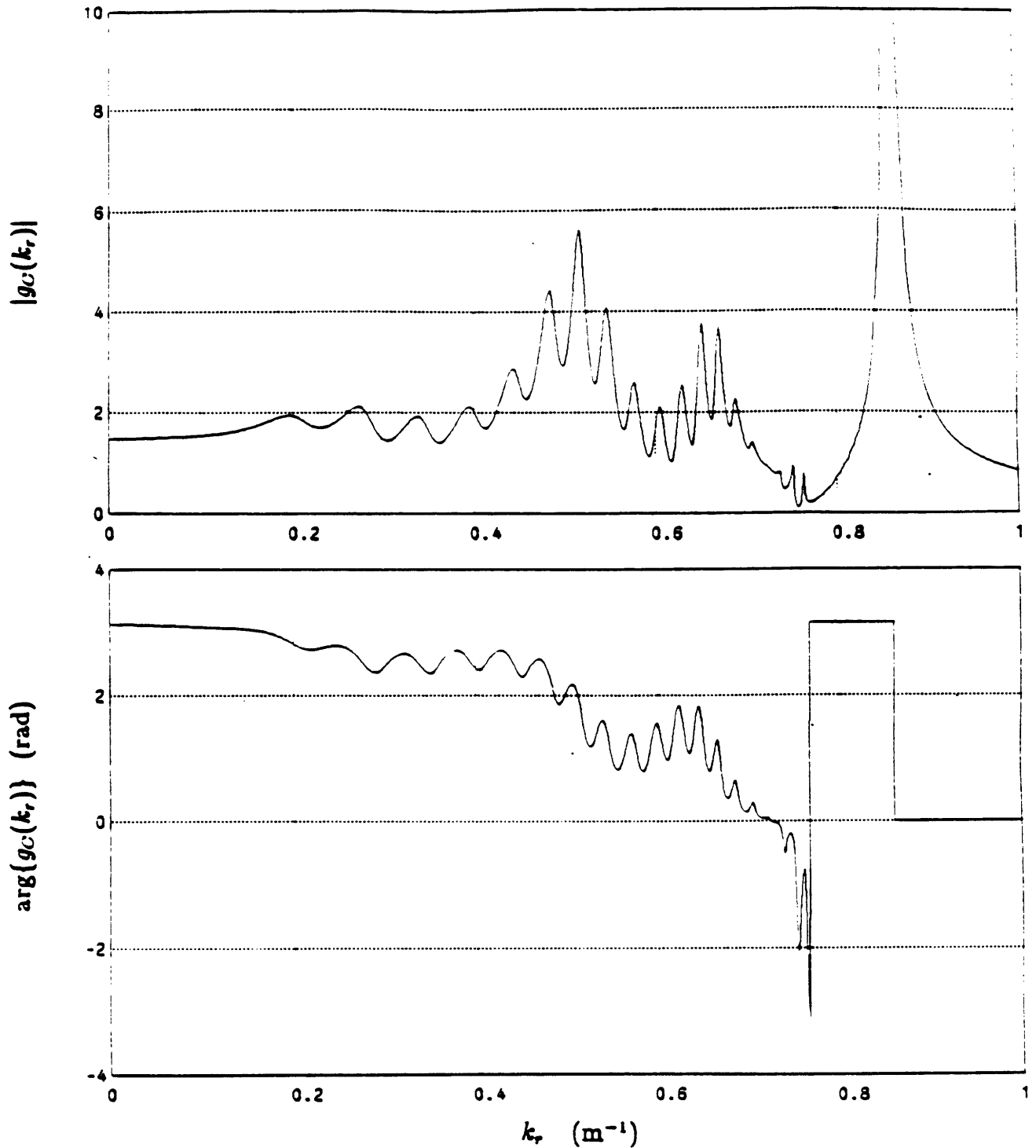
Figure 4.11: Magnitude and phase of the continuum portion of the Green's function, $g_C(k_r)$, after smoothing, corresponding to the geoacoustic model in Table 4.2. Only 13 of the 14 poles present were removed and the dominant pole at $k_r = 0.8597293$ was not removed. The preceding figure essentially shows the error in removing the effects of the dominant pole present here.

which is obtained by removing 13 of the poles and leaving the dominant pole. In effect, Figure 4.10 shows the error in removing the single pole present in Figure 4.11.

To summarize, an alternate approach for computing the poles and residues of $g(k_r)$ required in the hybrid method has been presented. The approach exploits the eigenfunction representation of $g_T(k_r)$. The advantage of the approach is that a larger number of poles can be accommodated and that existing normal-mode computer routines can be used to compute the poles and residues. In addition, the alternate approach can be used as an initialization step for more accurate schemes.

4.5.2 Computation of $p_C(r)$ Using Real-Part/Imaginary-Part Sufficiency

In the hybrid approach, the continuum portion of the field, $p_C(r)$, is computed as the Hankel transform of $g_C(k_r)$. One of the difficulties in this approach is obtaining the quantity $g_C(k_r)$. As pointed out previously, $g_C(k_r)$ can be obtained using $g_C(k_r) = g(k_r) - g_T(k_r)$ and thus the difficulty becomes obtaining $g_T(k_r)$. Several methods for obtaining $g_T(k_r)$ based on exploiting a priori knowledge of the Green's function were previously discussed. In this subsection, a completely different approach for generating $p_C(r)$ is presented. The technique is based on exploiting the real-part/imaginary-part sufficiency condition for $g(k_r)$ which was discussed in Chapter 3 [3]. In fact, this technique completely bypasses the step of determining $g_T(k_r)$ and no pole or residue estimation is required. The technique is best thought of as an alternate method for computing $p_C(r)$. Note that, in the hybrid scheme, $g_T(k_r)$ is still required in order to determine the modal portion of the field, $p_T(r)$. The technique to be discussed essentially decouples the problems of estimating $p_T(r)$ and $p_C(r)$.

One of the merits of this approach is that it provides a check on the original hybrid method. Establishing the validity of $g_C(k_r)$ or $p_C(r)$ without using this technique is quite difficult. This stems from the fact that evaluating $g_C(k_r)$ without using the expression $g_C(k_r) = g(k_r) - g_T(k_r)$ requires that a branch line integral must be performed for each value of k_r, as can be seen from equation (4.19). The alternate technique generates $p_C(r)$ without explicitly computing $g_C(k_r)$ and thus provides an independent way in which to verify the result of computing the Hankel transform of $g_C(k_r)$. In addition, the technique exploits the real-part/imaginary-part sufficiency property in the Green's function domain as opposed to the pressure field domain. The most obvious application of the real-part/imaginary-part sufficiency condition is in the acquisition and processing of a single channel of acoustic field data. However, the

---

[3] Specifically, Statement 6 for the unilateral inverse Fourier transform and Statement 6 for the Hilbert-Hankel transform is utilized.

proposed technique suggests that the real-part/imaginary-part sufficiency condition in the other domain may be of practical significance as well.

To begin the discussion, we first review two important properties on which the alternate technique for computing $p_C(r)$ is based. The first property is that $g_T(k_r)$ must be a purely real function for real-k_r. This can be simply derived by referring to the eigenfunction representation for $g_T(k_r)$, given in the previous subsection, and by recognizing that the eigenvalues and eigenfunctions are purely real. This implies that both a_i and k_{ri} are purely real and that

$$g_T(k_r) = \sum_i \frac{2a_i k_{ri}}{k_r^2 - k_{ri}^2} \tag{4.50}$$

must be purely real for real values of k_r. An implication of this property is that, although extracting $g_C(k_r)$ from $g(k_r)$ is a difficult problem and depends on estimating $g_T(k_r)$, extracting $Im\{g_C(k_r)\}$ *only* is much simpler. In fact,

$$Im\{g_C(k_r)\} = Im\{g(k_r)\} \tag{4.51}$$

for real-k_r as can be easily determined using the equation $g_C(k_r) = g(k_r) - g_T(k_r)$ and the fact that $g_T(k_r)$ is purely real for real-k_r.

As a numerical example of this property, consider the geoacoustic model described in Table 4.1. The magnitude and phase of $g(k_r)$ corresponding to this model were previously shown in Figure 4.3 and the magnitude and phase of $g_C(k_r)$ were previously shown in Figure 4.5. The function $g_C(k_r)$, in the latter figure, was obtained by estimating the position of the single pole and its residue and computing $g_C(k_r) = g(k_r) - g_T(k_r)$. The real and imaginary parts of the functions $g(k_r)$ and $g_C(k_r)$ are now shown in Figures 4.12 and 4.13. The plots of the imaginary portions of these functions confirm the property stated in equation (4.51) and thus $Im\{g_C(k_r)\}$ can be obtained from $g(k_r)$ in a straightforward manner. Note also that $Im\{g_C(k_r)\}$ is of finite extent to the wavenumber of the underlying halfspace, $k_N = 0.4888\ rad/m$. This follows from the property proved in Chapter 2 that $Im\{g(k_r)\} = 0$ for real-k_r greater than k_N and from equation (4.51).
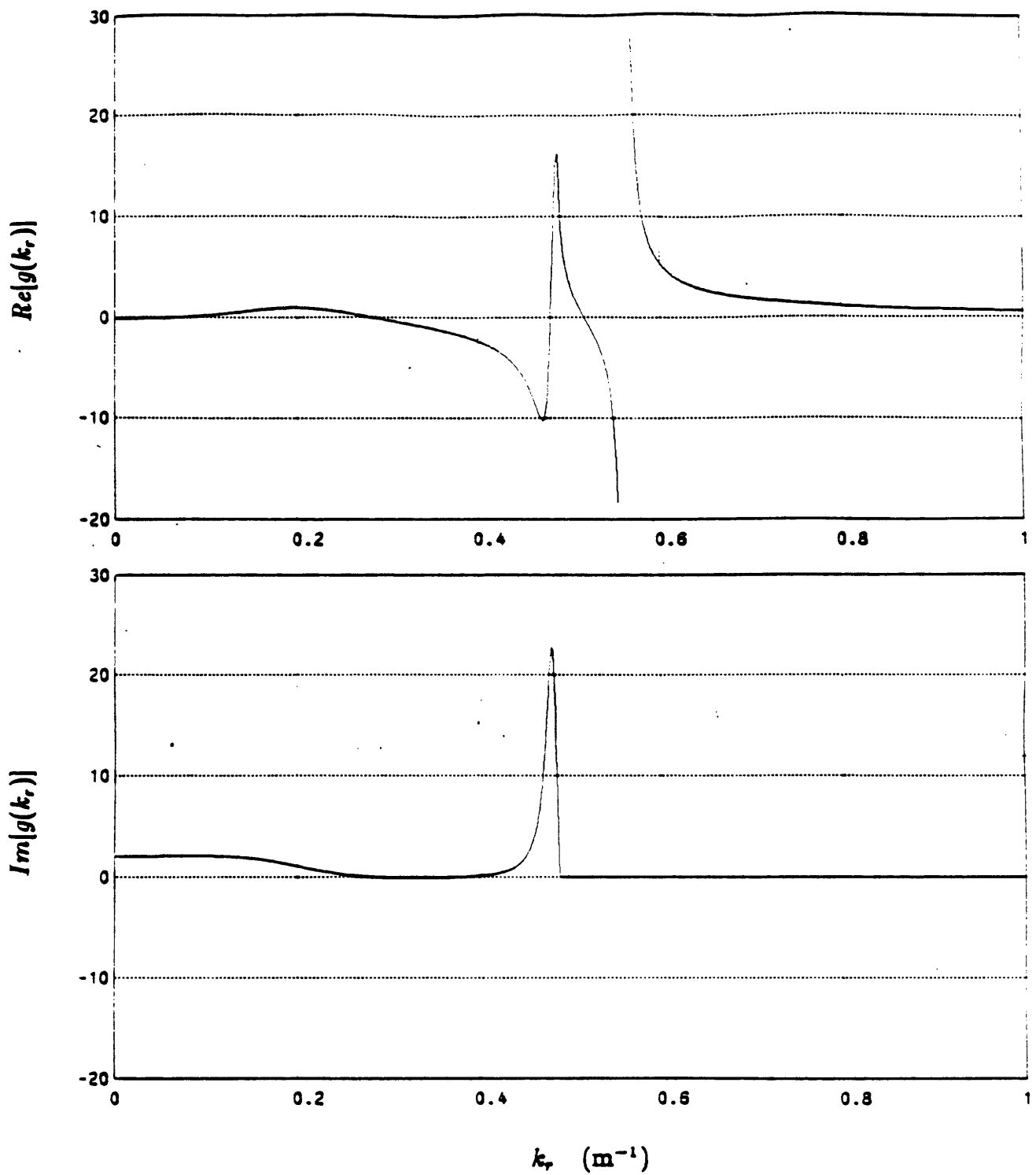
Figure 4.12: Real and imaginary parts of the Green's function, $g(k_r)$, for the geoacoustic model of Table 4.1
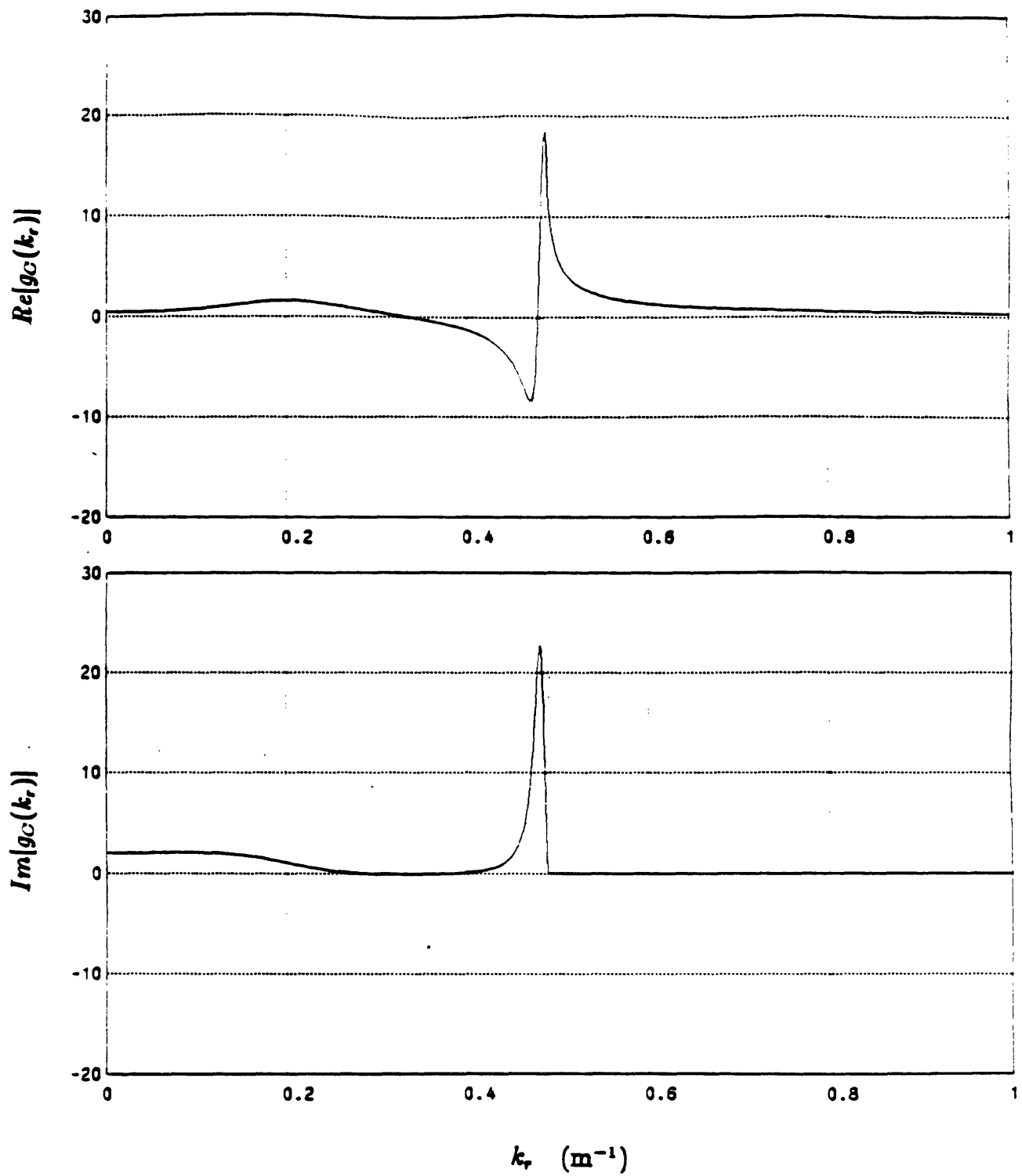
Figure 4.13: Real and imaginary parts of the continuum portion of the Green's function, $g_C(k_r)$, for the geoacoustic model of Table 4.1.

The second property required is that $g_C(k_r)$ and $p_C(r)$ can be related via the Hilbert-Hankel transform. This fact follows since $g_C(k_r)$ and $p_C(r)$ are related by a Hankel transform and since $g_C(k_r)$ has no singularities in quadrant II of the complex-k_r plane. Alternately, recalling that the Hilbert-Hankel transform applies to fields which radiate outward, we recognize that $p_C(r)$ must be such a field since $p(r) = p_T(r)+p_C(r)$ and both $p(r)$ and $p_T(r)$ are outgoing fields. Using the properties of the Hilbert-Hankel transform discussed in Chapter 3, it is apparent that the real-part/imaginary-part sufficiency conditions must apply to $g_C(k_r)$ and $p_C(r)$. In particular, it is possible to synthesize $p_C(r)$ from the imaginary part of $g_C(k_r)$ using $p_C(r) \sim 2j\,\mathcal{H}_a^{-1}\{Im[g_C(k_r)]\}$. It is also possible to utilize the asymptotic Hilbert-Hankel transform to perform this synthesis approximately.

The alternate technique for generating $p_C(r)$ from $g(k_r)$ without explicitly estimating $g_T(k_r)$ is summarized in Figure 4.14. As can be seen, the technique consists of computing the asymptotic Hilbert-Hankel transform of $2j\,Im\{g(k_r)\}$. The procedure is straightforward in comparison with the original hybrid method, in that no pole or residue estimates are required. The disadvantage is that an approximation has been introduced by using the Hilbert-Hankel transform or its asymptotic version. Additionally, the technique applies to only the restricted class of lossless, compressional geoacoustic models since the equivalence of the imaginary part of $g(k_r)$ with the imaginary part of $g_C(k_r)$ is valid only for the lossless case. However, a modification to this technique can be made which extends it to include attenuation, as will be discussed.

Two numerical examples of the technique for generating $p_C(r)$ are now presented. In the first example, the geoacoustic model summarized in Table 4.1 was used. A numerical Hankel transform algorithm based on the Abel/Fourier transform was applied to the smoothed version of $g_C(k_r)$ for this model. The continuum portion of the Green's function $g_C(k_r)$ was windowed to include values only up to $k_r \sim 1.0$ and 2048 points of $g_C(k_r)$ were used as input to the Hankel transform. The magnitude of the resultant field as a function of range out to 1500 m is shown in Figure 4.15. A discrete

211
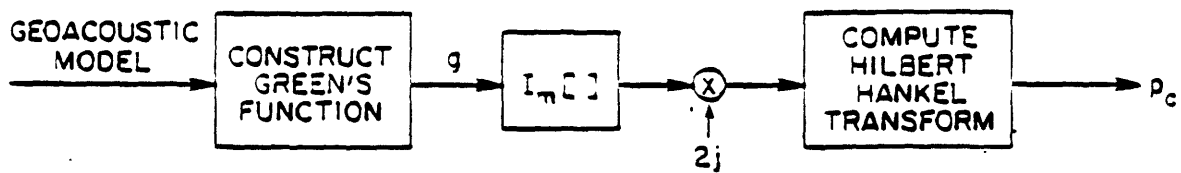
Figure 4.14: Block diagram of alternate technique for determining $p_C(r)$ based on the real-part/imaginary-part sufficiency condition of $g_C(k_r)$.
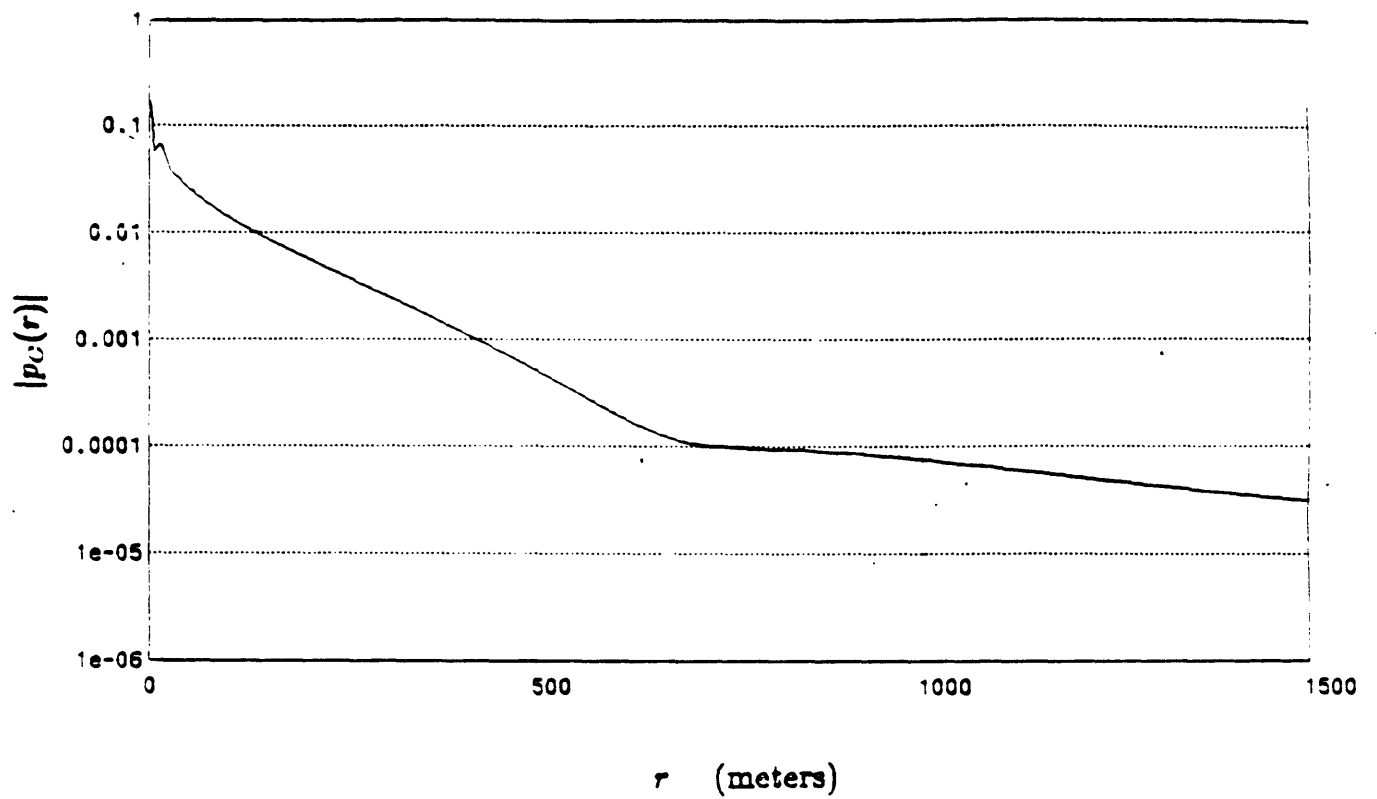
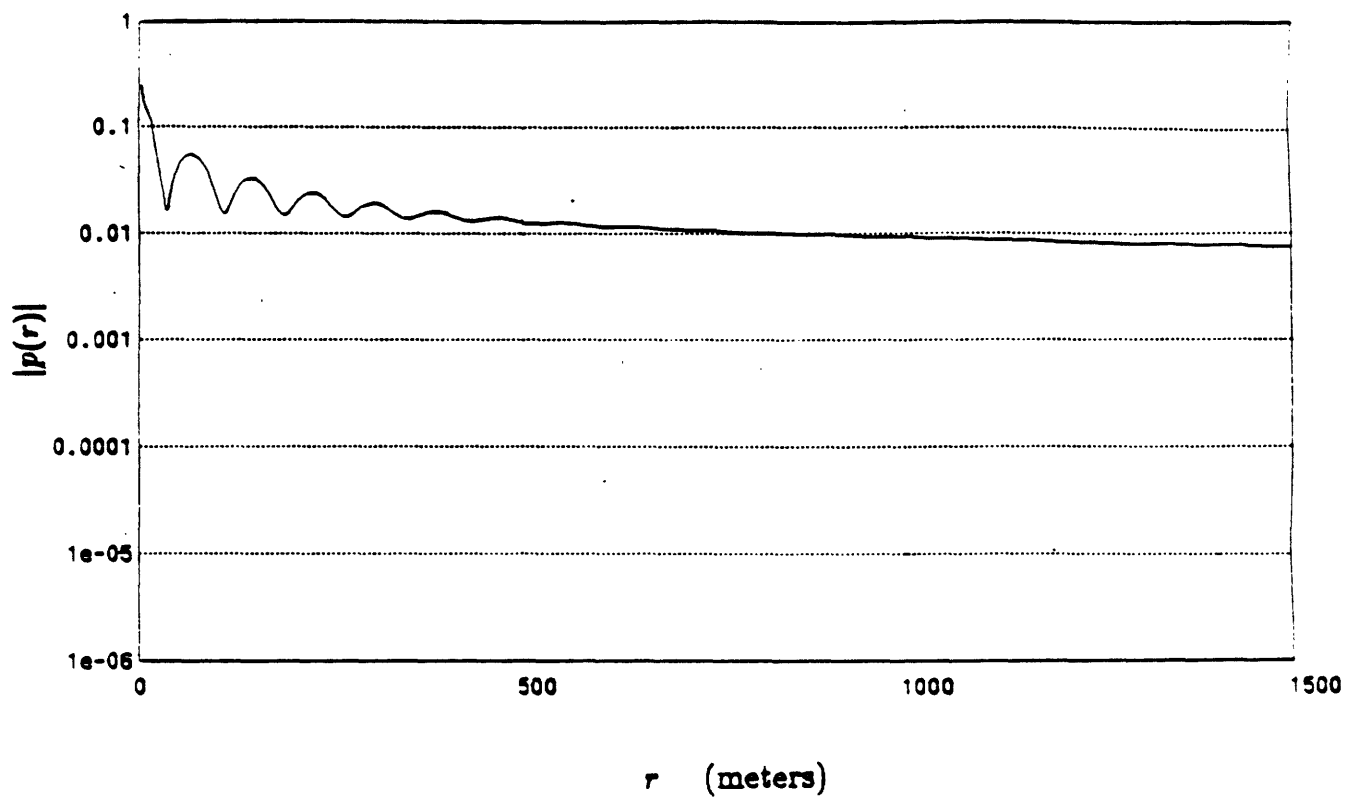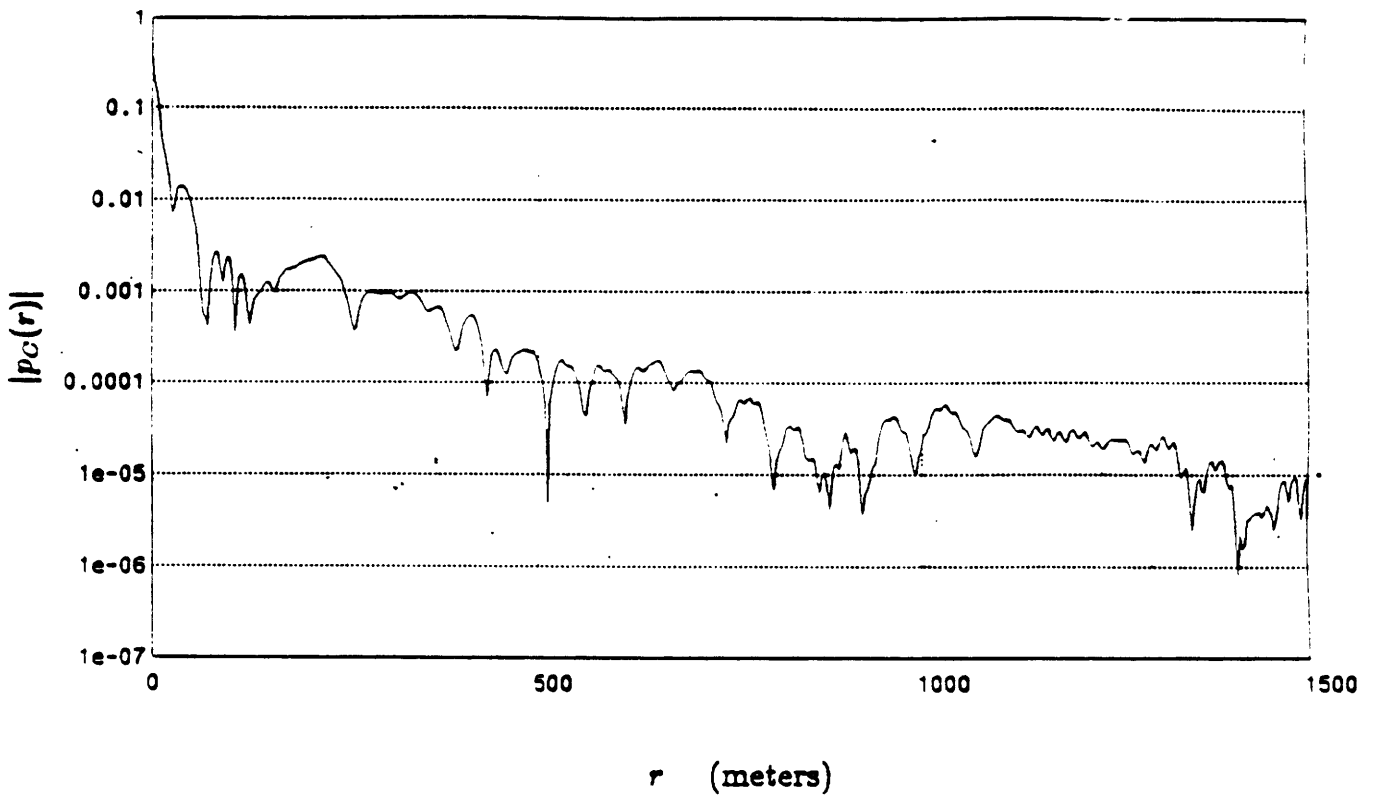Figure 4.15: Magnitude of the continuum portion of the field for the geoacoustic model in Table 4.1 generated by computing the Hankel transform of $g_C(k_r)$ based on the Abel/Fourier method.
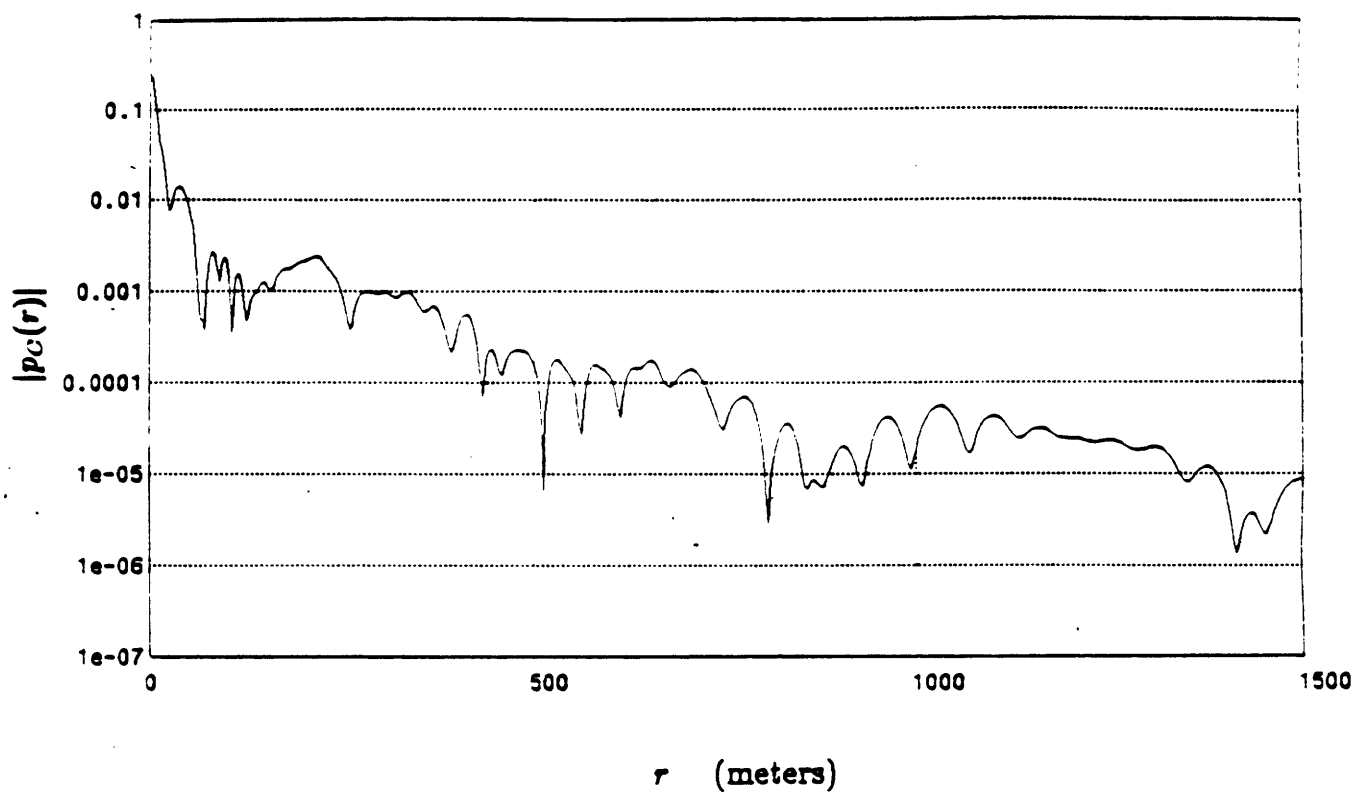
version of the asymptotic Hilbert-Hankel transform was also applied to the function $Im\{g(k_r)\}$ displayed in Figure 4.12b. The resultant continuum field magnitude is displayed in Figure 4.16.

In comparing the continuum field magnitudes in Figures 4.15 and 4.16, we see that although there are slight differences, the agreement is quite close. For reference purposes, we also include a plot of the magnitude of $p(r)$ in Figure 4.17, obtained by adding the analytically-computed modal field $p_T(r)$ and the numerically generated field $p_C(r)$. The oscillation in the magnitude of the total field in the first 500 m is due to the interference between the continuum portion of the field and the single trapped mode. This interference would not have been synthesized in a normal-mode method which incorporated the single mode only.

In Figure 4.18 is shown the magnitude of the total field, obtained by applying the asymptotic Hilbert-Hankel transform directly to $g(k_r)$, i.e. without using the hybrid method. Although the field magnitude in this figure is smoothly varying, it is evident that severe aliasing is present. The magnitude of the aliased field at far ranges in Figure 4.18 is approximately 10 times the magnitude of the correct field, generated using the hybrid method, in Figure 4.17. For the case of a single trapped mode, we have previously derived in Chapter 3 that the aliasing which results in the far-field consists of approximately a gain factor times the actual field. The gain factor was derived as $1/(1 - e^{jk_{ri}2\pi/\Delta k_r})$, where k_{ri} is pole location and Δk_r is the sample spacing of the Green's function. Using this formula, the magnitude of the gain factor is determined as 10.728 which is consistent with the actual aliasing observed.

In the second example, the geoacoustic model in Table 4.2 was used. The poles and residues of this model were determined using the normal-mode approach and the smoothed version of the corresponding $g_C(k_r)$ was previously shown in Figure 4.10. A numerical Hankel transform algorithm based on the Abel/Fourier method was applied to the smoothed version of $g_C(k_r)$ for this model. The continuum portion
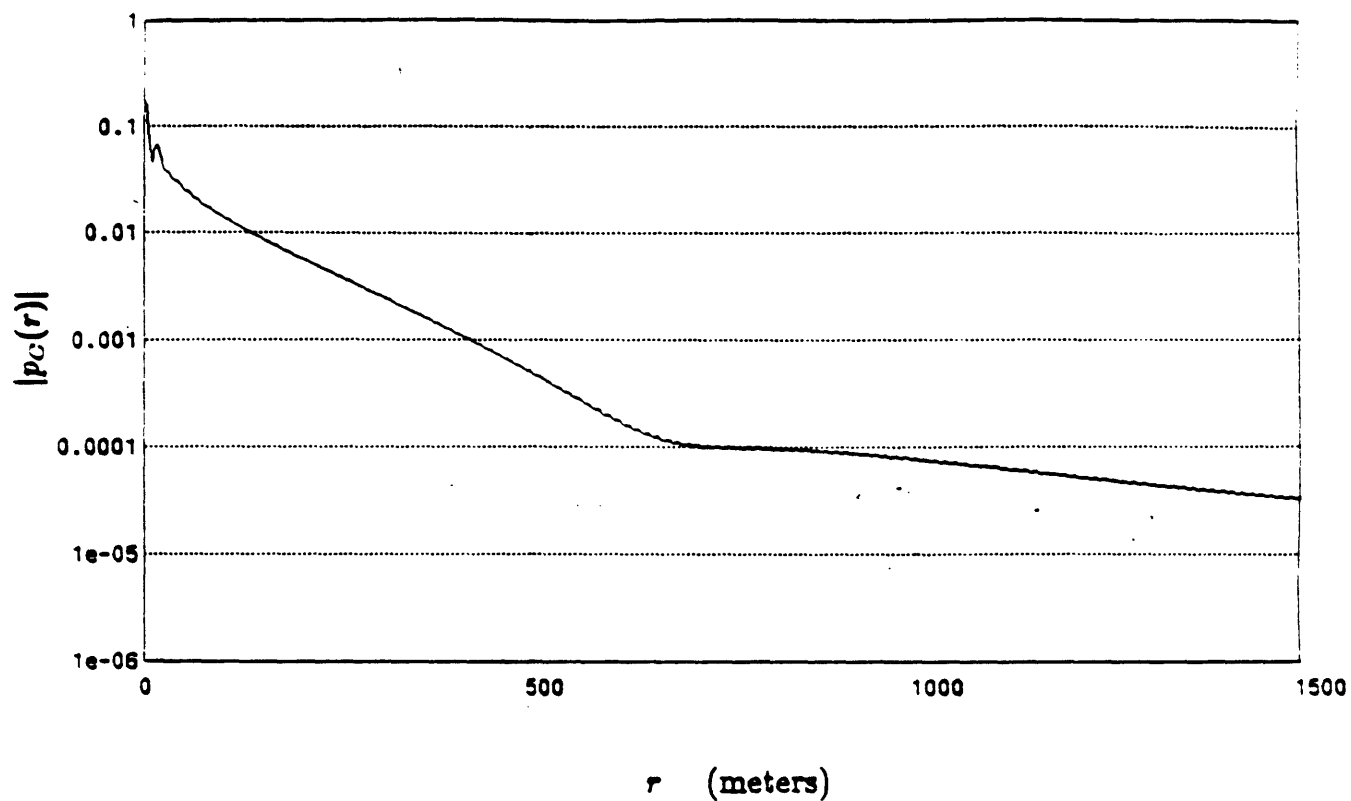
Figure 4.16: Magnitude of the continuum portion of the field for the geoacoustic model in Table 4.1 generated by computing the asymptotic Hilbert-Hankel transform of $2j\,Im[g]$.
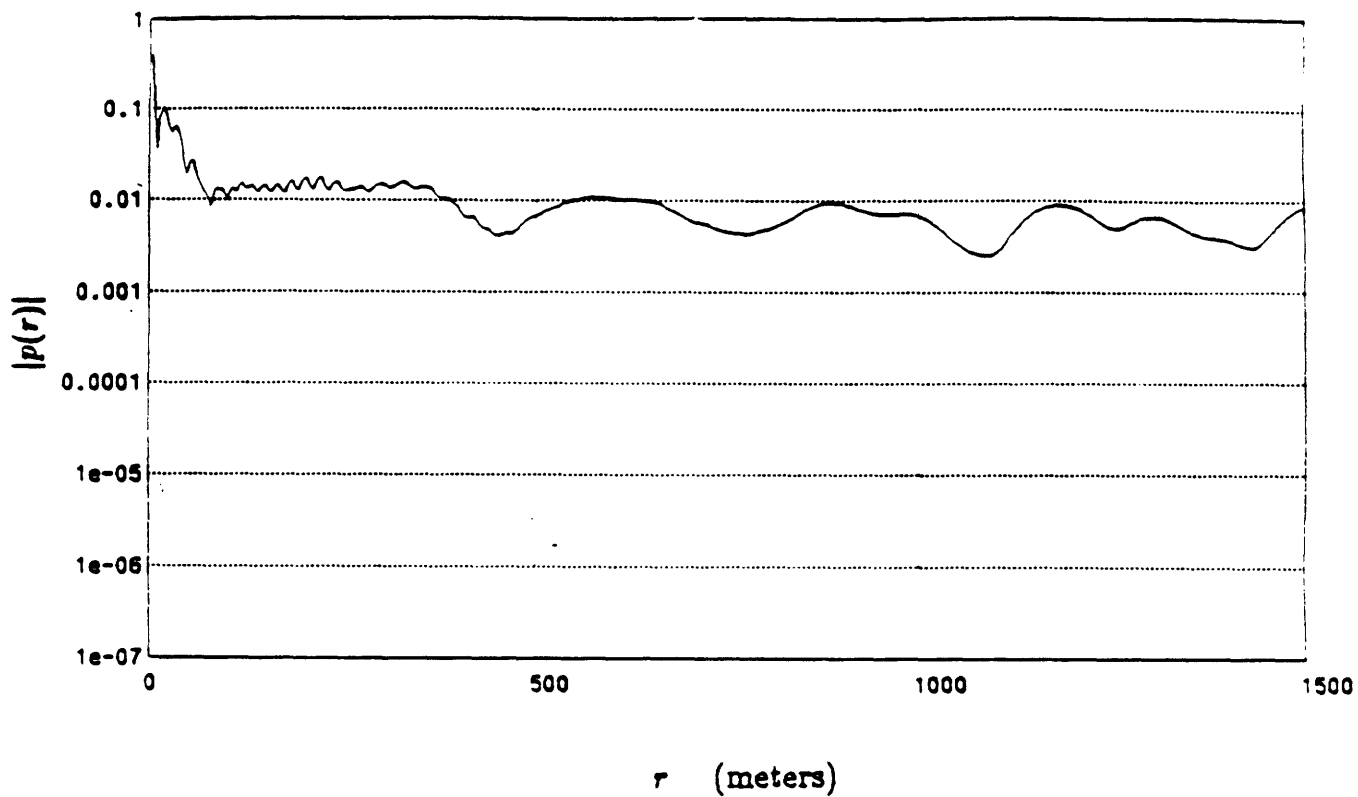
Figure 4.17: Magnitude of the total field for the geoacoustic model in Table 4.1 generated by adding $p_C(r)$ to $p_T(r)$. $p_C(r)$ was computed as the Hankel transform of $g_C(k_r)$ using the Abel/Fourier method.
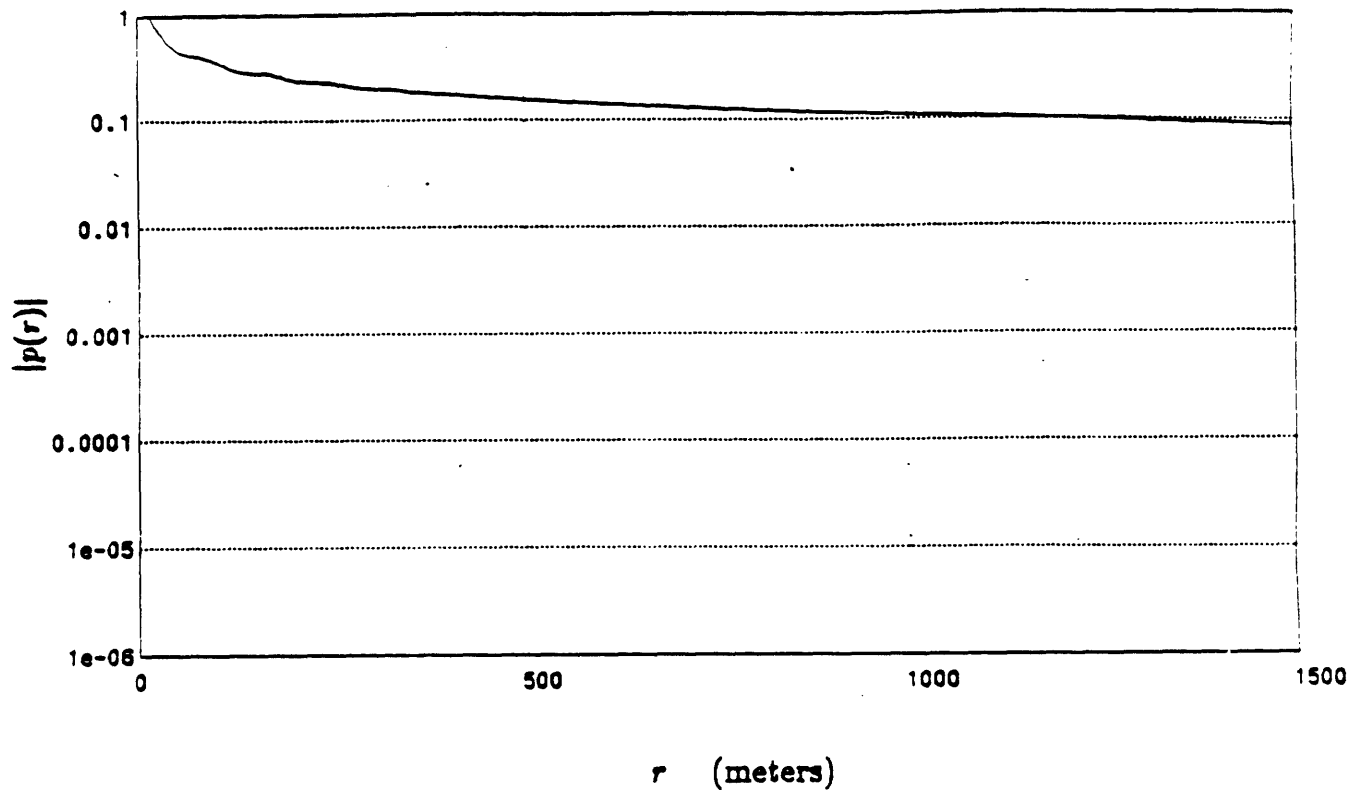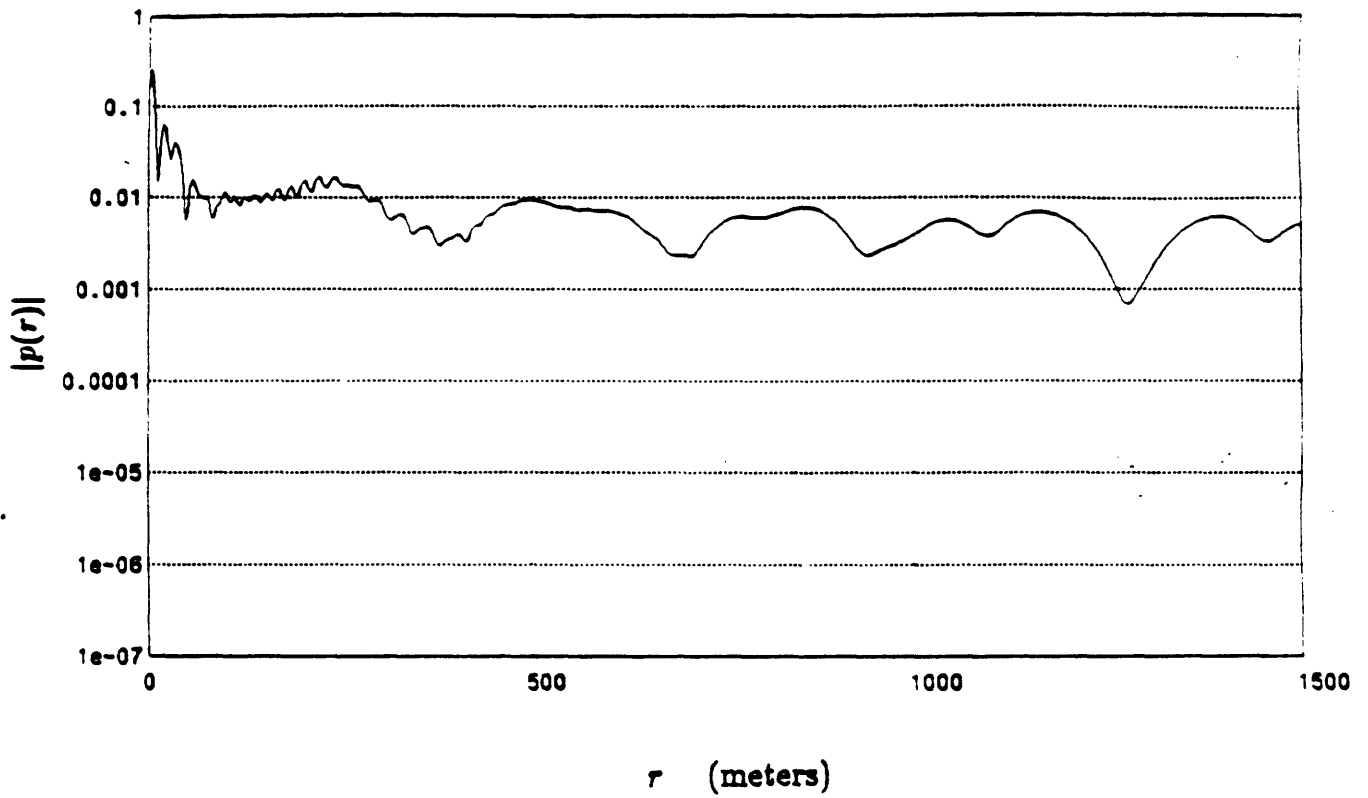
Figure 4.18: Magnitude of the total field for the geoacoustic model in Table 4.1 generated by applying the asymptotic Hilbert-Hankel transform directly to the Green's function without using the hybrid method. The field is severely aliased as can be seen by comparing it with the field in the preceding figure.

of the Green's function was windowed to include values only up to $k_r = 1.0$ and 2048 points of $g_C(k_r)$ were used as input to the Hankel transform. The magnitude of the resultant field as a function of range out to 1500 m is shown in Figure 4.19. The asymptotic Hilbert-Hankel transform was also applied to $Im\{g(k_r)\}$ and the resultant continuum field magnitude is displayed in Figure 4.20. Again, although there are small differences between the curves shown in Figures 4.19 and 4.20, the agreement is quite close. In fact, it is difficult to conclude which field is correct and which field is in error as different sources of error contribute in both approaches. The close agreement between the two curves confirms the validity of the two independent approaches. For reference purposes, we have also included a plot of the magnitude of $p(r)$ in Figure 4.21, obtained by adding the analytically-computed modal field $p_T(r)$ and the numerically generated field $p_C(r)$. The complexity of the field is due to the large number of resonances present within the Green's function, as can be seen from Figure 4.8. The rapid oscillation in the field out to ranges of about 500 m is due to the interference between the continuum portion of the field and the trapped mode portion and would not have been synthesized with a normal-mode technique. In Figure 4.22 a plot of the magnitude of the total field, obtained by applying the Hankel transform directly to $g(k_r)$, i.e. without using the hybrid method, is shown. The severe aliasing in the field computed without the use of the hybrid method is evident, as the two fields are substantially different.

On re-examining the alternate approach for computing $p_C(r)$ an apparent paradox becomes evident. The paradox can be phrased as follows: If both $g_C(k_r)$ and $g(k_r)$ have imaginary-part sufficiency, and $Im\{g(k_r)\} = Im\{g_C(k_r)\}$, then $p_C(r)$ must equal $p(r)$. However, $p_C(r)$ and $p(r)$ cannot be equal unless $p_T(r)$, and thus $g_T(k_r)$, is zero. If there are any poles present in $g(k_r)$, $g_T(k_r)$ cannot be zero and thus $p_C(r)$ must not equal $p(r)$. We now resolve this apparent paradox and in doing so, provide the basis for extending this technique to geoacoustic models which include attenuation.

The basis of the paradox is that although strictly speaking, $Im\{g_C(k_r)\} = Im\{g(k_r)\}$

Figure 4.19: Magnitude of the continuum portion of the field for the geoacoustic model in Table 4.2 generated by computing the Hankel transform of $g_C(k_r)$ based on the Abel/Fourier method.

Figure 4.20: Magnitude of the continuum portion of the field for the geoacoustic model in Table 4.2 generated by computing the asymptotic Hilbert-Hankel transform of $2j\,Im|g|$.

Figure 4.21: Magnitude of the total field for the geoacoustic model in Table 4.2 generated by adding $p_C(r)$ to $p_T(r)$. $p_C(r)$ was computed as the Hankel transform of $g_C(k_r)$ using the Abel/Fourier method.

Figure 4.22: Magnitude of the total field for the geoacoustic model in Table 4.2 generated by applying the Hankel transform directly to the Green's function without using the hybrid method. The field is severely aliased as can be seen by comparing it with the field in the preceding figure.

along the real-k_r axis, this result is not true for a contour displaced by ϵ below the axis. In particular, this equality condition is not true in the immediate vicinity of poles which are located on the real-k_r axis. The presence of these poles directly on the axis is of no concern in the original hybrid method because they are removed in the determination of $g_C(k_r)$. However, their presence is of concern if the Hankel transform of $g(k_r)$ is computed or if the Hilbert-Hankel transform of $Im\{g(k_r)\}$ is computed. In particular, in previous discussions we have considered the position of the integration contour as displaced ϵ below the real-k_r axis in order to avoid these pole singularities. If $g_T(k_r)$ is evaluated along the displaced contour, it is no longer a purely real function. The implication, using $g_C(k_r) = g(k_r) - g_T(k_r)$, is that $Im\{g_C(k_r)\}$ is not equal to $Im\{g(k_r)\}$ along this contour.

This effect is now illustrated using a numerical example. The real and imaginary parts of $g(k_r)$ as a function of real-k_r for the geoacoustic model in Table 4.1 have previously been shown in Figure 4.12. The function $g(k_r)$ was re-evaluated along a contour parallel to the real-k_r axis but displaced below it by $\epsilon = 1.0 * 10^{-6}$. The real and imaginary parts of $g(k_r)$, evaluated along this contour, are plotted in Figure 4.23. Note that the real and imaginary parts are nearly identical to those in Figure 4.12 with the exception of the presence of the spike near the pole located at $k_{ri} = 0.5623757$ in the imaginary component of $g(k_r)$ in Figure 4.23. The Hilbert-Hankel transform of the imaginary component in Figure 4.12b yields $p_C(r)$ while the Hilbert-Hankel of the imaginary component in Figure 4.23b yields $p(r)$. A numerical implementation of the latter transform would be difficult, of course, because of the sampling and aliasing effects previously discussed. Intuitively however, this result makes sense as the spike located at $k_r = k_{ri}$ in $Im\{g(k_r)\}$ contributes the term $\pi j a_i k_{ri} H_0^{(1)}(k_{ri}r)$ to the trapped portion of the field via the Hilbert-Hankel transform while the remaining portion of $Im\{g(k_r)\}$ contributes to the continuum portion of the field.

Thus, the apparent paradox is resolved as follows. The function $Im\{g(k_r)\}$ is equal to $Im\{g_C(k_r)\}$ for real-k_r if a lossless, compressional geoacoustic model is assumed.
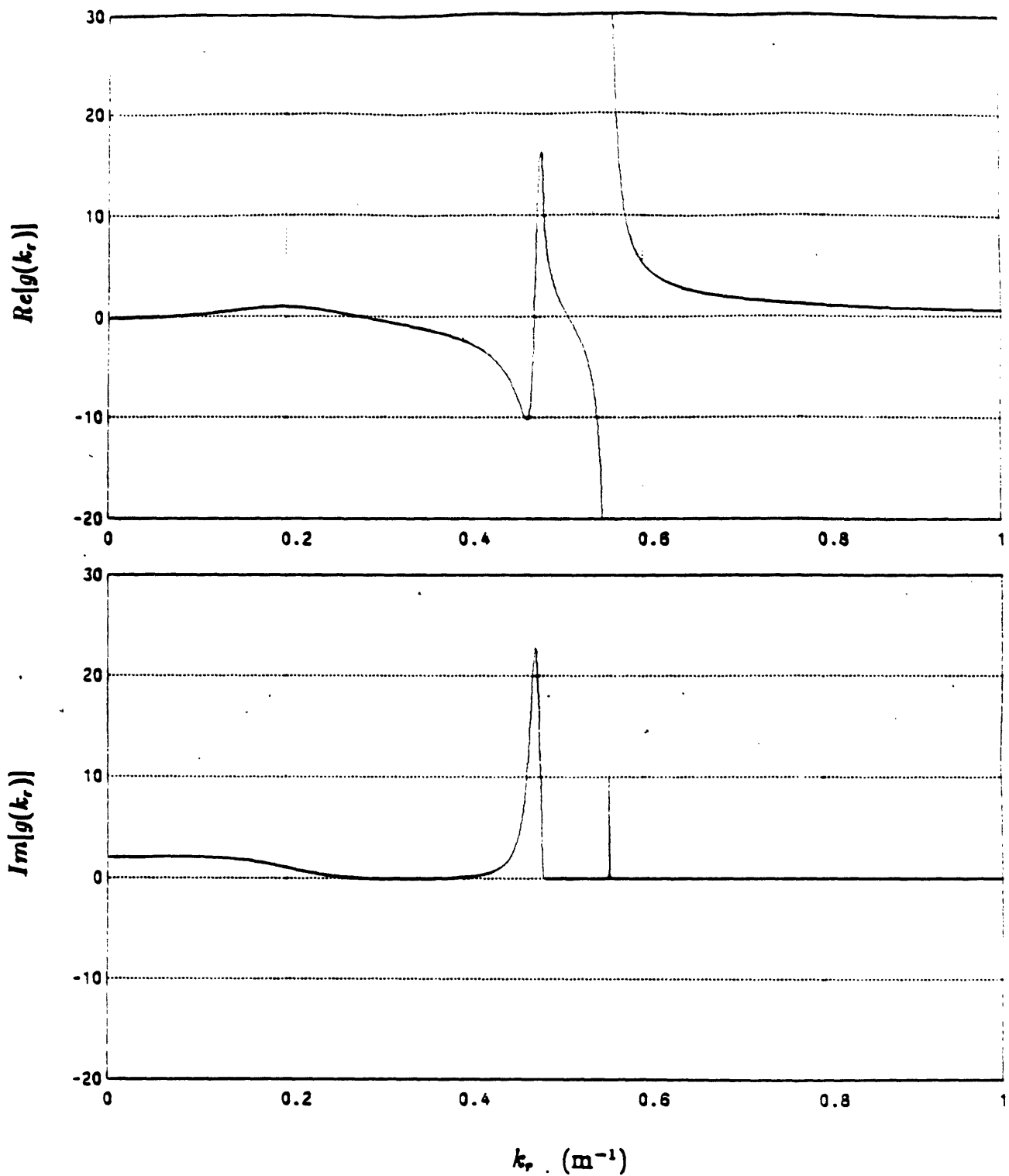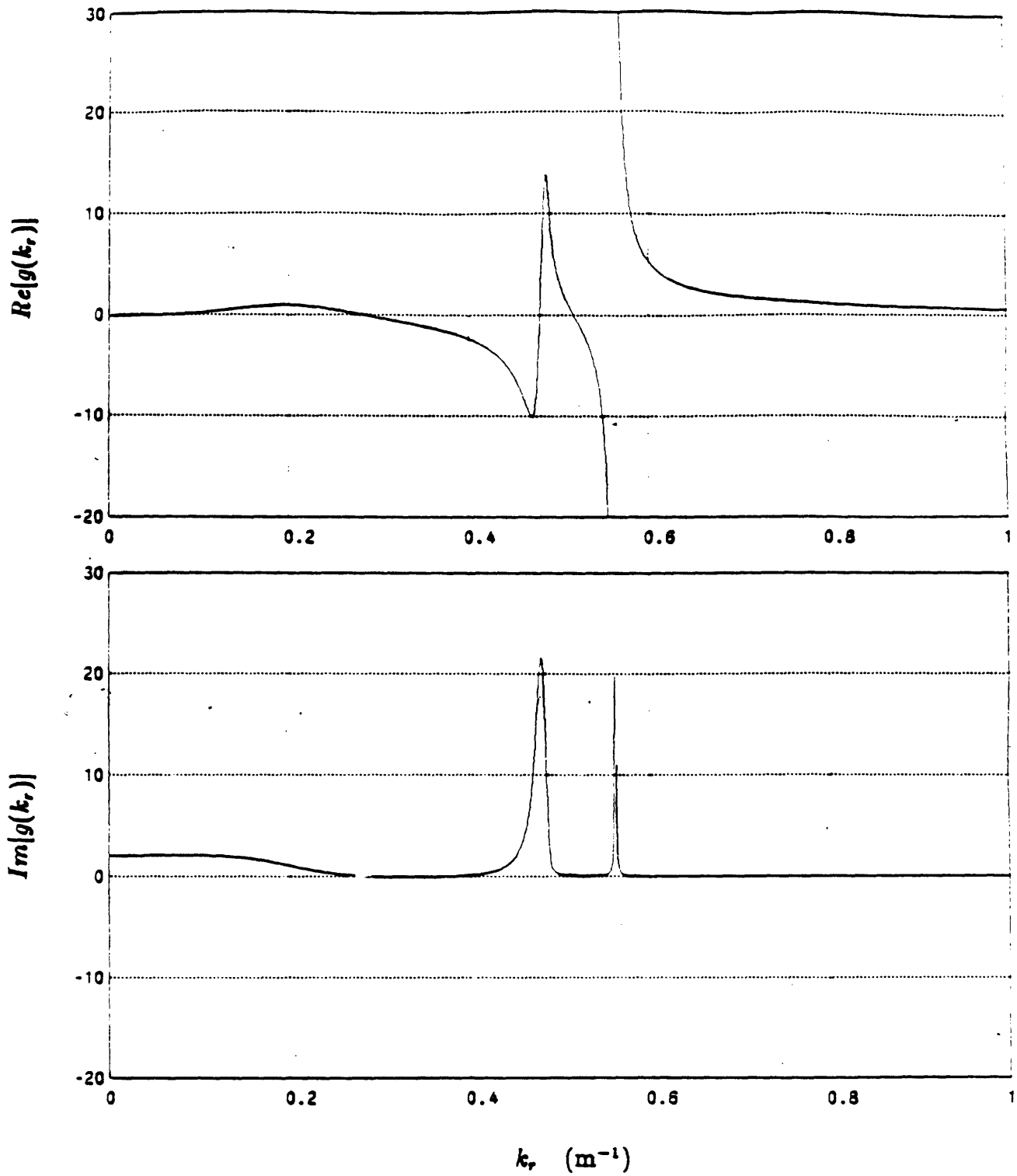
Figure 4.23: Real and imaginary parts of the Green's function corresponding to the geoacoustic model in Table 4.1 evaluated at a contour displaced by 1.0×10^{-6} below the real-k_r axis.

Furthermore, $p_C(r)$ can be generated from $Im\{g_C(k_r)\}$ by computation of its Hilbert-Hankel transform. However, $p(r)$ cannot be computed from $Im\{g(k_r)\}$ evaluated along the real-k_r axis because the contour of integration must be slightly displaced in order to avoid the poles.

The above argument addressed the conceptual question of whether $p_C(r)$ or $p(r)$ is generated when the Hilbert-Hankel transform of $Im\{g(k_r)\}$ is computed. The issue involved was the presence of the poles directly on the real-k_r axis. A more practical question arises if attenuation is included in the geoacoustic model. Here, we are no longer concerned with displacing the contour to avoid the poles and branch-point, as these are located slightly off the real-k_r axis in quadrant I of the complex-k_r plane. The question is whether or not the technique for generating $p_C(r)$ based on imaginary-part sufficiency is still applicable. It can be shown that when attenuation is included both the pole locations and residues become complex and thus $g_T(k_r)$ is no longer a real function for real-k_r. Therefore, we cannot argue that $Im\{g_C(k_r)\} = Im\{g(k_r)\}$. Strictly speaking, the alternate approach for generating $p_C(r)$ is no longer applicable. However, a modification to this approach can be made which yields acceptable $p_C(r)$ fields when realistic values of attenuation are considered.

The modification is based on the observation that $Im\{g_T(k_r)\} \sim 0$ for real-k_r everywhere except in the immediate vicinity of the real part of the pole location. In fact, it can be shown that if the pole is located at a position $k_{ri} = a + j\epsilon_0$ and the residue is $a_i = b + j\epsilon_1$, then $Im\{g(k_r)\}$ behaves as

$$Im\{g(k_r)\} \sim \frac{\epsilon_1(k_r - a) + \epsilon_0 b}{(k_r - a)^2} \qquad (4.52)$$

for real-k_r not in the vicinity of a. Because of the fact that ϵ_0 and ϵ_1 are small quantities for realistic values of attenuation in the model, it is noted that $Im\{g(k_r)\}$ is very small for real values of k_r not equal to a. In other words, for realistic amounts of attenuation, although $g_T(k_r)$ is not purely real, its imaginary part is non-zero only in a small wavenumber region near the location of the pole. Note that a similar statement cannot be made about the real part of $g_T(k_r)$ - if it could, then the original

225

technique for removing the poles from $g(k_r)$ could have been considerably simplified. In particular, the effect of a pole in the real part of $g_T(k_r)$ extends over a much wider interval along the real-k_r axis.

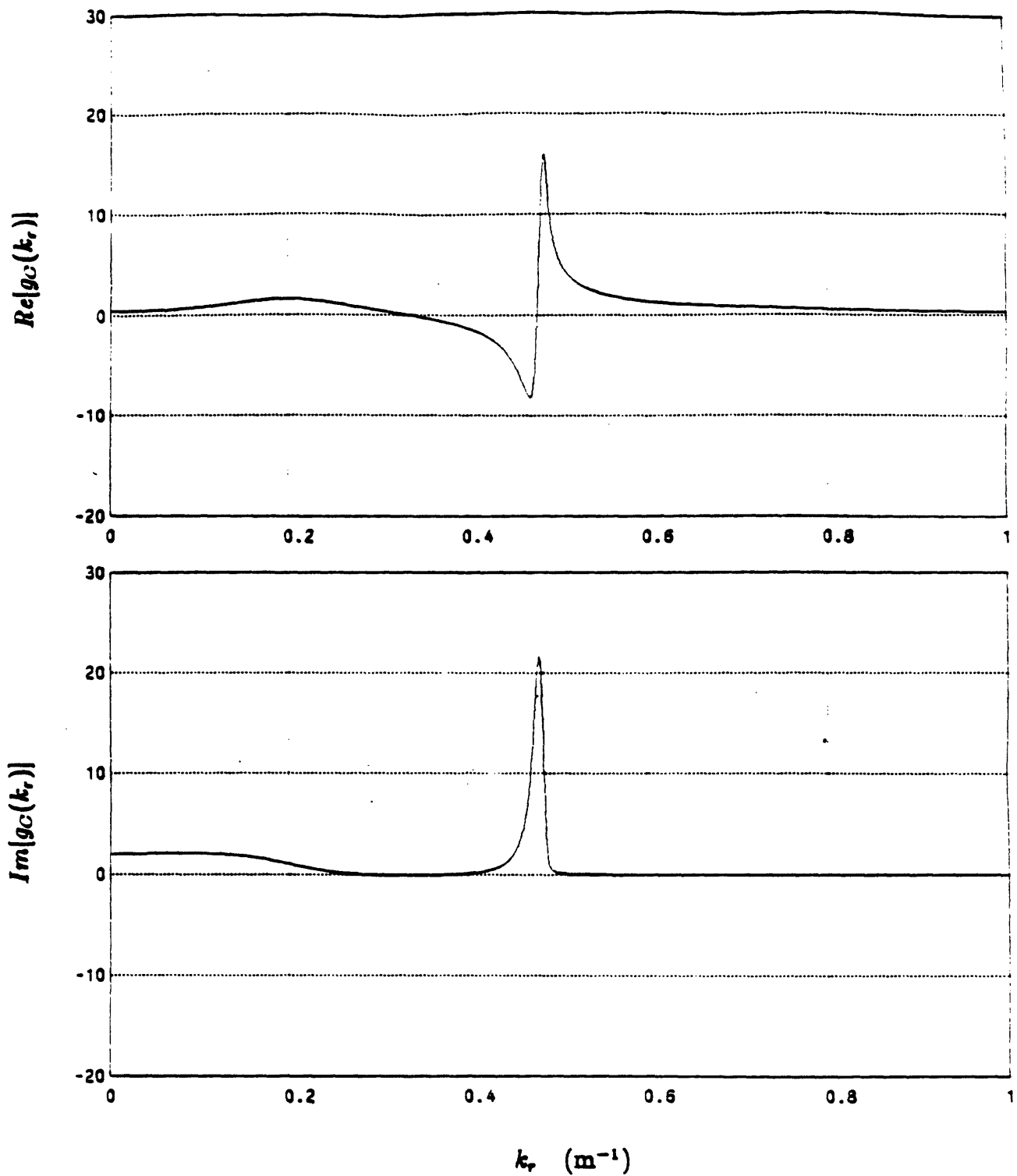As a numerical example of this, the Green's function corresponding to the geoacoustic model in Table 4.1 with attenuation in the underlying halfspace was computed. The attenuation factor, i.e. the imaginary part of the wavenumber within the underlying halfspace, was chosen as $0.015 dB/m$. The real and imaginary parts of the resultant Green's function, $g(k_r)$, are plotted in Figure 4.24. The pole position was determined, using the root-finding technique described earlier, as $k_{ri} = 0.5623747 + j9.0235437 * 10^{-5}$ and the residue was determined as $0.1558222 - j4.913016 * 10^{-4}$. The function $g_T(k_r)$ was then constructed and $g_C(k_r)$ was computed. The real and imaginary parts of $g_C(k_r)$ are plotted in Figure 4.25. By examining the imaginary parts of $g(k_r)$ and $g_C(k_r)$ in Figures 4.24b and 4.25b respectively, we see that they are nearly identical except in the immediate vicinity of the real part of the pole location. This is due to the fact that $Im\{g(k_r)\}$ is non-zero only in this region. This suggests that a way in which to obtain $Im\{g_C(k_r)\}$ from $Im\{g(k_r)\}$ is to apply a rectangular window to $Im\{g(k_r)\}$. As can be seen from Figures 4.24b and 4.25b, the effect of a low-wavenumber window applied to $Im\{g(k_r)\}$ is to eliminate the spike near the pole and preserve the behavior for lower values of wavenumber. It is apparent that this technique cannot be applied to the real parts of $g_C(k_r)$ and $g(k_r)$, as can be seen from these figures. As pointed out previously, in the lossless case, $Im\{g(k_r)\}$ is wavenumber limited to $k_r = k_N$ where k_N is the wavenumber in the underlying halfspace. In the case that attenuation is included, this is only an approximation, as can be seen by examining $Im\{g(k_r)\}$ in Figure 4.24b. However, this value of wavenumber does suggest the appropriate value at which to window $Im\{g(k_r)\}$ to determine $Im\{g_C(k_r)\}$.

The modification to the algorithm for generating $p_C(r)$ in the case that realistic attenuation is included thus consists of first windowing $Im\{g(k_r)\}$ at $k_r = k_N$ to obtain $Im\{g_C(k_r)\}$, and then computing the Hilbert-Hankel transform of $2j Im\{g_C(k_r)\}$.

226

Figure 4.24: Real and imaginary parts of the Green's function corresponding to the geoacoustic model in Table 4.1 with attenuation in the underlying halfspace of 0.015 dB/m

Figure 4.25: Real and imaginary parts of the continuum portion of the Green's function corresponding to the geoacoustic model in Table 4.1 with attenuation in the underlying halfspace of $0.015\ dB/m$

As a numerical example of this technique, $p_C(r)$ was first determined by computing the Hankel transform of $g_C(k_r)$, shown in Figure 4.25. The magnitude of the resultant $p_C(r)$ is shown in Figure 4.26. Next, $p_C(r)$ was determined by computing the asymptotic Hilbert-Hankel transform of a windowed version of $Im\{g(k_r)\}$ and the resultant magnitude is shown in Figure 4.27. Although there are differences between the two curves, their similarity suggests that the proposed approach has some merit. The dip in the magnitude of the field produced using both approaches is apparently related to a cancellation between the lateral wave and the virtual mode when the geoacoustic model includes attenuation. For reference, the continuum field magnitude, for the model with attenuation in Figure 4.26 may be compared with the continuum field magnitude, for the model without attenuation, in Figure 4.15. Note that the field magnitude in Figure 4.26, at a range of 1500 m, is down by $1500m * 0.015dB/m = 22.5dB$. Thus, the hybrid technique confirms that the far-field portion of the continuum, i.e. the lateral wave, decays at a rate determined by the attenuation factor within the underlying halfspace.

To summarize, an alternate method for generating $p_C(r)$ has been proposed. The method is based on exploiting the imaginary-part sufficiency condition of $g_C(k_r)$. In the lossless case, $g_T(k_r)$ is a purely real function and thus $Im\{g_C(k_r)\}$ can be determined directly from $Im\{g(k_r)\}$. The continuum portion of the field $p_C(r)$ can be generated using the Hilbert-Hankel transform, or asymptotic Hilbert-Hankel transform, of $Im\{g_C(k_r)\}$. In the case that attenuation is included in the model, $Im\{g_C(k_r)\}$ cannot be determined in this way. However, $Im\{g_C(k_r)\}$ is approximately wavenumber limited to the real-part of the branch point, corresponding to the velocity in the underlying halfspace. In effect, the pole contribution to $Im\{g(k_r)\}$ can be removed by simply windowing the function. The Hilbert-Hankel transform can then be applied to this function to determine $p_C(r)$. Thus, the alternate approach is based on both the imaginary-part sufficiency condition and the fact that the effects of a pole can be removed from the imaginary part of the Green's function without resorting to the full pole/residue estimation procedure.
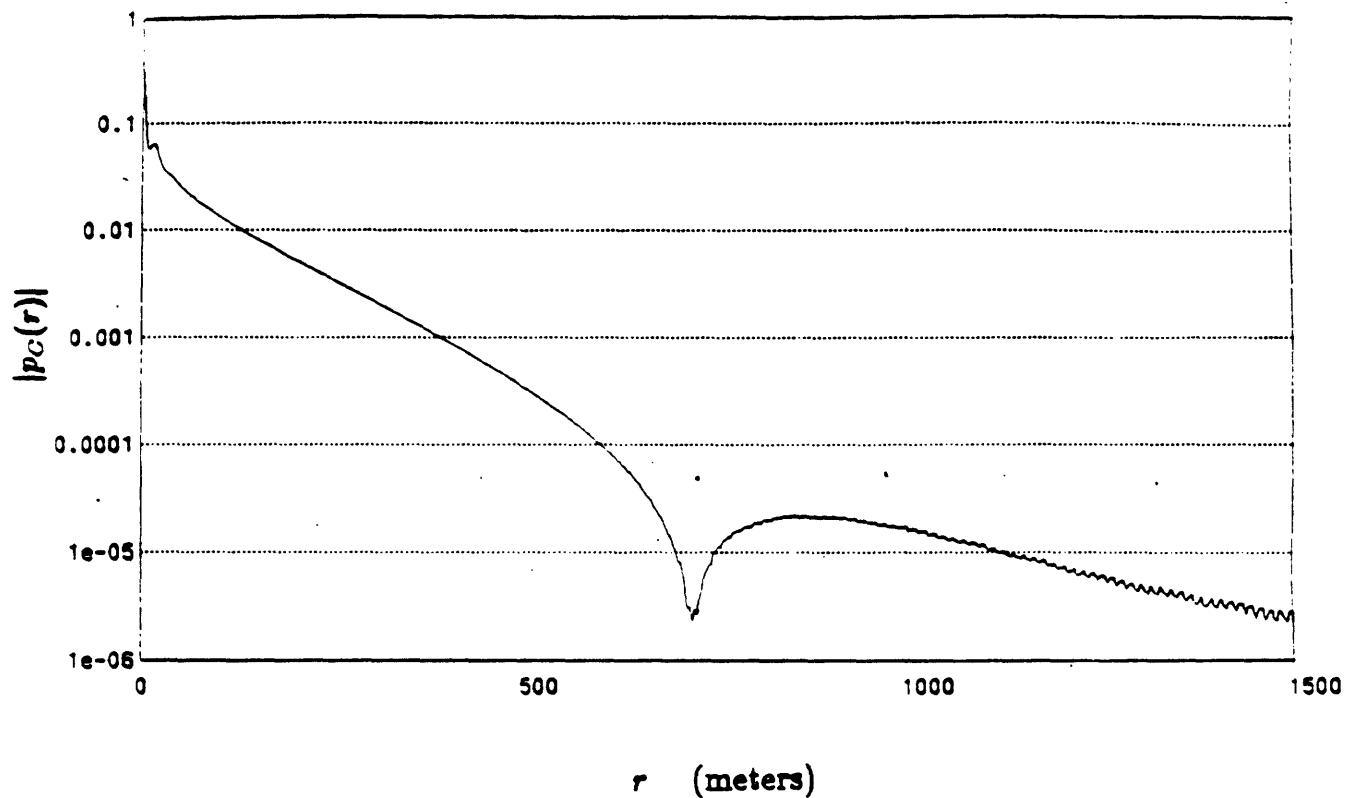
Figure 4.26: Magnitude of the continuum portion of the field for the geoacoustic model in Table 4.1 with attenuation in the underlying halfspace of 0.015 dB/m. The field was generated by computing the Hankel transform of $g_C(k_r)$ using the Abel/Fourier method.
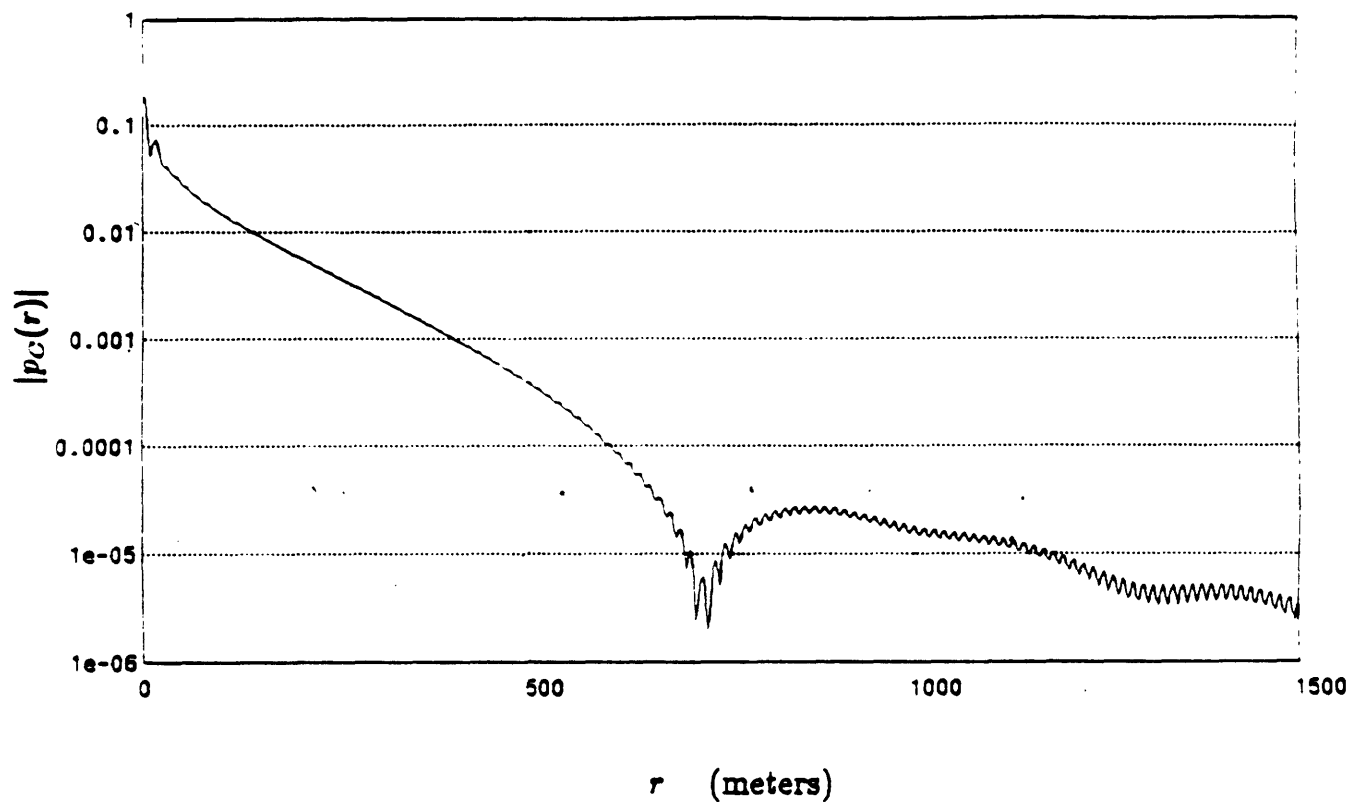
Figure 4.27: Magnitude of the continuum portion of the field for the geoacoustic model in Table 4.1 with attenuation in the underlying halfspace of 0.015 dB/m. The field was generated by computing the asymptotic Hilbert-Hankel transform of a windowed version of $2j\,Im[g(k_r)]$.

231

4.6 Relationship Between the Hybrid Method and Existing Methods

In this section, we discuss the relationship between the hybrid method for synthetic shallow water acoustic field generation and several other existing methods. The purpose of the discussion is to clarify some of the advantages and disadvantages of the hybrid approach and to highlight the differences between it and related techniques. We will consider three other existing techniques- the hybrid method of Kutschale and Thomson[6], the hybrid method for deep water acoustic field generation proposed by Mook [5] [27] and the uniform asymptotic method of Stickler and Ammicht [18] [19].

4.6.1 Relationship to Kutschale-Thomson Method

In this subsection, we consider the hybrid method of Kutschale and Thomson. Recall from Section 4.1 that this is a residue method in which the continuum portion of the field is computed using an FFP. Essentially, the FFP is used to approximately compute the branch-line integral. In the hybrid approach discussed in this chapter, the Hilbert-Hankel transform of $g_C(k_r)$ is computed. In order to develop the relationship between the two techniques, we must first directly relate the branch-line integral and the Hankel transform of $g_C(k_r)$. Previously, it was argued indirectly that both of these integrations must generate $p_C(r)$. A more direct relationship will now be established.

Recall that in the residue methods, Cauchy's theorem is applied to the Hankel transform integral

$$p(r) = \frac{1}{2} \int_{-\infty}^{\infty} g(k_r) H_0^{(1)}(k_r r) k_r \, dk_r \qquad (4.53)$$

The result is a sum due to the poles enclosed within the integration contour plus a contour integral around the branch-line. The branch-line integral yields the continuum

portion of the field and thus

$$p_C(r) = \frac{1}{2} \int_{BL} g(k_r) H_0^{(1)}(k_r r) k_r \, dk_r \qquad (4.54)$$

The decomposition of $g(k_r)$, discussed in section 4.3, can be substituted into this expression to yield

$$p_C(r) = \frac{1}{2} \int_{BL} [g_T(k_r) + g_C(k_r)] H_0^{(1)}(k_r r) k_r \, dk_r \qquad (4.55)$$

and thus

$$p_C(r) = \frac{1}{2} \int_{BL} g_T(k_r) H_0^{(1)}(k_r r) k_r \, dk_r + \frac{1}{2} \int_{BL} g_C(k_r) H_0^{(1)}(k_r r) k_r \, dk_r \qquad (4.56)$$

The first integral in the preceding expression is equal to zero as will now be argued. Previously, it was shown that $g_T(k_r)$ consists of a residue sum which contains only poles. In other words, there are no branch points in $g_T(k_r)$. The implication is that $g_T(k_r)$ must be continuous in the portion of the k_r-plane which includes the chosen branch-cuts of $g(k_r)$. Thus, since the branch-line contour in equation (4.55) traverses down one side of the cut and up the other side, and $g_T(k_r)$ is continuous across the cut, the first integral in equation (4.56) must be zero.

The expression for the continuum portion of the field thus becomes

$$p_C(r) = \frac{1}{2} \int_{BL} g_C(k_r) H_0^{(1)}(k_r r) k_r \, dk_r \qquad (4.57)$$

This is similar to the Hankel transform expression for $p_C(r)$ presented in section 4.3, but the limits of integration are along the branch-line and not from $k_r = -\infty$ to ∞. However, since $g_C(k_r)$ contains no poles, the integral around the branch line can be deformed, using Cauchy's theorem, as shown in Figure 4.28. Therefore,

$$p_C(r) = \frac{1}{2} \int_{-\infty}^{\infty} g_C(k_r) H_0^{(1)}(k_r r) k_r \, dk_r \qquad (4.58)$$

Note that this expression is identical to the expression used in the hybrid approach. In other words, the preceding integral prescribes $p_C(r)$ as the Hankel transform of $g_C(k_r)$.
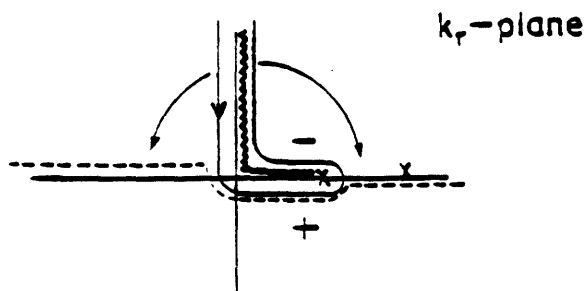
k_r-plane

Figure 4.28: Complex k_r plane showing the deformation of the branch-line contour to its position along the real axis. The + and − portions of the k_r plane are also shown.

The equivalence of the branch-line integral and the Hankel transform of $g_C(k_r)$ is thus summarized in the equivalence of the following expressions

$$
\begin{aligned}
p_C(r) &= \tfrac{1}{2} \int_{BL} g(k_r) H_0^{(1)}(k_r r) k_r\, dk_r \\
&= \tfrac{1}{2} \int_{BL} g_C(k_r) H_0^{(1)}(k_r r) k_r\, dk_r \\
&= \tfrac{1}{2} \int_{-\infty}^{\infty} g_C(k_r) H_0^{(1)}(k_r r) k_r\, dk_r
\end{aligned}
\tag{4.59}
$$

Note that the integration contour associated with the integral in equation (4.55) follows along both sides of the EJP branch-cut as shown in Figure 4.28. If we use the notation + to denote evaluation along one side of the cut and − to denote evaluation along the other side of the cut, an equivalent expression for the branch-line integral of equation (4.56) becomes

$$
p_C(r) = \frac{1}{2} \int_{BL_+} [g_+(k_r) - g_-(k_r)] H_0^{(1)}(k_r r) k_r\, dk_r
\tag{4.60}
$$

where $g_+(k_r)$ denotes $g(k_r)$ evaluated slightly below or to the left of the cut and $g_-(k_r)$ denotes $g(k_r)$ evaluated slightly above or to the right of the cut as shown in Figure 4.27. The integration contour corresponding to BL_+ starts at $j\infty$ to the left of the imaginary-k_r axis, proceeds parallel to this axis, then turns and proceeds just

below the real-k_r axis and continues to the branch point k_N. Using the definition $g_\Delta(k_r) \equiv g_+(k_r) - g_-(k_r)$, and splitting the integral along BL_+ into the sum of two contour integrals, we have that

$$p_C(r) = \frac{1}{2} \int_0^{jk_N} g_\Delta(k_r) H_0^{(1)}(k_r r) k_r \, dk_r + \frac{1}{2} \int_{j\infty}^0 g_\Delta(k_r) H_0^{(1)}(k_r r) k_r \, dk_r \qquad (4.61)$$

In the method proposed by Kutschale and Thomson, $p_C(r)$ is evaluated by neglecting the second integral in equation (4.61) and by using the FFP to evaluate the first integral. By examining equation (4.61), and neglecting the second term, it becomes apparent that their approach can be interpreted as the computation of the Hilbert-Hankel transform of $g_\Delta(k_r)$. Kutschale and Thomson use a closed-form expression for $g_\Delta(k_r)$ obtained from Stickler [13]. In order to further relate their approach with the hybrid method discussed earlier, it is necessary to relate $g_\Delta(k_r)$ with $g(k_r)$ and $g_C(k_r)$.

This relationship is easily described using the property developed in Chapter 2 that $g(k_r^*) = g^*(k_r)$ for the lossless, compressional geoacoustic model and the assumption of the EJP branch-cut. In particular, since $g_+(k_r) = g(k_r - j\epsilon)$ and $g_-(k_r) = g(k_r + j\epsilon)$ for real-k_r, then

$$g_\Delta(k_r) = g_+(k_r) - g_-(k_r) = g_+(k_r) - g_+^*(k_r) = 2j \, Im\{g_+(k_r)\} \qquad (4.62)$$

Taking the limit as $\epsilon \to 0$, we have that

$$g_\Delta(k_r) = 2j \, Im\{g(k_r)\} \qquad (4.63)$$

The approach of Kutschale and Thomson is actually equivalent to the technique for generating $p_C(r)$ using the imaginary-part sufficiency condition of $g(k_r)$ discussed in the previous subsection. In the Kutschale and Thomson approach, the EJP branch-line integral is evaluated approximately by integrating along the real-k_r axis only. The integration is implemented using an FFP. We have just shown that an alternate interpretation of this technique can be given using the imaginary-part sufficiency condition of $g_C(k_r)$ and $g(k_r)$ and the Hilbert-Hankel transform.

The method of Kutschale and Thomson applies only to the lossless, compressional geoacoustic model. In the previous subsection, we presented a method for extending the technique based on imaginary-part sufficiency of $g_C(k_r)$ to models in which attenuation is present. No such extension is provided in the Kutschale-Thomson method. Furthermore, recall that the method based on imaginary-part sufficiency was actually an extension to the original hybrid method based on the decomposition $g(k_r) = g_T(k_r) + g_C(k_r)$. This decomposition also applies to models which include attenuation and shear where it is recognized that the Hankel transform of $g_C(k_r)$ is equal to the sum of two branch-line integrals corresponding to the compressional contribution and the shear contribution.

4.6.2 Relationship to Mook Method

In this subsection, we relate the hybrid method based on the decomposition $g(k_r) = g_T(k_r) + g_C(k_r)$ with the hybrid numerical/analytic technique proposed by Mook [27] [5]. As pointed out previously, the two techniques actually address significantly different problems, as the new hybrid technique based on decomposing the Green's function has been applied to the shallow water problem, while the technique proposed by Mook was applied to the deep water problem. The common element of the two approaches is that both remove the effects of singularities from an integrand prior to the computation of its numerical transform. However, the integrand is different in the two cases, as is the method of singularity removal.

To briefly review the deep water problem, we first consider the plane-wave expansion for the field due to a point source which is located within an isovelocity halfspace which overlies a horizontally stratified media. The expression for the field, assuming that the receiver also lies within the halfspace, can be shown to be

$$p(r) = \int_0^\infty [\frac{je^{jk_s|z-z_0|}}{k_z} + \frac{je^{jk_s(z+z_0)}}{k_z}R_B(k_r)]J_0(k_r r)k_r dk_r \qquad (4.64)$$

This expression is in the form of a Hankel transform of the total deep water Green's function, $g(k_r)$, where

$$g(k_r) = [\frac{je^{jk_s|z-z_0|}}{k_z} + \frac{je^{jk_s(z+z_0)}}{k_z}R_B(k_r)] \qquad (4.65)$$

The notation here is identical to the notation presented in Chapter 2 with the exception that the z-axis is assumed to point upwards, with $z = 0$ located at the boundary between the isovelocity halfspace and the underlying media. Recall that in the shallow water case, the z-axis was chosen to point downward, with $z = 0$ located at the surface of the waveguide. The difference between the choice of the two coordinate systems arises mainly from the way in which the source and receiver positions, z_0 and z, are measured in deep and shallow water propagation experiments - z and z_0 are typically measured as heights off the bottom in a deep water experiment and as depths from the surface in a shallow water experiment.

The integral in equation (4.64), which describes the total deep water field, can be split into the sum of a direct field and a reflected field as

$$p(r) = p_D(r) + p_R(r) \qquad (4.66)$$

where

$$p_D(r) = \int_0^\infty \frac{j e^{jk_z |z-z_0|}}{k_z} J_0(k_r r) k_r dk_r \qquad (4.67)$$

and

$$p_R(r) = \int_0^\infty \frac{j e^{jk_z(z+z_0)}}{k_z} R_B(k_r) J_0(k_r r) k_r dk_r \qquad (4.68)$$

The corresponding deep water Green's function can also be split into the sum of a direct component and a reflected component as

$$g(k_r) = g_D(k_r) + g_R(k_r) \qquad (4.69)$$

where

$$g_D(k_r) = \frac{j e^{jk_z |z-z_0|}}{k_z} \qquad (4.70)$$

and

$$g_R(k_r) = \frac{j e^{jk_z(z+z_0)}}{k_z} R_B(k_r) \qquad (4.71)$$

Note that $g_D(k_r)$ and $p_D(r)$ form a Hankel transform pair as do $g_R(k_r)$ and $p_R(r)$. The first term on the right-hand side of equation (4.66) represents the direct propagation from the source to the receiver. The corresponding integral has the known analytic form $e^{jk_0 R_0}/R_0$, where k_0 is the total wavenumber of the isovelocity halfspace and $R_0 = (r^2 + (z-z_0)^2)^{1/2}$. The second term on the right-hand side of equation (4.66) represents the portion of the field which undergoes the single reflection off the boundary between the halfspace and the underlying media. Note that equation (4.68) expresses the reflected field as a plane-wave superposition and that each term in this superposition is weighted by the reflection coefficient evaluated at the proper horizontal wavenumber.

The decomposition of the field into the sum of a direct component plus a reflected component makes most sense in the context of deep water propagation. Although the shallow water field could also be decomposed into a direct portion plus a reflected

238

portion, there appears to be no advantage to representing the field in this way. This is due to the fact that the non-direct portion of the shallow water field actually consists of multiple reflections from both the bottom and surface of the waveguide as opposed to the single reflection in the deep water case. In neither case can the direct and reflected field be measured independently. However, the reflected field has a more intuitive interpretation in the deep water case. In addition, in the deep water problem, it is the reflected field alone which is most directly related to the bottom reflection coefficient.

In the hybrid approach of Mook, a method for determining the reflected field using equation (4.68) is proposed. Although this equation is in the form of a Hankel transform, a direct numerical implementation of the transform is not appropriate due to sampling requirements. Essentially, a high sampling rate is required due to the presence of the singularities in the integrand of equation (4.68) on, or near, the real-k_r axis. The singularities which cause the most difficulty are the poles of $R_B(k_r)$ which are located on the real-k_r axis and the branch-point at $k_r = k_0$. The difficulty associated with sampling near $k_r = k_0$ is associated not with the fact that k_0 is a branch point, but rather with the fact that the integrand becomes infinite at $k_r = k_0$ since k_z is zero here. The difficulty in performing the Hankel transform integral in equation (4.68) can be interpreted in the range domain as well, in that the reflected field decays at the slow rate of $1/r$. In order to avoid aliasing in the synthetic generation of this reflected field, it is necessary to sample at a high rate in the corresponding wavenumber domain.

To reduce aliasing artifacts associated with the generation of the reflected field, a technique for removing the singularity at $k_r = k_0$ was proposed [27][5]. In the wavenumber domain, a component is subtracted from the integrand so that the remaining portion is well-behaved in the neighborhood of $k_r = k_0$. The component subtracted is also chosen such that its Hankel transform has a known analytic form. Thus, the reflected field is determined by computing the numerical Hankel transform

239

of the modified kernel and adding the analytic portion associated with the singularity removed. There are two ways to interpret this technique. The first way is to consider it as a modelling of the kernel of the Hankel transform in the vicinity of the singularity at $k_r = k_0$. The alternate way is to consider it as a modelling of the reflected field at large r. Essentially, the difficulty in computing the transform is based on the fact that reflected field decays at the slow rate of $1/r$. The analytic portion of the integral can be chosen to match the form of the reflected field at large range such that the difference between the two falls off at a substantially faster rate. In the case at hand, the reflected field can be modelled as $R_B(k_0)e^{jk_0 R_1}/R_1$ where $R_1 = (r^2 + (z + z_0)^2)^{1/2}$. This suggests that the appropriate term to be removed from the kernel of the Hankel transform is $je^{jk_z(z+z_0)}R_B(k_0)/k_z$. This is precisely the term which Mook removes from the kernel of the Hankel transform integral.

The presence of low-speed layers within the underlying media can also give rise to infinities in the reflection coefficient at isolated values of $k_r = k_{ri}$. The reflection coefficient can be modelled as a residue over a pole near these points and Mook showed that removing terms of the form $a_i/(k_r^2 - k_{ri}^2)$ from $R_B(k_r)$ tends to reduce the effects of these infinities[5]. The method proposed for determining k_{ri} was to find the zeros of $1/R_B(k_r)$. The method proposed for determining a_i was to perform a least-squares fit using $a_i = R_B(k_r)(k_r^2 - k_{ri}^2)$ in the neighborhood of the pole at $k_r = k_{ri}$. With analogy to the singularity removal at $k_r = k_0$, $a_i/(k_r^2 - k_{ri}^2)$ can be removed from $R_B(k_r)$ and the numerical transform of the result can be computed. The integral

$$\int_0^\infty \frac{ja_i}{(k_r^2 - k_{ri}^2)} \frac{e^{jk_z(z+z_0)}}{k_z} J_0(k_r r)k_r \, dk_r \tag{4.72}$$

can also be evaluated analytically and this result can be added to the numerical transform to yield the desired reflected field.

The underlying problems of deep water and shallow water synthetic acoustic field generation are somewhat different. For example, by examining the form of the deep water Green's function shown in equation (4.65) and the form of the shallow water Green's function presented in Chapter 2, it is easily shown that an additional branch

240

point at the water wavenumber is present in the deep water case. Note also, that the term $1 - R_S(k_r)R_B(k_r)e^{j2k_z h}$, which contributes poles in the shallow water case, is not present in the deep water case. This term is responsible for guided wave propagation in shallow water due to constructive interference between the surface and bottom reflections. It does not contribute poles in the deep water Green's function since there is no surface reflection. Additionally, if there are low-speed layers within the bottom the reflection coefficient, $R_B(k_r)$, may also have poles. In the deep water case, these poles in $R_B(k_r)$ also contribute as poles in $g(k_r)$, signifying the fact that guided propagation within the low-speed layer can occur for certain specific values of horizontal wavenumber. This guiding occurs because of constructive interference between the reflections at the top and bottom of the low-speed layer. However, in the shallow water case, poles in $R_B(k_r)$ do not contribute as poles in $g(k_r)$. In fact, it can be shown that $g(k_r)$ remains finite at the pole locations of $R_B(k_r)$ and has the form

$$g(k_r) = \frac{2 \sin k_z z_l}{k_z} e^{-j k_z z_s}, \tag{4.73}$$

for the case of the source and receiver in the top layer. Physically, although the constructive interference between low-speed layer interfaces remains, there exist additional field components which have reflected off the surface of the waveguide which cancel this interference. The net result is that there is no guided propagation and thus the shallow water Green's function remains finite at these values of wavenumber. Despite these differences, there are also a number of similarities between the deep and shallow water propagation problems. In fact, we now show that the deep water Green's function is actually a special case of the shallow water Green's function.

To see this, consider the form for the field in an isovelocity waveguide overlying a horizontally stratified bottom which is

$$p(r) = \int_0^\infty g(k_r) J_0(k_r r) k_r \, dk_r \tag{4.74}$$

The form for $g(k_r)$ as presented in Chapter 2 is

$$g(k_r) = \frac{j(e^{-j k_z z_l} + R_S e^{j k_z z_l})(e^{j k_z z_s} + R_B e^{j k_z (2h - z_s)})}{k_z(1 - R_S R_B e^{j2k_z h})} \tag{4.75}$$

241

Previously, we have considered the surface of the waveguide as a water/air interface so that the surface reflection coefficient, R_S is -1. To transition from the shallow water field to the deep water field, we consider the latter as the field which exists within a waveguide which has no surface, i.e. $R_S = 0$. The implication in the deep water case is that there is no reflection at the surface of this waveguide and that any incident energy continues to propagate upward. Furthermore, it is convenient to redefine the z-coordinate axis as measured up from the bottom of the waveguide. Thus, z_g is replaced by $h - z_l$ and z_l is replaced by $h - z_g$. Substituting these values into equation (4.75) yields

$$g(k_r) = \frac{j}{k_z}[e^{jk_z(z_g-z_l)} + R_B(k_r)e^{jk_z(z_g+z_l)}] \qquad (4.76)$$

Using the facts that $z_g - z_l = |z - z_0|$ and $z_g + z_l = z + z_0$ it is apparent that

$$g(k_r) = \frac{j}{k_z}[e^{jk_z|z-z_0|} + R_B(k_r)e^{jk_z(z+z_0)}] \qquad (4.77)$$

Note that this Green's function, which was obtained by setting $R_S(k_r) = 0$ in the general shallow water Green's function expression and changing the orientation of the z-axis, is identical to the deep water Green's function presented earlier in equation (4.65).

The fact that the deep water Green's function can be obtained in this way has also been pointed out in [5]. However, this connection between the shallow water Green's function and the deep water Green's function has some important and useful consequences. Specifically, many of the properties developed for the more general shallow water Green's function must also be applicable to this special case, in which $R_S = 0$.

For example, the properties that $g(k_r) = g(-k_r)$ and $g(k_r^*) = g^*(k_r)$ developed in Chapter 2 also apply to the deep water Green's function. Recall that the property $g(k_r^*) = g^*(k_r)$ was also used to derive another property related to the finite extent of the imaginary part of the Green's function. The finite extent property also applies to the deep water case as can be verified by following the argument given in Chapter 2,

but with one important exception. The presence of the additional branch-cut, due to the ambiguity in the specification of the sign of the vertical wavenumber in the water, implies that the function $Im\{g(k_r)\}$ is wavenumber limited at $k_r = max(k_0, k_N)$ where k_0 is the water wavenumber and k_N is the wavenumber in the underlying halfspace. This result is distinctly different from the shallow water result that $Im\{g(k_r)\}$ is wavenumber limited at $k_r = k_N$. Since k_N is typically less than k_0, the implication is that, while the finite extent property still applies, it does not constitute a useful method for determining a geoacoustic parameter since presumably the water velocity is known.

Other useful properties of $g(k_r)$ also apply to the deep water Green's function including the real-part/imaginary part sufficiency condition for $g(k_r)$, and the decomposition of $g(k_r)$ into $g_T(k_r) + g_C(k_r)$, which formed the basis of the hybrid method for shallow water synthetic acoustic field generation. If this decomposition is applied to the deep water Green's function, it can be shown that the Hankel transform of $g_C(k_r)$ is actually the sum of the two branch-line integrals corresponding to the branch-points located at $k_r = k_0$ and $k_r = k_N$. In fact, unless there is a low-speed layer present within the bottom, $g_T(k_r)$ is zero. The implication is that under the condition that there are no poles present, $g(k_r) = g_C(k_r)$ and thus the integration contour along the real-k_r axis can be deformed to wrap around the branch-cuts. Therefore, in the case that there are no poles present, the Hankel transform of $g(k_r)$ is identical to the sum of the two branch-line integrals.

Note that the decomposition of $g(k_r)$ into $g_T(k_r) + g_C(k_r)$ is substantially different than the decomposition of $g(k_r)$ into its direct and reflected parts as done in equation (4.69). In fact, there are some interesting consequences of applying the decomposition $g(k_r) = g_T(k_r) + g_C(k_r)$ to the deep water problem. For example, consider the case in which there are no low-speed layers and thus no poles present. The decomposition becomes $g(k_r) = g_C(k_r)$ and the hybrid method for shallow water synthetic data generation can be directly applied. The acoustic field, in this case, consists of the

numerical transform of $g_C(k_r)$. Therefore, since $g_C(k_r) = g(k_r)$, application of the hybrid method to the deep water problem in which no poles are present trivially becomes computing the numerical Hankel transform of the total Green's function. The major difference between the method proposed by Mook and the method proposed here is that apparently no singularity removal at $k_r = k_0$ is performed in the latter case. However, in considering the difference between the two methods, we see that, in fact, the singularity is actually removed in the second technique as well. This is due to the fact that the numerical Hankel transform of the *total* Green's function is computed as opposed to the transform of the *reflected* portion of the Green's function alone, as was considered by Mook. The sampling requirements for computing the numerical Hankel transform of the total Green's function are reduced due to the fact that the total field decays as $1/r^2$, as opposed to a $1/r$ reflected field decay. In fact, in the lossless case, the two methods remove the singularity in essentially the same manner as will now be shown.

In removing the singularity at $k_r = k_0$ from the reflected Green's function, Mook exploits the fact that the numerical computation of the field $p_R(r) - R_B(k_0)e^{jk_0R_1}/R_1$ is better behaved than the computation of $p_R(r)$ alone. In the lossless case, $R_B(k_0) = -1$ and thus the portion of the field which is numerically computed is $p_R(r) + e^{jk_0R_1}/R_1$. In the hybrid approach based on $g_T(k_r) + g_C(k_r)$, the numerical field which is computed is the *total* field, which is $p_R(r) + e^{jk_0R_0}/R_0$. At large ranges, the fields computed numerically are nearly identical since $R_1 = (r^2 + (z+z_0)^2)^{1/2} \sim (r^2 + (z-z_0)^2)^{1/2} = R_0$. Issues associated with the generation of deep water synthetic acoustic pressure fields based on numerically generating the total field as opposed to numerically generating the reflected field have not been studied and merit further investigation. A numerical example which demonstrates the computation of the total field is now provided.

The realistic deep water geoacoustic model in Table 4.4 was considered. The reflection coefficient for the ocean bottom, consisting of 52 isovelocity layers overlying a halfspace, was generated. The reflected field was generated by removing the $1/k_z$

VELOCITY (m/s)

$\rho = 1$ g/cm³
$a = 0$ dB/m at 220 Hz

WATER-BOTTOM INTERFACE

$\rho = 1.6$ g/cm³
$a = .0039$ dB/m

SUBBOTTOM

$\rho = 1.6$ g/cm³
$a = .0039$ dB/m
$C_3 = 2200$ m/sec
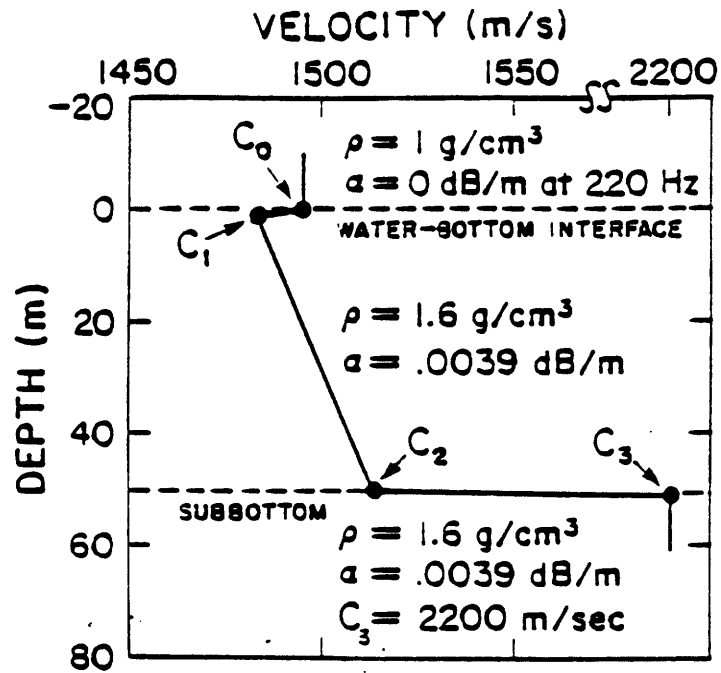
z_0	$=$	124.9 m
z	$=$	1.2 m
f	$=$	220 Hz

Table 4.4: Deep water geoacoustic model.

singularity as described in [5], and computing the Hankel transform based on the Abel/Fourier method. The total field was then constructed by adding the direct field, the analytic contribution of the singularity removed, and the numerical result of the Hankel transform. The magnitude of the corresponding total field is shown as a function of range r in Figure 4.29.

Alternately, the reflection coefficient was used in the expression for the total Green's function of equation (4.65). Although the resulting total Green's function could have been used as the input to a Hankel transform based on the Abel/Fourier method, we chose to use the asymptotic Hilbert-Hankel transform instead. The magnitude of the total field which resulted from the computation of the transform of the total Green's function is shown as a function of range in Figure 4.30. The similarity between the two fields in Figures 4.29 and 4.30, computed by substantially different methods, is apparent. They differ primarily in the near-field and this is most probably due to the fact that the asymptotic Hilbert-Hankel transform was used instead of the Hankel transform. Nevertheless, the two fields are remarkably close. This result shows the validity of generating the total field via a numerical transform as opposed to removing a singularity from the reflected portion of the Green's function, numerical generating the remaining portion of the reflected field, and adding the analytically-computed contribution of the singularity plus the direct field.

To conclude the example, an additional field magnitude is shown in Figure 4.31. This field was determined by computing the asymptotic Hilbert-Hankel transform of $2j\,Im\{g(k_r)\}$ for the geoacoustic model in Table 4.4. The similarity between this field and the fields in Figures 4.29 and 4.30 is apparent. This result confirms the fact that the real-part/imaginary-part sufficiency condition, previously discussed in the context of shallow water, applies to the deep water Green's function as well.

We can also consider the application of the hybrid method based on $g(k_r) = g_T(k_r) + g_C(k_r)$ to the deep water case when there are low-speed layers present. The
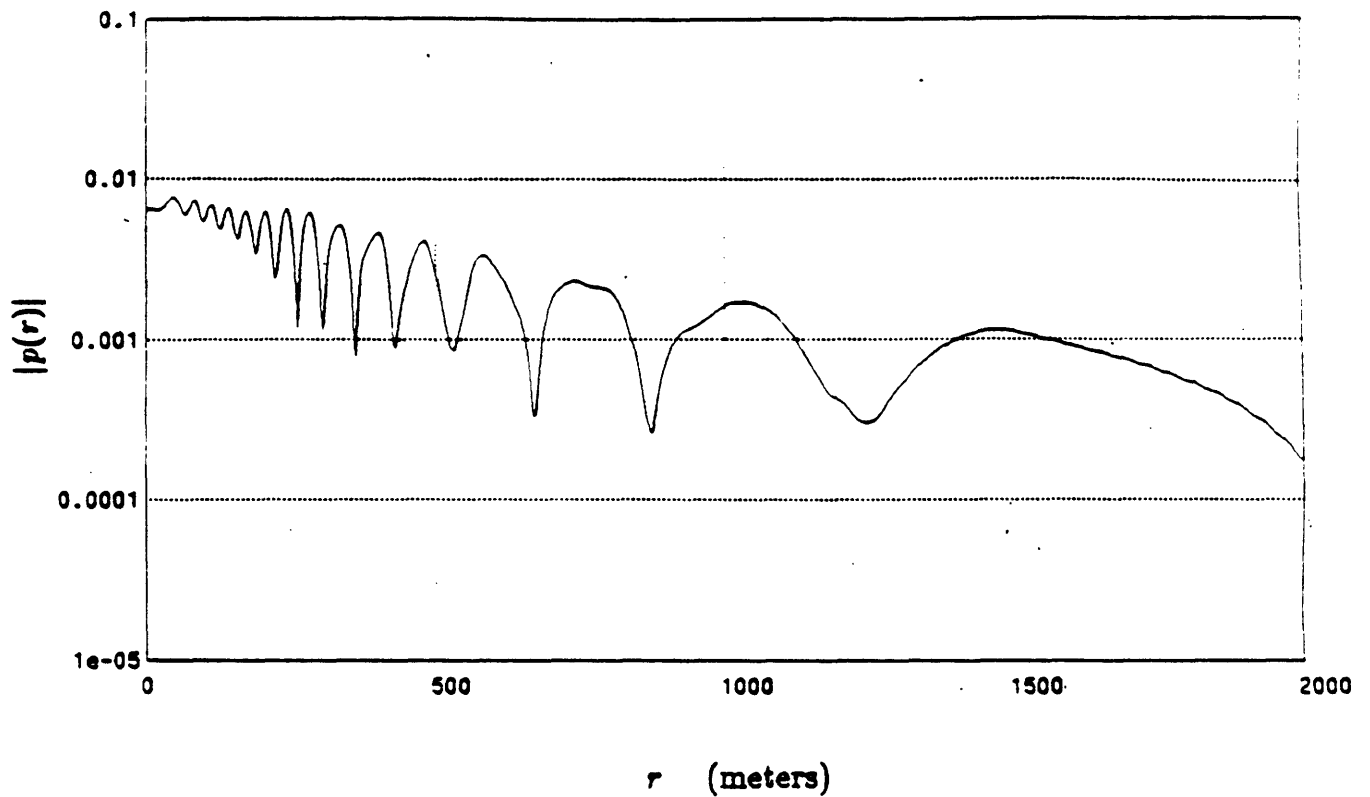
Figure 4.29: Magnitude of the total deep water field corresponding to the geoacoustic model in Table 4.4. The field was determined by numerically computing the reflected field and adding the analytically computed direct field.
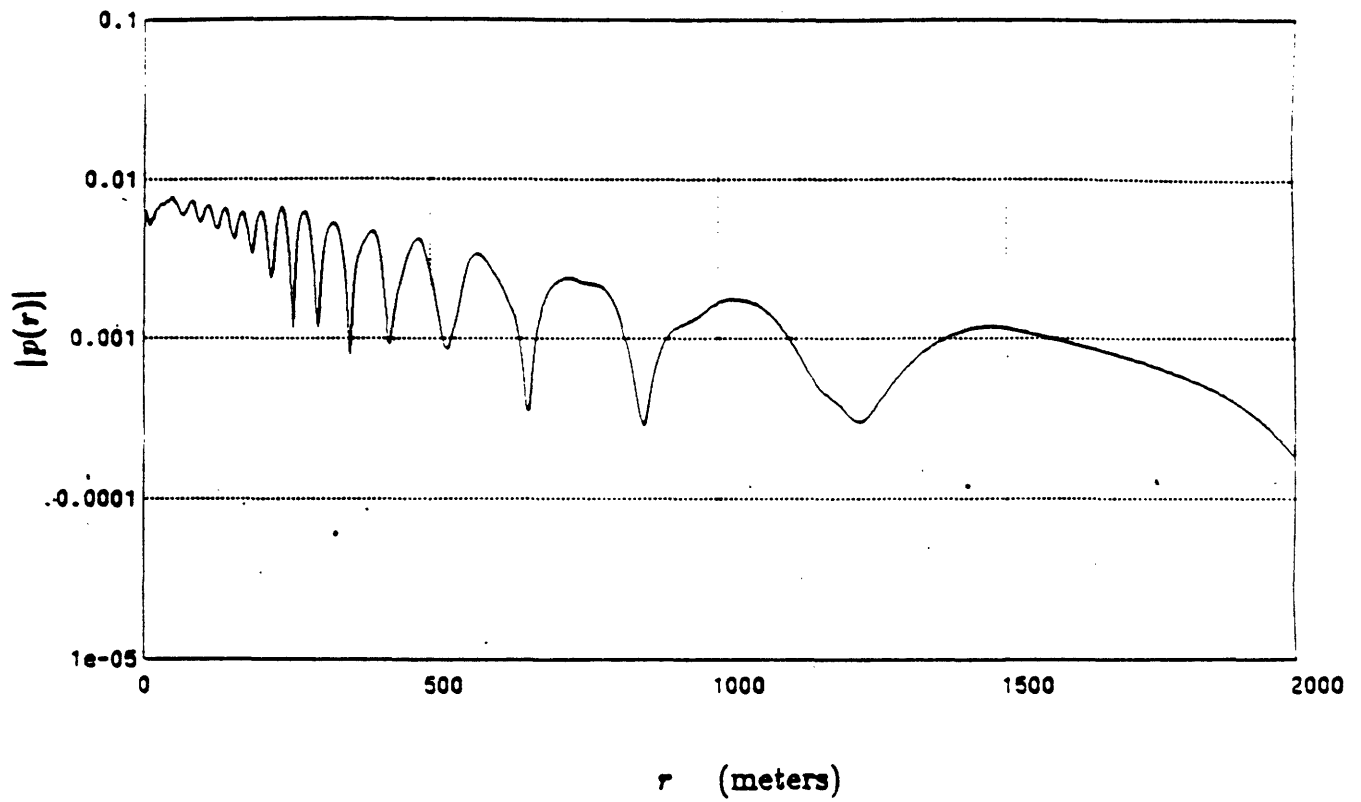
Figure 4.30: Magnitude of the total deep water field corresponding to the geoacoustic model in Table 4.4. The field was determined by computing the asymptotic Hilbert-Hankel transform of the total Green's function.
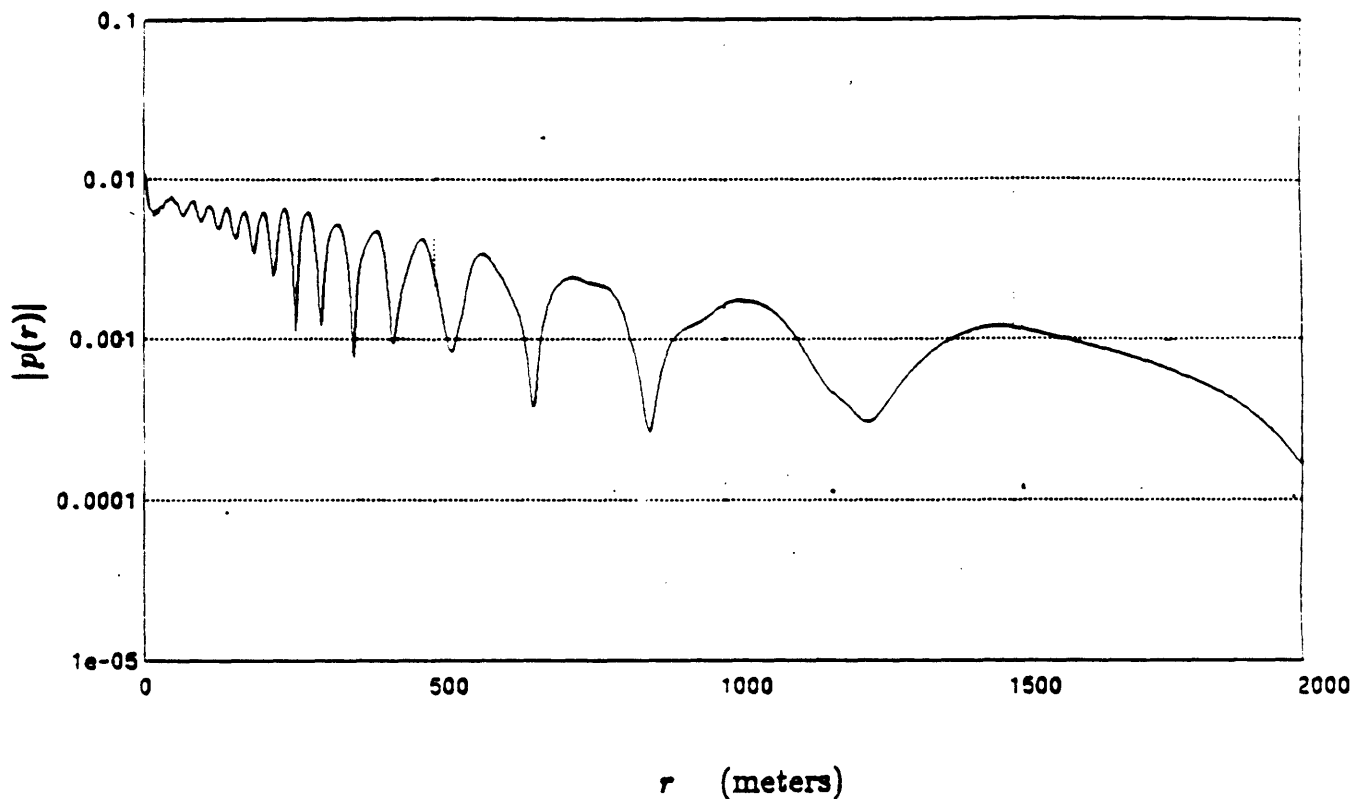
Figure 4.31: Magnitude of the total deep water field corresponding to the geoacoustic model in Table 4.4. The field was determined by computing the asymptotic Hilbert-Hankel transform of $2j\,Im[g(k_r)]$. The result demonstrates the property of real-part/imaginary-part sufficiency for the deep water Green's function.

presence of these layers implies that $g_T(k_r)$ may be non-zero. The relationship between this decomposition and the technique suggested by Mook[27] for removing poles from the reflection coefficient is now addressed. Initially, we assume that only a single pole at $k_r = k_{ri}$ is present in $R_B(k_r)$ and thus in $g(k_r)$. The expression for $g_T(k_r)$ thus becomes

$$g_T(k_r) = \frac{2a_i k_{ri}}{k_r^2 - k_{ri}^2} \tag{4.78}$$

where, as discussed previously,

$$a_i = \lim_{k_r \to k_{ri}} [(k_r - k_{ri})g(k_r)] \tag{4.79}$$

By writing $g(k_r)$ as the sum of its direct plus reflected components, i.e. $g(k_r) = g_D(k_r) + g_R(k_r)$, it is straightforward to show that the expression for a_i becomes,

$$a_i = \lim_{k_r \to k_{ri}} [(k_r - k_{ri})g_R(k_r)] \tag{4.80}$$

Introducing the expression for $g_R(k_r)$ into this equation yields

$$a_i = \lim_{k_r \to k_{ri}} [(k_r - k_{ri})R_B(k_r)\frac{je^{jk_z(z+z_0)}}{k_z}] \tag{4.81}$$

so that

$$a_i = \frac{je^{jk_{zi}(z+z_0)}}{k_{zi}} \lim_{k_r \to k_{ri}} [(k_r - k_{ri})R_B(k_r)] \tag{4.82}$$

where k_{zi} denotes the quantity k_z evaluated at the pole location $k_r = k_{ri}$. If the quantity b_i is defined as

$$b_i \equiv \lim_{k_r \to k_{ri}} [(k_r - k_{ri})R_B(k_r)] \tag{4.83}$$

then a_i and b_i are related as

$$a_i = (\frac{je^{jk_{zi}(z+z_0)}}{k_{zi}})b_i \tag{4.84}$$

and the expression for $g_T(k_r)$ becomes

$$g_T(k_r) = \frac{2jb_i k_{ri}}{k_{zi}}e^{jk_{zi}(z+z_0)}(\frac{1}{k_r^2 - k_{ri}^2}) \tag{4.85}$$

Using the definition of $g_C(k_r)$ in terms of $g(k_r)$ and thus in terms of $g_D(k_r) + g_R(k_r)$, we have that

$$g_C(k_r) = g_D(k_r) + g_R(k_r) - \frac{2jb_i k_{ri}}{k_{zi}}e^{jk_{zi}(z+z_0)}(\frac{1}{k_r^2 - k_{ri}^2}) \tag{4.86}$$

250

In the hybrid method based on $g_T(k_r)+g_C(k_r)$ the numerical transform of $g_C(k_r)$ is computed and added to $p_T(r)$, where $p_T(r) = j\pi a_i k_{ri} H_0^{(1)}(k_{ri}r)$. Using the relationship between a_i and b_i in equation (4.84) and equation (4.82) for a_i, the term $p_T(r)$ becomes

$$p_T(r) = \frac{-\pi b_i k_{ri}}{k_{zi}} e^{jk_{zi}(z+z_0)} H_0^{(1)}(k_{ri}r) \tag{4.87}$$

As pointed out previously, the inclusion of the first term in equation (4.86) for $g_C(k_r)$ effectively removes the singularity at $k_r = k_0$. The third term in equation (4.86) accounts for the pole singularity present. If the second term and third in equation (4.86) are grouped together, the process can be thought of as removing a pole singularity from $g_R(k_r)$ to form a new quantity $g_R'(k_r)$. Thus, in the hybrid method based on $g_T(k_r) + g_C(k_r)$ poles are removed from $g_R(k_r)$ via

$$g_R'(k_r) = g_R(k_r) - \frac{2j b_i k_{ri}}{k_{zi}} e^{jk_{zi}(z+z_0)}\left(\frac{1}{k_r^2 - k_{ri}^2}\right) \tag{4.88}$$

The method for removing poles due to low-speed layers, proposed by Mook in [27], can be shown to be

$$g_R'(k_r) = g_R(k_r) - \frac{2j b_i k_{ri}}{k_z} e^{jk_z(z+z_0)}\left(\frac{1}{k_r^2 - k_{ri}^2}\right) \tag{4.89}$$

Note that by comparing equations (4.88) and (4.89), it can be seen that the two techniques for pole removal differ due to the fact that k_z is a function of k_r while k_{zi} is not.

The corresponding analytic quantity which is added in Mook's method, written in the notation here, is

$$\int_0^\infty \frac{2j b_i k_{ri}}{k_z} e^{jk_z(z+z_0)}\left(\frac{1}{k_r^2 - k_{ri}^2}\right) J_0(k_r r) k_r \, dk_r \tag{4.90}$$

Although this integral can be evaluated by using a partial differential equation method [5], it is also possible to evaluate this integral in an alternate manner using the convolution property of the Fourier transform, and the Fourier transform relationship [35]

$$\frac{e^{jkR}}{R} = \int_{-\infty}^\infty [(\frac{1}{2j}) H_0^{(1)}((k^2 - k_z^2)^{1/2} r] e^{jk_z z} \, dk_z \tag{4.91}$$

251

where $R = (r^2 + (z + z_0)^2)^{1/2}$. The result is

$$\int_0^\infty \frac{2j b_i k_{ri}}{k_z} e^{jk_z(z+z_0)} \left(\frac{1}{k_r^2 - k_{ri}^2} \right) J_0(k_r r) k_r \, dk_r$$

$$= \frac{j b_i k_{ri}}{k_{zi}} \left(e^{-jk_{zi}|z|} *_z \frac{e^{jkR}}{R} \right)\Big|_{z=z+z_0} - \frac{\pi b_i k_{ri}}{k_{zi}} e^{jk_{zi}(z+z_0)} H_0^{(1)}(k_{ri} r) \qquad (4.92)$$

where $*_z$ denotes convolution with respect to z.

The above expression, which is the analytically computed part of the reflected field in Mook's method, is to be contrasted with $p_T(r)$ in equation (4.87) which is the analytic portion of the total field obtained from the hybrid method using $g_T(k_r) + g_C(k_r)$. They differ in that the quantity in equation (4.92) is the sum of $p_T(r)$ plus a convolution term. The advantage of Mook's decomposition is that both the numerically and analytically computed fields remain finite at $r = 0$ if $z + z_0 \neq 0$. This is not the case in the hybrid method based on $g_T(k_r) + g_C(k_r)$. Because $p(r)$ must be finite at zero, and $p_T(r)$ has a logarithmic singularity at $r = 0$, the numerically computed field, $p_C(r)$ must also be infinite at $r = 0$ in order to cancel the behavior of $p_T(r)$ at this point. The inability of the numerical technique to synthesize $p_C(r)$ at $r = 0$ is an apparent disadvantage of the new hybrid method based on $g_T(k_r) + g_C(k_r)$ for synthesizing a deep water field. It is noted however, that in equation (4.92), an additional convolution integral must be evaluated. There is apparently no closed-form solution for this integration and a potential disadvantage is that this convolution must be determined numerically for each value of desired r.

Another disadvantage of removing the pole in the manner shown in equation (4.89) is the re-introduction of the singularity due to the presence of the $1/k_z$ term. In other words, in removing the effects of a pole, the singularity at $k_r = k_0$, which was previously removed in Mook's technique by subtracting the term $j e^{jk_z(z+z_0)} R_B(k_0)/k_z$ from $g_R(k_r)$, is re-introduced. Because of the presence of this singularity, an aliased field may be generated when a numerical Hankel transform is applied to $g_R'(k_r)$. Potentially, the aliasing could be reduced by first removing the pole from $g_R(k_r)$ using equation (4.89) and then removing the singularity at $k_r = k_0$ by a modified method.

252

Therefore, an advantage of Mook's method for singularity removal is that a pole contributes a uniform finite contribution to the field as r approaches zero. The field remains finite at the cost of evaluating an additional integral numerically. The method for extracting the singularity at $k_r = k_0$ requires modification in order to avoid aliasing in the numerical transform. The hybrid approach based on $g_T(k_r) + g_C(k_r)$ for generating the deep water field when low-speed layers are present does not require the evaluation of this extra integral but is potentially less accurate in the determination of the extreme near-field. On the other hand, the hybrid technique based on $g_T(k_r) + g_C(k_r)$ can be applied to both deep and shallow water field generation. The method proposed by Mook applies only to the case of deep water. This is emphasized by the fact that Mook's method removes poles from the reflection coefficient. In deep water, poles of the reflection coefficient are also poles of the Green's function. However, this is not the case in shallow water. The hybrid method removes poles from the Green's function in both cases. A technique which removes poles from the shallow water Green's function in such a way that the numerically computed quantity remains finite at $r = 0$ has apparently not been developed and remains as a topic for further investigation.

To summarize, we have considered the relationship between the hybrid method based on the decomposition $g_T(k_r) + g_C(k_r)$ and the method proposed by Mook for computing synthetic acoustic pressure fields in deep water. In considering the relationship, we have pointed out that the deep water Green's function is actually a special case of the shallow water Green's function. The implication is that many of the useful properties discussed earlier in this thesis also apply in the deep water case. One such property is the decomposition of the deep water Green's function as $g_T(k_r) + g_C(k_r)$. In applying this decomposition to the deep water case, it was pointed out that the technique for removing the singularity at $k_r = k_0$ in generating the reflected field[5] is accomplished by applying the hybrid method based on $g_T(k_r) + g_C(k_r)$ to the total Green's function. A numerical example for a realistic geoacoustic model confirmed the similarity of the two techniques and also demonstrated the applicability

real-part/imaginary-part sufficiency condition to the deep water Green's function. In addition, it was shown that if there are low-speed layers present, the two techniques are actually remove the effects of the corresponding poles differently. Mook's method has an apparent advantage in that the field generated numerically is finite for very small ranges and an apparent disadvantage in that an additional integration is required and that special care must be taken to avoid aliasing in the result. Mook's method applies only to the deep water case, while the hybrid method presented in this chapter applies to both the shallow and deep water cases.

Perhaps the most interesting aspect of the relationship between the two approaches is the fact that the deep water Green's function is actually a special case of the shallow water Green's function. An implication is that since the Hilbert-Hankel transform can be applied to the shallow water Green's function, it also applies to the deep water Green's function. Therefore, the useful properties of the Hilbert-Hankel transform and the asymptotic Hilbert-Hankel transform can also be applied to deep water problems. Some of the interesting consequences of these properties, including a real-part/imaginary-part sufficiency condition for deep water fields, will be further considered in Chapter 6 of this thesis.

4.6.3 Relationship to Stickler-Ammicht Method

In the final portion of this section, the hybrid approach based on $g_T(k_r) + g_C(k_r)$ is related to the uniform asymptotic method of Stickler and Ammicht[18][19]. Their method is again a residue method in which the acoustic field within the waveguide is determined as the sum of the modal portion plus the continuum portion. The basis of their approach is to compute the continuum portion of the field by summing individual contributions. Each term in the sum represents the complete contribution due to a top or bottom sheet pole. The approach is uniform in that it is valid as any particular pole moves from the top sheet, through the branch point, to the bottom sheet. The technique is asymptotic in range due to the fact that each individual contribution is expressed as an integral which has no closed form solution and which is evaluated asymptotically. Although there are actually a infinite number of pole contributions, Stickler and Ammicht retain only the most important poles and thereby describe the continuum field by a finite number of contributions. Originally, their method was applied to the lossless Pekeris waveguide only. However, in later work the same idea was applied to the more general case which involved a lossless, layered model having a $1/c^2$-linear profile.

In order to relate their approach with the hybrid method discussed earlier in this chapter, we first review the basis of their method. As discussed previously, the continuum portion of the field is determined by the branch-line integral. If the branch-line is chosen to be the EJP cut, we have previously shown, in equation (4.62), that the expression for the continuum is

$$p_C(r) = \frac{1}{2} \int_{BL_+} g_\Delta(k_r) H_0^{(1)}(k_r r) k_r \, dk_r \qquad (4.93)$$

where $g_\Delta(k_r) \equiv [g_+(k_r) - g_-(k_r)]$ is the difference of the Green's function across the cut and where the contour BL_+ is along one side of the cut. This equation also forms the basis for the relationship between Kutschale and Thomson method and the hybrid method using imaginary part sufficiency discussed in first part of this section. It also

represents the point at which Stickler and Ammicht's method departs.

In their approach, the integral in equation (4.93) is mapped to the k_{zN} domain, where k_{zN} represents the vertical wavenumber in the underlying halfspace. The integral for the continuum thus becomes

$$p_C(r) = \frac{1}{2} \int_0^\infty g_\Delta(k_{zN}) H_0^{(1)}((k_N^2 - k_{zN}^2)^{1/2} r) k_{zN} dk_{zN} \qquad (4.94)$$

where k_N is the wavenumber in the underlying halfspace. As pointed out by Stickler and Ammicht, the advantage of considering the integration in the k_{zN} plane is that the function $g_\Delta(k_{zN})/k_{zN}$ becomes a function which contains only poles and not branch points. For example, we have previously presented the example of the Pekeris waveguide continuum, where $N = 1$, using this formulation in Chapter 2. The form of the $g_\Delta(k_{zN})/k_{zN}$ was shown to be

$$\frac{g_\Delta(k_{z1})}{k_{z1}} = \frac{4jm \sin k_{z0} z_0 \sin k_{z0} z}{k_{z0}^2 m^2 \cos^2 k_{z0} h + k_{z1}^2 \sin^2 k_{z0} h} \qquad (4.95)$$

We note that the function is even in both the variables k_{z0} and k_{z1} and thus contains no branch points.

In Stickler and Ammicht's technique, the function $g_\Delta(k_{zN})/k_{zN}$ is expanded in a partial fraction expansion in the variable k_{zN}. The poles in this expansion, k_{zN_i}, are locations in the k_{zN}-plane which correspond to the pole locations in the k_r-plane through the mapping $k_r = (k_N^2 - k_{zN}^2)^{1/2}$. Poles on both Riemann sheets of the k_r-plane are mapped in this manner. Using this approach, Ammicht and Stickler write the form for $p_C(r)$ as

$$p_C(r) = \int_0^\infty \sum_i \frac{c_i}{k_{zN}^2 - k_{zN_i}^2} H_0^{(1)}((k_N^2 - k_{zN}^2)^{1/2} r) k_{zN}^2 dk_{zN} \qquad (4.96)$$

where c_i is a parameter which is related algebraically to the residue at the pole in the k_{zN}-plane. Stickler and Ammicht also developed asymptotic expressions for integrals of the form

$$J(r, k_{zN_i}) = \int_0^\infty \frac{k_{zN}^2}{k_{zN}^2 - k_{zN_i}^2} H_0^{(1)}((k_N^2 - k_{zN}^2)^{1/2} r) dk_{zN} \qquad (4.97)$$

256

and in this way, compute the continuum contribution as

$$p_C(r) = \sum_i c_i J(r, k_{zN_i})$$ (4.98)

Therefore, their method consists of determining the poles and residues in the k_{zN}-plane and evaluating the expression in equation (4.98). Perhaps the most interesting aspect of their approach is that it can be considered as a modelling technique for $p_C(r)$. In fact, Stickler and Ammicht point out that $p_C(r)$ is well-approximated by considering only those poles which lie within a radial region of the k_{zN}-plane of $|k_{zN}| < k_N$. The corresponding statement in the k_r-plane is that $p_C(r)$ can be modelled by including the effects of poles on both sheets which lie within the neighborhood of the branch-point at $k_r = k_N$. In typical cases, there may be only several significant poles and in this case, the continuum is approximately expressed as

$$p_C(r) = \sum_{i=1}^{N} c_i J(r, k_{zN_i})$$ (4.99)

where N is a small integer and represents the number of significant poles.

This approach for computing the continuum differs significantly from the hybrid method in which $p_C(r)$ is determined by computing the numerical Hankel transform of $g_C(k_r)$. In the hybrid method, no modelling of $g_C(k_r)$ or $p_C(r)$ is involved. Thus, $p_C(r)$ is not computed as the sum of a small number of finite terms but rather as the output of a numerical transform.

It is also possible to apply the concept of modelling $p_C(r)$ using the framework of the hybrid decomposition based on $g(k_r) = g_T(k_r) + g_C(k_r)$. In this case, $g_C(k_r)$ is modelled as the sum of a finite terms. However, there are significant differences between the two modelling approaches in that the hybrid method has difficulty in treating poles in the immediate neighborhood of the branch-point. To describe this further and to relate it to the method of Stickler and Ammicht, we now discuss how the modelling approach can be applied to the hybrid method.

Recall from discussions earlier that, assuming the selection of the EJP branch-cut, $g_T(k_r)$ consists of a partial fraction expansion which includes all of the poles on the top sheet. The remaining portion of the Green's function, $g_C(k_r)$, contains no top sheet poles. However there are resonances within $g_C(k_r)$ which are due to the proximity of poles on the bottom sheet to the real-k_r axis. As discussed in Chapter 2, the branch-cut can be re-defined such that it exposes additional poles on the top Riemann sheet. Since the new function $g_C(k_r)$ now contains poles on the top Riemann sheet, it can be decomposed into the sum of two components in an analogous manner as was done for the original Green's function. Thus, $g_C(k_r)$ can be written as

$$g_C(k_r) = g_{C_1}(k_r) + g_{C_2}(k_r) \tag{4.100}$$

where

$$g_{C_1}(k_r) = \sum_{i=1}^{M} \frac{2a_i k_{ri}}{k_r^2 - k_{ri}^2} \tag{4.101}$$

and where

$$g_{C_2}(k_r) = g_C(k_r) - g_{C_1}(k_r) \tag{4.102}$$

The value of M here is dependent on the number of poles which reside on the top sheet, which in turn is dependent on the definition of the new branch-cut. Note that both the poles and residues of $g_{C_1}(k_r)$ are complex-valued. Their values can be determined exactly in the manner discussed earlier for determining the trapped poles and residues. Namely, a root-finding technique can be used to determine the pole locations and the residues can be determined using the analytic expression in terms of the reflection coefficient and its derivative at the poles. The Hankel transform of $g_C(k_r)$ now becomes

$$p_C(r) = p_{C_1}(r) + p_{C_2}(r) \tag{4.103}$$

and $p_{C_1}(r)$ can be written in terms the poles and residues as

$$p_{C_1}(r) = \pi j \sum_{i=1}^{M} a_i k_{ri} H_0^{(1)}(k_{ri}r) \tag{4.104}$$

As discussed in Chapter 2, this portion of the field decays exponentially in range due to the fact that k_{ri} has a positive imaginary part. This expression is the virtual mode

contribution to the total field. It differs from the virtual mode method of Tindle in that no approximations have been made here. Furthermore, it applies to the more general layered model as opposed to the Pekeris model considered by Tindle.

As a numerical example of this technique, we consider the geoacoustic model summarized in Table 4.5. The Green's function for this model was computed and·its magnitude and phase are shown in Figure 4.32. From this figure it can be seen that two trapped poles are present. The positions of these poles and their corresponding modal amplitudes, $m_i = \pi a_i k_{ri}$, were determined using the root-finder and the expression for a_i in terms the reflection coefficient and its derivative at each pole location, and are listed in Table 4.6. The continuum portion of the Green's function $g_C(k_r)$ was computed and its magnitude and phase are shown in Figure 4.33. The continuum portion of the field, $p_C(r)$ was computed by performing a numerical Hankel transform of $g_C(k_r)$ and the magnitude of the result is shown in Figure 4.34. Note from Figures 4.32 and 4.33 that, although the trapped mode resonances have been removed, there still remain three significant resonances within $g_C(k_r)$, which are due to the off-axis poles which reside on the bottom Riemann sheet. If the branch-cut is twisted in such a way that these poles are exposed, they can be removed from $g_C(k_r)$ using the decomposition $g_C(k_r) = g_{C_1}(k_r) + g_{C_2}(k_r)$. The root-finder was used to determine the location of the poles and the analytic expression for the residues in terms of the reflection coefficient and its derivative at the pole locations was used to determine the associated residues. The pole locations and modal amplitudes, m_i, are listed in Table 4.6. The magnitude and phase of the function $g_{C_2}(k_r)$ is shown in Figure 4.35. It is noted that the three resonances in $g_C(k_r)$ have been removed using this technique. In addition the numerical Hankel transform of $g_{C_2}(k_r)$ was computed and the magnitude of the resultant field, $p_{C_2}(r)$ is shown in Figure 4.36. In Figure 4.37 is shown the magnitude of the field which results from the addition of $p_{C_1}(r)$, computed using equation (4.104), and $p_{C_2}(r)$ computed by performing a numerical Hankel transform of $g_{C_2}(k_r)$. It is noted that the fields in Figures 4.34 and 4.37 are identical i.e. $p_C(r)$ in Figure 4.34 is identical to $p_{C_1}(r) + p_{C_2}(r)$ in Figure 4.37. This result is a numerical

$$1500 \text{ m/sec}, \ 1.0 \text{ g/cm}^3 \qquad 22.5 \text{ m}$$

$$1650 \text{ m/sec}, \ 1.5 \text{ g/cm}^3 \qquad 2 \text{ m}$$

$$1800 \text{ m/sec}, \ 1.8 \text{ g/cm}^3$$
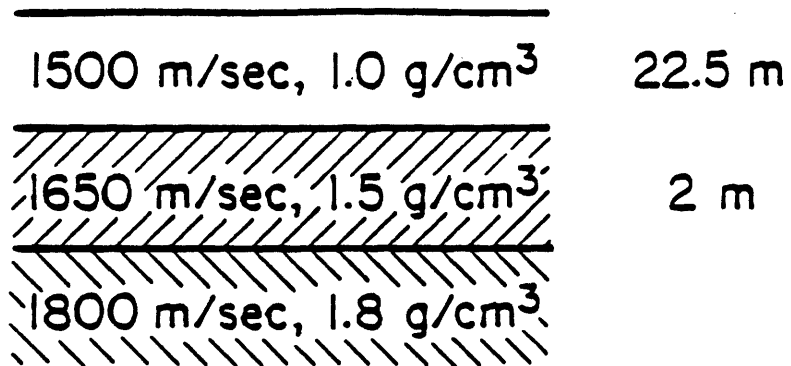
z_0	=	3.5 m
z	=	7.5 m
f	=	140.056 Hz

Table 4.5: Geoacoustic model consisting of an isovelocity water column overlying a thin layer overlying a halfspace.

260
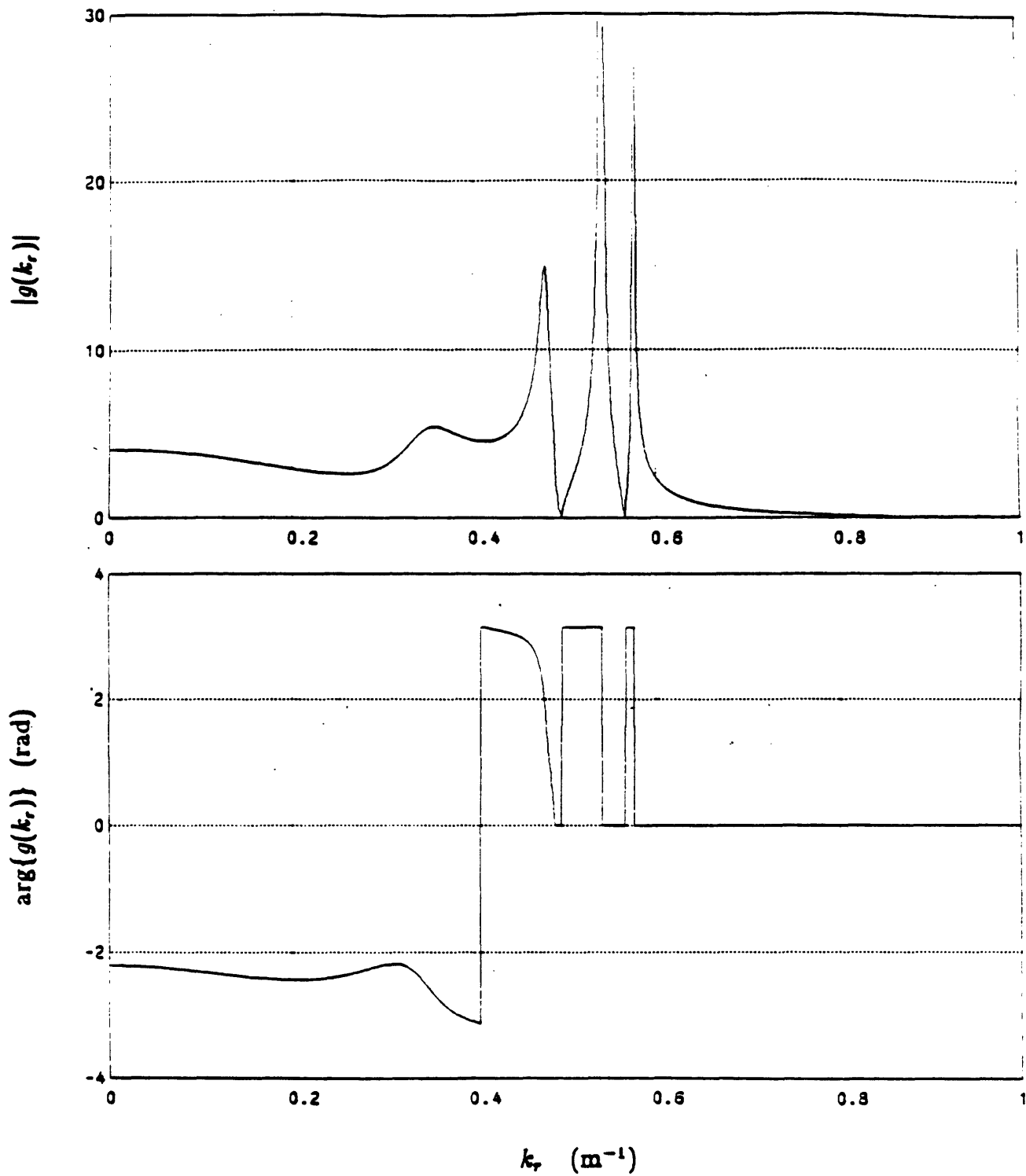
Figure 4.32: Magnitude and phase of the Green's function, $g(k_r)$, corresponding to the geoacoustic model in Table 4.5.

	Real	Imag
k_{r1}	0.5759144	$2.9533481e - 10$
m_1	$-1.7048060e - 07$	$5.5761382e - 02$
k_{r2}	0.5406027	$8.3109626e - 09$
m_2	$-9.1754220e - 07$	0.1467160
k_{r3}	0.4798682	$5.8425809e - 03$
m_3	$2.7451498e - 02$	0.1365754
k_{r4}	0.3472330	$3.4899876e - 02$
m_4	$-5.8755945e - 02$	-0.1084604
k_{r5}	0.1101135	0.2067913
m_5	$-2.5215799e - 02$	-0.2813639

Table 4.6: Summary of pole locations and mode amplitudes, $m_i = \pi a_i k_{ri}$, for the geoacoustic model in Table 4.5. The last three poles are on the bottom Riemann sheet when the EJP cut is selected.
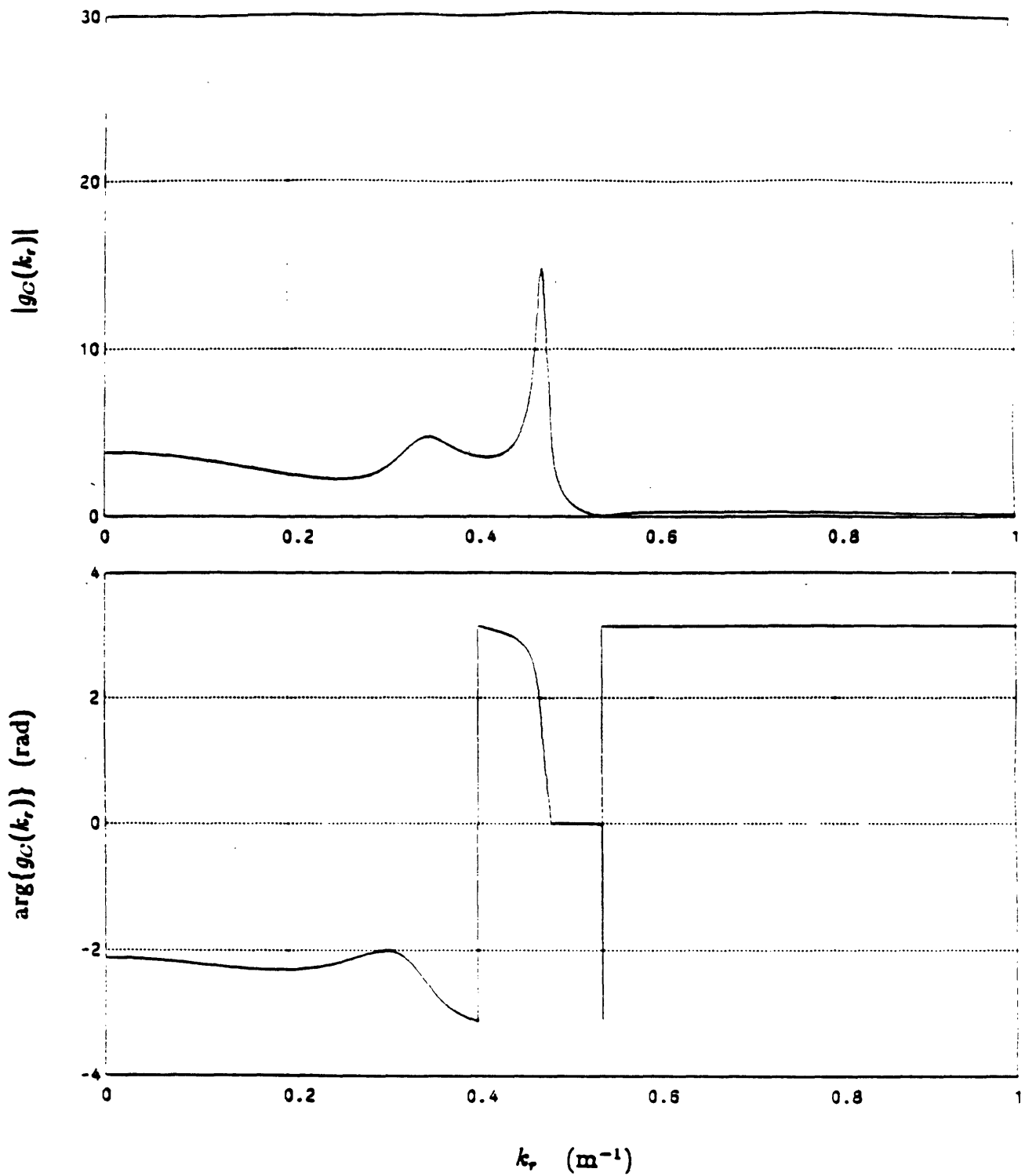
Figure 4.33: Magnitude and phase of the continuum portion of the Green's function, $g_C(k_r)$, corresponding to the geacoustic model in Table 4.5.
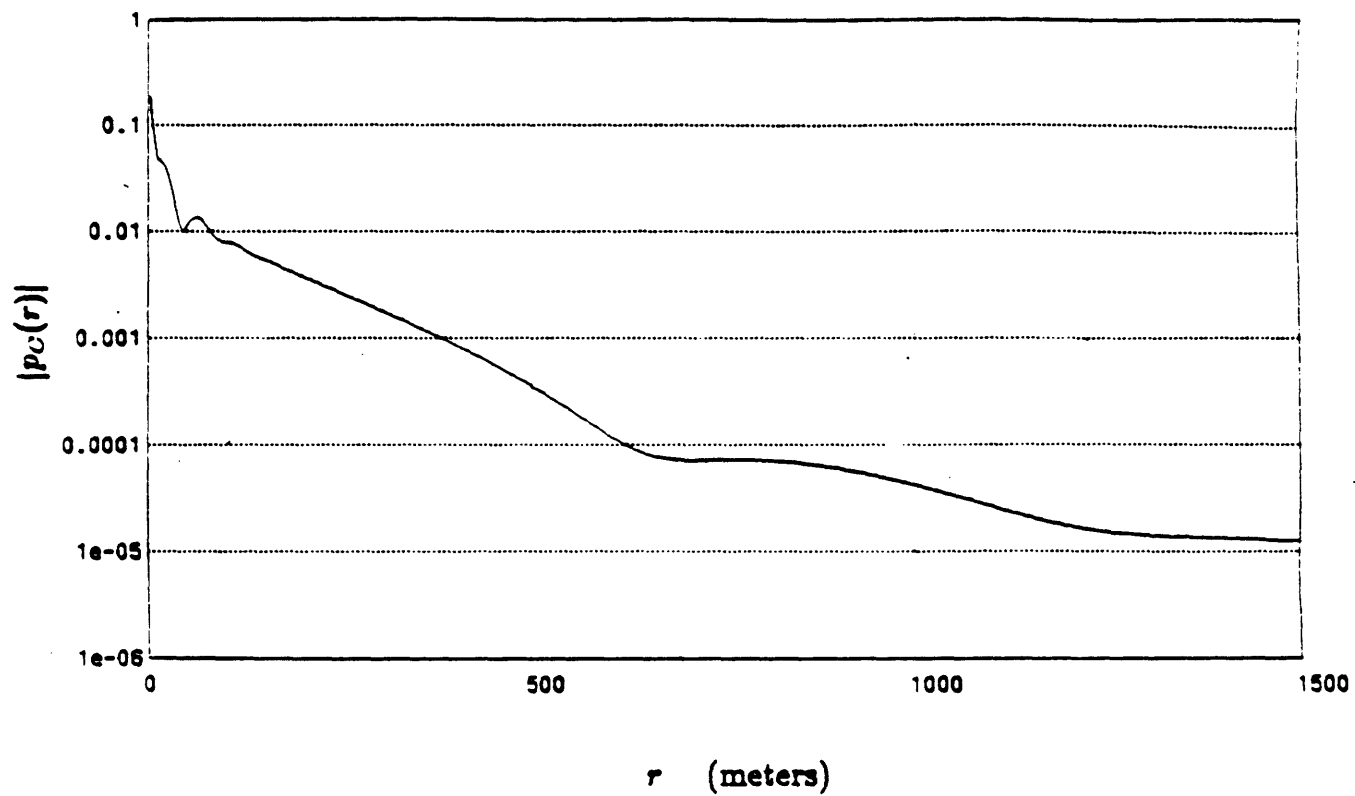
Figure 4.34: Magnitude of the continuum portion of the field, $p_C(r)$, for the geoacoustic model in Table 4.5 generated by computing the Hankel transform of $g_C(k_r)$.
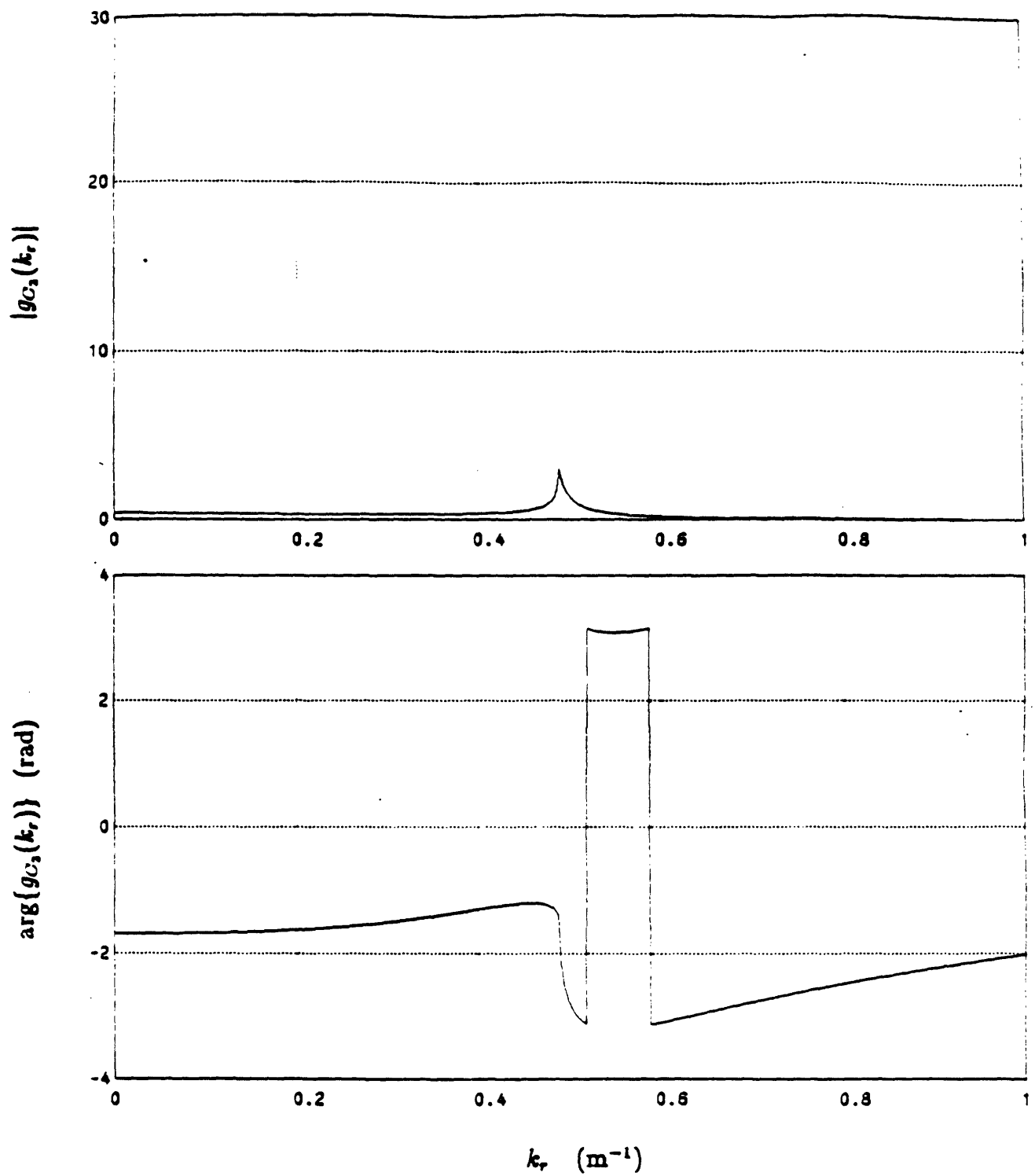
Figure 4.35: Magnitude and phase of the function $g_{C_2}(k_r)$ for the model in Table 4.5 obtained by removing the three off-axis poles from $g_C(k_r)$.
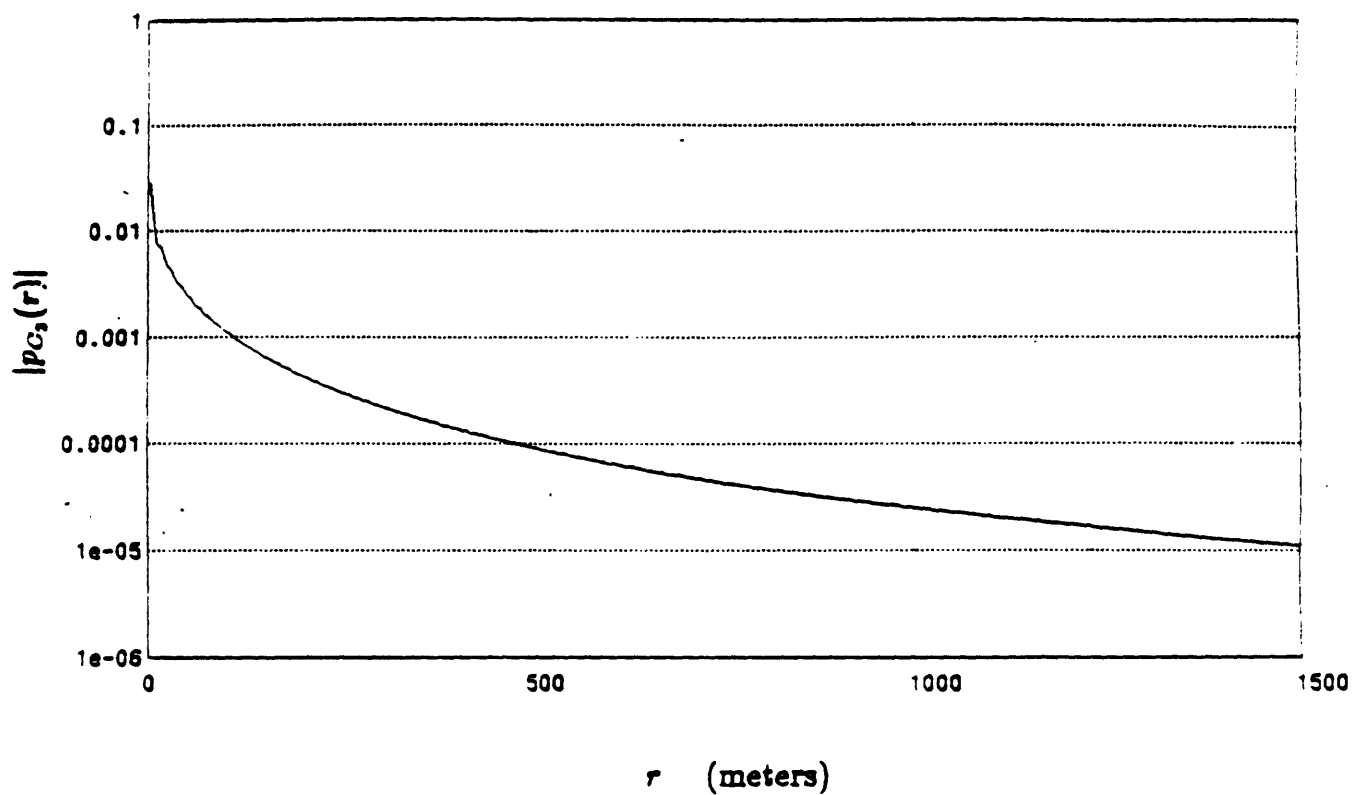
Figure 4.36: Magnitude of the field $p_{C_3}(r)$ obtained by computing the Hilbert-Hankel transform of $g_{C_3}(k_r)$ for the geoacoustic model in Table 4.5. This field represents the contribution to the continuum portion of the field other than the contribution due to three virtual modes.
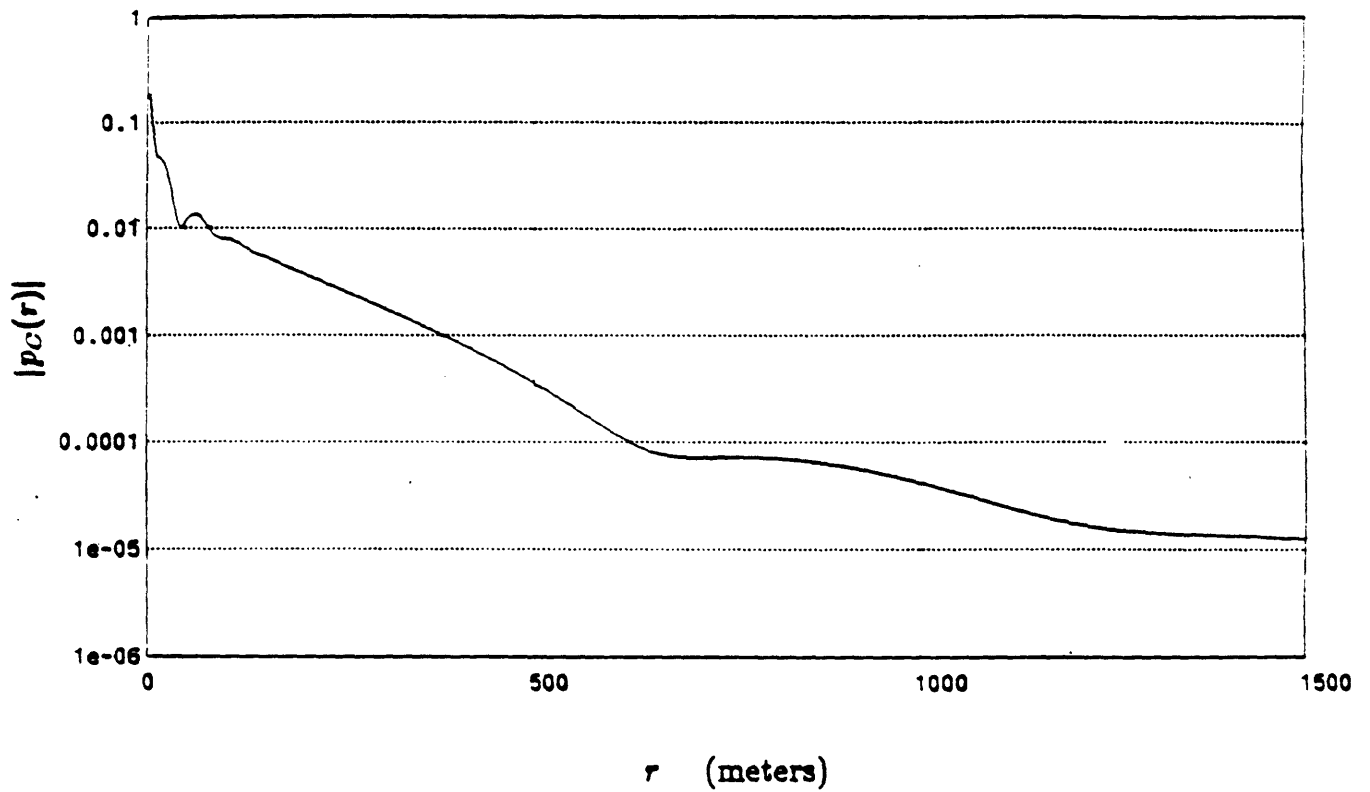
Figure 4.37: Magnitude of the continuum portion of the field, $p_C(r)$, obtained by adding fields $p_{C_1}(r)$ and $p_{C_2}(r)$. The result is identical to the continuum portion of the field computed as the Hankel transform of $g_C(k_r)$.

verification of Cauchy's theorem and of the decomposition $g_C(k_r) = g_{C_1}(k_r) + g_{C_2}(k_r)$.

In effect, the continuum portion has been modelled as the sum of the three off-axis pole contributions. As further evidence of this, the magnitude of the virtual mode field $p_{C_1}(r)$ is shown in Figure 4.38. The similarity of the field $p_C(r)$ in Figure 4.34 and the field $p_{C_1}(r)$ in Figure 4.38 is representative of the approximation of the virtual mode field to the actual continuum field. The virtual mode sum does not approximate the continuum at far ranges, as can be seen from in comparing these two figures, however, the trapped mode contributions dominate the total field at these far ranges. For reference, the magnitude of the total field obtained using the hybrid method, is shown in Figure 4.39. Therefore, by twisting the branch-cut so that additional bottom sheet poles are exposed on the top sheet, $g_C(k_r)$ can be modelled, using the decomposition $g_C(k_r) = g_{C_1}(k_r) + g_{C_2}(k_r)$, as $g_{C_1}(k_r)$.

We note that, although $g_{C_1}(k_r)$ can be considered as a model for $g_C(k_r)$, there are some differences as evidenced by the fact that $g_{C_2}(k_r)$ is, in general, non-zero. In effect, $g_{C_2}(k_r)$ represents the modelling error in representing $g_C(k_r)$ as the sum of a finite number of off-axis pole contributions. As can be seen from the plot of the magnitude of $g_{C_2}(k_r)$ in Figure 4.35, a broad resonance exists near $k_r = 0$ and a sharp peak exists near $k_r = 0.6$. The broad resonance is due to the remaining bottom sheet poles which have not been included in the model $g_{C_1}(k_r)$. Numerical experiments have shown that this resonance can be substantially reduced by including additional pole contributions in the virtual mode sum. The effect of excluding these contributions from the model is exactly analogous to the method of Stickler and Ammicht of retaining only the finite number of significant poles. However, the peak near $k_r = 0.6$ cannot be removed in this way. In fact, it can be verified that this peak is not located at a position related to the pole positions, but rather is located at the branch-point, i.e. at the halfspace wavenumber. The contribution of this peak to the field is referred to as the branch-point contribution.
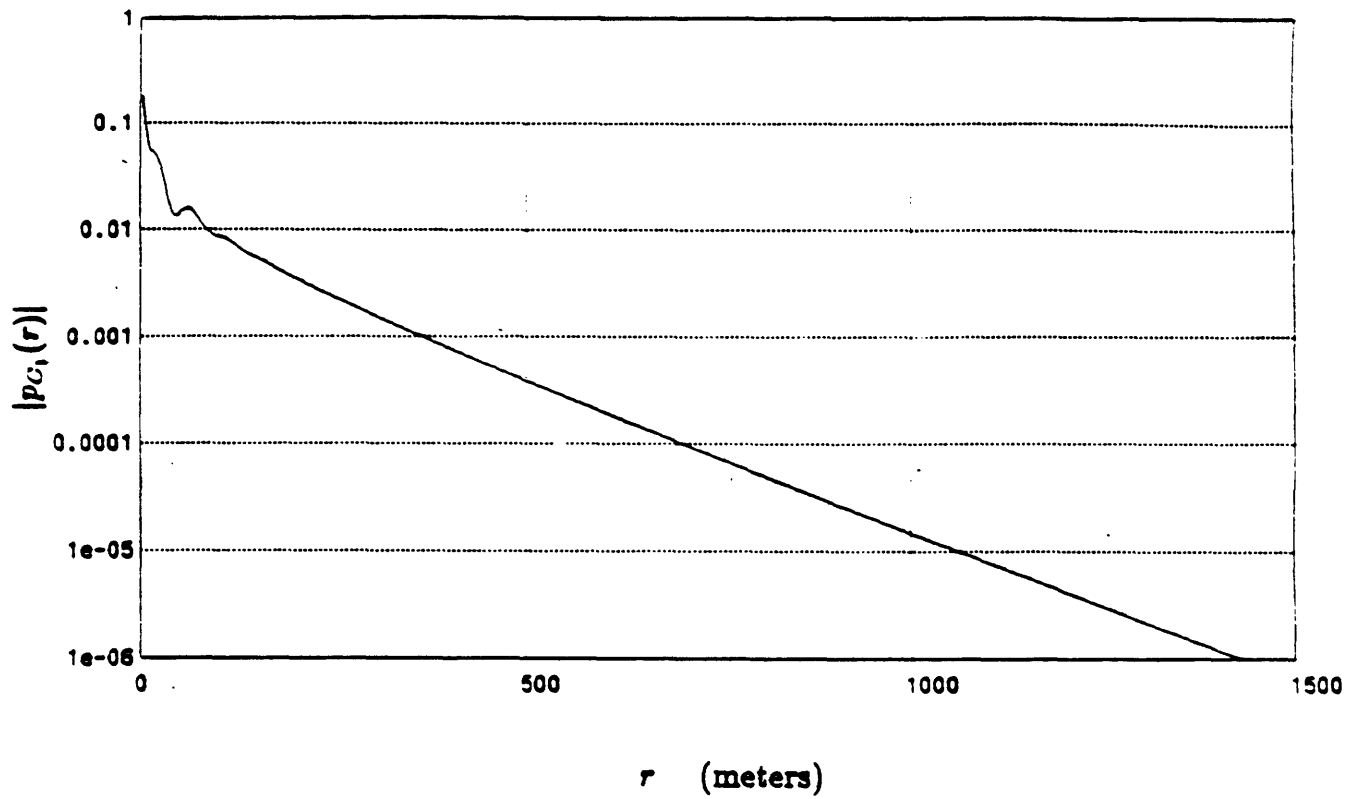
Figure 4.38: Magnitude of the field $p_{C_1}(r)$ obtained using the analytic formula for the contribution of the three off-axis poles. This field represents the contribution of the three virtual modes to the continuum portion of the field.
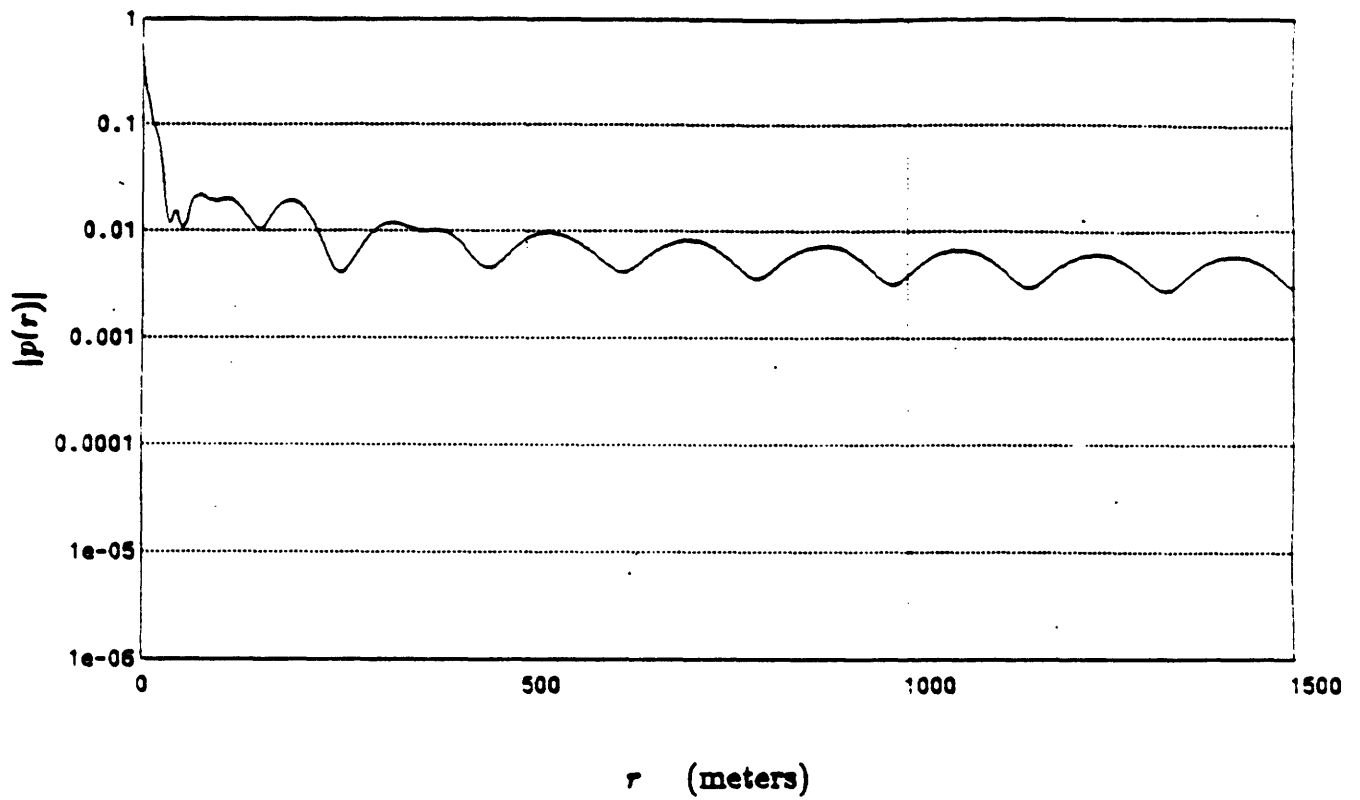
Figure 4.39: Magnitude of the total field for the geoacoustic model in Table 4.5 generated by adding $p_T(r)$ to $p_C(r)$. $p_C(r)$ was computed using the asymptotic Hilbert-Hankel transform of $g_C(k_r)$.

The physical interpretation of this branch-point contribution is that it yields the lateral wave contribution to the field. This wave propagates along the interface between the halfspace and the overlying layer at the halfspace phase velocity. Its contribution to the field can be seen by examining the magnitude of $p_{C_1}(r)$ in Figure 4.36. The interference pattern in the near-field is caused by the interference between the remaining virtual modes and the lateral wave. The remaining virtual modes decay at a very rapid rate because the associated poles have large positive imaginary parts. As range increases, and the virtual modes have decayed, the field which remains is the lateral wave.

The significant lateral wave contribution is due to the fact that one or more poles are present in the vicinity of the branch-point. Numerical experiments have shown that if the geoacoustic model is changed such that the nearest pole moves farther away from the branch-point, then the branch-point contribution is diminished. This effect is noted for both top and bottom sheet poles, assuming the EJP-cut, although it is more pronounced for the bottom sheet poles. In fact, as the model is changed so that a bottom sheet pole approaches the branch-point, and proceeds on to the top sheet, the branch-point contribution increases and decreases in a corresponding manner. The implication of this in the hybrid model, is that although the decomposition is mathematically correct, the presence of a pole in the immediate vicinity of the branch-point not only contributes as a pole to $g_T(k_r)$ but also contributes a significant contribution to $g_C(k_r)$ near the branch-point. Although the exact Hankel transform of $g_C(k_r)$ yields $p_C(r)$, a numerical implementation of the transform may be subject to sampling and aliasing errors due to the behavior of $g_C(k_r)$ near the branch-point. This effect is a potential limitation of the new hybrid technique which does not occur in Stickler and Ammicht's method. We note that in the preceding numerical example, the off-axis pole at $0.47986982 + j5.8425809 * 10^{-3}$ is located quite close to the branch-point at 0.488888, and the hybrid technique does not produce an aliased result. In situations when a pole is much closer to the branch-point, the hybrid method may produce aliased results.

In the approach of Stickler and Ammicht, the effect of a pole in $g(k_r)$ is modelled exactly. This applies to all poles including those in the vicinity of the branch-point. This suggests that Stickler and Ammicht's approach might be incorporated within the framework of the hybrid method based on the decomposition $g(k_r) = g_T(k_r) + g_C(k_r)$ in order to improve the performance of the hybrid method when a pole lies in the immediate vicinity of the branch-point. In other words, their approach potentially might be used to model $g(k_r)$ differently by modifying the form of $g_T(k_r)$ particularly for those poles in the immediate vicinity of the branch-point. In order to investigate this possibility, we remapped the integral in equation (4.96) back to k_r-plane as

$$p_C(r) = \int_{BL_+} \sum_i \frac{c_i k_{sN}}{k_r^2 - k_{ri}^2} H_0^{(1)}(k_r r) k_r \, dk_r \qquad (4.105)$$

We note that poles in this sum must also appear in complex conjugate pairs as opposed to the sum for $g_{C_1}(k_r)$ in equation (4.101) which contains only the exposed off-axis poles in quadrant I. In order to further relate this expression to the pole model for $g_{C_1}(k_r)$, it was necessary to relate the coefficient c_i in Stickler and Ammicht's expansion to the residue at the pole in the k_r-plane. The algebraic details of this are not included here, however, the resulting expression for $p_C(r)$ was determined to be

$$p_C(r) = \int_{BL_+} \sum_i \frac{2a_i k_{ri} k_{sN}}{k_{sN_i}(k_r^2 - k_{ri}^2)} H_0^{(1)}(k_r r) k_r \, dk_r \qquad (4.106)$$

It is noted that the kernel of this expression is identical to the form proposed by Kurkjian for modelling the effects of a pole near a branch-point in a borehole acoustics context [36]. Kurkjian hypothesized this form from the properties of $g(k_r)$ when a pole is in the vicinity of the branch-point. It is interesting to note that an identical form is obtained by mapping Stickler and Ammicht's expansion, based on the Mittag-Leffler theorem to the k_r-plane.

In order to relate the form for $p_C(r)$ in equation (4.106) with the hybrid technique, equation (4.93) is used. The implication is that

$$g_\Delta(k_r) = [g_+(k_r) - g_-(k_r)] = \sum_i \frac{2a_i k_{ri} k_{sN}}{k_{sN_i}(k_r^2 - k_{ri}^2)} \qquad (4.107)$$

272

for values of k_r along the branch-cut. Using the properties developed in Chapter 2 that $g(k_r^*) = g^*(k_r)$ and $g(k_r) = g(-k_r)$, it can be shown that the quantity $[g_+(k_r) - g_-(k_r)]$ is $2j \, Im\{g(k_r)\}$ for values of k_r along the EJP branch-cut. The implication is that

$$2j \, Im\{g(k_r)\} = \sum_i \frac{2a_i k_{ri} k_{zN}}{k_{zN_i}(k_r^2 - k_{ri}^2)} \tag{4.108}$$

along the branch-cut. In order to further relate Stickler and Ammicht's approach to the modelling of $g_C(k_r)$, we use the fact proved earlier that $Im\{g(k_r)\} = Im\{g_C(k_r)\}$ for real values of k_r. Thus,

$$2j \, Im\{g_C(k_r)\} = \sum_i \frac{2a_i k_{ri} k_{zN}}{k_{zN_i}(k_r^2 - k_{ri}^2)} \tag{4.109}$$

for real values of k_r along the branch-cut.

There are several important observations concerning (4.109) which are now made. First, it is apparent that although Stickler and Ammicht's technique has been mapped to the k_r-plane, it suggests a technique for modelling only the imaginary part of $g_C(k_r)$. Nothing is implied about modelling of the real part. This was to be expected as their modelling technique consists of expanding the difference of the Green's function across the cut in a partial fraction expansion. As previously pointed out, the difference is across the EJP-cut is the imaginary part of $g_C(k_r)$. Secondly, the model is only applicable to the imaginary part of $g_C(k_r)$ for real values of k_r less than the branch-point. It implies nothing about modelling the behavior of $g_C(k_r)$ for values of k_r greater than this value.

In effect, this result points out that the method for modelling the contribution of a pole proposed by Stickler and Ammicht is not directly applicable to the hybrid method based on $g_T(k_r) + g_C(k_r)$. The primary reason is that their form applies to modelling $Im\{g_C(k_r)\}$ only while we are concerned with modelling both the real and imaginary parts of $g_C(k_r)$. Potentially, some combination of the two methods which exploits the imaginary-part sufficiency condition of $g_C(k_r)$ might be applicable. For example, a pole could be removed from $Im\{g_C(k_r)\}$ using equation (4.109). The Hilbert-Hankel transform of the imaginary part of the remaining portion could be

computed and added to the analytic contribution computed using equation (4.97). The result, added to the expression for $p_T(r)$, would comprise the total field.

To summarize, we have discussed the relationship between the hybrid approach and the method proposed by Stickler and Ammicht. The latter method is uniform with respect to poles near the branch-point while the former is not. In particular, a weakness of the hybrid approach is that it cannot effectively deal with the poles which are in the immediate vicinity of the branch-point. It was pointed out that removal of these poles may leave a substantial contribution within $g_C(k_r)$ at the branch-point. Sampling and aliasing artifacts may result from the numerical computation of the transform of this function. The hybrid method can be also be considered within the framework of modelling $g_C(k_r)$. The behavior of $g_C(k_r)$ at the branch-point when a pole is nearby suggests that a better model than $2a_i k_{ri}/(k_r^2 - k_{ri}^2)$ might exist. The possibility of mapping the model proposed by Stickler and Ammicht to the k_r-plane was discussed. The resulting model became $2a_i k_{ri} k_{sN}/[k_{sN_i}(k_r^2 - k_{ri}^2)]$ for $Im\{g_C(k_r)\}$. Thus, their method provides the basis for modelling only the imaginary part of $g_C(k_r)$. An alternate method which exploits the advantages of both approaches may exist. In particular, a specific algorithm which incorporates the model of Stickler and Ammicht along with the property of imaginary-part sufficiency was proposed.

4.7 Summary

In this chapter, we have discussed a hybrid method for the synthetic generation of shallow water acoustic fields. To provide background, we first presented a review of existing methods. The theory of the new method was then developed in terms of decomposing the Green's function into a modal portion and a continuum portion. In this method, the modal contribution to the field is computed analytically and the continuum contribution is computed by applying a numerical Hankel transform to the continuum portion of the Green's function. Although the method is theoretically straightforward, several implementation aspects were discussed. Numerical examples of synthetic acoustic fields in both isovelocity and non-isovelocity waveguides were presented. Two important extensions to the method were next discussed. In the first extension, we pointed out that the modal portion of the Green's function can be determined by using existing normal-mode techniques. In the second extension, we combined the finite extent property of the imaginary part of the Green's function, with the real-part sufficiency property of the Hilbert-Hankel transform, to develop an alternate method for computing the continuum portion of the field. This method does not explicitly require the determination of the poles and residues of the Green's function. The method was also considered in the case that realistic attenuation is present in the geoacoustic model. In the final section of the chapter, we related the hybrid method to three existing methods for synthetic data generation. In making this comparison, we provided additional numerical examples of the hybrid method and suggested that it may be useful in deep water applications as well.

Bibliography

[1] F.D. Tappert. Selected applications of the parabolic equation method in underwater acoustics. Intern. Workshop on Low-Frequency Propagation and Noise (Woods Hole, MA), Oct. 1974.

[2] F.D. Tappert. The parabolic equation method. In J.B. Keller and J.S. Papadakis, editors, *Wave Propagation and Underwater Acoustics*, Springer-Verlag, New York, 1977.

[3] F.R. DiNapoli and R.L. Deavenport. Theoretical and numerical Green's function solution in a plane multilayered medium. *J. Acoust. Soc. Am.*, 67:92–105, 1980.

[4] H.W. Marsh and S.R. Elam. Internal Document Raytheon Company Marine Research Laboratory, New London CT, 1967.

[5] Douglas R. Mook, George V. Frisk, and Alan V. Oppenheim. A hybrid numerical/analytic technique for the computation of wave fields in stratified media based on the Hankel transform. *J. Acoust. Soc. Am.*, 76(1):222–243, July 1984.

[6] D.J. Thomson. *Implementation of the Lamont-Doherty Geological Observatory Normal Mode/Fast Field Model on the NUSC Vax 11/780 Computer*. Technical Report TR7221, Naval Underwater Systems Center, Sept. 1984.

[7] Henrik Schmidt and Finn B. Jensen. A full wave solution for propagation in multilayered viscoelastic media with application to Gaussian beam reflection at fluid-solid interfaces. *J. Acoust. Soc. Am.*, 77(3):813–825, Mar. 1985.

[8] A.V. Newman and F. Ingenito. *A Normal Mode Computer Program for Calculating Sound Propagation in Shallow Water with an Arbitrary Velocity Profile.* Technical Report NRL 2381, Naval Research Laboratory, Jan. 1972.

[9] John F. Miller and Frank Ingenito. *Normal Mode Fortran Programs for Calculating Sound Propagation in the Ocean.* Technical Report NRL 3071, Naval Research Laboratory, June 1975.

[10] F.B. Jensen and M.C.Ferla. SNAP: The Saclanten normal-mode acoustic propagation model. Rep. SM-121, SACLANT Research Centre, La Spezia, Italy, 1979.

[11] A.B. Baggeroer. A numerical approach to the solution of the acoustic wave equation. Unpublished paper, 1985.

[12] George V. Frisk and Henrik Schmidt. Private communication, Dec. 1985.

[13] D.C. Stickler. Normal-mode program with both the discrete and branch line contributions. *J. Acoust. Soc. Am.*, 57(4):856–861, Apr., 1975.

[14] H.P. Bucker. Propagation in a liquid layer lying over a liquid half-space (Pekeris cut). *J. Acoust. Soc. Am.*, 65(4):906–908, Apr., 1979.

[15] C.T. Tindle, A.P. Stamp, and K.M. Guthrie. Virtual modes and the surface boundary condition in underwater acoustics. *J.Sound Vib.*, 49:231–240, 1976.

[16] A.O Williams. Pseudoresonances and virtual modes in underwater sound propagation. *J. Acoust. Soc. Am.*, 64(5):1487–1491, Nov., 1978.

[17] C.T. Tindle. Virtual modes and mode amplitudes near cutoff. *J. Acoust. Soc. Am.*, 65(6):1423–1427, June, 1979.

[18] D.C. Stickler and E. Ammicht. Uniform asymptotic evaluation of the continuous spectrum contribution for the Pekeris model. *J. Acoust. Soc. Am.*, 67(1):2018–2024, 1980.

[19] E. Ammicht and D.C. Stickler. Uniform asymptotic evaluation of the continuous spectrum contribution for a stratified ocean. *J. Acoust. Soc. Am.*, 76:186–191, July 1984.

[20] H. Weinberg. Application of ray theory to acoustic propagation in horizontally stratified oceans. *J. Acoust. Soc. Am.*, 58:97–109, 1975.

[21] F.D. DiNapoli. *Fast Field Program for Multilayered Media*. Technical Report NUSC 4103, Naval Underwater Systems Center, New London, CT, Aug. 1971.

[22] J.W. Cooley and J.W. Tukey. An algorithm for the machine calculation of complex Fourier series. *Mat. Computation*, 19:297–301, 1965.

[23] H.W. Kutschale. *The Integral Solution of the Sound Field in a Multilayered Liquid-Solid Halfspace with Numerical Computations for Low-Frequency Propagation in the Arctic Ocean*. Technical Report 1, Lamont-Dohert Geological Observatory, Palisades, NY, 1970.

[24] F.D. DiNapoli. *The Collapsed Fast Field Program*. Technical Report TA11-317-72, Naval Underwater Systems Center, New London, CT, Oct. 1972.

[25] P.M. Morse and H. Feshbach. *Methods of Theoretical Physics*. Volume 1,2, McGraw-Hill, New York, 1953.

[26] Imsl library, version 8. International Mathematical and Statistical Libraries Inc., Houston, TX:.

[27] D.R. Mook. *The Numerical Synthesis and Inversion of Acoustic Fields Using the Hankel Transform with Application to the Estimation of the Plane Wave Reflection Coefficient of the Ocean Bottom*. Technical Report, Sc.D. Thesis, MIT/WHOI Joint Program, Cambridge Ma., Jan. 1983.

[28] Ronald N. Bracewell. *The Fourier Transform and Its Applications*. McGraw-Hill, New York, 1978.

[29] Alan V. Oppenheim, George V. Frisk, and David R. Martinez. Computation of the Hankel transform using projections. *J. Acoust. Soc. Am.*, 68(2):523–529, Aug. 1980.

[30] D.R. Mook. An efficient algorithm for the numerical evaluation of the Hankel and Abel transforms. *IEEE Trans. Acoustics, Speech, and Signal Processing*, 31:979–985, 1983.

[31] Eric W. Hansen and Alexander Jablokow. State variable representation of a class of linear shift-variant systems. *IEEE Trans. Acoustics, Speech, and Signal Processing*, 30(6):874–880, Dec. 1982.

[32] Eric W. Hansen. New algorithms for Abel inversions and Hankel transforms. *Proc. 1983 ICASSP*, 2:1260–1263, 1983.

[33] Cornelius Lanczos. *Linear Differential Operators*. D. Van Nostrand Co., London, 1960.

[34] E.C. Titchmarsh. *Eigenfunction Expansions*. Oxford University Press, London, 1946.

[35] I.S. Gradshteyn and I.M Ryzhik. *Tables of Integrals, Series, and Products*. Academic Press, 1965.

[36] Andrew L. Kurkjian. Numerical computation of individual far-field arrivals excited by an acoustic source in a borehole. *Geophysics*, 50(5):852–866, May 1985.

Chapter 5

Shallow Water Acoustic Field Inversion

5.1 Introduction

In this chapter, the problem of inverting shallow water acoustic fields is discussed. In the inversion problem, information about the waveguide and the underlying ocean bottom is extracted from measurements of the complex-valued acoustic pressure field collected as a function of range. The general inverse problem of extracting the complete geoacoustic model from measurements of the pressure field due to a harmonic point source is a difficult and as-of-yet unsolved problem. Some idea of the complexity of the problem can be obtained by considering the complexity of the related forward problem, discussed in Chapter 4 of this thesis. As discussed in that chapter, the field is related to the Green's function by the Hankel transform, the Green's function is in turn algebraically related to the reflection coefficient, and the reflection coefficient is related to the geoacoustic parameters within each layer. The theoretical difficulty lies within the final step of obtaining the model from the reflection coefficient, although there are also experimental difficulties associated with the other steps.

There have been a number of approaches proposed to solve this general problem [1] [2] [3] [4]. In one approach, the model is obtained using an analysis-by-synthesis or forward modelling procedure. In this procedure, a computer model is used to synthetically generate a field which is then compared with an experimentally measured field. The geoacoustic parameters which form the input to the computer model are varied in such a way as to most closely match the synthetic and experimental fields.

An essential element in the forward modelling approach is the computer model which generates a synthetic shallow water acoustic field in an accurate and computationally efficient manner. We point out that the hybrid method discussed in the previous chapter is a good candidate in such an application. This method not only provides an accurate synthetic field using a fast algorithm but has an important intrinsic property as well - it is directly related to alternate and simpler methods for synthetic data generation. In particular, the field synthesized in the hybrid method is the sum of the field produced by a simpler method, such as a normal-mode technique, plus the more complicated continuum portion which effectively requires a branch-line integral computation. In some forward modelling situations, only the modal portion, and not the complete acoustic field, is required. By using the hybrid method to produce the continuum field only, it is possible to determine whether or not this portion is important in the forward modelling procedure over a specific range interval, and thus whether or not a simpler method is appropriate.

Forward modelling in underwater acoustics problems is still something of an art because of the complex ways in which the geoacoustic parameters influence the synthetically generated field. Although it is possible, in theory, to automate the forward modelling process, the criteria for evaluating the closeness of the match may be quite difficult to determine and quantify. For these reasons, we have chosen not to make forward modelling using the hybrid method a major thrust of our research. Instead, in the second section of this chapter, we will focus on the related question of what to forward model. In particular, in conventional forward modelling schemes, it is usually

the magnitude of the acoustic field which is matched as opposed to other quantities such as the quadrature components of the field or the phase. The primary reason for this is that the magnitude tends to vary at a much slower rate as a function of range than other quantities. Typically, the phase is not considered in the forward modelling procedure and is often not plotted due to its rapidly varying nature. However, in our work, we have found that the phase of the acoustic field contains important information about the propagation of an acoustic field within a waveguide. Because of its importance, we will discuss the role of a quantity which is directly related to the phase, referred to as residual phase, in forward modelling methods. In addition, we will discuss several other applications of the residual phase.

An alternate approach for solving the inverse problem is to perform the steps described for synthesizing the field in reverse. The complexity of performing this procedure is apparent. Not only are there important and difficult signal processing issues involved, such as the amount of data required and optimal methods for processing this data, but more fundamental issues are involved as well. For example, the uniqueness and sensitivity of several steps in the inversion procedure are not well understood. Nevertheless, several developments in recent years including improvements in the experimental procedure for acquiring the data and theoretical advances in relating the reflection coefficient to the properties of the underlying media are indicative of the feasibility of this approach.

Because of the difficulty in solving the inversion problem in this way, the problem is typically partitioned into two separate sub-problems - 1) determination of the reflection coefficient given the measurements of the acoustic field in shallow water, 2) determination of the geoacoustic properties given the reflection coefficient. There are a number of advantages to partioning the problem in this way. The solution of the first sub-problem essentially removes any geometry features of the shallow water experiment. The solution of the second sub-problem is also common to other disciplines in which the properties of some medium are to be determined from measurements

282

of the complex amplitude of the scattered field. Thus, one advantage is that theoretical strides made toward solving the second, more general sub-problem can be incorporated and exploited in the context of this particular inversion problem.

Another advantage of this partitioning is that important and fundamental information about the nature of the propagation within the waveguide can be derived from the solution of the first sub-problem alone. For example, a reasonable assumption is that accurate determination of the reflection coefficient implies accurate determination of the shallow water Green's function. The Green's function contains information relating to the preferred modes of propagation, indicated by the presence of poles or peaks in its amplitude. If the Green's function is accurately determined, these features can be extracted and interpreted. Extracting information directly from the Green's function about the geoacoustic model represents the basis for a series of less ambitious but potentially more robust inversion methods. Here only certain geoacoustic parameters are extracted or else a model-based method is used. As one example of this, we have shown in Chapter 2 that the velocity in the underlying halfspace can be determined directly from the imaginary part of the Green's function using the finite extent property, i.e. without specifically relying on the solution of the second sub-problem. As another example, it has been shown that the eigenvalues, i.e. peaks in the Green's function, can be used in a model-based perturbative inverse procedure to determine the velocity profile [5].

Thus, the partioning of the inversion problem into a sequence of these two steps is advantageous for several reasons. In Section 5.3 of this chapter, we will address several of the theoretical issues related to the first sub-problem, that is, determining the reflection coefficient from measurements of the shallow water acoustic field. We will show that there are some fundamental differences involving the sensitivity of extracting the reflection coefficient from shallow water field measurements, as compared with extracting the reflection coefficient from measurements in the deep-water, non-reverberant environment. Additionally, we will suggest an experimental means

by which the points of highest sensitivity, i.e. points at which the largest errors in the inverted reflection coefficient are expected, can be placed in regions which are not of interest.

In Section 5.4 of this chapter, we will demonstrate the feasibility and limitations of obtaining the reflection coefficient from a shallow water acoustic field using synthetic data. In this approach, accurately produced synthetic data is used as the input to the inversion technique in which the reflection coefficient is extracted. Although demonstrating that the reflection coefficient can be obtained from a synthetically produced shallow water acoustic field has been considered elsewhere [3], only limited success has been achieved. In particular, it has been previously difficult to isolate those effects which are due to approximations in the synthetic data generation method from effects associated solely with the inversion procedure. By taking advantage of the hybrid method discussed in the preceding chapter, it is possible to better isolate these two effects. To demonstrate the utility of studying the inversion of synthetic data, we will present implications of the theoretical sensitivity results, discussed in Section 5.3, using numerical examples of synthetic data.

5.2 The Residual Phase of a Shallow Water Acoustic Field

In shallow water forward modelling methods, it is usually the magnitude of the acoustic field which is modelled as opposed to other quantities, such as the quadrature components of the complex-valued field, or the phase. Typically, the magnitude varies as a function of range at a much slower rate than these other quantities. Even though a great deal of information regarding the propagation of the field and the underlying geoacoustic parameters may be contained within these other quantities [1], their rapidly varying nature may obscure this information. One method for utilizing both magnitude and phase information is to first determine the Green's function, and to then apply forward modelling methods in the horizontal wavenumber domain. Since determination of the Green's function requires knowledge of both the magnitude and the phase, more information is utilized in this forward modelling procedure than in a forward modelling procedure based on matching the field magnitude only [6]. In this section, we define the residual phase of a shallow water acoustic field. Because of its slowly varying nature and its direct relationship to the phase of the field, the residual phase can be used, along with the magnitude of the field, in alternate methods for forward modelling directly in the range domain. These methods do not require the computation of a Hankel transform and thus have several advantages over the Green's function method. In addition to forming a quantity useful for forward modelling based inversion, the residual phase has several other important applications, as will be discussed in this section.

As an example of a shallow water acoustic field, consider the field for the Pekeris geoacoustic model previously presented in Table 4.1. The hybrid method for synthetic

---

[1] The interpretation of the quadrature components will not be specifically addressed in this section. However, in the next chapter we will show that sufficient information is contained within the quadrature components such that one component can be reconstructed from the other.

field generation was used and the magnitude and phase of the corresponding field are shown in Figure 5.1. From this figure, it can be seen that while the magnitude is a slowly varying function of range, the phase is not. The real and imaginary parts of this field are shown in Figure 5.2. Again, both of these quantities are rapidly varying functions of range. Interpretation of the acoustic field phase or quadrature components, when displayed in this way, is difficult.

A similar effect was noted by Mook in the study of deep water acoustic fields [7]. However, Mook pointed out the important fact that although the phase of the deep water field varied rapidly as a function of range from the source, its variation about a known trend was much less rapid. In particular, if the form of a deep water reflected pressure field, for a particular source and receiver depth, is

$$p(r) = M(r)e^{j\theta(r)} \tag{5.1}$$

where $M(r)$ represents the field magnitude and $\theta(r)$ represents the field phase, Mook defined a quantity referred to as the residual phase $\epsilon(r)$, as

$$\epsilon(r) = \theta(r) - k_o R \tag{5.2}$$

where $R = (r^2 + (z - z_0)^2)^{1/2}$ and k_0 is the water wavenumber.

The residual phase $\epsilon(r)$ formed an essential component in a method for unwrapping the phase of a deep water field [7] [8]. The method is based on a technique of adding multiples of 2π to the principal value of a phase function, computed using an inverse tangent routine, until the discontinuities induced by the modulo 2π operation are removed [9] [10]. Such an algorithm relies on the detection of a discontinuity by computing the difference of the phases of two adjacent samples. Whenever the phase difference exceeds a threshold, a discontinuity has occurred. The procedure yields the unwrapped phase whenever the sampling is fine enough so that the difference between adjacent samples of the unwrapped phase is less than the threshold. Mook's contribution was to apply this phase unwrapping scheme not to $\theta(r)$ directly, but rather to the quantity $\theta(r) - k_0 R$. Essentially, in his method the phase function $\epsilon(r)$

286
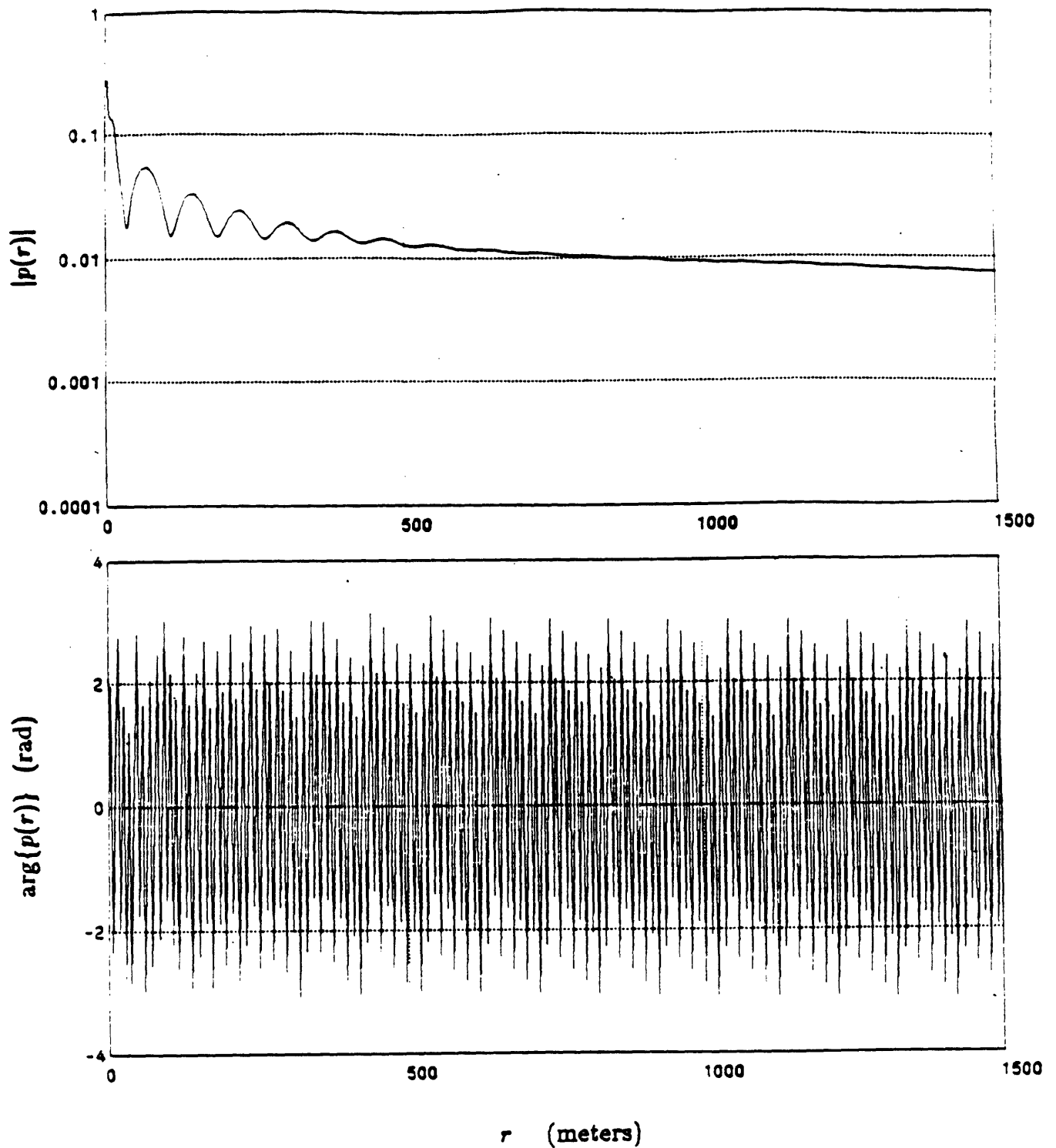
Figure 5.1: Magnitude and phase of the Pekeris model shallow water field.
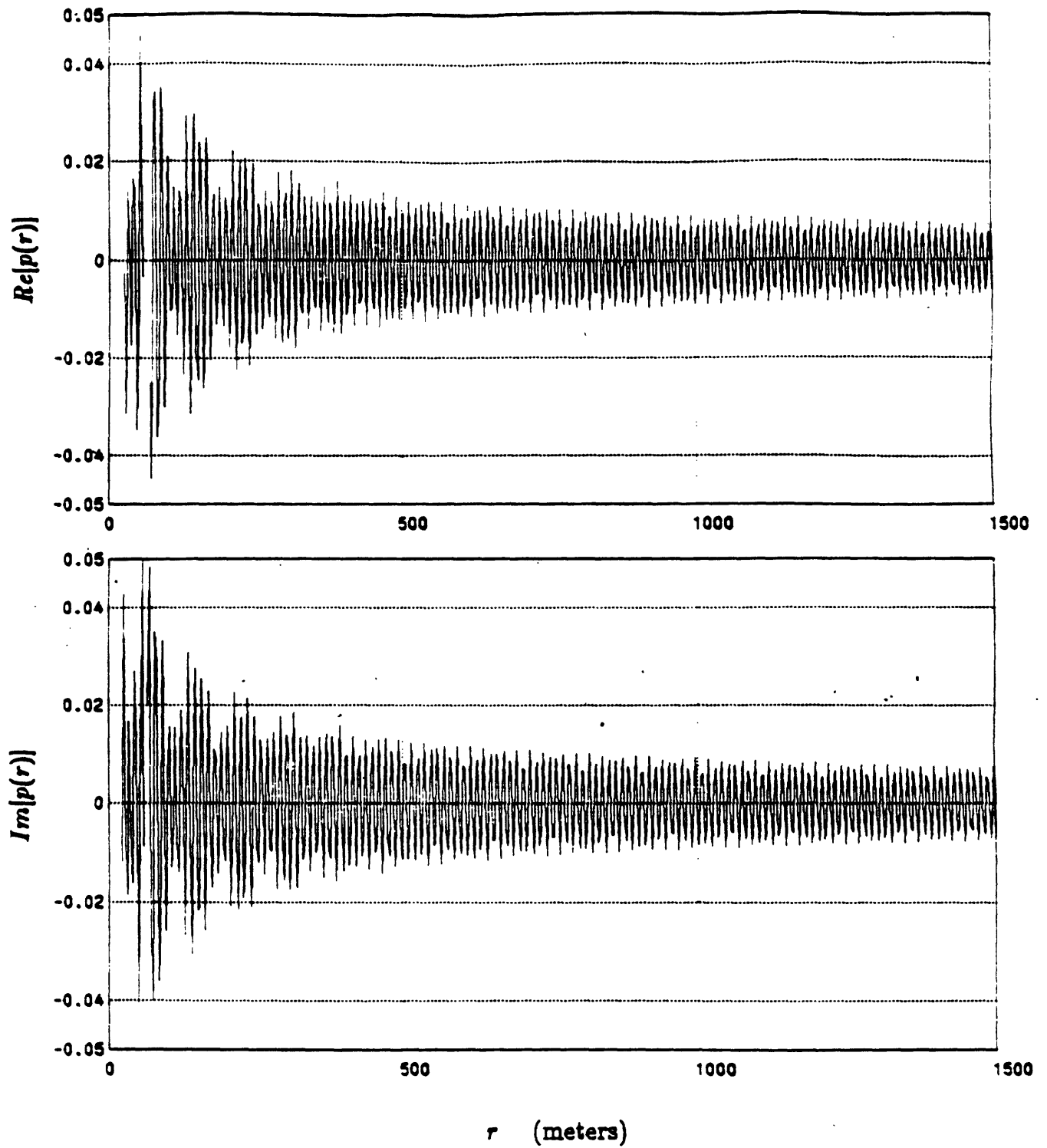
Figure 5.2: Real and imaginary components of the Pekeris model shallow water field.

288

is unwrapped by detecting discontinuities in its principal value. After the unwrapped phase function $\epsilon(r)$ is determined, the unwrapped phase function $\theta(r)$ is computed by adding $k_0 R$ to $\epsilon(r)$. In Mook's application, the unwrapped phase function was used in an interpolation method for obtaining a deep water acoustic field on an alternate grid more suitable for processing. In related work, plots of the deep water residual phase were presented and interpreted [8]. The deep water residual phase was found to useful in other applications including a technique for compensating for source-height variation [8].

The utility of the deep water residual phase function led us to investigate a similar quantity for shallow water acoustic fields. In our work, we found that a useful shallow water phase function is given by

$$\phi(r) \equiv P\{\theta(r) - k_\phi r\} \tag{5.3}$$

where the operator $P\{\}$ denotes principal value over the interval $(-\pi, \pi]$. To distinguish between the phase function $\phi(r)$ and the phase function $\epsilon(r)$ defined for the deep water field, we will henceforth refer to $\phi(r)$ as the residual phase, and $\epsilon(r)$ as the unwrapped deep water residual phase. Although there are some similarities between the residual phase $\phi(r)$ and the unwrapped deep water residual phase $\epsilon(r)$, there are also essential differences, which are now discussed.

First, $\phi(r)$ is defined in terms of horizontal range r, rather than in terms of slant range $R = (r^2 + (z - z_0)^2)$. In deep water, the dependence of $\theta(r)$ on slant range can be justified using a specular phase or geometric argument. Essentially, when the field is comprised of a single path from the source to the receiver, the phase is determined by the path length multiplied by the wavenumber of the medium. In shallow water, there are an infinite number of paths from the source to the receiver, corresponding to the reverberation within the shallow water waveguide, and a simpler specular argument does not apply. Because of the trapping effect within the waveguide, it is more meaningful to interpret the field in terms of a modal sum, where the phase of each mode is determined by the product of its horizontal wavenumber with the horizontal

range r. The difference between R and r is not particularly significant at large ranges in shallow water however. Secondly, the residual phase $\phi(r)$ is defined in terms of an arbitrary wavenumber k_ϕ, rather than in terms of the water wavenumber k_0. The choice of an alternate wavenumber is again related to the fact that a trapping effect can occur at a wavenumber which differs from the water wavenumber. Thus, the choice of the term $k_\phi r$ indicates that although the phase of the shallow water field has a strong linear dependence, the linear phase term is not $k_0 R$, but rather the model-dependent term $k_\phi r$. Finally, the phase function $\phi(r)$ is an unambiguously defined, principal valued quantity. In contrast, there is some ambiguity in the definition of $\epsilon(r)$, in that it is defined in terms of the unwrapped phase $\theta(r)$. The precise definition of an unwrapped phase function is difficult, although statements regarding its relationship to an integrated phase derivative with initial condition can be made [9]. Alternately, the residual phase function $\phi(r)$ does not require phase unwrapping in its definition. This statement can be justified using the following identity

$$\phi(r) \equiv P\{\theta(r) - k_\phi r\} = P\{P\{\theta(r)\} - k_\phi r\} \qquad (5.4)$$

which indicates that the residual phase $\phi(r)$ can be determined from the principal value of the phase of the acoustic field.

There exists a simple computational algorithm for computing $\phi(r)$ given the real and imaginary components of the shallow water acoustic field and k_ϕ. The algorithm consists of computing $\phi(r)$ via

$$\phi(r) = \tan^{-1}\{Im[p_d(r)]/Re[p_d(r)]\} \qquad (5.5)$$

where $p_d(r)$ is the demodulated version of $p(r)$, i.e.

$$p_d(r) \equiv p(r)[\cos k_\phi r - j \sin k_\phi r] \qquad (5.6)$$

In addition to its computational simplicity, the definition of the residual phase $\phi(r)$ as a principal valued function has other advantages, including reduced dynamic range of the phase plot, and insensitivity to errors in the phase unwrapping. If an unwrapped

version of $\phi(r)$ is required, one of a number of existing methods for phase unwrapping can be applied.

One use of the unwrapped deep water residual phase was in an interpolation algorithm for obtaining the field on a particular grid from its measurements obtained an alternate grid. We point out that it is also possible to use the wrapped residual phase $\phi(r)$ in a shallow water interpolation algorithm, which consists of 1) determining the residual phase using equation (5.5), 2) deriving the corresponding quadrature components by multiplying the magnitude of the field times the cosine of the residual phase, and the magnitude of the field times the sine of the residual phase 3) interpolating the quadrature components using a method such as linear interpolation, 4) multiplying the resultant complex-valued quantity by $e^{jk_\phi r}$. This interpolation scheme is essentially bandlimited interpolation and is expected to work well only when the field is adequately sampled initially – that is, the field must be sampled at roughly the appropriate average rate prior to its interpolation to an alternate grid. This interpolation algorithm is currently being studied and we will present an example of its application to an experimental shallow water acoustic field in the next chapter.

As an example of the use of residual phase in shallow water forward modelling, the magnitude and residual phase of the field previously shown in Figure 5.1 are shown in Figure 5.3. The water wavenumber k_0 was chosen as the value of k_ϕ for this example. As can be seen, the residual phase $\phi(r)$ is a more slowly varying quantity than the original phase $P\{\theta(r)\}$, shown in Figure 5.1. It can also be seen that the residual phase still contains a linear phase component, as indicated by its periodic wrapping as a function of range. This implies that by selecting a different value of k_ϕ, the trend can be removed. An appropriate choice can be determined by computing the averaged phase derivative of the phase function displayed in Figure 5.3.

There are numerous methods for computing this averaged phase derivative. For example, it can be estimated manually by observing that the phase function rolls by

291
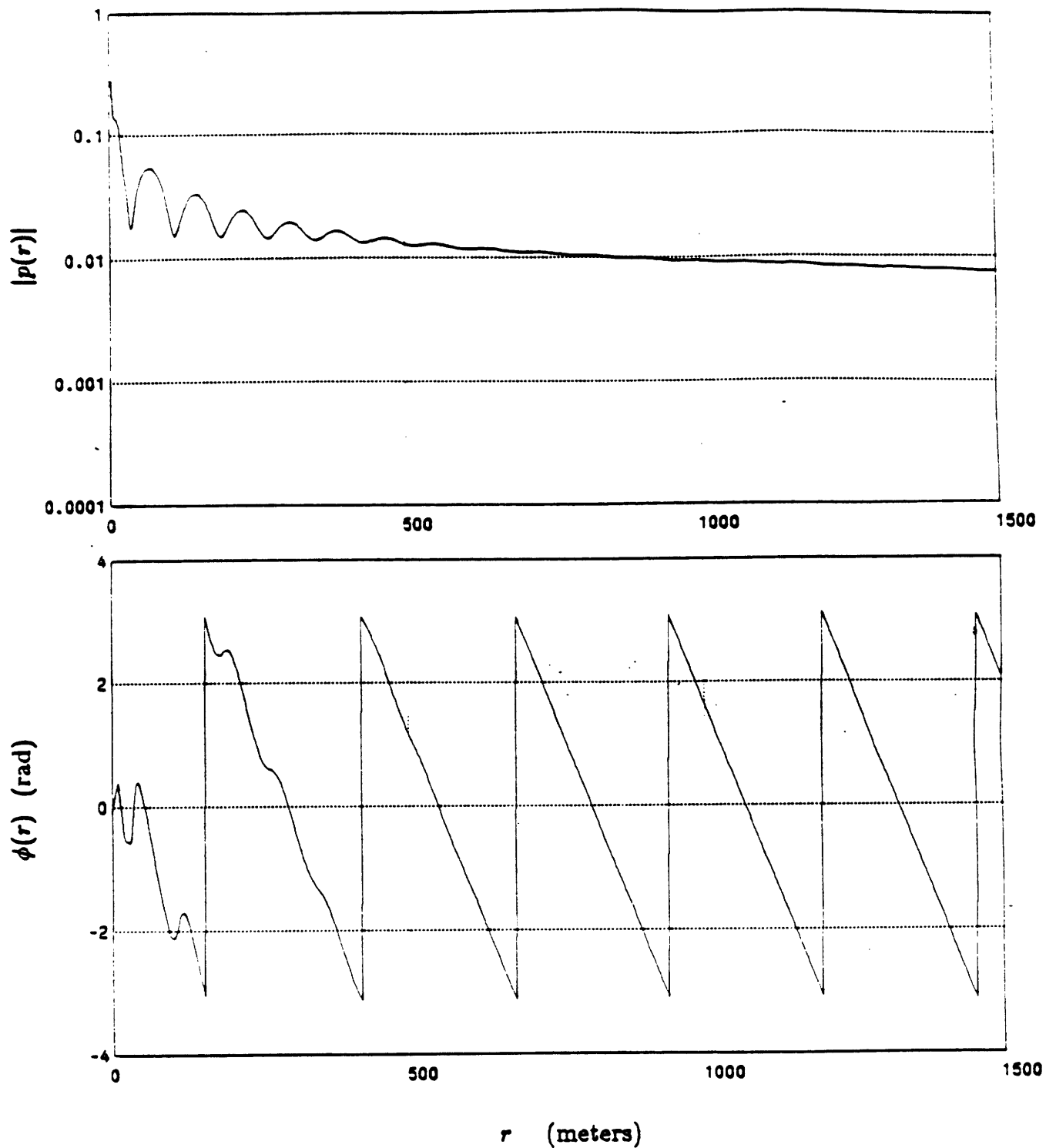
Figure 5.3: Magnitude and residual phase of the Pekeris model shallow water field assuming k_o is chosen as the water wavenumber.

-2π over the range interval from 420 to 680 m in the figure. Thus, an alternate choice for k_ϕ which effectively removes the remaining linear component is $k_0 - 2\pi/(680 - 420) \approx .5623$. Alternately, the determination of an averaged phase derivative can be automated. For example, if the residual phase function computed using $k_\phi = k_0$ is unwrapped, an averaged phase derivative can be obtained by averaging the difference in phase between adjacent samples. Unfortunately, this method may again be sensitive to phase unwrapping errors. An alternate technique which also determines the phase derivative without phase unwrapping is described in [9] [10]. The method computes the phase derivative of a function by multiplying its Fourier transform by an appropriate factor and computing the inverse Fourier transform. We have applied the technique to this example, and have computed by averaged phase derivative by combining the phase derivative at each range sample, over the range interval of 500 m to 1500 m. The averaged phase derivative was determined as $-.0242\ rad/m$, thereby implying that an appropriate choice of k_ϕ is $k_0 - .0242 \approx .5624$. In our work, we have not investigated the tradeoffs between various automated methods for estimating k_ϕ. In particular, since experimental acoustic fields are usually obtained on non-uniform grids, the automated algorithms must account for this. An investigation of these algorithms and their performance when applied to synthetic and experimental shallow water fields is suggested as future work. In the remainder of this section, k_ϕ will be selected manually, or from a priori knowledge about the shallow water waveguide model.

In Figure 5.4, the magnitude and residual phase of the field, computed using $k_\phi = 0.5623$, is shown. We note that the residual phase is again slowly varying, and that no unwrapping was required to determine it. The behavior of the phase of the field at large values of r is particularly simple for this example - a constant value. The simple behavior of the residual phase for the field, which corresponds to a non-trivial geoacoustic model, is actually not surprising. As discussed in Chapter 4, the total shallow water field can be considered as the sum of a modal portion plus a continuum portion. In this example, only a single mode is present, and at large values of range it
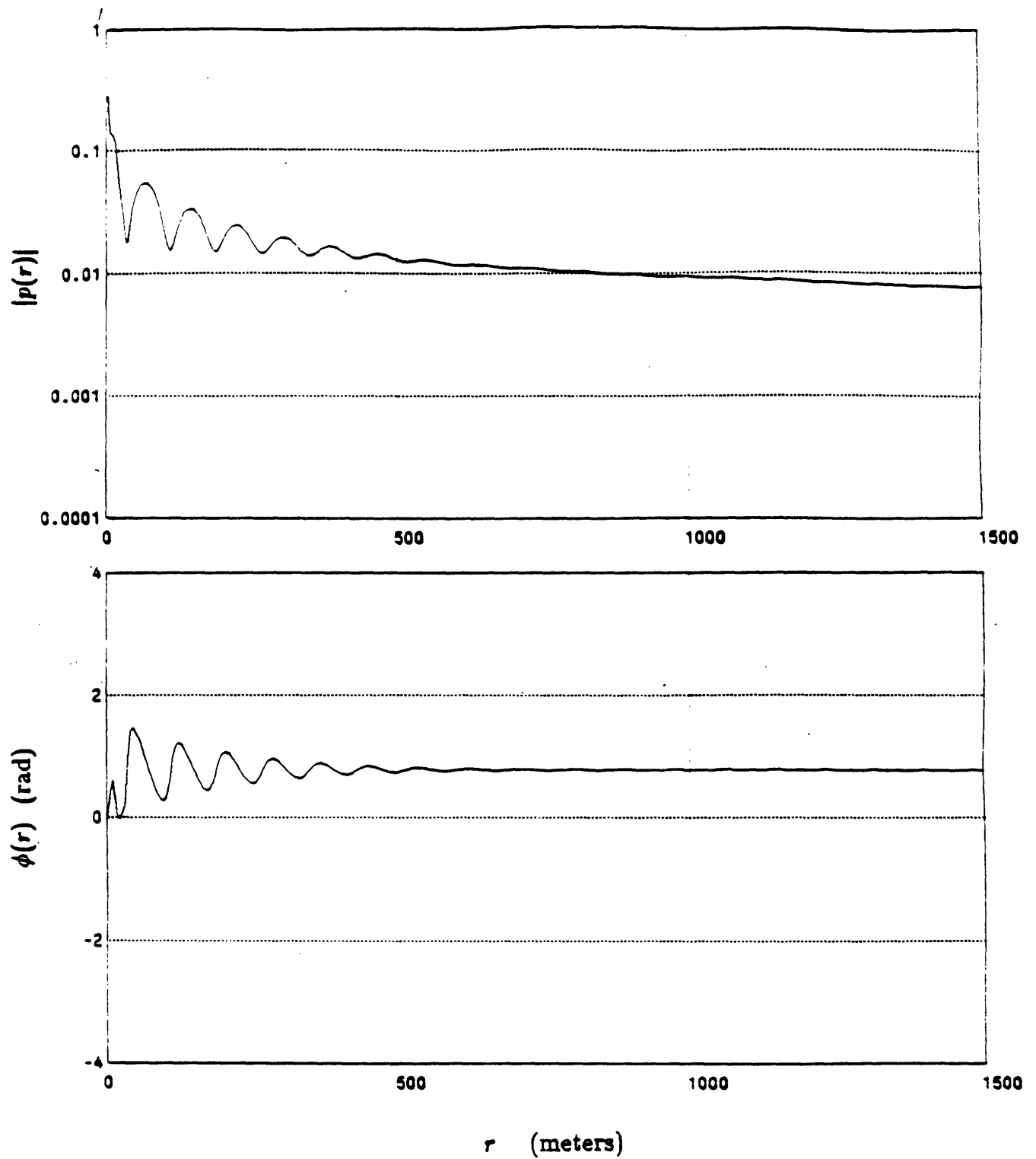
Figure 5.4: Magnitude and residual phase of the Pekeris model shallow water field assuming k_ϕ is chosen as 0.5623.

dominates over the continuum portion. Therefore, the field at large r is approximately

$$p(r) \approx p_T(r) = j\pi a_i k_{ri} H_0^{(1)}(k_{ri}r) \tag{5.7}$$

from equation (4.12) of Chapter 4. Next, using the asymptotic form of the Hankel function, valid at these ranges, it is easily seen that

$$p(r) \approx j(2\pi)^{1/2} a_i k_{ri} \frac{e^{j(k_{ri}r - \pi/4)}}{(k_{ri}r)^{1/2}} \tag{5.8}$$

so that

$$p(r) \approx c e^{j\pi/4} \frac{e^{jk_{ri}r}}{r^{1/2}} \tag{5.9}$$

where c is a real constant. Therefore, in the far-field, the residual phase consists of

$$\phi(r) = P\{\pi/4 + k_{ri}r - k_\phi r\} \tag{5.10}$$

and if k_ϕ is chosen to be exactly k_{ri}, the residual phase is simply $\pi/4$. In this example, the value of k_{ri} is 0.5623757, nearly identical to the value which we have chosen to compute the residual phase. The value $\pi/4$ is consistent with the value of the residual phase displayed in Figure 5.4 at large ranges. Essentially, we have determined the eigenvalue for the trapped mode in this model by systematically selecting the parameter k_ϕ so that the residual phase approached a constant value at large ranges. The modal eigenvalue was determined without resorting to more sophisticated methods, such as computation of the Hankel transform.

Additionally, the residual phase in the near-field indicates the presence of an interference pattern with a cycle distance d of approximately 78 m. An implication is that there may be an additional virtual mode present with a wavenumber which has the real part determined by $k_\phi - 2\pi/d = .4817$. This value is consistent with the theoretical value of the virtual mode at $0.481675 + j7.980302 * 10^{-3}$, as discussed in Chapter 4. We point out that the calculation of cycle distance is typically performed using the magnitude function only. By considering the behavior of the residual phase however, we were able to not only confirm the cycle distance observed in the magnitude

but to closely approximate the real parts of the corresponding horizontal wavenumbers as well. The procedure indicates that information normally available only in the wavenumber decomposition, i.e. the positions of several peaks in the Green's function, can be extracted from range domain signals as well.

The preceding example implies that generalizing the definition of residual phase from a function which is related to the water wavenumber k_0, to a function which is related to the horizontal wavenumber of the dominant mode present may be quite useful in shallow water forward modelling. As a more realistic example of the method of using residual phase in this context, we consider the magnitude and phase of an experimental 50 Hz acoustic field collected in September 1985 in the Gulf of Mexico [11]. The magnitude and phase of this field as a function of range to 1500 m are shown in Figure 5.5. By manually adjusting the value of k_ϕ, we have determined that an appropriate value for determining the residual phase for this case is 0.1974. The magnitude and the residual phase [2] , corresponding to this choice of k_ϕ, are shown in Figure 5.6. The residual phase is quite flat for this example and exhibits no linear trend. The implication is that there is a dominant mode which contributes to the field over these ranges which has the horizontal wavenumber equal to k_ϕ.

The relatively constant value of the residual phase in this figure is of importance for another reason as well. In particular, the value of the flat residual phase at large ranges can be used in a method for determining the phase of the complex gain of the acoustic source/receiver pair. This complex gain is required in the subsequent processing for extracting the reflection coefficient. The phase portion of this complex gain is sometimes referred to as the source phase because its total effect can be included by assuming that only the source has a phase offset. In contrast with the deep water case, there is no existing method for determining the source phase in the shallow water case. We propose that the residual phase determination provides a way

_____

[2] We have added π to the residual phase curve shown here in order to avoid plotting artifacts near $-\pi$.
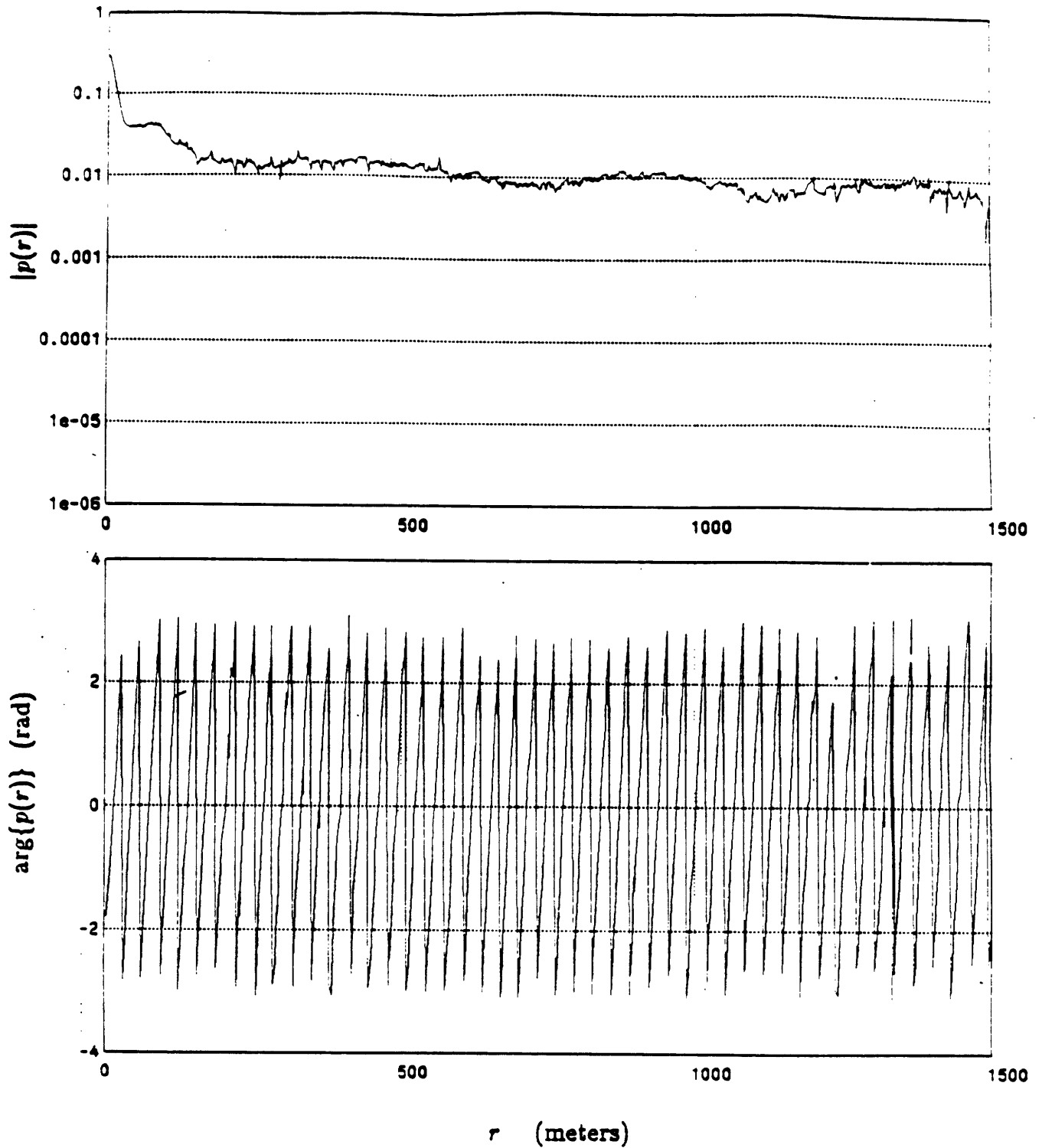
Figure 5.5: Magnitude and phase of the 50 Hz field from a shallow water experiment conducted in the Gulf of Mexico in September 1985.
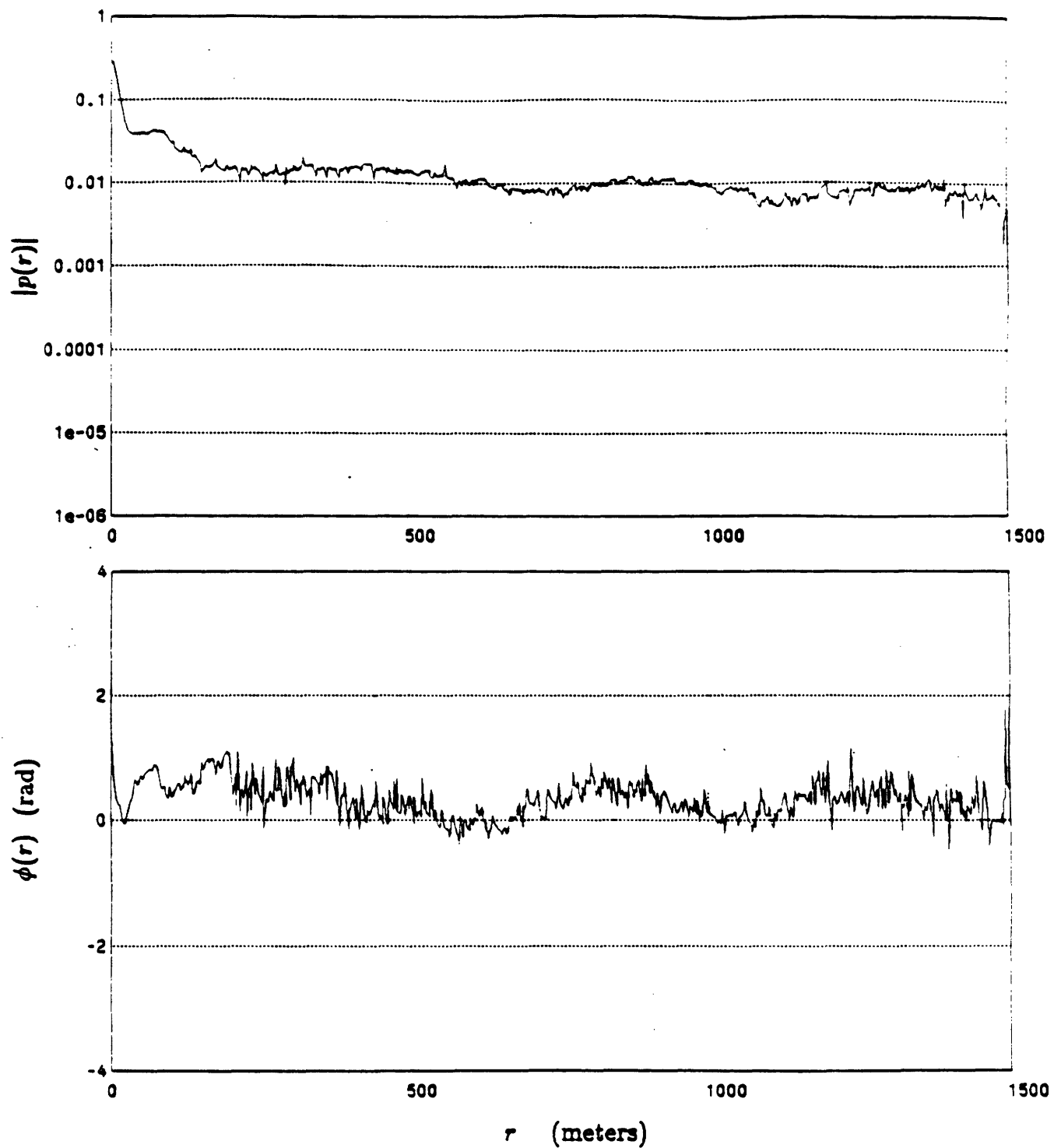
Figure 5.6: Magnitude and residual phase of the 50 Hz field from a shallow water experiment conducted in the Gulf of Mexico in September 1985. k_o was chosen as 0.1974.

in which the source phase can be extracted directly from the acoustic measurements. In other words, the residual phase provides a convenient way in which to separate information about the medium and the measurement procedure.

In particular, if the acoustic source is assumed to have the complex gain $Ge^{j\psi}$, where G and ψ are fixed constants, then the form of the far-field when a dominant mode is present is

$$p(r) \approx Ga_i k_{r_i}^{1/2} \frac{e^{j(k_{r_i}r + \pi/4 + \psi)}}{r^{1/2}} \tag{5.11}$$

Using the definition of residual phase, it is easily seen that

$$\phi(r) = P\{\psi + \pi/4 + k_{r_i}r - k_\phi r\} \tag{5.12}$$

If k_ϕ is chosen to match k_{r_i}, then the source phase ψ can be determined from the residual phase $\phi(r)$, assuming that no wrapping is involved as $\psi = \phi(r) - \pi/4$. In general, a number of values of $\phi(r)$ can be averaged to improve the stability of the estimate. The computation of the parameter G cannot be determined using this procedure. However, G is typically easier to determine using other methods, and remains fixed from experiment to experiment.

As the above example points out, the residual phase can provide important information related to propagation of acoustic fields in a waveguide. In particular, in the case that the field is dominated by a single component, the residual phase measurement is particularly valuable. In the previous examples, the dominant component consisted of the trapped mode. However, in a more general setting, the residual phase can provide information related to the dominant component which may vary as a function of range. Typically, this type of information is obtained from the magnitude of the field. For example, the asymptotic behavior of the magnitude may provide information about the propagation. However, we point out that the residual phase is also rich in information about propagation within the waveguide.

As a further example of this, we examine the continuum portion of the field for the model in Table 4.1. The magnitude and phase of this field are shown in Figure 5.7.

Features of the continuum portion of the field were previously discussed in Chapter 4. In particular, by varying different choices of parameters in the forward modelling process, we demonstrated that the field at far ranges consists of the lateral wave, and that the change in the behavior of the magnitude which occurs at $r = 750\ m$ is due to the lateral wave becoming dominant with respect to the virtual mode. The behavior is even more apparent when the residual phase of this field is examined. In Figure 5.8 is shown the magnitude and residual phase using the $k_\phi = 0.4888$, which is the wavenumber in the underlying halfspace. The fact that the residual phase stabilizes to a constant value at ranges past 750 m indicates that a dominant component of the continuum field, which has a horizontal wavenumber of 0.4888, is present at these ranges. Therefore, the residual phase confirms that the continuum field is dominated by the lateral wave here. In addition, the differing residual phase behavior at smaller values of r indicates that there are other dominant contributions at these ranges. The approximate value of the linear slope of the phase in the first several hundred meters is consistent with the value of the real part of the virtual mode wavenumber for this geoacoustic model. Therefore, by examining the residual phase of the continuum, it can be concluded that the virtual mode dominates the lateral wave in the near field but at ranges greater than 750 m, the lateral wave becomes dominant. The example points out that the residual phase can be an important tool for understanding the theory of propagation within a waveguide.

In the situation where there are many modes present, the appropriate choice for k_ϕ may be more difficult. In some cases, there may be a particular mode which is dominant as indicated by a relatively large modal amplitude m_i, as defined in Chapter 4. For example, in the geoacoustic model in Table 4.2, there are 14 trapped modes present, although the mode at $k_{ri} = 0.8597293$ has a modal amplitude which is several times larger than any other mode. In Figure 5.9 is shown the magnitude and phase of the total field for this model and in Figure 5.10 is shown the magnitude and residual phase using $k_\phi = 0.8597293$. The smooth variation in the residual phase can be seen for this choice of k_ϕ. In the more general case, an appropriate choice for k_ϕ could
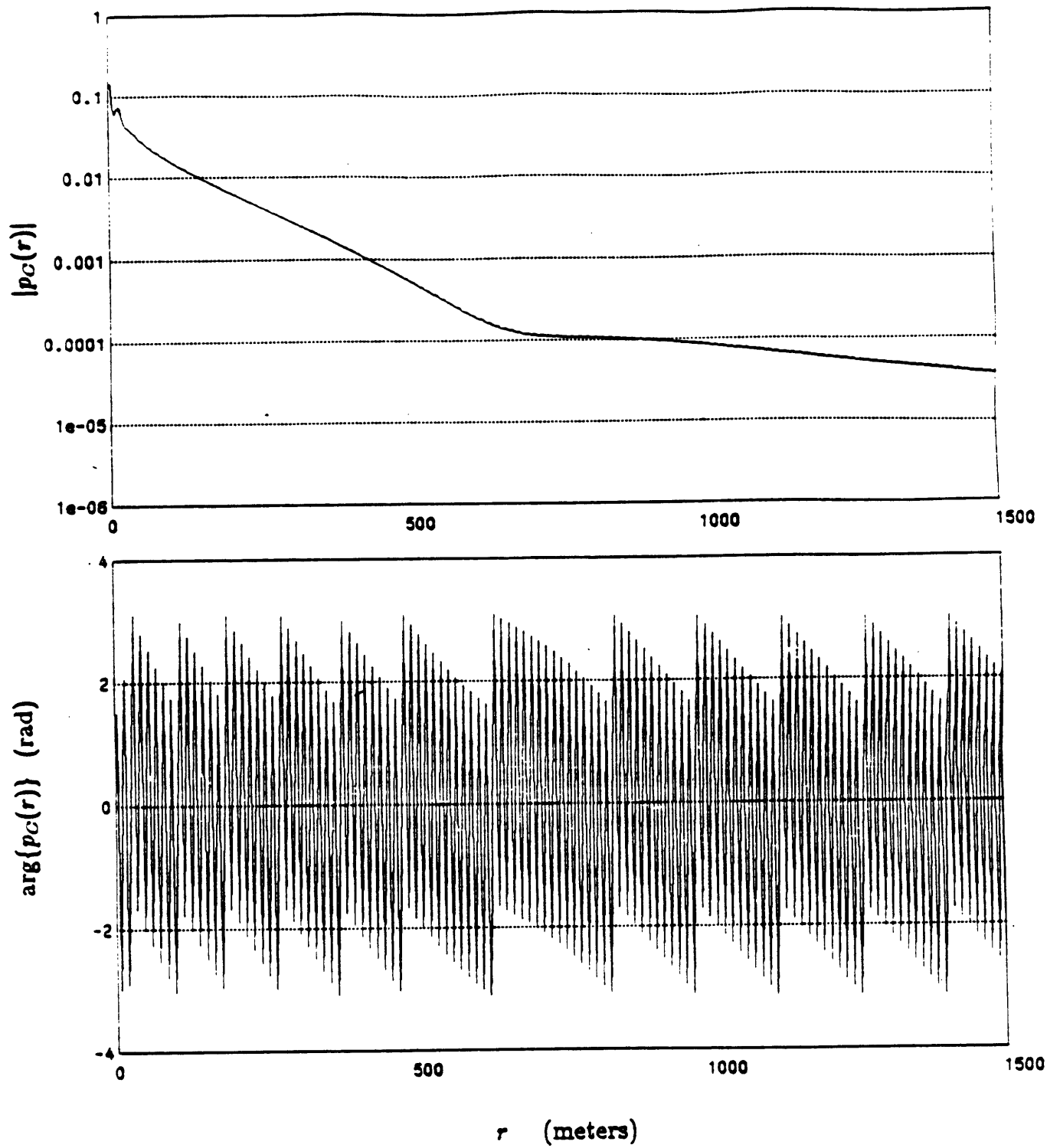
Figure 5.7: Magnitude and phase of the continuum portion of the Pekeris model shallow water field.
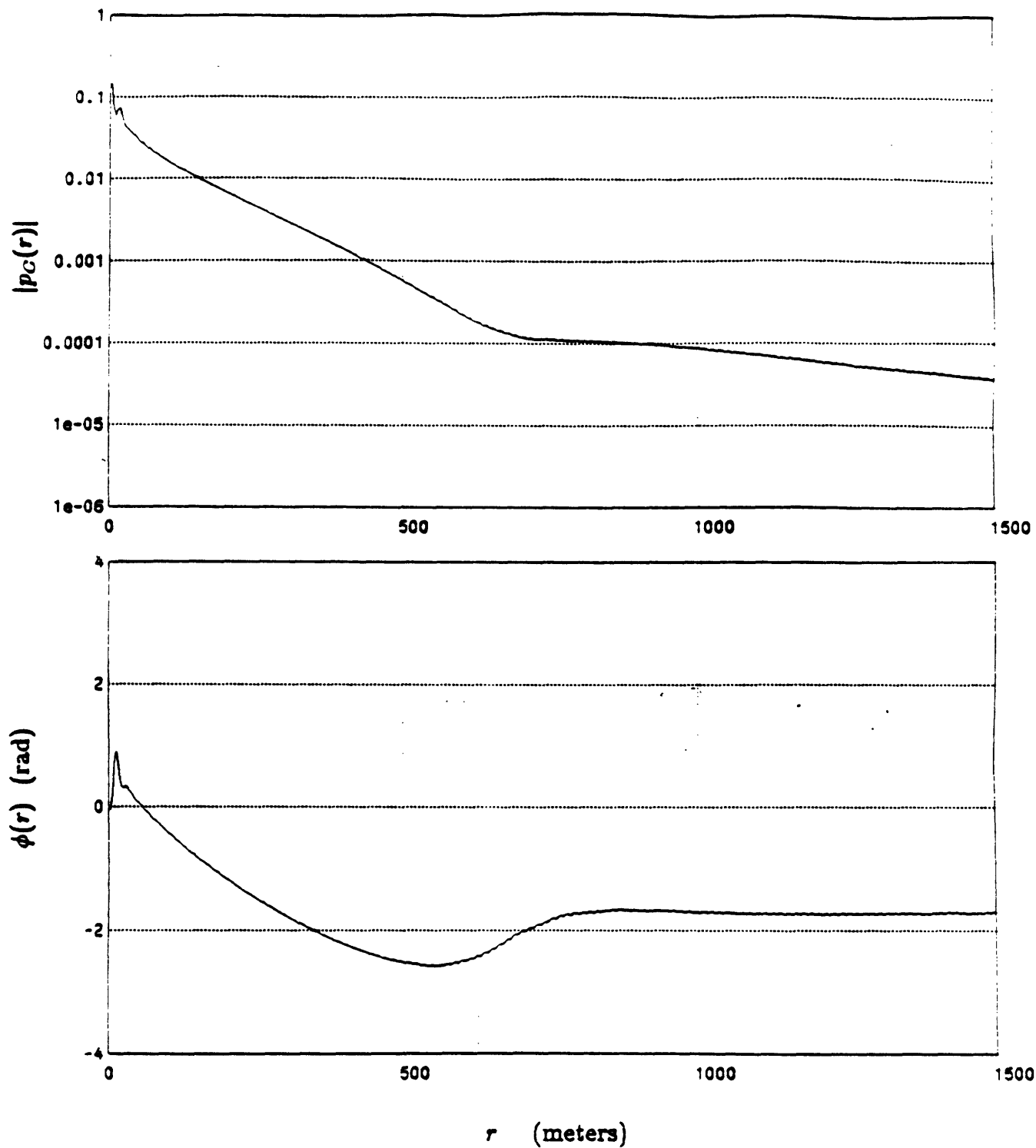
Figure 5.8: Magnitude and residual phase of the continuum portion of the Pekeris model shallow water field. k_o was chosen as the wavenumber in the underlying halfspace.
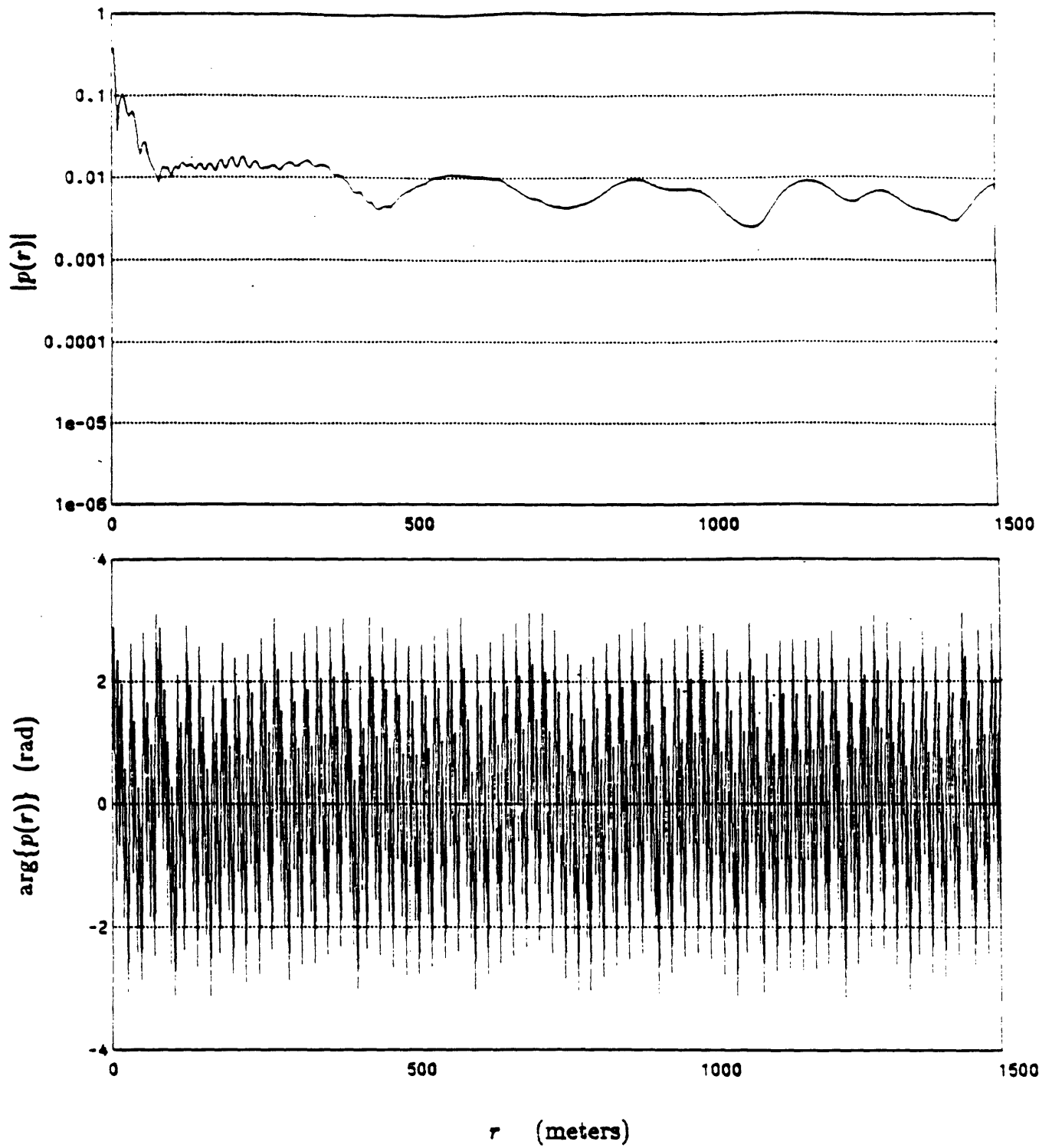
Figure 5.9: Magnitude and phase for the shallow water field described by the geoacoustic model in Table 4.2.
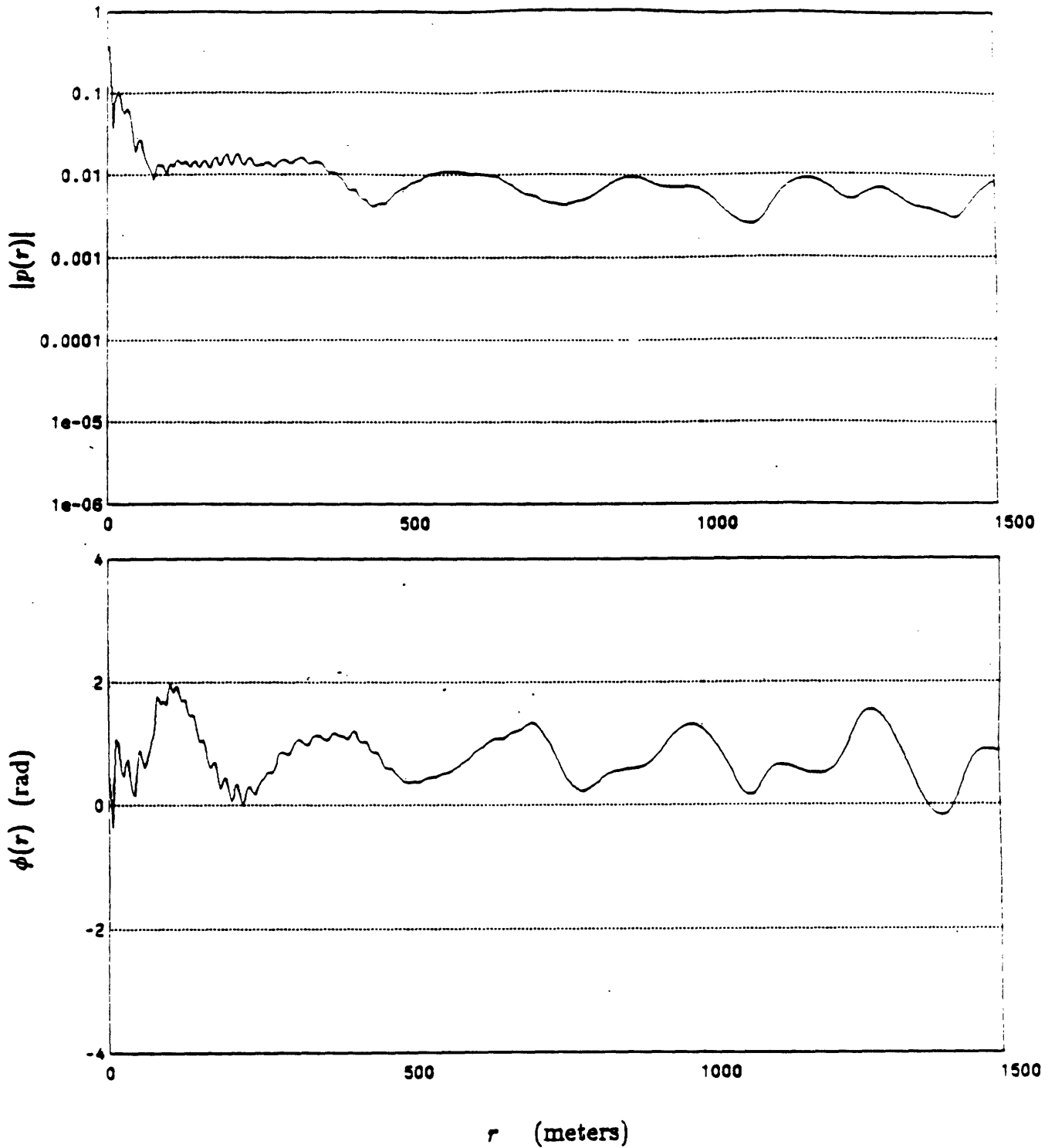
Figure 5.10: Magnitude and residual phase for the shallow water field described by the geoacoustic model in Table 4.2. k_o was chosen as the wavenumber of the dominant mode.

consist of a weighted average of the modal eigenvalues, where the weights are the modal amplitudes.

The residual phase may form a key element in characterizing acoustic propagation in more complicated range varying media as well. As an example of this, the magnitude and residual phase for the 140 Hz experimental shallow field collected in the Nantucket Sound in May 1984 [6] are shown in Figure 5.11. The value of k_ϕ used to determine the residual phase was chosen as 0.575. Several features are apparent from the examination of the residual phase for this example. First, although the residual phase is somewhat noisy, it exhibits no linear trend at ranges past 500 m for at least 700 m. This indicates that there is probably only a single mode present with a horizontal wavenumber of 0.575, accurate to at least three decimal places. In particular, if the wavenumber were in error by 0.001, an additional 0.001 $rad/m * 700$ $m = 0.7$ rad phase roll in the residual phase would occur over the range of 500 to 1200 m. No such behavior is observed however. The behavior of the residual phase in the near-field is partially obscured by the wrapping which occurs, and a display of the unwrapped residual phase might be more meaningful here. However, it is noted that a linear trend in the residual phase of approximately 4 /250 = 0.016 rad/m occurs within the near field and that the trend abruptly terminates at a range of 500 m. This behavior in the residual phase indicates that the dominant horizontal wavenumber has changed from 0.559 to 0.575 at the range cf 500 m. The exact reason for this change is not clear. However, an interesting speculation is that it is due to a variation with respect to range of the experimental geoacoustic model. In particular, the depth of the waveguide varied as a function of range in this experiment. The abrupt change in the residual phase could be attributed to a variation in the horizontal wavenumber of the dominant mode, caused by the change in waveguide thickness. We have not been able to precisely correlate the behavior of the phase with actual measurements of the waveguide thickness, obtained from an echosounding instrument. Nevertheless, a conjecture is that the change in the behavior of the residual phase is due to a range-dependent variation in the geoacoustic model. The example points out that the
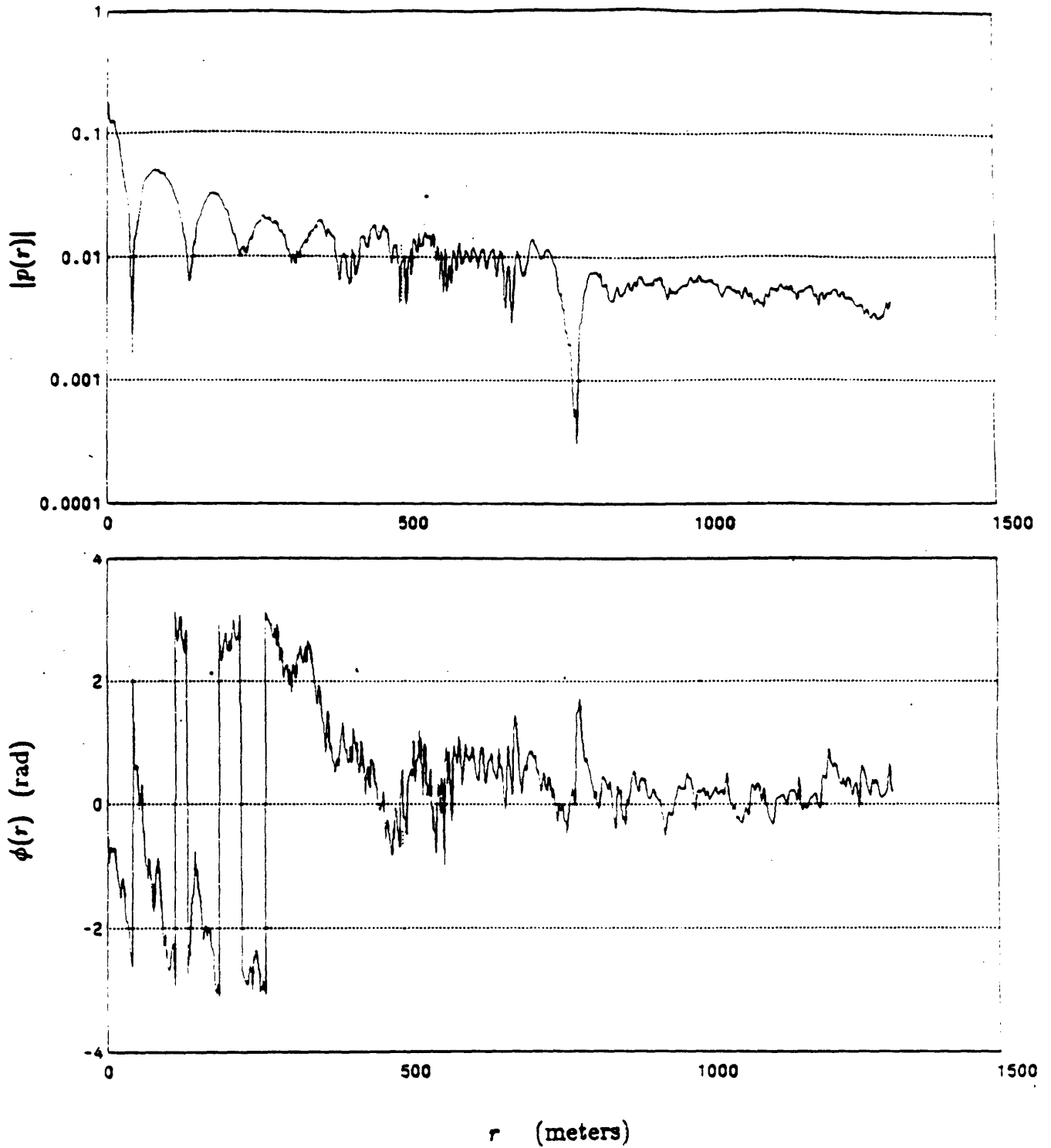
Figure 5.11: Magnitude and residual phase of the 140 Hz field from a shallow water experiment conducted in Nantucket Sound in May 1984. k_o was chosen as 0.575.

interpretation of the residual phase in range-dependent problems might be extremely interesting, and it is felt that this topic represents an area for further research.

Thus far, the residual phase has been defined in terms of the fixed parameter k_ϕ which is chosen to match the wavenumber of the dominant component of the field. It is also possible to allow the parameter k_ϕ to vary as a function of the position within the waveguide. Mathematically, the more general expression for residual phase can be expressed as

$$\phi(r) = P\{\theta(r, z) - k_\phi(r, z)r\} \qquad (5.13)$$

This generalization may provide the basis for improving forward modelling procedures involving more complicated range dependent models. For example, in the approach proposed by Bordley [12], forward modelling is performed by iteration of a paraxial method. Essentially, the acoustic wave equation is solved by guessing a value used to split the field into outgoing plus incoming components, applying a paraxial approximation, and determining a new split value from the apparent horizontal wavenumber of the resulting field. One of the problems with the technique is that the determination of the apparent horizontal wavenumber is difficult, as it requires that the derivative of the logarithm of the field be determined. Thus, since the logarithm is a multi-valued function, the phase of the field must be unwrapped prior to the computation of the derivative. The unwrapping of the rapidly varying phase has proven to be quite difficult in this context. Alternate techniques, such as computing the derivative of the field and dividing by the field, have other disadvantages, as pointed out by Bordley. The introduction of residual phase into this method may yield alternate algorithms which improve the performance of Bordley's method. For example, one approach might consist of determining the residual phase within an iteration using $k_\phi(r, z)$, unwrapping the residual phase prior to the computation of the derivative and then re-adding the term $k_\phi(r, z)$. Presumably, the residual phase is easier to unwrap as compared with the total phase, if $k_\phi(r, z)$ is properly chosen. However, it is possible to relate $k_\phi(r, z)$, used to determine the residual phase with the apparent horizontal

wavenumber. The implication is that within the iteration scheme $k_\phi(r,z)$ could be determined based on the apparent horizontal wavenumber in the past iteration.

In summary, we have defined the residual phase of a shallow water acoustic field and have discussed several applications. The residual phase was defined such that phase unwrapping is not required in its computation. Additionally, the residual phase was based on removing the product of a horizontal wavenumber and the horizontal range, as opposed to the product of the water wavenumber and the slant range. The definition is particularly important in shallow water propagation in which a particular dominant mode is present. Several synthetic and experimental examples confirmed that the residual phase can be important for establishing the wavenumber of the dominant mode, and also for determining the acoustic source phase. It was pointed out that the residual phase can be used for determining the dominant wavenumber component in a range dependent medium. There appear to be important applications for the residual phase when the wavenumber used to compute it is assumed to be spatially-varying. In this case, the residual phase may provide the basis for improving methods for forward modelling and inversion of range dependent acoustic fields.

5.3 Reflection Coefficient Sensitivity

In the previous section, we pointed out that the residual phase forms an additional quantity to the magnitude which is useful in forward modelling inversion methods. In another class of inversion methods, the inversion is based on computing the Hankel transform of the acoustic field to obtain the Green's function, extracting the reflection coefficient from the Green's function, and determining the geoacoustic model from the reflection coefficient. In this section, we will first review this technique and then point out that there is a fundamental instability which exists, in some circumstances, in the step of extracting the reflection coefficient from the Green's function. The points of instability, or infinite sensitivity, are then related to the invariant zeros of the Green's function and its imaginary part. These invariant zeros are due to the cancellation which can occur between various upgoing and downgoing components within the shallow water waveᴚuide.

The technique for obtaining the reflection coefficient of the ocean bottom from measurements of the shallow water acoustic field is based on the fact that the Hankel transform is its own inverse Since the acoustic pressure field is related to the shallow water Green's function via a Hankel transform, determining the Hankel transform of the field yields the Green's function. In an experimental context, the field measurements are not available out to an infinite range and in addition, are subject to a number of degradations including ranging uncertainty, non-uniform sampling and additive noise. Therefore, in computing the Hankel transform of these measurements, it is an estimate, rather than the Green's function itself which is obtained.

From the estimate of the Green's function it is possible to determine an estimate of the reflection coefficient. For example, in the case of an isovelocity waveguide with a pressure-release surface ($R_S = -1$), the relationship between the Green's function

and the reflection coefficient was shown to be

$$g(k_r) = \frac{2\sin k_z z_l}{k_z} \frac{(e^{jk_z z_s} + R_B(k_r)e^{jk_z(2h-z_s)})}{(1 + R_B(k_r)e^{j2k_z h})} \tag{5.14}$$

This expression can be algebraically inverted to yield an expression for the reflection coefficient in terms of the Green's function as follows

$$R_B(k_r) = \frac{2\sin k_z z_l e^{jk_z z_s} - g(k_r)k_z}{k_z e^{j2k_z h} g(k_r) - 2\sin k_z z_l e^{jk_z(2h-z_s)}} \tag{5.15}$$

In the case that only an estimate of $g(k_r)$ is available, the reflection coefficient, which is derived using this expression, is also an estimate.

In going from the expression for $g(k_r)$ in terms of $R_B(k_r)$ to the expression for $R_B(k_r)$ in terms of $g(k_r)$ only simple algebra was required. However, the transition from $g(k_r)$ to $R_B(k_r)$ actually represents the more fundamental operation of dereverberating the acoustic field [13]. In other words, by computing the Hankel transform of the field $p(r)$ within the waveguide and inverting algebraically to obtain $R_B(k_r)$, the result is identical to that which would have been obtained had the surface not been present. Phrased in terms of a filtering operation, a dereverberated field can be obtained by determining the wavenumber decomposition of the field within the waveguide (performing the Hankel transform), applying an inverse filter (determining $R_B(k_r)$ from $g(k_r)$), reapplying a new filter (multiplying by a new phase factor which corresponds to propagation from the source to the receiver) and resynthesizing the field (performing the Hankel transform).

The dereverberation of the field in this way also applies to more complicated, non-isovelocity waveguides. In particular, we have previously derived expressions which relate the extended Green's function to the reflection coefficient between the layer in which z_g resides and the underlying media. This reflection coefficient is in turn related to the ocean bottom reflection coefficient, i.e. the reflection coefficient at the water/sediment interface, via the reflectivity series, as described in Chapter 2. The use of the extended Green's function and the reflectivity series in this context is mentioned not only as a means for justifying that the dereverberation can be applied to

more complicated models, but also as the basis for a practical method for extracting the reflection coefficient which avoids the unwieldy algebra required for the determination of $R_B(k_r)$ in these cases. In the discussions which follow, we will tend to focus on the simpler isovelocity waveguide which has a pressure-release surface, with the implication that many of the results apply to more complicated waveguide models as well.

Although the relationship in equation (5.15) is mathematically exact, there may be values, or regions, of real-k_r at which the inversion is ill-conditioned. By ill-conditioned, we mean that a slight change in $g(k_r)$ may yield a large change in the reflection coefficient. In other words, at these values, $R_B(k_r)$ may be highly sensitive to changes in $g(k_r)$. In order to study this effect further, it is convenient to define a measure of the sensitivity, $S(k_r)$ referred to as the *sensitivity function* as follows

$$S(k_r) = |\frac{\partial R_B(k_r)}{\partial g(k_r)}| \tag{5.16}$$

From this definition, it is apparent that if the sensitivity function, $S(k_r)$ is large, then a small change in $g(k_r)$ is responsible for a large change in $R_B(k_r)$. Thus, when the sensitivity function is large, $R_B(k_r)$ is most sensitive to errors which occur in estimating $g(k_r)$. Computing the partial derivative of $R_B(k_r)$ for the isovelocity waveguide case, and expressing the result not as a function of $g(k_r)$ but rather as a function of $R_B(k_r)$, it can be shown that

$$S(k_r) = |\frac{k_z(1 + e^{j2k_z h} R_B(k_r))^2}{4 \sin k_z z_l \sin k_z z_s} e^{-j2k_z h}| \tag{5.17}$$

for values of real-k_r including evanescent values where $k_r > k_0$ and k_0 is the water wavenumber.

The numerator of the sensitivity function is related to the characteristic equation for the waveguide. As discussed previously, the zeros of the characteristic equation determine the poles of the Green's function, which in turn determine the modes of propagation. The sensitivity function thus has zeros at the values of k_r corresponding

311

to the trapped modes. The determination of the reflection coefficient is particularly insensitive to errors in $g(k_r)$ at these values of k_r. This fact is not surprising as $g(k_r)$ is quite large in regions near the poles and one could expect a unit change in $g(k_r)$ to have a small effect in the determination of $R_B(k_r)$ here. Similarly, at real values of k_r corresponding to the virtual modes, i.e. off-axis poles, the sensitivity function will have local minima and thus we expect to obtain a less sensitive estimate of the reflection coefficient at these values of k_r. If the source or receiver is located in a null of a trapped mode then both the numerator and denominator of the sensitivity function are zero. A straightforward application of L'Hopital's rule shows that the sensitivity is zero in this case as well. Additionally, it can be seen that the numerator and denominator of the sensitivity function become zero when k_z is identically zero, i.e when $k_r = k_0$. Application of L'Hopital's rule to this case also indicates that $S(k_r) = 0$. However, this result depends on the fact that, for real k_0,

$$R_B(k_r)|_{k_r=k_0} = -1 \tag{5.18}$$

for any underlying bottom, a interesting fact which can be proved using the properties of the reflectivity series discussed earlier. The implication is that the sensitivity is zero due to the fact that the reflection coefficient is known a priori to be -1, at this value of k_r. However, if there are any slight deviations in the underlying model which cause the reflection coefficient to depart from this value, for example a very slight roughness at the interface, the sensitivity function becomes infinite at $k_r = k_0$. This value represents an interesting special case of the theory which we are about to present.

Note also, that for values of k_r greater than the water wavenumber, the sensitivity function does not depend strongly on $R_B(k_r)$, and for $k_r \gg k_0$, the sensitivity function approaches

$$S(k_r) = \gamma e^{\gamma(2h-(z_s+z_l))} \tag{5.19}$$

where $\gamma = +(k_r^2 - k_0^2)^{1/2}$. From this expression, it can be seen that for z_s and z_l near the bottom of the waveguide, the sensitivity function increases slowly as a function

of k_r for $k_r > k_0$. However, as z_q and z_l become smaller, i.e. the source and receiver are located at shallower depths, the sensitivity function increases at an exponential rate for $k_r > k_0$. The implication is that determination of the reflection coefficient becomes increasingly more sensitive as the source and receiver are moved away from the bottom, for values of $k_r > k_0$.

Such an effect has also been noted for the deep water case. That is, as the source and receiver heights, z_0 and z, become larger in a deep water experiment, accurate determination of the reflection coefficient at values of $k_r > k_0$ becomes more difficult. This result can also be predicted by computing the sensitivity function for the deep water case, which can be shown to be

$$S(k_r) = |k_z e^{-jk_z(z+z_0)}| \tag{5.20}$$

for values of real-k_r including evanescent values where $k_r > k_0$. We note that for values of $k_r \gg k_0$, the deep water and shallow water sensitivity functions are identical due to the fact that the vertical wavenumber is purely imaginary - the surface has no effect due to the exponential decay of the field in the vertical direction. However, for values of $k_r < k_0$ the deep water sensitivity function is considerably simpler than the shallow water sensitivity function as can be seen by comparing equations (5.20) and (5.17). In particular, the sensitivity function for the deep water case is a smoothly varying function of k_r which decreases from k_0 to zero as k_r varies from zero to k_0. The deep water sensitivity function does not exhibit the interesting behavior of the shallow water sensitivity function and it will not be further considered in this section. We will refer to equation (5.17) as the definition of the sensitivity function henceforth.

As can be seen from equation (5.17), the sensitivity function may become infinite at values of real-k_r which are solutions [3] to either

$$\sin k_z z_l = 0 \tag{5.21}$$

---

[3]Strictly speaking, this is true only for the non-trivial solutions, i.e, for $k_r \neq k_0$. However, as discussed earlier, the point $k_r = k_0$ is a special case at which the sensitivity function is zero in theory, but actually infinite in practice, if any deviation in the assumed model is allowed.

$$\sin k_z z_g = 0 \qquad\qquad (5.22)$$

It is noted that these value are independent of the reflection coefficient and thus *independent* of the media underlying the waveguide - they depend only on the depths of the source and receiver and the water wavenumber.

In fact, by examining the form of the Green's function in equation (5.14), the fact that one of these equations appears becomes obvious. At values of k_r which satisfy the equation $\sin k_z z_l = 0$, the sensitivity becomes infinite and the Green's function becomes identically zero. Essentially, at these values, $g(k_r)$ contains no information, at least in its zeroth derivative, regarding the reflection coefficient - the Green's function becomes zero *independent* of the value of $R_B(k_r)$. A key point here is that the infinite sensitivity occurs not because the Green's function becomes zero, but rather because it becomes zero independent of $R_B(k_r)$. As will be pointed out later, there may exist other zeros of $g(k_r)$ at which the sensitivity does not exhibit this behavior. In addition, points of infinite sensitivity predicted by the equation $\sin k_z z_g = 0$ do not correspond to zeros of $g(k_r)$.

It is also possible to relate the other equation, i.e. equation (5.22) for points of infinite sensitivity to the Green's function. To do this, the Green's function in equation (5.14) is written in terms of its real and imaginary parts. Performing the required algebra, we find that

$$g_R(k_r) \equiv Re\{g(k_r)\} = \frac{2\sin k_z z_l}{k_z}\frac{[(1+a^2)\cos k_z z_g + 2a\cos(\theta + k_z(2h-z_g))]}{(1+2a\cos(\theta+2k_z h)+a^2)} \qquad (5.23)$$

$$g_I(k_r) \equiv Im\{g(k_r)\} = \frac{2\sin k_z z_l \sin k_z z_g (1-a^2)}{k_z(1+2a\cos(\theta+2k_z h)+a^2)} \qquad (5.24)$$

for real values of k_r less than k_0 where $a = a(k_r) = |R_B(k_r)|$ and $\theta = \theta(k_r) = arg\{R_B(k_r)\}$. From equation (5.24) for the imaginary part of $g(k_r)$, it can be seen that $g_I(k_r)$ becomes zero at the points of infinite sensitivity described by the equation $\sin k_z z_g = 0$. Furthermore, from equation (5.23), the real part of $g(k_r)$ is $\pm 2\sin k_z z_l / k_z$ at these values. This fact follows since $\cos k_z z_g = \pm 1$ when $\sin k_z z_g = 0$ and from the

use of trigonometric identities applied to the numerator of equation (5.23). The infinite sensitivity results because $g(k_r)$ contains no information about $R_B(k_r)$ at values of k_r which are solutions to $\sin k_z z_s = 0$ - the imaginary part of $g(k_r)$ is identically zero and the real part is $\pm 2 \sin k_z z_l / k_z$, a quantity *independent* of $R_B(k_r)$.

Thus far, we have shown that points of infinite sensitivity imply that either $g(k_r)$ is zero or else its imaginary part $g_I(k_r)$ alone is zero. We will refer to these zeros as *invariant zeros* because they do not depend on the reflection coefficient and are thus invariant with respect to the media underlying the waveguide. We will distinguish between the two types of zeros, although it is recognized that the imaginary part of $g(k_r)$ is zero in either case. In fact, the presence of invariant zeros of $g(k_r)$ and $g_I(k_r)$ has not been previously pointed out in the literature. The existence of these zeros which do not depend on the properties of the underlying media is quite interesting because the Green's function itself is highly dependent on the underlying media. The fact that $g(k_r)$ and $g_I(k_r)$ are known a priori to be zero at these locations may represent an important piece of information in an inversion scheme. Because of the potential importance of exploiting the positions of these points, and because of the important connection between the invariant zeros and the points of infinite sensitivity, several statements concerning the zeros and invariant zeros of $g(k_r)$ and $g_I(k_r)$ are now made.

The terminology of pre-critical and post-critical will refer respectively to real values of $k_r \leq Re\{k_N\}$ and real values of $k_r > Re\{k_N\}$ where k_N is the wavenumber of the underlying halfspace. We will assume that k_0 is purely real, i.e. that there is no attenuation in the water column, and that $Re\{k_N\} < k_0$, as is typically the case. Additionally, only real zeros will be considered. We will distinguish a zero of $g_I(k_r)$ as a particular value of k_r at which the imaginary part of $g(k_r)$ is zero and the real part is non-zero.

Statement 1 *All pre-critical zeros of $g(k_r)$ must be invariant and must satisfy the equation $\sin k_z z_l = 0$.*

Statement 2 *Post-critical zeros of $g(k_r)$ may or may not be invariant. If invariant, they must satisfy $\sin k_z z_l = 0$.*

Statement 3 *Any zero which occurs in the region $Re\{k_r\} > k_0$ cannot be invariant.*

Statement 4 *All pre-critical zeros of $g_I(k_r)$ must be invariant and must satisfy $\sin k_z z_s = 0$.*

Statement 5 *There are no isolated post-critical zeros of $g_I(k_r)$ if k_N is purely real.*

The proof of these statements is straightforward. Statement 1 follows directly from equation (5.14) and also from the fact that the reflection coefficient magnitude, a must be less than unity for pre-critical values of k_r. The latter fact follows from the properties of the reflectivity series, discussed in Chapter 2. Statement 2 follows from equation (5.14) and the fact that additional zeros of $g(k_r)$ can occur in this region since a may be unity. Statement 3 follows from the fact that $\sin k_z z_l$ cannot be zero for purely imaginary k_z. Statement 4 follows directly from equation (5.24) and the fact that a must be less than unity at pre-critical values of k_r. Statement 5 follows from the fact that $g_I(k_r) = 0$ for all real values of $k_r > k_N$, a fact proved in Chapter 2, and equation (5.24). We will next present several statements which relate the invariant zeros of $g(k_r)$ and $g_I(k_r)$ to points of infinite sensitivity.

Statement 6 *All pre-critical zeros of $g(k_r)$ or $g_I(k_r)$ must be points of infinite sensitivity. In addition, all pre-critical points of infinite sensitivity must occur at zeros of $g(k_r)$ or $g_I(k_r)$. In both cases, these points are invariant.*

Statement 7 *All post-critical points of infinite sensitivity, except those due to poles in $R_B(k_r)$, must satisfy either $\sin k_z z_l = 0$ or $\sin k_z z_s = 0$. If $\sin k_z z_l = 0$ is satisfied, the point is an invariant zero of $g(k_r)$.*

316

Statement 8 *All post-critical solutions of either* $\sin k_z z_l = 0$ *or* $\sin k_z z_q = 0$ *are points of infinite sensitivity unless* $1 + R_B(k_r)e^{j2k_z h} = 0$ *is satisfied. If the latter equation is satisfied, the corresponding value of* k_r *is a point of zero sensitivity.*

The proof of these statements is straightforward. Statement 6 follows from equation (5.17) and from Statements 1 and 4. Statement 7 follows from equation (5.17) and from Statement 2. Statement 8 follows from equation (5.17), Statement 2, and L'Hopital's rule. The second statement in statement 8 occurs when either the source or receiver is positioned exactly in the null of a perfectly trapped mode.

A numerical example demonstrating some of the statements related to the invariant zeros and the associated peaks in the sensitivity function is now provided. The geoacoustic model is identical to the model previously considered in Chapter 4, Table 4.1. The magnitude and phase of the Green's function corresponding to this model are shown in Figure 5.12. The water wavenumber in this example is $k_0 = 0.5866652$, and the wavenumber in the underlying halfspace is $k_N = k_1 = 0.488888$. By examining these curves, we can see that an invariant zero of $g(k_r)$ is present at $k_r \approx 0.28$. The location of this zero is evident because the magnitude function becomes zero here, and further this zero must be invariant (Statement 1). It can be verified that this zero satisfies the equation $\sin k_z z_l = 0$, and that its exact value is 0.28033. Additionally, there exists an invariant zero of $g_I(k_r)$ at $k_r \approx 0.375$. The location of this zero is evident because of the behavior of the phase at this point. Since the phase is either $\pm \pi$ or zero, the imaginary part of $g(k_r)$ must be zero. This zero of $g_I(k_r)$ must be invariant (Statement 4). It can be verified that this zero satisfies the equation $\sin k_z z_q = 0$, and that its exact value is 0.38052. Note that the phase function also crosses zero at $k_r = 0.48888$. However, this point is related only to the halfspace velocity since $g_I(k_r)$ must be zero for k_r greater than 0.48888. Therefore, this point is not an invariant zero (Statement 5) and thus not a point of infinite sensitivity (Statement 6). Additionally, we note that another zero of $g(k_r)$ is present at $k_r \approx 0.51$. This zero may or may not be invariant (Statement 2). It turns out in this case, that it is not because it does not
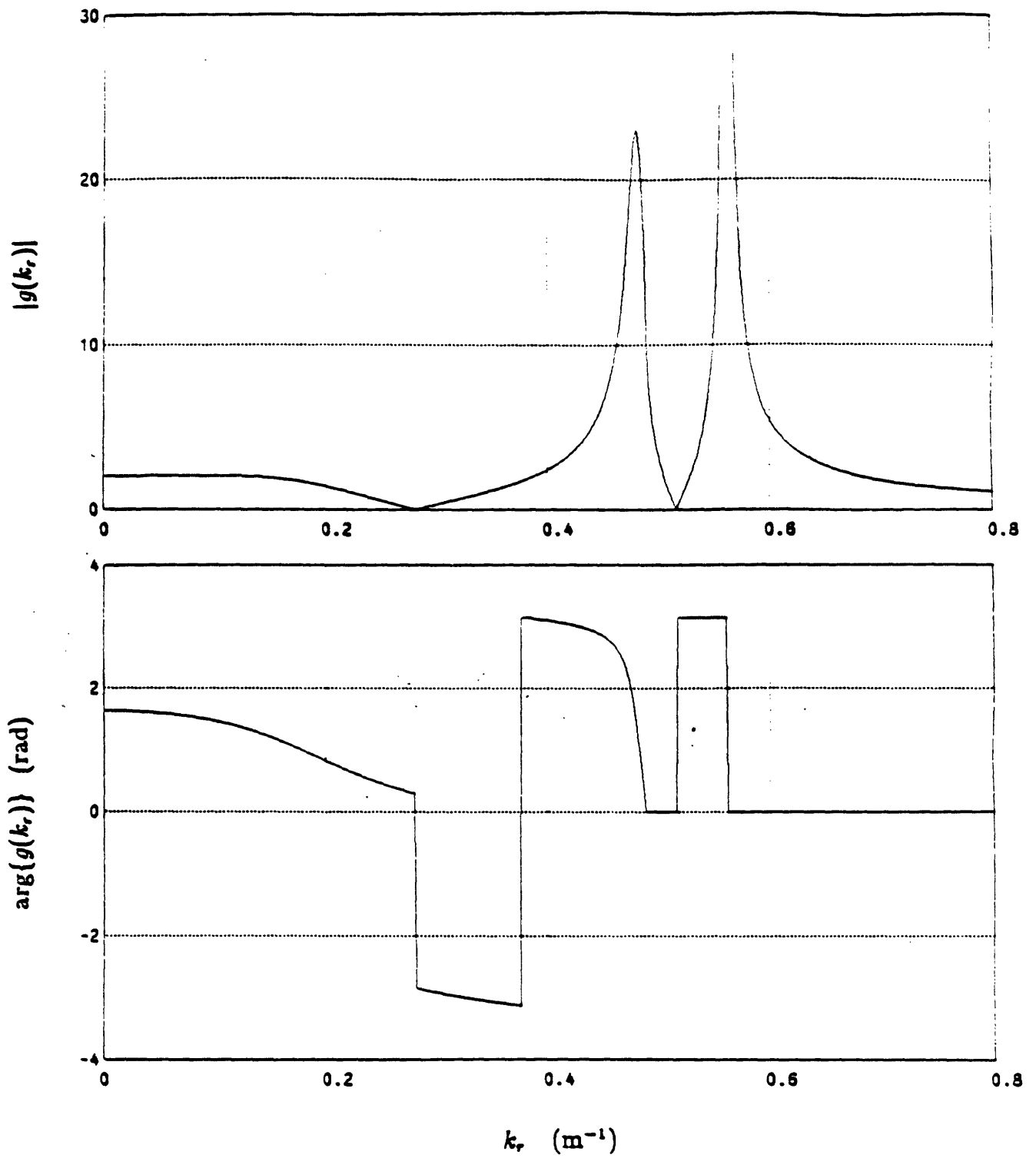
Figure 5.12: Magnitude and phase of the Pekeris model Green's function.

satisfy the equation required for an invariant zero of $g(k_r)$, $\sin k_z z_l = 0$ (Statement 2). In fact the position of this zero depends strongly on the phase of the reflection coefficient.

For reference, a plot of the sensitivity function for this model is included in Figure 5.13. Note from this figure that there are two points of infinite sensitivity which correspond exactly to the two invariant zero positions (Statement 6). In addition, the presence of a local minimum at the virtual mode location is noted, as is the point of zero sensitivity at the trapped pole location. For values of k_r greater than the water wavenumber, i.e. in the evanescent region, the sensitivity function increases at an exponential rate as a function of k_r, as predicted by equation (5.19).

The geoacoustic model summarized in Table 5.1 was next considered. Note that this model differs significantly from the model just considered - the depth of the water column has increased, and the properties of the underlying media have changed from a lossless isovelocity halfspace, to a layer with velocity gradient and attenuation overlying a halfspace with attenuation. As can be seen from the plot of the magnitude and phase of the corresponding Green's function in Figure 5.14, two additional modes have appeared in this model due to the increased thickness of the waveguide and presence of an additional layer. Nevertheless, the zero of $g(k_r)$ (indicated by the zero in the amplitude function) and the zero in $g_I(k_r)$ (indicated by the phase behavior) remain in identical locations as in the previous model, confirming their invariant nature. Note that the zero present at $k_r \approx 0.51$ in the first model is not present in the same position in the second model, in support of the conclusion that this zero is not invariant. For reference, a plot of the sensitivity function for the model in Table 5.1 is shown in Figure 5.15. The correspondence between the nulls in the sensitivity function and the positions of the peaks in the magnitude of the Green's function is apparent. Note that the sensitivity function for the second model grows at a substantially faster rate than that of the first model. This is due to the fact that although the source and receiver depths have not been altered, their relative distance

319
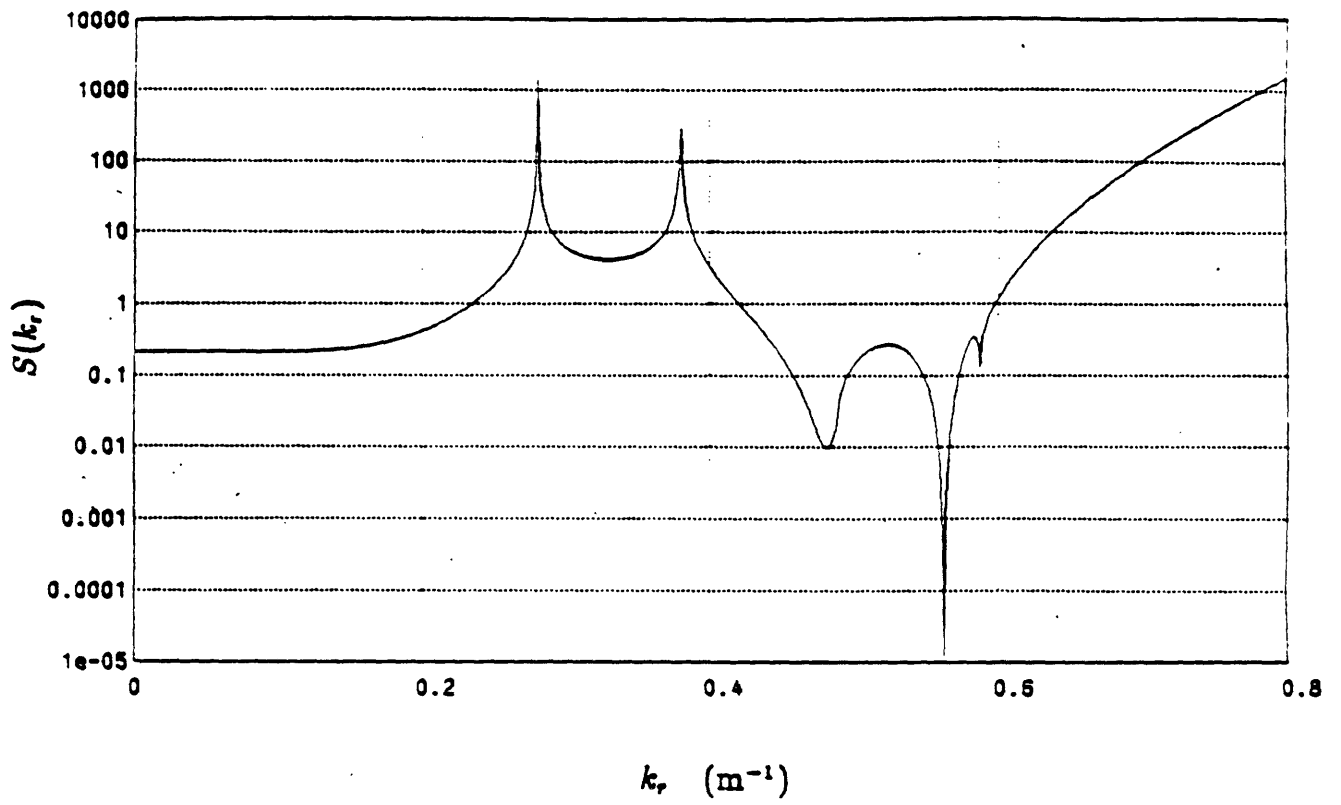
Figure 5.13: Sensitivity function for the Pekeris model Green's function.

$$25\ m \qquad 1500\ m/s \qquad 1530\ m./s \qquad \rho = 1.0\ g/cm^3$$

WATER

BOTTOM

LINEAR
GRADIENT $= 14s^{-1}$

$\rho = 1.7\ g/cm^3$

$\alpha = 0.1\ dB/\lambda$

$15\ m$

$1740\ m/s$

$\rho = 1.7\ g/cm^3$

$\alpha = 0.1\ dB/\lambda$
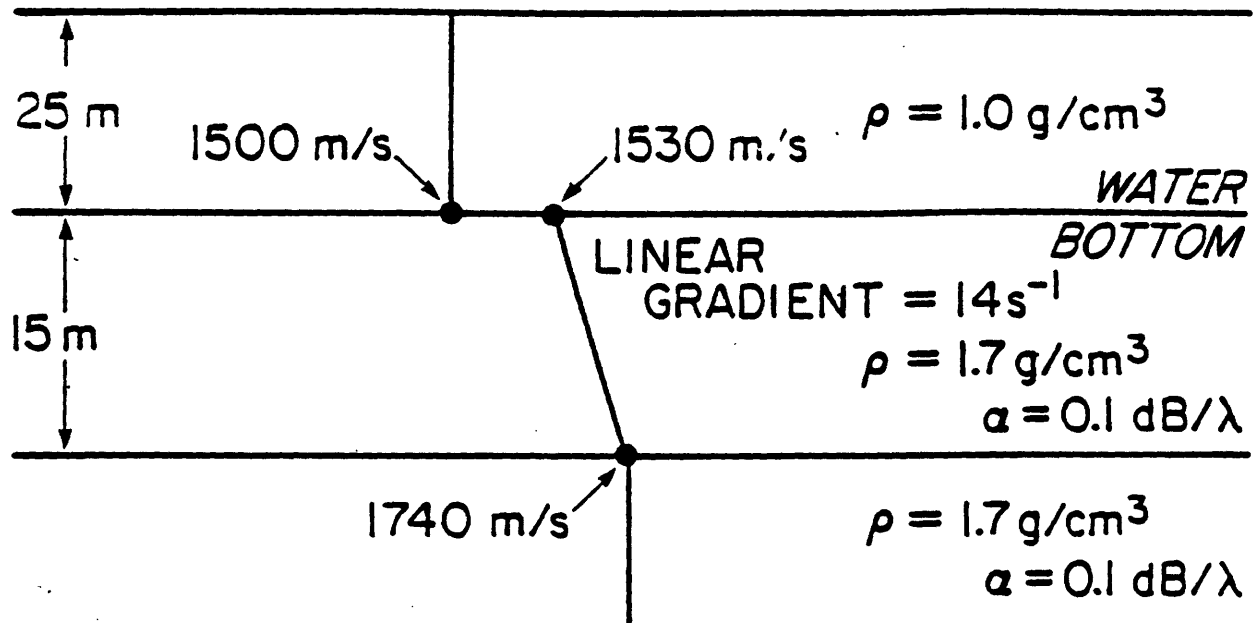
z_0	$=$	6.096 m
z	$=$	7.03579 m
f	$=$	140.056 Hz

Table 5.1: Geoacoustic model for a realistic shallow water case.

321
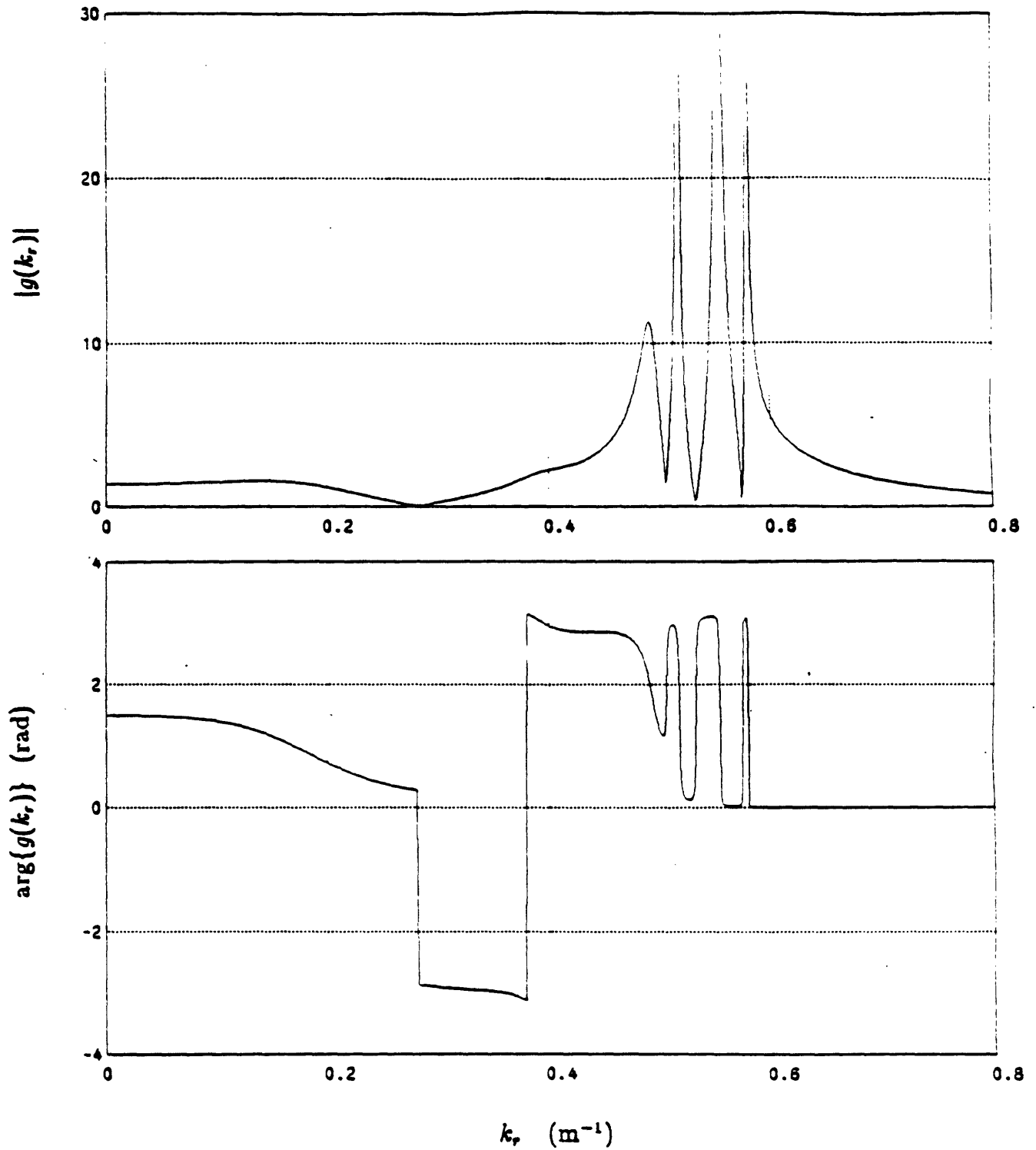
Figure 5.14: Magnitude and phase of the Green's function for the geoacoustic model described in Table 5.1.
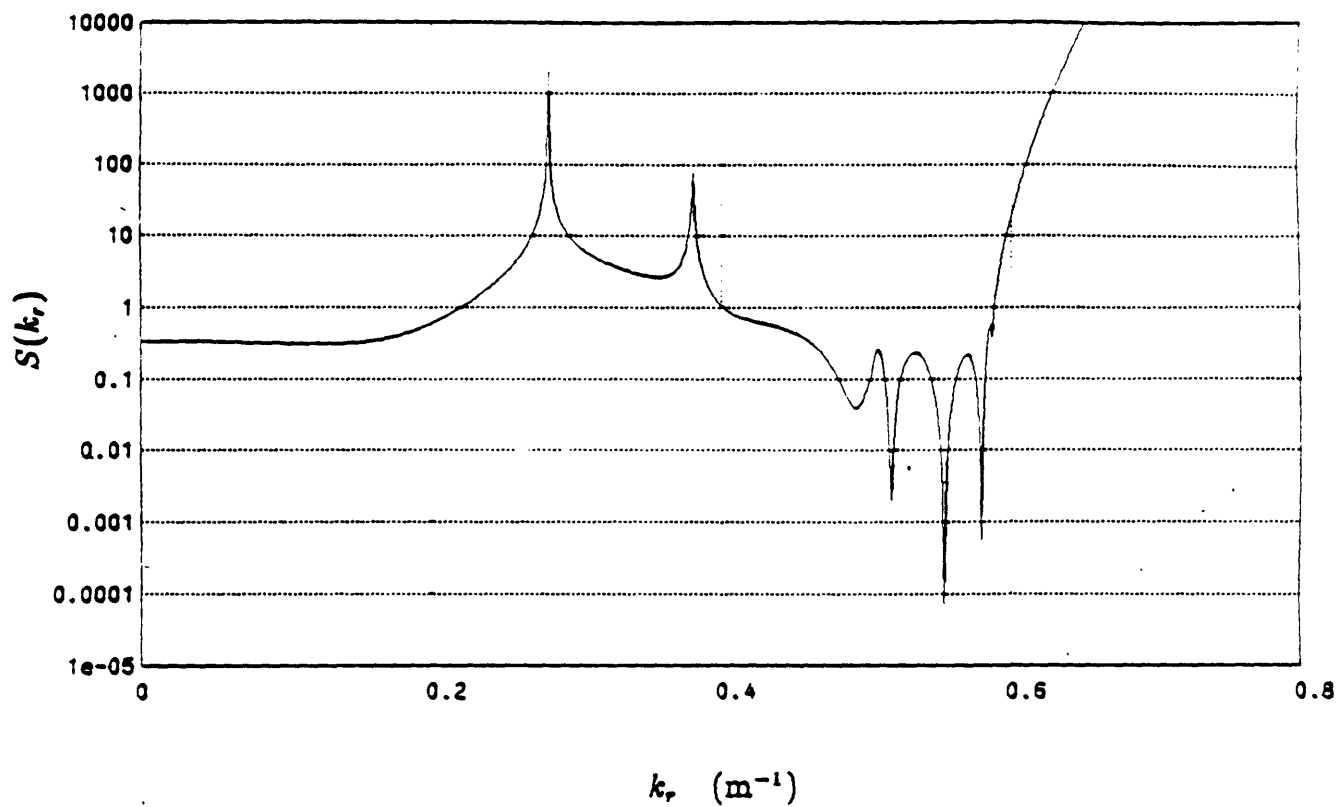
Figure 5.15: Sensitivity function for the geoacoustic model described in Table 5.1.

from the bottom has increased, due to the increased thickness of the waveguide. Also, note that although the sensitivity function is substantially different than the previously displayed sensitivity function, both exhibit infinite sensitivity at the same values of k_r, because of the invariant nature of these points.

In the preceding discussion, the sensitivity function was related to the Green's function primarily as a means for simplifying the determination of the peaks in sensitivity. The discussion implied that the sensitivity of inverting the Green's function to obtain the reflection coefficient can be discerned from a plot of the Green's function itself. [4] The peaks in sensitivity occur at invariant zero locations and minima occur at pole locations - either trapped or virtual. However, the connection between the sensitivity function and the Green's function also provides a basis for a more physical explanation for these invariant zeros and associated infinite peaks in sensitivity. This explanation is now provided.

In Chapter 2, it was pointed out that one of the ways in which to derive the Green's function is based on a plane wave decomposition of the source into an upgoing and a downgoing plane wave at each value of horizontal wavenumber. It was shown that the acoustic field at the receiver, when decomposed into a plane wave representation, consists of the infinite sum of four types of plane wave components - those downgoing at the source and downgoing at the receiver (dd), those upgoing at the source and downgoing at the receiver (ud), those downgoing at the source and upgoing at the receiver (du), and those upgoing at the source and upgoing at the receiver (uu). In Figure 5.16 several of the infinite number of plane waves which arrive at the receiver are symbolically illustrated within the waveguide. The type of component has been labelled in the figure as uu, ud, du, or dd and in addition, has been subscripted to indicate the additional number of interactions it has had with both the surface and

---

[4]There is actually one case when this is not strictly true. If k_N is purely real, any post-critical points of infinite sensitivity are not easily seen in the behavior of the Green's function. Here the real part of $g(k_r)$ is non-zero and the imaginary part is zero due to the fact that $k_r > k_N$.
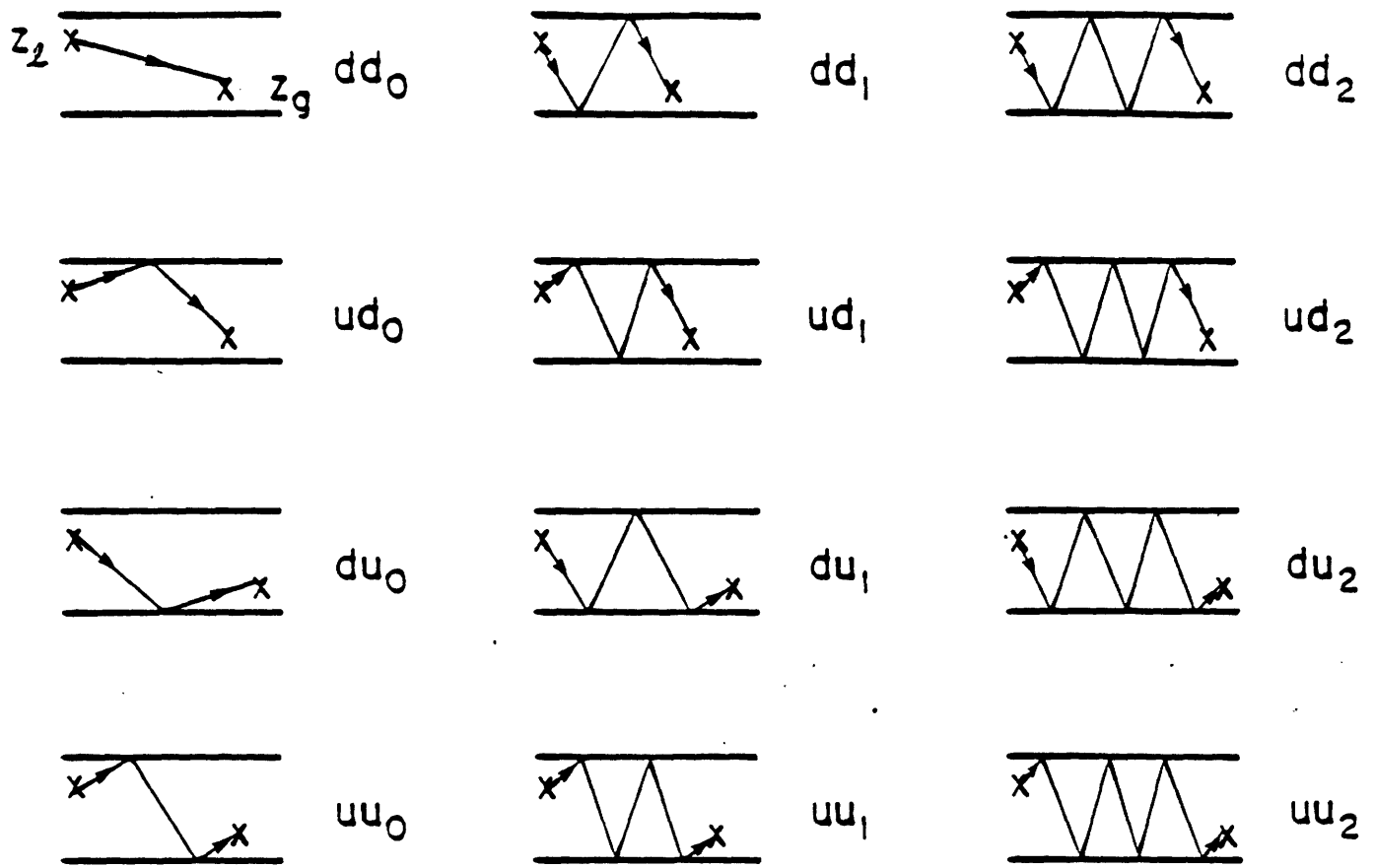
Figure 5.16: Symbolic diagram of multiple components within a waveguide.

bottom. For example, the plane wave component labelled ud_1 in this figure is upgoing at the source, downgoing at the receiver and has had one additional reflection from both the surface and bottom of the waveguide as compared with component ud_0. We have arbitrarily placed the source at a shallower depth than the receiver in this example, although this choice is of no significance from reciprocity - the alternate choice simply reverses the direction of all arrowheads in this figure. Note that the angles at which the various plane wave components interact with the surface and bottom are only symbolic - in fact, all components shown plus the remaining higher order multiples not shown correspond to a single value of k_r, i.e. a single angle of incidence, in the plane wave expansion of the field. The components in this diagram represent plane waves and not eigenrays.

Using the diagram shown in Figure 5.17, it is possible to show that various plane wave components can interfere with each other under certain conditions. For example, consider the components dd_0 ud_0 du_0 and uu_0. It is possible for dd_0 and ud_0 to cancel and for du_0 and uu_0 to cancel. Note that the component ud_0 undergoes an additional phase rotation of $e^{j2k_z z_i}$ in propagating from z_i to z_s as compared with component dd_0, excluding any other phase change due to its interaction with the surface. Therefore, excluding surface interaction, these two components will arrive perfectly in phase at z_s if the phase factor $e^{j2k_z z_i}$ is unity. However, the surface reflection coefficient is actually -1 and therefore if the phase factor is unity, the two components will actually arrive at z_s perfectly *out* of phase. In other words, if the condition $k_z z_i = n\pi$ is met, where n is any positive non-zero integer, the components dd_0 and ud_0 will cancel exactly. By examining Figure 5.17, it can be seen that if this condition is satisfied, components du_0 and uu_0 will cancel also. Note that this cancellation will occur even though du_0 and uu_0 have undergone a reflection at the bottom of the waveguide. In general, the amplitude and phase of these two components will be modified after interaction with the bottom. The important point however, is that both interact exactly once with the bottom, and are thus modified *identically* . In other words, these two components undergo a cancellation which
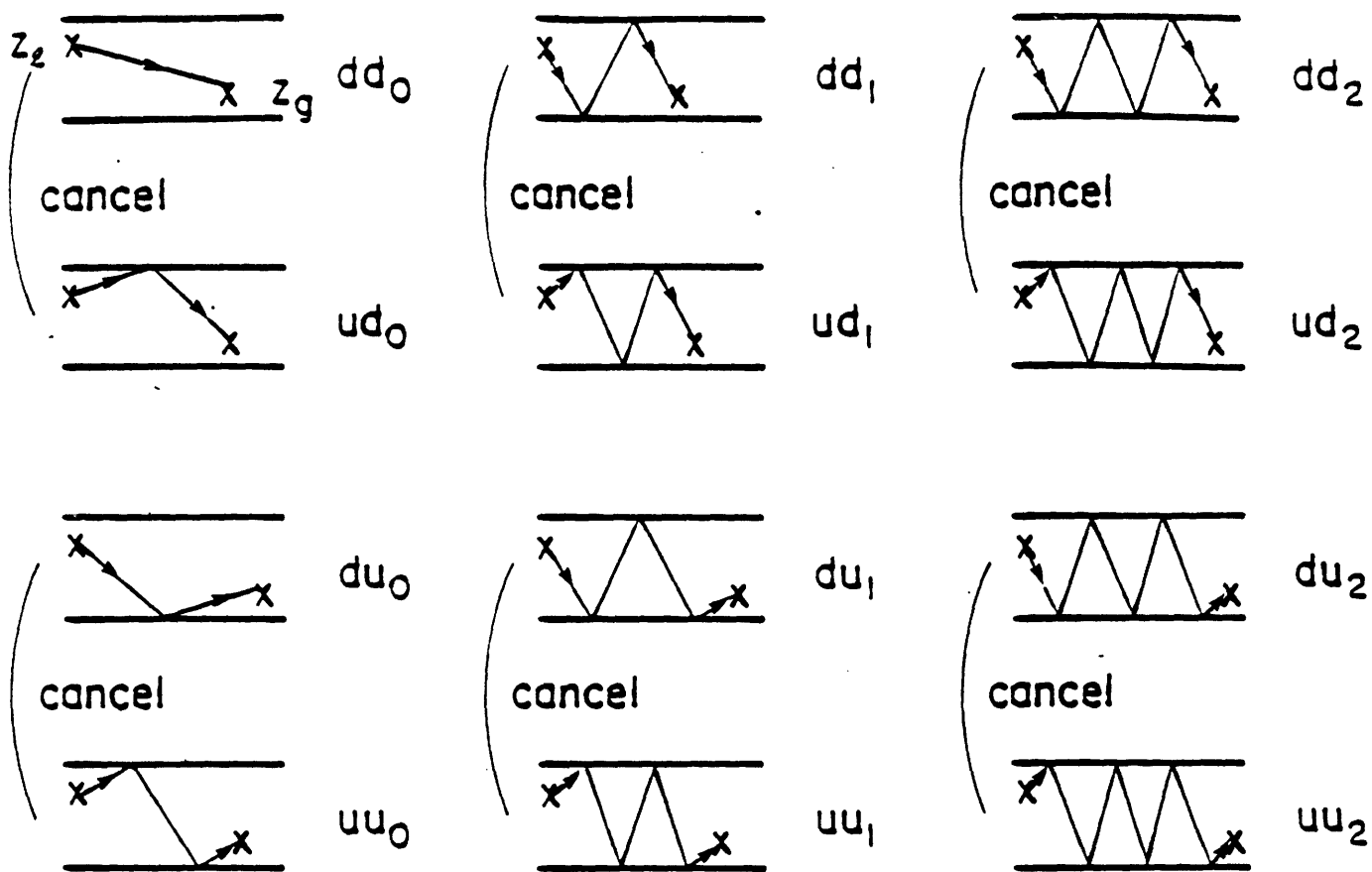
Figure 5.17: Symbolic diagram of components within a waveguide indicating the cancellation which yields a zero in $g(k_r)$.

is invariant with respect to the properties of the bottom. In fact, it can be easily shown that higher order components will cancel in an similar fashion, if the condition $k_z z_l = n\pi$ is satisfied. This cancellation will occur even though the higher order multiples experience a larger number of bottom interactions. It is apparent that the condition $k_z z_l = n\pi$ is equivalent to the condition $\sin k_z z_l = 0$, which is the equation for an invariant zero of $g(k_r)$. The Green's function is identically zero for values of k_r which satisfy $\sin k_z z_l = 0$ because of the cancellation which occurs between components in the plane wave expansion. The corresponding sensitivity in inverting for $R_B(k_r)$ also becomes infinite at these values because there is no information about the bottom present due to cancellation between components dd_i and ud_i and between components du_i and uu_i for all $i \geq 0$.

We have previously seen that infinite sensitivity can also occur at other values of k_r which satisfy the equation $\sin k_z z_s = 0$. These values are also determined by a second type of interference which can occur within the waveguide. In this case, cancellation occurs between a lower order multiple and the next higher multiple, as depicted symbolically in Figure 5.18. Note that all components which cancel interact with the bottom an identical number of times. The cancellation is again invariant with respect to bottom properties as well as to waveguide thickness. Furthermore, it is apparent from Figure 5.18 that under the condition that $\sin k_z z_s = 0$, all components will cancel in pairs *except* for components dd_0 and ud_0. There are no remaining components to which these two can be paired and they do not cancel each other. Therefore, we expect that the Green's function will be non-zero at these values of k_r and that it will be comprised only of the sum of these two components, as follows

$$g(k_r) = \frac{j}{k_z}(e^{jk_z(z_s-z_l)} - e^{jk_z(z_s+z_l)}) = \pm\frac{2\sin k_z z_l}{k_z} \tag{5.25}$$

since $e^{jk_z z_s} = \pm 1$ at these values of k_r. Note that $g(k_r)$ is purely real, and that this is precisely the result which was presented earlier when the real and imaginary parts of $g(k_r)$ were determined under the condition that $\sin k_z z_s = 0$.

The relationship between the invariant zeros of $g(k_r)$ and $g_I(k_r)$ and the points of

328
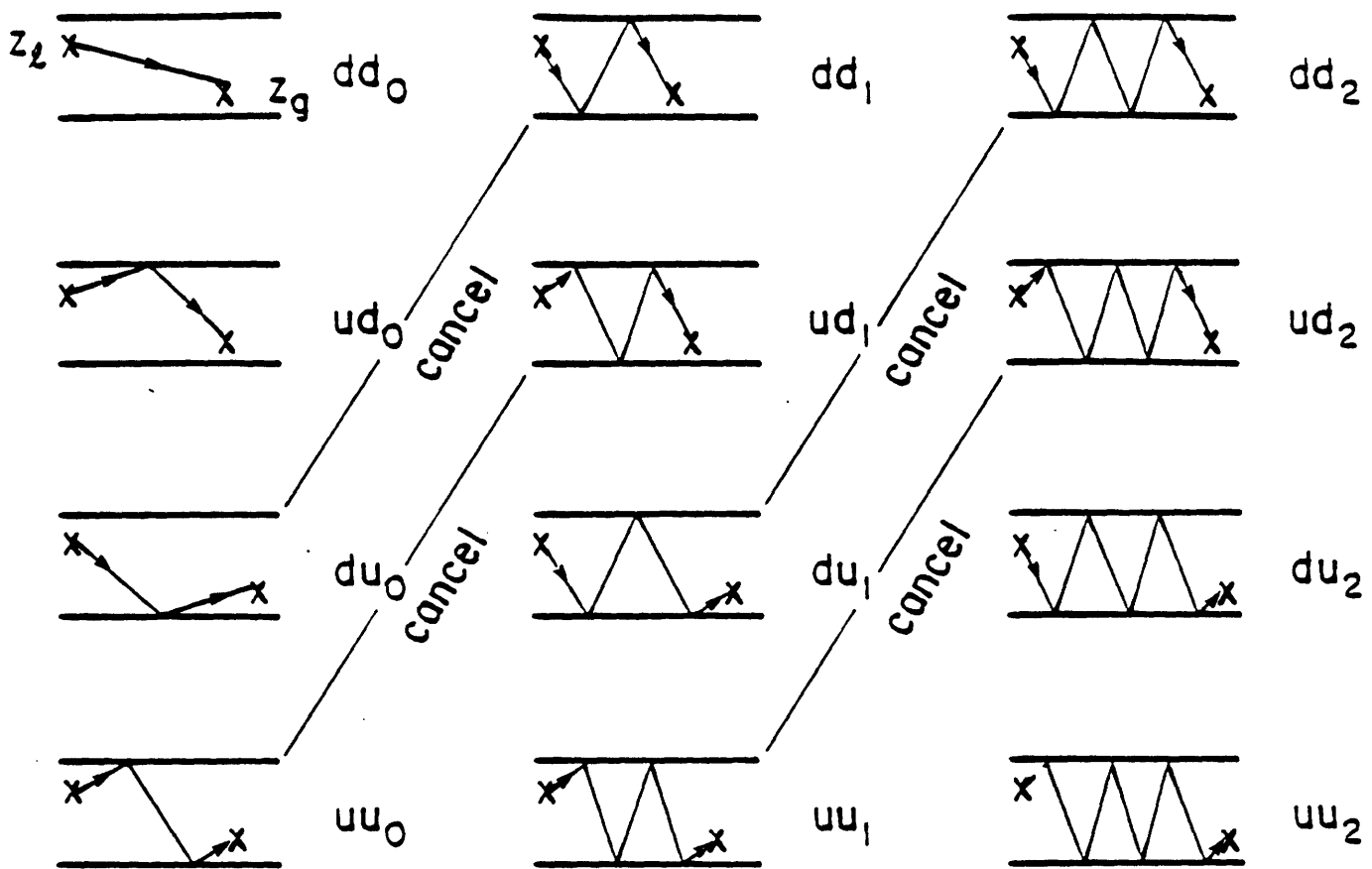
Figure 5.18: Symbolic diagram of components within a waveguide indicating the cancellation which yields a zero in $g_I(k_r)$.

infinite sensitivity can be thus be physically interpreted as a cancellation which occurs due to the presence of the surface of the waveguide. In the deep water problem when there is no surface present, no such effect occurs as can be confirmed by examining the sensitivity function in equation (5.20) or from physical considerations.

A practical implication of the preceding results concerning invariant zeros and points of infinite sensitivity is the definition of an *invariant critical depth* z_c. If either the source or receiver is positioned within the waveguide at depths deeper than the invariant critical depth, at least one point of infinite sensitivity is guaranteed to occur in the determination of the reflection coefficient for non-evanescent values of k_r, i.e. for $k_r < k_0$. The expression for the invariant critical depth for an isovelocity waveguide can be determined, using equations (5.21) and (5.22), as

$$z_c = \frac{\pi}{k_0} \tag{5.26}$$

where k_0 is the water wavenumber. The invariant critical depth is independent of the waveguide thickness and it scales inversely with frequency, i.e. at lower frequencies, the source and receiver can be placed closer to the bottom without incurring a point of infinite sensitivity. It is pointed out that the selection of the depths at which to place the source and receiver in an actual experiment involves tradeoffs among a number of factors including nulls in the modal amplitude functions, excitation of shear waves in the bottom, determination of the evanescent portion of the reflection coefficient, and surface scattering. The determination of optimal depths which must include all of these factors has not been fully studied and represents an important area for further study in the context of shallow water acoustic inversion. The critical depth definition is interesting however, in that it suggests that the inversion problem becomes inherently better conditioned as instruments are moved farther away from the media to be imaged - at least until both are shallower than the critical depth.

Many of these results can be generalized to non-isovelocity waveguides. The location of the points of infinite sensitivity which occur in obtaining the bottom reflection coefficient can be determined from physical considerations, without resorting to the

algebra required for determination of the invariant zeros of the extended Green's func-
tion, or the invariant zeros of the imaginary part of the extended Green's function.
In Figure 5.19 is depicted a non-isovelocity waveguide with the source and receiver
located in different layers. Components dd_0 and ud_0 must cancel in order to have the
first type of interference discussed earlier and components du_0 and dd_1 must cancel
in order to have the second type of interference. It is apparent from this figure that
the equations which describe the conditions for cancellation are

$$\sin[\sum_{i=0}^{J-1} k_{zi} h_i + k_{zJ}(z_l - \sum_{i=0}^{J-1} h_i)] = 0 \qquad (5.27)$$

and

$$\sin[\sum_{i=0}^{K-1} k_{zi} h_i + k_{zK}(z_g - \sum_{i=0}^{K-1} h_i)] = 0 \qquad (5.28)$$

where k_{zi} is the vertical wavenumber in layer i, h_i is the thickness of layer i, z_l is
located in layer J and z_g is located in layer K. From arguments presented earlier,
we may also conclude that these equations precisely describe the locations of points
of infinite sensitivity - no information about the reflection coefficient is contained
within $g(k_r)$ at the corresponding values of k_r. Because of the cancellation of plane
wave components at these values, the extended Green's function must also have an
invariant zero, or invariant zero of its imaginary part, at these same values of k_r. The
zeros of the extended Green's function are invariant with respect to the properties
of the media underlying z_l. The zeros of the imaginary part of the Green's function
are invariant with respect to the properties of the media underlying z_l. The invariant
critical depth for the non-isovelocity waveguide is given by the solution to

$$\sin[\sum_{i=0}^{J-1} k_i h_i + k_J(z_c - \sum_{i=0}^{J-1} h_i)] = 0 \qquad (5.29)$$

where z_c is within layer J. Numerical experiments, including the prediction of the
locations of zeros of the extended Green's function using equations (5.27) and (5.28)
and the confirmation of their invariant nature, have provided further support for these
conclusions. The extension of these results to the cases including waveguides with high
speed layers and to continuously varying waveguides represents an interesting area for
further research.
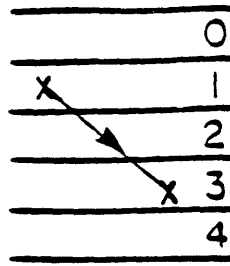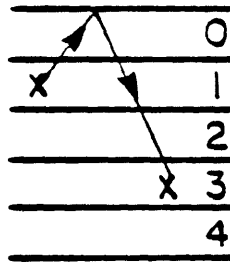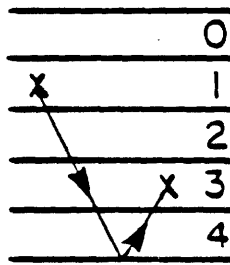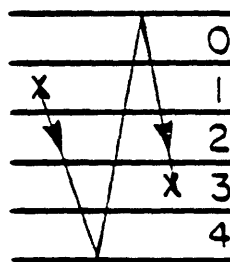
Figure 5.19: Symbolic diagram of components within a non-isovelocity waveguide which can cancel under some circumstances.

In this section we have developed the sensitivity function in order to understand how errors in estimating the Green's function affect the extracted reflection coefficient. The sensitivity function was shown to have a number of interesting theoretical properties which are related to the poles and zeros of the Green's function. Although the sensitivity function can be similarly derived for the deep water case, the resultant function is smoothly varying and the interesting behavior caused by the presence of the surface is not seen. One of the most interesting properties of the sensitivity function is that it possesses points of infinite sensitivity at wavenumber locations which do not depend on the medium being investigated, i.e. on the ocean bottom. Rather, these points are invariant with respect to the media underlying the waveguide and are determined primarily by the configuration of the experiment. These positions of infinite sensitivity are connected in an interesting way to the zeros of the Green's function and the zeros of its imaginary part only. We presented a number of statements regarding these zeros and their invariant nature, as well as their connection with points of infinite sensitivity. Additionally, a physical explanation relating cancellation within the waveguide to the invariant zeros and points of infinite sensitivity was provided. Finally, some of the results presented were extended to the non-isovelocity waveguide.

5.4 Inversion of Synthetic Data

In this section, we consider the application of the inversion scheme to obtain the reflection coefficient from synthetically generated shallow water acoustic fields. Although the inversion method is actually based on using experimentally collected data as input, there are a number of important reasons to consider, at least initially, the use of synthetic data as input. First, and perhaps foremost, the use of synthetic data provides a means for verifying that the inversion technique produces a valid result. Additionally, the use of synthetic data provides a means for studying how various parameters can affect the quality of the inversion. Understanding the variation caused by a particular parameter can impact the design of an actual ocean experiment and may also facilitate interpretation of inversion results. In the prior section of this chapter we presented a number of theoretical results concerning the sensitivity of extracting the reflection coefficient from shallow water field measurements. In this section, we will use the inversion of synthetic data to numerically demonstrate the consequences of sensitivity and the invariant critical depth.

Developing a numerical simulation which produces a synthetic shallow water acoustic field and inverts to obtain an accurate estimate of the bottom reflection coefficient is actually a very difficult task. In order to justify this, let us provide a list of the some of the considerations and difficulties involved. First, a means for generating a high quality synthetic shallow water acoustic field must be developed. Without such a scheme, it is difficult to separate degradations which are the result of inaccuracies in the synthetic data production from degradations which are incurred in the inversion process itself. We have found that various approximate techniques, including those which synthesize the field as a sum of trapped modes alone or as a sum of trapped plus virtual modes, do not produce synthetic data of sufficient accuracy to produce a good reflection coefficient estimate. Accurate computation of the continuum portion of the total field is quite important in the context of obtaining an accurate reflection

coefficient.

As pointed out in earlier chapters, the acoustic field can be mathematically expressed as the Hankel transform of the Green's function. However, unless special care is taken, a numerical Hankel transform when applied to typical shallow water Green's functions produces fields which are degraded due to aliasing. In contrast with the problem of deep water synthetic field generation, the shallow water Green's function nearly always contains pole singularities which must be estimated and removed as one means of eliminating the degradation due to aliasing.

Although the Hankel transform can be computed accurately using the Fourier-Bessel series under certain circumstances, this method is computationally quite slow and may be prohibitively so for some applications. Alternately, other methods including the Abel/Fourier approach or the FFP are much faster, but can introduce other errors. For example, the FFP does not produce accurate results for small values of range because several underlying assumptions are violated. This may be quite acceptable in producing fields which are accurate everywhere except in the near-field, but may be unacceptable in a numerical simulation in which the inverted reflection coefficient is to be determined. For example, in shallow water applications where the source and receiver are close to the bottom, the range at which the specular reflection becomes critical may be quite small, typically only a few wavelengths. Therefore, in these cases, accurate synthetic data in the near-field may be required for accurate determination of the reflection coefficient, especially at pre-critical values of k_r. The use of the FFP in the synthesis method may not be desirable in these situations. Additionally, the hybrid method, by its very nature, may not produce data of sufficiently high quality near $r = 0$ as pointed out in the previous chapter. For example, the trapped mode contribution is actually infinitely large at $r = 0$ and must cancel the continuum portion precisely so that a finite field results. Also, an asymptotic expression for the modal contributions to the total field may not be sufficiently accurate, particularly at small ranges.

Another difficulty which occurs in a simulation which demonstrates inversion of synthetic data is assuring that the inversion technique does not undo an error incurred in the synthesis technique. For example, under some circumstances, it is possible to synthesize an aliased field, which when inverted, yields a good estimate of the Green's function. The numerical simulation should be constructed to avoid this cancellation of errors.

Additionally, there are tradeoffs to be made in the selection of the technique for computing the Hankel transform of the acoustic field to obtain the Green's function. The Fourier-Bessel series can again be used although it is computationally quite slow. Additionally, the input field data is required on a non-uniform grid which is related to the zeros of a Bessel function. Thus, the data must either be produced on such a grid, or else interpolated to this grid. There are several issues associated with the interpolation of shallow water fields which are not encountered in the interpolation of deep water fields. Also, although the Abel/Fourier method for performing the Hankel transform was found to be successful in synthesizing the field from the Green's function, it appears to work poorly in the context of inverting the field to obtain the Green's function. Although the precise reasons for this are not completely understood, the problem appears to be related to the rapid variation of the field versus the less-rapid variation of the Green's function. In particular, we have found that the Abel/Fourier method works well when applied to the field, only when the field is highly oversampled. Presumably, the problem is with the state equation method[14] for determining the Abel transform when the input data is rapidly varying. Alternate Abel transform algorithms have other disadvantages. For example, techniques based on convolution on a square-root grid tend to concentrate the sampling away from the origin as opposed to near the origin where the field may be most rapidly varying.

Despite these difficulties, it is possible to construct a valid numerical simulation which inverts a synthetically generated shallow water acoustic field to obtain the bottom reflection coefficient. We have used this simulation to study the effects various

parameters have on the quality of the inverted reflection coefficient. In the remainder of this section, we will focus only on effects of differing source and receiver depths and their relationship to the invariant critical depth, defined in the prior section. In order to do this, several numerical examples of the simulation will be presented and issues such as algorithm selection will be simultaneously considered.

To begin the discussion, we consider the geoacoustic model previously presented in Table 4.1. Note that in this model, both the source and receiver exceed the invariant critical depth of $\pi/k_0 = 5.355\ m$ and thus there will be at least two points of infinite sensitivity which will occur in obtaining the bottom reflection coefficient. The magnitude and phase of the corresponding Green's function, plotted to a maximum value of $k_r = 0.6$ are shown in Figure 5.20. In the example to be discussed, we have chosen to examine the inversion only for values of k_r less than the water wavenumber, $k_0 = 0.58666$, and all wavenumber related functions will be displayed to approximately this maximum value of k_r.

1024 samples of the Green's function, windowed to a maximum value of $k_r = 1.0$ were used as input to the hybrid method for synthetic field generation. The Abel/Fourier method for computing the Hankel transform was selected and the resultant continuum and total fields were computed to a maximum range of $3217\ m$ at a range interval of $3.14\ m$. The magnitudes of these fields as a function of range were previously shown in Figures 4.15 and 4.17 of Chapter 4. In producing the continuum portion of the field, we have also chosen to remove the virtual pole and to re-add its contribution analytically to the field. This was done as a means of assuring that the inverse process does not undo any degradation incurred in the synthesis, process. In other words, the two dominant contributions to the field were actually generated based on analytic expressions for their modal forms, although the inversion technique is completely numerical and does not use these analytic expressions. It is stressed that the remaining portion of the field must be included in order to assure that an accurate reflection coefficient estimate results from the inversion.
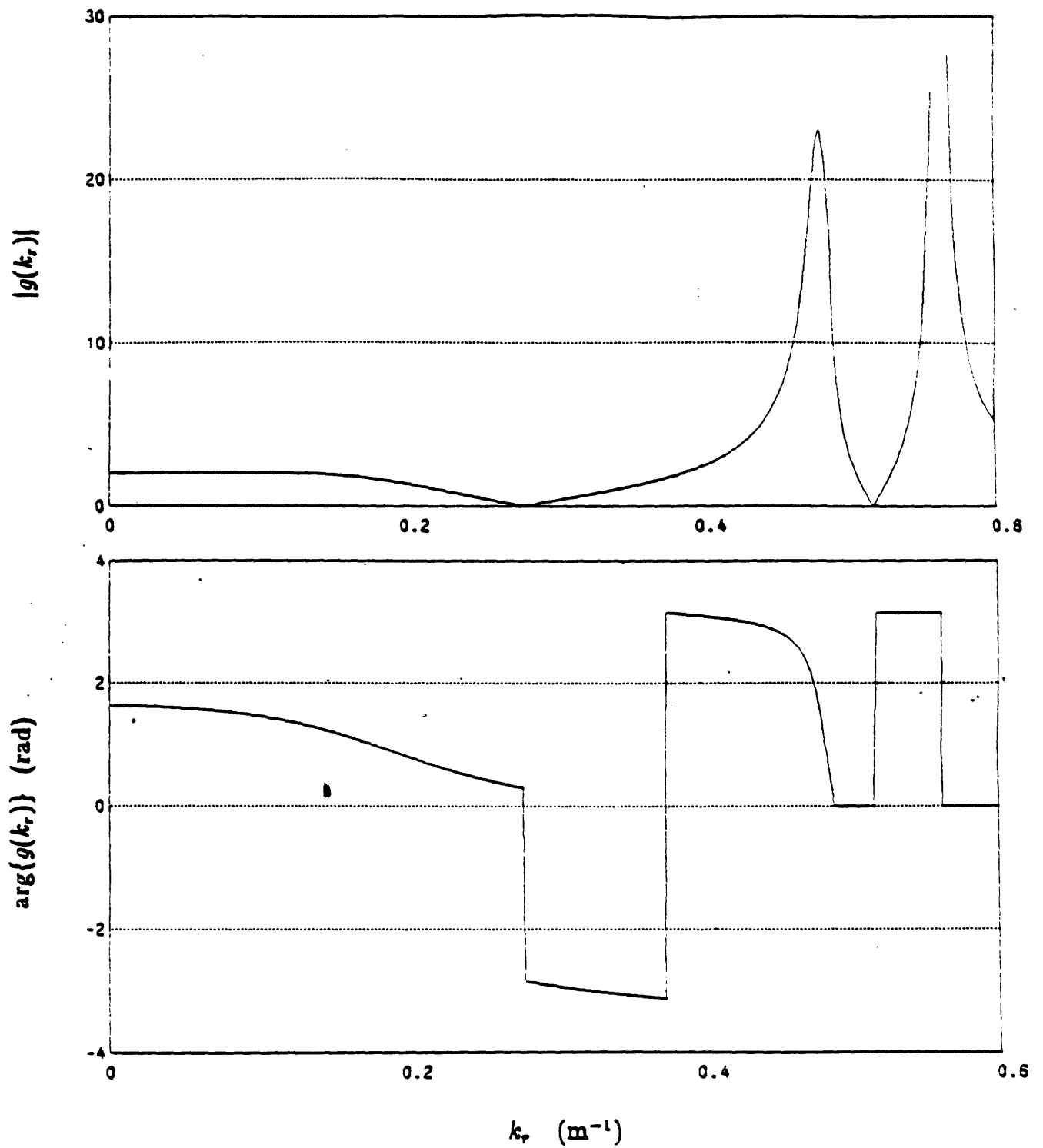
Figure 5.20: Magnitude and phase of the Pekeris model Green's function.

A projection-based Hankel transform algorithm which differs from the Abel/Fourier method was selected as the means for obtaining the Green's function estimate from the synthetic acoustic field. As pointed out previously, we encountered difficulty in applying the Abel/Fourier method to the rapidly varying acoustic field. Severe degradation was noted in the resulting Green's function, which was presumably due to errors in the numerical Abel transform when it was applied to the rapidly varying field. Instead, we chose to use the dual algorithm for computing the Hankel transform which consists of first performing an inverse Fourier transform and then performing an inverse Abel transform. The application of the inverse Fourier transform tends to reduce much of the rapid variation in the data prior to the application of the inverse Abel transform. The method will be referred to as the Fourier^{-1}/Abel^{-1} method and it is the dual algorithm in the following sense.

Projection algorithms for computing the Hankel transform are based on the projection-slice theorem for two-dimensional functions. Because of the symmetry of the forward and inverse Fourier transforms, the projection-slice theorem can be applied in either direction. The implication is that a slice in the frequency (wavenumber) domain can be obtained in two ways, 1) by first computing the projection of the two-dimensional function and then computing its one-dimensional Fourier transform or 2) by first computing a one-dimensional inverse Fourier transform and then computing its back-projection. In the case that the underlying functions are circularly symmetry, the projection operation becomes an Abel transform and the backprojection operation becomes an inverse Abel transform [15]. By relating the Hankel transform to the two-dimensional Fourier transform of a circularly symmetric function, it becomes apparent that the Abel/Fourier and Fourier^{-1}/Abel^{-1} techniques are dual methods for computation of the Hankel transform.

Furthermore, as pointed out by Bracewell, the forward and inverse Abel transforms have the similar forms

$$f_A(y) = 2 \int_y^\infty \frac{f(x)x}{(x^2 - y^2)^{1/2}} dx \qquad (5.30)$$

339

and

$$f(x) = -\frac{1}{\pi} \int_s^\infty \frac{f_A'(y)}{(y^2 - x^2)^{1/2}} dy \qquad (5.31)$$

where $f(x)$ represents the original function, $f_A(y)$ represents its Abel transform, and $f_A'(y)$ represents the derivative of $f_A(y)$ with respect to y. The fact that a derivative is present, and the similar forms of the forward and inverse transforms is not surprising, from the following line of reasoning. If $f(x)$ and $f_A(y)$ are expressed on square-root grids, i.e. $F(X) = f(x^2)$ and $F_A(y^2) = f_a(y)$, then $F_A(x)$ consists of a scale factor times the half-order integral of $F(x)$. In other words, their Laplace transforms are related via the factor $1/s^{1/2}$. Thus, to compute the inverse of $F_A(x)$, we must compute its half-order derivative. This may be performed, in turn, by first computing its derivative and then computing its half-order integral. Therefore, the inverse Abel transform can be performed by use of the derivative and Abel transform operations. The additional factor x which appears in equation (5.30) but not in (5.31) is due to the relationship between derivatives on uniform versus square-root grids.

It is noted that the dual algorithm for computing the Hankel transform, based on the Fourier^{-1}/Abel^{-1} method, is actually comprised of the same building blocks used in the Abel/Fourier method. That is, an FFT is used to compute the inverse Fourier transform and the state-equation method is used to compute the Abel transform of the function $-f_A'(y)/2\pi y$ in order to derive the required inverse Abel transform. We have used a first-order difference technique to approximate the derivative, although it is recognized that other methods may yield better performance, including multiplication by r prior to computing the inverse Fourier transform. In fact, the selection of the algorithm which approximates the derivative is a key issue in other applications which involve a backprojection operation, including medical CT and NMR tomography. An exhaustive evaluation of the performance of the dual algorithm for computing the Hankel transform has not been performed, although the performance of the state-equation approach for computation of the inverse Abel transform has been discussed elsewhere. Instead, we have chosen this algorithm as one possible way to compute the

340

Hankel transform of the rapidly varying acoustic field in a computationally efficient manner.

The magnitude and phase of the inverted Green's function, obtained by applying the $Fourier^{-1}/Abel^{-1}$ method to the synthetic acoustic field to a range of 3217 m is shown in Figure 5.21. In comparing the inverted Green's function in Figure 5.21 with the true Green's function shown in Figure 5.20, it can be seen that their magnitudes match quite well. However, the agreement in phase behavior is less striking. We point out however, that the interpretation of the phase of a function, particularly as a means for comparing it with another function must be done carefully. For example, if the principal value of the phase is defined over the interval $-\pi$ to π, a function which has the complex value $Ae^{j\pi-\epsilon}$ might be quite similar to a function which has the value $Ae^{j\pi+\epsilon}$, yet their phase functions would look quite different. Additionally, if the amplitude of a complex function is very small, slight errors in either the real or imaginary parts can cause large variations in phase. To demonstrate this further, the real and imaginary parts of the true Green's function are shown in Figure 5.22, and the real and imaginary parts of the inverted Green's function are shown in Figure 5.23. The two functions may appear to be more similar to each other using this method of display, as compared with the previously shown magnitude/phase format. The example points out that the interpretation of the phase differences between two Green's functions must be done carefully.

To continue with the simulation example, the reflection coefficient was extracted from the inverted Green's function using equation (5.15) and the resultant magnitude and phase are shown in Figure 5.24. For reference, plots of the magnitude and phase of the theoretical reflection coefficient for this model are shown in Figure 5.25. As can be seen by comparing the two figures, there are striking differences between the two functions. In particular, one might infer that the critical k_r for this model is at $k_r = 0.28$ by examining the inverted reflection coefficient magnitude, when in fact the actual critical k_r is 0.48888. Additionally, the dip in the inverted reflection coefficient
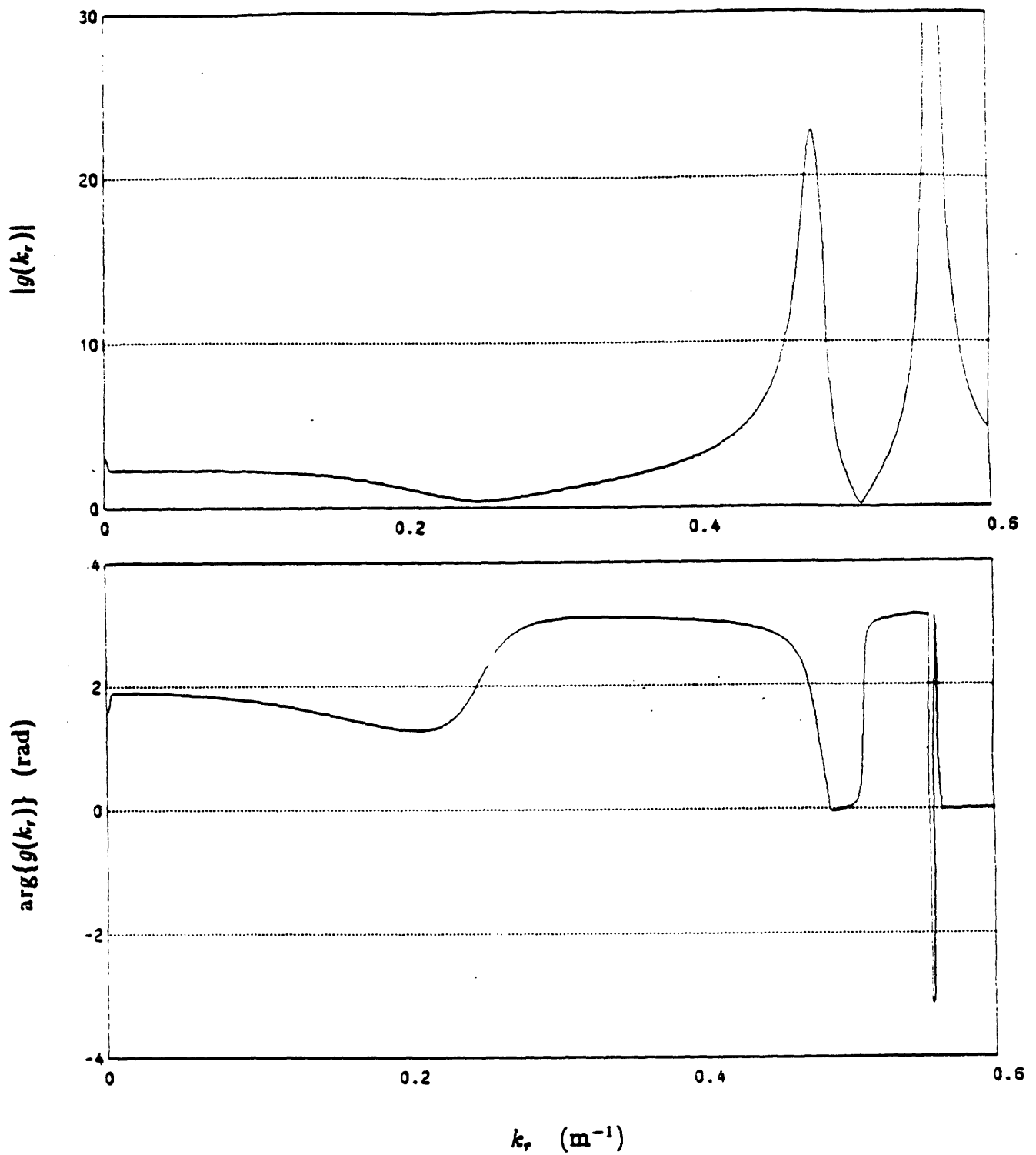
Figure 5.21: Magnitude and phase of the inverted Pekeris model Green's function. This function was obtained by computing the Hankel transform of the total shallow water field.
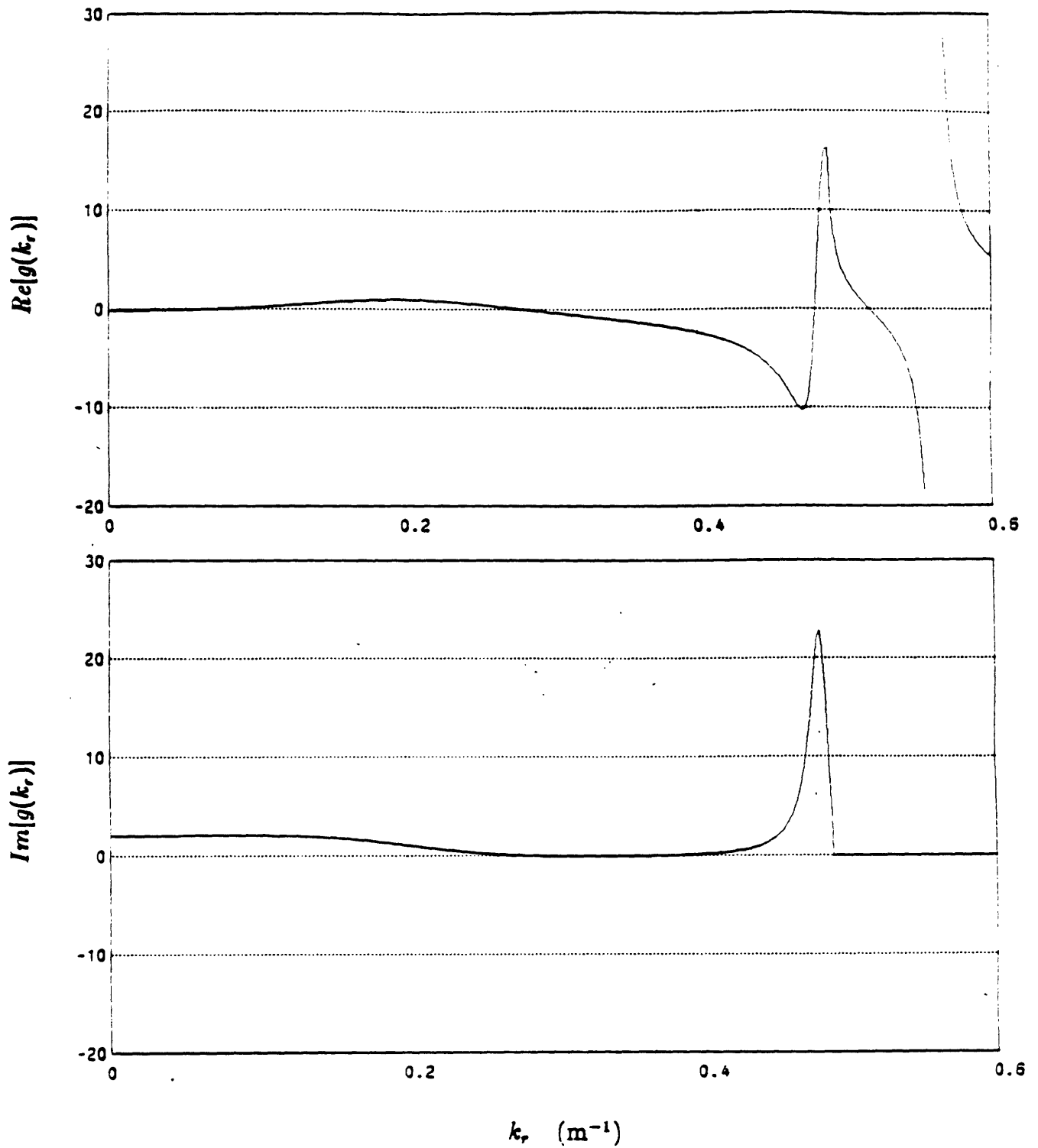
Figure 5.22: Real and imaginary components of the Pekeris model Green's function.
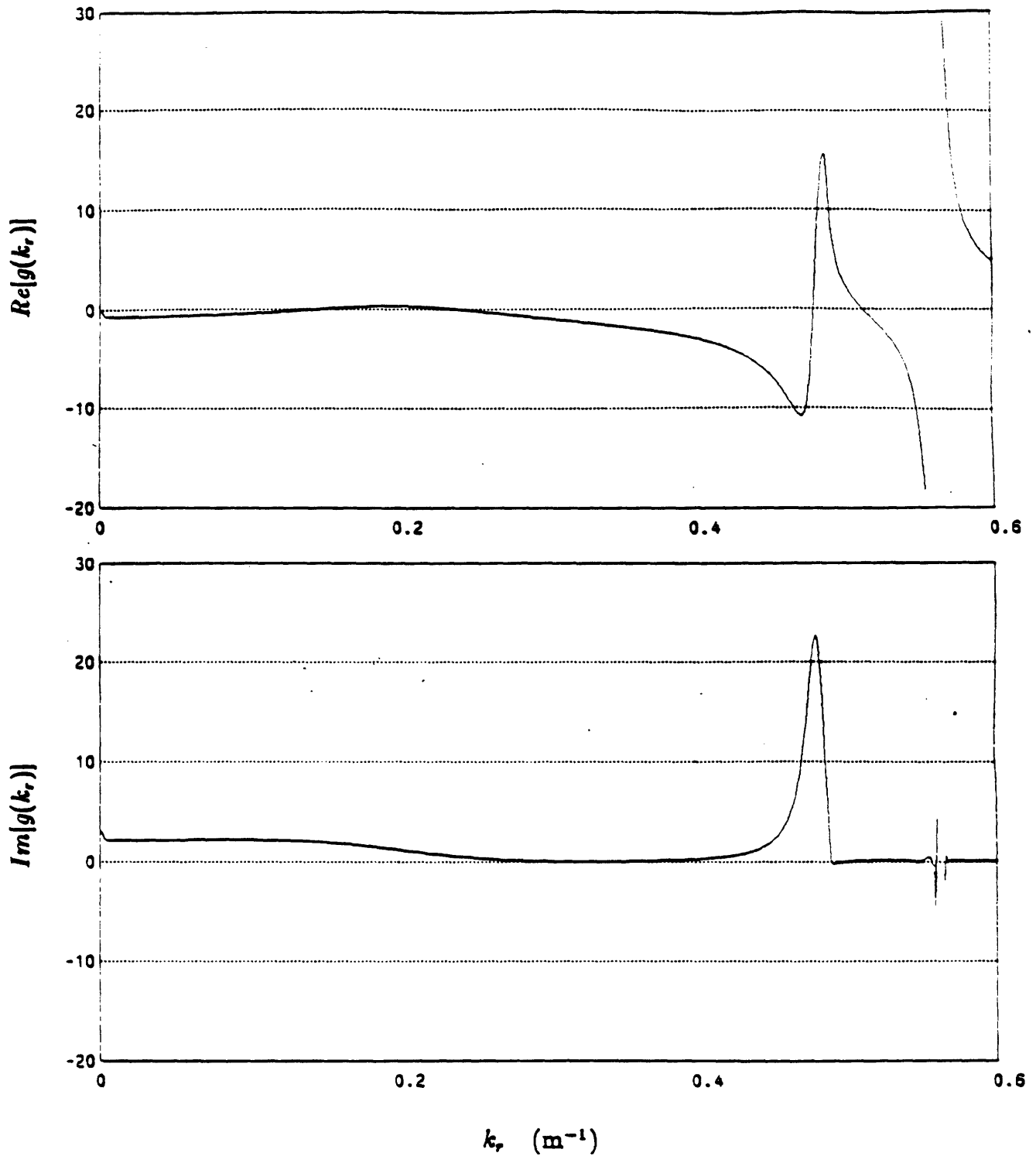
Figure 5.23: Real and imaginary components of the inverted Pekeris model Green's function. This function was obtained by computing the Hankel transform of the total shallow water field.
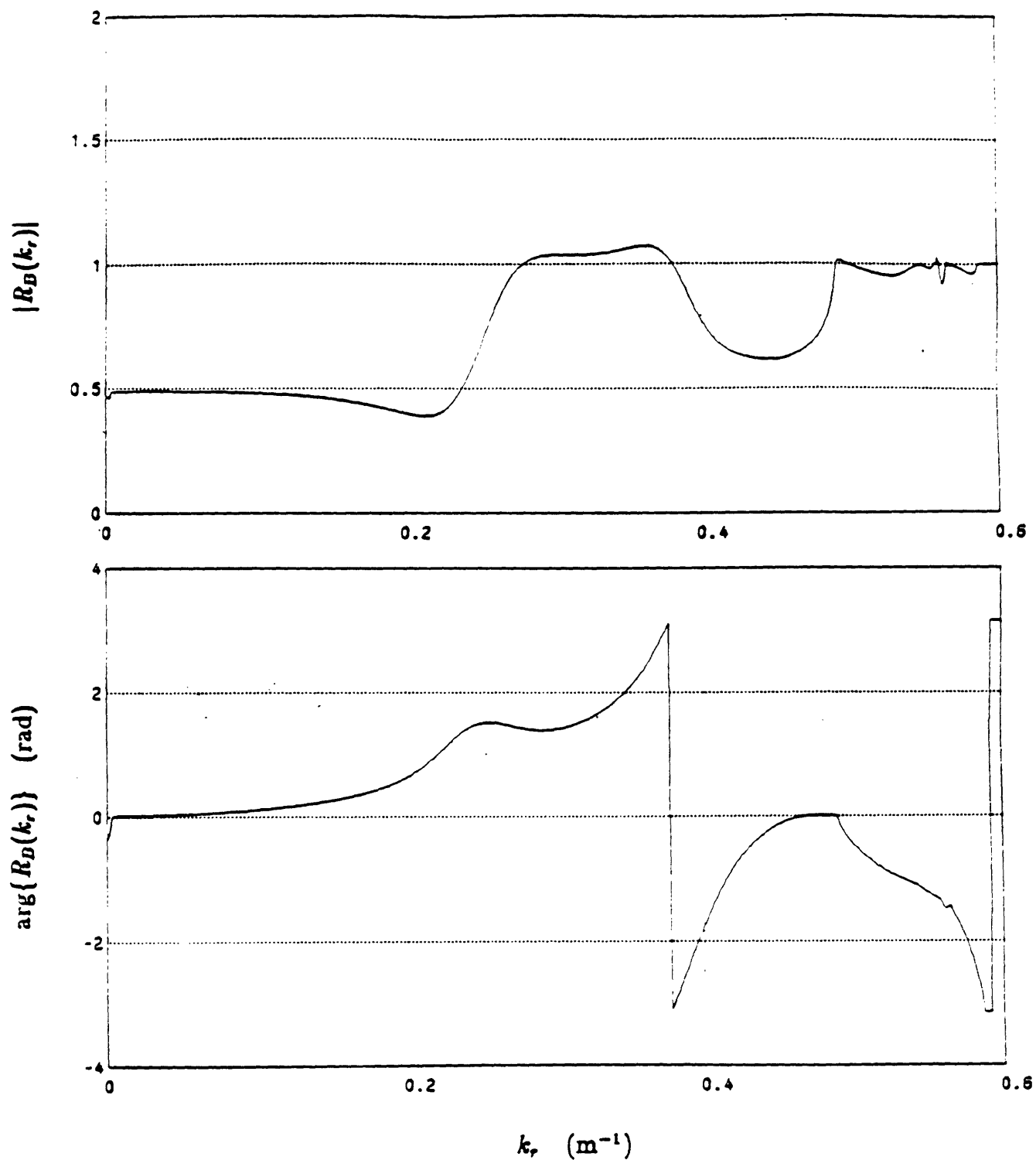
Figure 5.24: Magnitude and phase of the inverted reflection coefficient. This function was obtained by computing the Hankel transform of the total shallow water field to determine the Green's function and then extracting the reflection coefficient.
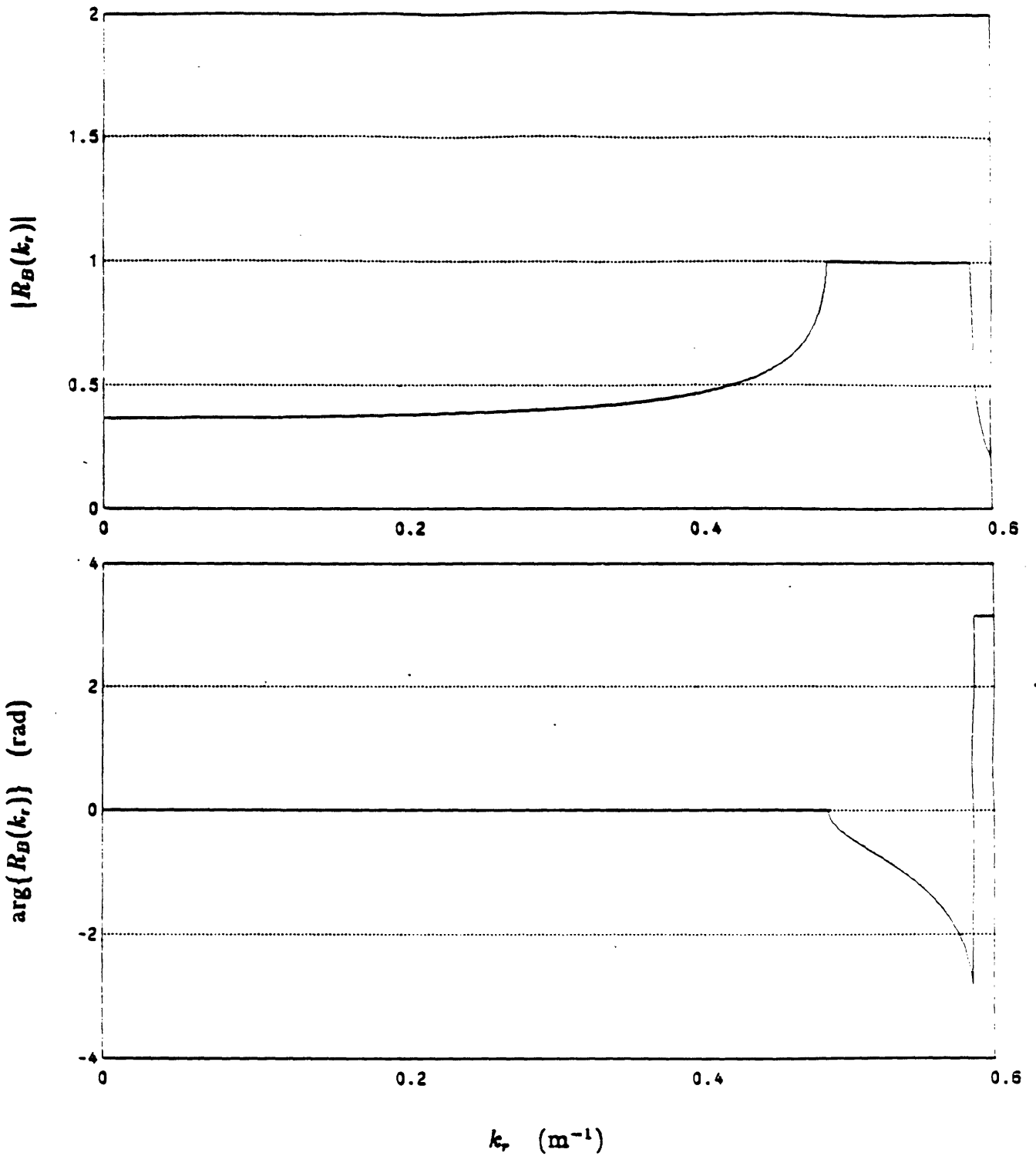
Figure 5.25: Magnitude and phase of the theoretical reflection coefficient for the Pekeris model.

magnitude at $k_r = 0.4$ to 0.5 suggests that some complicated layered structure may be present in the bottom, when in fact the model is a Pekeris model, i.e. the bottom is a simple isovelocity halfspace. It is further noted that the functions agree quite well for values of k_r which exceed the theoretical critical value of k_r and which do not exceed the water wavenumber at $k_r = 0.58688$.

A possible conjecture about the cause of the difference between the theoretical reflection coefficient and the inverted reflection coefficient is that it is due to the windowing implicit in computing the Hankel transform of a finite portion of the synthetic field. In fact, the hybrid method for synthetic data generation provided a convenient means for testing this hypothesis. To investigate this, the following numerical simulation was performed. The hybrid method was used to produce only the continuum portion of the field. The virtual mode contribution was again computed by using its analytic form so that errors incurred in the synthesis of the continuum were not undone in its inversion. The continuum portion of the field was inverted by using the Fourier^{-1}/Abel^{-1} method in order to estimate the function $g_C(k_r)$ and the resultant magnitude and phase functions are shown in Figure 5.26. For reference, the magnitude and phase of the theoretical $g_C(k_r)$ function for this model are shown in Figure 5.27. It is noted that, in performing this simulation, the effects of the windowing in range have been drastically reduced. In other words, because the trapped mode portion of the field was not included and because the continuum portion of the field has decayed significantly over the aperture of $3217\ m$, the effects of windowing should be quite small. The difference between the theoretical $g_C(k_r)$ and inverted $g_C(k_r)$ functions is most probably due to the use of the asymptotic expression for the virtual mode contribution as well other slight numerical errors in the simulation. To derive the inverted reflection coefficient for this case in which the windowing effects have been minimized, the theoretical $g_T(k_r)$ function was added to the inverted $g_C(k_r)$ function prior to the use of equation (5.15). The magnitude and phase of the resulting reflection coefficient are shown in Figure 5.28.
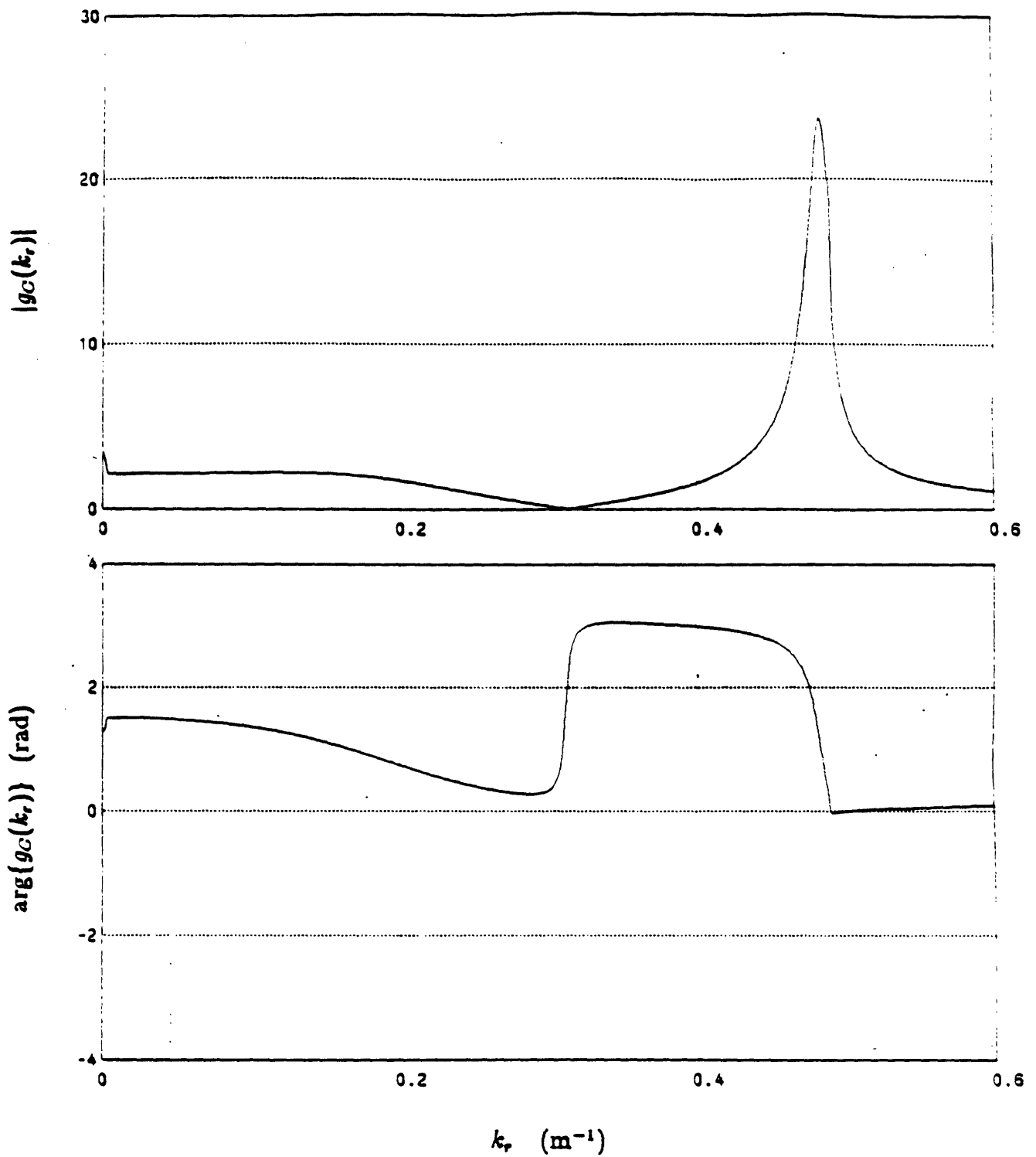
Figure 5.26: Magnitude and phase of the inverted continuum portion of the Green's function. This function was obtained by computing the Hankel transform of the continuum portion of the field.
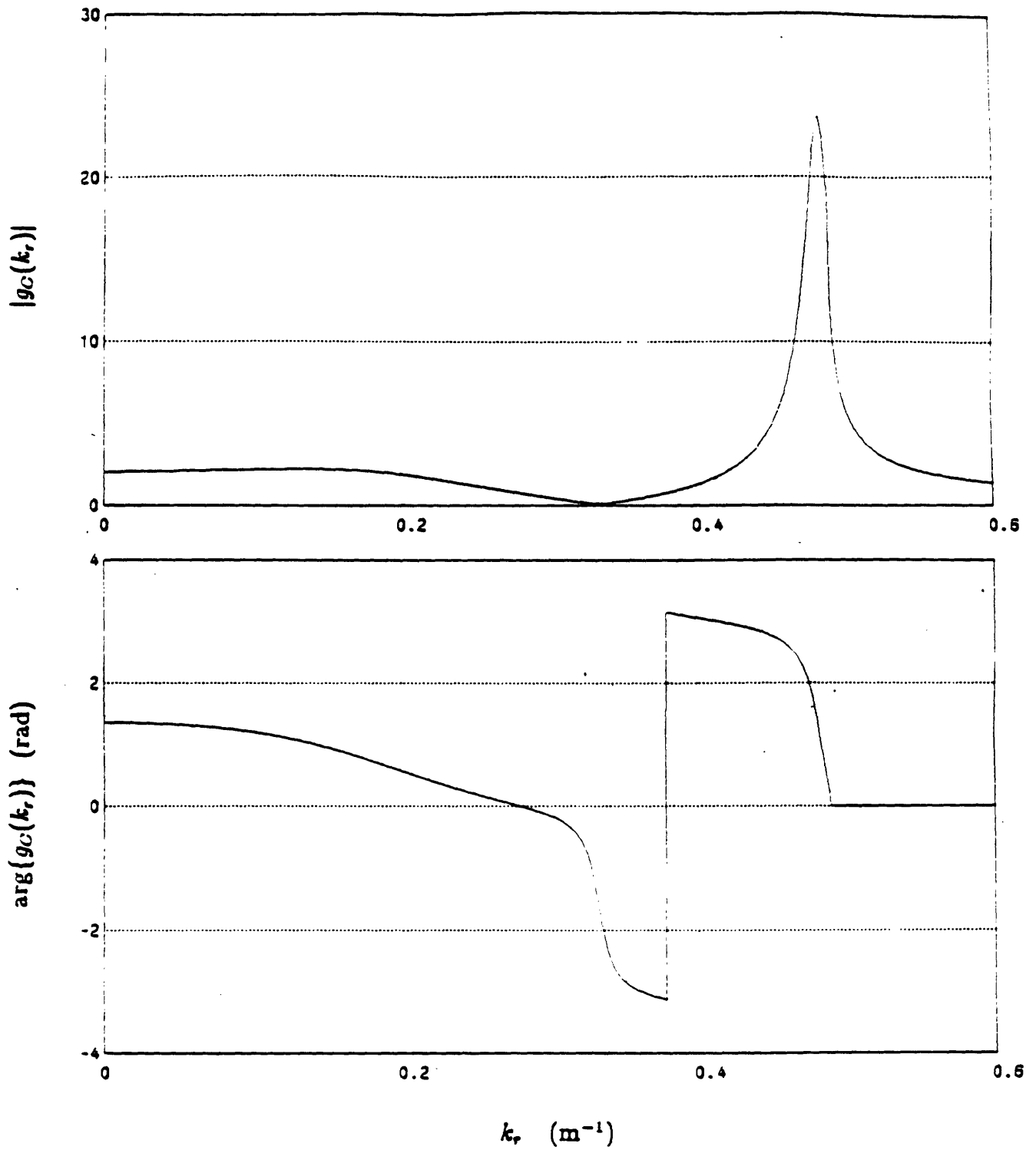
Figure 5.27: Magnitude and phase of the theoretical continuum portion of the Green's function.
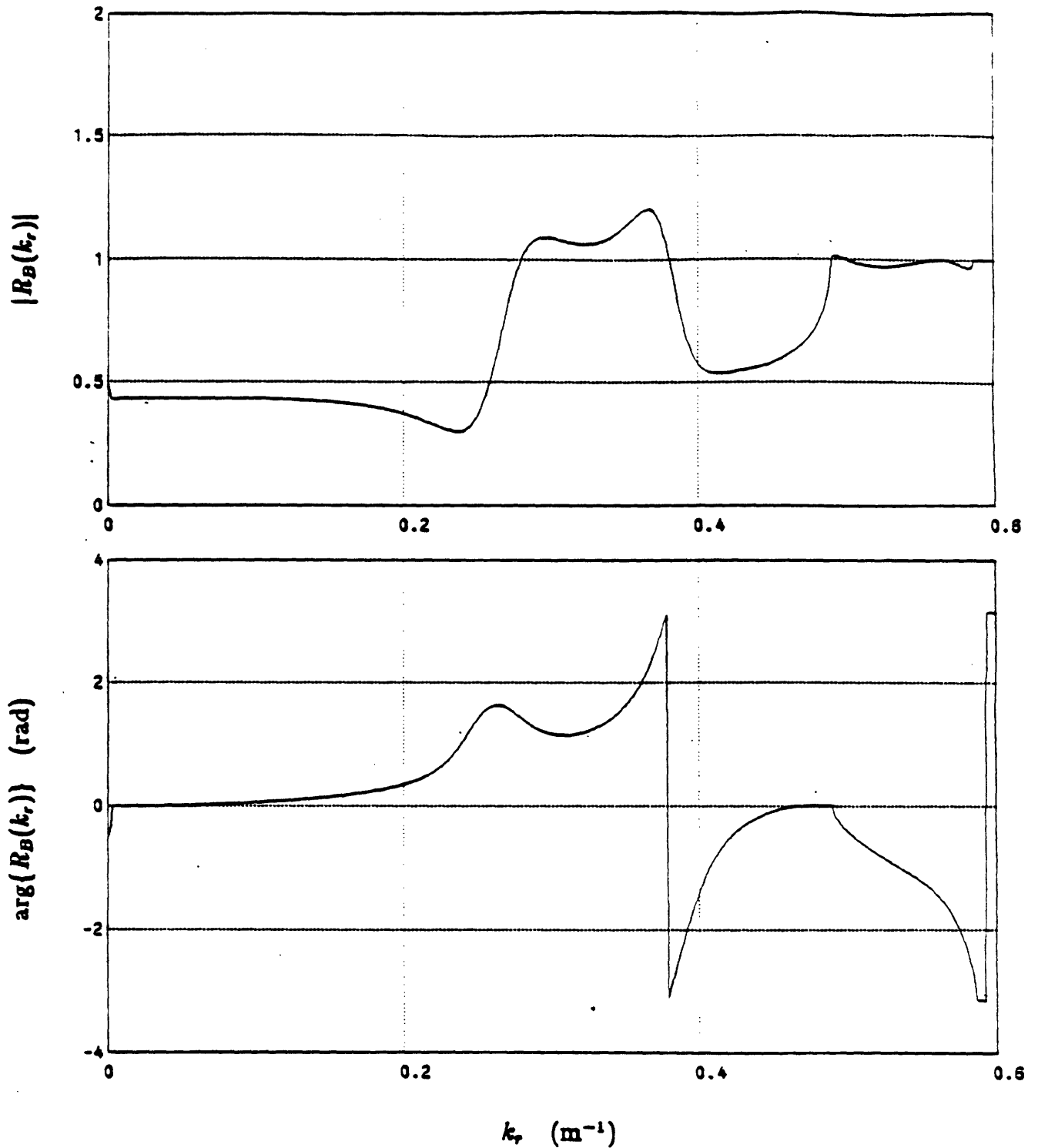
Figure 5.28: Magnitude and phase of the inverted reflection coefficient. This function was obtained by computing the Hankel transform of the continuum portion of the field, adding the theoretical trapped portion of the Green's function and then extracting the reflection coefficient.

There are several points to be made concerning the reflection coefficient derived in this way. First, in comparing it with the theoretical reflection coefficient and the reflection obtained from inverting the total field, it is apparent that some improvement in the estimate has occurred at values of k_r near the trapped mode locations. This result is not surprising, as in the second method of inversion the trapped mode contribution is included exactly and thus any degradations due to the windowing of the trapped portion of the field are reduced. However, the most striking feature of the reflection coefficient obtained by inverting only the continuum and adding $g_T(k_r)$ analytically is that still exhibits incorrect behavior at values of k_r from 0.25 to 0.4. In particular, the reflection coefficient still indicates an incorrect critical k_r even though the effects of windowing have been drastically reduced. Apparently, the incorrect behavior of the reflection coefficient in this region cannot be attributed to a windowing effect.

The poor behavior of the reflection coefficient can be attributed to the fundamental sensitivity of the inversion process in this interval. As pointed out previously, since both the source and receiver are located below the critical depth, there must be at least two points of infinite sensitivity for values of k_r less than the water wavenumber. It can be shown that there are exactly two points of infinite sensitivity for this particular source/receiver configuration. These points, determined by the solution of the equations $\sin k_z z_l = 0$ and $\sin k_z z_g = 0$, are at $k_r = 0.2803$ and $k_r = 0.3805$. The complete sensitivity function for this case is shown in Figure 5.29 and it is noted that the two peaks are located at precisely these values of k_r.

In comparing the sensitivity function with the inverted reflection coefficient functions, it can be seen that the reflection coefficients differ from their true values in the regions of k_r at which the sensitivity is large. For example, in the region where the inverted reflection coefficients exceed unity, near $k_r = 0.3$, it can be seen that the inversion is roughly 50 times more sensitive to any error in $g(k_r)$ versus the sensitivity at low values of k_r. Thus, we hypothesize that the errors in the reflection coefficient
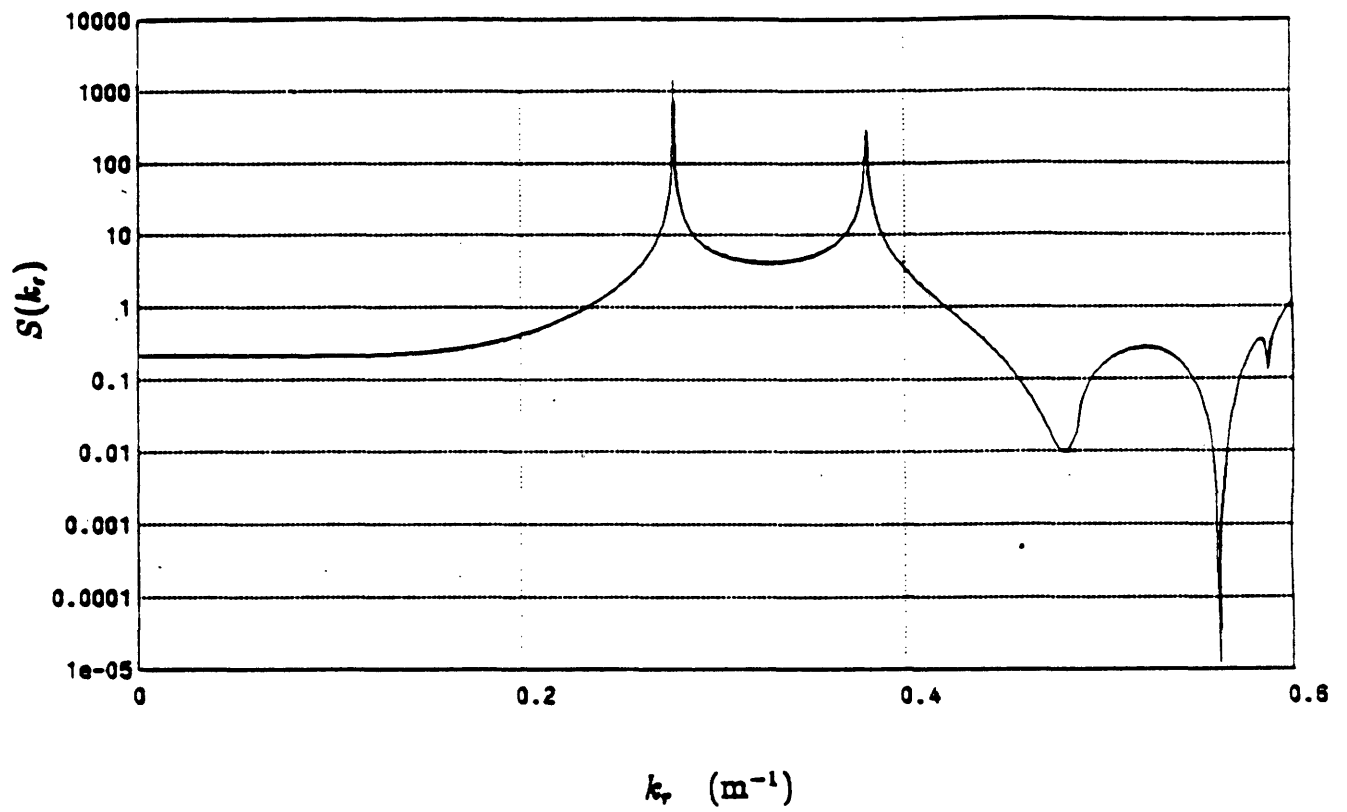
Figure 5.29: Sensitivity function for the Pekeris geoacoustic model.

estimation are due to the large magnification of small errors which have occurred in the process of generating a synthetic field and then inverting it. The small errors in the simulation have occurred for reasons we have discussed earlier including use of the asymptotic forms of the trapped and virtual modes, windowing of the continuum and performance of the Hankel transform algorithms. We point out that, although this effect has been discussed in the context of inverting synthetic data, the magnification of error can also be anticipated in the inversion of actual experimental fields.

As a further example of this effect, the simulation was re-run for the identical geoacoustic model except that the source and receiver were raised slightly within the waveguide, so that their positions did not exceed the invariant critical depth of 5.355 m. In particular, both were raised by 2.0 m so that $z_0 = 4.096$ m and $z = 5.03579$ m. The magnitude and phase of the theoretical Green's function for the displaced case are shown in Figure 5.30. By examining the magnitude and phase, it is seen that no invariant zeros of $g(k_r)$ or $g_I(k_r)$ are present, as expected. The theoretical sensitivity function for the case of the displaced source and receiver, shown in Figure 5.31, also confirms that there are no points of infinite sensitivity. In fact, by examining this curve, we see that it is nearly flat over the entire range of k_r from zero to the water wavenumber, excluding the dips near the virtual and trapped mode locations at which the sensitivity is predictably smaller, i.e. an even better reflection coefficient estimate is to be expected here. The magnitude and residual phase of the field for the case of the displaced source and receiver is shown in Figure 5.32. Note that it does not appear to be significantly different than the field obtained for the previous model as shown in Figure 4.17 except for perhaps slight changes in the positions of the nulls and peaks in the near-field. In Figure 5.33 is shown the magnitude and phase of the inverted Green's function for the displaced source/receiver obtained by computing the Hankel transform of the total field using the Fourier^{-1}/Abel^{-1} method. In Figure 5.34 is shown the magnitude and phase of the inverted reflection coefficient. From this figure it is apparent that a much improved reflection coefficient estimate has been obtained with respect to the reflection coefficient obtained for the original
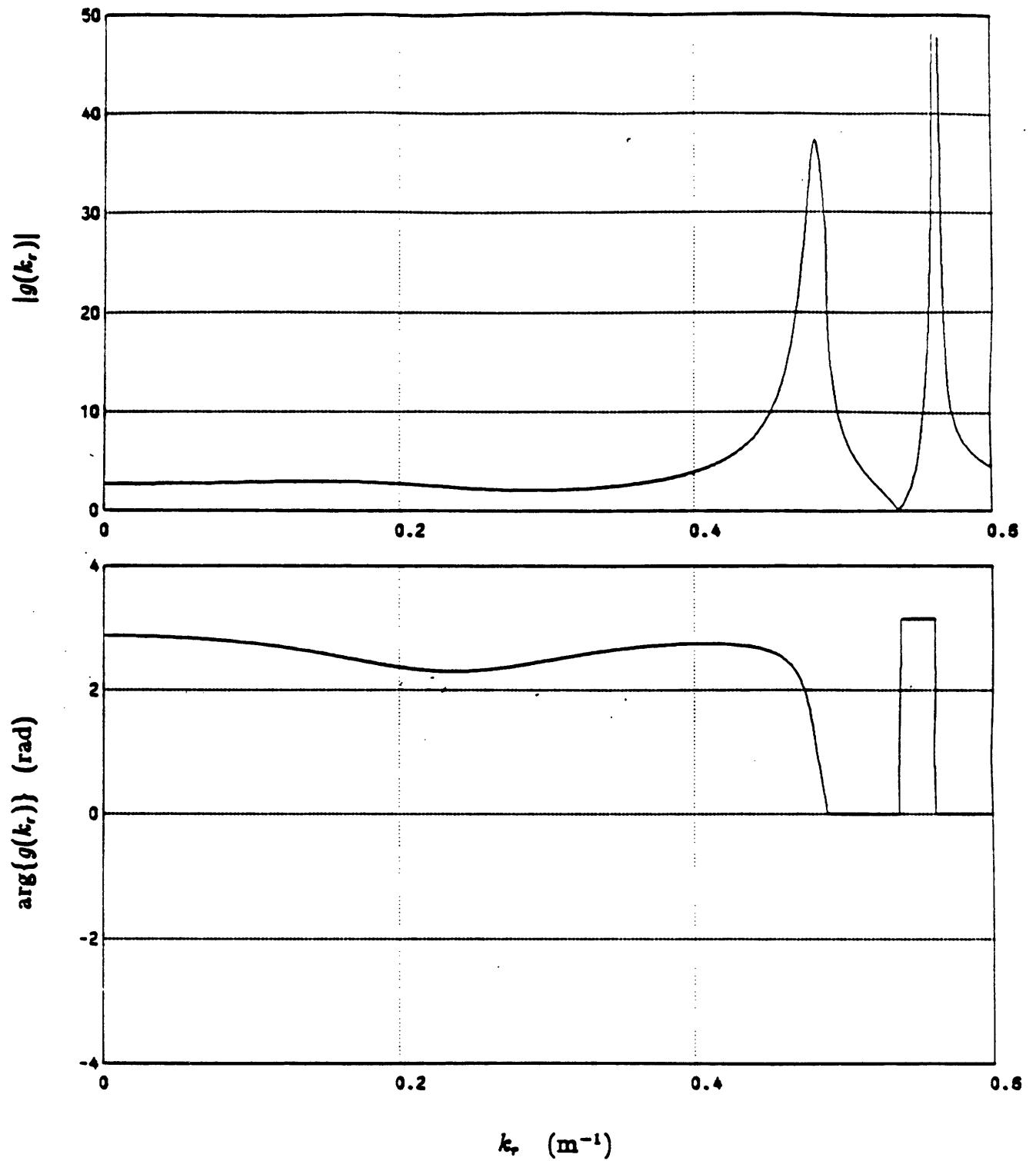
Figure 5.30: Magnitude and phase of the Pekeris model Green's function with displaced source and receiver.
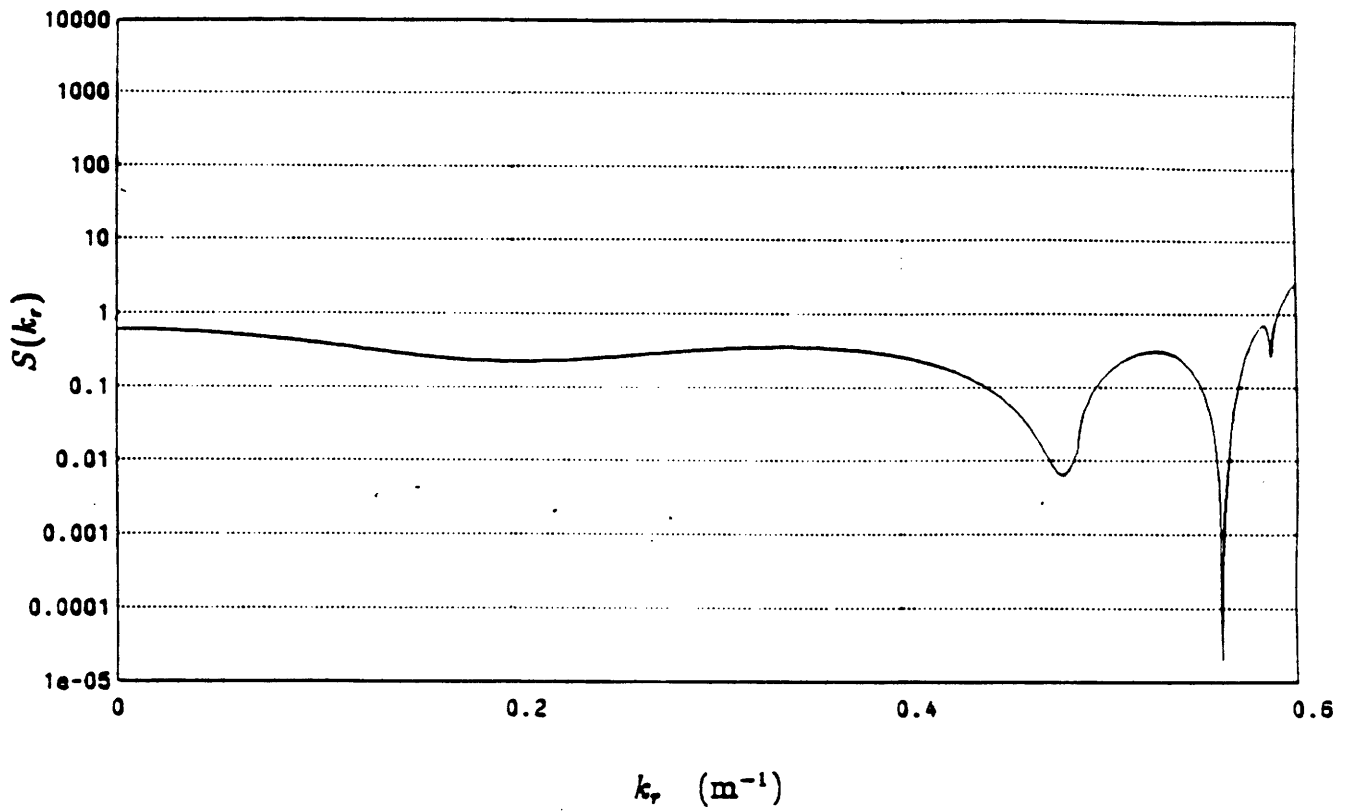
Figure 5.31: Sensitivity function for the Pekeris model with displaced source and receiver. The invariant critical depth is not exceeded in this model.
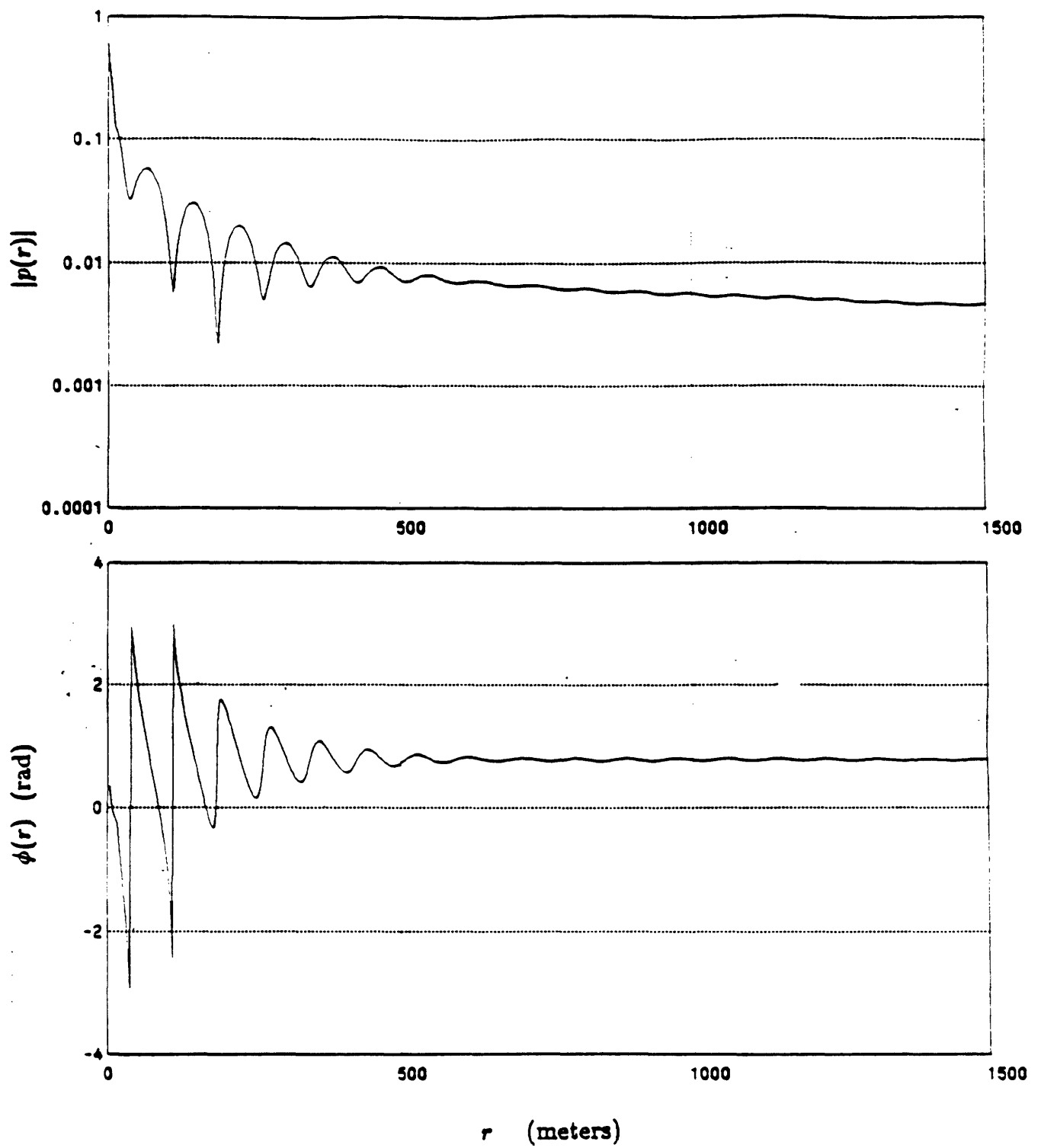
Figure 5.32: Magnitude and residual phase of the Pekeris model field with displaced source and receiver.
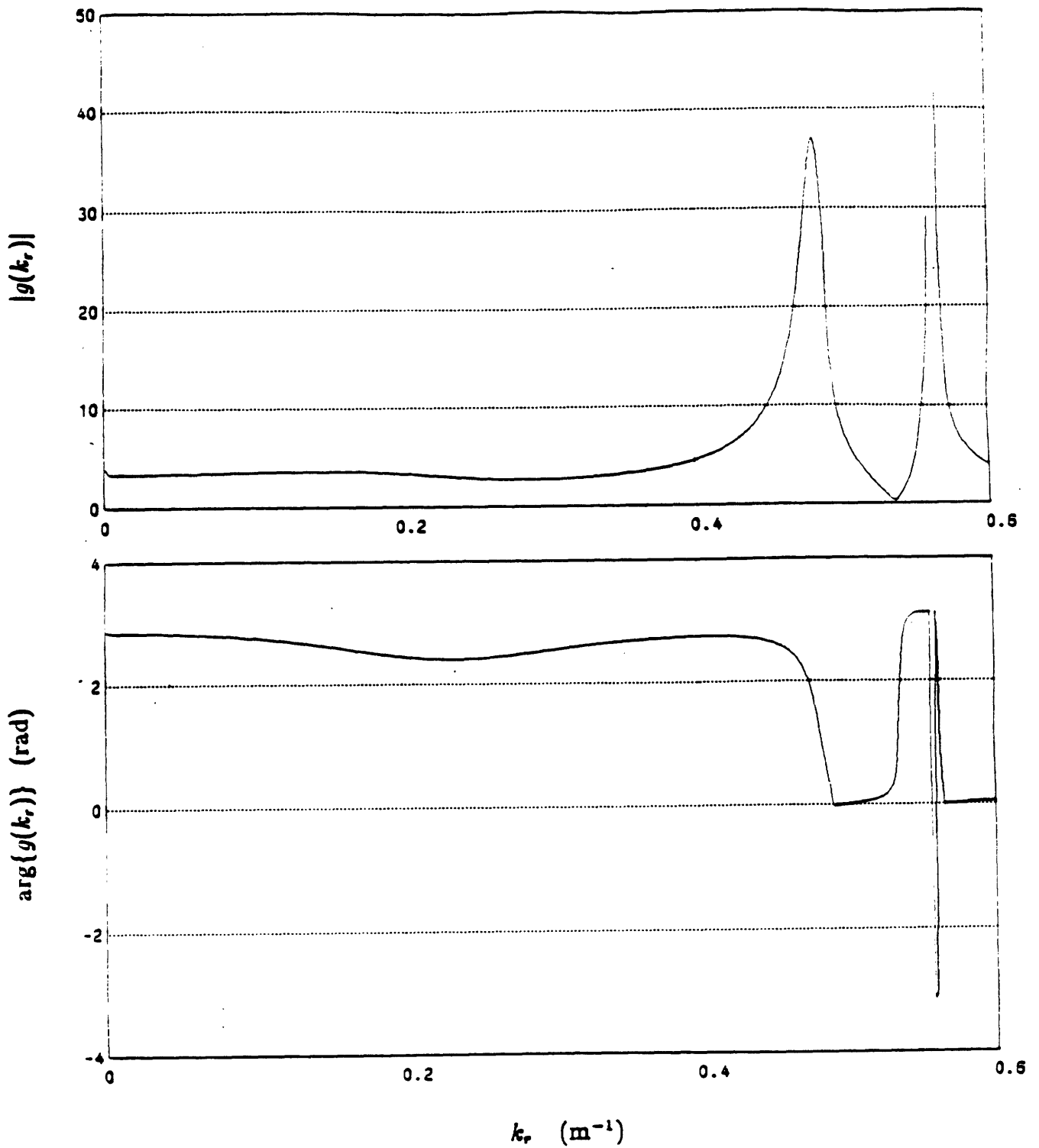
Figure 5.33: Magnitude and phase of the inverted Pekeris model Green's function with displaced source and receiver. This function was obtained by computing the Hankel transform of the total shallow water field.
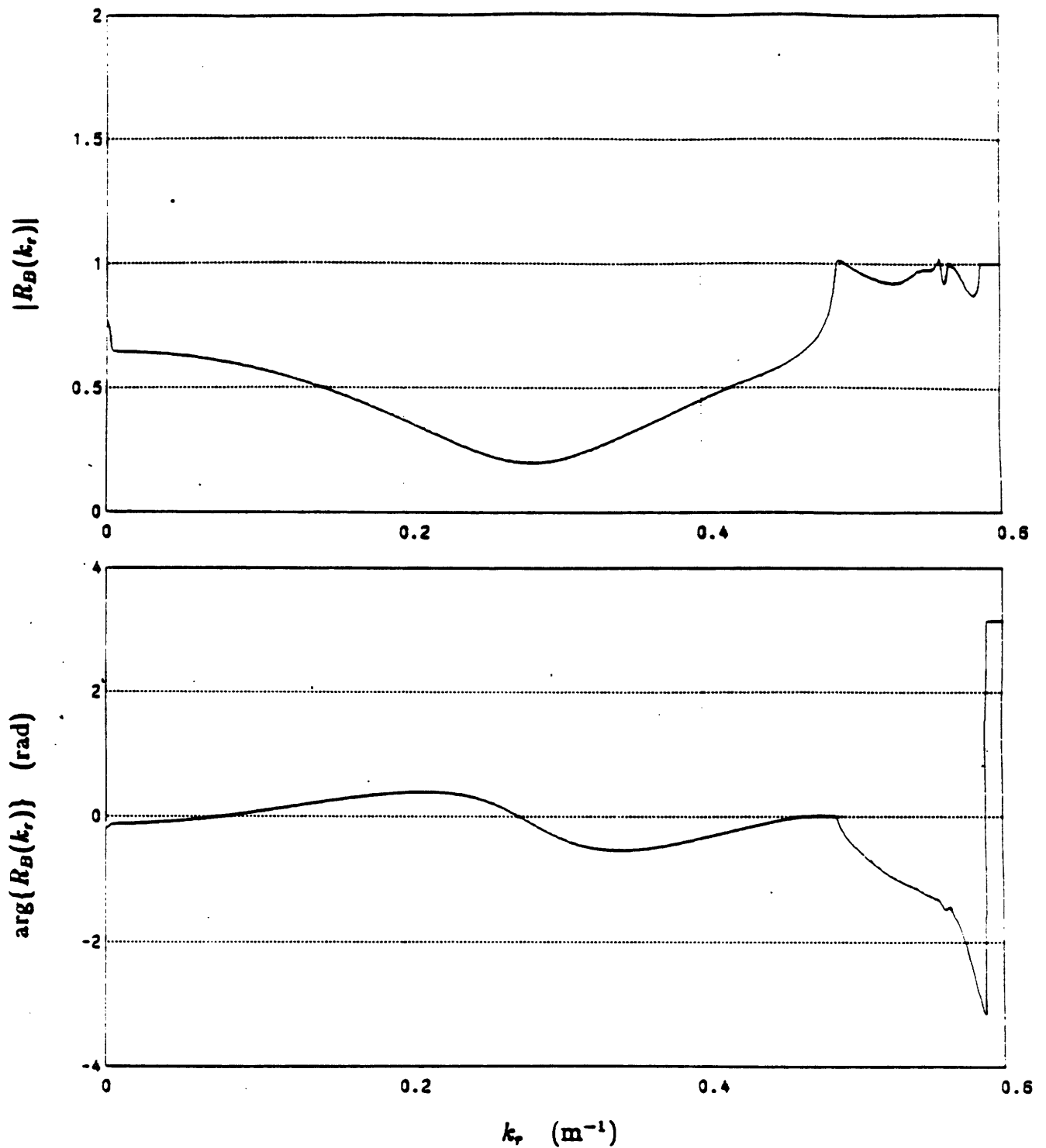
Figure 5.34: Magnitude and phase of the inverted reflection coefficient for the case in which the source and receiver are displaced such that the invariant critical depth is not exceeded. This function was obtained by computing the Hankel transform of the total shallow water field to determine the Green's function and then extracting the reflection coefficient.

source/receiver configuration. In particular, the reflection coefficient no longer exceeds unity at an incorrect value of k_r and its behavior in the region $k_r = 0.25$ to 0.4 is much closer to the behavior of the theoretical reflection coefficient here. The numerical simulation has confirmed that an improvement in the reflection coefficient estimate can be obtained by simply changing the positions of the source and receiver so that the critical depth is not exceeded, i.e. in order to avoid the presence of invariant zeros.

In fact, the quality of the reflection coefficient obtained in the numerical simulation, even for the case of the displaced source and receiver which do not exceed the critical depth, is a bit disappointing. It represents the net effect of all numerical errors in the simulation as well as the errors which occur from processing only a finite portion of the total field. It is our conjecture that the primary source of error is in the use of the asymptotic expressions for the virtual and trapped modes. To investigate this further, the simulations were run again except that the virtual mode was not extracted and added analytically to the field. Rather, it was included as part of $g_C(k_r)$ and was incorporated within the field by computing the Hankel transform of the Green's function with just the single trapped pole removed. The total field was computed by adding the trapped mode contribution to the continuum. The corresponding inverted reflection coefficient is shown in Figure 5.35 for the case of the source and receiver deeper than the critical depth. Although this reflection coefficient is slightly different than that shown in Figure 5.24, it still indicates poor behavior in the region of high sensitivity. Finally, the simulation was run in an identical manner except that the source and receiver were located at depths which did not exceed the critical depth. The corresponding inverted reflection coefficient magnitude and phase are shown in Figure 5.36. Its agreement with the theoretical reflection coefficient, shown in Figure 5.25 is apparent. The two curves again confirm the improvement in the reflection coefficient estimate which results from designing the experiment so that the invariant critical depth is not exceeded.

In summary, we have discussed a numerical simulation method for inverting syn-
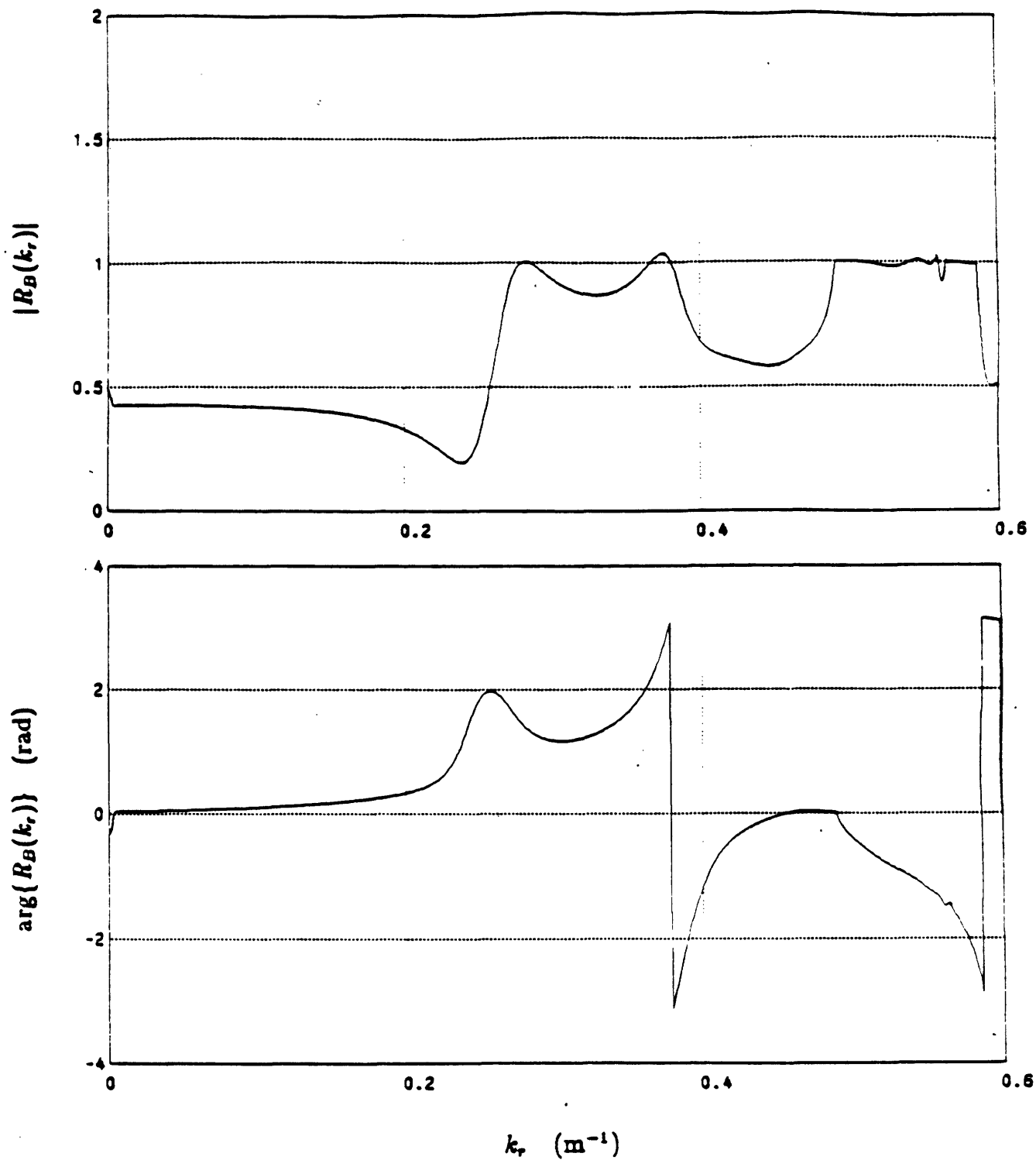
Figure 5.35: Magnitude and phase of the inverted reflection coefficient for the case in which both the source and receiver exceeded the invariant critical depth. The method used to generate the synthetic data included the virtual mode within $g_C(k_r)$.
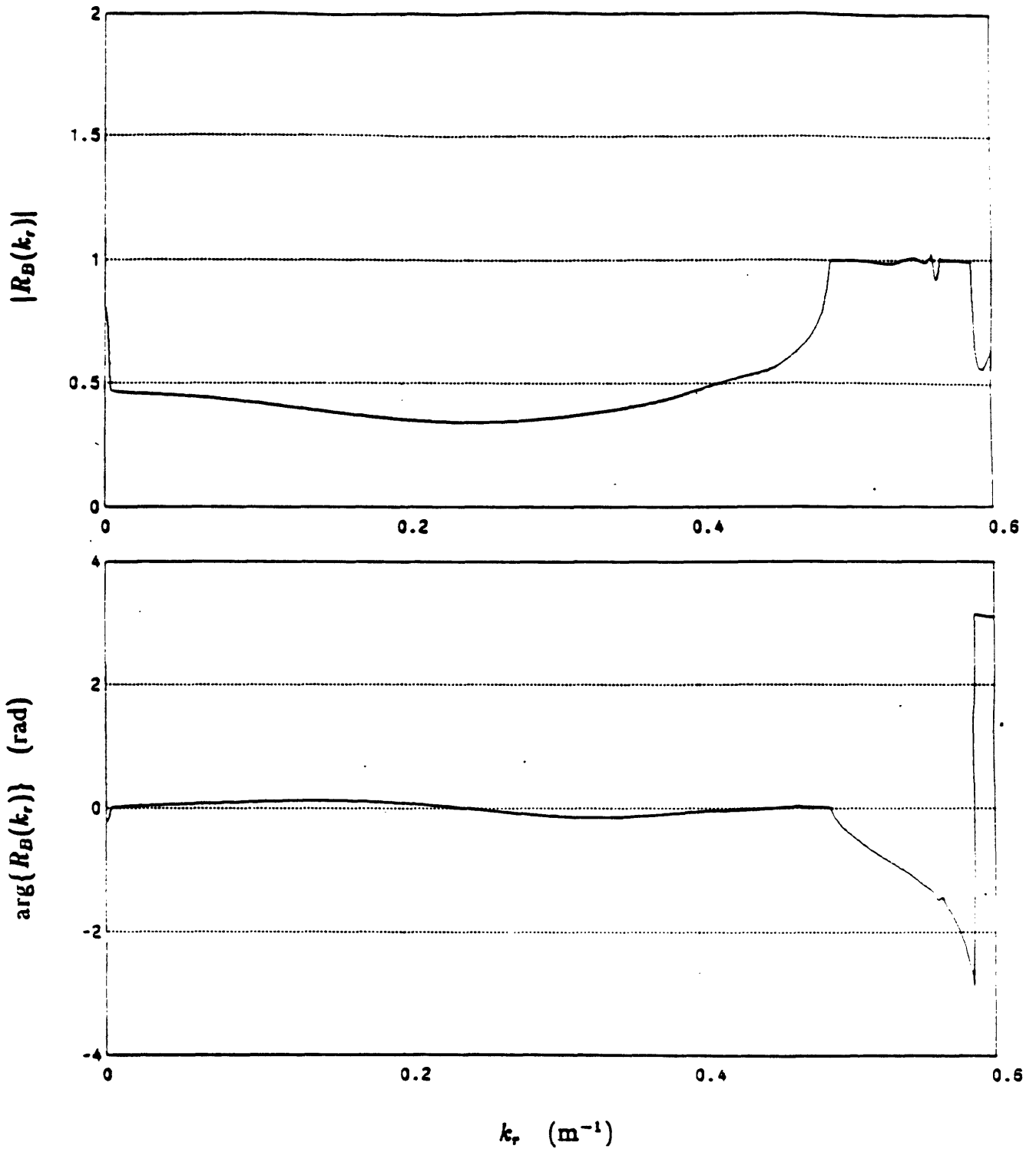
Figure 5.36: Magnitude and phase of the inverted reflection coefficient for the case of the displaced source and receiver. The method used to generate the synthetic data included the virtual mode within $g_C(k_r)$.

thetic acoustic shallow water fields to obtain an estimate of the bottom reflection coefficient. There are a number of difficulties involved in constructing a simulation of this type, including separating the degradations incurred in the synthesis process versus the inversion process, and cancellation of errors. A particular method for constructing a valid simulation which avoids many of these difficulties was presented. An example of the simulation was given as a demonstration of the improvement in the reflection coefficient that can be obtained if the invariant critical depth is not exceeded. The simulation indicated that the primary source of degradation is not the windowing effect, as had been previously suspected, but rather the inherent fundamental sensitivity of the inversion if invariant zeros are present.

5.5 Summary

In this chapter, we have discussed a number of aspects related to the inversion of shallow water acoustic fields. We pointed out that this problem is difficult and is currently not completely solved. Nevertheless, it is felt that the ideas and methods presented in this chapter represent fundamental and important strides towards the solution.

In particular, we asserted that the hybrid method, discussed in Chapter 4, may form a key element in a forward modelling, or analysis-by-synthesis approach. The hybrid method has a number of advantages including speed, accuracy, and a direct relationship between alternate and simpler methods. However, we chose not to make the solution of the inverse problem by forward modelling a major thrust of our research. Rather, we chose to examine other aspects of the shallow water acoustic inversion problem.

Specifically, in the second section of this chapter, we discussed a related question of what to forward model. We proposed that the residual phase of the shallow water acoustic field contains valuable information which can be used both in forward modelling methods and in other applications as well. In order to demonstrate this, we determined the residual phase for a number of different fields, both synthetic and experimental. We demonstrated that the residual phase, in some cases, can be used to accurately determine the wavenumber of a dominant mode. In fact, we found the results of the computation and interpretation of residual phase to be competitive with other methods for extracting information about the waveguide, including the Hankel transform. It is felt that a combination of several of these techniques may represent the best way in which to solve the general inverse problem. Other applications of the residual phase were discussed, including determination of the source phase, which is required in the method for extracting the reflection coefficient, interpretation and correlation with range-varying parameters, and potential utility in methods for syn-

thetically generating fields in range-variant environments.

In the third section of this chapter, we reviewed the theory of extracting the reflection coefficient from measurements in a reverberant waveguide. We pointed out that the theory of the extended Green's function and reflectivity series, discussed earlier in this thesis, may be applied to the more general problem of extracting the reflection from measurements in a non-isovelocity waveguide. Rather than focus on the more complex cases, we chose instead to define and investigate the sensitivity function. This function is a quantitative measure of how ill-conditioned or sensitive the inversion is to errors in the Green's function. A number of theoretical properties of the sensitivity function were derived and its close relationship with the Green's function was developed. Perhaps the most interesting property is that points of infinite sensitivity correspond to invariant zeros of the Green's function or its imaginary part only. The connection was also made via the statement of a number of theorems.

One important practical implication of these results is the definition of the invariant critical depth. This parameter suggests a guideline for conducting an acoustic experiment in which the reflection coefficient is to be extracted from measurements in shallow water. In particular, we showed that if the source and receiver exceed the invariant critical depth, i.e. are located too close to the medium being probed, at least one point of infinite sensitivity is guaranteed in the inversion. Conversely, if neither instrument exceeds the critical depth, no points of infinite sensitivity can be incurred, at least for pre-critical values of horizontal wavenumber.

As a means for further justifying these results, we presented a physical explanation in terms of the cancellation of upgoing and downgoing plane-wave components within the waveguide. The physical argument might also prove to be useful in extending these results to other applications, including non-isovelocity waveguides. Several results involving invariant zeros and points of infinite sensitivity were extended to these cases and the need for further study was suggested.

Finally, in the fourth section of the chapter, we considered the inversion of synthetic shallow water acoustic fields. In doing so, we provided the motivation for solving the experimental inversion problem in terms of studying the synthetic inversion problem. A number of issues involving algorithms, sampling grids, and apertures were discussed. We proposed a particular method for inverting synthetic data, which effectively separates the degradations in the synthesis process itself from effects incurred in the inversion process. The method was used to demonstrate the implications of the sensitivity function theory and the invariant critical depth.

Bibliography

[1] George V. Frisk, Alan V. Oppenheim, and D.R. Martinez. A technique for measuring the plane-wave reflection coefficient of the ocean bottom. *J. Acoust. Soc. Am.*, 68(2), Aug. 1980.

[2] Michael Schoenberg. Nonparametric estimation of the ocean bottom reflection coefficient. *J. Acoust. Soc. Am.*, 64:1165–1170, Oct. 1984.

[3] G.V. Frisk and J.F. Lynch. Shallow water waveguide characterization using the Hankel transform. *J. Acoust. Soc. Am.*, 76(1), July 1984.

[4] D.C. Stickler. Inverse scattering in a stratified medium. *J. Acoust. Soc. Am.*, 74:994–1005, Sept. 1983.

[5] S.D. Rajan, J.F. Lynch, and G.V. Frisk. A direct perturbative inversion scheme to obtain bottom acoustical parameters in shallow water from modal eigenvalues. To be submitted to J.Acoust.Soc.Am, Dec. 1985.

[6] George V. Frisk, James F. Lynch, and James A. Doutt. The determination of geoacoustic models in shallow water. Presented at Symposium on Ocean Seismo-Acoustics, La Spezia, Italy, June 10-14 1985.

[7] D.R. Mook. *The Numerical Synthesis and Inversion of Acoustic Fields Using the Hankel Transform with Application to the Estimation of the Plane Wave Reflection Coefficient of the Ocean Bottom.* Technical Report, Sc.D. Thesis, MIT/WHOI Joint Program, Cambridge Ma., Jan. 1983.

[8] George V. Frisk, Douglas R. Mook, James A. Doutt, Earl E. Hays, Michael S. Wengrovitz, and Alan V. Oppenheim. The application to experimental data of a technique for measuring the plane-wave reflection coefficient of the ocean bottom. To be submitted to J.Acoust.Soc.Am., Dec. 1985.

[9] Jose M. Tribolet. A new phase unwrapping algorithm. *IEEE Trans. Acoustics, Speech, and Signal Processing*, 25(2):170–177, Apr. 1977.

[10] Alan V. Oppenheim and Ronald W. Schafer. *Digital Signal Processing*. Prentice-Hall, Englewood Cliffs, NJ, 1975.

[11] George V. Frisk. Private communication, Nov. 1985.

[12] Thomas E. Bordley. *Improved Paraxial Methods for Modelling Underwater Acoustic Propagation*. Technical Report, Sc.D. Thesis, Massachusetts Institute of Technology, Cambridge, Ma., May 1985.

[13] Andrew L. Kurkjian. *The Estimation of the Cylindrical Wave Reflection Coefficient*. Technical Report, Ph.D. Thesis, Massachusetts Institute of Technology, Cambridge, Ma., July 1982.

[14] Eric W. Hansen. New algorithms for Abel inversions and Hankel transforms. *Proc. 1983 ICASSP*, 2:1260–1263, 1983.

[15] Ronald N. Bracewell. *The Fourier Transform and Its Applications*. McGraw-Hill, New York, 1978.

Chapter 6

Reconstruction of a Complex-Valued Acoustic Field From its Real or Imaginary Part

6.1 Introduction

In this chapter, we discuss the reconstruction of a complex-valued acoustic field from its real or imaginary part. The reconstruction method is based on the approximate real-part/imaginary-part sufficiency condition for outgoing acoustic fields discussed in Chapter 3. An intuitive explanation for this condition is obtained by exploiting the similarity between a complex-valued outwardly propagating field and a complex-valued signal which has a one-sided Fourier transform. The implication is that only one component of the field or signal is required and that the alternate component can be reconstructed. There exist several methods for performing the reconstruction and issues related to the reconstruction of sampled fields, required sampling rate, and algorithm selection will be discussed in this chapter. Additionally, because the underlying assumption on which the real-part/imaginary-part sufficiency

condition is based is only an approximation, i.e. that the Hilbert-Hankel transform can be used to approximately synthesize the acoustic field, characterizing the quality of the approximation, particularly in the context of a reconstruction scheme, is quite important. In order to do this, we will present a number of examples of the reconstruction method applied to various acoustic fields which vary in complexity from simple free-space fields to actual experimental fields which have interacted with the surface and bottom of a shallow ocean.

In this section, we will provide some motivation for developing an algorithm for reconstructing one component from the alternate quadrature component. We will also address the question of how measurements of a complex-valued field are obtained in the first place, when in a strictly practical sense, the pressure field due to a point source must certainly be a real-valued quantity. The relationship between quadrature demodulation, sampling, the real-part/imaginary-part sufficiency condition, and the reconstruction method will be discussed.

In acoustical signal processing, the three-dimensional wave equation is used as the model which describes the propagation of sound. Thus, the equation for the acoustic sound pressure field $p(\mathbf{r}, t)$ within a layer is

$$(\frac{\partial^2}{\partial x^2} + \frac{\partial^2}{\partial y^2} + \frac{\partial^2}{\partial z^2})p(\mathbf{r}, t) - \frac{1}{c^2(\mathbf{r})}\frac{\partial^2 p(\mathbf{r}, t)}{\partial t^2} = s(\mathbf{r}, t) \qquad (6.1)$$

where the quantity $s(\mathbf{r}, t)$ on the right-hand of this equation is a general complex-valued source field. The solution of the partial differential equation is linear with respect to the source $s(\mathbf{r}, t)$. In other words, doubling the source strength will cause a doubling of the pressure field $p(\mathbf{r}, t)$ and the pressure field due to the coherent sum of the sources must consist of the coherent sum of the pressure fields due to each individual source. In previous chapters of this thesis, we have chosen the specific form of the source field as

$$s_1(\mathbf{r}, t) = e^{-j\omega t}\delta(\mathbf{r}) \qquad (6.2)$$

It may be shown in a straightforward manner that $e^{-j\omega t}$ represents a temporal eigen-

function of the wave equation. That is, if the source on the right-hand side of the wave equation is harmonic in time, the pressure field on the left-hand side must also be harmonic with the same functional form. Therefore, the pressure field $p_1(\mathbf{r}, t)$ due to the harmonic point source $s_1(\mathbf{r}, t)$ must be of the form

$$p_1(\mathbf{r}, t) = p(\mathbf{r})e^{-j\omega t} \tag{6.3}$$

If these forms for $s_1(\mathbf{r}, t)$ and $p_1(\mathbf{r}, t)$ are substituted into the wave equation, the Helmholtz equation results. Additionally, it is the complex-valued quantity $p(\mathbf{r})$ which is of fundamental importance in the context of inversion, i.e. it is $p(\mathbf{r})$ which is directly related to $g(k_r)$ and the bottom reflection coefficient $R_B(k_r)$.

In practice, a realistic acoustic source cannot have the complex-valued form shown in equation (6.2), but rather must be of the general real-valued form

$$s_2(\mathbf{r}, t) = A\cos(\omega t + \theta)\delta(\mathbf{r}) \tag{6.4}$$

where A and θ are arbitrary constants. Note that even though the source is real-valued, the linearity of the wave equation can be exploited to determine the complex-valued pressure $p(\mathbf{r})$. In particular, we see that if the realistic source is re-written as

$$s_2(\mathbf{r}, t) = \frac{A}{2}(e^{-j(\omega t + \theta)} + e^{j(\omega t + \theta)})\delta(\mathbf{r}) \tag{6.5}$$

then

$$s_2(\mathbf{r}, t) = \frac{A}{2}(\,e^{-j\theta}s_1(\mathbf{r}, t) + e^{j\theta}s_1^*(\mathbf{r}, t)\,) \tag{6.6}$$

From linearity, the pressure response, $p_2(\mathbf{r}, t)$ to the realistic source must therefore have the form

$$p_2(\mathbf{r}, t) = \frac{A}{2}(\,e^{-j\theta}p_1(\mathbf{r}, t) + e^{j\theta}p_1^*(\mathbf{r}, t)\,) \tag{6.7}$$

so that

$$p_2(\mathbf{r}, t) = A\,Re\{p(\mathbf{r})e^{-j(\omega t + \theta)}\} \tag{6.8}$$

Note that the total response to the real-valued source is also real-valued and that the desired quantity, $p(\mathbf{r})$ is complex-valued.

There are several methods by which $p(\mathbf{r})$ can be extracted from $p_2(\mathbf{r}, t)$. For example, if $p_2(\mathbf{r}, t)$ is available at a given range for all time, the one-dimensional temporal Fourier transform can be applied and evaluated at the frequency ω to obtain $Ap(\mathbf{r})e^{-j\theta}/2$. The complex number $p(\mathbf{r})$ is easily extracted from this quantity, assuming that the complex source gain $Ae^{-j\theta}$ is known. The transform can be computed using the discrete Fourier transform if a temporally sampled version of $p_2(\mathbf{r}, t)$ is available. This method is usually not practical however, due to the large sampling rate which is required - the bandwidth of the signal is 2ω, where ω is the frequency of the harmonic acoustic source.

A more typical method employed is quadrature demodulation [1] [2] [3]. In this method, $p_2(\mathbf{r}, t)$ at each range point is multiplied by $\cos\omega t$ and integrated over time to yield $ARe\{p(\mathbf{r})e^{-j\theta}\}$. Similarly, $p_2(\mathbf{r}, t)$ is multiplied by $\sin\omega t$ and integrated over time to yield $AIm\{p(\mathbf{r})e^{-j\theta}\}$. The two quantities can be combined and divided by the complex source gain to yield $p(\mathbf{r})$. Alternately, the quantity $Ae^{-j\theta}p(\mathbf{r})$ can be directly processed and the source gain can be eliminated later. In practice, quadrature demodulation is implemented in analog circuitry. The multiplication operation is performed using a mixer and the integration operation is approximated using a low-pass filter.

For example, a block diagram of the data acquisition harware, used in acquiring the experimental acoustic fields presented in this thesis, is shown in Figure 6.1. As can be seen from the figure, the quadrature demodulation is performed to obtain range samples of $p(\mathbf{r})$, which are then digitized and stored. Of critical importance in this data acquisition technique is that the separate $\cos\omega t$ and $\sin\omega t$ oscillators in the mixer remain in perfect synchrony. Additionally, if there are any differences in the gain or phase through the two channels, the quadrature demodulation result will be imperfect and thus the samples of $p(\mathbf{r})$ will be corrupted. Furthermore, the hardware which performs the operations shown in this block diagram is typically moored underwater. Maintenance of the conditions of perfect synchrony and identical gains through the
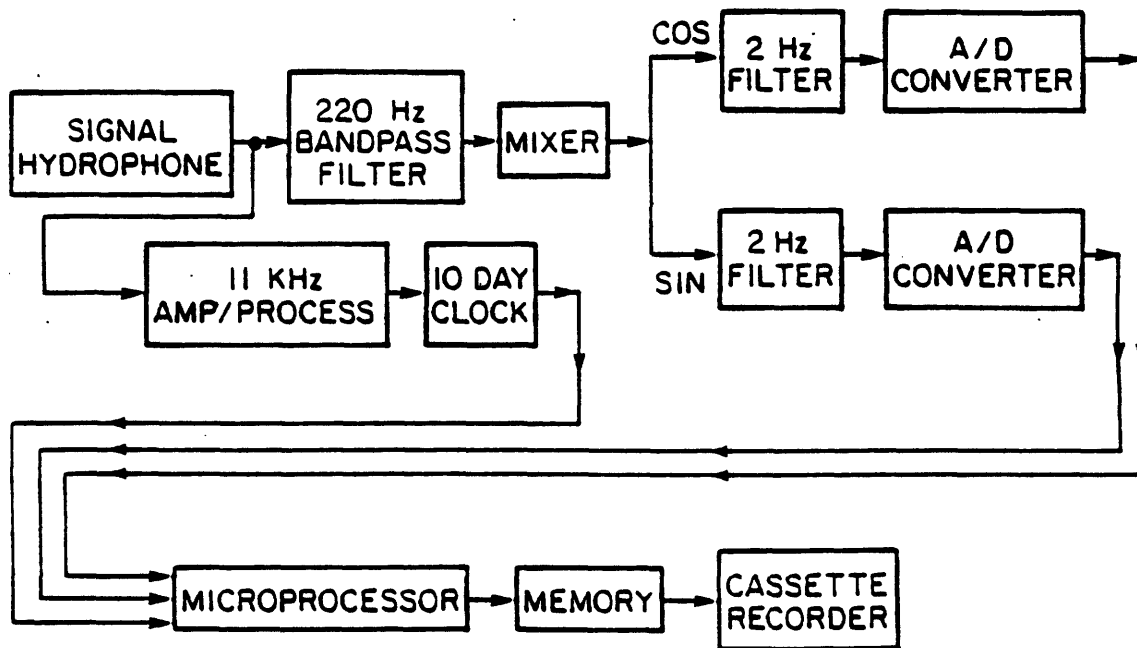
Figure 6.1: Block diagram of data acquisition hardware.

two channels may be difficult to achieve, particularly in the harsh environment in which the hardware is located.

In this chapter, we will discuss a reconstruction algorithm for obtaining real (or imaginary) samples of $p(r)$ from imaginary (or real) samples of $p(r)$. There are several practical advantages of a software reconstruction method in which one of these channels is recovered from samples of the alternate channel. In particular, a large portion of the data acquisition hardware shown in Figure 6.1 can be eliminated and digital storage requirements can be reduced. Additionally, the requirements of perfect synchrony and identical channel gains are no longer of necessity. It is still essential to establish the complex gain through the single channel which remains, if the inversion to obtain the reflection coefficient is to be performed, but we point out that the reconstruction method does not depend on this knowledge. Additionally, as discussed earlier, it may be possible to determine the phase portion of this complex gain directly from the residual phase of the field, or reconstructed field.

An essential point to be made here is the distinction between the sampling rate in range and the real-part/imaginary-part sufficiency condition for $p(r)$. In general, it is not possible to double the sampling rate of some arbitrary complex-valued function of range, and eliminate one of the sampled channels, without loss of information. In fact, if the real and imaginary components of the function $p(r)$ are independent of each other, it is not possible to reconstruct the real (or imaginary) component of $p(r)$ from a sampled version of the imaginary (or real) component even if the sampling rate is infinite. The fact that $p(r)$ has a real-part/imaginary-part sufficiency condition is not related to the sampling rate but rather is a consequence of the applicability of the Hilbert-Hankel transform. However, there is a consequence of the real-part/imaginary-part sufficiency condition which is related to sampling. As pointed out in Chapter 3, if both the real and imaginary components are sampled, the real-part/imaginary-part sufficiency implies that the sampling rate can be reduced by a factor of two, as compared with the conventional sampling rate of two complex

373

samples per water wavelength.

The algorithm for reconstruction is now discussed. In Chapter 3 we showed that an outgoing acoustic field can be approximated as

$$p(r) \sim p_{as}(r) \quad r \gg 0 \tag{6.9}$$

where $p_{as}(r)$ is the asymptotic Hilbert-Hankel transform of the Green's function $g(k_r)$, i.e.

$$p_{as}(r) = \mathcal{H}_{as}^{-1}\{g(k_r)\} = \frac{1}{2}\int_0^\infty g(k_r)(\frac{2}{\pi k_r r})^{1/2}e^{j(k_r r - \pi/4)}k_r dk_r \tag{6.10}$$

We also showed that $p_a(r)$ and thus $p_{as}(r)$ are approximately causal if the field is approximated by the Hilbert-Hankel transform, and thus

$$p(r)r^{1/2}u(r) \sim \frac{1}{2\pi}\int_0^\infty g(k_r)(\frac{2\pi}{k_r})^{1/2}e^{j(k_r r - \pi/4)}k_r dk_r \tag{6.11}$$

which implies that $Re[p(r)u(r)r^{1/2}]$ and $Im[p(r)u(r)r^{1/2}]$ form an approximate Hilbert transform pair. When sampled versions of these signals are involved, there exist several methods for determining the Hilbert transform [4] [5]. In the method we chose, a sampled version of $Re[p(r)u(r)r^{1/2}]+jIm[p(r)u(r)r^{1/2}]$ is obtained by computing the FFT of $Re[p(r)u(r)r^{1/2}]$ (or $jIm[p(r)u(r)r^{1/2}]$), multiplying by $2u(k_r)$, and computing the inverse FFT. An investigation of alternate methods for computing the Hilbert transform has not been done in the context of acoustic field reconstruction, however we point out that a discrete Hilbert transform based on an optimal FIR filter [6] [7] may have application to this problem.

In the remaining sections of this chapter, we will apply this reconstruction algorithm to a number of deep and shallow water acoustic fields. A large number of examples will be presented for several reasons. First, the fact that some underlying assumptions are involved suggests that the reconstruction algorithm might perform well in certain cases but not in others. In fact, we have not found this to be the case and a variety of examples has been chosen as a demonstration. Second, several example fields which have known analytic expressions have been selected so that the issue

of synthetic generation, particularly with regard to use of the Hankel transform or Hilbert-Hankel transform, is completely decoupled from the reconstruction method. The examples chosen are also indicative of the fact that the reconstruction method is applicable to both deep and shallow water coherent processing applications, in which information about the ocean bottom is to be determined from a single sampled channel. Finally, the reconstruction method will be applied to several experimental acoustic fields in order to demonstrate that it can be applied not only in theory, but in practice as well.

6.2 Reconstruction of Simple Acoustic Fields

We begin this discussion by considering the simplest possible acoustic field - the field in free space due a point time-harmonic source. We will further choose the source and receiver for this example to be of nearly identical heights with respect to an arbitrary reference plane as shown in Figure 6.2. The heights were chosen as nearly identical as opposed to exactly identical to avoid the issues related to the singular behavior of the pressure field at zero range in the latter case. We point out that, ironically, this simplest field yields the poorest results in the context of reconstruction of one channel from the alternate channel. The reason for this, related to the required sampling rate for this field, will be explained shortly. The parameters chosen for this example are also indicated in Figure 6.2. This field can be expressed in closed-form as

$$p(r) = \frac{e^{jk_0 R}}{R} \tag{6.12}$$

where k_0 is the water wavenumber and where $R = (r^2 + (z - z_0)^2)^{1/2}$. Using this expression, we have plotted the corresponding field magnitude and residual phase, using $k_\phi = k_0$ in Figure 6.3. The simplicity of the field, when displayed in this manner, is apparent. The magnitude decays as $1/r$ since $R \sim r$ for $r \gg |z - z_0|$, as can be verified by examining the magnitude at $r = 1000 \ m$ where the field magnitude is 0.001. The residual phase, $\phi(r)$ quickly approaches the constant value of zero since

$$\phi(r) = P\{arg\{p(r)\} - k_\phi r\} = P\{k_0 R - k_\phi r\} \sim 0 \tag{6.13}$$

for $r \gg |z - z_0|$. The rapidly varying real and imaginary components for this field are displayed in Figure 6.4. In the reconstruction scheme, one of these components must be obtained from the other.

Previously, it was suggested that in order to adequately sample an acoustic field, two complex samples per water wavelength [1] were required [3] [8] Apparently, it seems

---

[1] The water wavelength λ_0 is defined as $2\pi/k_0$, where k_0 is the water wavenumber.
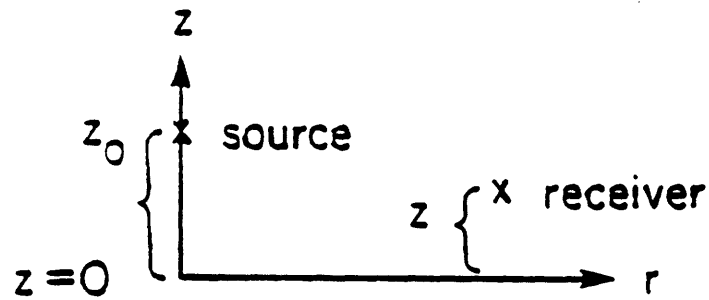
$\lvert z_0 - z \rvert$	=	1 m
f	=	220 Hz
c	=	1500 m/sec
k_0	=	.9215 rad/m

Figure 6.2: Geoacoustic model for a free-space field with source and receiver of nearly identical heights with respect to a reference plane.
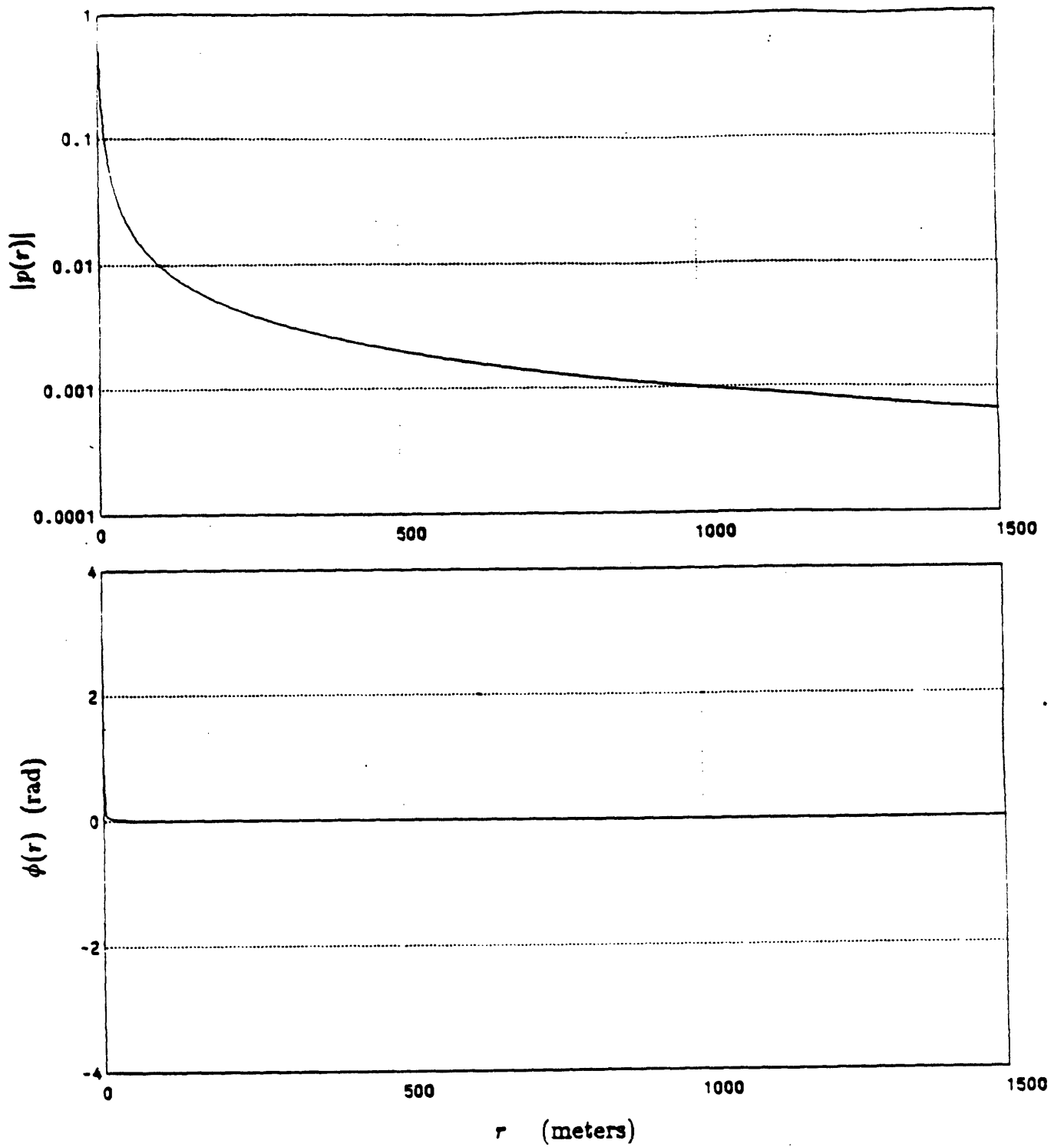
Figure 6.3: Magnitude and residual phase of free-space field.
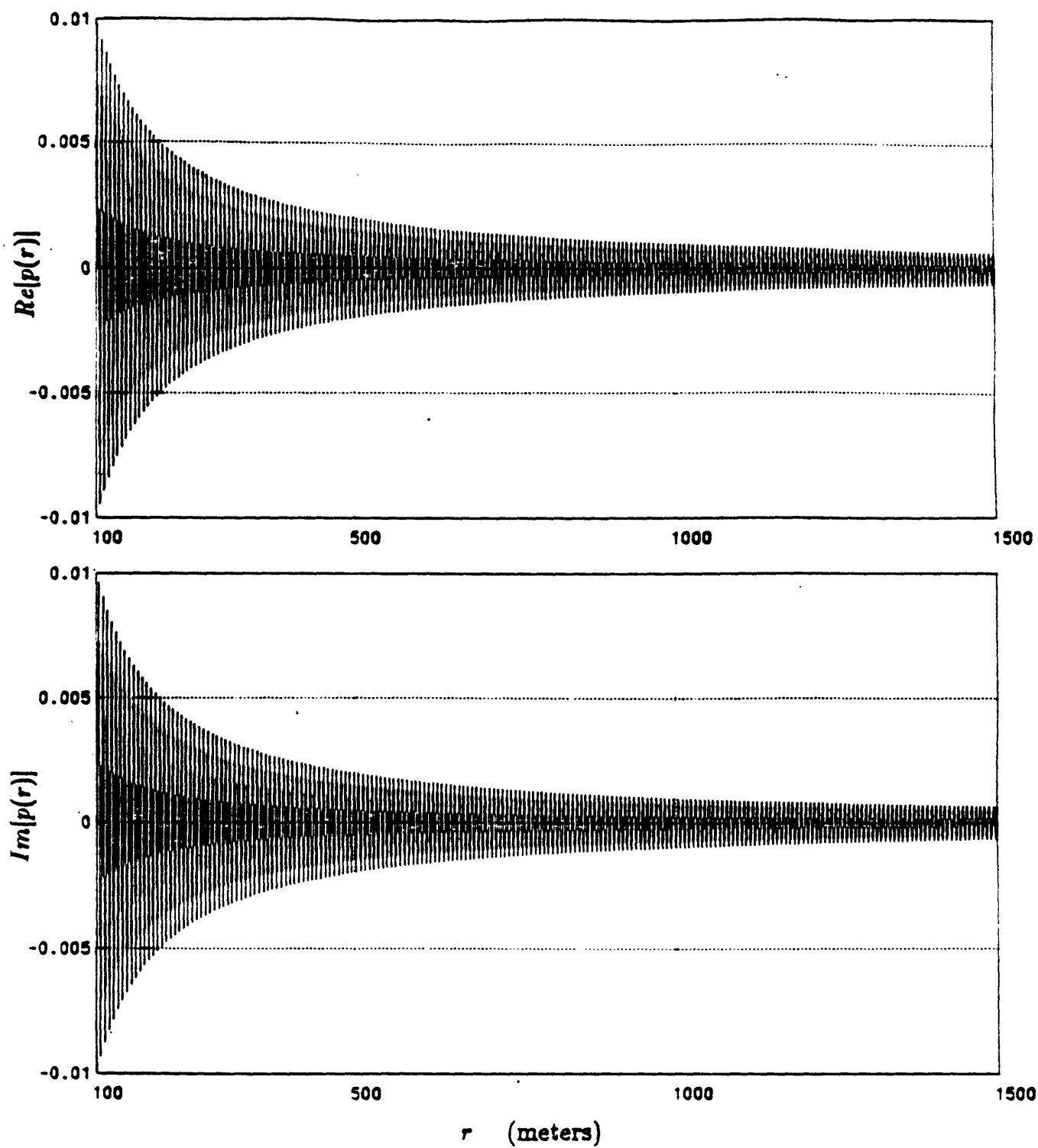
Figure 6.4: Real and imaginary components of the free-space field.

that there must be some loss of information or reduction in the number of degrees of freedom when the real or imaginary parts of these samples are discarded and then reconstructed. In fact, no information is lost, but we will postpone a discussion of why this is the case until later. Thus, we will choose the sampling rate for this example as four complex samples per water wavelength. For the selected parameters this corresponds to sampling the acoustic field once every 1.7 m. We again point out that in general, complex sampling *cannot* be replaced by simply doubling the sampling rate of a single channel.

To perform the reconstruction, the real part of the field shown in Figure 6.4 was set to zero and 1024 samples of the imaginary part were retained. Thus, the imaginary component, sampled every 1.7 m from $r = 0$ to $r = 1745$ m, was used in the reconstruction algorithm. In using an aperture of this size, the effects of windowing may be quite substantial in the context in inverting the field to extract a Green's function. An exhaustive study of how windowing and the number of samples affects the reconstruction has not been performed. However, we have found that typical apertures of this size yield good reconstruction results and the performance of the algorithm does not appear to be highly sensitive to the choice of these parameters.

The results of the reconstruction algorithm are shown in Figure 6.5. The top curve shows the true real part of the field and the bottom curve shows the reconstructed real part. The rapidly varying nature of the components in this figure makes it difficult to assess the quality the reconstruction. Apparently, some other display or related measurement must be determined. We have chosen two other methods which are perhaps more indicative of the algorithm's performance. The first method is to recompute the field magnitude and residual phase using the reconstructed channel and the original alternate channel. By comparing the magnitude and residual phase after reconstruction with the original magnitude and residual phase, it is possible to qualitatively assess the performance of the reconstruction technique. Unfortunately, although the display of magnitude and residual phase is quite meaningful, the reconstructed channel
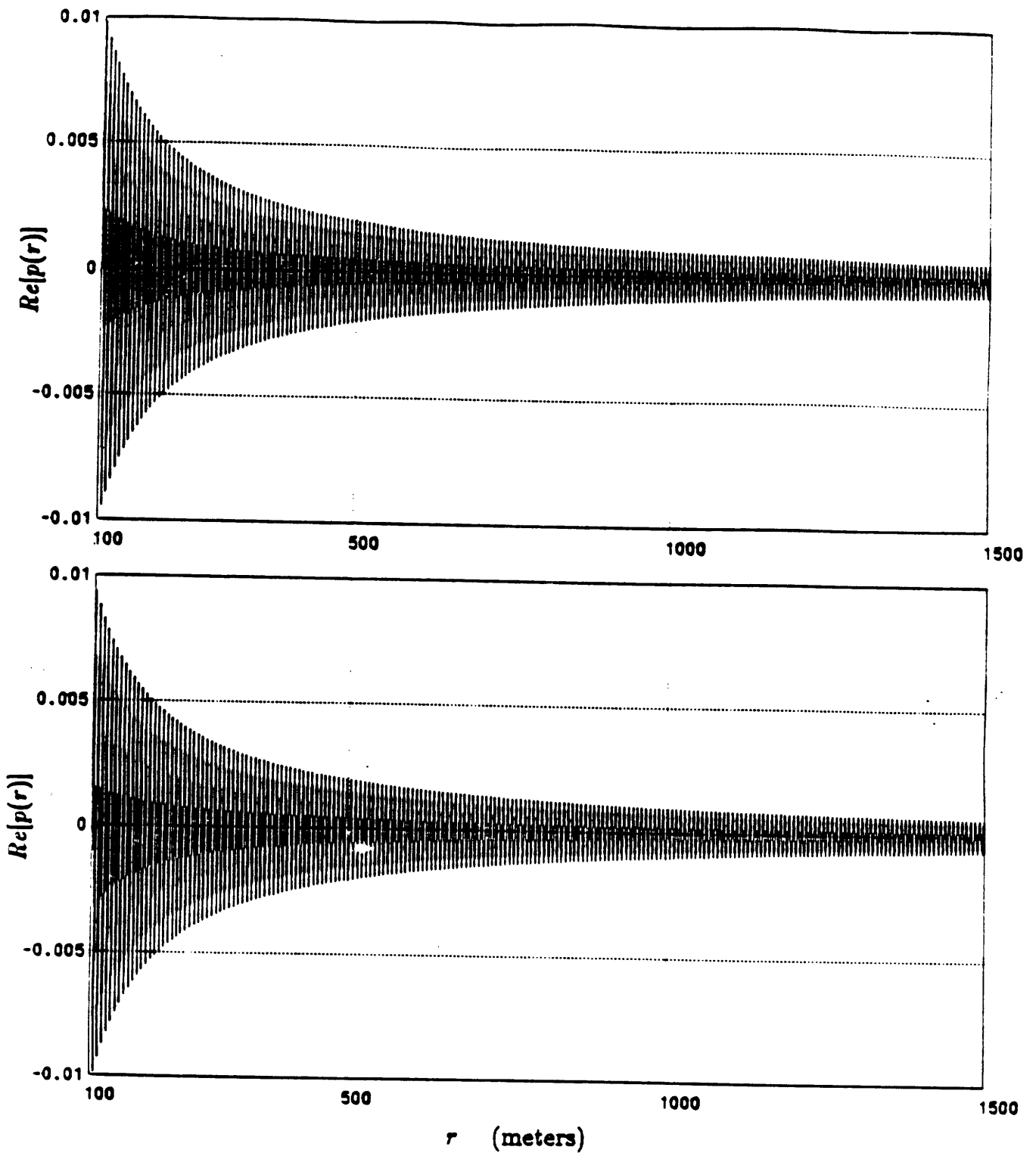
Figure 6.5: Original real component (top) and reconstructed real component (bottom) for the free-space field.

and the true alternate channel are mixed together in this representation. Alternately, we have chosen to display the magnitude of the difference between the reconstructed channel and its true version. We will refer to this measurement as the *error signal* and it will typically be plotted along with the magnitude of the true field, both as a function of range, as an indication of its relative importance.

The magnitude and residual phase of the reconstructed field are shown in Figure 6.6. These curves are to be compared with the true magnitude and residual phase previously displayed in Figure 6.3. As can be seen, the reconstructed field magnitude decays at the correct $1/r$ rate and the residual phase is nearly flat. There is some ringing in the residual phase however and the overall quality of this reconstruction is certainly not perfect. Ironically, as pointed out previously, although this field has the simplest form the quality of its reconstruction is the worst of any example we have found.

In this example, the field has not been adequately sampled due to the fact that $z \sim z_0$. As pointed out in Chapter 4, it may not always be appropriate to consider the Green's function as wavenumber limited at the water wavenumber particularly when $z \sim z_0$. As an example of this, the magnitude and phase of the theoretical Green's function for this field are displayed in Figure 6.7. The peak in the magnitude function, which occurs at $k_r = k_0$ where $k_{z0} = 0$, is finite only because of plotting artifacts. From the figure, it is apparent that the wavenumber decomposition for this field contains components at values significantly higher than the water wavenumber. For example, at twice the water wavenumber there are components present with amplitudes greater than ten-percent of the amplitudes of the low-wavenumber components. [2] The implication is that in order to adequately represent this field, the sampling rate should be much larger than two complex samples per water wavelength. The quality

---

[2] Although the Green's function is slowly decaying, its imaginary part is zero for values of k_r greater than the water wavenumber, k_0. This is an example of the property discussed in Chapter 4 related to the finite-extent of the imaginary part of the total deep water Green's function.
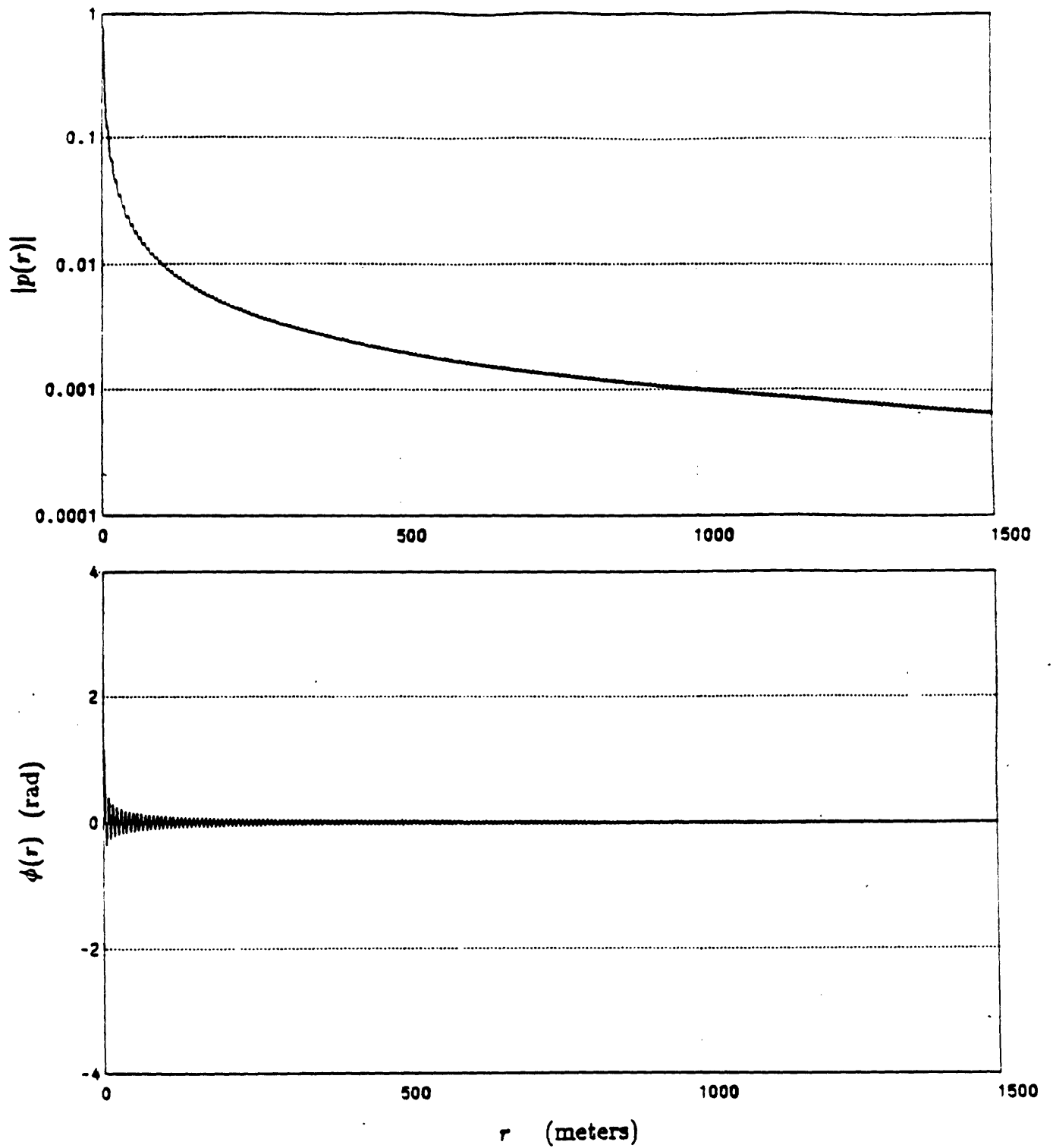
Figure 6.6: Magnitude and residual phase of the reconstructed free-space field.
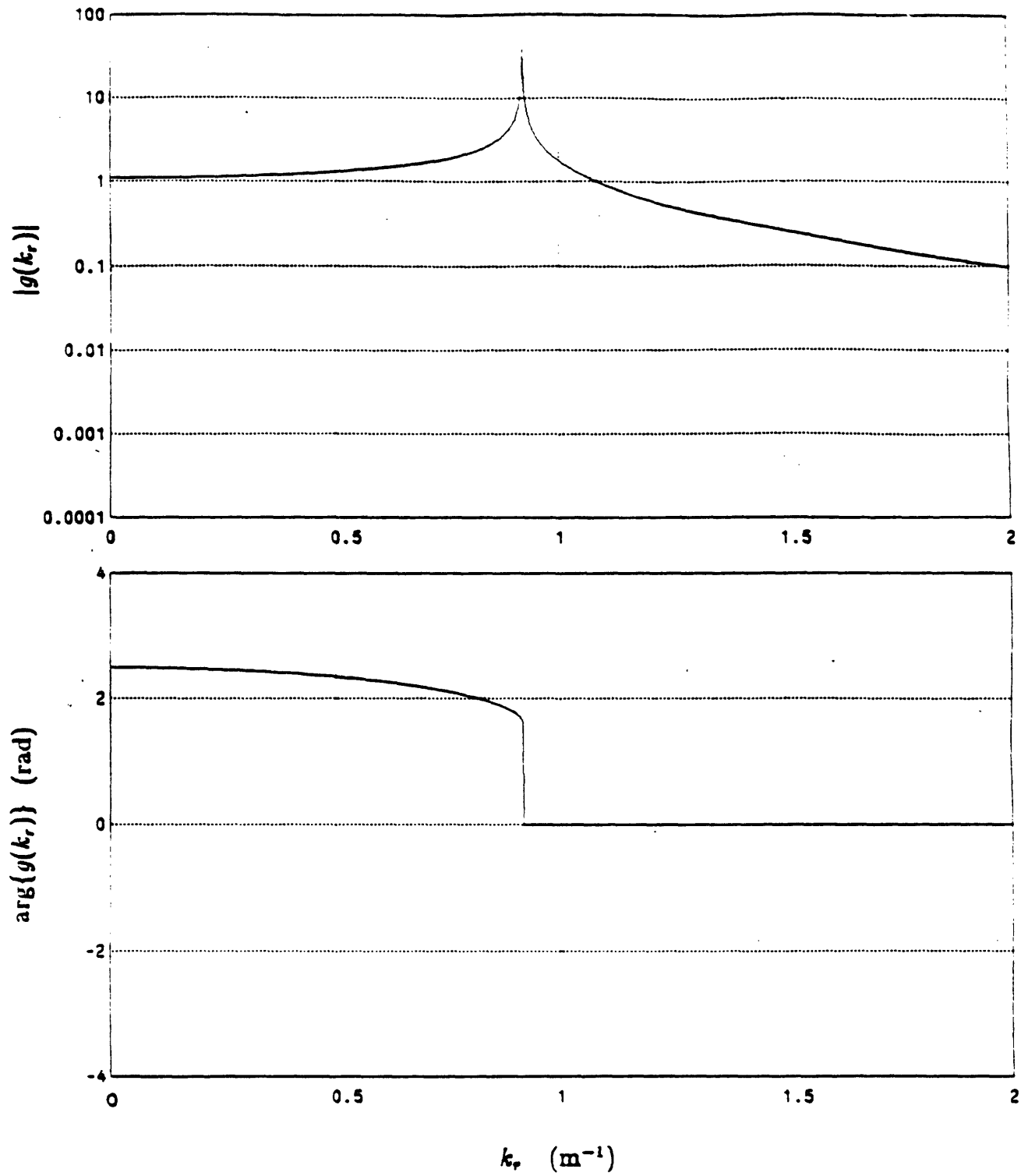
Figure 6.7: Magnitude and phase of the theoretical total Green's function for the free-space field.

of the reconstruction of this field is perhaps more an indication of the fact that the field was undersampled initially than any other effect.

The error signal for the reconstruction in this example is shown as the bottom curve in Figure 6.8 along with the magnitude of the true field shown as the top curve. The error curve indicates that the reconstruction error is at least one to two orders of magnitude below the intensity of the field at all ranges except the near-field. We will consider the behavior in the near-field in more detail in later examples in which the field has been adequately sampled initially. This example has been included to show that even if this simple field is undersampled, the reconstructed results do not exhibit significant degradation.

In the next example, the geoacoustic model is identical to the one just considered except that the source and receiver have been vertically displaced, as is shown in Figure 6.9. The field is still a free-space field which can be synthetically generated using its closed-form expression. However, the assumption that the corresponding Green's function is wavenumber limited is much more realistic in this case due to the displaced source and receiver as can be concluded by examining the magnitude of the theoretical Green's function, shown in Figure 6.10. Therefore, a sampling rate of two complex samples or four real samples is certainly adequate in this case and we will note a significant improvement in the quality of the reconstruction for this example.

In Figure 6.11 is shown the true magnitude and residual phase of this field. The rapid variation of the residual phase, particularly in the near-field, indicates that a different choice of k_ϕ, used to compute the residual phase, might have been more effective in displaying a slowly varying quantity directly related to the phase of the field. Nevertheless, we will retain the definition of residual phase provided earlier for consistency among the examples to be discussed. In Figure 6.12, the rapidly varying real and imaginary parts of this field are shown. In a reconstruction scheme, one of these components must be determined from the other. In further examples, we
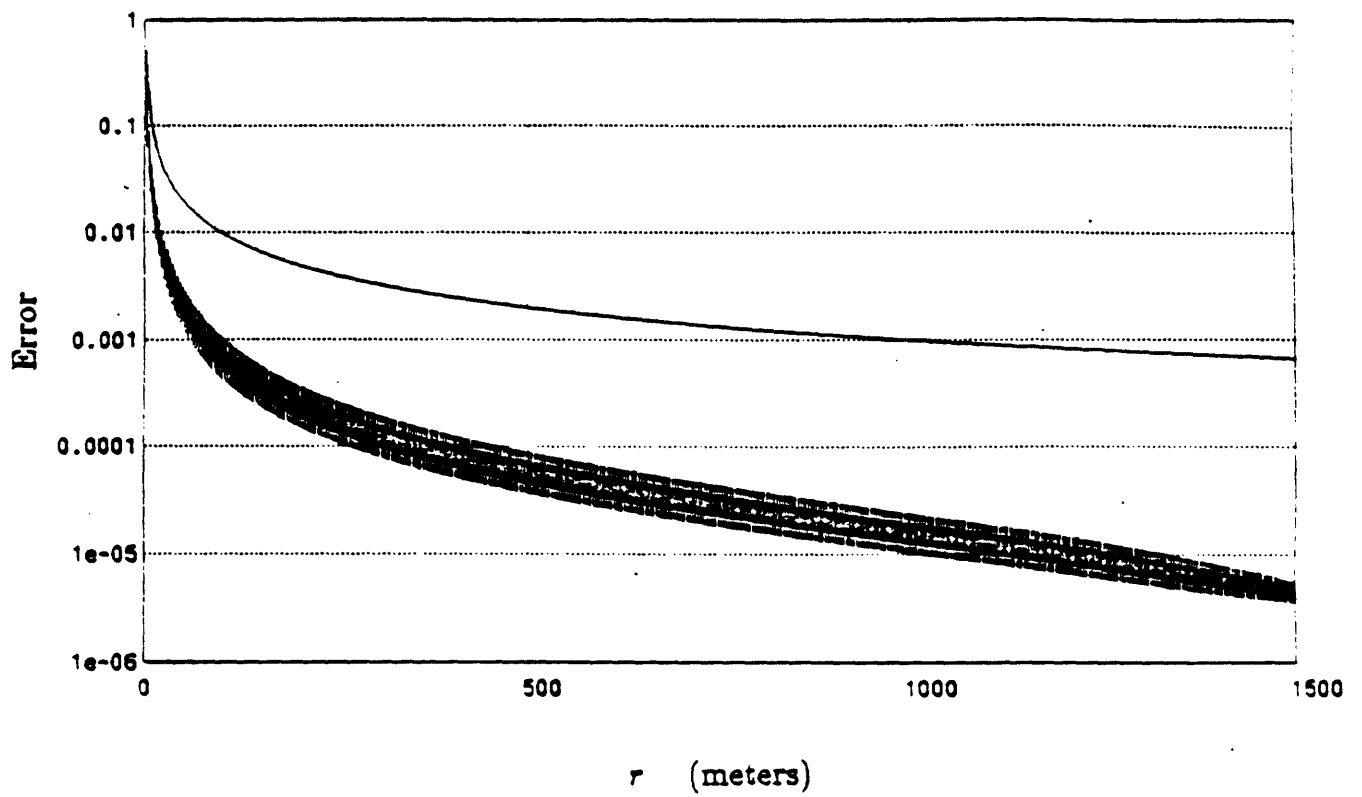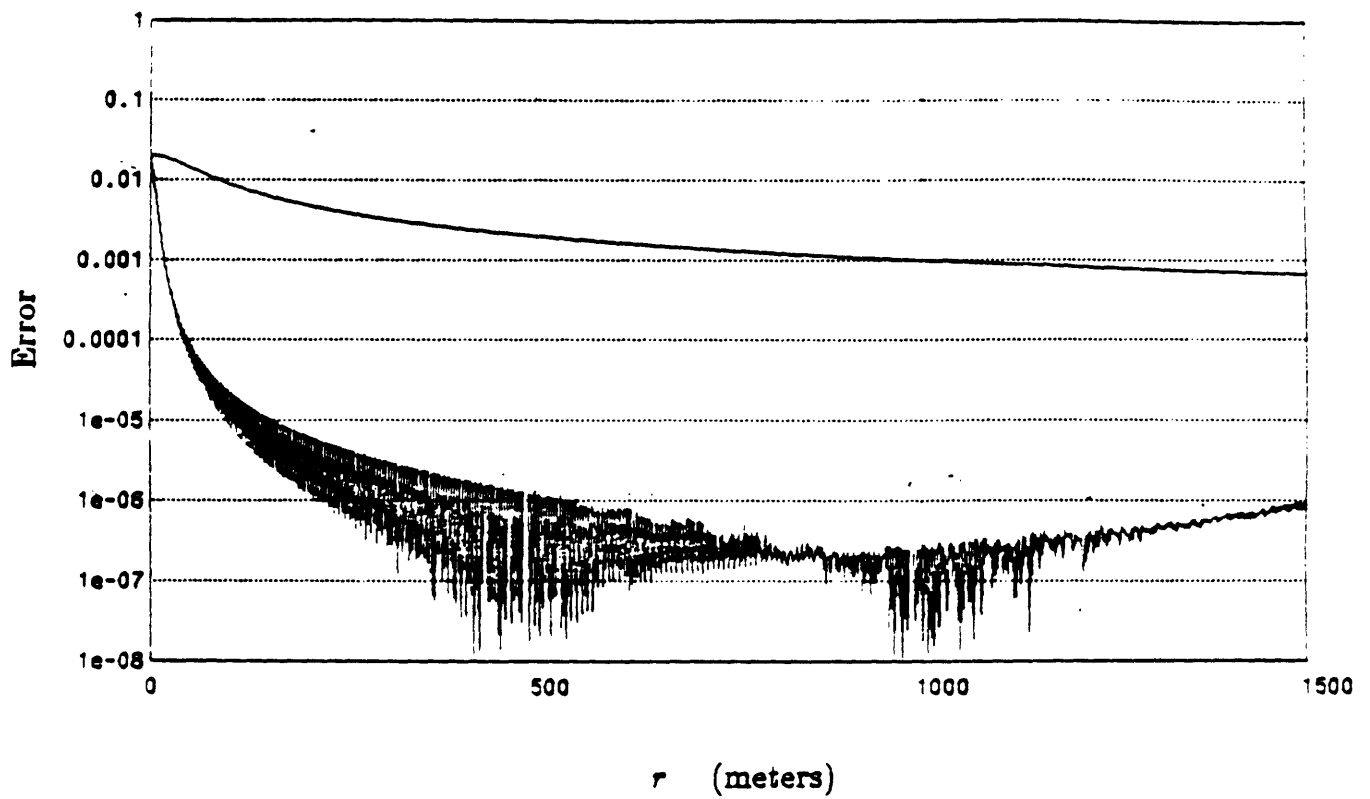
Figure 6.8: Error in the reconstruction of the real component (bottom curve) and true field magnitude (top curve).
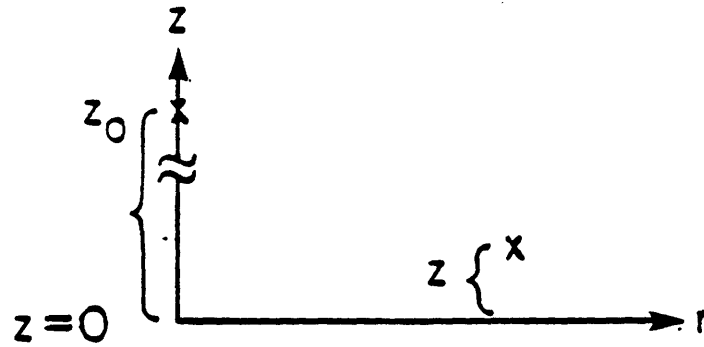
$\|z_0 - z\|$	=	50 m
f	=	220 Hz
c	=	1500 m/sec
k_0	=	.9215 rad/m

Figure 6.9: Geoacoustic model for a free-space field with source and receiver of displaced heights with respect to a reference plane.
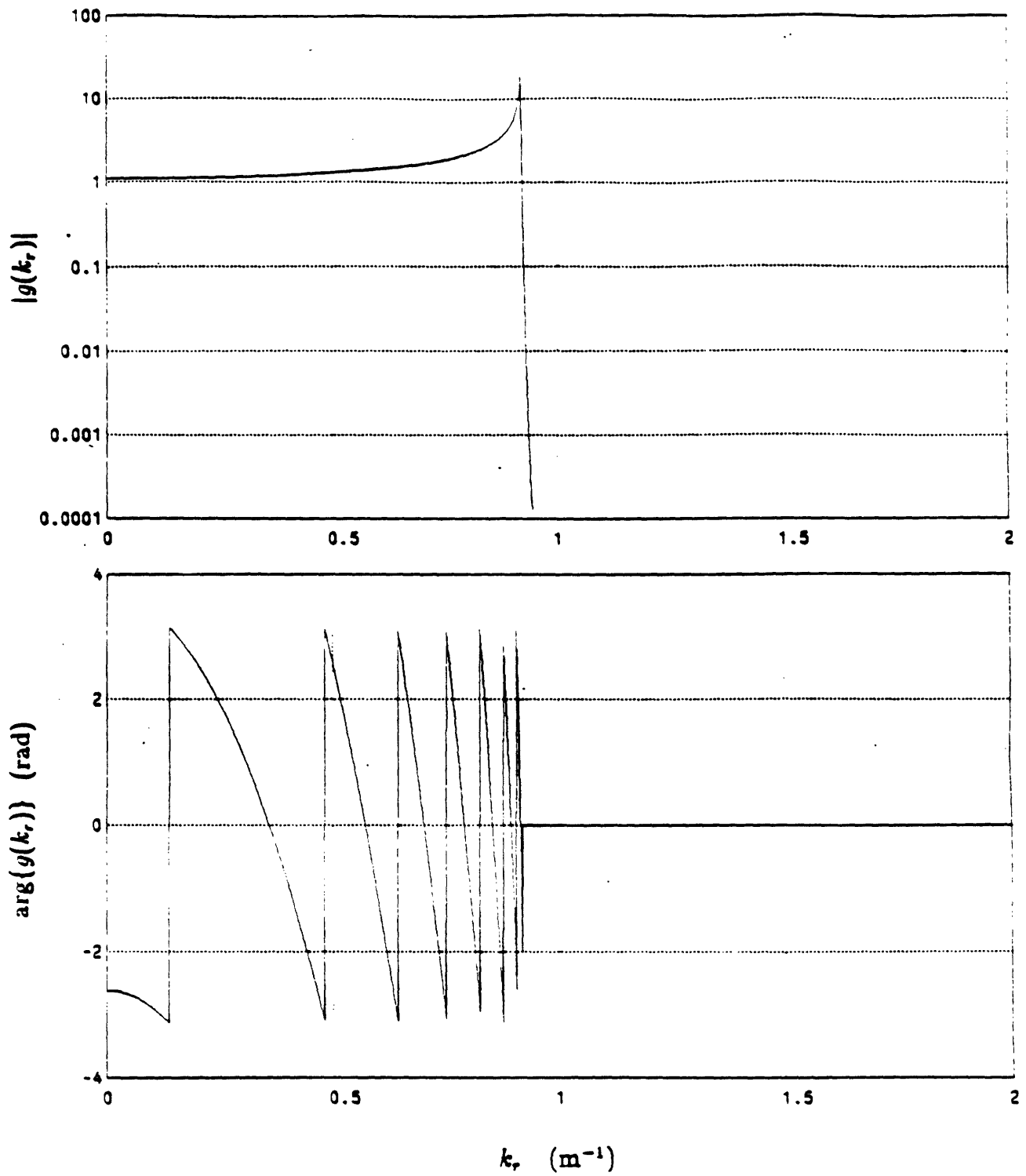
Figure 6.10: Magnitude of the theoretical total Green's function for the free-space field with displaced source and receiver.
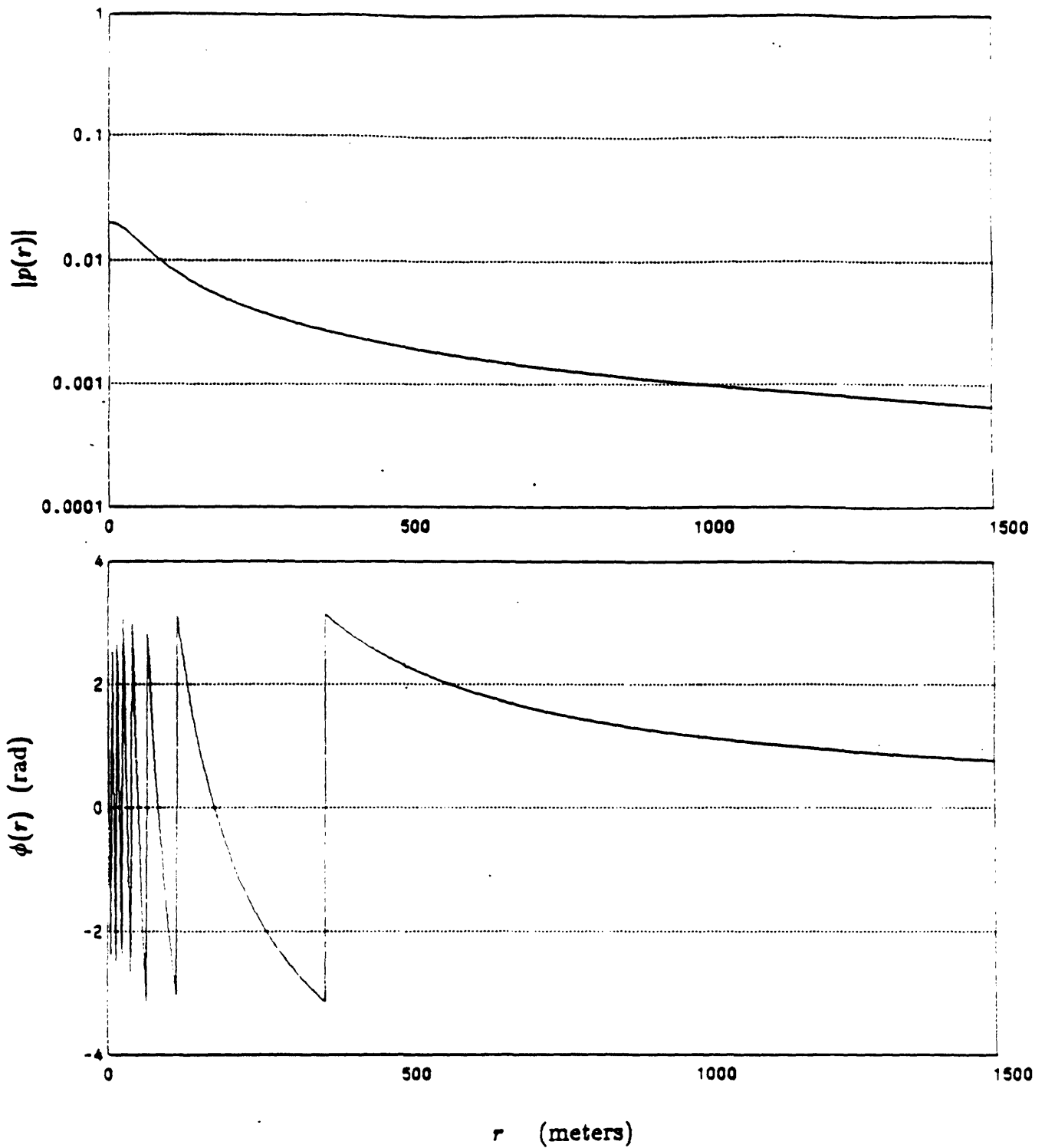
Figure 6.11: Magnitude and residual phase of the free-space field with displaced source and receiver.
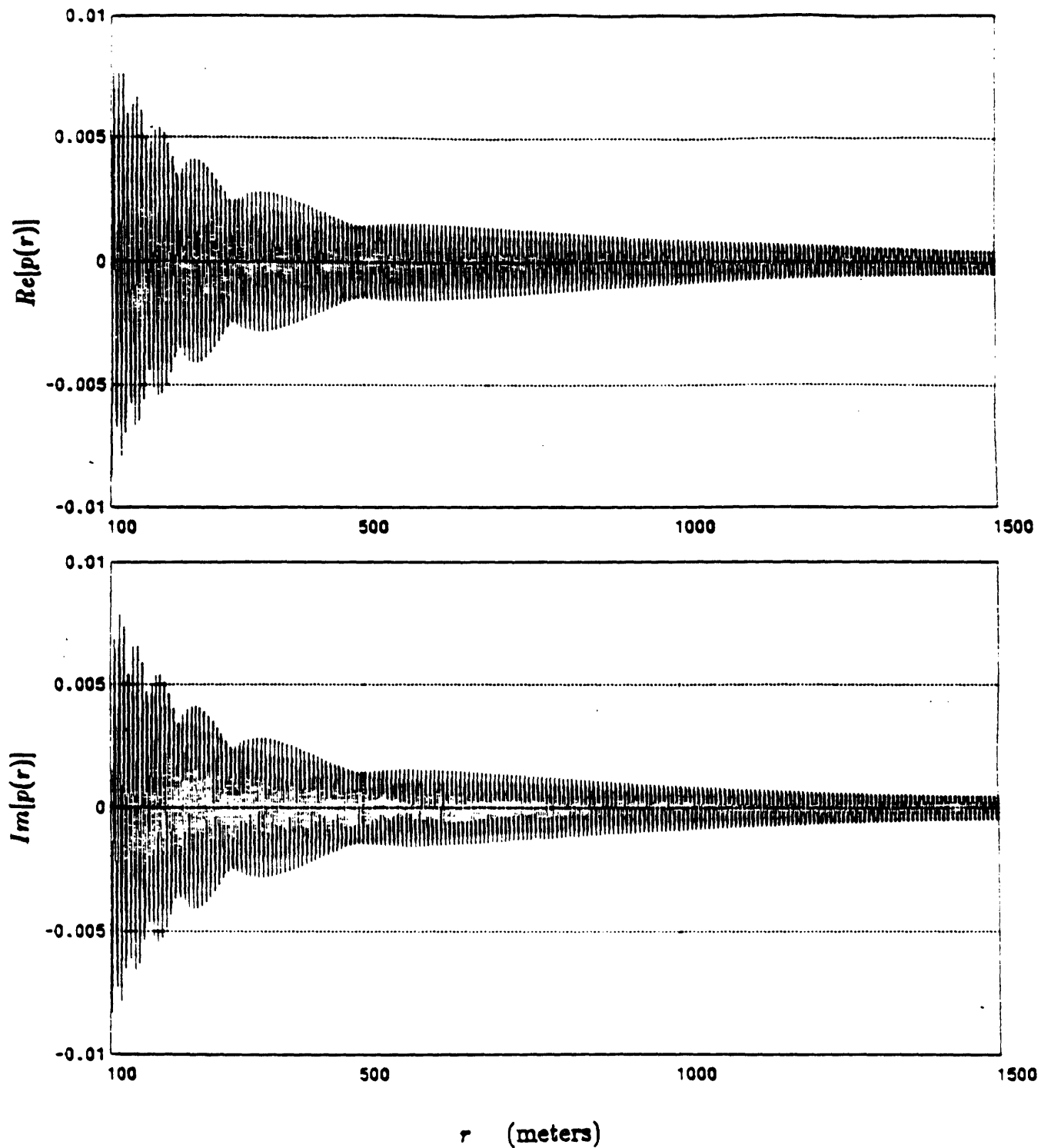
Figure 6.12: Real and imaginary components of free-space field with displaced source and receiver.

will suppress the display of these components as they present very little additional information except that the quantities involved are rapidly varying. Similarly, the display of the true signal versus its reconstruction will be suppressed. In Figure 6.13 is shown the magnitude and residual phase of the reconstructed field. The reconstruction was performed by using 1024 samples of the imaginary part of the field spaced at an interval of 1.7 m. As can be seen by comparing Figure 6.13 with Figure 6.11, the quality of the reconstruction is quite good except for the behavior in the near-field. As additional evidence of this, the error signal and the true field magnitude are displayed in Figure 6.14. As can be seen, the error signal falls more than an order of magnitude below the intensity of the field in the first 25 $m \sim 4\lambda_0$. The error drops rapidly to at least three orders of magnitude below the true intensity at the remaining ranges. In order to more clearly show the degradation in the near-field, we have included expanded plots of the true magnitude and residual phase and the reconstructed magnitude and residual phase in Figure 6.15 and 6.16 respectively. The figures again show the high quality of reconstruction at ranges greater than about 25 m and also indicate significance of the degradation in the near-field.

The degradation in the reconstructed near-field can be attributed to two effects. First, the assumption that the acoustic field can be synthesized using the Hilbert-Hankel transform, i.e. using positive wavenumbers only, is not strictly valid at very short ranges. Second, the asymptotic expressions, obtained from the asymptotic Hilbert-Hankel transform, which are used in the reconstruction method are not valid at short ranges. In the examples which follow, we will see that the reconstruction method consistently yields some degradation in the near-field. In many coherent processing applications, this degradation may not be significant but we point out that it is a limitation of the theory and method for reconstruction which we have proposed.

In the previous two examples, the acoustic fields were generated by using their known analytic forms and the quality of the reconstruction was assessed. In more re-
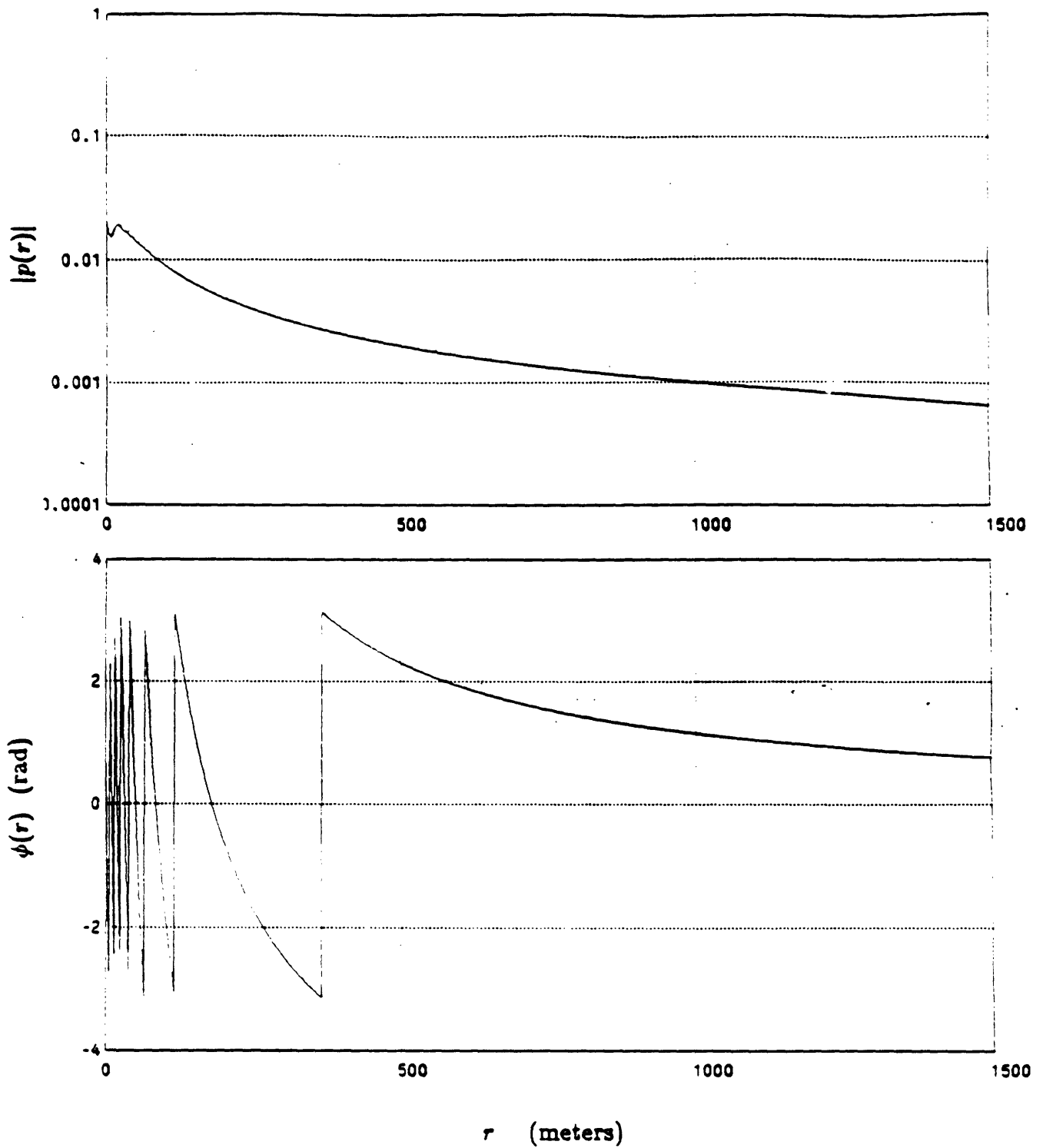
Figure 6.13: Magnitude and residual phase of the reconstructed free-space field with displaced source and receiver.

Figure 6.14: Error in the reconstruction of the real component (bottom curve) and true field magnitude (top curve) of the free-space field with displaced source and receiver.
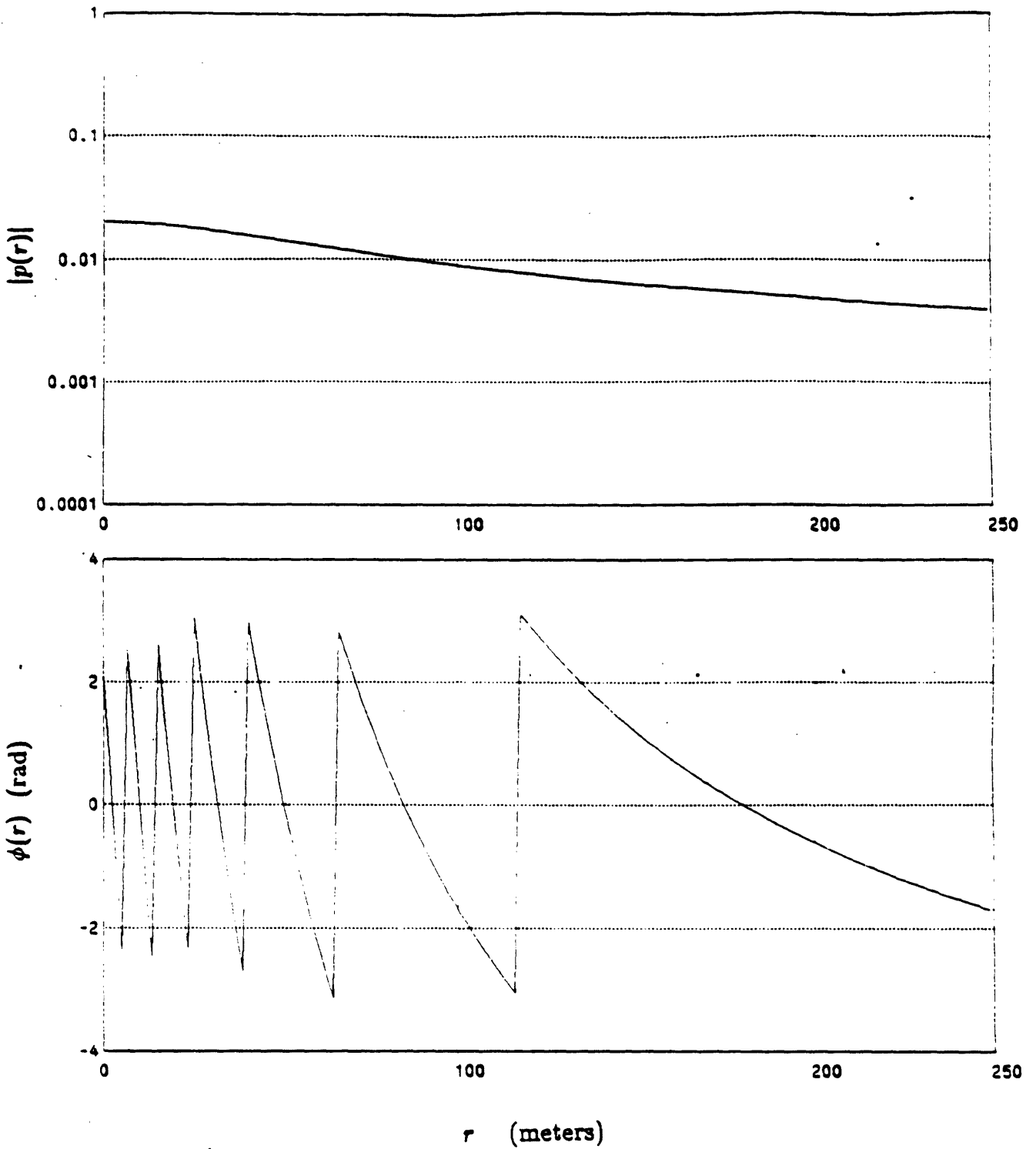
Figure 6.15: Expanded versions of the near-field magnitude and residual phase for the free-space field with displaced source and receiver.
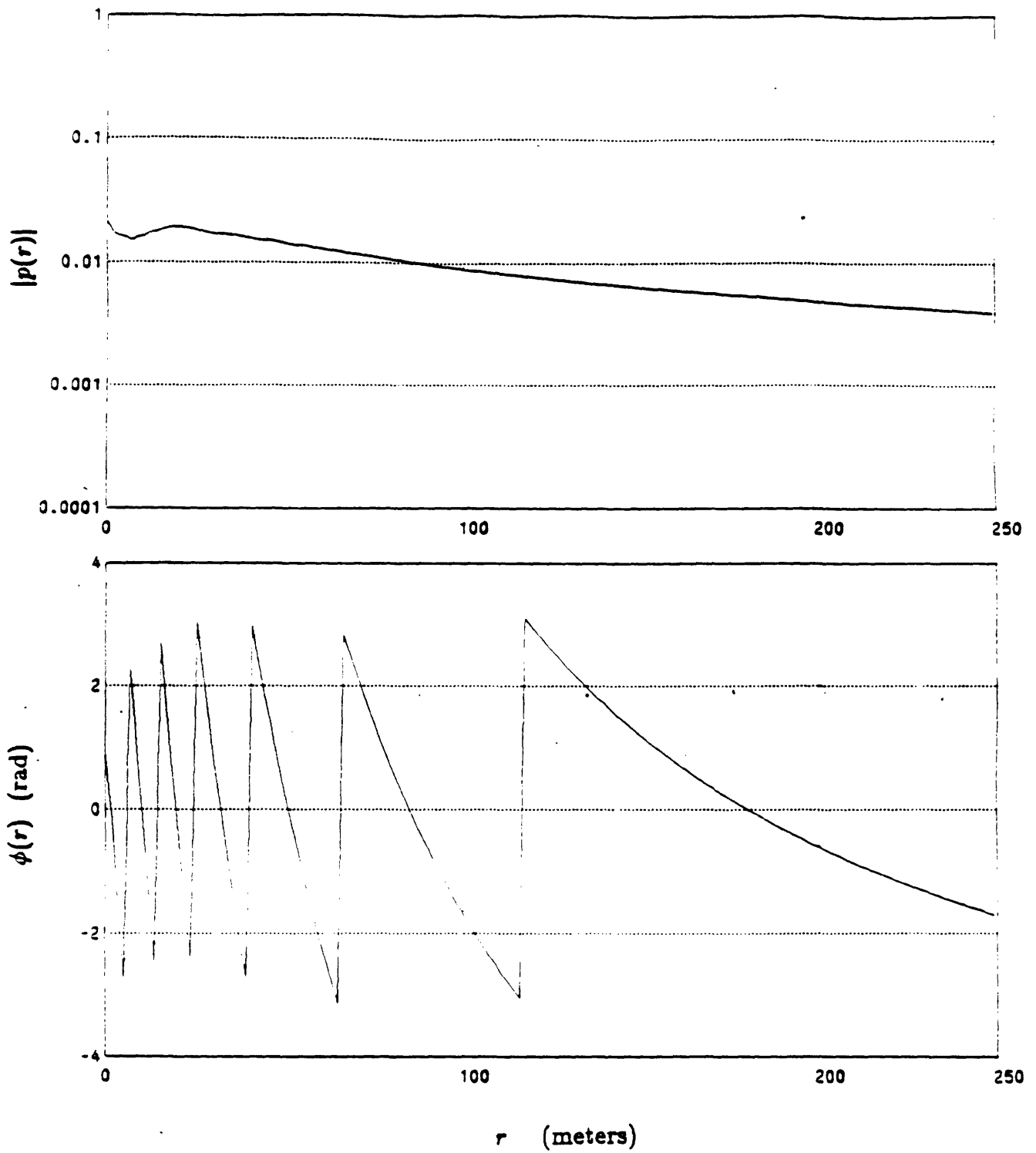
Figure 6.16: Expanded versions of the reconstructed near-field magnitude and residual phase for the free-space field with displaced source and receiver.

alistic acoustic propagation situations, there are boundaries which are present which complicate the behavior of the field. In most cases involving boundaries, closed-form expressions for the field are not available and a numerical method must be introduced in order to generate the synthetic field. However, if the boundary is particularly simple, a closed-form expression can be obtained. For example, if the boundary consists of a pressure-release surface, the field can be simply described and its corresponding behavior is referred to as the Lloyd mirror effect [9]. We will consider this field as the next reconstruction example. The example was chosen to indicated that the reconstruction algorithm applies to non-free-space fields. Additionally, the method for synthetically generating this field is completely decoupled from the reconstruction technique.

The geoacoustic model for the Lloyd mirror field is described in Figure 6.17. The corresponding field can be written in closed-form as

$$p(r) = \frac{e^{jk_0 R_0}}{R_0} - \frac{e^{jk_0 R_1}}{R_1} \tag{6.14}$$

where $R_0 = (r^2 + (z - z_0)^2)^{1/2}$ and $R_1 = (r^2 + (z + z_0)^2)^{1/2}$. The field can be interpreted as the sum of a direct field plus a reflected field which has interacted with the pressure-release boundary, which has a reflection coefficient of -1. The magnitude and residual phase of this field, where the residual phase has been computed using $k_\phi = k_0$, are shown in Figure 6.18. The nulls and peaks in the field are characteristic of the constructive and destructive interference between the direct and reflected fields for this model. The reconstructed magnitude and residual phase are next shown in Figure 6.19 and their similarity with the true magnitude and residual phase shown in the preceding figure is apparent. Additionally, the first 250 m of the true and reconstructed magnitude/residual phase curves are shown in Figures 6.20 and 6.21 respectively.

The quality of the reconstruction, even in the near-field, can be seen from these figures.
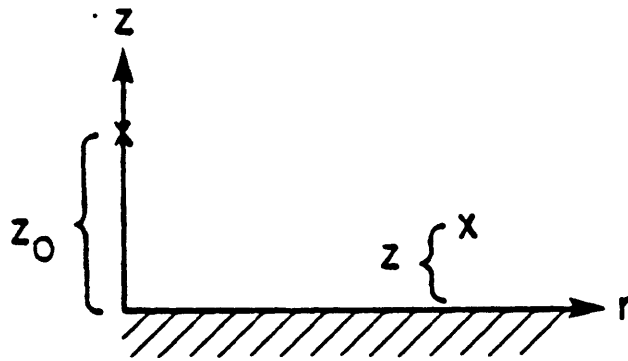
R_B	$=$	-1
$|z_0 - z|$	$=$	50 m
f	$=$	220 Hz
c	$=$	1500 m/sec
k_0	$=$	.9215 rad/m

Figure 6.17: Geoacoustic model for the Lloyd mirror field corresponding to the sum of a direct field plus a field which has interacted with a pressure-release bottom.
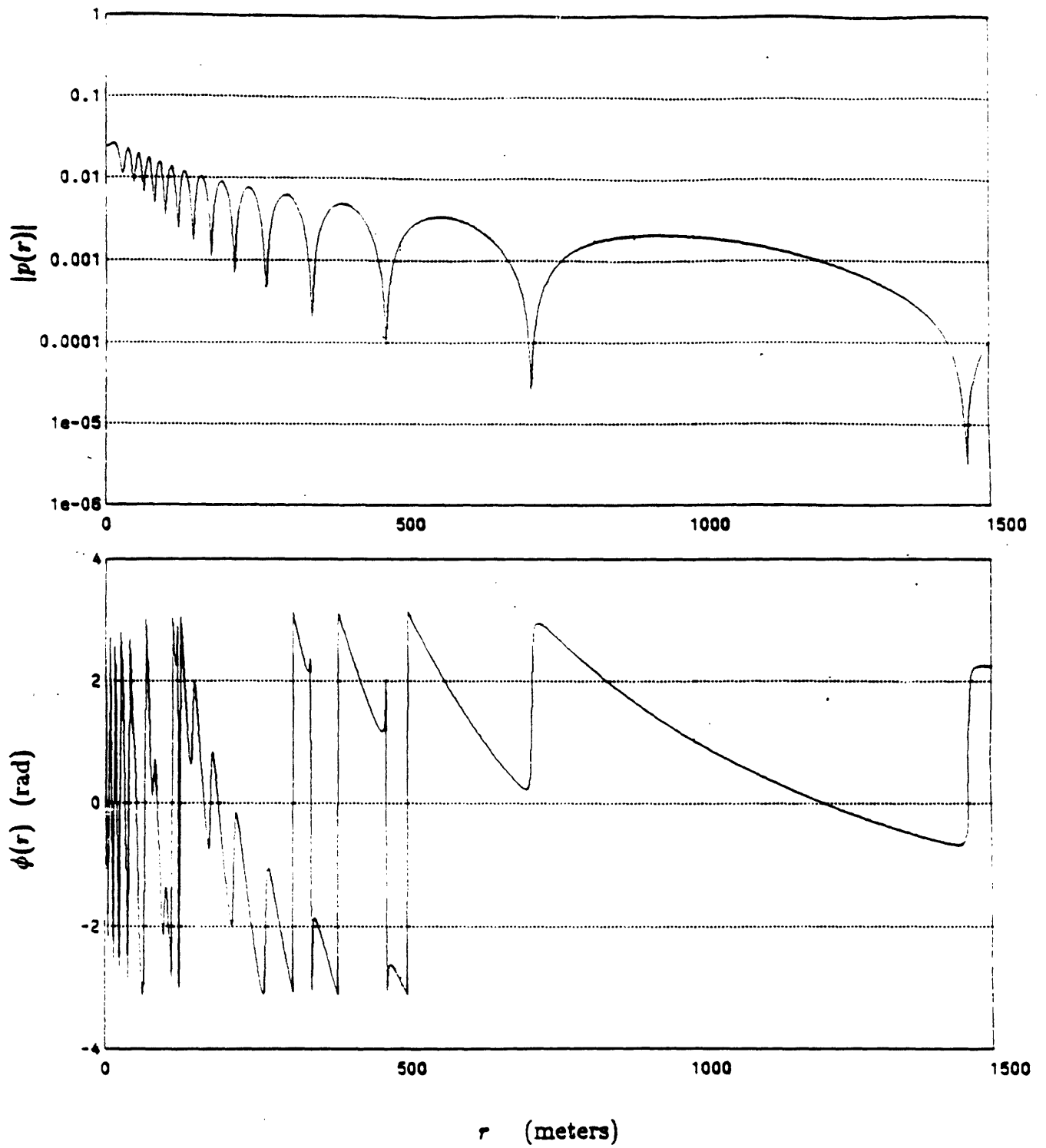
Figure 6.18: Magnitude and residual phase of the Lloyd mirror field.
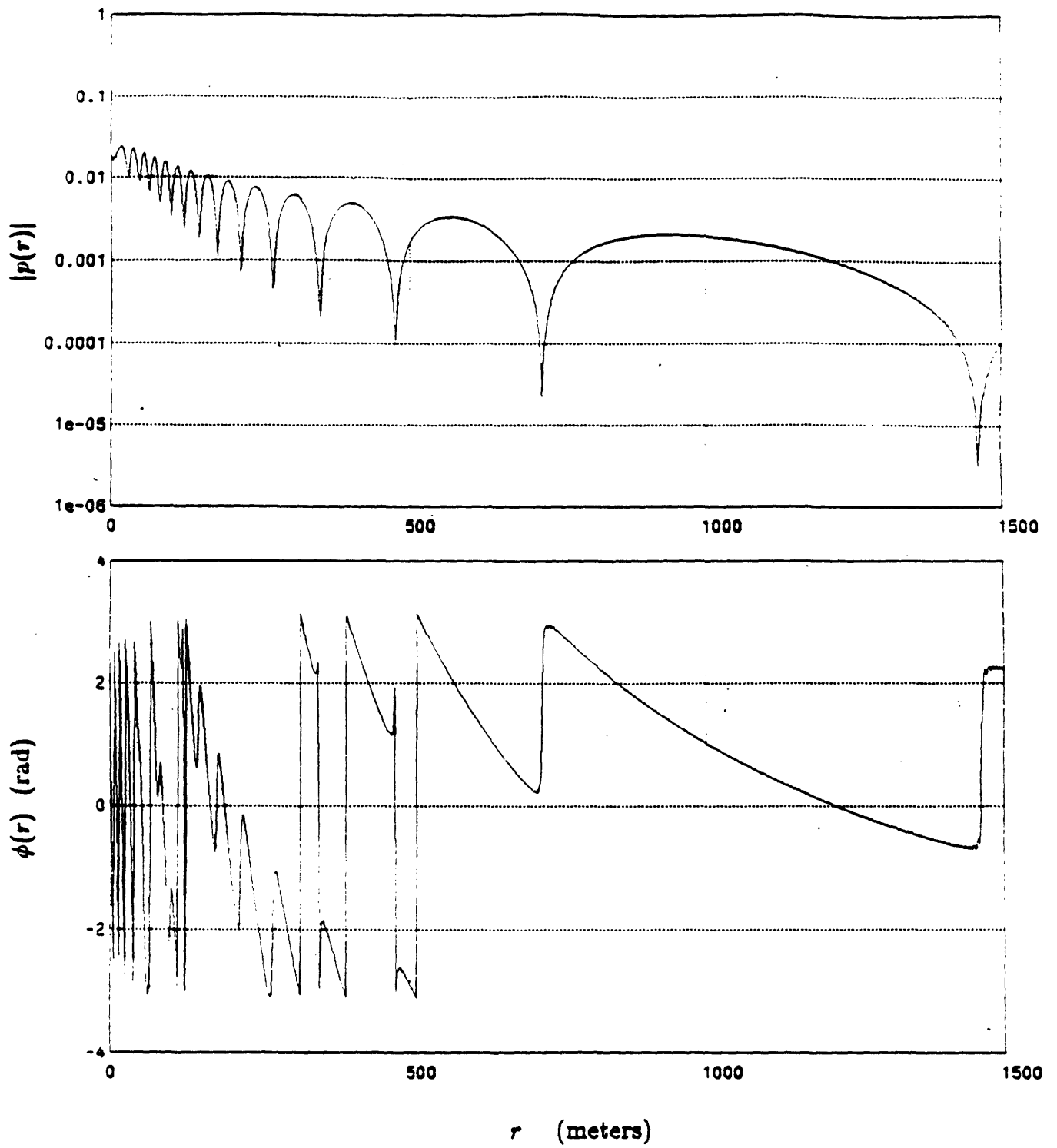
Figure 6.19: Magnitude and residual phase of the reconstructed Lloyd mirror field.
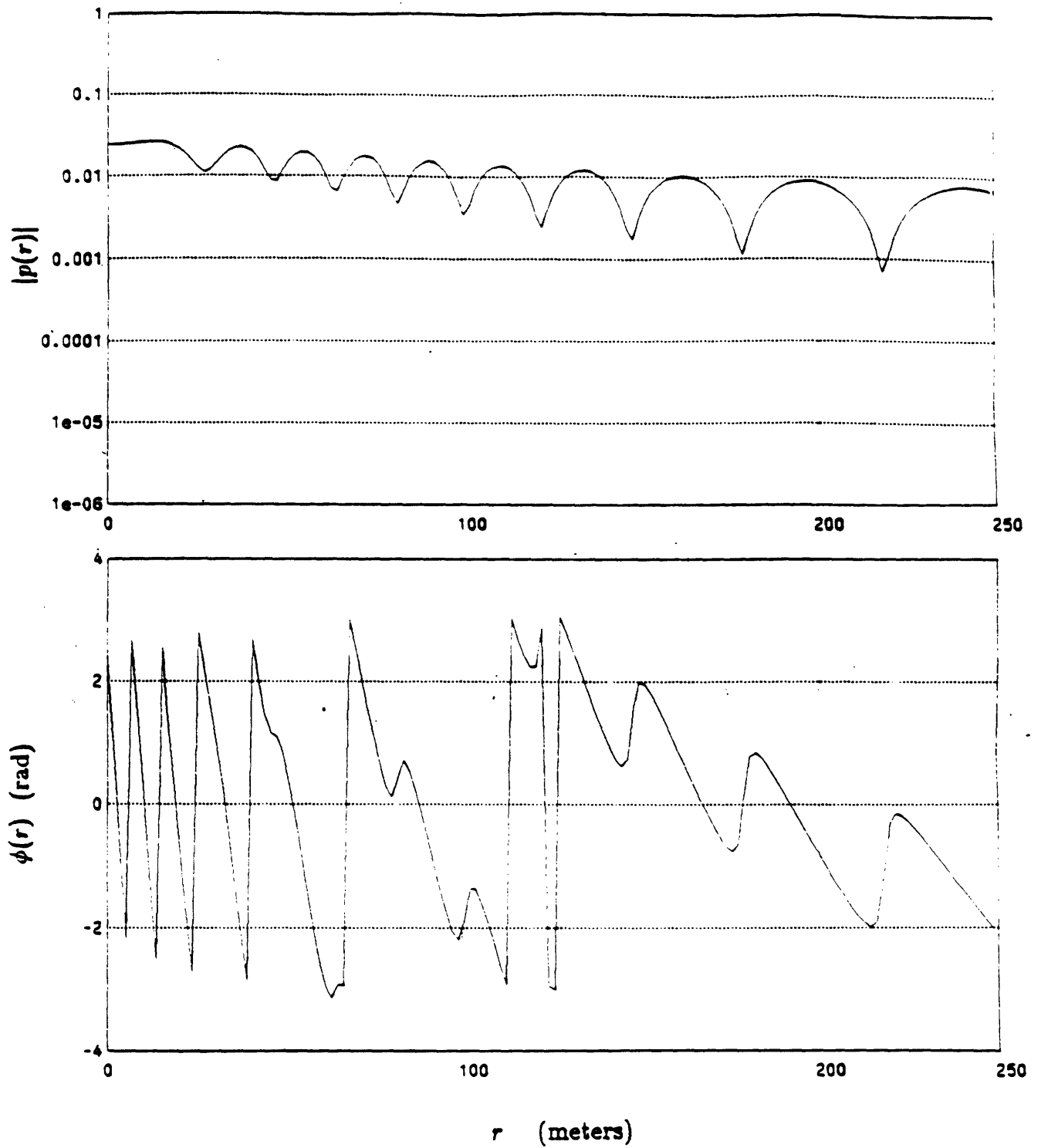
Figure 6.20: Expanded versions of the near-field magnitude and residual phase for the Lloyd mirror field.
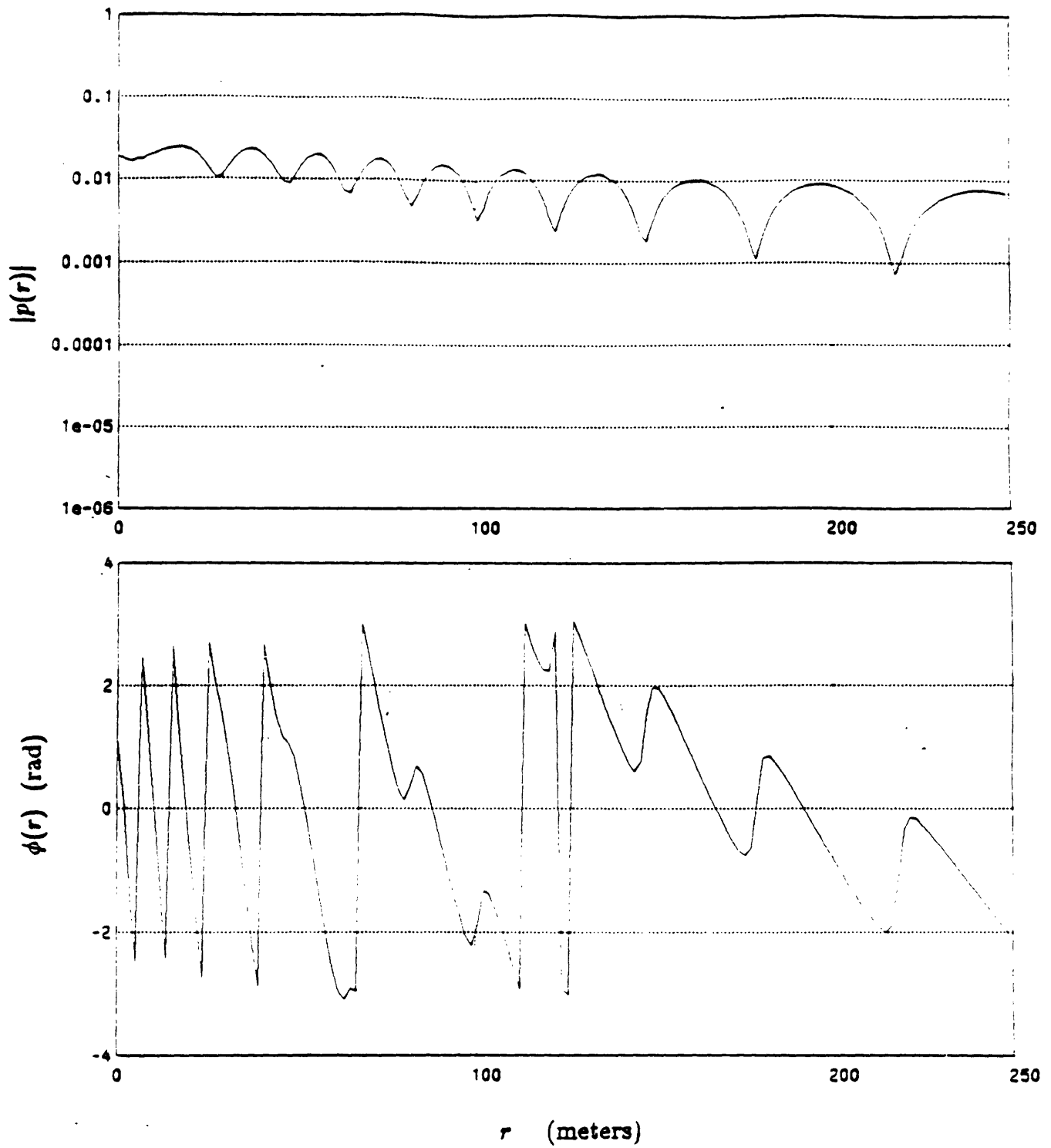
Figure 6.21: Expanded versions of the reconstructed near-field magnitude and residual phase for the Lloyd mirror field.

In the previous examples, we have chosen to sample at a rate of four real samples per water wavelength and then reconstruct the alternate channel. In fact, the sampling rate can be reduced so that the field can be reconstructed from slightly more than two real samples per water wavelength. Initially, it seems that some loss of information must occur here. That is, if the field is adequately represented by two complex samples per water wavelength, then apparently there must be some loss if the real (or imaginary) parts of these two samples are discarded or not collected. However, there is no loss of information as is now explained.

As discussed in Chapter 3, if the Green's function corresponding to a particular field is wavenumber limited to the water wavenumber, actually only *one* complex sample or two real samples per water wavelength are required to adequately represent the field. This stems from the fact that the field is outgoing and therefore, only positive wavenumbers are required for its synthesis. Essentially, the one-sided nature of the wavenumber decomposition makes the acoustic field a special case of more general complex-valued functions which are synthesized using a Hankel transform. The implication is that the sampling rate of the field may be reduced by a factor of two due to the one-sided nature of its wavenumber decomposition. In practice, we have found that the minimum sampling rate should be slightly larger than this to accommodate cases when the Green's function is not precisely wavenumber limited. As an example of this, we will examine the reconstruction of the real part of the Lloyd mirror field which has been sampled at an average rate which is ten percent higher than the minimum rate of one complex sample per water wavelength - i.e. the imaginary part of the field was sampled at a rate of 22 samples per 10 λ_0. The magnitude and residual phase of the reconstructed field are shown in Figure 6.22. The reconstruction is quite good as can be seen by comparing this figure with the true magnitude and residual phase in Figure 6.18. Additionally, the error signal for the reconstruction is shown, along with the true field magnitude, in Figure 6.23.

One additional point is to be made here. The reconstruction technique should
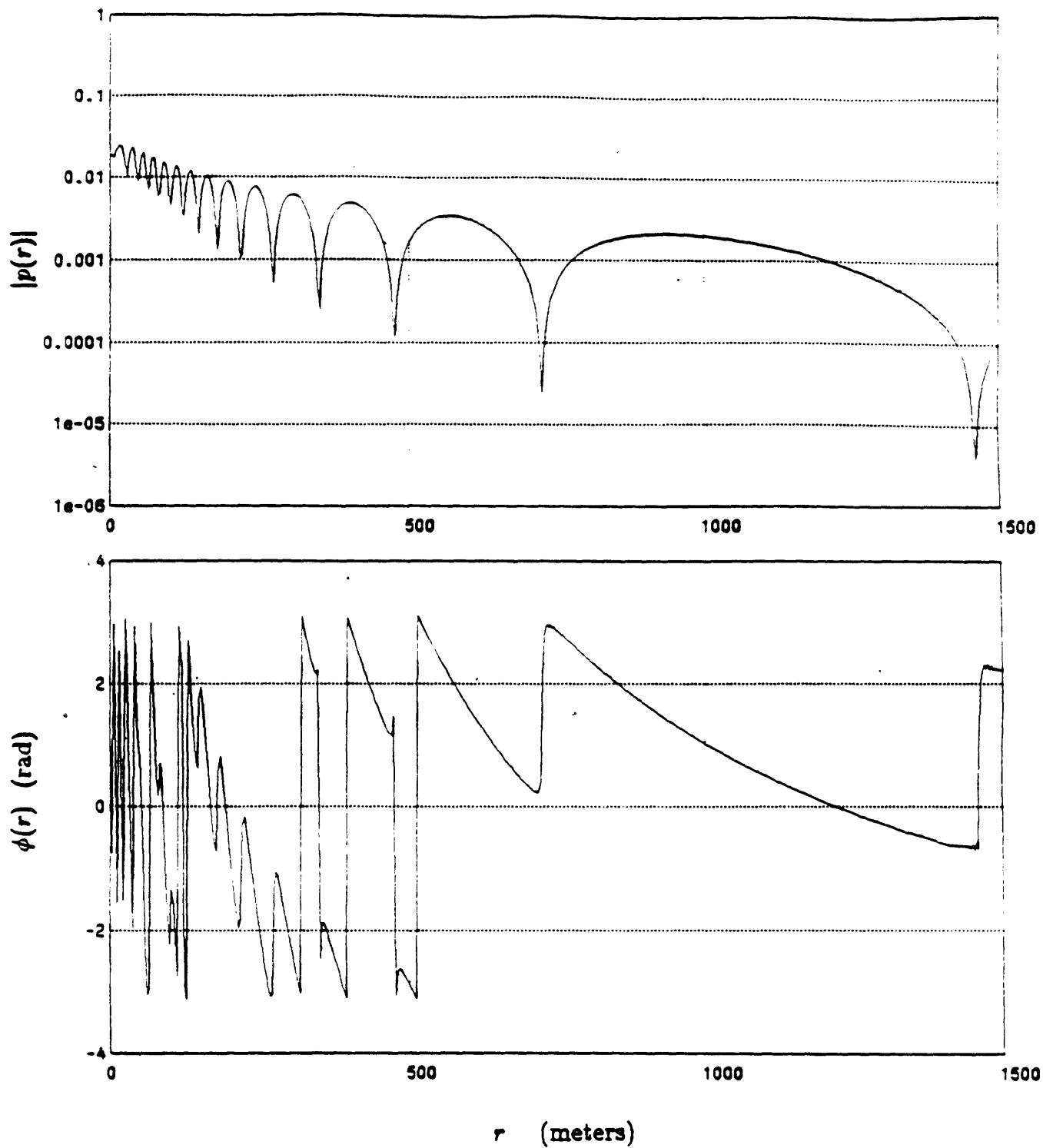
Figure 6.22: Magnitude and residual phase of the reconstructed Lloyd mirror field. The imaginary component was sampled at an average rate of 2.2 samples per water wavelength and the real part was reconstructed.
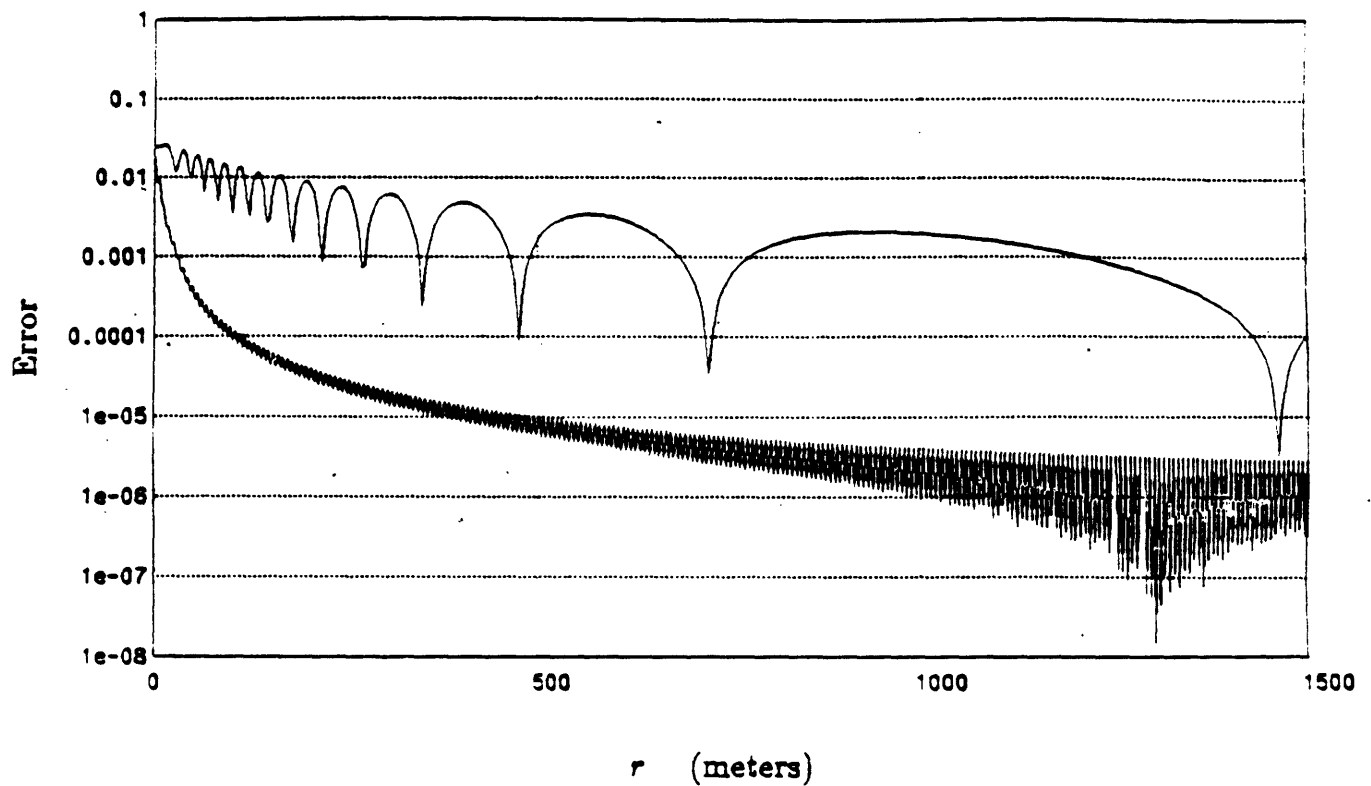
Figure 6.23: Error in the reconstruction of the real component (bottom curve) obtained from 2.2 samples of the imaginary component per water wavelength, and true field magnitude (top curve) of the Lloyd mirror field.

not be thought of a method for obtaining only the magnitude of the field from a single component. To emphasize this, we have always shown accompanying residual phase curves in the examination of the reconstruction technique. It may be possible to obtain a reasonable estimate of the magnitude only from a single channel by an envelope detection scheme, where it is assumed that the phase of the field varies at a much larger rate than the magnitude. As an example of this, we have plotted the absolute value of the real part of the Lloyd mirror field in Figure 6.24. The dashed line in the figure indicates the true magnitude of the field. The similarity of the envelope of the rapidly varying signal and the true magnitude suggests that a simpler scheme, such as averaging the absolute value of a component,i.e. performing an envelope detection, may produce a reasonable estimate of the magnitude only. In the reconstruction scheme we are proposing however, not only is an accurate estimate of the magnitude obtained but an accurate estimate of the phase is obtained as well. The reconstruction technique is thus applicable in coherent processing schemes in which both the magnitude and phase are required but in which only one of the corresponding quadrature channels is collected.
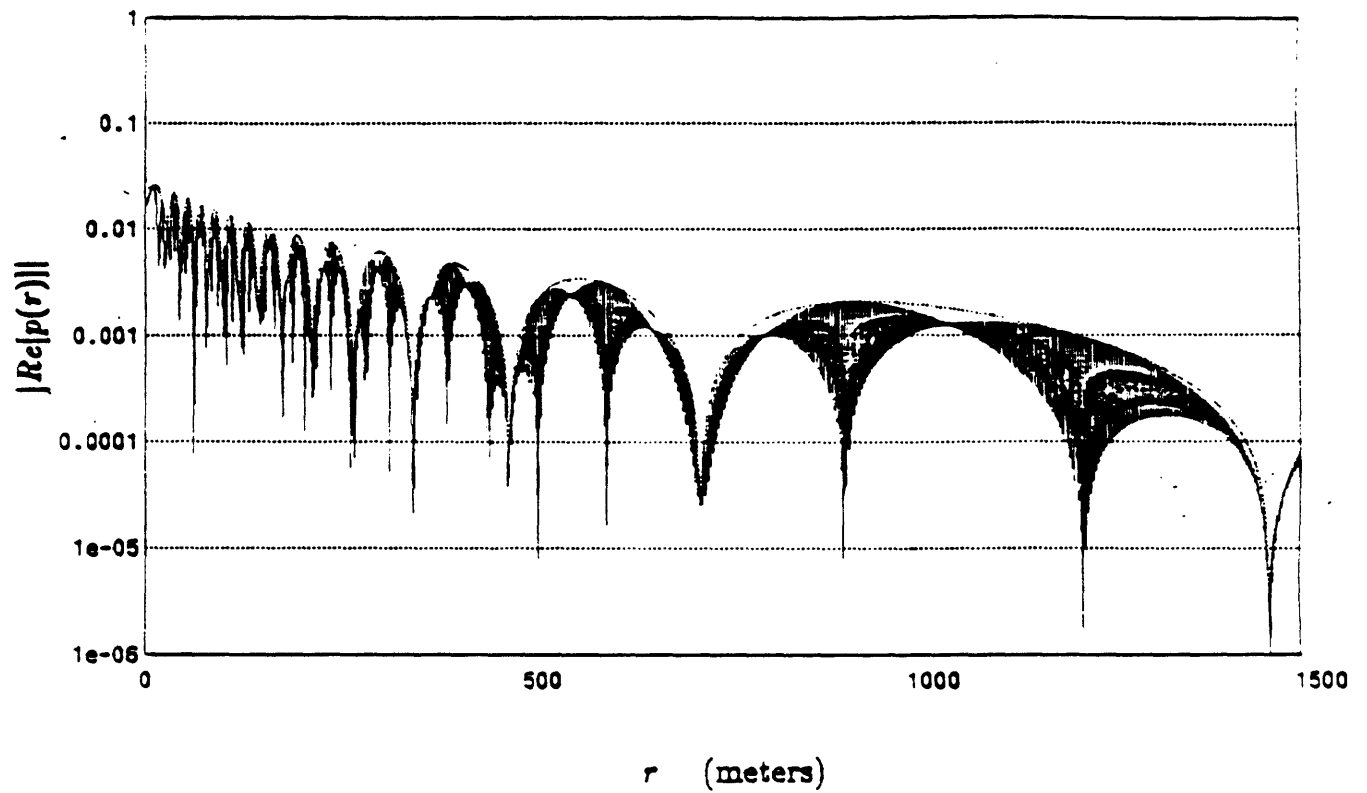
Figure 6.24: Absolute value of the real part of the Lloyd mirror field. Dashed line depicts theoretical magnitude of the field.

6.3 Reconstruction of Deep Water Acoustic Fields

In the previous section, fields which have known analytic forms have been used to demonstrate the reconstruction method. It is of interest to assess the quality of the reconstruction algorithm under more realistic circumstances which include, for example, fields which interact with a layered ocean bottom. However, convenient closed-form expressions for these fields do not exist and a technique for synthetic data generation must be used. The synthetic data generation method we have chosen consists of computing the Hankel transform of the reflected portion of the Green's function using the Abel/Fourier method and adding the direct field using its closed-form expression. The method is identical to the method proposed by Mook [2] [8], and is described in detail in Chapter 4. Although we have previously pointed out that it is also possible to directly determine the field by computing the Hankel transform of the total Green's function, the alternate approach has been chosen as means for decoupling the synthesis and reconstruction procedures. Specifically, it is the reflected field only which is synthesized using the Hankel transform algorithm while it is the total field which is used in the reconstruction.

As the first example of a realistic deep water field, we will consider the geoacoustic model previously given in Table 4.4 .The parameters for this model were determined using a forward modelling procedure for experimentally collected data. As such, the model, which includes attenuation in the underlying media, is considered as realistic and will serve as the basis for demonstrating the reconstruction method when the acoustic field has interacted with a layered ocean bottom. The corresponding total field magnitude for this example has been previously displayed in Chapter 4. Alternate approaches for its generation based on the real-part/imaginary-part sufficiency in the k_r domain were discussed there as well. Here, we wish to consider the real-part/imaginary-part sufficiency condition in the range domain and as a consequence of the condition, show that the field can be reconstructed from only one component.

The magnitude and the residual phase of the field, computed using $k_\phi = .9215$, are shown in Figure 6.25. To demonstrate the reconstruction, 1024 samples of the imaginary part of the field, sampled at a rate of 3.14 m, corresponding to a rate of approximately four samples per water wavelength were retained and the real part of the field was set to zero. In Figure 6.26 is shown the magnitude and residual phase of the reconstructed field. These quantities are apparently quite similar to the true magnitude and residual phase displayed in the previous figure. Additionally, the error signal in the reconstruction is displayed in Figure 6.27 along with the true field magnitude for reference. The error signal is approximately two orders of magnitude below the field intensity for ranges greater than about 25 m. The expanded versions of the near-field magnitude and residual phase for the true and reconstructed fields are shown for additional reference in Figure 6.28 and 6.29. Additionally, the same experiment was repeated except that the real part of the field was retained and the imaginary part was reconstructed. The magnitude and residual phase of the corresponding field are shown in Figure 6.30. Their similarity with the true field magnitude and residual phase, shown in Figure 6.25, is apparent. This last example demonstrates that there is no preferred component to be used in the reconstruction procedure, i.e. the real part can be reconstructed from the imaginary part or the imaginary part can be reconstructed from the real part. In the examples which follow in this chapter, we will typically set the real component of the field to zero and reconstruct it from the sampled imaginary component.

Of importance in coherent deep water signal processing is the extraction of the Green's function and the bottom reflection coefficient. There are at least two methods by which these quantities can be obtained given that only a single component of the data is available. In the first method, the total field is reconstructed and then forms the input to a numerical Hankel transform algorithm in order to obtain the Green's function. The bottom reflection coefficient can be extracted algebraically from the Green's function. In the second method, the properties of unilateral transforms, developed in Chapter 3, are exploited to obtain an approximation to the Green's
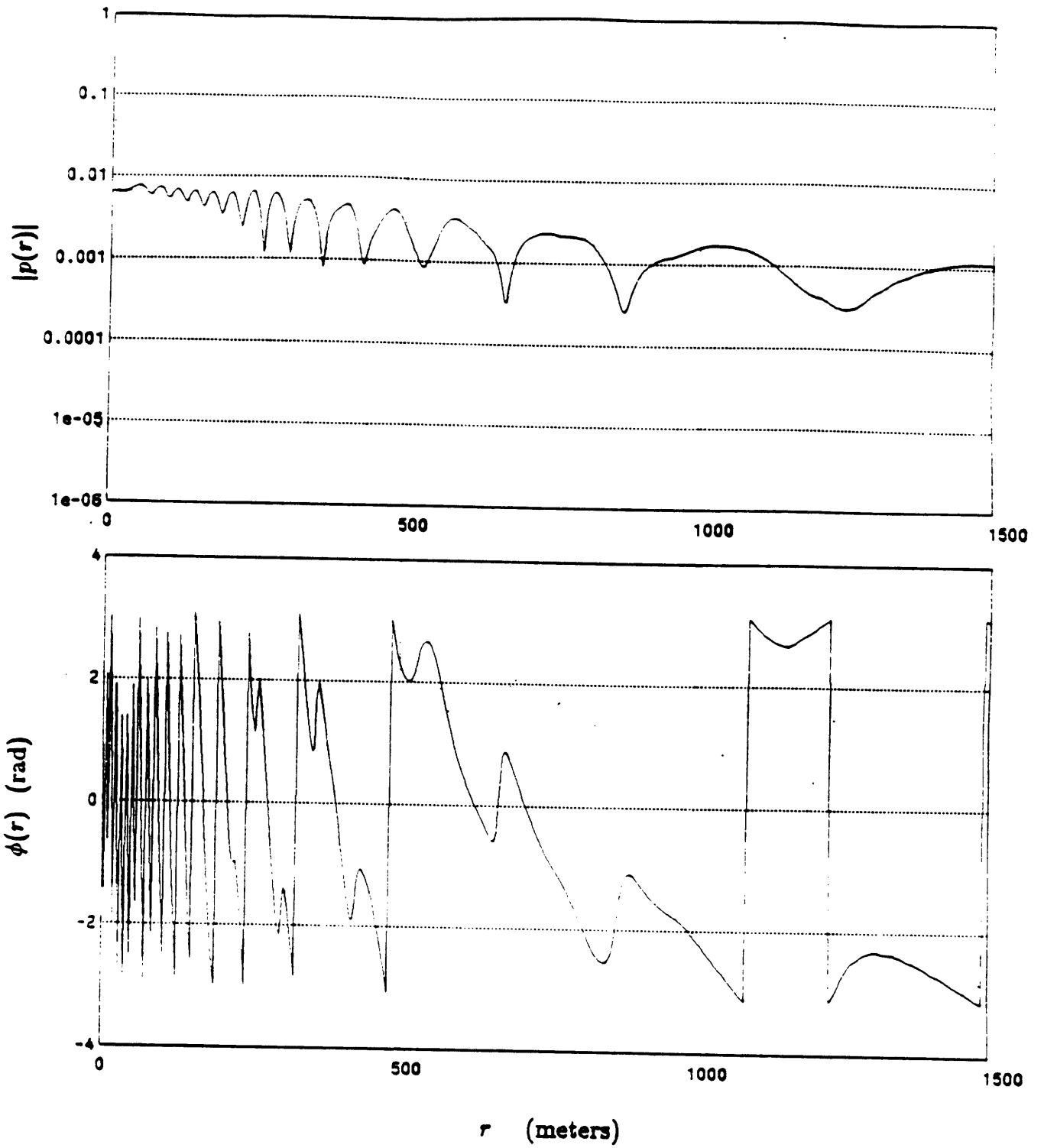
Figure 6.25: Magnitude and residual phase of realistic deep water field.
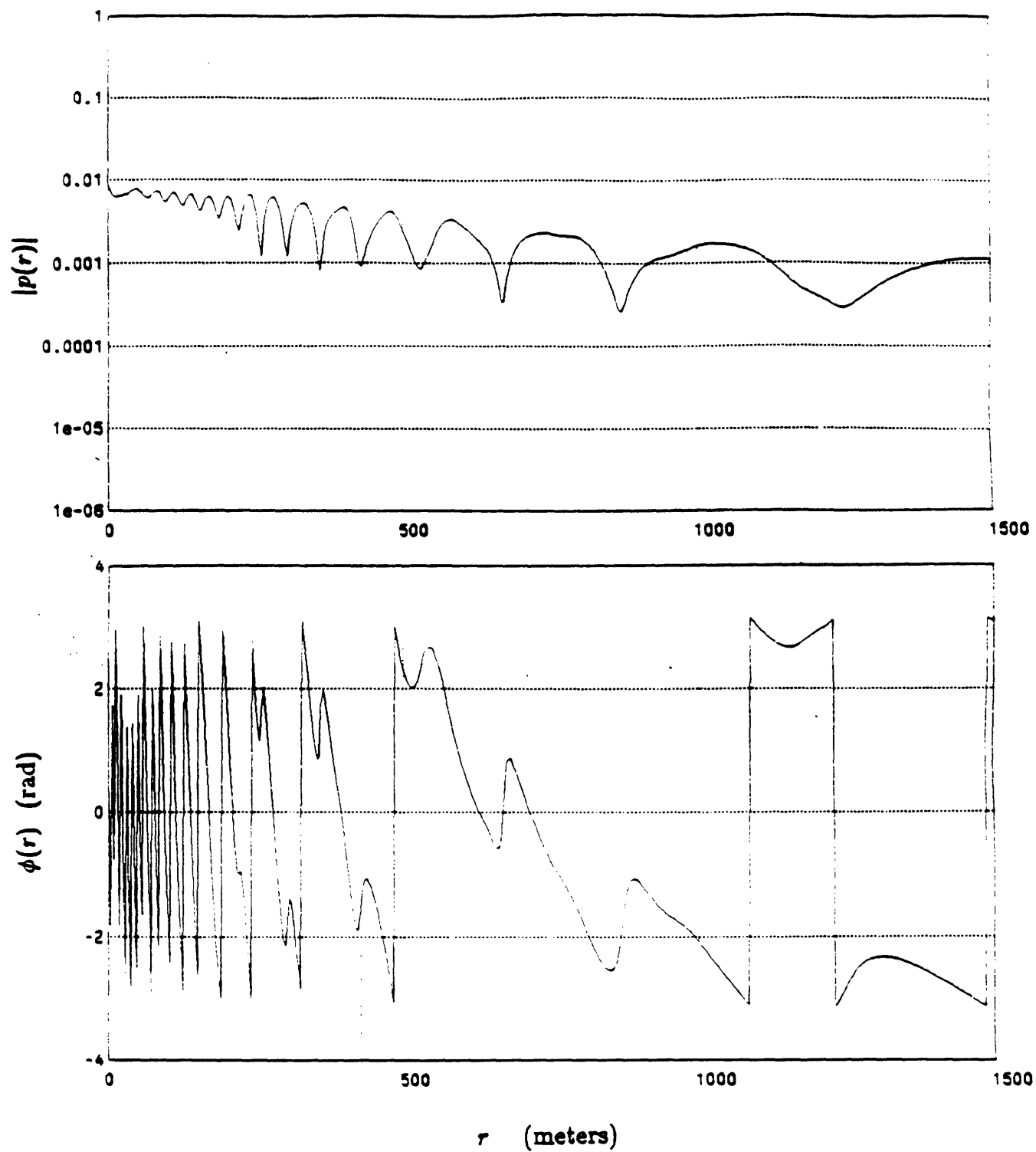
Figure 6.26: Magnitude and residual phase of reconstructed realistic deep water field.
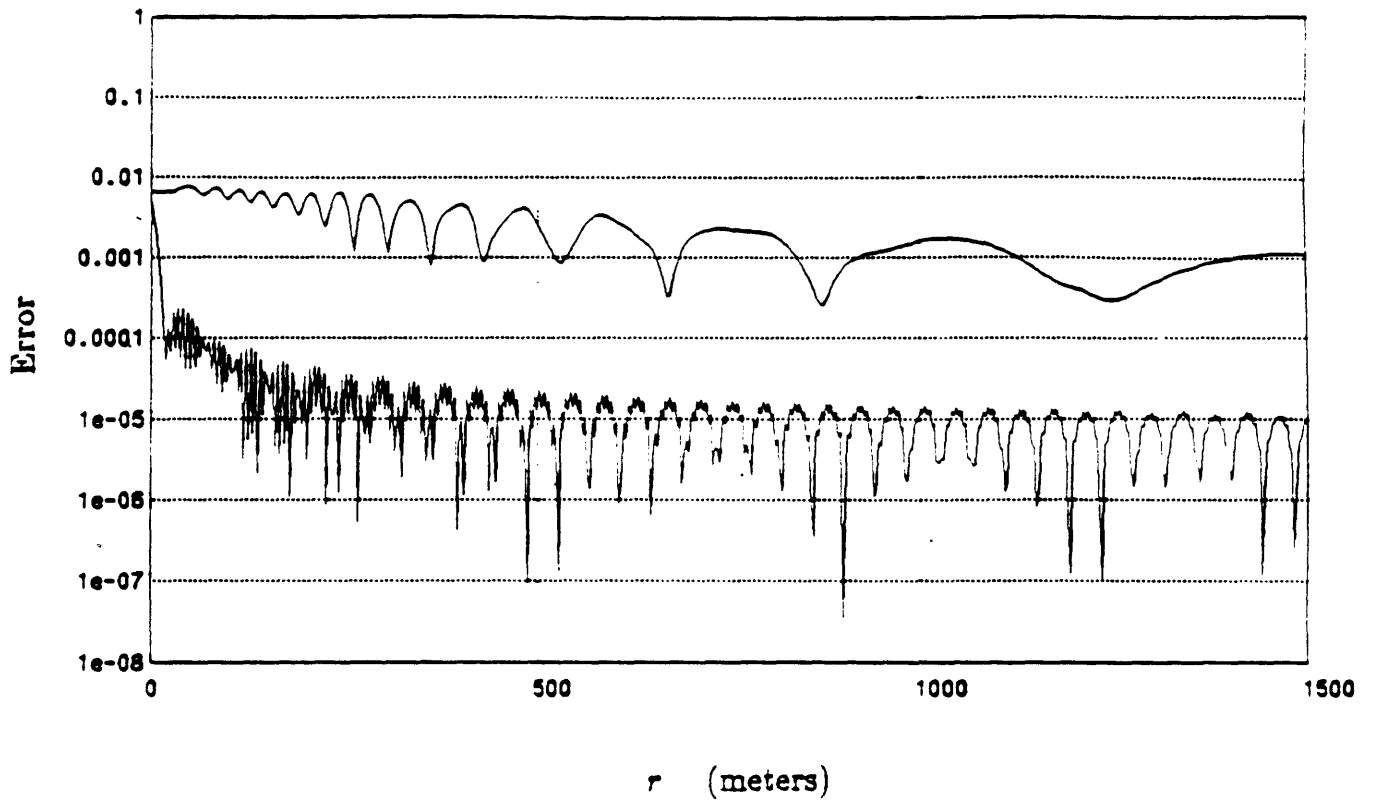
Figure 6.27: Error in the reconstruction of the real component (bottom curve) and true field magnitude (top curve) for the realistic deep water field.

411
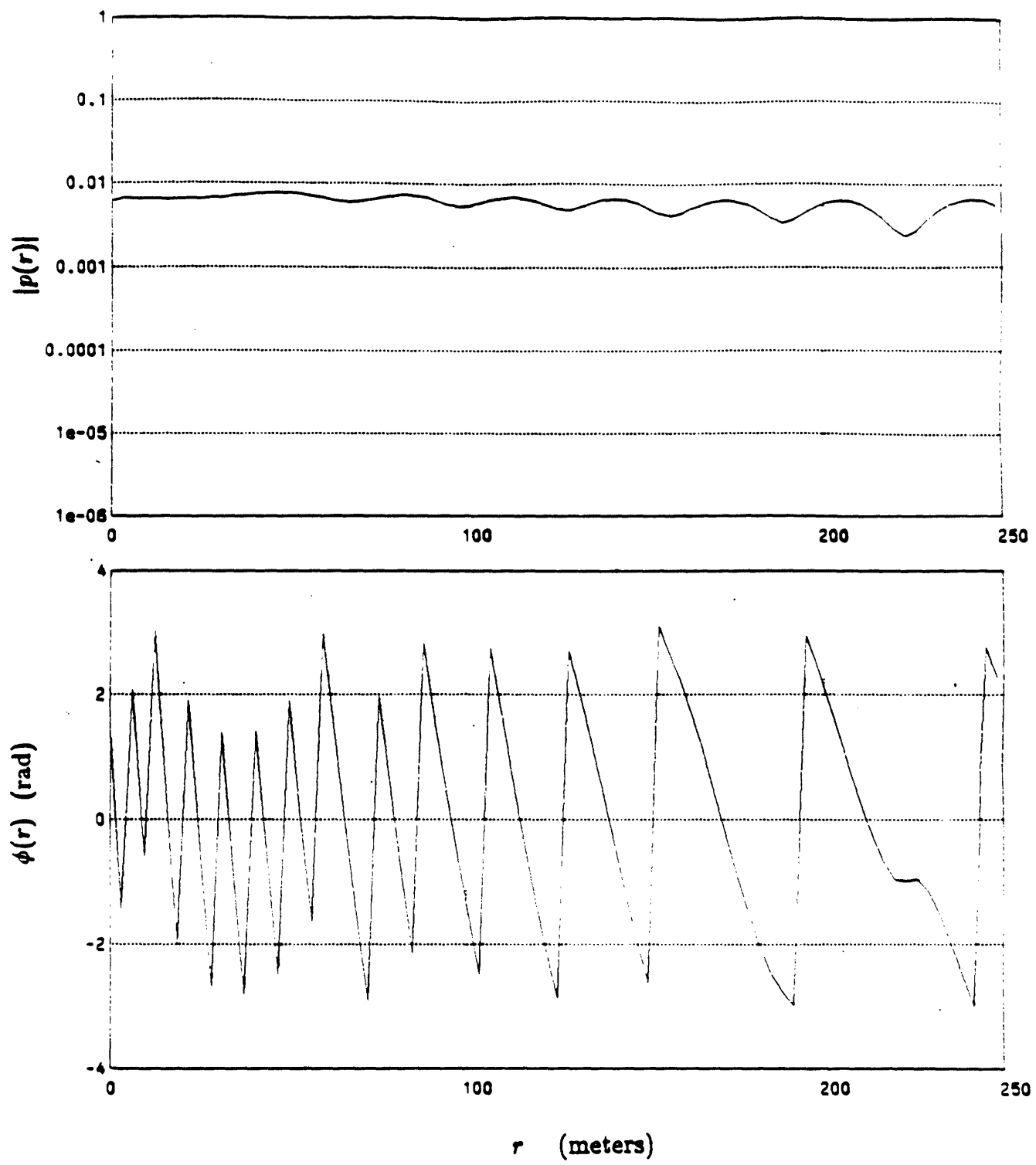
Figure 6.28: Expanded versions of the near-field magnitude and residual phase for the realistic deep water field.
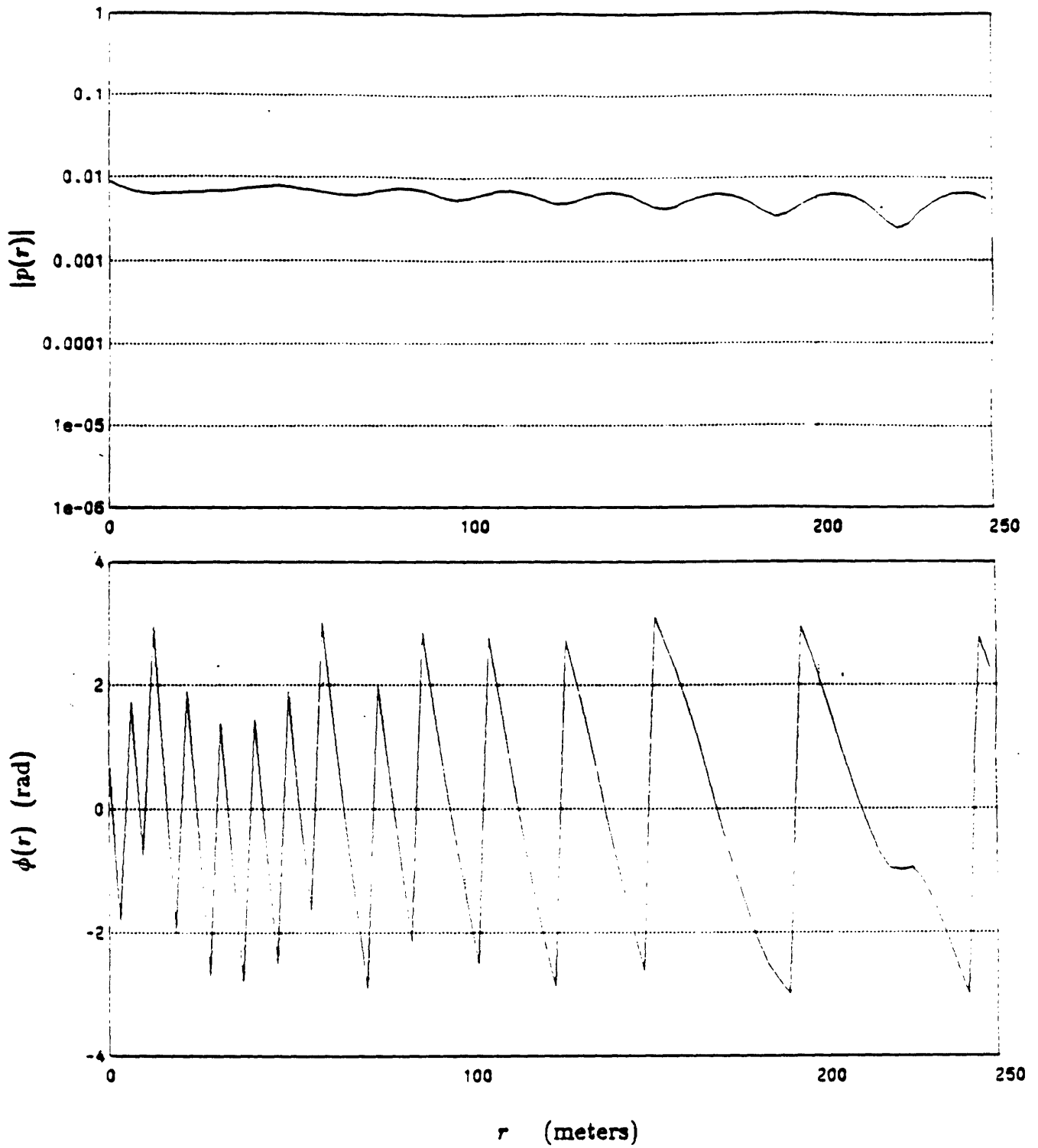
Figure 6.29: Expanded versions of the near-field magnitude and residual phase for the reconstructed realistic deep water field.
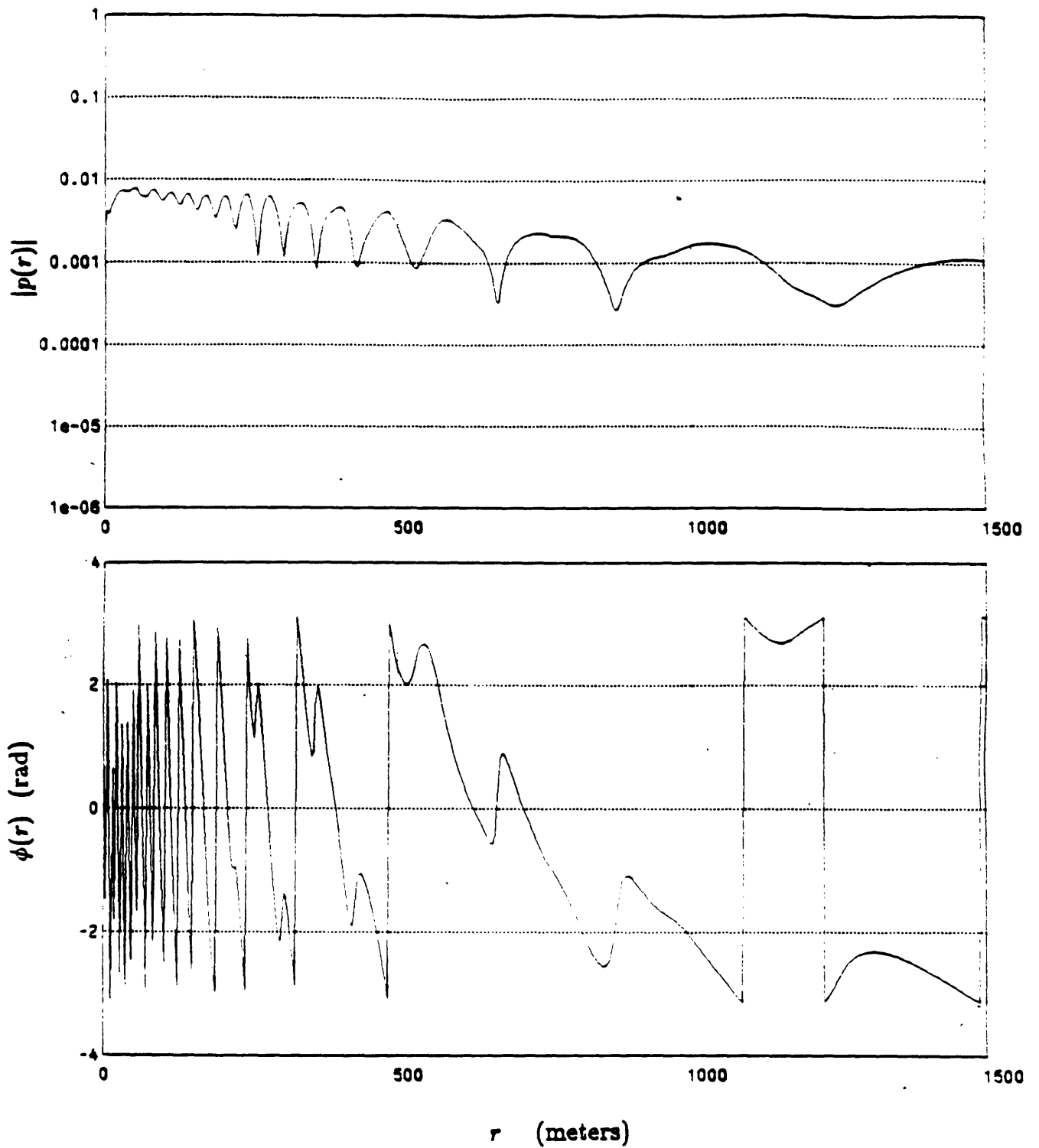
Figure 6.30: Magnitude and residual phase of the reconstructed realistic deep water field. The imaginary part was reconstructed from the real part.

414

function directly from a single component of the field.

For example, in Chapter 3, we showed that if

$$r^{1/2}p(r) \sim r^{1/2}p_{ou}(r) \quad r > 0 \tag{6.15}$$

where

$$r^{1/2}p_{ou}(r) = \mathcal{F}_u^{-1}\{\bar{g}(k_r)\} \tag{6.16}$$

and

$$\bar{g}(k_r) = (2\pi|k_r|)^{1/2}g(k_r)e^{-j\pi/4} \tag{6.17}$$

then

$$\bar{g}(k_r) \sim 2\mathcal{F}_u\{r^{1/2}Re[p(r)]\} \tag{6.18}$$

$$\bar{g}(k_r) \sim 2j\,\mathcal{F}_u\{r^{1/2}Im[p(r)]\} \tag{6.19}$$

Thus, in the second method, $\bar{g}(k_r)$ is estimated by computing a unilateral Fourier transform of the single component, multiplied by $r^{1/2}$ and the Green's function is extracted from $\bar{g}(k_r)$. While we are not proposing that the unilateral Fourier transform by adopted as a general method for obtaining the Green's function, we will present a numerical example which demonstrates the feasibility of the approach. The example illustrates that a reasonable estimate of the Green's function and reflection coefficient can be obtained from a single channel of a realistic, synthetically-generated, deep water field.

To demonstrate this, the total 52-layer field was synthesized using the technique described earlier. 1024 complex samples of the total field were produced at a range interval of 3.14 m, corresponding to a rate of approximately four complex samples per water wavenumber. The real part of this field was then set to zero, and the imaginary part, after being scaled by $2jr^{1/2}$ formed the input to a 1024 point unilateral Fourier transform. The magnitude and phase of the resultant Green's function are displayed in Figure 6.31. For comparison purposes, the magnitude and phase of the theoretical total Green's function for this example are shown in Figure 6.32. The comparison

415
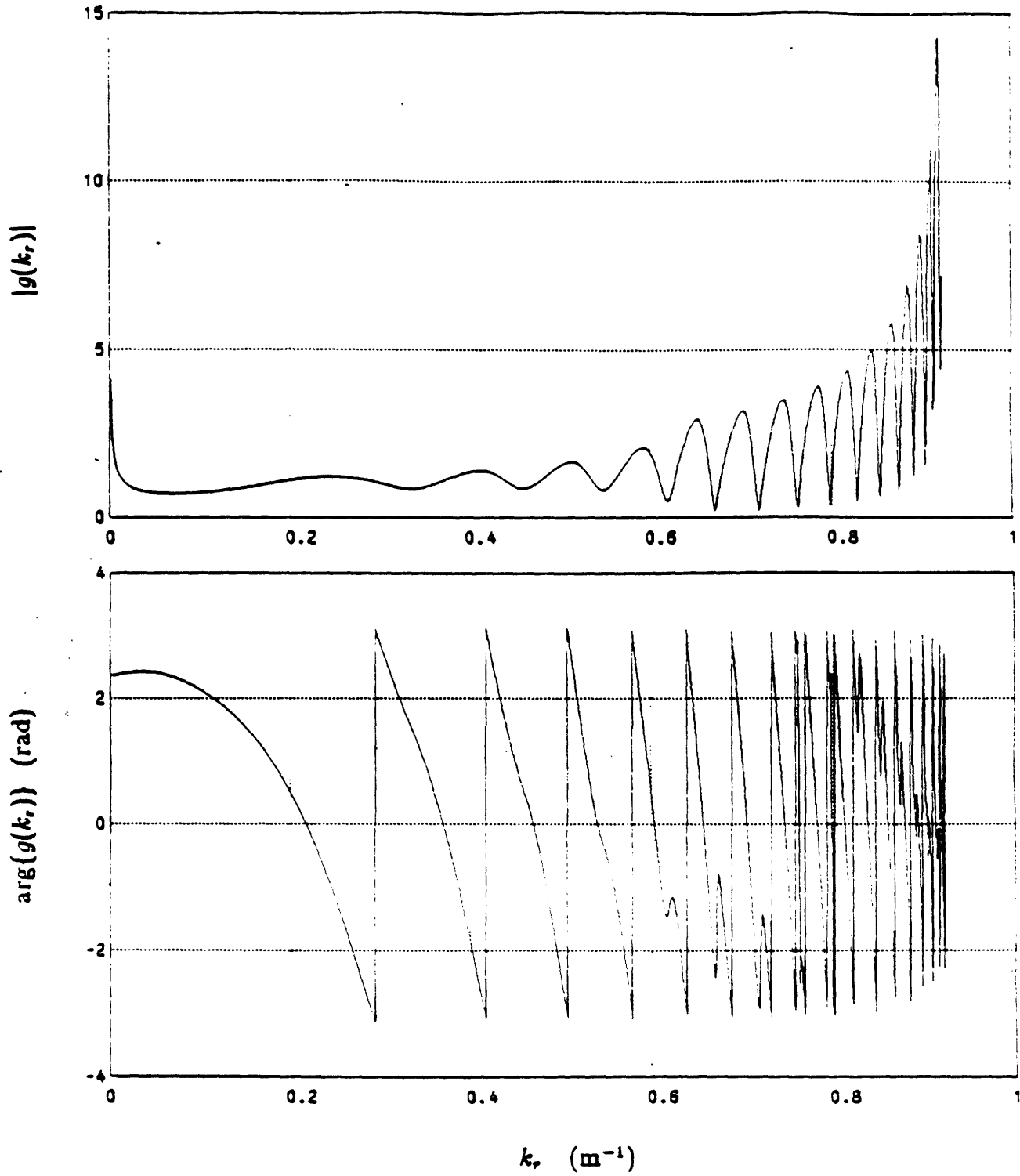
Figure 6.31: Magnitude and phase of the total Green's function obtained by processing only a single channel of the realistic deep water field.
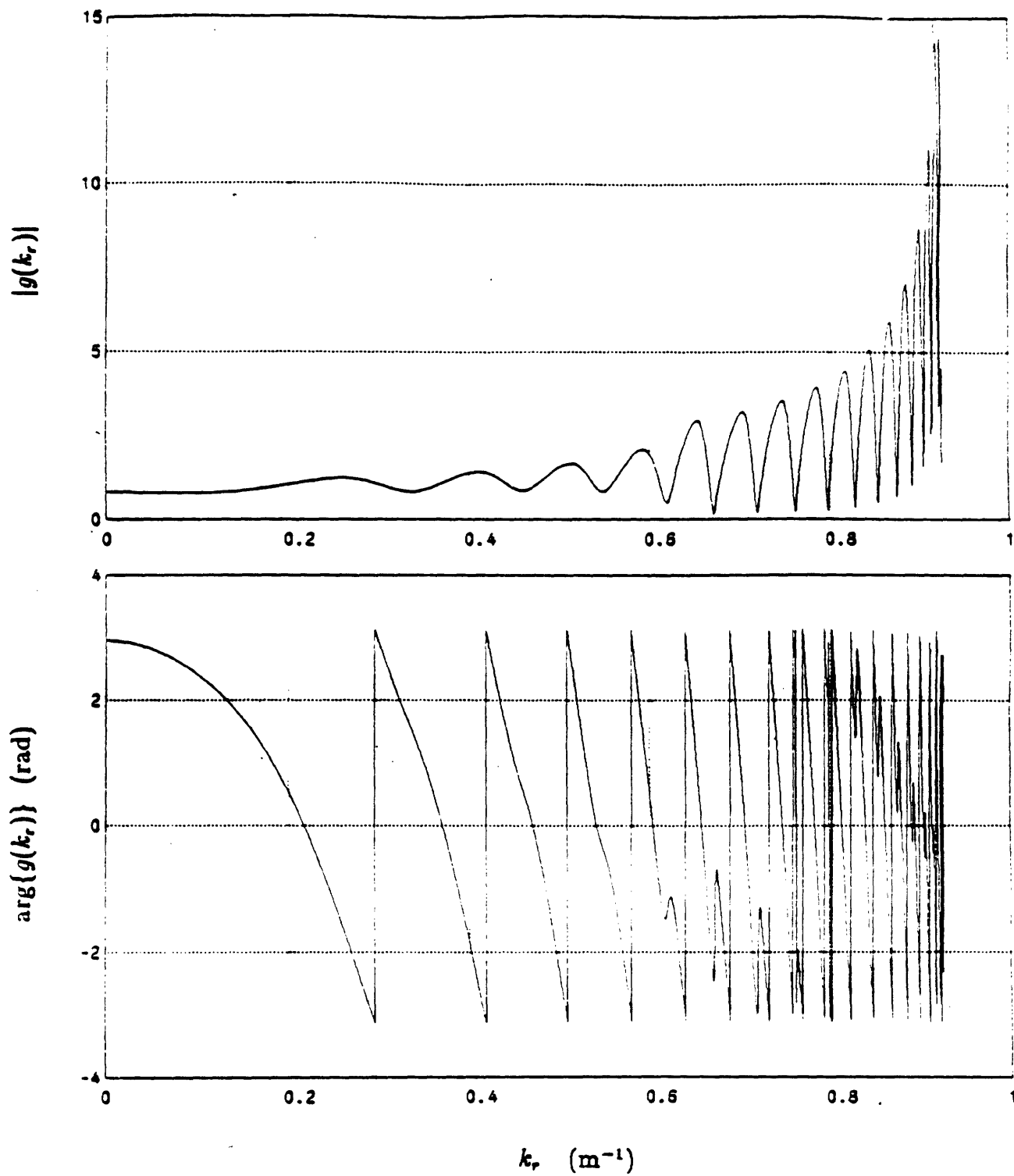
Figure 6.32: Magnitude and phase of the theoretical total Green's function for the realistic deep water case.

between the two Green's functions is quite good and it is apparent that they differ primarily at low values of k_r. The degradation here is primarily due to the fact that

$$p(r) \sim p_{a\omega}(r) \qquad (6.20)$$

is based on two assumptions which are not strictly valid at small ranges.

Additionally, the reflection coefficient was extracted from the Green's function obtained by processing only the single component, and its magnitude and phase are displayed in Figure 6.33. For reference, the magnitude and phase of the theoretical reflection coefficient for this example are shown in Figure 6.34. The comparison between the two reflection coefficient functions is quite good except at small values of k_r, despite the fact that only a single component of the field was used as the basis for this coherent signal processing inversion. In addition, we point out that some of the degradation in the extracted reflection coefficient may be due to the windowing effects, as described by Mook [2], which have been caused by processing a fairly small aperture of data, i.e. $1024 \times 3.14 \, m = 3217 \, m$. The example points out that reasonable estimates of the Green's function and reflection coefficient can be obtained by appropriately processing only one sampled component of the total realistic deep water acoustic field. It is stressed that appropriate processing does not consist of performing the Hankel transform of the single component - this method will produce an estimate of the real or imaginary part of the Green's function only.

Although it is not our intention here to suggest that the unilateral Fourier transform be used as a substitute for the Hankel transform in inversion methods [10], we point out that its properties may have other important applications in the processing of deep water acoustic fields. As one example of this, we consider the use of the shift theorem, discussed in Chapter 3, as a means for compensating for a fixed range registration error. In this numerical example, we will simulate the effect of incorrectly establishing the position of the origin, i.e. $r = 0$, in a deep water data collection experiment. Thus, instead of processing the deep water field starting at $r = 0$, the shifted version of the field $p(r + r_0)$ will be processed. In Chapter 3, it
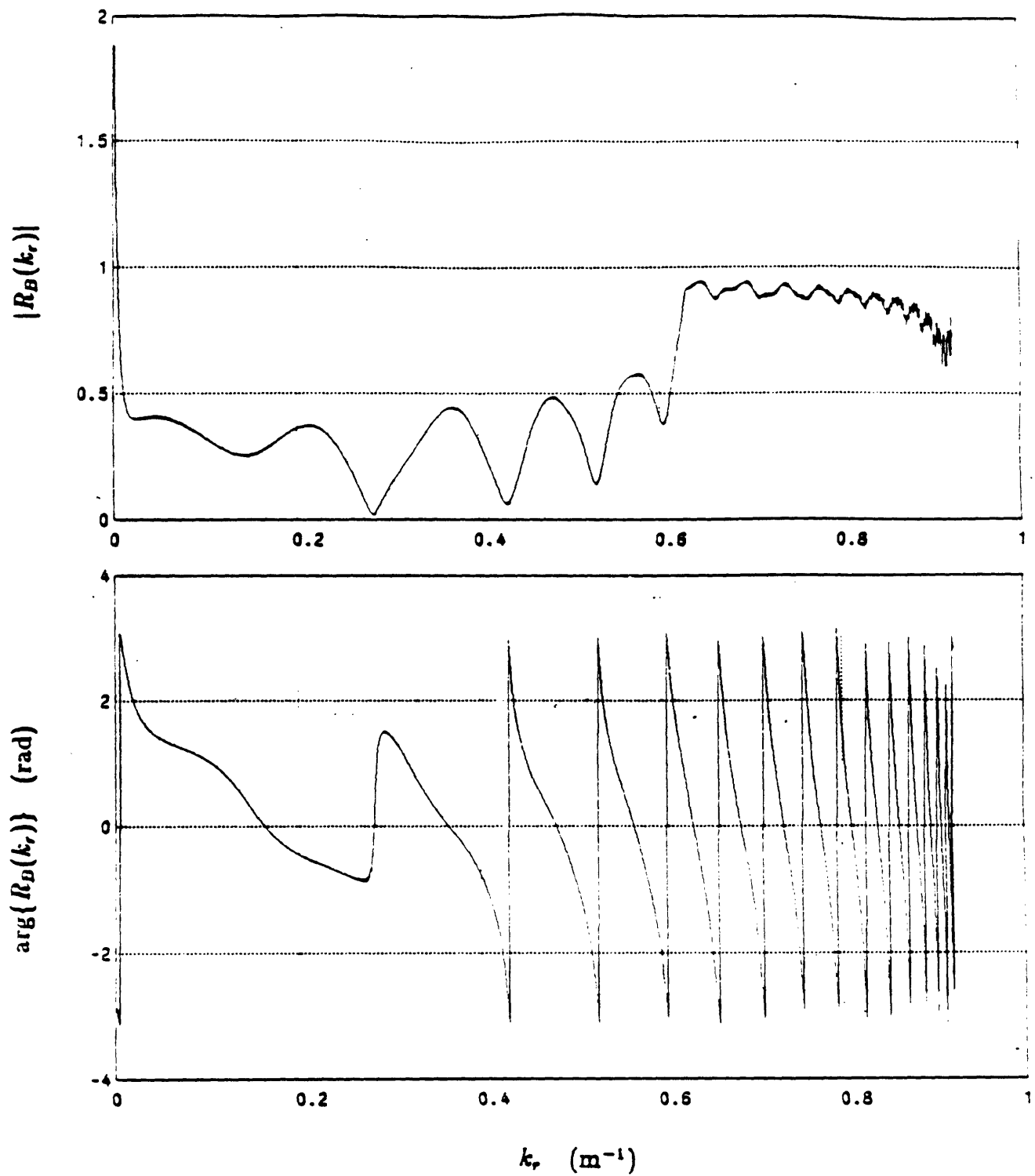
Figure 6.33: Magnitude and phase of the extracted bottom reflection coefficient which was obtained by processing only a single channel of the realistic deep water field.
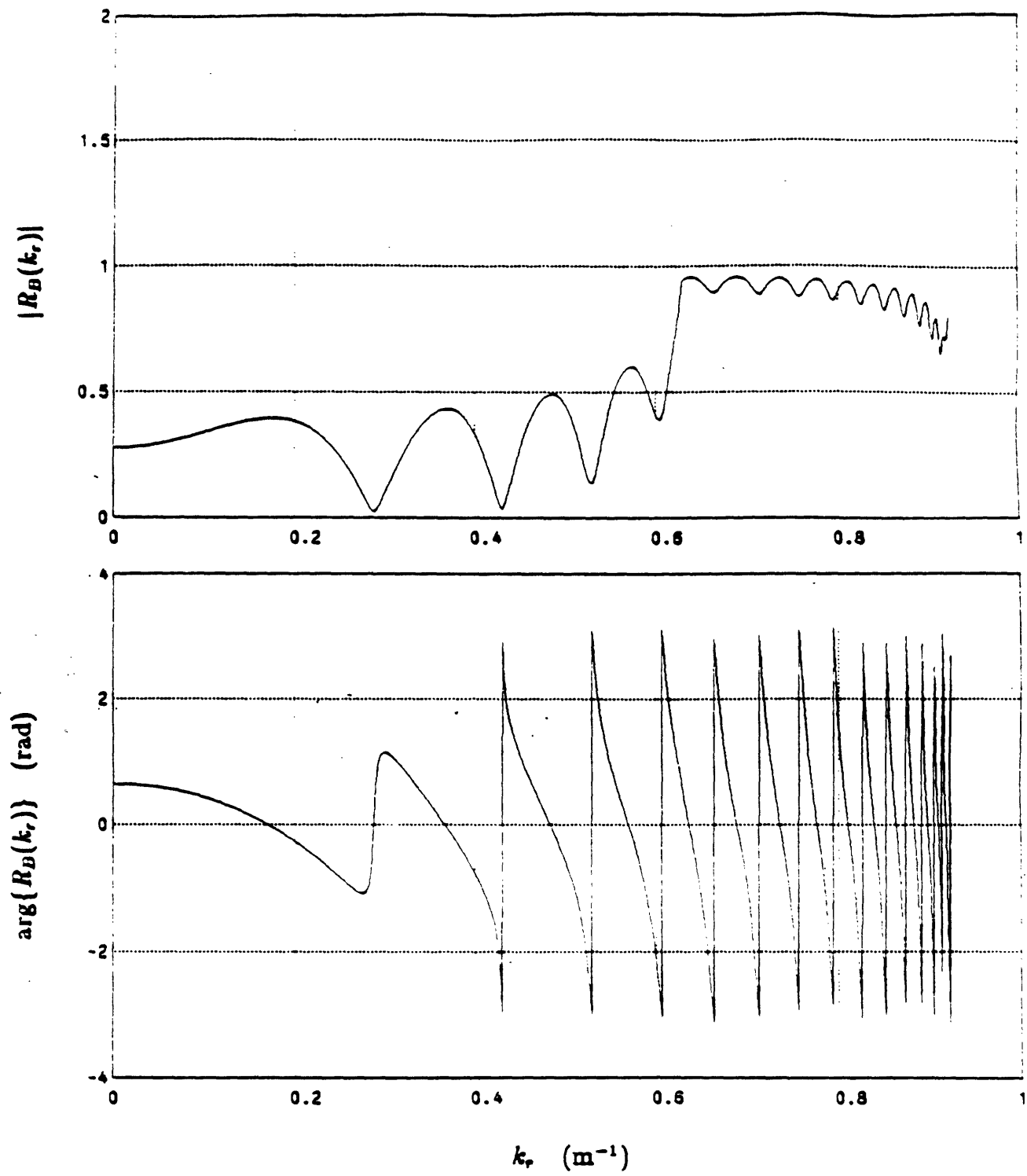
Figure 6.34: Magnitude and phase of the theoretical reflection coefficient for the realistic deep water case.

was pointed out that the effect can be partially compensated for by multiplying the Green's function of the shifted field by the linear phase factor $e^{-jk_r r_0}$. In the numerical example, we have processed 1024 points of the total 52-layer deep water field which has been shifted by approximately 9.42 m (three range samples). The first 9.42 m of the field was discarded. The field was then multiplied by $r^{1/2}$ and its unilateral Fourier transform was computed. [3] The reflection coefficient of the uncompensated Green's function was extracted and its magnitude and phase are displayed in Figure 6.35. In comparing the magnitude and phase of this estimate of the reflection coefficient with the theoretical reflection coefficient shown in the preceding figure, we see that the extracted reflection coefficient shows significant degradation. If the shift theorem is applied, and the same Green's function is multiplied by the linear phase factor, the reflection coefficient can again be extracted. The reflection coefficient which results from this sequence of processing steps is displayed in Figure 6.36. The improvement in the result is apparent as can be seen by comparing this figure with the previous two figures. The degradation at low values of k_r is primarily due to the fact that the first 9.42 m of data have been discarded in the processing which was performed and is also be due to the error in approximating $p(r)$ with $p_{as}(r)$ at small ranges. A method based on the above technique might also be applied to experimental data in order to partially compensate for a fixed range registration error and is suggested as a direction for further investigation. It is our conjecture that the shift theorem might also form the basis of a method for the compensation of source height variation.

As another example of the use of the unilateral Fourier transform, the processing of the total 52-layer deep water field which has been sampled at a lower rate will be considered. In particular, by appropriately processing the synthetic deep water acoustic field which has been sampled at the approximate rate of one complex sample per water wavelength, we will show that it is possible to obtain reasonable estimates of both the Green's function and the reflection coefficient. As pointed out previously, this

---

[3] The determination of the Green's function using the unilateral Fourier transform was done for convenience. A more exact method could have also been used.
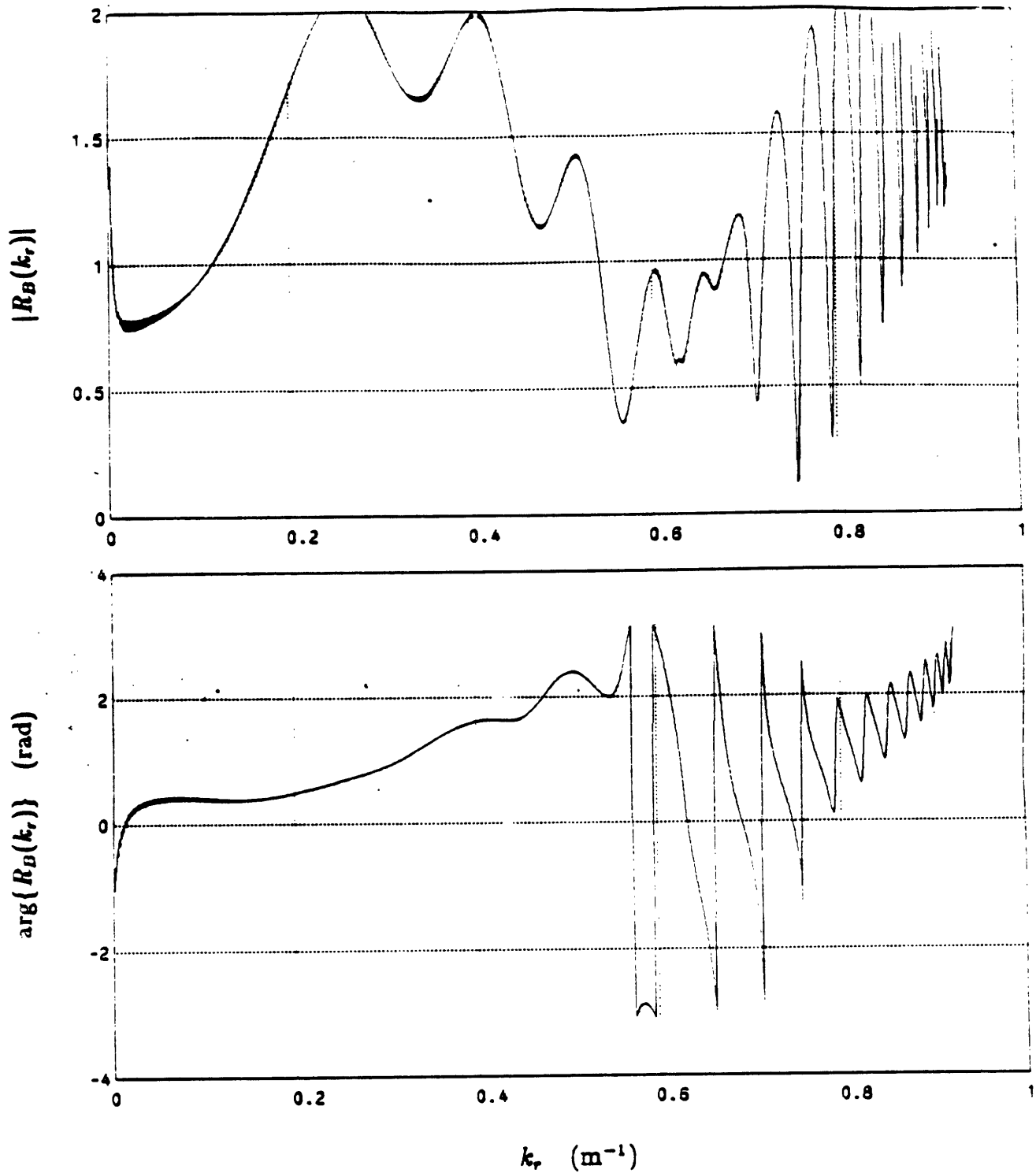
Figure 6.35: Magnitude and phase of the reflection coefficient which results from processing the deep water field with fixed range offset.
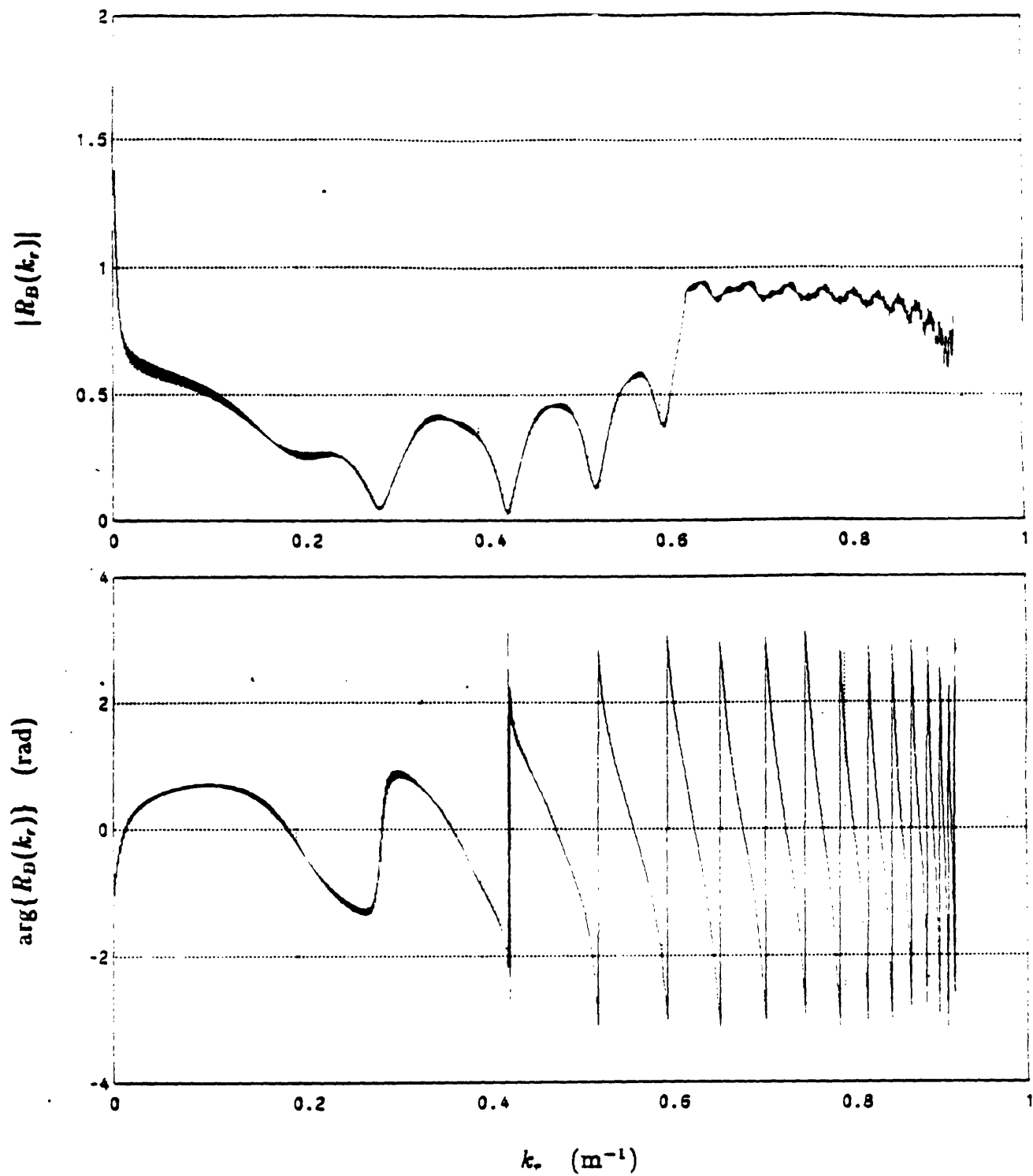
Figure 6.36: Magnitude and phase of the reflection coefficient which results from processing the deep water field with fixed range offset. The Green's function was first multiplied by a linear phase factor.

sampling rate should be adequate to completely represent the field if the assumption that the field can be synthesized using positive wavenumbers only is valid. The implication is that if the field is adequately represented, it should be possible to extract the corresponding Green's function and reflection coefficient. A method for accomplishing this is now described.

In the numerical example, 512 points of the complex-valued 52-layer total synthetic deep water field were multiplied by $r^{1/2}$ and were processed using the unilateral Fourier transform. The field was sampled every 6.28 m which is a rate slightly larger than one sample per water wavelength. The rate was chosen as slightly higher partly to accommodate the effects of the pole in the reflection coefficient and Green's function at a value of k_r higher than the water wavenumber. In Figure 6.37 is shown the magnitude and phase of the Green's function obtained by processing the field sampled at this rate. It is quite similar to the theoretical Green's function, shown in Figure 6.32, except at low values of k_r where several assumptions are not valid. The exact reason for the presence of the spike at $k_r \sim 0.1$ is not known. A conjecture is that it is related to aliasing, due to the pole in the reflection coefficient at a value of k_r greater than the water wavenumber. It may also be due to some inaccuracy in the method for synthetic data generation chosen. In particular, the effects of this pole were not removed in the technique used to generate this field, discussed earlier. The magnitude and phase of the corresponding reflection coefficient extracted from this Green's function are next shown in Figure 6.38. The spike is again evident as is the poor quality of the reflection coefficient at small values of k_r. Nevertheless, the quality of the reflection coefficient obtained by processing a realistic synthetic deep water field which has been sampled at approximately one (complex) sample per wavelength is quite good as can be seen by comparing Figure 6.38 with the theoretical reflection coefficient in Figure 6.34.

To briefly summarize, we have demonstrated that a realistic deep water acoustic field can be reconstructed from samples of only one of the quadrature components.
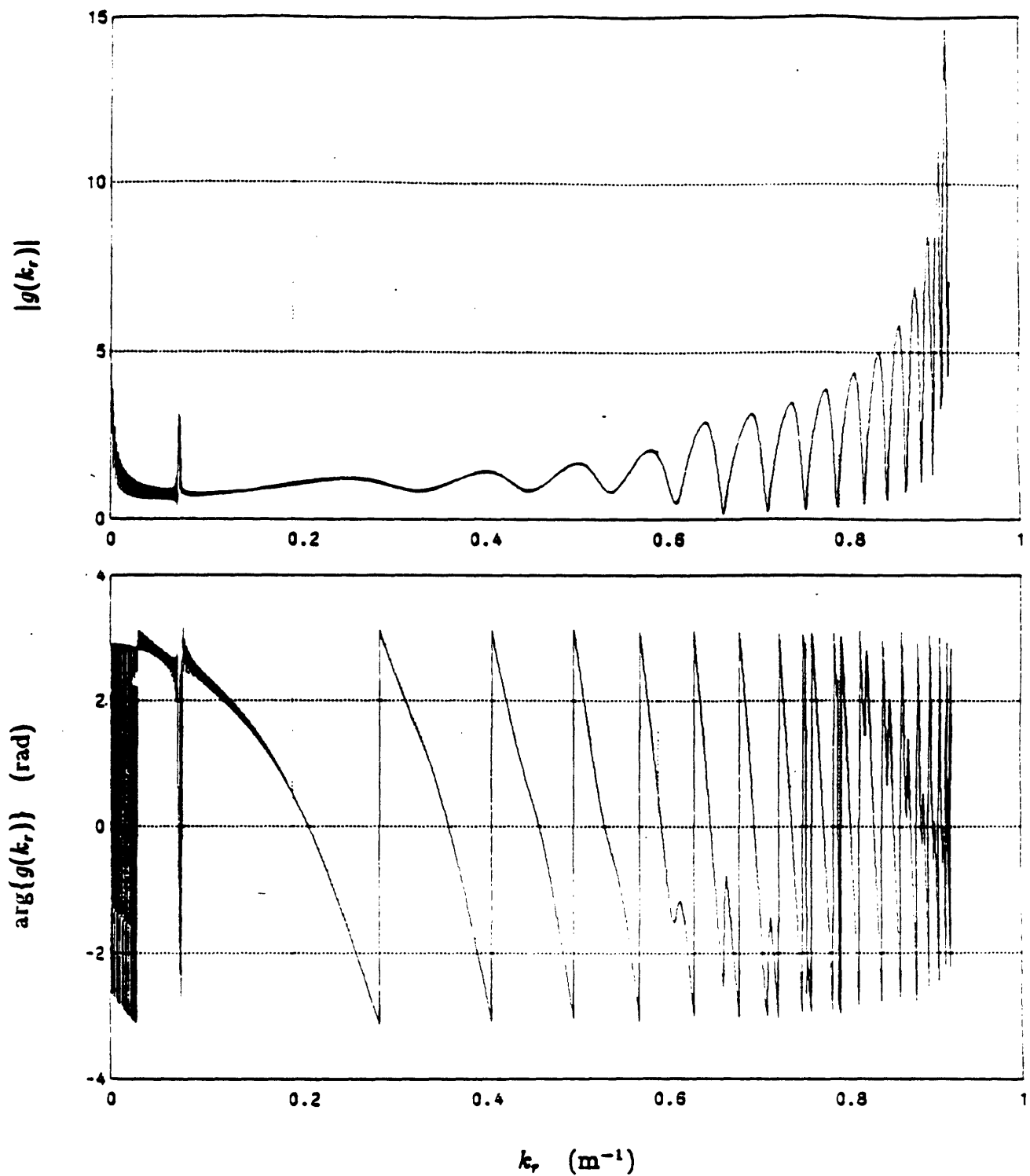
Figure 6.37: Magnitude and phase of the Green's function obtained by sampling the realistic deep water at a rate of approximately one complex sample per water wavelength and processing using the unilateral Fourier transform.
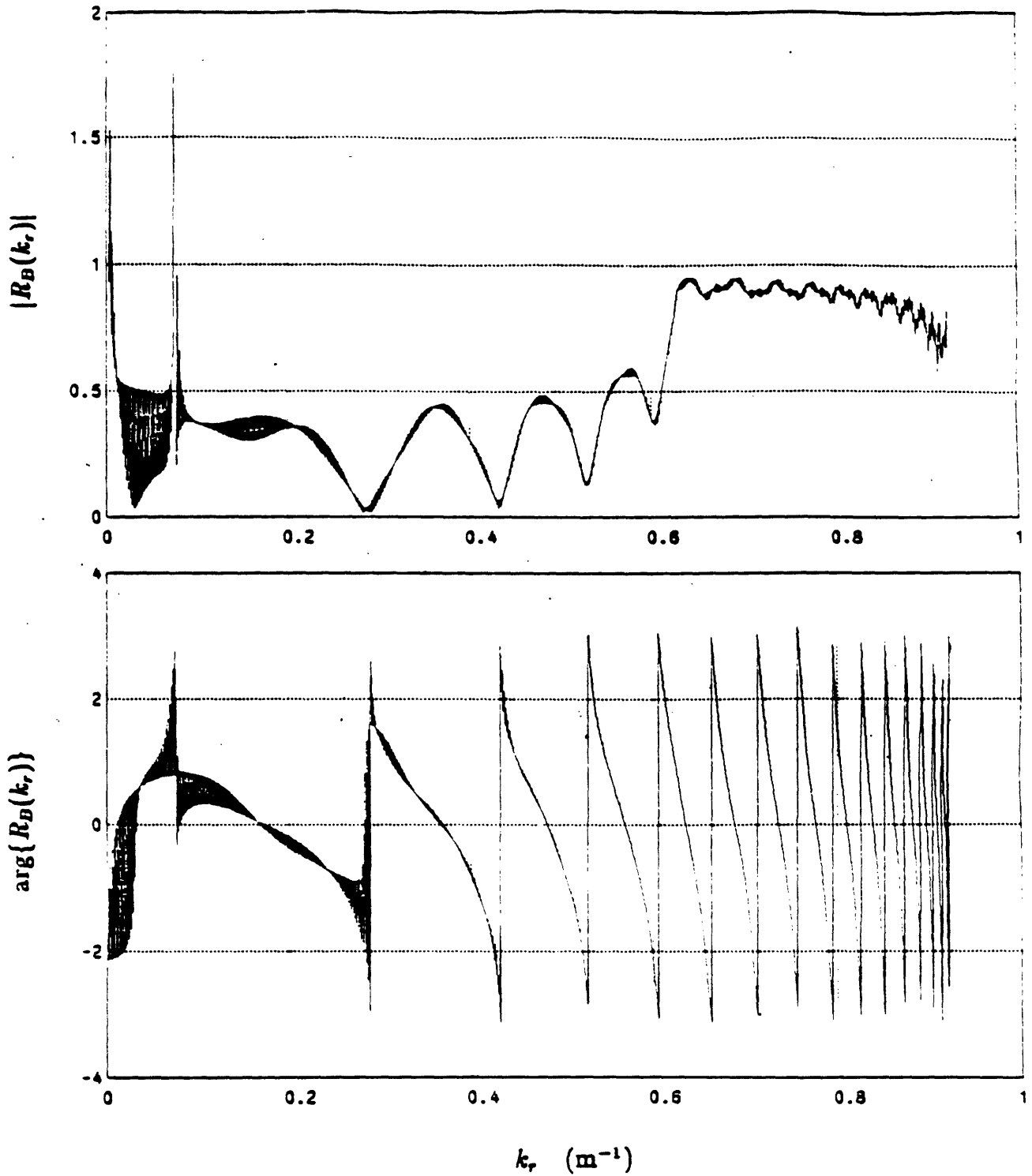
Figure 6.38: Magnitude and phase of the reflection coefficient obtained by sampling the realistic deep water at a rate of approximately one complex sample per water wavelength and processing using the unilateral Fourier transform.

Although the relationship between the technique used for synthetic data generation and the technique used for reconstruction is certainly an issue, we have described a technique which effectively decouples the two. The reconstruction results indicate that the error in the reconstructed signal is small except in the first several wavelengths. Additionally, it was pointed out that, at least for this realistic example, the real-part/imaginary-part sufficiency condition leads to the development of coherent processing techniques which can be performed using only a single channel of the data. In particular, it was shown that only a single channel is required in order to obtain reasonable estimates of both the Green's function and the ocean bottom reflection coefficient. Finally, it was shown that the unilateral Fourier transform can be used as the basis for processing an acoustic field which has been sampled at a rate of approximately one complex sample per wavelength, i.e. at half the rate as was previously predicted. It is our conjecture that the properties of the unilateral Fourier transform and asymptotic Hilbert-Hankel transform may have other important applications in the context of modifying current methods and developing new methods for the signal processing of deep water acoustic fields.

6.4   Reconstruction of Shallow Water Acoustic Fields

In previous sections of this chapter, we have examined the reconstruction of free-space acoustic fields and acoustic fields which have interacted with a single boundary only. In the case of acoustic propagation in shallow water, it is of interest to consider the effects of adding another boundary, i.e. the top of the waveguide, on the reconstruction. We point out that although there are reverberant field components within the waveguide which travel upwards and downwards due to the reflection at the bottom and top of the waveguide, each component is still outgoing in range r. Thus, it is expected that the condition of real-part/imaginary-part sufficiency is still valid and that the reconstruction method can be applied. Two numerical examples of the reconstruction of a shallow water acoustic field from a single channel will be discussed in this section. The first example consists of a simple Pekeris waveguide model. The second example consists of a more realistic waveguide model which was obtained from the forward modelling of an experimental shallow water field.

The Pekeris model was chosen as an example of a simple shallow water field to which the reconstruction algorithm can be applied. In fact, the field is not so simple, and as pointed out in Chapter 3, an accurate numerical method is required in order to generate this field. Perhaps a simpler model consisting of a waveguide overlying a hard bottom could have been considered. Although a closed-form expression for the field in this type of model exists, it requires the computation of an infinite number of terms corresponding to the evanescent modes. In practice, the hard bottom shallow water field is approximated by retaining only a finite number of these contributions. Although we have not previously made this point, the hybrid method for synthetic field generation, discussed in Chapter 4, can be applied in this case as well. However, the hard bottom model is quite unrealistic of shallow water propagation and we will select the Pekeris model as our first shallow water example. As pointed out previously, the field produce by the hybrid method may be slightly in error at very short ranges.

In comparing the results of the reconstructed field with the initial synthetic field, it is therefore apparent that there may be errors in both at these ranges. However, we will show that the reconstruction method produces a close approximation to the synthetic field produced using the hybrid method.

The Pekeris model selected is identical to the one previously considered in Chapter 4 and is summarized in Table 4.1. The synthetic field was generated by computing the Hankel transform of $g_C(k_r)$ using the Abel/Fourier method and adding $p_T(r)$ corresponding to the single mode for this model. The magnitude and residual phase, computed using $k_\phi = 0.5623757$, are shown in Figure 6.39. Although these quantities are smoothly varying, the associated real and imaginary components of the field are again rapidly varying as can be seen from their display in Figure 6.40. In the reconstruction method, one of the components in Figure 6.40 is to be determined from the other.

To demonstrate the reconstruction method, 1024 samples of the imaginary part of the field, sampled at a range interval of 3.14 m, [4] were retained and the real part was set to zero. The real part was then reconstructed and the magnitude and residual phase of the reconstructed field are shown in Figure 6.41. In comparing this field with the true field shown in the preceding figure, it can be seen that the reconstruction is quite good, except in the near-field. As further evidence of this, the error signal in the reconstruction is plotted in Figure 6.42 along with the true magnitude of the field. In the next two figures, Figure 6.43 and 6.44, the true field magnitude/residual phase and the reconstructed field magnitude/residual phase are shown expanded in the first 250 m. The significance of the degradation in the near-field due to the reconstruction is apparent in comparing these figures. The example points out that a high-quality reconstruction can be obtained everywhere except in the near-field assuming the Pekeris model for shallow water propagation.

---

[4] This rate corresponds to approximately 3.4 samples per water wavelength.
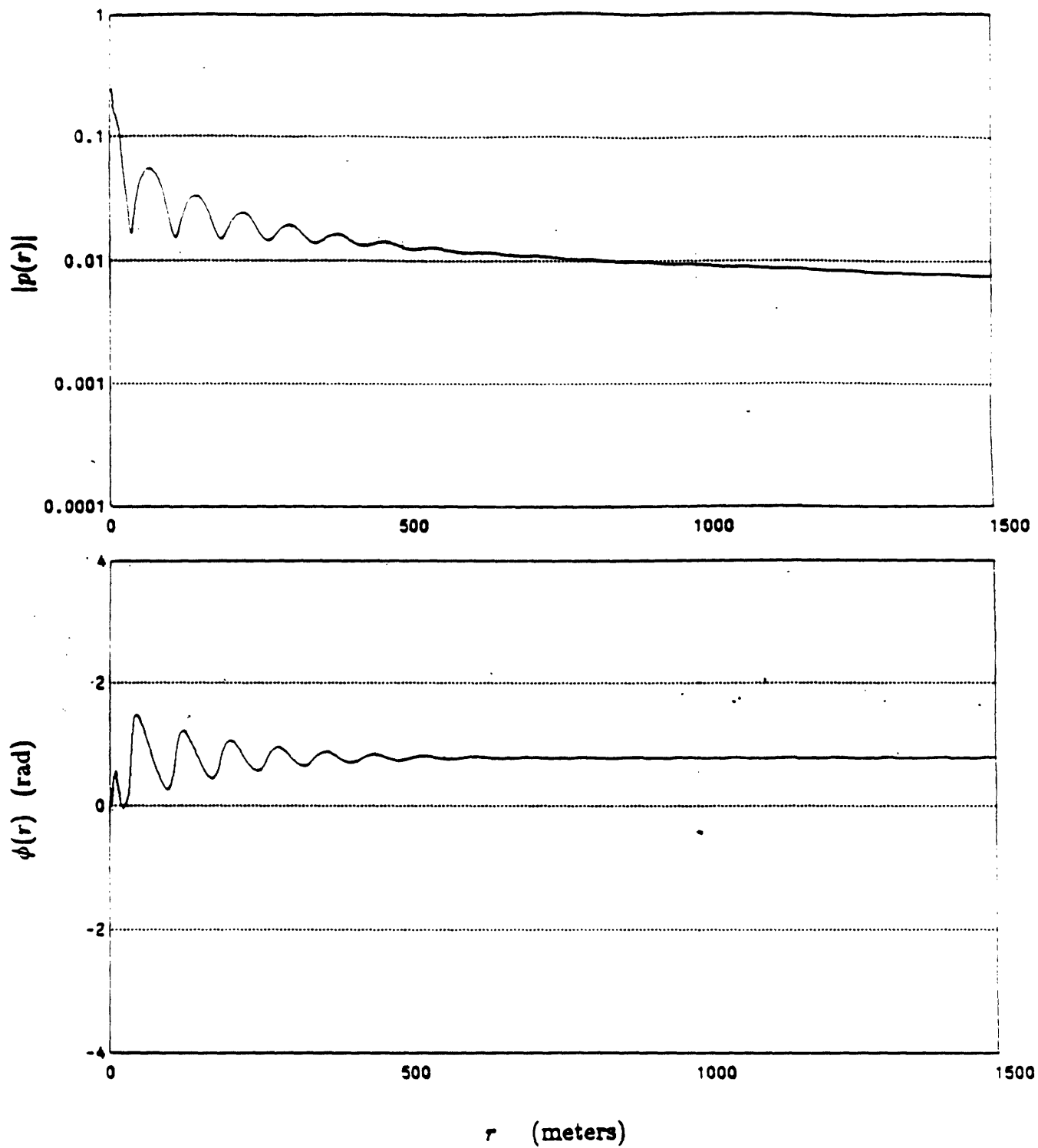
Figure 6.39: Magnitude and residual phase of the Pekeris model shallow water field.
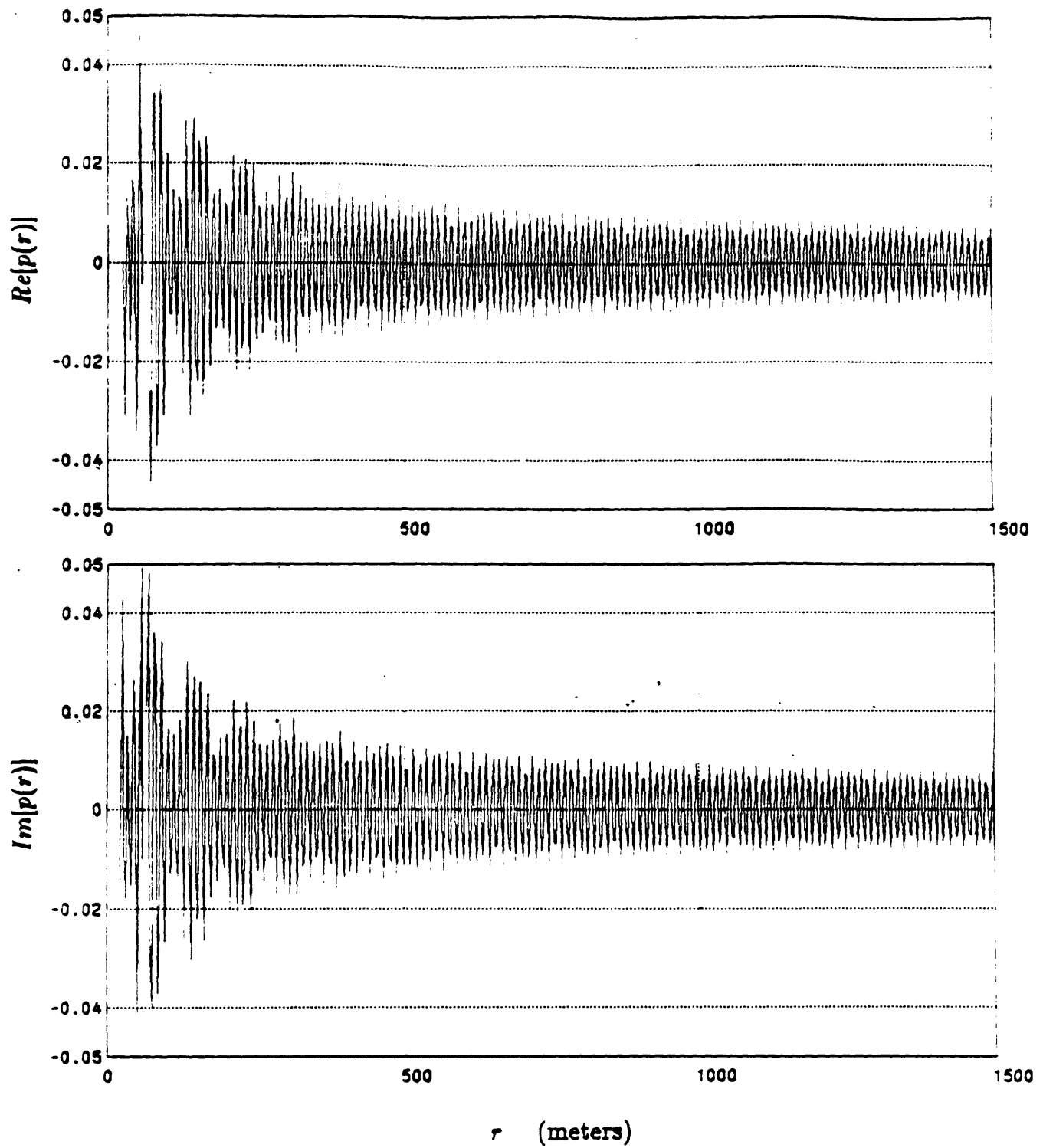
Figure 6.40: Real and imaginary components of the Pekeris model shallow water field.
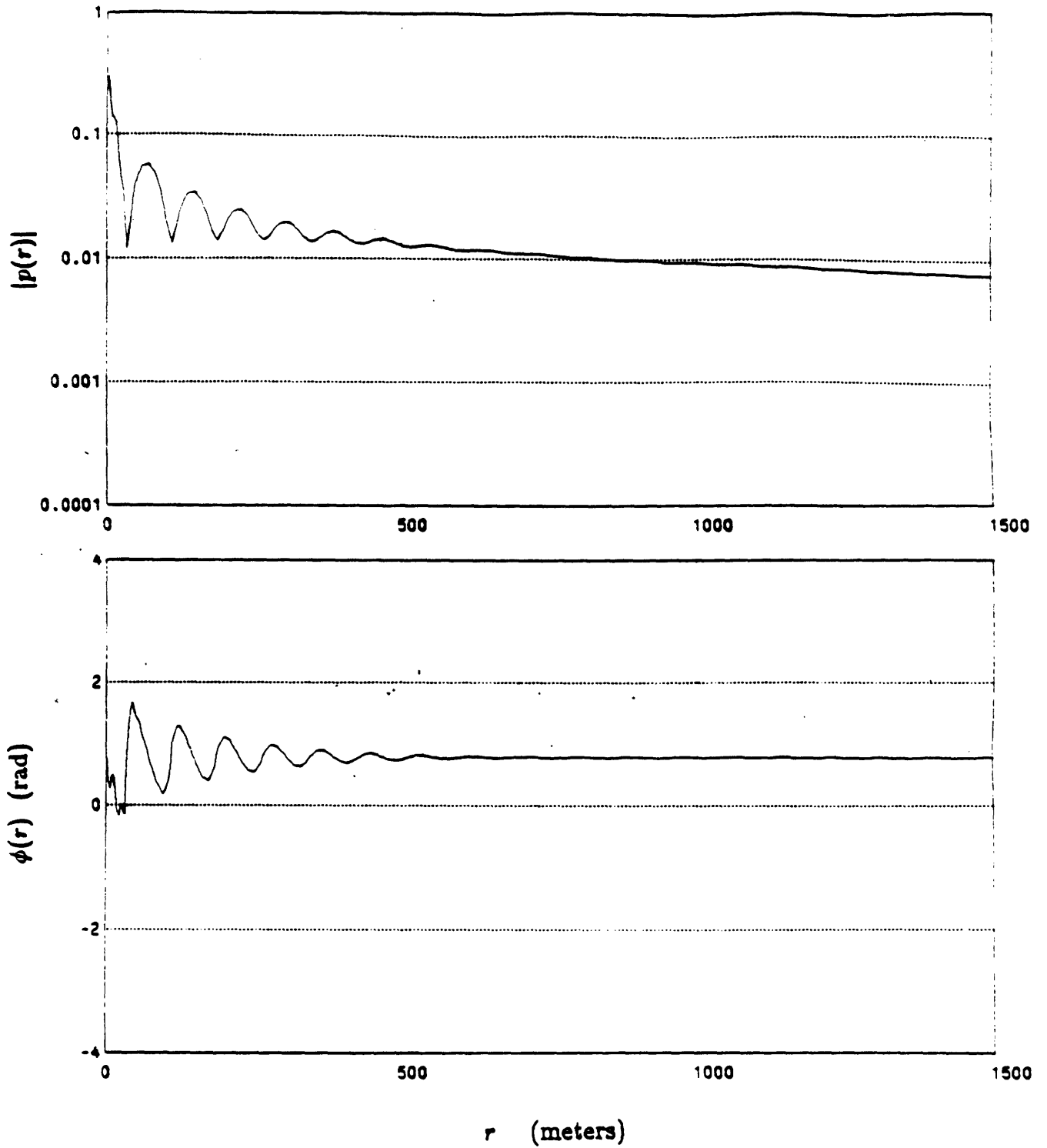
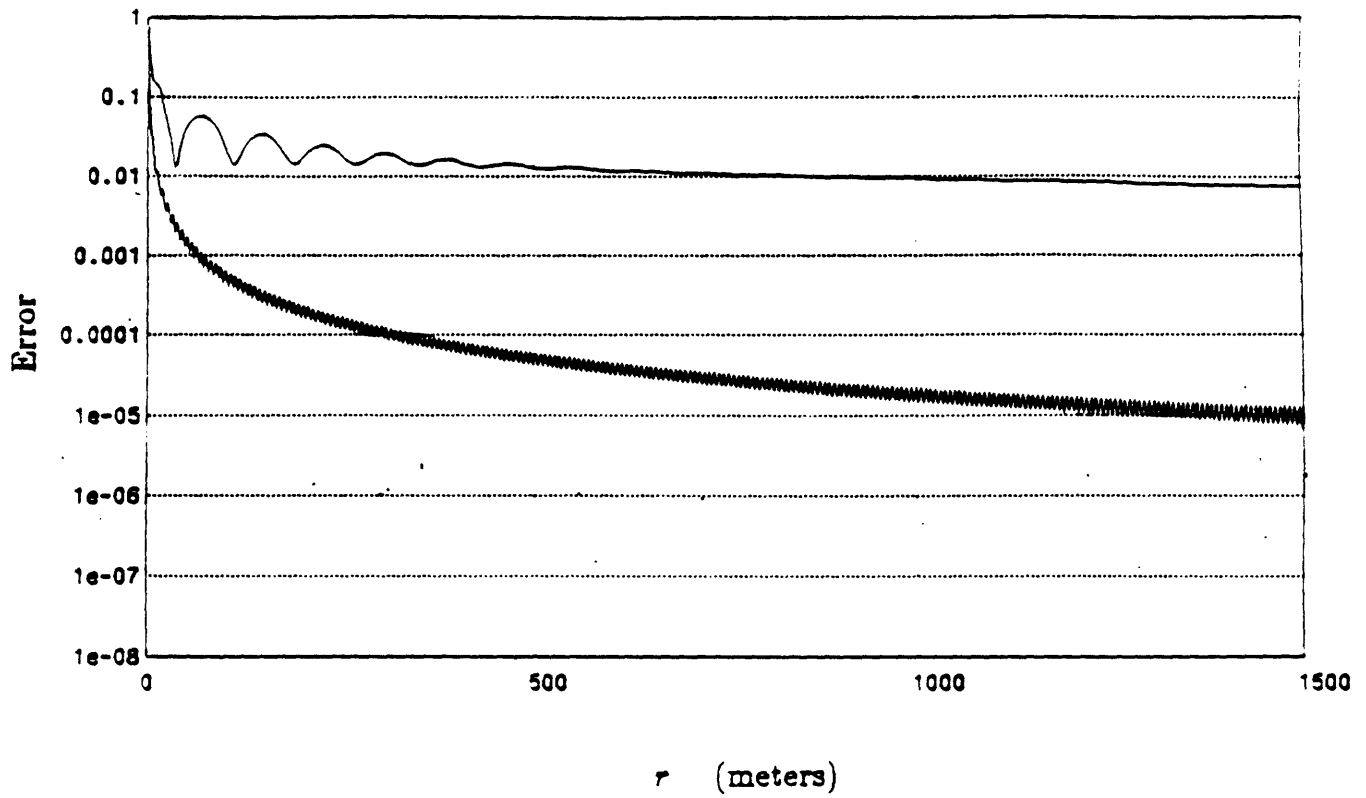Figure 6.41: Magnitude and residual phase of the reconstructed Pekeris model shallow water field.

Figure 6.42: Error in the reconstruction of the real component (bottom curve) and true field magnitude (top curve) for the Pekeris model shallow water field.
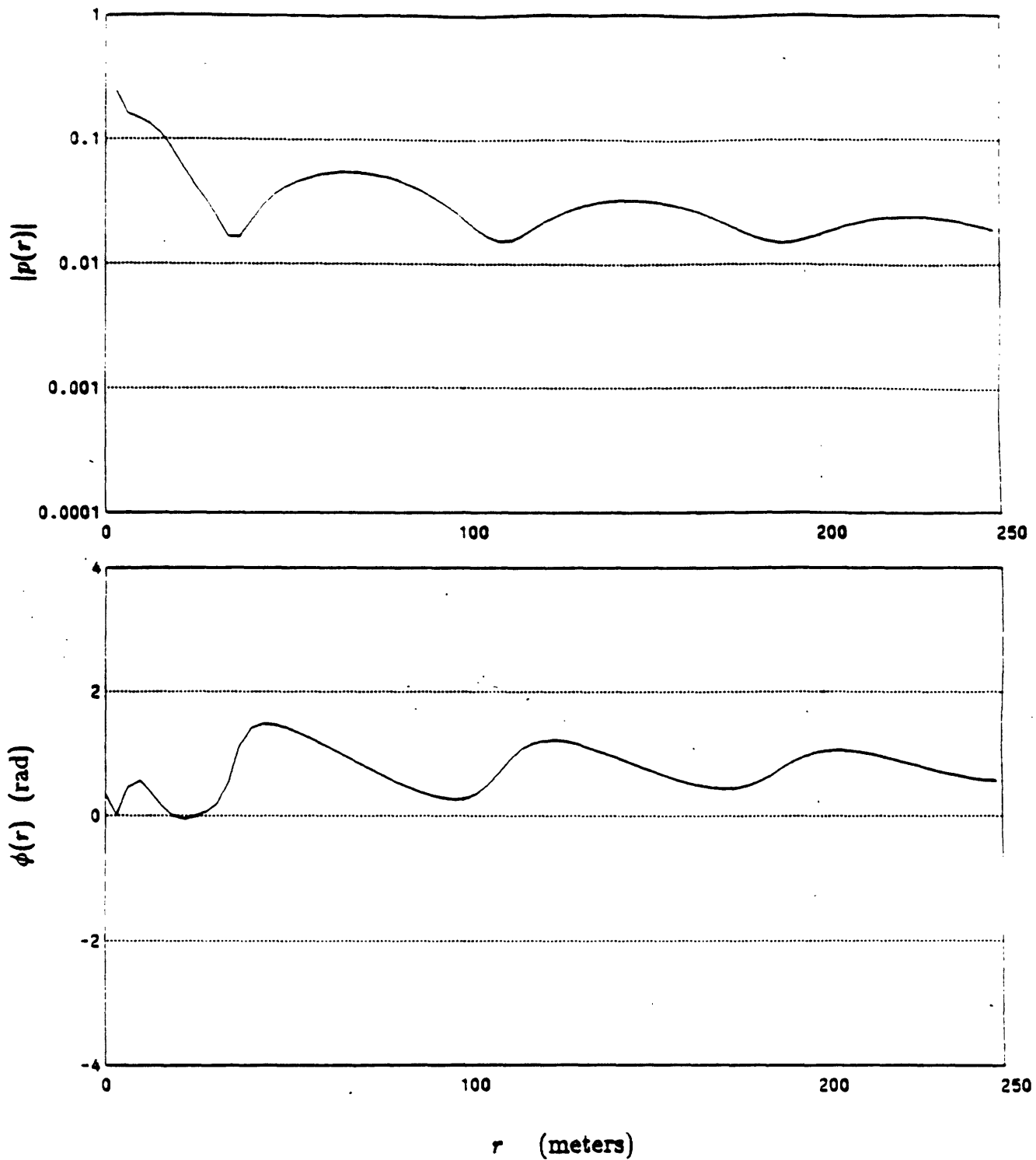
Figure 6.43: Expanded versions of the near-field magnitude and residual phase for the Pekeris model shallow water field.
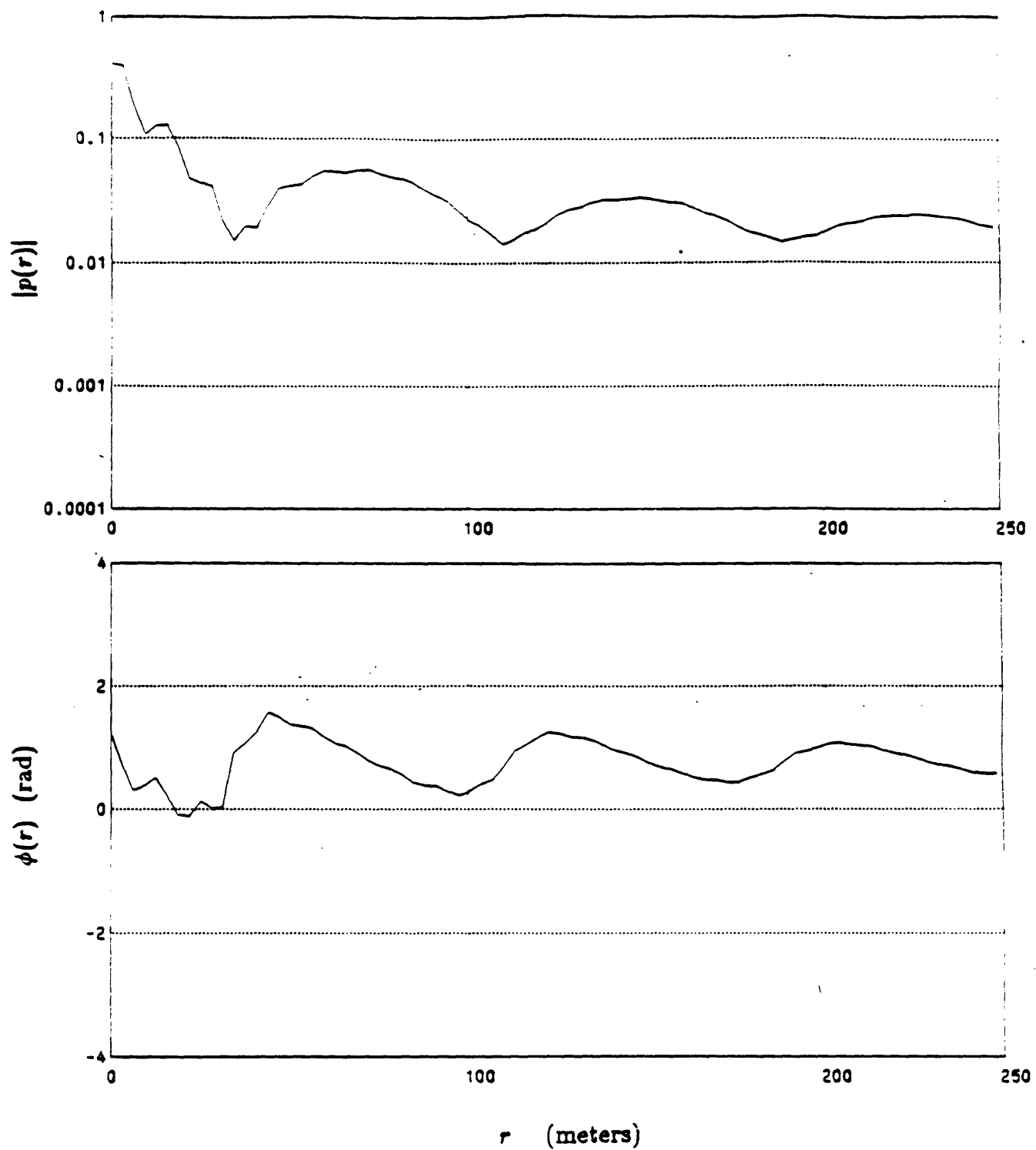
Figure 6.44: Expanded versions of the near-field magnitude and residual phase for the reconstructed Pekeris model shallow water field.

As a more realistic example, the geoacoustic model in Table 6.1 will next be considered. This geoacoustic model was obtained by the forward modelling of an experimental acoustic field [11], measured in Nantucket Sound, Mass. in May 1984, and includes realistic attenuation in the underlying ocean bottom. The hybrid method for synthetic data generation was used to produced the synthetic field for this geoacoustic model. In Chapter 4, we pointed out that care must be taken to avoid aliasing in the synthetic generation of shallow water fields if the Hankel transform is applied directly to the total Green's function. This aliasing can occur not only for simple Pekeris models, but also for more complicated models which consist of a layered bottom with realistic attenuation. Furthermore, the aliased field may appear to be smoothly varying therefore not giving any apparent indication that aliasing has occurred.

To demonstrate this, we have computed the acoustic field for the realistic shallow water geoacoustic model which includes attenuation by using the hybrid method and by using the direct method. In both cases, 1024 samples over a wavenumber interval of $k_r = 0.0$ to 1.0 were used although the hybrid method used samples of $g_C(k_r)$ while the direct method used samples of $g(k_r)$. For reference, the magnitude and phase of $g(k_r)$ and the magnitude and phase of $g_C(k_r)$ are displayed in Figures 6.45 and 6.46 respectively. [5] The magnitude and residual phase of the field computed using the hybrid method are shown as dashed curves in Figure 6.47 and the magnitude and residual phase of the field computed using the direct method are shown as solid curves in this figure. For the particular sampling of the Green's function chosen, the real-part of the dominant pole, located at $k_r = 0.5688832$ for this example, lies nearly halfway between two consecutive samples. The differences between the magnitude curves, and the differences between the residual phase curves, can be attributed to the aliasing

[5] This realistic shallow water Green's function, corresponding to a layered bottom with attenuation, nicely displays the property of the finite extent of the imaginary part of the Green's function. In particular, the value at which the phase is approximately either $\pm\pi$ or 0 is $k_r = 0.50878$ which corresponds to the total wavenumber in the underlying halfspace. In addition, the presence of two invariant zeros is noted.
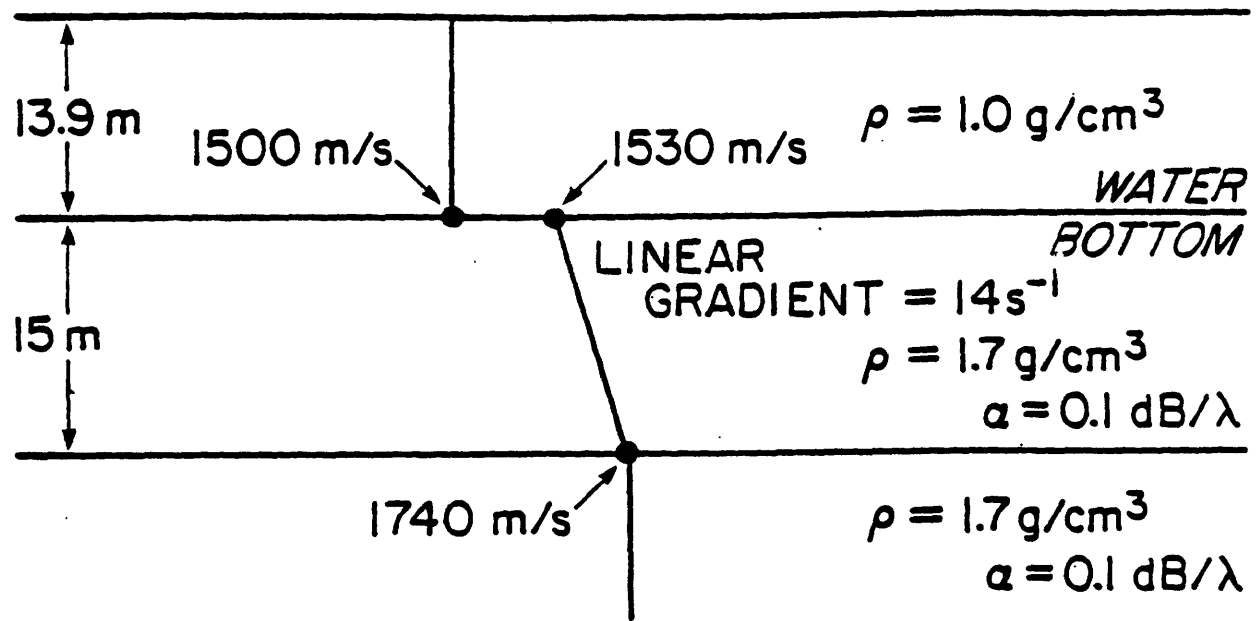
z_0	=	6.096 m
z	=	7.03579 m
f	=	140.056 Hz

Table 6.1: Geoacoustic model for the realistic shallow water case.
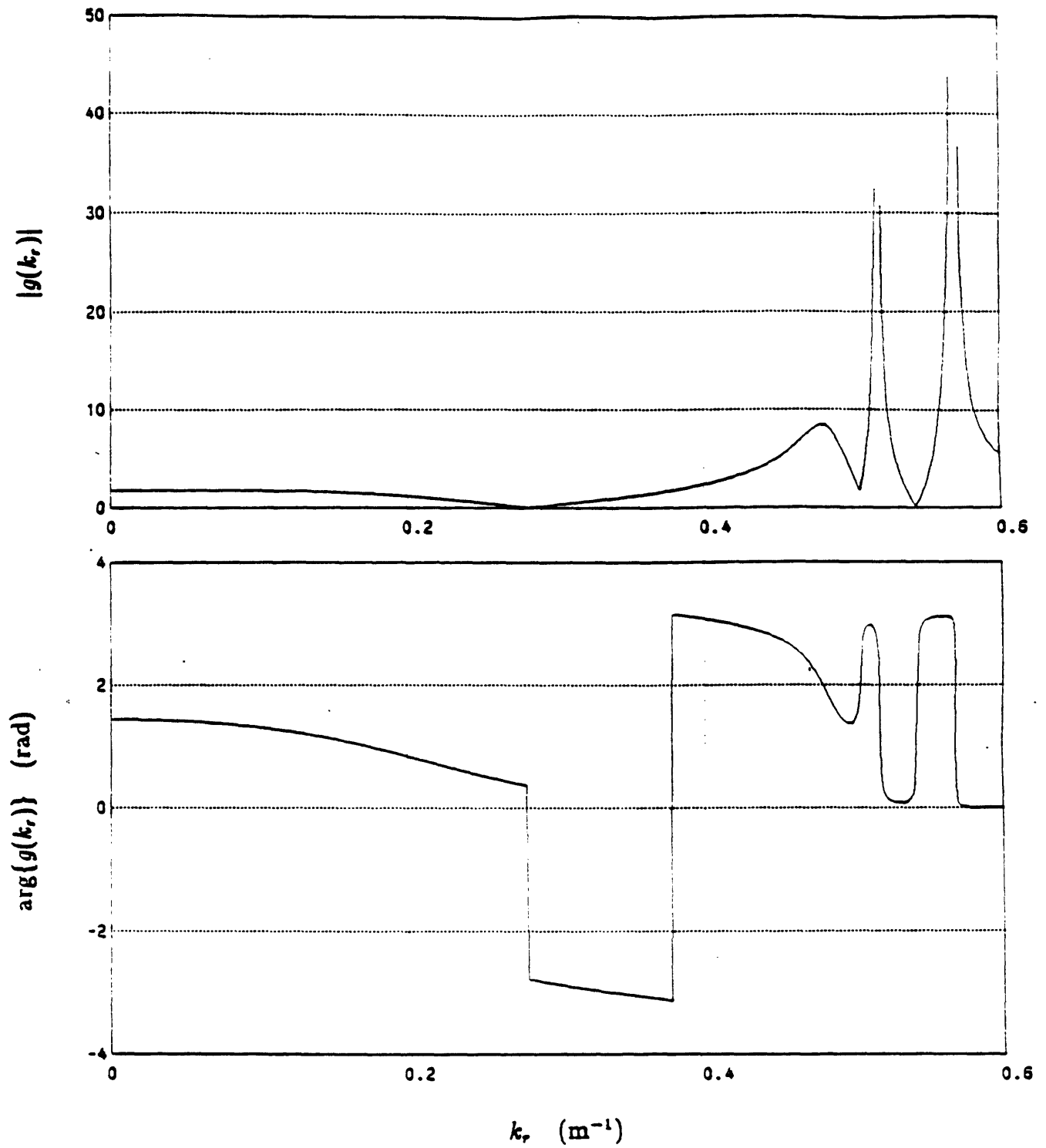
Figure 6.45: Magnitude and phase of the Green's function for the realistic shallow model summarized in Table 6.1.
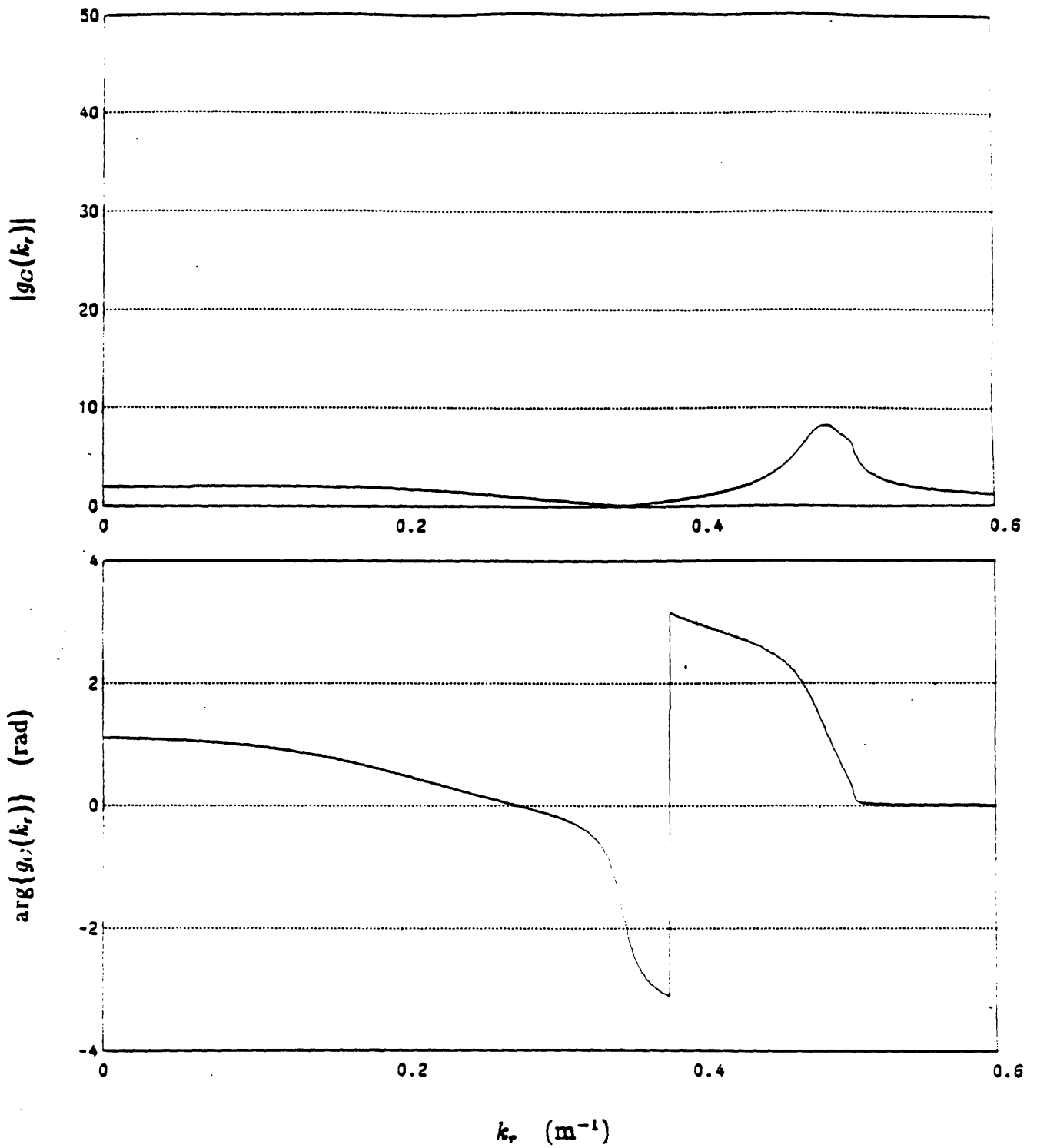
Figure 6.46: Magnitude and phase of the continuum portion of the Green's function for the realistic shallow water model.
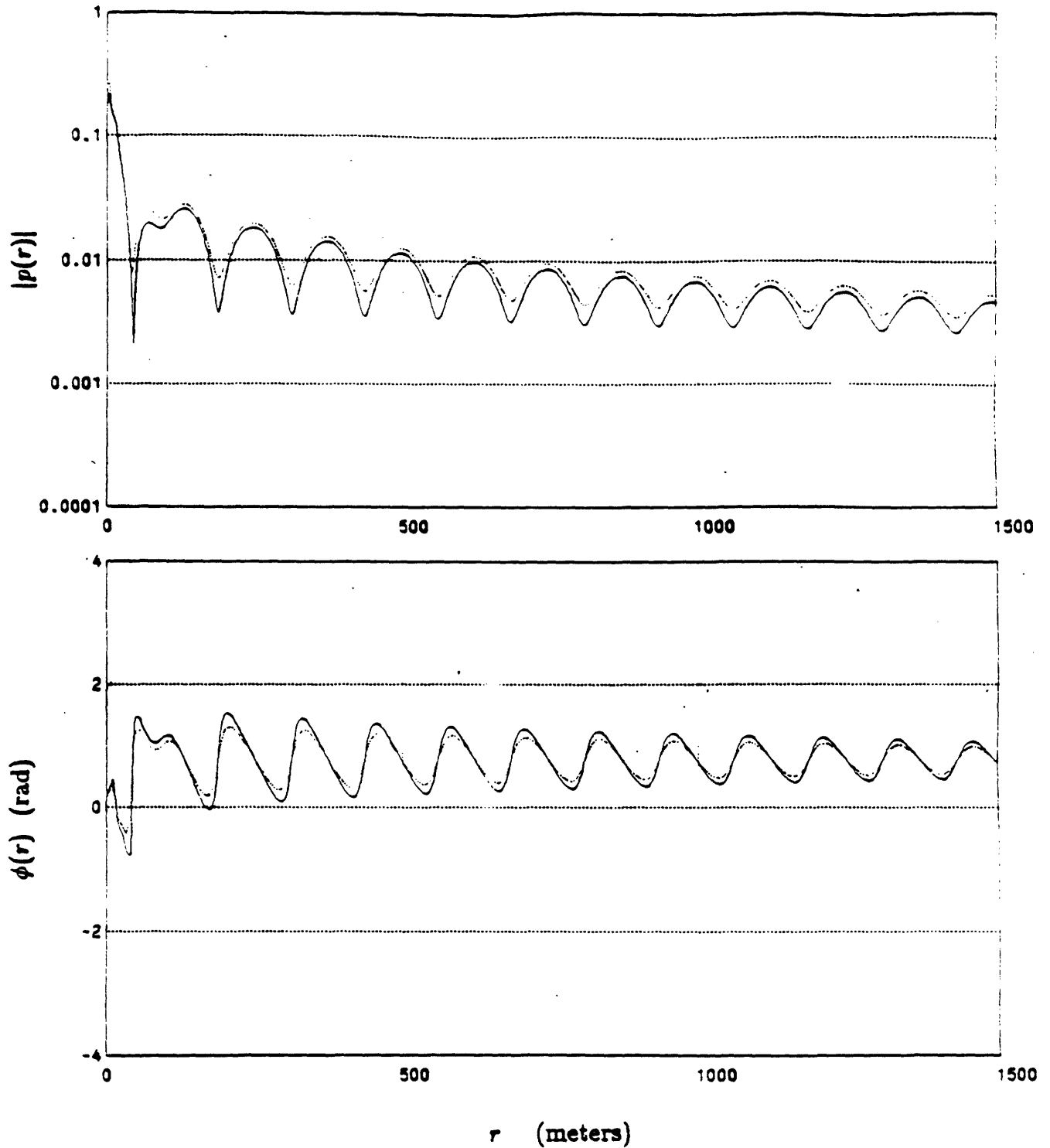
Figure 6.47: Magnitude and residual phase of the realistic shallow water field. The solid curves represent the field which was computed directly, without removal of the poles. The dashed curves represent the field computed using the hybrid method.

in the range domain, which has occurred in the use of the direct method. As further evidence of this, the sampling of the Green's function was changed very slightly so that 1024 samples were taken over a wavenumber interval of $k_r = 0.0$ to $1.0 - \epsilon$, where $\epsilon = 7.952 * 10^{-4}$. The exact value of ϵ was computed such that the real part of the dominant pole lies exactly on a sampling point. The magnitude and residual phase of the field computed using the hybrid method are shown as dashed curves in Figure 6.48, and the magnitude and residual phase of the field computed using the direct method are shown as solid curves in this figure. In comparing this figure with the previous figure, we note that the hybrid method has produced identical fields for the two choices of sampling. However, in comparing the solid curves, it is seen that significant changes have occurred in the fields produced using the direct method, even though the sampling rate was changed very slightly, i.e. less than 0.01%.

The example demonstrates that if the direct method is chosen, care must be taken to avoid aliasing in the synthetic data generation of realistic shallow water fields even if attenuation is present in the model. The effects of aliasing may be of particular importance in forward modelling applications in which the model is determined based on the approximate matching of the peaks and nulls in the field and their relative significance. In particular, an incorrect model may result due to the fact that aliasing is present in the forward modelling procedure if the direct method is used. In addition, the above example suggests a method for determining how severe the aliasing is, if a direct method is used. In particular, by fixing the number of samples and varying the maximum wavenumber over a range of half a sample, it is possible to assess the significance of the aliasing present. This method may be of importance for applications in which it is impractical to use a more exact method for synthetic data generation and a bound on the quality of the data produced is desired.

To continue with the discussion of the reconstruction of a realistic shallow water acoustic field, we consider the magnitude and residual phase of the field produced using the hybrid method shown in Figure 6.49. This field was produced assuming the
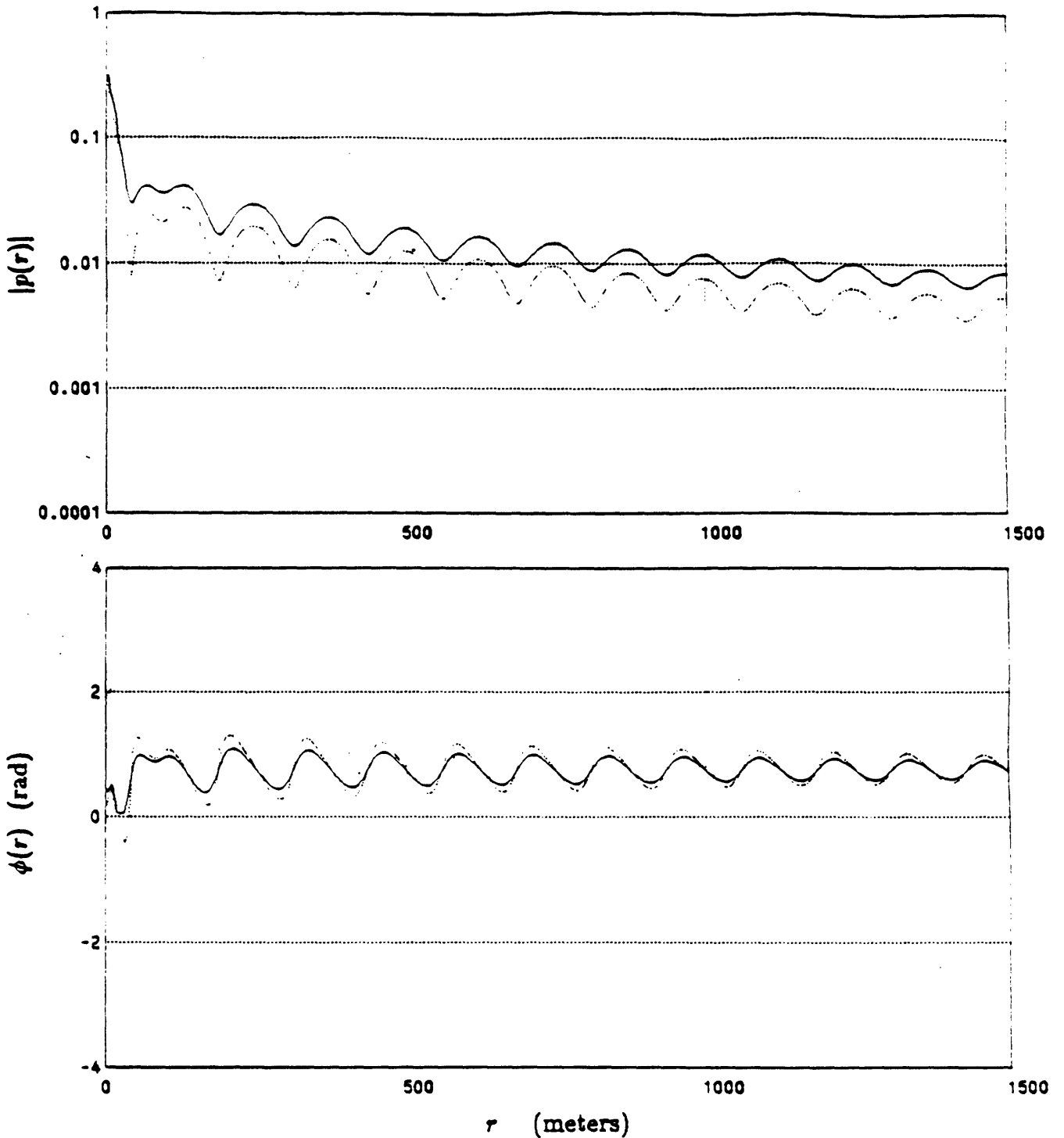
Figure 6.48: Magnitude and residual phase of the realistic shallow water field. The solid curves represent the field which was computed directly without removal of the poles. The dashed curves represent the field computed using the hybrid method. The maximum wavenumber in the integration was changed by ϵ compared with the results in the preceding figure.
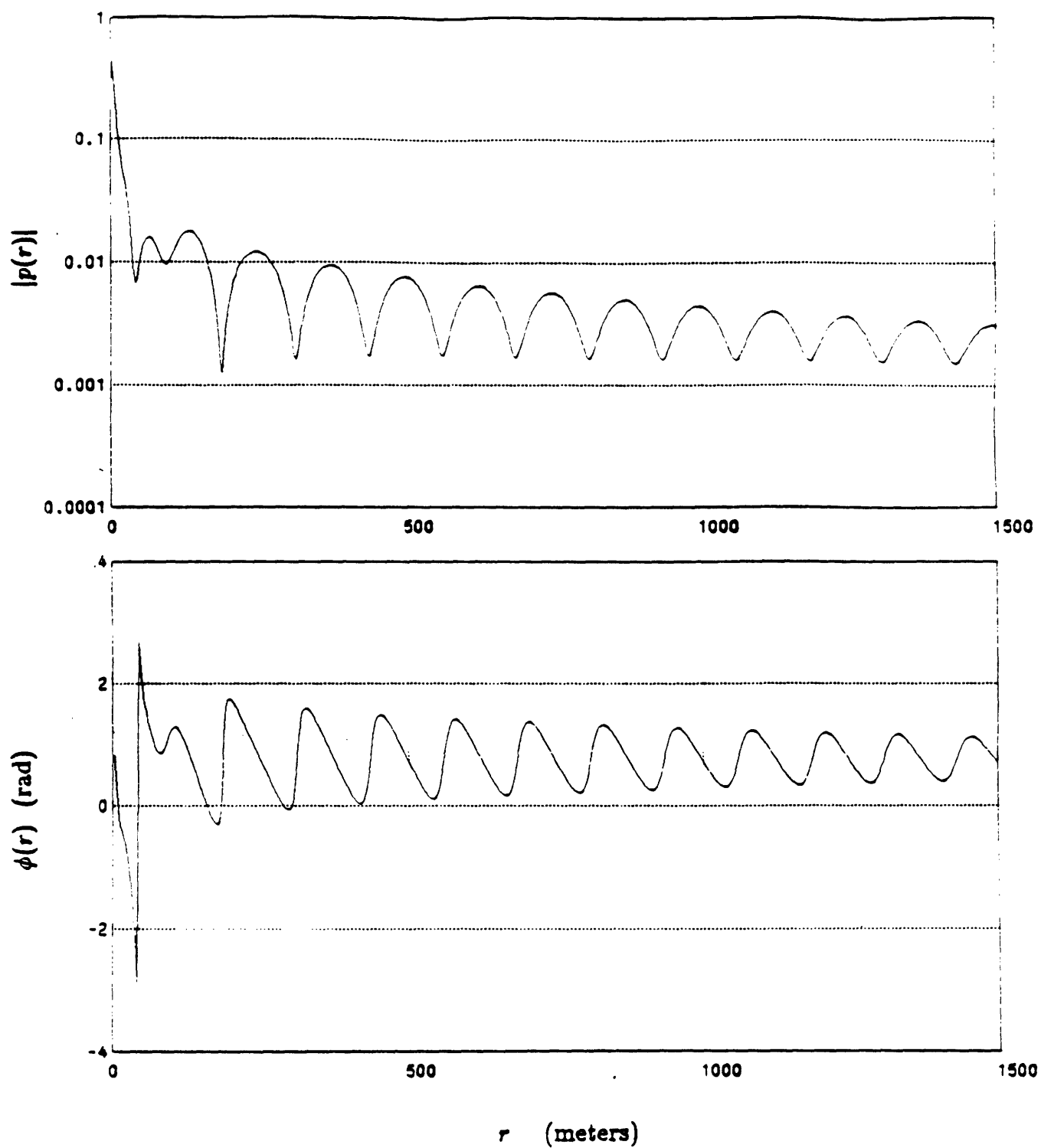
Figure 6.49: Magnitude and residual phase of the realistic shallow water field with raised receiver.

geoacoustic model in Table 6.1 except that the receiver was raised from its position described in this table to a depth of 3.174 m. To derive the synthetic field, 1024 samples of $g_C(k_r)$ over a wavenumber interval of $k_r = 0.0$ to 1.0 were used and the Hankel transform was computed using the Abel/Fourier method. We note that the residual phase wraps at a range of approximately 40 m while no such behavior was observed in the residual phase of the field for the receiver at the lower depth, as can be concluded by examining the dashed residual phase curve in Figure 6.47. We will return to the significance of this shortly. The real part of the synthetic field displayed in Figure 6.49 was set to zero and 1024 samples of the imaginary part, sampled at a rate of 3.14 m, were used as the input to the reconstruction algorithm. The magnitude and residual phase of the reconstructed field are displayed in Figure 6.50 and by comparing these quantities with those in the preceding figure, it is apparent that the reconstruction is quite good. As further evidence of this, the error signal for the reconstruction is displayed in Figure 6.51 along with the magnitude of the true field. This example indicates that reasonable reconstructions of synthetic fields within a realistic waveguide can be obtained from a single channel only.

As a more graphic example of the reconstruction method, we have generated the acoustic field as a function of range *and* depth for the geoacoustic model in Table 6.1. To do this, the source position was fixed and the receiver depth was varied incrementally from just below the surface to just above the bottom. The hybrid method was used to generate a separate field for each receiver depth, and 128 such fields were produced. The locations and residues of the two poles present were estimated and removed in order to generate $g_C(k_r)$ for each receiver depth. The field previously shown in Figure 6.49 comprises one of these fields, and the field previously shown in dashed in Figure 6.47 comprises another. The magnitude and residual phase for the two-dimensional field are shown in Figure 6.52 to a range of 400 m as intensity modulated functions of position - white corresponds to the maximum intensity in the magnitude display. The black vertical line in the residual phase at a range of approximately 40 m can be seen. This line corresponds to the wrap in the residual phase
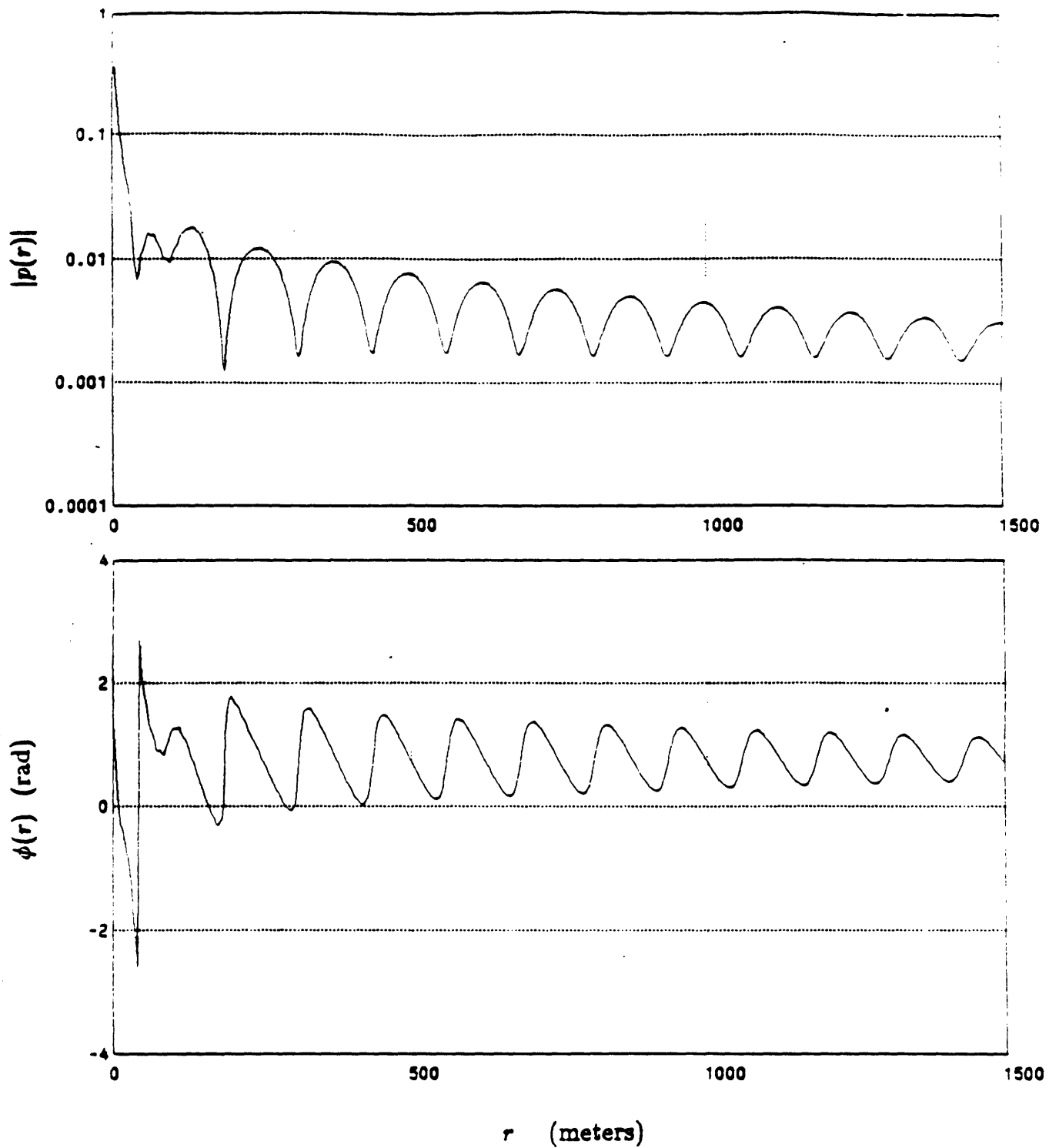
Figure 6.50: Magnitude and residual phase of the reconstructed realistic shallow water field with raised receiver.
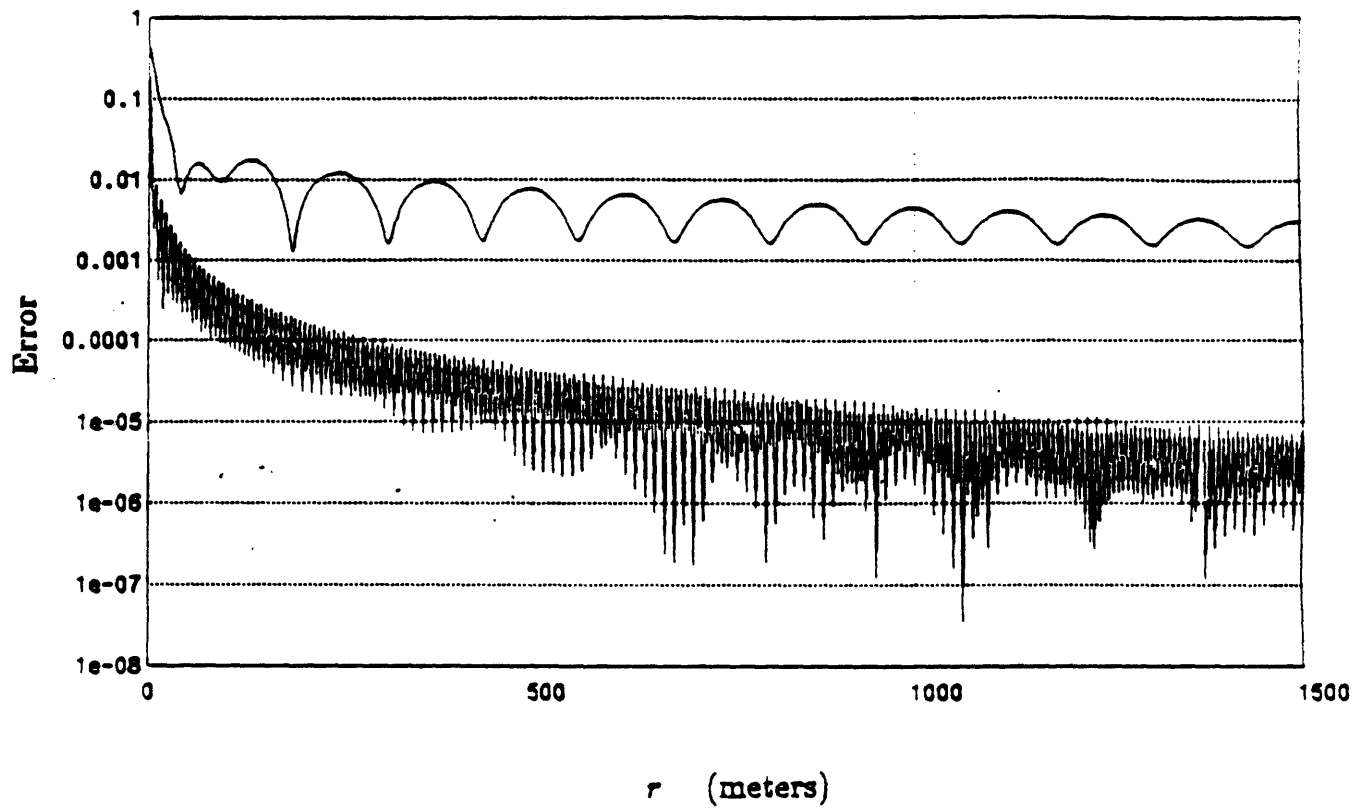
Figure 6.51: Error in the reconstruction of the real component (bottom curve) and true magnitude (top curve) for the realistic shallow water field with raised receiver
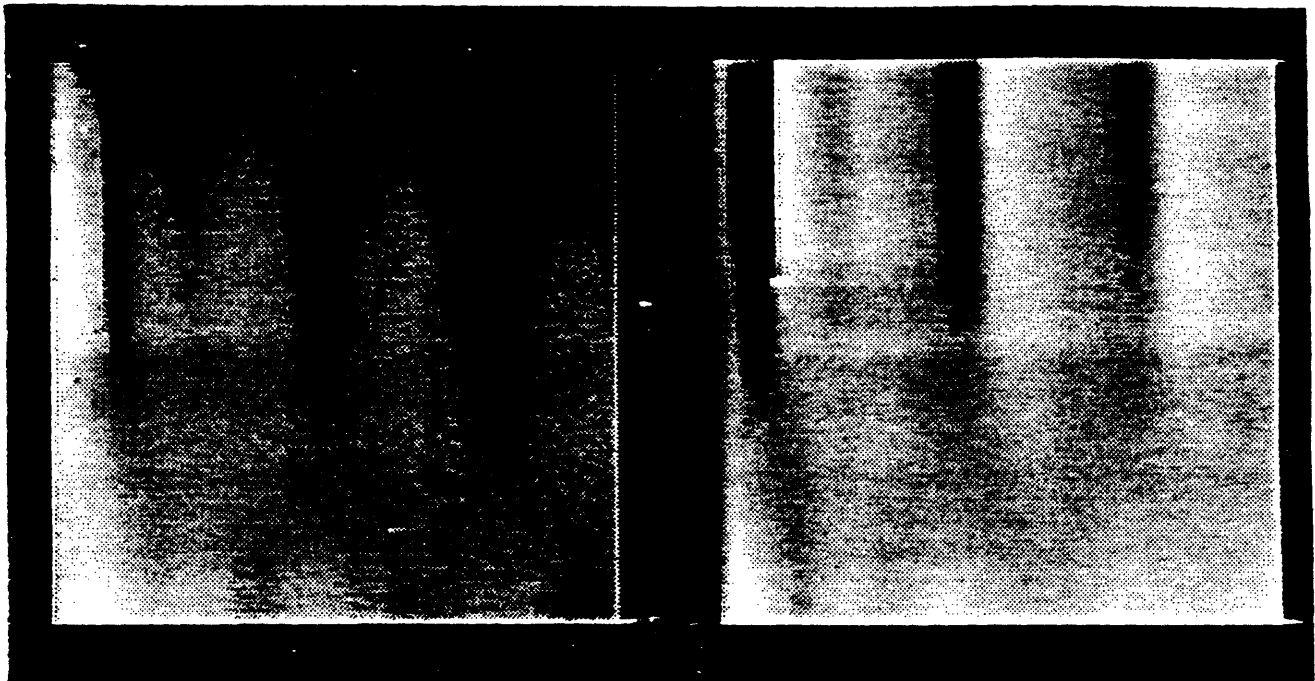
Figure 6.52: Magnitude (left) and residual phase (right) of the realistic field as a function of both range and depth. The waveguide thickness is 13.9 m and the first 400 m of range data are displayed.

which we have previously pointed out in Figure 6.49. Note that no wrap occurs for the deeper positions of the receiver within the waveguide and this is also confirmed by examining the residual phase in Figure 6.47. To demonstrate the reconstruction, the real part of the entire field was set to zero and then reconstructed using the imaginary part as a function of range for each particular receiver depth. No attempt to exploit the similarity of fields in depth was made in the reconstruction process, i.e. the field was reconstructed on a row-by-row basis. In comparing the true two-dimensional field with the reconstructed field, shown in Figure 6.53, their similarity is evident. In particular, the vertical line corresponding to the wrap in the residual phase is preserved as are many other features in both the residual phase and magnitude. The differences between the true and reconstructed fields occur primarily in the very-near field, a fact which we have consistently observed before.
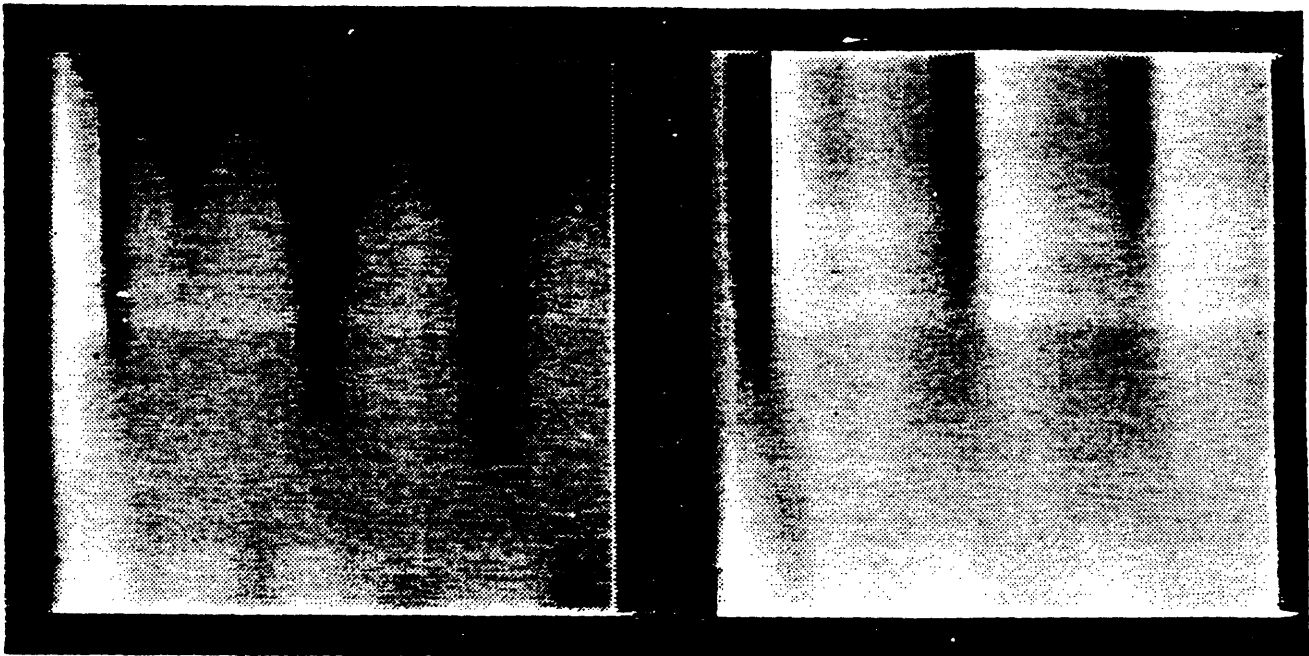
Figure 6.53: Magnitude (left) and residual phase (right) for the reconstructed realistic field as a function of both range and depth. The waveguide thickness is 13.9 m and the first 400 m of range data are displayed.

6.5 Reconstruction of Experimental Acoustic Fields

In previous sections, we have examined the reconstruction of synthetically generated complex-valued fields from a single component. Of particular interest however, is the application of the reconstruction technique to acoustic fields which have been collected experimentally. In this section, we will consider several of the issues related to the reconstruction of these fields and examples of the reconstruction method applied to two shallow water experiments will be presented.

There are a number of factors which can cause experimentally collected fields to differ from the synthetic fields previously discussed. Theoretically, the reconstruction algorithm is based on the real-part/imaginary-part sufficiency condition which applies to outgoing fields. In an ocean environment, the effects of velocity changes within the water column, as well as violations of both the horizontal stratification and radial symmetry, may yield acoustic fields which are not completely outgoing. Additionally, in shallow water, the effects of a non-perfect surface may yield scattered acoustic components which are not outgoing. It is to be expected therefore, that there are theoretical reasons which can account for errors in the reconstruction of experimentally collected fields.

In addition, there are several practical aspects related to the collection and range registration of experimental fields which can also affect the quality of the reconstruction. In particular, experimental acoustic fields are typically not acquired on the uniform range grid which we have assumed for the synthetic cases previously discussed. The exact spacing in range is dependent on a number of factors including the drift rate. As an example of the non-uniformity of a typical sampling grid, a plot of the range versus the sample number is shown in Figure 6.54 for a shallow water acoustic experiment conducted in Nantucket Sound in May 1984[11]. The curve indicates a global change in the sampling rate which occurred at a range of approximately 600 m due to a change in the drift rate during the experiment. The corresponding field for
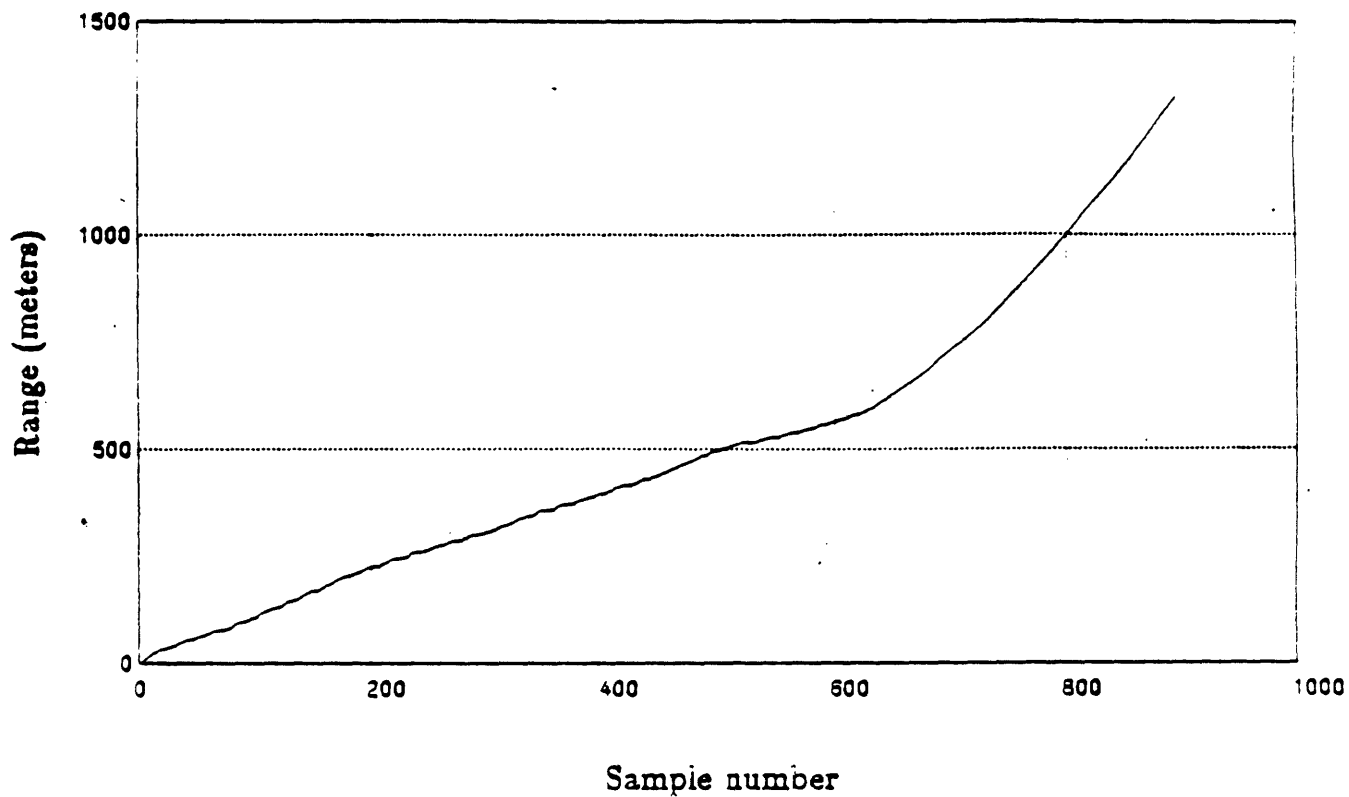
Figure 6.54: Range registration versus sample number for a shallow water 140 Hz acoustic experiment conducted in Nantucket sound.

this 140 Hz acoustic experiment has been previously presented in Chapter 5, Figure 5.11, and will also form the basis for the first reconstruction example here. On a local level, the sampling rate in range may be non-uniform due to variations in source height and offset due to ocean surface effects. For example, an expanded version of the preceding registration function within the first 100 m, is shown in Figure 6.55. The deviation of the curve from linear is indicative of the variation in the sampling rate on a wavelength scale - the acoustic wavelength in the water for this 140 Hz example is 10.71 m. Additionally, the problem of establishing the exact range which corresponds to a particular sample is difficult in an experiment of this sort. Typically, several ranging methods are simultaneously employed and the results are combined to yield an estimate of the range. Errors in this estimate may also impact the quality of a field which is reconstructed from only a single component. Thus, it is apparent that for both theoretical and practical reasons related to the acquisition of experimental fields, there may be degradation in the quality of the reconstruction of experimental fields as compared with the quality previously demonstrated on synthetic fields.

To reduce the effects caused by non-uniform sampling, we will first re-sample the complex-valued field to a uniform grid. The re-sampling algorithm is based on the interpolation technique discussed in Chapter 5. This technique is based on the use of the residual phase and thus requires both the real and imaginary parts of the non-uniformly sampled field. After re-sampling to a uniform grid, one component of the complex-valued field is set to zero and then reconstructed from the alternate component. Because of the fact that both components of the experimental data were originally recorded, it is also possible to compare the reconstructed component with the re-sampled original, and thereby obtain an error signal. This method however is not a true test of the reconstruction of the original experimental field from a single component – both components are used in the interpolation scheme to obtain uniformly spaced samples prior to the elimination and reconstruction of one component.

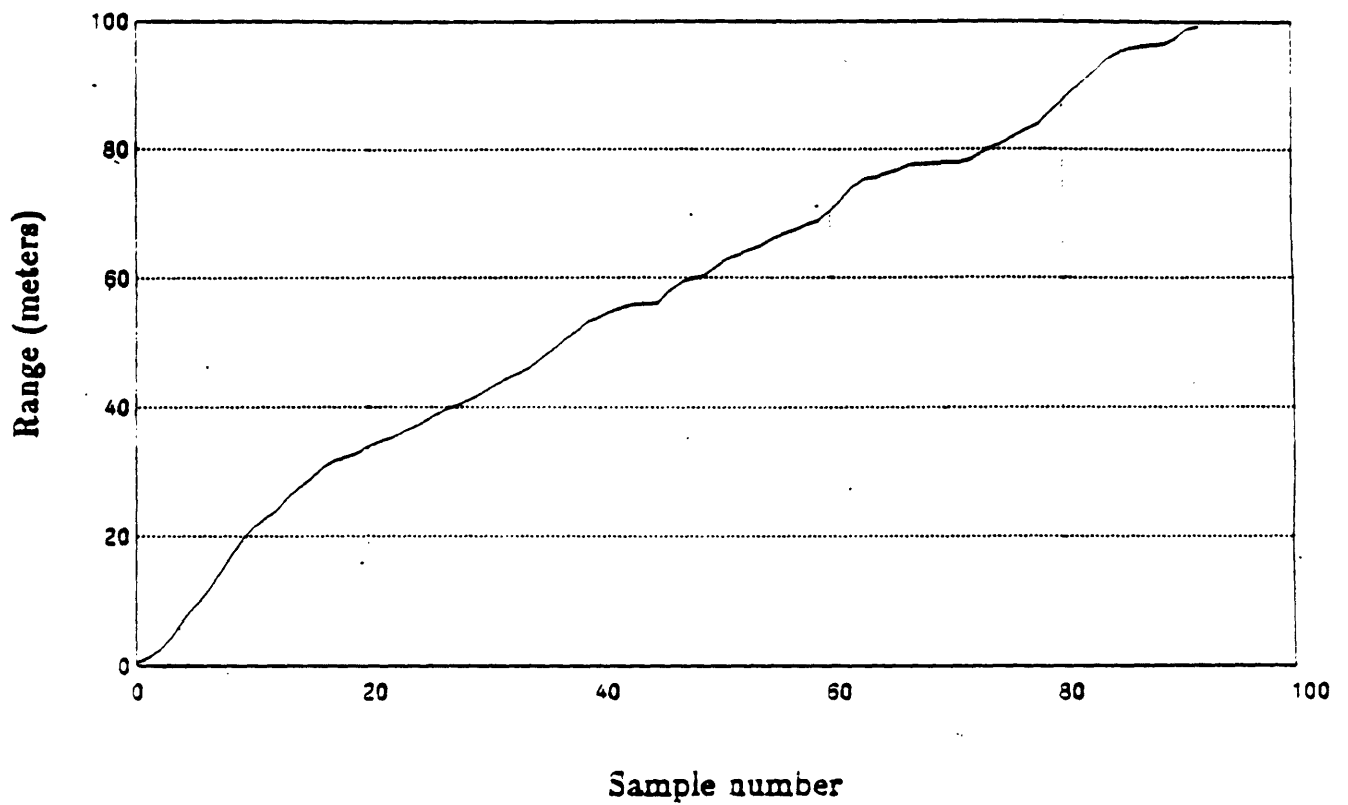As an example of this procedure, consider the magnitude and unwrapped residual

Figure 6.55: Expanded range registration versus sample number for a shallow water acoustic experiment conducted in Nantucket sound.

phase for the May 1984 experimental field, shown in Figure 6.56. The value of k, chosen to determine the residual phase was 0.575. For reference, the real and imaginary components of the original experimental field are displayed in Figure 6.57 and their rapidly varying nature is evident. The real and imaginary parts of the field with residual phase only, i.e. the quadrature components of the demodulated field, are displayed in Figure 6.58. The quadrature components in this figure were linearly interpolated to a uniform grid and the field was then re-modulated using $k_\phi = 0.575$. The process, discussed previously in Chapter 5, can be thought of as bandlimited interpolation for a non-uniformly sampled complex signal. It is stressed that both the real and imaginary parts of the original, non-uniformly sampled field are required in this procedure.

The magnitude and unwrapped residual phase of the re-sampled signal are displayed in Figure 6.59. There are only very slight differences between the re-sampled field and the original field as can be concluded by examination of Figures 6.59 and 6.56. In the original field, there were 896 samples collected over an aperture of 1320 m corresponding to an average rate of 7.3 samples per water wavelength. The interpolated field consists of 1024 uniformly spaced samples over the 1320 m aperture. To demonstrate the reconstruction, the real part of this signal was set to zero and then reconstructed from the imaginary part. The magnitude and unwrapped residual phase of the reconstructed field are shown in Figure 6.60. The similarity of the reconstructed field with the original and re-sampled fields is evident. In particular, the behavior of the unwrapped residual phase is preserved, as are the peaks and nulls in the magnitude of the field. If the curves are examined in further detail, it can be seen that the some of the finer details differ. These slight differences occur not only at near ranges, as was the case for reconstructed synthetic fields, but at far ranges as well. These differences are also evident from examination of the error signal for this example, shown in Figure 6.61, along with the magnitude of the experimental field. We attribute these differences to aspects mentioned previously which may cause experimental fields to depart from synthetic fields with regard to the real-part/imaginary-part sufficiency
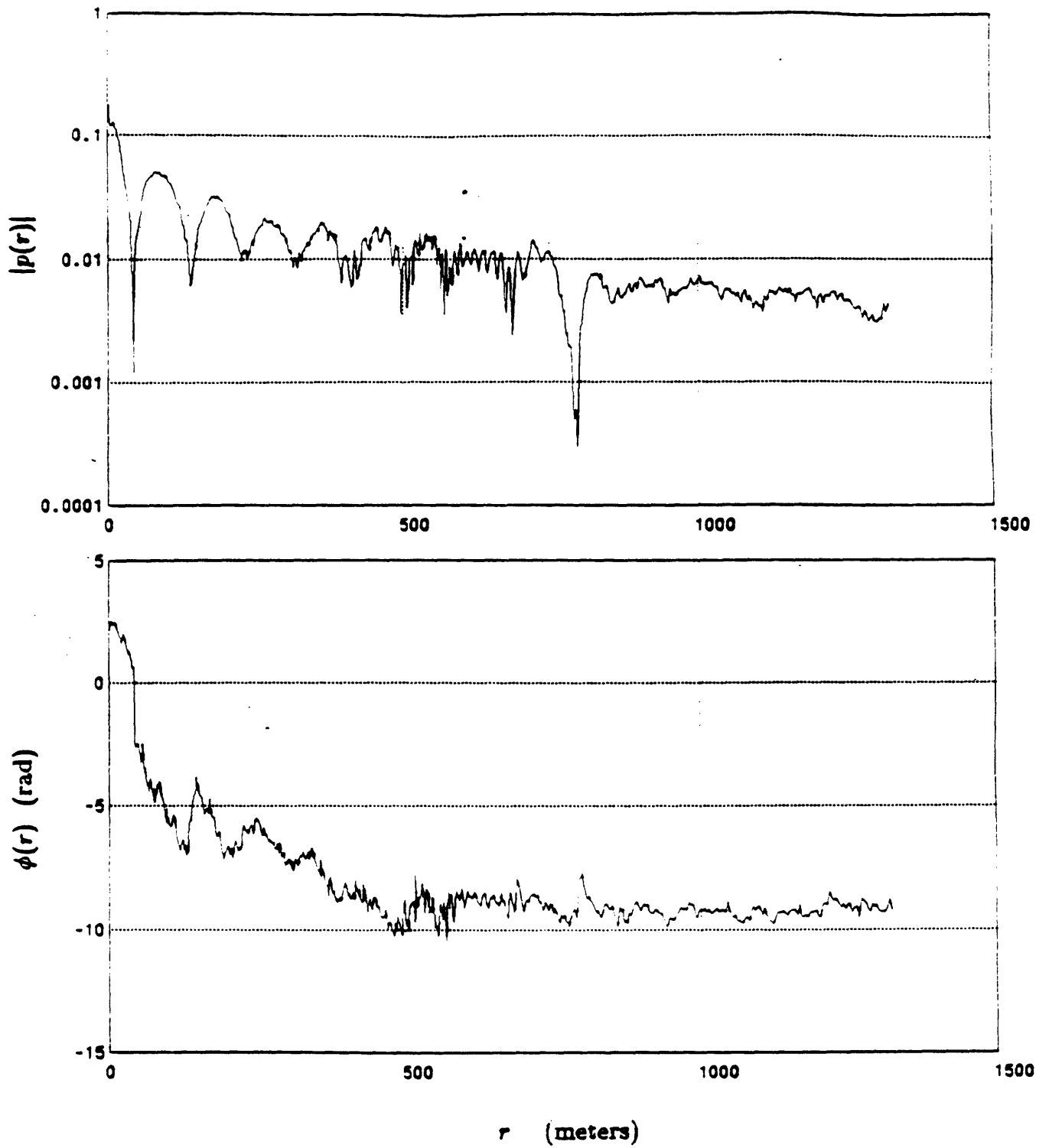
Figure 6.56: Magnitude and unwrapped residual phase of the 140 Hz experimental shallow water field.
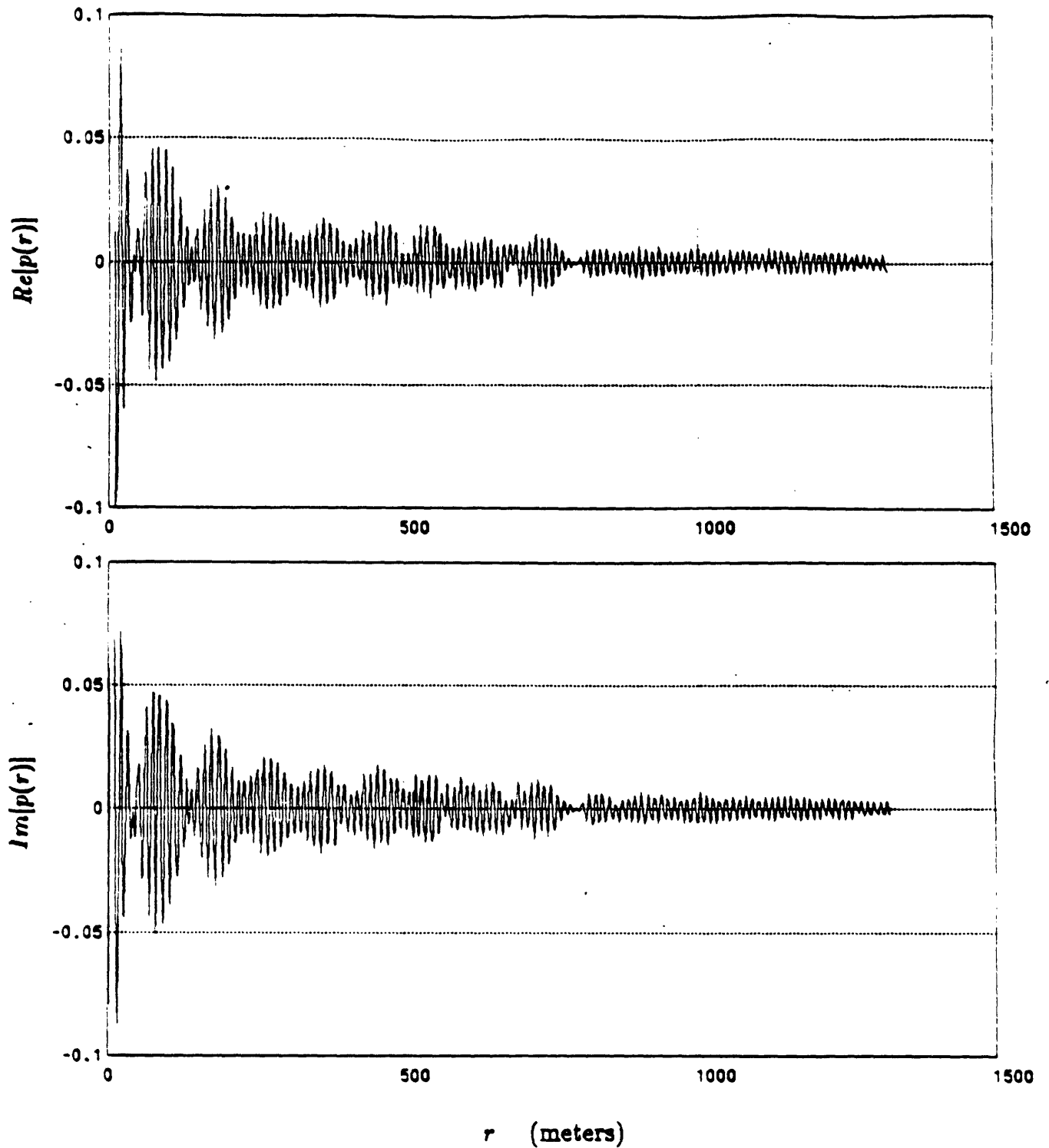
455

Figure 6.57: Real and imaginary components of the 140 Hz experimental shallow water field.
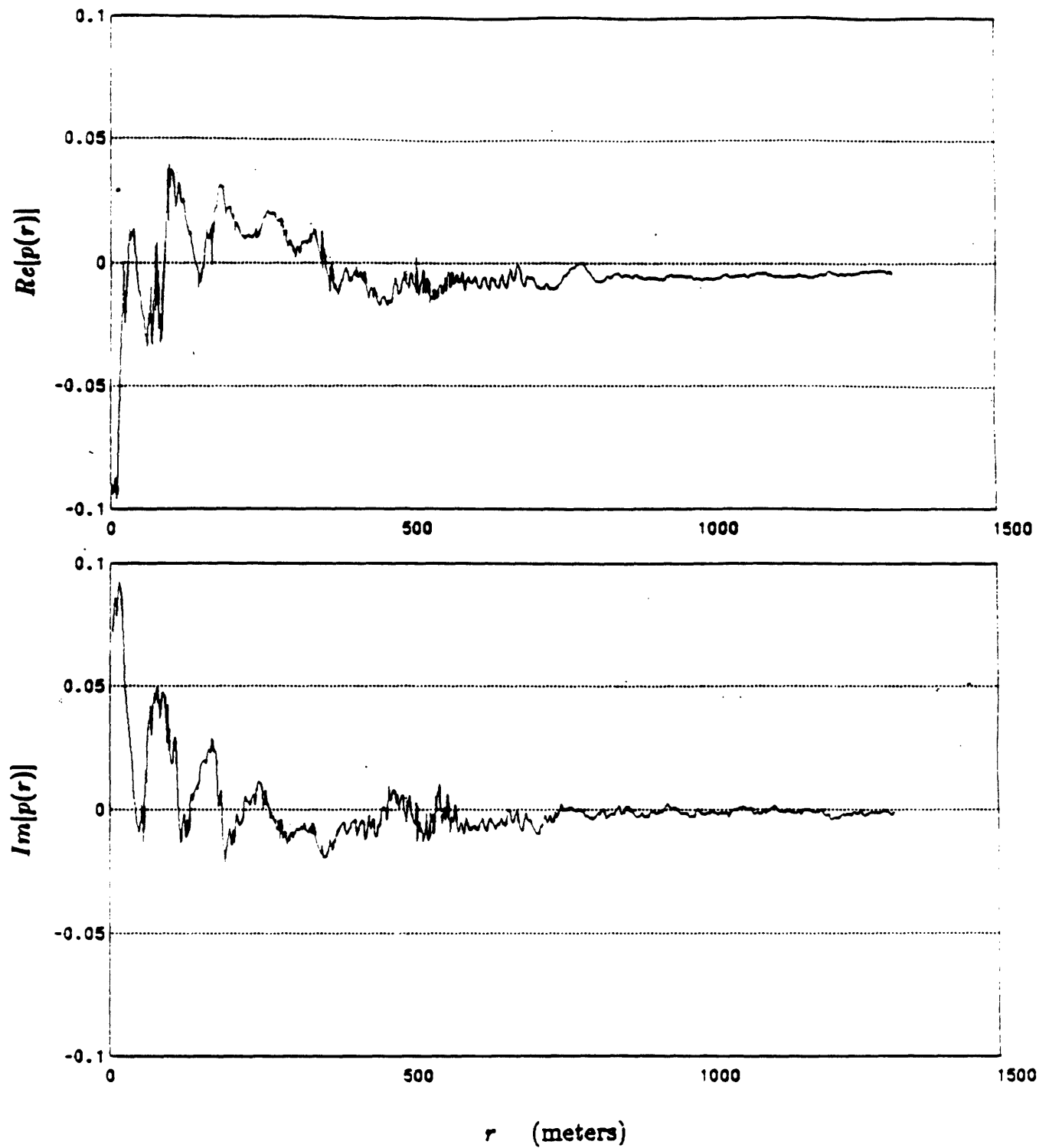
Figure 6.58: Real and imaginary components of the 140 Hz experimental shallow water field which has been processed to retain the residual phase only.
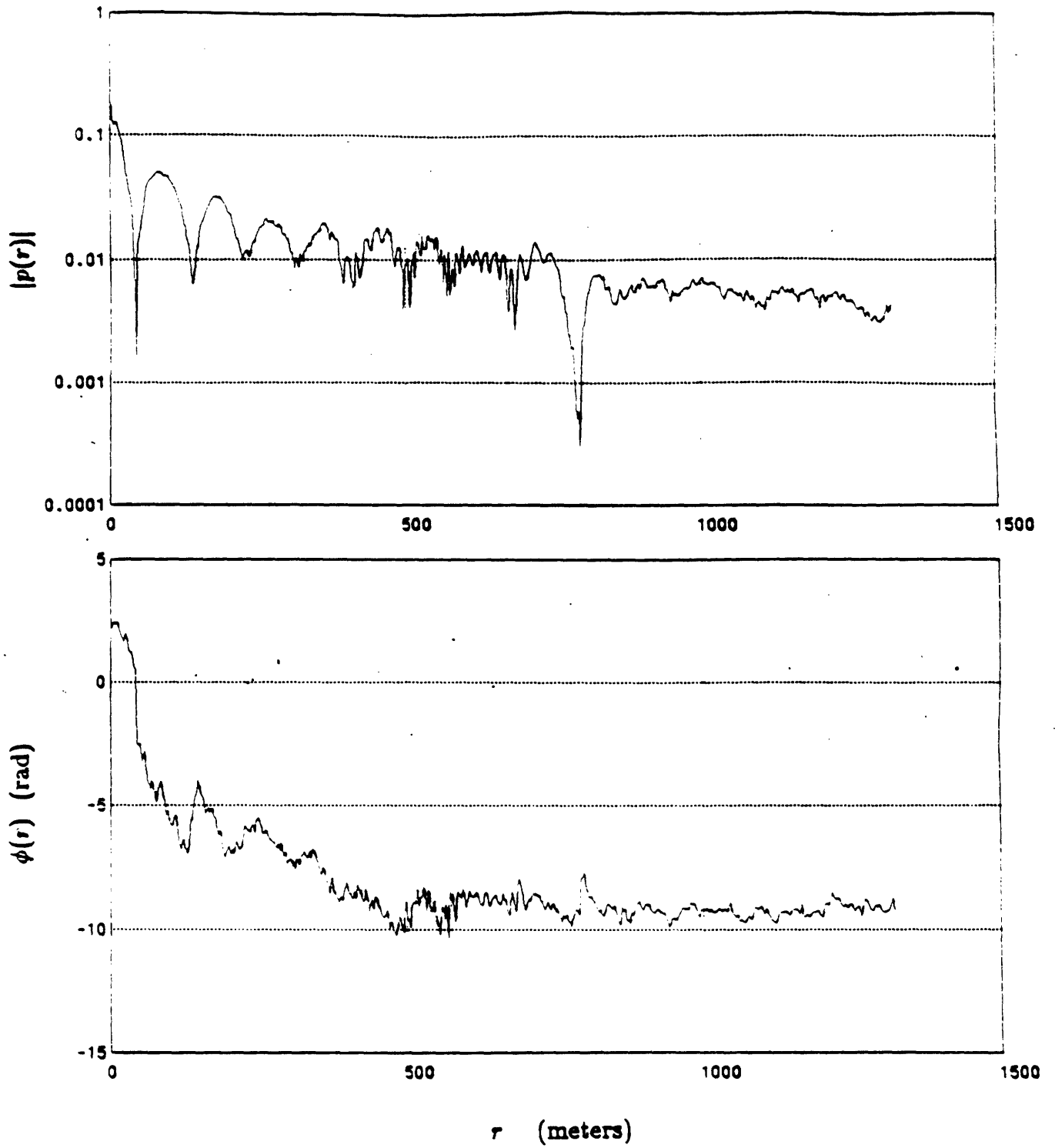
Figure 6.59: Magnitude and unwrapped residual phase of the interpolated 140 Hz experimental shallow water field.
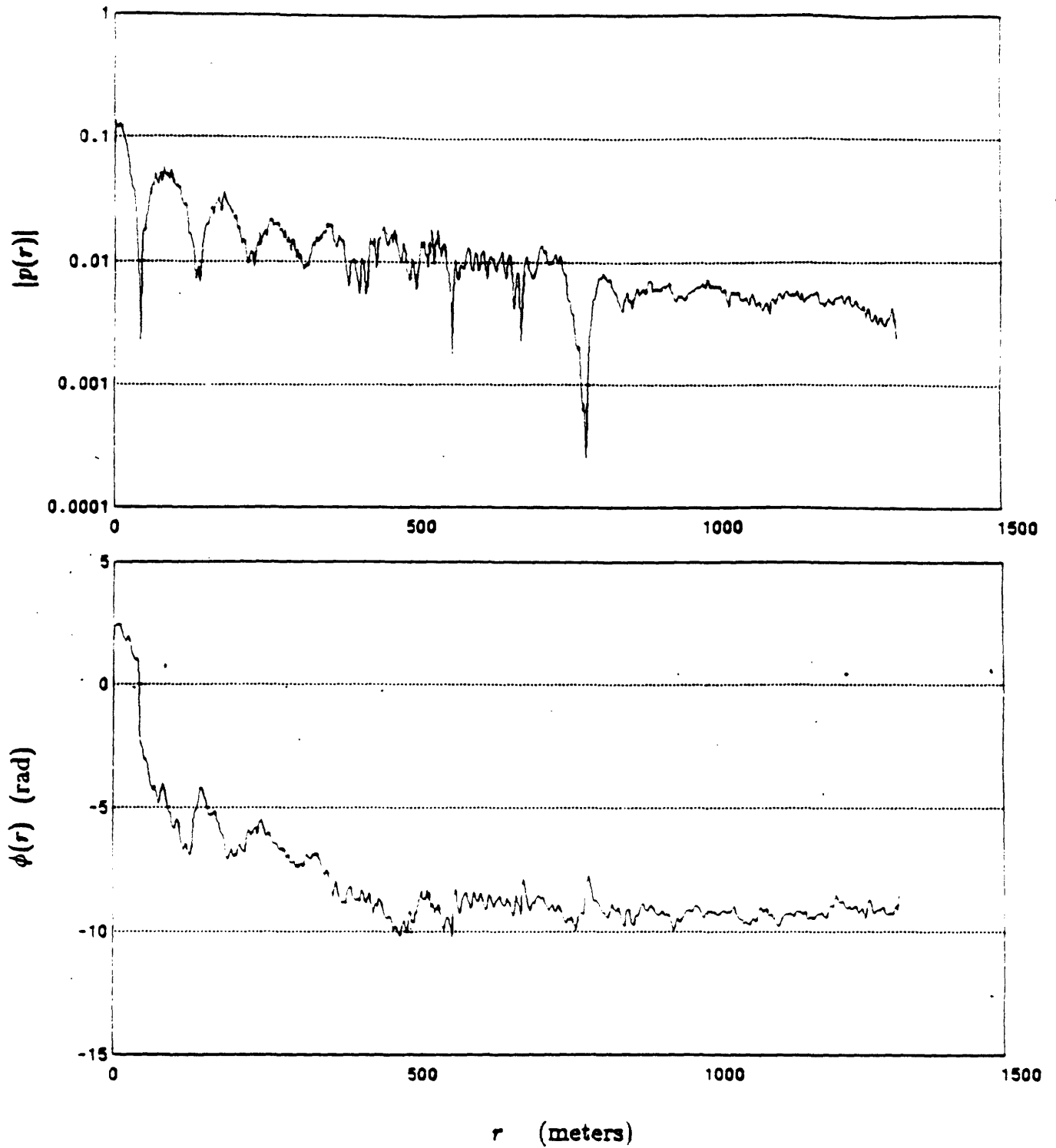
Figure 6.60: Magnitude and unwrapped residual phase of the reconstructed 140 Hz experimental shallow water field. Both components were required in the initial interpolation scheme.

property.

Nevertheless, the reconstructed field is quite similar to the original field. In fact, the agreement between the curves suggests that this method might also be used as a measure of the quality of the experimental data collected. In this approach, both components are recorded and re-sampled to a uniform grid. One component is then set to zero and reconstructed from the alternate component. A similar procedure can also be performed using the alternate component. Presumably, if the reconstructed and original fields differ substantially, there is an implication that effects such as errors in range registration, surface scattering and media inhomogeneity cannot be treated as negligible. Such a procedure may also provide important information about the scattering properties of the media as a function of position. In numerical experiments, we have seen a correlation in the quality of the reconstruction with the accuracy of the ranging method established independently. Thus, in this context, the reconstruction method is used not as a means for eliminating hardware in the data acquisition system, but rather as an important consistency check on the quality of the sampled complex-valued acoustic field.

In the preceding reconstruction, we have *not* demonstrated that the experimental field can be reconstructed from a single component since both components were required in the interpolation method for obtaining uniformly-spaced samples. In the case that only a single component is collected, it is not possible to use an interpolation method which is based on the use of the residual phase. The field must now be reconstructed from a single component which has been sampled on a non-uniform grid. There are two classes of methods for the reconstruction of a field given these constraints. In the first class, the single component is interpolated to a uniform grid using some scheme, and the imaginary part is then reconstructed. Iterative methods in which the results of the previous reconstruction are used to re-interpolate the field also fall within this class. In the second class, the imaginary part is directly reconstructed from the non-uniformly sampled real part. In our work, we have explored
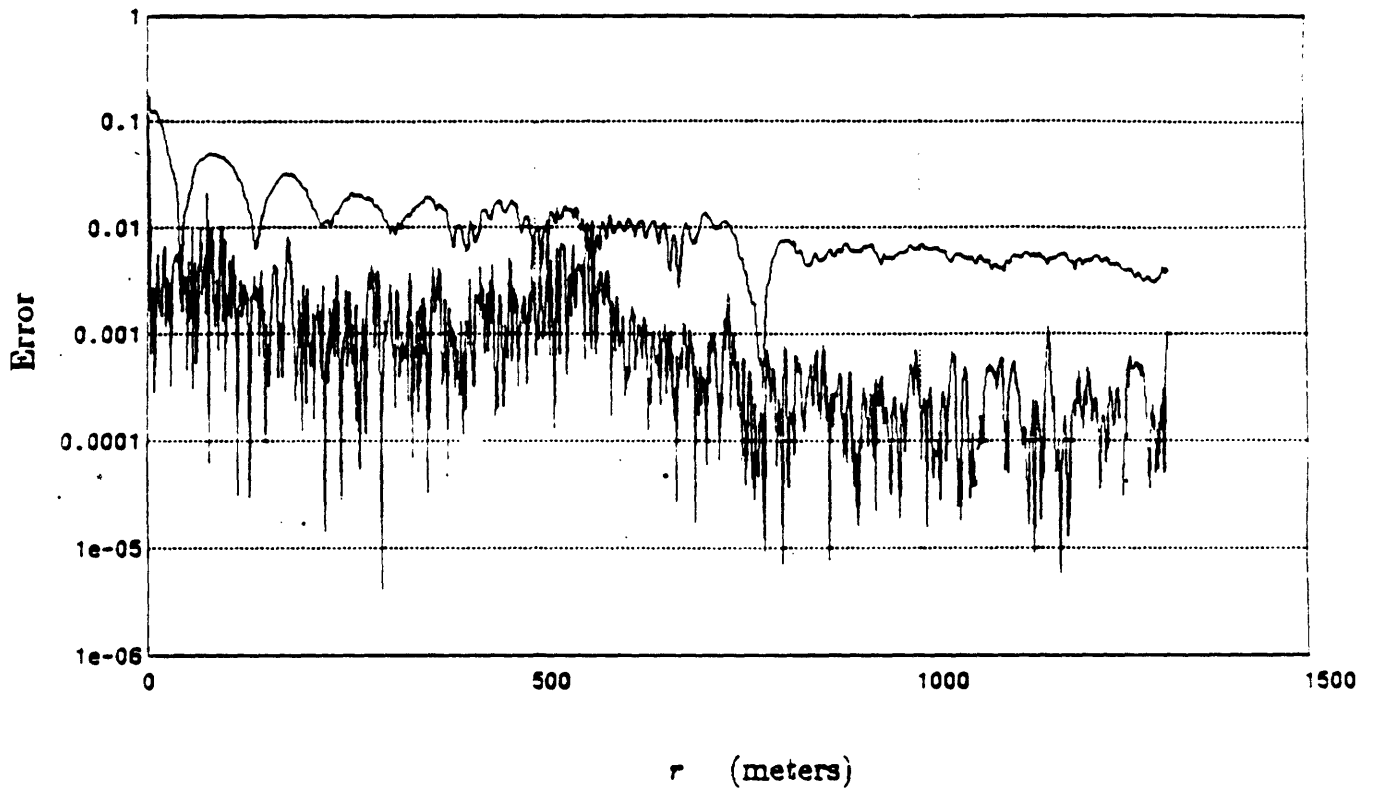
Figure 6.61: Error in the reconstruction of the real component (bottom curve) and true field magnitude (top curve) for the experimental 140 Hz shallow water field.

only the simplest method in the first class. In this method, the single non-uniformly sampled channel is linearly interpolated to a uniform grid and the reconstruction is then performed. More sophisticated interpolation methods are also applicable but have not been explored in this context. It is apparent that the linear interpolation is adequate only in the case that the field is oversampled, and this method is not expected to work well in cases in which the average sampling rate approaches the minimum rate of two real samples per wavelength. In situations when the experimental average sampling rate exceeds the theoretical minimum rate by a factor of four or more, we have found that the method based on linear interpolation yields reconstruction results which are quite good.

To demonstrate this, the real part of the experimental field displayed in Figure 6.57 was zeroed and the imaginary part was linearly interpolated to a uniform grid. The magnitude and unwrapped residual phase of the field which was reconstructed from the linearly interpolated single channel are displayed in Figure 6.62. In comparing these quantities with the original field in Figure 6.59, we see that the reconstruction is quite good. Additionally, the degradation which was introduced in the reconstruction by performing the linear interpolation can be seen in comparing this figure with Figure 6.60. In particular, we see that the reconstruction appears most degraded at large ranges. Here, the error in the linear interpolation is most severe due to the reduced sampling rate caused by the increase in drift rate as depicted in Figure 6.54. The local sampling rate at these ranges is approximately 3.6 samples per water wavelength and the corresponding increase in the degradation of the reconstructed field is noted.

As the final example, we will demonstrate the reconstruction using a single channel of a 50 Hz shallow water experimental acoustic field collected in the Gulf of Mexico in September, 1985. The magnitude and unwrapped residual phase, using $k_\phi = 0.1974$ for this example are displayed in Figure 6.63. The real part of the field was set to zero and the imaginary part was linearly interpolated to a uniform grid. This particular field was highly oversampled due to the slow drift rate of the experiment – approx-
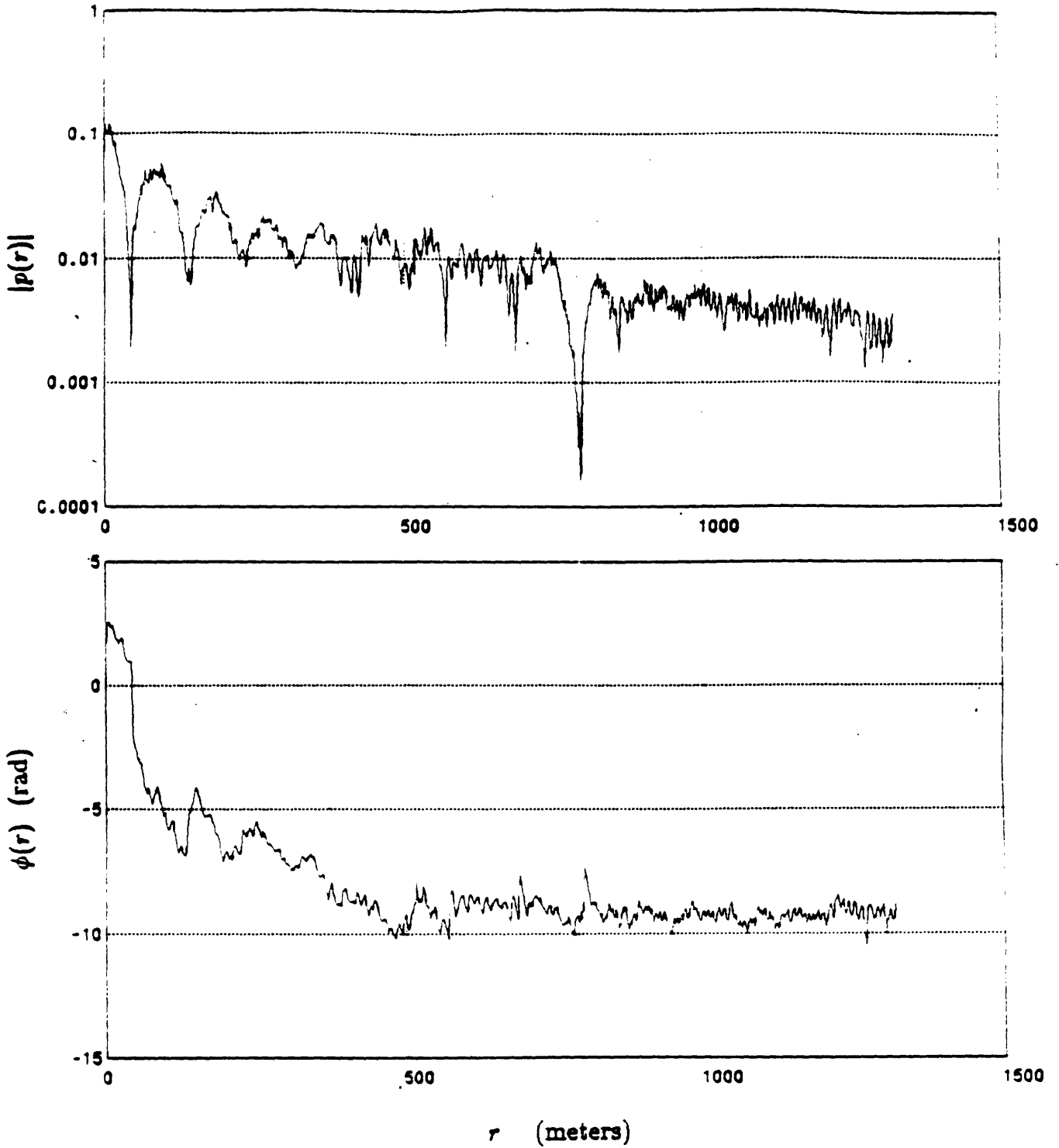
Figure 6.62: Magnitude and unwrapped residual phase of the reconstructed 140 Hz experimental shallow water field. The real channel was discarded as the first step in the processing and then reconstructed from the linearly interpolated imaginary channel.
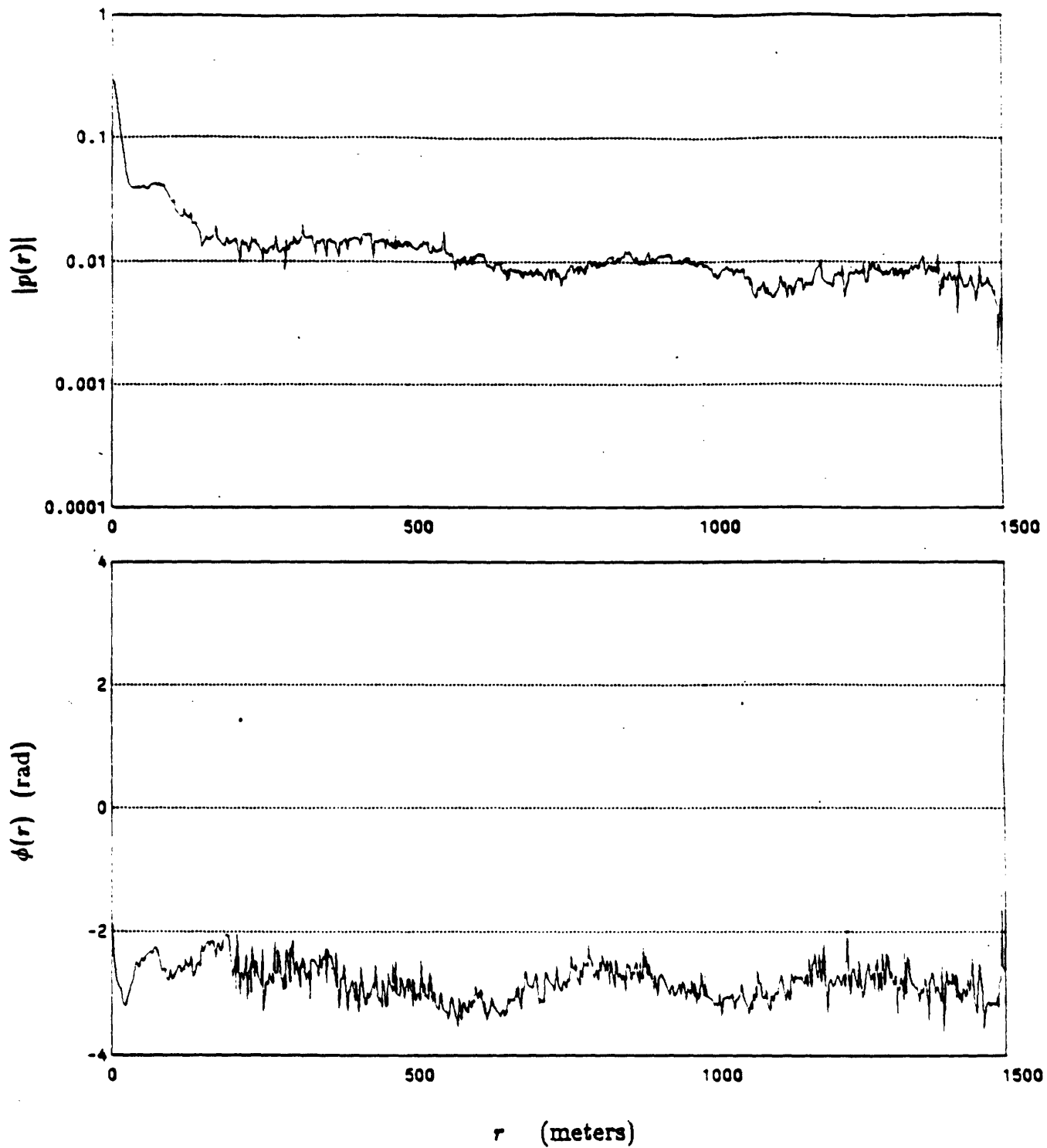
Figure 6.63: Magnitude and unwrapped residual phase of the $50Hz$ field from a shallow water acoustic experiment conducted in the Gulf of Mexico in September 1985.

imately 11 samples per water wavelength were recorded. The real part of the field was reconstructed and the corresponding magnitude and unwrapped residual phase are shown in Figure 6.64. The similarity of the reconstructed field and original field, shown in Figure 6.63 is apparent, again confirming the validity of the reconstruction method applied to experimental shallow water acoustic fields.
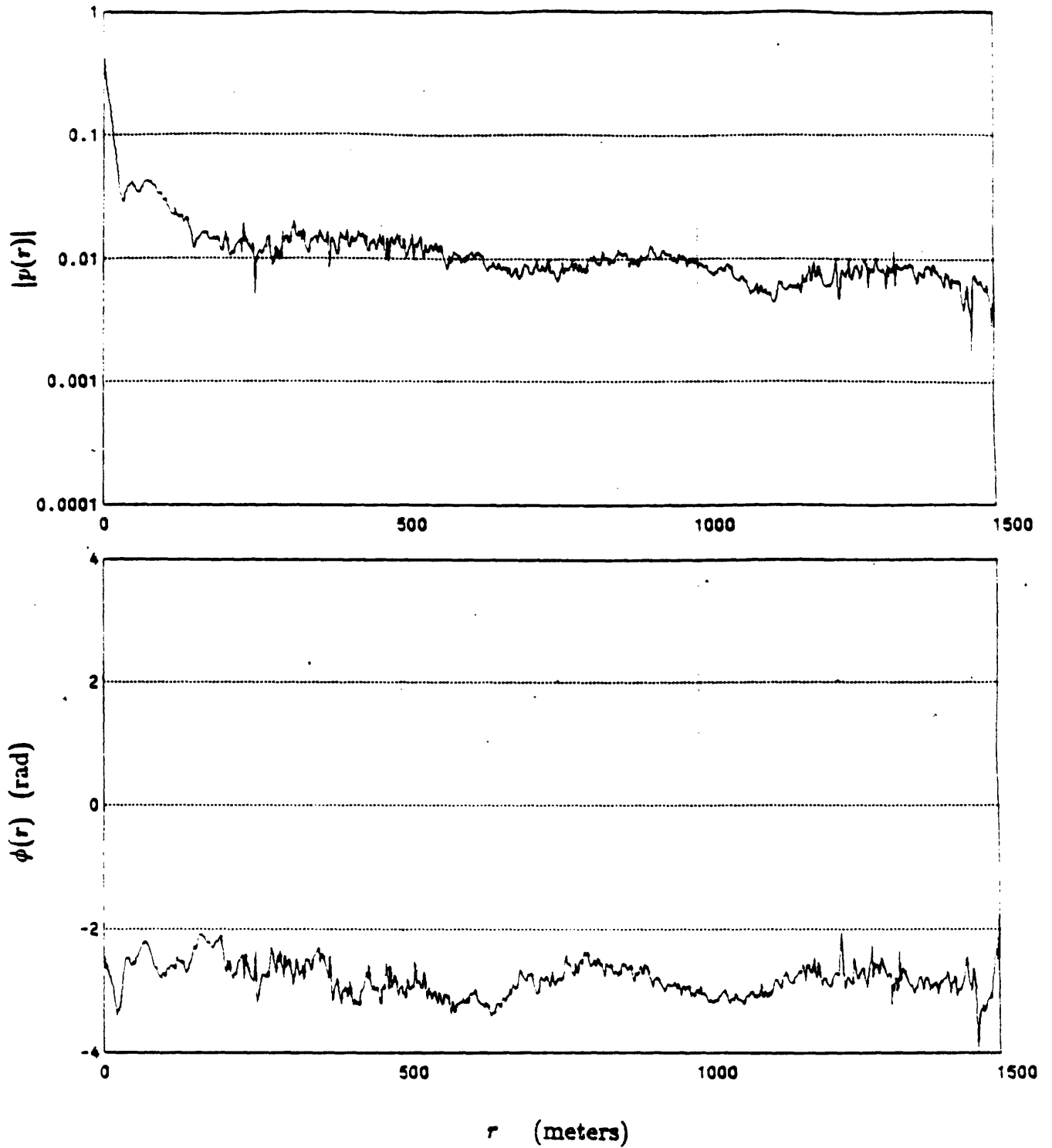
Figure 6.64: Magnitude and unwrapped residual phase of the reconstructed $50Hz$ field from a shallow water acoustic experiment conducted in the Gulf of Mexico in September 1985.

6.6 Summary

In this chapter, we have discussed the application of a reconstruction method which is based on the real-part/imaginary-part sufficiency condition for acoustic fields. In the reconstruction method a single sampled channel is retained and samples of the alternate channel are reconstructed. In order to separate the effects of synthetic data generation from the reconstruction procedure, we first considered several examples of acoustic fields which have closed-form expressions. Next, an example of a realistic deep water field was considered. This field, obtained from forward modelling an experimentally collected deep water field, was reconstructed and examined. Additionally, it was shown that it is possible to obtain reasonable estimates of the Green's function and reflection coefficient by processing only a single channel of this realistic field. Other related applications of the unilateral Fourier transform were suggested, including processing a field which has been sampled at a rate approaching one complex sample per wavelength, and compensating for incorrectly range-registered fields. Next, we considered two examples of the reconstruction applied to shallow water acoustic fields. The first example consisted of a Pekeris model and the second example consisted of a realistic shallow water model obtained by forward modelling an experimentally collected field. It was pointed out that it is important to consider the effects of aliasing when a direct method for synthetic shallow water data generation is applied, even for the case of a layered model with realistic attenuation. Finally, the reconstruction of two experimentally collected shallow water fields was discussed. A distinction was made between the algorithm for obtaining this field on a uniformly-sampled grid and the algorithm for reconstruction. A simple method for reconstructing an experimental acoustic field from a non-uniformly sampled single channel was demonstrated.

Bibliography

[1] John M. Wozencraft and Irwin M. Jacobs. *Principles of Communication Engineering*. John Wiley and Sons, New York, 1965.

[2] D.R. Mook. *The Numerical Synthesis and Inversion of Acoustic Fields Using the Hankel Transform with Application to the Estimation of the Plane Wave Reflection Coefficient of the Ocean Bottom*. Technical Report, Sc.D. Thesis, MIT/WHOI Joint Program, Cambridge Ma., Jan. 1983.

[3] G.V. Frisk and J.F. Lynch. Shallow water waveguide characterization using the Hankel transform. *J. Acoust. Soc. Am.*, 76(1), July 1984.

[4] B. Gold, A.V. Oppenheim, and C.M. Rader. Theory and implementation of the discrete Hilbert transform. In *Proc. Symp. Computer Processing in Communications, Vol.19*, Polytechnic Press, New York, 1970.

[5] Alan V. Oppenheim and Ronald W. Schafer. *Digital Signal Processing*. Prentice-Hall, Englewood Cliffs, NJ, 1975.

[6] J. McClellan, T. Parks, and L. Rabiner. A computer program for designing optimum FIR linear phase digital filters. *IEEE Trans. on Audio and Electroacoustics*, AU-21(6):506–526, 1973.

[7] L.R. Rabiner and B. Gold. *Theory and Application of Digital Signal Processing*. Prentice-Hall Inc., Englewood Cliffs, N.J., 1975.

[8] Douglas R. Mook, George V. Frisk, and Alan V. Oppenheim. A hybrid numerical/analytic technique for the computation of wave fields in stratified media based on the Hankel transform. *J. Acoust. Soc. Am.*, 76(1):222–243, July 1984.

[9] C.B. Officer. *Introduction to the Theory of Sound Transmission with Application to the Ocean.* McGraw-Hill, New York, 1958.

[10] F.D. DiNapoli. *The Inverse Fast Field Program: An Application to the Determination of the Acoustic Properties of the Ocean Bottom.* Technical Report TM 771160, Naval Underwater Systems Center, New London, CT, Aug. 1977.

[11] George V. Frisk, James F. Lynch, and James A. Doutt. The determination of geoacoustic models in shallow water. Presented at Symposium on Ocean Seismo-Acoustics, La Spezia, Italy, June 10-14 1985.

Chapter 7

Summary

7.1   Contributions

In the first portion of Chapter 2, a unified treatment of poles, branch-cuts, and Riemann sheets associated with the Green's function for shallow water acoustic propagation was presented. For the Pekeris waveguide, this led to exact expressions for both trapped and virtual mode contributions. In considering the more general layered waveguide, the method of Green's function migration was developed which formed the basis for computational algorithms used throughout the thesis. This method also led to the development of several important properties including a finite-extent property for the imaginary part of the Green's function. This property can be exploited to determine the velocity in the underlying halfspace from knowledge of the Green's function.

In Chapter 3, we developed the theory for one and two-dimensional unilateral transforms. In one dimension, it was shown that if the causal portion of an even signal can be approximately synthesized by the unilateral inverse Fourier transform, there are important consequences. Specifically, such a signal possesses an approx-

imate real-part/imaginary-part sufficiency condition, as does its Fourier transform. Additionally, the approximation was shown to imply an inverse relationship between the unilateral inverse Fourier transform and the unilateral Fourier transform, as well as other relationships between the cosine and sine transforms of the real and imaginary components of the signal, and its Fourier transform. In extending the theory to two dimensions, we developed a bilateral version of the Hankel transform and a unilateral version referred to as the Hilbert-Hankel transform. It was shown that if the causal portion of a circularly symmetric signal can be approximately synthesized by the Hilbert-Hankel transform there are important consequences. Specifically, such a signal possesses an approximate real-part/imaginary-part sufficiency condition as does its Hankel transform. Additionally, the approximation implies an inverse relationship between the Hilbert-Hankel transform and the complex Hankel transform, as well as other relationships between the J_0, Y_0, and H_0 transforms of the real and imaginary components of the signal and its Hankel transform. As was pointed out, the unilateral synthesis in two dimensions is particularly applicable to harmonic acoustic fields which are outwardly propagating. An asymptotic version of the Hilbert-Hankel transform was discussed and related to the unilateral inverse Fourier transform, the Fast-Field-Program, and the Hartley transform. In addition, several properties of the asymptotic Hilbert-Hankel transform were exploited to show that an outgoing acoustic field can be approximately represented in terms of its samples spaced once per water wavelength. In the ocean acoustics context, this rate is a factor of two smaller than has been previously stated. If the field is sampled at the conventional rate of at least two complex samples per water wavelength, there is redundant information, and the asymptotic Hilbert-Hankel transform provides the basis for an efficient reconstruction algorithm for obtaining samples of one quadrature component from the alternate component.

In Chapter 4, we presented a new hybrid method for computing synthetic shallow water acoustic fields. The effects of aliasing due to the presence of poles in the Green's function are substantially reduced in the new method. The technique, which

471

computes the trapped and continuum portions of the acoustic field separately, has several advantages including accuracy and computational efficiency. Although the acoustic field is conventionally decomposed into a trapped and continuum portion, the method exploits the fact that the related Green's function can be decomposed in an analogous manner. In extending the hybrid method, we pointed out that existing normal mode codes, which compute only the trapped portion of the acoustic field, can be used to determine the trapped portion of the Green's function. It was shown that it is also possible to generate the continuum portion of the field without explicitly determining the poles and residues, by using the finite extent property of the imaginary part Green's function, developed in Chapter 2, and the real-part/imaginary-part sufficiency condition, developed in Chapter 3. In relating the new technique with an existing hybrid deep water technique, it was pointed out that the new method can be used for synthetic deep water field synthesis as well. In this application, the Hankel transform of the total deep water Green's function is determined, as opposed to the Hankel transform of only the reflected portion. Additionally, using a numerical example, we showed that the Hilbert-Hankel transform can also be applied to deep water acoustic fields.

In Chapter 5, we defined the residual phase function for a shallow water acoustic field and demonstrated its importance in several applications. In particular, it was shown that the residual phase is a complementary quantity to the shallow water acoustic field magnitude and that it is useful in forward modelling applications. The residual phase can also be used to determine the phase of the acoustic source, which is required in the extraction of the ocean bottom reflection coefficient. It was also pointed out that the residual phase is useful for determining range-dependent waveguide properties. In the second portion of the chapter, the sensitivity function for reflection coefficient determination from shallow water acoustic field measurements was defined. This function relates errors in the extracted reflection coefficient to errors in the Green's function estimate. We pointed out that under certain circumstances, the sensitivity function can become infinite at specific horizontal wavenumbers. The

472

result suggests that the reflection coefficient extracted from shallow water measurements cannot be accurately determined at these wavenumbers and in surrounding wavenumber regions. The points of infinite sensitivity were related to invariant zeros of the Green's function and its imaginary part. These points are invariant with respect to the geoacoustic properties of the media underlying the waveguide, and depend only on the depths of the acoustic source and receiver from the ocean surface, and on the water wavenumber. The theory led to the definition of the invariant critical depth. If either the source or receiver is positioned below the invariant critical depth, at least point of infinite sensitivity is guaranteed to occur for non-evanescent values of horizontal wavenumber. Conversely, if both instruments are shallower than the critical depth, there can be no points of infinite sensitivity. The sensitivity effect was related to two kinds of cancellation which can occur between the upgoing and downgoing plane wave components of the field within the waveguide. The invariant critical depth, points of infinite sensitivity, and invariant zeros of the Green's function were also discussed using a numerical example which involved the inversion of synthetically produced shallow water data.

In Chapter 6, a reconstruction algorithm for obtaining the real (or imaginary) component of an acoustic field from the imaginary (or real) component was applied to synthetic and experimental fields. Two means of assessing the quality of the reconstruction were discussed. High quality reconstruction results were obtained in all of the examples, including the two experimentally collected acoustic fields. It was shown that a reasonable approximation to the ocean bottom reflection coefficient can be obtained, using synthetic deep water data, from samples of the field collected at a rate of one sample per water wavelength.

7.2 Future Research

In this section, we suggest future work, directions and applications based on the results presented in this thesis.

In Chapter 2, the reflection coefficient migration technique and Green's function migration technique were used to develop various properties of the reflection coefficient and Green's function. The theory was developed for fluid layered media, however the idea can be extended to the more general elastic layered case as well. In the proposed reflection coefficient migration approach, four reflection coefficients are required at each layer interface in order to represent all of the possible conversions which can occur[1]. Thus, four reflection coefficient migration equations must be developed in order to migrate these reflection coefficients across a layer. The method could form the basis of a computational algorithm and in addition, could be used to develop properties of the reflection coefficient in an analogous manner as was done in Chapter 2. Similarly, the Green's function and the extended Green's function expressions could be developed for the elastic layered media case. These equations could be used to investigate properties of the Green's function including the finite extent property.

In Chapter 3, we developed the theory of one and two-dimensional unilateral transforms. Our interest was primarily in the application of the two-dimensional theory to wave propagation problems. However, the general nature of the theory suggests that it may be applicable to other problems as well. In particular, an investigation of one-dimensional applications is suggested. Also, the development of the general multi-dimensional theory incorporating different symmetry conditions is suggested. This includes, for example, two-dimensional even signals which can be approximated by the unilateral inverse two-dimensional Fourier transform. In addition, we developed the theory for an approximate real-part/imaginary-part sufficiency condition. It is also possible to develop the analogous theory for an approximate magnitude/phase sufficiency condition by applying the complex logarithm to the Fourier transform[2].

474

Essentially, in one dimension there exists a duality between the even signal and the even cepstrum, and between the approximate real-part/imaginary-part sufficiency condition and the approximate magnitude/phase sufficiency condition. The duality suggests that there exists an approximate Hilbert transform relationship between the magnitude and phase for a special class of mixed-phase signals. The relationship between the unilateral transform and cepstrum may have some important consequences in applications which include reconstruction of a signal from its magnitude only, phase unwrapping, and general homomorphic signal processing. An investigation of these applications is suggested as further work.

As an additional application, we suggest that the definition of the unilateral inverse transform be extended to include some portion of the negative frequencies, as well as all of the positive frequencies. The extended definition of the transform could be applied to signals which cannot be exactly synthesized in terms of positive frequencies only, but which can be approximated by including an additional small portion of the negative frequencies. The concept may be particularly applicable to CT and NMR tomography problems where the data is obtained directly in the frequency domain and there is a cost associated with collecting additional data.

In Chapter 4, we developed a hybrid method for synthesizing a shallow water acoustic field. Although the technique was developed for the fluid case only, it is also possible to develop a similar technique for the elastic case in which shear is supported in the underlying ocean bottom. In this case, the Green's function is still decomposed into the sum of a modal and a continuum portion, however the poles and residues of the modal portion are more difficult to determine. One means for implementing the decomposition algorithm might be based on applying a root finding algorithm to the elastic Green's function which is computed using the global matrix method of SAFARI[3]. The investigation of the hybrid method in this more general context is suggested as future work.

475

As an additional extension of the ideas presented in both Chapters 4 and 5 of this thesis, we suggest that a dual hybrid method for shallow water acoustic inversion be developed. The hybrid inversion method could consist of determining the modal and continuum portions of the field, $p_T(r)$ and $p_C(r)$, separately. The advantage is that if $p_T(r)$ can be determined accurately, it can be inverted analytically to obtain $g_T(k_r)$. The remaining portion of the field, $p_C(r)$ can be inverted numerically to obtain $g_C(k_r)$. Inverting the field in this way may eliminate some of the windowing problems associated with computing the numerical transform of the total field. The method is the dual method for the synthesis procedure discussed in Chapter 4 – both trade off the difficulty in determining one quantity with the difficulty of accurately computing the numerical transform of another quantity. The hybrid synthesis method was simplified by recognizing that the poles and residues of $g_T(k_r)$ and $g(k_r)$ are identical. The dual inversion method can be simplified by recognizing that $p_T(r)$ and $p(r)$ are nearly identical for large r. As was discussed in Chapter 2, it is possible to write a parametric description for $p_T(r)$ based on a modal sum. Thus, if the parameters can be determined using only the far-field data, they suffice to describe $p_T(r)$ at all ranges. The determination of the parameters may be simplified by exploiting the asymptotic form of the modal sum and its relationship to a sum of complex exponentials.

In Chapter 5, we suggested that the residual phase of a shallow water acoustic field is useful in several applications including forward modelling and extraction of range dependent waveguide features. The detailed investigation of these applications is suggested as future research. In this chapter, we also developed the theory of invariant zeros of the Green's function and the relationship of invariant zeros to points of infinite sensitivity. We pointed out that by changing the experimental configuration, it is possible to eliminate the points of infinite sensitivity. On the other hand, exploiting the presence of invariant zeros may be prove to useful. For example, observing an invariant zero in the Green's function obtained from experimental data provides a confirmation of the integrity of the data. Incorporating the location of invariant zeros as a priori knowledge in an inversion scheme might also be useful. In addition,

the investigation of invariant zeros in other waveguide problems, such as the borehole problem, is suggested as future work. This investigation could lead to certain preferred experimental configurations such as an off-axis hydrophone array for acoustic probing within a borehole.

In Chapter 6, we presented numerical examples of the reconstruction of acoustic fields. The quality of the reconstruction obtained even from experimentally collected fields suggests that the real-part/imaginary-part sufficiency condition for an outgoing field is quite robust. In fact, if both components of an experimental field are recorded, the reconstruction method can provide the basis for assessing the quality and integrity of the data collected. The technique may also form the basis for measuring the scattering properties of an inhomogeneous medium in which the field has both an incoming and an outgoing component. In addition, although we have explored outgoing acoustic fields only, the real-part/imaginary-part sufficiency condition may apply to other outgoing fields. The investigation and application of this property in other areas including seismics, optics and electromagnetics is suggested as future research.

Bibliography

[1] K. Aki and P.G. Richards. *Quantitative Seismology Theory and Methods.* W.H. Freeman and Co., San Francisco, 1980.

[2] Alan V. Oppenheim and Ronald W. Schafer. *Digital Signal Processing.* Prentice-Hall, Englewood Cliffs, NJ, 1975.

[3] Henrik Schmidt and Finn B. Jensen. A full wave solution for propagation in multilayered viscoelastic media with application to Gaussian beam reflection at fluid-solid interfaces. *J. Acoust. Soc. Am.,* 77(3):813–825, Mar. 1985.

DISTRIBUTION LIST

	DODAAD Code	
Director **Defense Advanced Research Project Agency** 1400 Wilson Boulevard Arlington, Virginia 22209 Attn: Program Management	HX1241	(1)
Head Mathematical Sciences Division **Office of Naval Research** 800 North Quincy Street Arlington, Virginia 22217	N00014	(1)
Administrative Contracting Officer E19-628 **Massachusetts Institute of Technology** **Cambridge, Massachusetts 02139**	N66017	(1)
Director **Naval Research Laboratory** Attn: Code 2627 **Washington, D.C. 20375**	N00173	(6)
Defense Technical Information Center Bldg 5, Cameron Station Alexandria, Virginia 22314	S47031	(12)
Dr. Judith Daly **DARPA / TTO** 1400 Wilson Boulevard Arlington, Virginia 22209		(1)